Advances in Experimental Medicine and Biology 923

Qingming Luo
Lin Z. Li
David K. Harrison
Hua Shi
Duane F. Bruley *Editors*

Oxygen Transport to Tissue XXXVIII

Springer

Advances in Experimental Medicine and Biology

Volume 923

Editor-in Chief for ISOTT Oxygen Transport to Tissue Proceedings:
DUANE F. BRULEY, Synthesizer, Inc., Ellicott City, MD, USA

Editorial Board:

IRUN R. COHEN, *The Weizmann Institute of Science, Rehovot, Israel*
ABEL LAJTHA, *N.S. Kline Institute for Psychiatric Research, Orangeburg, NY, USA*
JOHN D. LAMBRIS, *University of Pennsylvania, Philadelphia, PA, USA*
RODOLFO PAOLETTI, *University of Milan, Milan, Italy*

More information about this series at http://www.springer.com/series/5584

Qingming Luo • Lin Z. Li • David K. Harrison
Hua Shi • Duane F. Bruley
Editors

Oxygen Transport to Tissue XXXVIII

Springer

Editors
Qingming Luo
Britton Chance Center for Biomedical Photonics
Wuhan National Laboratory for Optoelectronics
Huazhong University of Science and Technology
Wuhan, China

David K. Harrison
Microvascular Measurements
St. Lorenzen, Italy

Duane F. Bruley
ISOTT Historian, Ellicott City, MD, USA
Synthesizer, Inc., Ellicott City, MD, USA

Lin Z. Li
Molecular Imaging Laboratory
Department of Radiology
Britton Chance Laboratory of Redox Imaging, Johnson Research Foundation
Department of Biochemistry and Biophysics
Perelman School of Medicine
University of Pennsylvania
Philadelphia, PA, USA

Hua Shi
Britton Chance Center for Biomedical Photonics
Wuhan National Laboratory for Optoelectronics
Huazhong University of Science and Technology
Wuhan, China

ISSN 0065-2598 ISSN 2214-8019 (electronic)
Advances in Experimental Medicine and Biology
ISBN 978-3-319-38808-3 ISBN 978-3-319-38810-6 (eBook)
DOI 10.1007/978-3-319-38810-6

Library of Congress Control Number: 2016949471

© Springer International Publishing Switzerland 2016
Chapters 24, 26 and 33 are licensed under the terms of the Creative Commons Attribution 4.0 International License (http://creativecommons.org/licenses/by/4.0/). For further details see license information in the chapters.
This work is subject to copyright. All rights are reserved by the Publisher, whether the whole or part of the material is concerned, specifically the rights of translation, reprinting, reuse of illustrations, recitation, broadcasting, reproduction on microfilms or in any other physical way, and transmission or information storage and retrieval, electronic adaptation, computer software, or by similar or dissimilar methodology now known or hereafter developed.
The use of general descriptive names, registered names, trademarks, service marks, etc. in this publication does not imply, even in the absence of a specific statement, that such names are exempt from the relevant protective laws and regulations and therefore free for general use.
The publisher, the authors and the editors are safe to assume that the advice and information in this book are believed to be true and accurate at the date of publication. Neither the publisher nor the authors or the editors give a warranty, express or implied, with respect to the material contained herein or for any errors or omissions that may have been made.

Printed on acid-free paper

This Springer imprint is published by Springer Nature
The registered company is Springer International Publishing AG Switzerland

The 43rd ISOTT Conference Presidents,
Qingming Luo and Lin Z. Li, would like to dedicate this volume
to the memory of Britton Chance.

Brit at Britton Chance Center for Biomedical Photonics, Wuhan National Laboratory for Optoelectronics, Huazhong University of Science and Technology, Wuhan, China, in November 2007

In Memory of Professor Britton Chance

During the early morning of November 16th, 2010, Eastern Standard Time in the United States, Professor Britton Chance passed away at the age of 97 in Philadelphia. I was devastated and couldn't hold back my tears when I heard the news. The scientific community lost a great man; we lost a beloved mentor and friend, and spiritual leader. B.C.'s life was a great life, a legendary life and a brilliant, beautiful life.

I had known B.C. for 16 years. Looking back, there are many fond memories. In June 1995, I was fortunate enough to be one of his students. When I first arrived in Philadelphia, I lived in his house. I woke up every morning to the "tick-tock, tick-tock" sound in one room. It was from his ham radio transmitting Morse codes. It turned out that B.C. really loved amateur radio, often using a traditional transceiver to communicate with his friends.

B.C.'s laboratory at the University of Pennsylvania was situated next to the library of the Johnson Research Foundation, said upon his special request. This way the library could be used at any time for academic exchange. The laboratory is a big hall and B.C.'s office was in one of its corners. With a row of cabinets behind him filled with all kinds of reference materials and notes of scientific research, he sat on a high seat, a good vantage point with a view of everyone's daily activities.

B.C. paid great attention to scientific experiments. We were encouraged to make our own instrument and equipment; minor mechanical parts were often designed and made by ourselves. When in the lab, B.C. would drop in at any time to check on our work and give us feedback. We were pressured but motivated, and worked hard so that we would have something new to report to him each day. If you had a good idea, you could work on it, as long as you had already completed the research assignments. As a result, I was able to design and put together a NIR functional brain imaging system. After the system was completed and produced results, B.C. was very happy. He would often bring people in for a visit, a discussion, or to collaborate on experiments so that the system could be put to greater and more comprehensive performance testing. Looking back, I now realize that this may have been his special way of training us. Now, when I train my own students, if the work is of highly innovative nature, I take them on "study tours" so that they will get additional feedback and comments.

B.C. also paid great attention to academic exchanges. We each had to do a weekly presentation summarizing our own project. In addition to the review by B.C. himself, experts in the field were invited to review and comment on our work. The group meeting was lively and the brainstorming most exciting. I enjoyed every minute of it and felt a renewed commitment each time. B.C.'s laboratory is one of the most important international centers for biomedical photonics research. Every so often we got a chance to hear from the most prominent experts in the field, and we were able to talk with them in person. The reason I decided to return to China to build up the new field of biomedical photonics was that I had been exposed to a lot of lectures given by "the masters." These lectures made me realize that this was an important field that China had yet to catch up with. And I felt a responsibility and obligation to contribute my bit.

Working hard and enjoying life were two of B.C.'s most prominent characteristics. At the time, he was over 80 years old, but he came to the lab at 7 am and did not leave until 8 pm. Legend has it that he kept a "crazier" schedule during his younger years, and very few people working with him stayed for more than 3 years. I was lucky that I was strong physically, but could barely "keep pace" with him. For me, the biggest advantage was that I could always find him for a question. And no matter what we were asking, he would always offer amazing suggestions. He had a whole lot of GREAT ideas. When on business trips, we had to send daily reports to him by fax, and each time we would receive his reply. He led a simple life and dressed casually, but paid great attention to his diet and nutrition, and even more to sports. He would return to his New Jersey or Florida beach home on weekends to enjoy the fun of sailing. He was an Olympic gold medalist in the sport of sailing, and had a special attachment for both boat and sea. I ventured out with him during one of his sailings, which was thrilling and breathtaking. While at sea, you realize the importance of lighthouse. B.C. is a perpetual beacon to my heart, forever illuminating my way forward.

When I decided to return home for a new start and asked for his opinion, he said he was proud of me. He said China needed me, and that I would get his full support. He kept his promise.

I returned to China at the end of February 1997. We started from scratch, carving out the way to success. At the beginning of our venture, we selected six young teachers and graduate students and sent them to B.C.'s laboratory. Four of them have become key members of our research center. B.C. suggested that we host an international conference in China in the field to promote its development. Now the International Conference on Photonics and Imaging in Biology and Medicine we initiated and organized has become the largest conference series of its kind in the Asia-Pacific region. B.C. attended almost all of our conferences. Because of his appeal, several well-known experts in the field have also come to the conference. Under his influence, many of his former students have joined in the collaborative research with us. These have greatly promoted the development of our center. Since 1999, B.C. visited our laboratory in Wuhan many times, sometimes a week, sometimes more than a month, providing guidance and extending cooperation. As I recall, the happiest thing for B.C. was to discuss scientific issues with his students.

B.C. had a special and personal connection to China. In the 1940s in Cambridge, he and Prof. Zou Chenglu, an academician of the Chinese Academy of Sciences, were classmates; in the 1950s in Philadelphia, Prof. Chia-Chih Yang, who later became one of the "Two Bombs and One Satellite" "Meritorious Scientists" and the academician of Chinese Academy of Sciences, was a postdoctoral fellow under his supervision; in the 1980s, also in Philadelphia, the former Executive Vice President of Beijing Medical University, Prof. Cheng Boji, was a visiting researcher in his lab. In the 1990s, B.C. had many Chinese students, including me. On his 90th birthday, we presented him with a plaque, which says "Favorite Teacher with Students around the World (Tao2 Li3 Tian1 Xia4)" to express gratitude from all his Chinese students. In 2008, the Chinese government awarded B.C. the "Friendship Award"; Premier Wen Jiabao cordially met with him in the Great Hall of the People in Beijing. In 2009, B.C. won the "China International Science and Technology Cooperation Award," and it was well deserved. In April 2009, B.C. was awarded an honorary doctorate degree from Huazhong University of Science and Technology; this turned out to be his last trip to Wuhan.

In April 2010, I paid a visit to Prof Chance's home in Tainan. Originally he planned to visit Mainland China in September, but could not make it because of visa problem. In early September, one of my colleagues visited him in his Philadelphia home, while he still kept a regular schedule in his lab. In early November, we held the fourth meeting of the International Advisory Board for our Britton Chance Center in Wuhan, and his colleagues from the University of Pennsylvania brought the good news that he was gradually recovering his health. We were happily planning for his visit the following spring and never expected the sad news of his passing, which came as an unbearable shock.

Recalling the past, I was sleepless. Even though B.C. is gone, his spirit will stay with us forever. Under the guidance of his spirit, we at the Britton Chance Center for Biomedical Photonics will continue on, to scale the heights of science, to overcome difficulties, to exert extra effort, to pursue excellence, and to honor the name of "Britton Chance."

B.C. will always live in our hearts.

Wuhan, China Qingming Luo, Ph.D.

Obituary

Grieving Message for Dr. Masaji Mochizuki

Dedication by Dr. Tomiyasu Koyama

Curriculum vitae:

1922.3.3:	Born in Shizuoka prefecture, Japan
1945.9:	Graduated from School of Medicine, Hokkaido Imperial University
1945.12:	Research Associate, School of Medicine and Microwave Research Institute, Hokkaido Imperial University
1946.3:	Hokkaido University, Research Associate, Research Institute of Applied Electronics, Hokkaido University (by the rule change of the Japanese education system)
1952.4:	Associate Professor, Hokkaido University
1953.8:	Guest Researcher, Göttingen University, West Germany
1958.10:	Professor, Hokkaido University, Research Institute of Applied Electronics, Hokkaido University

1961.3:	Guest Researcher, Department of Medical Physiology, University of Pennsylvania, USA
1970.4:	Director of Research Institute of Applied Electronics, Hokkaido University
1970.4:	University Senate, Hokkaido University
1973.11:	Professor, School of Medicine, Yamagata University
1979.4:	Dean, School of Medicine. Yamagata University
1979.4:	University Senate, Yamagata University
1986.4:	President for the 63rd Conference of Japanese Physiological Society
1987.3:	Retired from the position Dean of the School of Medicine, Yamagata University
1987.4:	Professor emeritus, Yamagata University
1987.4:	Head of the Research Center of the Respiratory Function in Senescent Patients, Keijinnkai Nishimaruyama Byouin Hospital
1987.8:	President of the 1987 meeting of ISOTT in Sapporo
1995.4:	Honorable member of Japanese Society for Physiology
1996.11:	Honored with the order of Sacred Treasure
2014.10.24:	Dr. Mochizuki died at the age of 92 years

Dr. Mochizuki, a very dedicated scientist, repeated the measurements of reaction time of oxygenation and deoxygenation in erythrocytes and analyzed detailed molecular level mechanisms, theoretically. He concluded that the process could be understood precisely only when the diffusion gap was considered in the calculations. In the analysis, he determined that oxygen can diffuse through molecular pores having a diameter of 4.5 Å with transfer coefficients of O_2, CO_2, and CO being equally 2.5×10^{-6} cm $\cdot$ s^{-1} $\cdot$ torr^{-1} and a permeability of $\lambda / \sqrt{2mKT}$. Further, he succeeded in describing O_2, CO_2, and HCO_3^- exchange dynamics in the lung in senescent patients and in chicken eggs.

As an established researcher, Dr. Mochizuki spent 35 years working with O_2, CO_2, and HCO_3^- diffusions. During the long period of his research, he had the good fortune to meet and discuss the diffusing molecular processes with Drs. F.J.W. Roughton, H. Bartels, R.E. Foster, I.S. Longmuir, and D.F. Bruley. He wished to express his cordial thanks to them for their valuable input and encouragements. Dr. Mochizuki and his wife attended almost every ISOTT meeting from the very first meeting in Clemson/Charleston, SC, USA, in 1973 until his illness prevented them from doing so.

Preface

The 43rd Annual Meeting of the International Society on Oxygen Transport to Tissue (ISOTT 2015), hosted by Britton Chance Center for Biomedical Photonics (BC CBMP), Wuhan National Laboratory for Optoelectronics (WNLO), Huazhong University of Science and Technology (HUST), was held in Wuhan, China, on July 11–16th, 2015. This volume contains the papers submitted, peer-reviewed (at least by two reviewers), and accepted from presentations at that meeting.

During the 43 years of ISOTT history, this was the first conference ever held in China. We have gone through an 8-year journey to this milestone. As Dr. Duane Bruley (ISOTT historian) discussed with Dr. Li in 2007 about organizing of an ISOTT conference in China, this proposal immediately gained strong support from Dr. Britton Chance. Brit then wrote to Dr. Luo in HUST who was a former postdoc fellow in the Chance lab in the 1990s and now an established senior research leader in China. For the sake of Brit, our beloved mentor, Dr. Luo kindly accepted the invitation for a couple of plenary lectures in ISOTT and started to attend and send participants to ISOTT since 2012. After a few years of planning and development and with strong support from both local HUST and ISOTT communities, we organized the 2015 meeting successfully in Wuhan, finally fulfilling our promises to Brit and Duane.

The ISOTT 2015 conference brought together 109 participants (33 from Mainland China and 76 from other regions and countries) in a unique cross-disciplinary forum for discussions on a broad range of topics related to oxygen transport and metabolism in health and disease. In total there were 103 presentations (4 keynote and 22 invited lectures, 30 oral presentations, and 47 poster presentations). The meeting featured "Britton Chance Memorial" sessions with a number of diversified and interesting research presentations and an invited talk by Duane entitled "ISOTT from the beginning: a tribute to our deceased members (icons)," reflecting on the ISOTT's long history of 43 years and people who have made major contributions to the society especially Brit. In total 16 meeting sessions covered various research topics including Multi-Modal Imaging/Spectroscopy and Instrumentation; Cancer Metabolism; Cellular Hypoxia and Mitochondrial Function; Brain Oxygenation and Function; Other Organ Function and Metabolism;

Oxygen Transport in Sports, Diseases and Clinical Care; Acupuncture, Meridians, and Primo Vascular System; and EPR, MRS and MRI. Extensive discussion time was allocated to each oral presentation to enhance and facilitate full scientific interaction. Each poster presenter was given 2 min to highlight orally the key points in the posters to the general audience. Interested participants were also invited to visit Wuhan National Laboratory for Optoelectronics and Britton Chance Center for Biomedical Photonics.

In addition to the academic programs, many participants expressed their satisfaction with and enjoyment of the social events and the hospitality of local hosts and the nice environment of the conference site PUYU hotel. The social events included the welcome reception hosted in the PUYU hotel, the farm food dinner in a restaurant nearby the East Lake served with the unique Wuhan style food, the Yangtze River cruise enjoying a spectacular night views of the city, and the exercise program of Taiji Walk and Ba Duan Jin instructed in the mornings throughout the conference.

We would like to acknowledge earnestly the great work done by our conference coordinators Dr. Hua Shi and Ms. Weiwei Dong plus a number of staff members and volunteers that have made the conference smooth and successful. Deep appreciation also goes to the Members of Local Organizing Committee, Scientific Committee, ISOTT Executive Board, and all the session chairs, speakers, and presenters for their participation, support, advice, and help. Together we have made the first ISOTT conference in China an outstanding and memorable experience. Great thanks also go to all the editors and reviewers that make the publication of this ISOTT 2015 proceeding possible.

Wuhan, China — Qingming Luo
Philadelphia, PA, USA — Lin Z. Li

Acknowledgements

As organizers of the 2015 Meeting of the International Society on Oxygen Transport to Tissue, held on July 11–16, 2015, in Wuhan, China, we would like to gratefully acknowledge the support of our sponsors.

www.hust.edu.cn

www.wnlo.cn

bmp.hust.edu.cn

www.hamamatsu.com.cn

Lin Z. Li and several other conference participants would like to acknowledge the support and fund from the 111 Project of China (B07038). “In Memory of Professor Britton Chance” was translated from Chinese to English by Ms. Ling Mao in Philadelphia, USA.

Panel of Reviewers

Reviewer	Affiliation
Gemma Bale	University College London, UK
Duane F. Bruley	Synthesizer, Inc. Ellicott City, USA
David Busch	University of Pennsylvania, USA
Alexander Caicedo	Katholicke Universitaet Leuven, Belgium
Chris Cooper	University of Essex, Colchester, UK
Yong Deng	Huazhong University of Science and Technology, China
Paula Dore-Duffy	Wayne State University, USE
Clare Elwell	University College London, UK
Boris Epel	University of Chicago, USA
Ann Flood	EPR Center at Dartmouth, Hanover, USA
Howard Halpern	University of Chicago, USA
David Harrison	Microvascular Measurements, St Lorenzen, Italy
Huagang Hou	EPR Center at Dartmouth, Hanover, USA
Kyung Kang	University of Louisville, USA
Peter Keipert	Keipert Corp. Consulting, San Diego, USA
Ryatoro Kime	Tokyo Medical University, Japan
Joseph LaManna	Case Western Reserve University, Cleveland, USA
Terence Leung	University College London, UK
Lin Z. Li	University of Pennsylvania, USA
Pengcheng Li	Huazhong University of Science and Technology, China
Qingming Luo	Huazhong University of Science and Technology, China
Avraham Mayevsky	Bar Ilan University, Israel
Edwin Nemoto	University of New Mexico, USA
Shoko Nioka	Chen Kung University, Taiwan
George Perdrizet	University of California, San Diego, USA
Dominik Pesta	University of Düsseldorf, Germany
Zimei Rong	University of Nottingham Ningbo, China
Kaoru Sakatani	Nihon University School of Medicine, Japan
Brian Salzberg	University of Pennsylvania, USA
Jiangang Shen	University of Hong Kong, China

Hua Shi	Huazhong University of Science and Technology, China
Kuangyu Shi	Technical University Munich, Germany
Justin Skowno	The Children's Hospital at Westmead, Australia
Nannan Sun	Huazhong University of Science and Technology, China
Kwang-Sup Soh	Seoul National University, Korea
Harold Swartz	EPR Center at Dartmouth, Hanover, USA
IliasTachtsidis	University College London, UK
Shun Takagi	Waseda University, Japan
Eiji Takahashi	Saga University, Japan
Oliver Thews	University of Halle, Germany
Valery Tuchin	Saratov State University, Russia
Sabine Van Huffel	Katholicke Universitaet Leuven, Belgium
Peter Vaupel	University Medical Centre, Mainz, Germany
Takashi Watanabe	Hamamatsu Photonics K.K., Japan
Martin Wolf	University of Zurich, Switzerland
Ursula Wolf	University of Bern, Switzerland
Christopher Wolff	St. Mary's College and Barts, London, UK
He N. Xu	University of Pennsylvania, USA
Kui Xu	Case Western Reserve University, Cleveland, USA
Xiaoquan Yang	Huazhong University of Science and Technology, China
Shaoqun Zeng	Huazhong University of Science and Technology, China
Zhihong Zhang	Huazhong University of Science and Technology, China
Dan Zhu	Huazhong University of Science and Technology, China
Technical Reviewer	
Laraine Visser-Isles	Rotterdam, The Netherlands
Eileen Harrison	St. Lorenzen, Italy

Group Photos

Local Organizing Committee

Qingming Luo
Lin Z. Li
Hua Shi
Weiwei Dong
Xiaoying Hu
Pengcheng Li
Zhihong Zhang
Hui Gong
Shaoqun Zeng
Dan Zhu
Yong Deng
Xiaoquan Yang

Scientific Committee

Qingming Luo, Huazhong University of Science and Technology, China
Lin Z. Li, University of Pennsylvania, USA
Kyung A. Kang, University of Louisville, USA
Joseph C. Lamanna, Case Western Reserve University, USA
Avraham Mayevsky, Bar Ilan University, Israel
Shoko Nioka, University of Pennsylvania, USA
Jiangang Shen, Hong Kong University, Hong Kong, China
Harold M. Swartz, Dartmouth College, USA
Eiji Takahashi, Saga University, Japan
Terence Leung, University College London, UK
Peter Vaupel, University of Mainz Medical Center, Germany
Lihong V. Wang, Washington University in St. Louis, USA

ISOTT Officers and Executive Committee

Presidents
Name: Qingming Luo
Country: China
Telephone: (+86) 27-8779-2033
Fax: (+86) 27-8779-2034
Email: qluo@mail.hust.edu.cn

Name: Lin Z. Li
Country: USA
Telephone: (+1) 215-898-1805
Fax: (+1) 215-573-2113
Email: linli@mail.med.upenn.edu

Past President
Name: Clare Elwell
Country: UK
Telephone: (+44) 20-7679-0270
Fax: (+44) 20-7679-0255
Email: c.elwell@ucl.ac.uk

President-Elect
Name: Howard Halpern
Country: USA
Telephone: (+1) 773-702-6871
Fax: (+1) 773-702-5940
Email: h-halpern@uchicago.edu

Secretary
Name: Oliver Thews
Country: Germany
Telephone: (+49) 345-557-4048
Fax: (+49) 345-557-4019
Email: oliver.thews@medizin.uni-halle.de

Treasurer
Name: Peter Keipert
Country: USA
Phone: (+1) 858-699-4789
Fax: (+1) 858-792-7489
Email: peterkeipert@gmail.com

Chairman, **Knisely Award Committee**
Name: Duane F. Bruley
Country: USA
Telephone: (+1) 410-313-9939
Fax: (+1) 410-313-9939
Email: bruley33@verizon.net

Executive Committee Members
Alexander Caicedo Dorado (Belgium)
Chris Cooper (UK)
Ann Flood (USA)
Malou Friedrich-Perrson (Sweden)
Jerry D. Glickson (USA)
Terence Leung (UK)
Frederik Palm (Sweden)
Eiji Takahashi (Japan)

ISOTT Award Winners

The Melvin H. Knisely Award

The Melvin H. Knisely Award was established in 1983 to honor Dr. Knisely's accomplishments in the field of the transport of oxygen and other metabolites and anabolites in the human body. Over the years, he has inspired many young investigators and this award is to honor his enthusiasm for assisting and encouraging young scientists and engineers in various disciplines. The award is to acknowledge outstanding young investigators. This award was first presented during the banquet of the 1983 annual conference of ISOTT in Ruston, Louisiana. The award includes a Melvin H. Knisely plaque and a cash prize.

Melvin H. Knisely Award Recipients

1983 Antal G. Hudetz (Hungary)
1984 Andras Eke (Hungary)
1985 Nathan A. Bush (USA)
1986 Karlfried Groebe (Germany)
1987 Isumi Shibuya (Japan)
1988 Kyung A. Kang (Korea/USA)
1989 Sanja Batra (Canada)
1990 Stephen J. Cringle (Australia)
1991 Paul Okunieff (USA)
1992 Hans Degens (The Netherlands)
1993 David A. Benaron (USA)
1994 Koen van Rossem (Belgium)
1995 Clare E. Elwell (UK)
1996 Sergei A. Vinogradov (USA)

1997 Chris Cooper (UK)
1998 Martin Wolf (Switzerland)
1999 Huiping Wu (USA)
2000 Valentina Quaresima (Italy)
2001 Fahmeed Hyder (Bangladesh)
2002 Geofrey De Visscher (Belgium)
2003 Mohammad Nadeem Khan (USA)
2004 Fredrick Palm (Sweden)
2005 Nicholas Lintell (Australia)
2006 –
2007 Ilias Tachtsidis (UK)
2008 Kazuto Masamoto (Japan)
2009 Rossana Occhipinti (USA)
2010 Sebatiano Cicco (Italy)
2011 Mei Zhang (USA)
2012 Takahiro Igarashi (Japan)
2013 Malou Friederich-Persson (Sweden)
2014 David Highton (UK)
2015 Alexander Caicedo Dorado (Belgium)

The Dietrich W. Lübbers Award

The Dietrich W. Lübbers Award was established in honor of Professor Lübbers's long-standing commitment, interest, and contributions to the problems of oxygen transport to tissue and to the society. This award was first presented in 1994 during the annual conference of ISOTT in Istanbul, Turkey.

Dietrich W. Lübbers Award Recipients

1994 Michael Dubina (Russia)
1995 Philip E. James (UK/USA)
1996 Resit Demit (Germany)
1997 Juan Carlos Chavez (Peru)
1998 Nathan A. Davis (UK)
1999 Paola Pichiule (USA)
2000 Ian Balcer (USA)
2001 Theresa M. Busch (USA)
2002 Link K. Korah (USA)
2003 James J. Lee (USA)
2004 Richard Olson (Sweden)
2005 Charlotte Ives (UK)
2006 Bin Hong (China/USA)
2007 Helga Blockx (Belgium)

2008 Joke Vanderhaegen (Belgium)
2009 Matthew Bell (UK)
2010 Alexander Caicedo Dorado (Belgium)
2011 Malou Friedrich (Sweden)
2012 Maria Papademetriou (UK)
2013 Nannan Sun (China/USA)
2014 Felix Scholkmann (Switzerland)
2015 Shun Takagi (Japan)

The Britton Chance Award

The Britton Chance Award was established in honor of Professor Chance's long-standing commitment, interest, and contributions to the science and engineering aspects of oxygen transport to tissue and to the society. This award was first presented in 2004 during the annual conference of ISOTT in Bari, Italy.

Britton Chance Award Recipients

2004 Derek Brown (Switzerland)
2005 James Lee (USA)
2006 Hanzhu Jin (China/USA)
2007 Eric Mellon (USA)
2008 Jianting Wang (USA)
2009 Jessica Spires (USA)
2010 Ivo Trajkovic (Switzerland)
2011 Alexander Caicedo Dorado (Belgium)
2012 Felix Scholkmann (Switzerland)
2013 Tharindi Hapuarachchi (UK)
2014 Anne Riemann (Germany)
2015 Wenhao Xie (China)

The Duane F. Bruley Travel Awards

The Duane F. Bruley Travel Awards were established in 2003 and first presented by ISOTT at the 2004 annual conference in Bari, Italy. This award was created to provide travel funds for student researchers in all aspects of areas of oxygen transport to tissue. The awards signify Dr. Bruley's interest in encouraging and supporting young researchers to maintain the image and quality of research associated with the society. As a cofounder of ISOTT in 1973, Dr. Bruley emphasizes cross-disciplinary research among basic scientists, engineers, medical scientists, and clinicians. His pioneering work constructing mathematical models for oxygen and other anabolite/metabolite transport in the microcirculation, employing computer solutions, was the

first to consider system nonlinearities and time dependence, including multidimensional diffusion, convection, and reaction kinetics. It is hoped that receiving the Duane F. Bruley Travel Award will inspire students to excel in their research and will assist in securing future leadership for ISOTT.

The Duane F. Bruley Travel Award Recipients

2004 Helga Blocks (Belgium), Jennifer Caddick (UK), Charlotte Ives (UK), Nicholas Lintell (Australia), Leonardo Mottola (Italy), Samin Rezania (USA/Iran), Ilias Tachtsidis (UK), Liang Tang (USA/China), Iyichi Sonoro (Japan), Antonio Franco (Italy)

2005 Robert Bradley (UK), Harald Oey (Australia), Kathy Hsieh (Australia), Jan Shah (Australia)

2006 Ben Gooch (UK), Ulf Jensen (Germany), Smruta Koppaka (USA), Daya Singh (UK), Martin Tisdall (UK), Bin Wong (USA), Kui Xu (USA)

2007 Dominique De Smet (Belgium), Thomas Ingram (UK), Nicola Lai (USA), Andrew Pinder (UK), Joke Vanderhaegen (Belgium)

2008 Sebastiano Chicco (Italy)

2009 Lei Gao (UK), Jianting Wang (USA), Obinna Ndubuizu (USA), Joke Vanderhaegen (Belgium)

2010 Zareen Bashir (UK), Tracy Moroz (UK), Mark Muthalib (Australia), Catalina Meßmer (USA), Takashi Eriguchi (Japan), Yoshihiro Murata (Japan), Jack Honeysett (UK), Martin Biallas (Switzerland)

2011 Catherine Hesford (UK), Luke S. Holdsworth (UK), Andreas Metz (Switzerland), Maria D. Papademetriou (UK), Patrik Persson (Sweden), Felix Scholkmann (Switzerland), Kouichi Yoshihara (Japan)

2012 Allann Al-Armaghany (UK), Malou Friederich-Persson (Sweden), Tharindi Hapuarachchi (UK), Benjamin Jones (UK), Rebecca Re (Italy), Yuta Sekiguchi (Japan), Ebba Sivertsson (Sweden), Andre´ Steimers (Germany)

2013 Allann Al-Armaghany (UK), Gemma Bale (UK), Alexander Caicedo Dorado (Belgium), Luke Dunne (UK)

2014 Geraldine De Preter (Belgium), Benjamin Jones (UK), Stefan Kleiser (Switzerland), Nassimsadat Nasseri (Switzerland), Marie-Aline Neveu (Belgium), Shinsuke Nirengi (Japan), Takuya Osawa (Japan)

2015 Nannan Sun (China), Gemma Bale (UK), Chenyang Gao (China), Guennadi Saiko (Canada), Kuangyu Shi (Germany), Phong Phan (UK), Chae Jeong Lim (Korea)

Kovach Lecture

The Kovach Lecture is presented periodically to honor a career dedicated to oxygenation research. Arisztid Kovach was a world-renowned cardiovascular physiologist and one of the early leaders of ISOTT. This lecture is dedicated to his remarkable scientific and teaching career.

Kovach Lecture Recipients

2011 John Severinghaus
2012 Peter Vaupel
2013 No Recipient
2014 Edwin Nemoto
2015 No Recipient

Contents

Part III Brain Oxygenation and Function

The original version of this book was revised. An erratum to this book can be found at DOI 10.1007/978-3-319-38810-6_59

Chapter 1
ISOTT from the Beginning: A Tribute to Our Deceased Members (Icons)

Duane. F. Bruley and E.E. Thiessen

Abstract ISOTT was founded by Drs. Duane F. Bruley and Haim I. Bicher in the state of South Carolina, USA in 1973. The symposium was jointly held at Clemson University (Clemson, SC, USA) and the Medical College of South Carolina (Charleston, SC, USA), which are geographically located 260 miles apart. This venue resulted from Dr. Bruley's (Clemson University) wish to have a meeting on Oxygen Transport to Tissue and with it to honor the research collaboration between the two universities and Dr. Melvin H. Knisely's accomplishments on studies regarding "blood sludging" in the microcirculation. Because of the unexpected large response to the symposium, Drs. Bruley and Bicher decided to found an international society at this meeting (ISOTT). The purpose of this paper is to summarize the formalization of ISOTT and to **honor important contributors** to the society who have since passed away. The authors did their best to include a brief overview of our past icons who have excelled in leadership as well as science/engineering, and apologize if someone has been mistakenly left out or if data is inaccurate or incomplete.

1 Introduction

The founding of a formal international society on oxygen transport to tissue (ISOTT) took a tortuous path, similar to many scientific and engineering investigations [1]. The process included the evolution of joint "engineering science and medical science collaborations" with a variety of oxygen-related studies being presented and published through various societies around the world. Most notably the European Society for Microcirculation and the American Society for Microcirculation.

D.F. Bruley (✉)
ISOTT Historian, Ellicott City, USA

Synthesizer, Inc., 2773 Westminster Road, Ellicott City, MD 21043, USA
e-mail: bruley33@verizon.net

E.E. Thiessen
Synthesizer, Inc., 2773 Westminster Road, Ellicott City, MD 21043, USA

© Springer International Publishing Switzerland 2016

Q. Luo et al. (eds.), *Oxygen Transport to Tissue XXXVIII*, Advances in Experimental Medicine and Biology 923, DOI 10.1007/978-3-319-38810-6_1

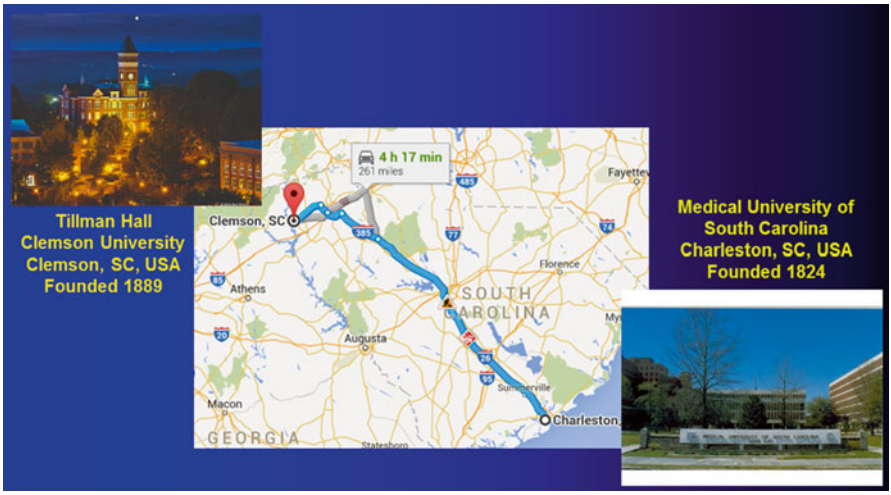

Fig. 1.1 ISOTT Founding Meeting, Clemson/Charleston, SC, USA, 1973

ISOTT was founded by Drs. Duane F. Bruley and Haim I. Bicher in the state of South Carolina, USA in 1973. The symposium was jointly held at Clemson University (Clemson, SC: Mathematical Modelling and Computer Simulation) and the Medical College of South Carolina (Charleston, SC: Experimental PO_2 Measurements and Anticoagulants), which are geographically located 260 miles apart (254 attendees transported between by bus, Fig. 1.1). This venue resulted from Dr. Bruley's wish to have a meeting on Oxygen Transport to Tissue and with it to honor the collaboration between the two universities (the first joint research collaboration between the two institutions) and Dr. Melvin H. Knisely's accomplishments on blood sludging in the microcirculation. The decision to have a joint meeting with the Medical College of SC led Dr. Bruley to invite Dr. Bicher to help with the meeting organization. Because of the unexpected large response, Drs. Bruley and Bicher decided to found an international society at this meeting (ISOTT).

Throughout our history, many engineers, scientists, medical researchers and clinicians have made major contributions in the evolution of ISOTT. However, the purpose of this paper is to honor important contributors to the society who have since passed away. The authors hope to include here all of our past icons who have contributed in science, engineering, and medicine or in major leadership or supporting roles. We apologize if someone has been left out or if important information has been missed. We did not include the investigator if we could not establish their passing. The authors would like to add that all of these individuals had so many achievements in their lifetime that it is impossible to do them justice in a single limited paper.

2 Our Historical Icons

We would like to begin this section with our *first honorary president*, who was appointed by Drs. Bruley and Bicher at the Founding meeting. He was selected because of his many professional accomplishments as a pioneer in the study of the microcirculation. Of course, this icon is **Dr. Melvin H. Knisely** (1904–1975), who served at the University of Chicago, and later as Chairman of Anatomy at the Medical College of South Carolina. Dr. Knisely's most notable contribution was developing the quartz rod crystal technology for illumination and being credited as the first human being to observe the clumping (sludging) of particulate matter in the microcirculation. His research demonstrated this phenomenon in over 100 disease states [2]. Dr. August Krogh nominated Dr. Knisely's work for a Nobel Prize in physiology in 1947, 1948, and 1949. He was later nominated twice in 1951 by Larus Einarson and C. Holten. Failure to receive the award in no way diminishes the significance of his contributions. The rest of his life was spent trying to solve the problem of blood sludging and improve the process of oxygen transport to tissues [3], particularly in the gray matter of the human brain. The society will forever be indebted to his original work. Dr. Knisely was futuristic in that he appreciated the potential of applied mathematics [4] along with wet laboratory studies to aid in the solution of this complex problem. To obtain more accurate studies of oxygen gradients in tissue, he hired Dr. Haim Bicher in 1967 to join our group to develop oxygen microelectrodes (polarography) to make micromeasurements of tissue pO_2. In addition to his scientific career, Dr. Knisely had a wide variety of interests. For example, he was friends with John Steinbeck and together they met with President Roosevelt during World War II to discuss a plan they had devised to dump fake currency into enemy states. In 1983, as president of ISOTT, Dr. Bruley established the Melvin H. Knisely award, the premier award of the society.

Another extremely important member in the development of our society is **Dr. Britton Chance** (1913–2010). His scientific contributions, example, and mentorship are unmatched and have given great credibility to ISOTT [5, 6]. He was the Eldridge Reeves Johnson University Professor Emeritus of Biochemistry and Biophysics, as well as Professor Emeritus of Physical Chemistry and Radiological Physics at the University of Pennsylvania, School of Medicine. Dr. Chance served as the second elected president of ISOTT in 1976 at the Anaheim, CA meeting. Britt was a steadfast supporter of ISOTT efforts and attended almost every meeting, including the founding meeting in 1973. He always sat in the first row and had penetrating questions for almost all of the presenters. Close to his death, I asked him why he never queried me about my zymogen protein C projects. His answer was that he didn't understand what I was doing. Later, after his stroke, while I was in his lab, he asked me if I thought that the infusion of the natural anticoagulant protein C (ZPC) would have prevented his stroke. I answered that I was sure it could have been a benefit. He then asked for copies of my papers, which I provided, but shortly after that, Britt passed away. I have fond memories of the work that we did together [7] and cherish the time that I had to be and work with Britt. Britt was truly a

multi-dimensional achiever and earned an Olympic gold medal (1952) for his sailing skills. Amongst his numerous awards and recognitions, Britt joined the United States National Academy of Sciences in 1952, received the National Medal of Science in 1974, was elected a Foreign Member of the Royal Swedish Academy of Sciences in 1968, and a Foreign Member of the Royal Society (London) in 1981. In 2004, Dr. Bruley, along with others, nominated Dr. Chance for the establishment of the Chance Award, which is now a big part of the society. It is definitely a pleasure to have the opportunity to give this presentation in Wuhan at an institute named in his honor, the "Britton Chance Center for Biomedical Photonics".

Dr. Gerhard Thews (1926–2003) is internationally known for his contributions to oxygen transport to tissue [8, 9]. His many recognitions include the 1961 Wolfgang-Heubner Prize in Berlin, Germany, the 1964 first prize from the Carl-Diem Foundation of the German Sports Federation, the 1969 Adolf Fick Prize in Wurzburg, Germany, and the Great Cross of Merit in 1991. In 1964, Dr. Thews was appointed to the chair of physiology at the University of Mainz, along with the directorship of the Institute of Physiology. He served as chairman of the German Physiological Society and as Dean of the Faculty of Medicine from 1968 to 1969. Among his many honored positions, he served as president of the academy of sciences and literature in Mainz, Germany from 1985 to 1993. After a very active career, he retired in 1994. One of his most important works involved expanding the studies of August Krogh on the Capillary Tissue system to include both the capillary and the tissue. His mathematical models were linear since at that time he had to use analytical techniques to obtain oxygen tension solutions for both the capillary and the tissue. As computers became available and more easily used, nonlinearities were introduced (Bruley Model, 1967) [4]. It is significant that Dr. Gerhard Thews served as the *first elected president* of our society in 1975 at the University of Mainz in Germany.

Dr. Dietrich Lübbers' (1917–2005) research goal was to understand the entire pathway and regulation of oxygen supply from the blood into the mitochondria [10]. In his quest to accurately measure and understand oxygen supply [11], he held numerous patents for photometry, electrochemical sensors, pO_2 and pCO_2 measurements in situ and optical sensors with absorbent and fluorescent optical indicators. For his work he was awarded the Diesel Gold Medal in 1997 at the German Institute for Inventions. He was appointed the Director of the Max Planck Institute for Occupational Physiology in Dortmund in 1968, which was renamed the Max Planck Institute for Systems Physiology to reflect the work he was doing. In 1971, he organized a meeting on oxygen supply at the Max Planck Institute in Dortmund which was well attended. He was a member of the first International Committee of ISOTT, president in 1982 in Dortmund, Germany, and attended almost every meeting until 2000. In 1994, the Dietrich W. Lübbers award was established to honor his long-standing commitment, interest, and contributions to the problems of oxygen supply to tissue and to the society.

Dr. Leland C. Clark, Jr. (1918–2005) received his formal education at Antioch College in Ohio, USA, and his Ph.D. in biochemistry and physiology from University of Rochester in NY, USA. He served as a professor of biochemistry at

Antioch College and became head of the department. He then held a simultaneous appointment at the University of Cincinnati, College of Medicine. In 1958, he moved to the department of surgery at the University of Alabama Medical College. He then became professor of research pediatrics at the Cincinnati Children's Hospital Research Foundation in 1968 and remained there until he retired in 1991. He is best known as the inventor of the Clark Electrode [12] for measuring oxygen in blood and is considered the father of biosensors [13]. He conducted pioneering research on heart-lung machines and was holder of more than 25 patents. Dr. Clark attended and was a member of the International Committee for the founding meeting of ISOTT at Clemson/Charleston in 1973. His contributions to polarography to sense oxygen resulted in great advances in the understanding of oxygen transport in human tissue.

Dr. Manfred Kessler (1934–2013) was trained as a medical doctor and joined Professor Lübbers in Marburg and later followed him to the Max Planck Institute für Arbeitsmedizin in Dortmund (1968), after which he became a chairman at the Institut für Physiologie und Kardiologie in Erlangen, directing interdisciplinary research related to the regulation mechanisms of oxygen supply to tissue. He used multiwire surface electrode (MDO) and tissue micro spectrometry to study the heterogeneity of oxygen supply to tissues. He helped determine that the heterogeneity and redistribution of oxygen pattern indicated the highly regulated tissue supply and the existence of protective mechanisms that prevented tissue damage during oxygen deficiency. From this work, he postulated that oxygen supply is redistributed at the capillary level in critical oxygen supply situations. Also, the reduction of oxygen uptake rate and cell function enable the cells to survive and prevent anoxia for a longer period of time. It was the basis of pathological tissue protection like the "Hibernating Myocardium", well known in cardiac surgery today. Dr. Kessler also did pioneering research for the measurement of oxygen and minimally invasive electrode techniques for other biologically-important substances [14, 15].

Dr. Frans Frederik Jobsis (1929–2006) was born in Jakarta, Indonesia and moved to the Netherlands with his family at age 9 before coming to the United States at 19. He graduated from the University of Maryland and received his Ph.D. from the University of Michigan and then completed several postdoctoral studies in biophysics. Frans began his career in physiology research at the University of Pennsylvania before accepting a position with Duke University Medical Center in 1964. An eminent physiologist, Dr. Jobsis made major contributions to the understanding of muscle contraction and brain metabolism, and was one of the early pioneers in the field of near-infrared light spectrophotometry, allowing the measurement of oxygen levels in tissue and blood [16, 17]. This was a profoundly significant contribution to the advancement of healthcare for the benefit of mankind. He was a recipient of many professional awards, including a Guggenheim Foundation Fellowship and the Semmelweis Award. Dr. Jobsis published extensively throughout his prestigious career and was considered a pioneer in his professional endeavors and all aspects of life.

Dr. Arisztid G. B. Kovách (1920–1996) was well known as the founder and director for over 30 years of the Experimental Research Department in Semmelweis

Medical University, where he created a school of cardiovascular physiological research that has inspired many on the international stage [18]. He was the president of our Society and host of the Annual Meeting in Budapest, Hungary in 1980 [19]. His energy, enthusiasm, and insightful observations encouraged many of us who knew him. The year after his death, Dr. Antal G. Hudetz (ISOTT President, 1997, Milkwaukee, WI, USA) established the Arisztid G. B. Kovách Memorial Lectures to remember his dedication and contribution to ISOTT, science, and education.

Dr. David J. Maguire (1945–2012) was a devoted scientist who established a national and international reputation for his work in fundamental phenomena in the respiration of basal cell carcinomas and the effects of hypo- and hyperthermia on oxygen profiles in tumor spheroids [20, 21]. He was a true leader in our society and served as the president in Brisbane, Australia in 2005. He stood out in any situation and when in the room, his friendly and genuine openness touched everyone present. To each meeting, he brought a spirit of adventure and organized competitive swimming events to enhance the social aspects of ISOTT. All of those who worked or played with David will have fond memories to accompany his legacy in research.

Dr. Ferdinand Kreuzer (1919–2005) served as President of ISOTT in 1984 at the Radboud University in Nijmegen, The Netherlands. His main research interest was the transportation and diffusion of oxygen through blood about which he published extensively [22, 23]. Dr. Kreuzer led a brilliant career as practitioner, researcher, and teacher in various institutions in The Netherlands and the United States, particularly the Radboud University in Nijmegen, where he was appointed professor and head of the department of physiology and served from 1951 to 1985. In his private life, Dr. Kreuzer loved art and produced many paintings, as well as being involved in local history research that led to many publications outside of science.

Dr. Ian Stewart Longmuir (1922–2011) was born and raised in Glasgow, Scotland. He received his bachelor's degree in 1943 and his Master of Arts and Bachelor of Medicine in 1948 all at Cambridge University in Cambridge, England. Steps in his career included house physician at St. Bartholomew, England in 1948 and a junior member of the faculty at the University of Cambridge from 1948 to 1951. He served as principal scientist in Porton, England from 1951 to 1954, and as senior lecturer at the University London from 1956 to 1965. In 1965, he joined North Carolina State University in Raleigh, USA as Professor, where he served until his retirement at 1991. He contributed over 100 articles and papers to professional journals during his career. Some of those papers include his work related to cytochrome P-450 [24] and his histochemical stain technology for determining intracellular oxygen [25]. Among his many contributions to the evolution of ISOTT, Dr. Longmuir served as president of the society in 1985.

Dr. Masaji Mochizuki (1922–2014) served ISOTT throughout his illustrious career, most of it taking place at the Research Institute of Applied Electricity at Hokkaido University in Sapporo, Japan. He organized our first ISOTT meeting in Japan (1987), serving as the president of the society, along with his colleague Dr. Carl Honig as honorary president. As all of Dr. Mochizuki's endeavors, it was a huge success and attracted a large number of new society members, which has continued to grow over the years. He contributed to the society in many areas. However, his

single, greatest contribution closely focused on the interactions between carbon dioxide and oxygen under various conditions in the microcirculation [26, 27]. In addition to his high-level scholarly research, he was also an accomplished painter. He would frequently bring some of his artwork to our meetings and personally presented my wife Suzanne and me with several of his works. Both he and his wife were very active in the society and were involved in the beginning in the scholarship and social functions annually. Dr. Mochizuki and his wife attended almost every meeting from the very first in 1973 until his illness prevented them from doing so.

Dr. René Bourgain (1926–2011) had a broad area of interest in tissue oxygenation. However, one of his unique niches involved studies of the blood proteins involved in coagulation. This is an extremely important area for oxygen transport to the cells in the tissues and only lightly touched on throughout our society. His work included many of the blood factors, but of high interest was the impact of protein C deficiency and the resulting medical pathology associated with this condition. He first alerted me in 1980 to the research that was taking place in Belgium related to protein C and its function in the blood and the possibility of thrombosis associated with deficiencies. Among other work that he contributed to our society was the use of oxygen as a regulator of tissue perfusion [28] and using photo-optics to study blood clotting [29]. On the athletic side, Dr. Bourgain had a passion for the game of tennis and brought his racquet to all the meetings to play with anyone interested. He and I had many wonderful tennis sessions together.

Dr. Carl A. Goresky (1932–1996) was a Professor of Medicine at McGill University, a Career Research Investigator in the Medical Research Council of Canada, and Director of Gastroenterology at the Montreal General Hospital where he practiced medicine for 36 years. He was honored many times by his peers for his contributions to biomedical science as well as the impact he had on Canadian and North American medicine. He was a physician and scientist who actively engaged in research to the final days of his life. As a teacher, he consistently took every opportunity to illustrate that a clinician scientist should bring knowledge from bedside to the bench and back. His greatest achievement in research was in his successful application of rigorous mathematical methods, coupled with carefully designed experiments, to explore fundamental physiological phenomena. His first paper [30] is often considered as one of the main foundation stones for the entire area of whole-organ tracer kinetics. From his time as editor of *Clinical and Investigative Medicine* beginning in 1984 until this death, he significantly raised the scientific standards of the articles via best peer review and put the journal on sound financial basis. He was a prodigious researcher and author, resulting in 140 peer-reviewed publications, 28 chapters in books, and editor on two books. For a lifetime of devoted service to medical science, he was inducted into the Order of Canada as Officer. He was a dedicated ISOTT member attending the majority of meetings while he was alive, including the first meeting [31], where his quiet presence encouraged others.

Dr. Carl R. Honig (1925–1993) received his B.S. in Chemistry from University of Rochester in 1945, and returned to the Rochester school of Medicine and Dentistry in 1957 as Senior Instructor in Physiology and Professor of Physiology in 1967. He also served as acting chair from 1968 to 1969. From 1972, he served as

Visiting Professor of Physiology at the University of Hawaii. His research in the cardiovascular system [32] was well supported by funds from the national heart institute of the US Public Health Service. His book *Modern Cardiovascular Physiology* [33] was well received and suitable for both specialists and generalists, and gave an engineering flavor to the study of the circulation system. Dr. Honig was a dedicated teacher of both undergraduate and graduate medical students and was chosen Teacher of the Year three times as well as awarded the Manuel D. Goldman Prize in 1985. Carl had a great humanitarian side to him and demonstrated his concern when he organized a reunion of the Civilian Public Service (CPS) Unit 115-R, a group of people who had volunteered to be human subjects in physiological experiments designed to test the limits of human body tolerance for high temperature, high altitudes and starvation. He received a Merit Award from the U.S. Public Health Service in 1988. Carl served as honorary president in 1987 at the Sapporo, Japan ISOTT meeting, along with Dr. Masaji Mochizuki (President).

Dr. Johannes Piiper [34, 35] (1924–2012) was a physiologist and a foreign member of the Estonian Academy of Sciences. He graduated from the Faculty of Medicine of the University of Göttingen in 1952 and received his doctorate in medicine in 1954. He continued his training at the University of Buffalo in the early 60s and became a professor at the University of Göttingen in 1966. He was also associated with the Max Planck Institute for Experimental Medicine in Göttigen for many years, serving as the head of the Department of Physiology (1973–1992) and executive director of the institute (1975–1977, 1987–1989). He served as President of ISOTT in 1989, in Göttingen, Germany.

Dr. Berend Oeseburg (1939–2000) was a remarkable figure in medical research in the Netherlands at both facilities where he worked in Nijmegen and Groningen as well as in the Dutch Association for Medical Education (NVMO), where he was a member of the General Board. His research focused on oxygen transport by both the myoglobin and hemoglobin molecules [36, 37]. He had a passion for experimentation and teaching and was active and innovative in the area of examinations. He served as ISOTT President in 2000 in Nijmegen, The Netherlands.

Dr. Eors Dóra (1947(?)–1992) was an accomplished scientist and influential teacher. Throughout his career, he focused purely on science without diversion, and finding out the secrets of physiology and pathology. He spent a large portion of his career at Semmelweis University Medical School with Dr. Kovách, where he was known to be an accomplished scientist, inspirational teacher, and mentor, with an original way of looking at findings [38]. He spent some time at the University of Lund, where he studied isolated blood vessel systems, which he then brought back to Hungary to continue his studies. He also worked with the Cerebral Vascular Research Center in the Department of Neurology at the University of Pennsylvania, where he studied cat brain cortex [39]. Unfortunately, the field of oxygen transport lost a valuable researcher when Dr. Dóra passed away at an early age.

Dr. Mamoru Tamura (1943–2011) was one of the great pioneers in biomedical optics and functional near-infrared spectroscopy, as well as a solid and constant presence in ISOTT. His researched revolved around the use of light as a tool for *in vivo* investigation of human function, especially in the transport and utilization of oxygen in cells, tissues, organs, and whole body [40]. *Chance* brought him to

Dr. Britton Chance's laboratory in 1971 as a post-doc, where their work together ended up as a lifelong influence on Dr. Tamura's research [41]. He was an active member of ISOTT and attended almost every meeting from the third official conference in 1977 (Churchill College, Cambridge, UK) until his death. He served as Honorary President in 2008, Sapporo, Japan.

Dr. Heinz Bartels (d.2000) was a native of Friedrichshaven, Germany and a graduate of the University of Kiel, where he began his research making measurements of hemoglobin-oxygen affinity and of the Bohr effect in a variety of mammals to discern differences in blood oxygen transport [42]. He also studied high-altitude species that showed a high oxygen affinity to explain adaptive features for low-oxygen environments. Dr. Bartels was known for his forefront research in prenatal respiration [43]. He studied the complexities of maternal and fetal blood gas dissociation curves and the Bohr effect applied to oxygen transfer in the placenta and in fetal tissues. We apologize for not being able to include a photograph and date of birth for Dr. Bartels. Extensive attempts were made to do this.

Dr. Lars-Erik Gelin (1920–1980), often called the "Charlie Gelin", was a professor of General Surgery and Transplantation Surgery at Gothenburg University and the director of Surgery I in Sahlgrenska Hospital. He initiated the renal transplant program in 1965, firmly establishing the hospital as one of the world's largest renal transplant units and held the first chair of transplant surgery in Sweden. He was known both nationally and internationally for his pioneering research in transplantation. As an example of his efforts to understand better the process of reoxygenation after surgery, we have included a pertinent reference [44]. A year after his death, the Foundation Professor Lars-Erik Gelin Memorial Foundation was established to award grants to scientific research and development projects related to transplantation. The Gelin Scholarship was established in 1996 and is awarded annually to applicants who intend to develop their clinical skills at a foreign clinic or institution. Dr. Gelin served on the first International Board for ISOTT [45].

Dr. Ludwig Schleinkofer (1952–2012) was the Director of Research and Development at Hamamatsu Deutschland GmbH for more than 30 years [46]. He was a leading expert in medical applications of near-infrared spectroscopy and joined ISOTT in 2004. He served on the executive committee from 2008 to 2011 and was a major sponsor of meetings and active supporter in the society. He passed away suddenly in 2012.

3 Conclusion

This paper is intended to speak for the history and founding of our society, ISOTT, and to honor many of the members who have made great contributions to its development to what we are today. These deceased members must be recognized to ensure our history is maintained intact for those who will come after us. It has been an *honor* and a *privilege* to be able to write and document this story. We have included a photo gallery to preserve our memories of our beloved colleagues (Fig. 1.2).

Fig. 1.2 Gallery of past Icons of ISOTT

References

1. Bruley DF (2014) The founding of ISOTT: the Shamattawa of engineering science and medical science. Adv Exp Med Biol 812:59–63
2. Goro FW (1948) Blood sludge. Life Mag 24(22):49–59
3. Bicher HI, Bruley DF, Knisely MH (1973) Anti-adhesive drugs and tissue oxygenation. Adv Exp Med Biol 37A:657–667
4. Reneau DD, Bruley DF, Knisely MH (1967) A mathematical simulation of oxygen release, diffusion and consumption in the capillaries and tissue of the human brain. In: Chemical engineering in medicine and biology. Plenum Press, New York, pp 135–241
5. Li LZ, Xu HN, Ranji M, Nioka S, Chance B (2009) Mitochondrial redox imaging for cancer diagnostic and therapeutic studies. J Innov Opt Health Sci 2(4):325–341
6. Chance B, Luo Q, Nioka S, Alsop DC, Detre JA (1997) Optical investigations of physiology: a study of biomedical contrast: intrinsic and extrinsic. Phil Trans R Soc Lond B 352:707–716
7. Kang KA, Bruley DF, Chance B (1997) Feasibility study of a single and multiple source NIR phase modulation device for biological system characterization. Biomed Instrum Technol 31(4):373–386
8. Grote J, Reneau DD, Thews G (eds) (1976) Oxygen transport to tissue, II: Adv Exp Med Bio, vol 75
9. Thews G (1960) Oxygen diffusion in the brain. A contribution to the question of the oxygen supply of the organs. Pflugers Arch 271:197–226
10. Kessler M, Bruley DF, Clark LC Jr, Lübbers DW, Silver IA, Strauss J (eds) (1973) Oxygen supply. Urban & Schwarzenberg, Dortmund
11. Huch R, Lübbers DW, Huch A (1974) Reliability of transcutaneous monitoring of arterial Po_2 in newborn infants. Arch Dis Child 49(3):213–218
12. Clark LC Jr, Wolf R, Granger D, Taylor Z (1953) Continuous recording of blood oxygen tensions by polarography. J Appl Physiol 6:189–193
13. Clark LC Jr, Clark EW (1973) Differential anodic enzyme polarography for the measurement of glucose. Adv Exp Med Biol 37A:127–133
14. Schönleben K, Hauss JP, Spiegel U, Bünte H, Kessler M (1978) Monitoring of tissue PO_2 in patients during intensive care. Adv Exp Med Biol 92:593–598
15. Kessler M, Lübbers DW (1966) Aufbau und Anwendungsmöglichkeiten verschiedener pO_2-Elektroden. Pflüg Arch ges Physiol 291:32
16. Jobsis FF (1980) Method and apparatus for monitoring metabolism in body organs in vivo. Duke University, BB Olive, French Patent
17. Jobsis FF, Jobsis PD (2000) Method and apparatus for determining oxygen saturation of blood in body organs. BB Olive, US Patent
18. Kovách AGB (1972) Metabolic changes in hemorrhagic shock. Adv Exp Med Biol 23:275–278
19. Kovách AGB, Dóra E, Kessler M (1981) Oxygen transport to tissue: satellite symposium of the 28th international congress of physiological sciences, Budapest, Hungary, 1980. Elsevier Science, Burlington
20. Maguire DJ, Lintell NA, McCabe M et al (2003) Genomic and phenomic correlations in the respiration of basal cell carcinomas. Adv Exp Med Biol 540:251–256
21. Maguire DJ, McCabe M, Piva T (1988) The effects of hypo- and hyperthermia on the oxygen profile of a tumour spheroid. Adv Exp Med Biol 222:741–745
22. de Koning J, Hoofd LJ, Kreuzer F (1981) Oxygen transport and the function of myoglobin. Theoretical model and experiments in chicken gizzard smooth muscle. Pflugers Arch 389(3):211–217
23. Kreuzer F, Hoofd JC (1976) Facilitated diffusion of CO and oxygen in the presence of hemoglobin or myoglobin. Adv Exp Med Biol 75:207–215
24. Longmuir IS, Pashko L (1976) The induction of cytochrome P-450 by hypoxia. Adv Exp Med Biol 75:171–175

25. Longmuir IS, Knopp JA (1973) A new histochemical stain for intracellular oxygen. Adv Exp Med Biol 37A:55–57
26. Mochizuki M, Shibuya I, Uchida K, Kagawa T (1987) A method for estimating contact time of red blood cells through lung capillary from O_2 and CO_2 concentrations in rebreathing air in man. Jpn J Physiol 37(2):283–301
27. Mochizuki M, Kagawa T (1988) Relationship between alveolar-arterial Po2 and Pco2 differences and the contact time in the lung capillary. In: Mochizuki M, Honig CR, Koyama T et al (eds) Oxygen transport to tissue X, vol 222, Advances in experimental medicine and biology., pp 497–504
28. McCabe MG, Bourgain R, Maguire DJ (2003) Oxygen as a regulator of tissue perfusion. Adv Exp Med Biol 540:287–290
29. Van Rossem K, Vermarien H, Decuyper K, Bourgain R (1992) Photothrombosis in rabbit brain cortex: follow up by continuous pO_2 measurement. Adv Exp Med Biol 316:103–112
30. Goresky CA (1963) A linear method for determining liver sinusoidal and extravascular volumes. Am J Physiol 204:626–640
31. Goresky CA, Goldsmith HL (1973) Capillary-tissue exchange kinetics: diffusional interactions between adjacent capillaries. Adv Exp Med Biol 37B:773–781
32. Honig CR, Bourdeau-Martini J (1973) O_2 and the number and arrangement of coronary capillaries: effect on calculated tissue PO_2. Adv Exp Med Biol 37A:519–524
33. Honig CR (1988) Modern cardiovascular physiology. Little, Brown and Company, Boston
34. di Prampero PE, Piiper J (2003) Effects of shortening velocity and of oxygen consumption on efficiency of contraction in dog gastrocnemius. Eur J Appl Physiol 90(3-4):270–274
35. Piiper J (2000) Perfusion, diffusion and their heterogeneities limiting blood-tissue O_2 transfer in muscle. Acta Physiol Scand 168(4):603–607
36. Lamers-Lemmers JP, Hoofd LJC, Oeseburg B (2003) Oxygen diffusion coefficient and oxygen permeability of metmyoglobin solutions determined in a diffusion chamber using a non-steady state method. Adv Exp Med Biol 530:509–517
37. Hoofd LJC, Oeseburg B (2003) A modeling investigation to the possible role of myoglobin in human muscle in near infrared spectroscopy (NIRS) measurements. Adv Exp Med Biol 530:637–643
38. Kovách AG, Dóra E, Farago M, Horvath IH, Szabo C (1989) Regional differences in the regulation of contraction-relaxation machinery of vascular smooth muscle. Adv Exp Med Biol 248:601–609
39. Dóra E, Tanaka K, Greenberg JH, Gonatas NH, Reivich M (1986) Kinetics of microcirculatory, NAD/NADH, and elecrocorticographic changes in cat brain cortex during ischemia and recirculation. Ann Neurol 19:536–544
40. Hoshi Y, Hazeki O, Kakihana Y, Tamura M (1997) Redox behavior of cytochrome oxidase in the rat brain measured by near-infrared spectroscopy. J Appl Physiol 83:1842–1848
41. Tamura M, Oshino N, Chance B, Silver IA (1978) Optical measurements of intracellular oxygen concentration of rat heart in vitro. Arch Biochem Biophys 191(1):8–22
42. Baumann R, Bartels H, Bauer C (1987) Blood oxygen transport. Compr Physiol 147–172
43. Bartels H (1970) Prenatal respiration, vol 17, North-Holland: research monographs frontiers of biology. North Holland Publishing Co, Amsterdam and London
44. Dawidson I, Eriksson B, Gelin LE, Söderberg R (1979) Oxygen consumption and recovery from surgical shock in rats: a comparison of the efficacy of different plasma substitutes. Crit Care Med 7(10)
45. Gelin LE (1973) Intravascular aggregation of blood cells and tissue metabolic defects. Adv Exp Med Biol 191:647–656
46. Schleinkofer L, Tsuchia Y (1989) Electrical signal observing device. Patent #4870350

Part I
Cell Metabolism, Tissue Oxygenation and Treatment

Chapter 2
A Compelling Case for the Use of Perioperative Zymogen Protein C for Increased Patient Safety

Duane. F. Bruley, J.M. Abdallah, M.B. Streiff, T.W. McGuire, K.C. Bruley, M. Duncan, R. Duncan, E.E. Thiessen, M. White, K.C. Bruley Jr., and S.B. Bruley

Abstract It is imperative to maintain normal blood flow to provide adequate oxygen supply to specific organs and cells, as well as for the removal of metabolic byproducts. Therefore, any situation that results in blood clotting can injure or kill living tissues. In this paper, we describe a case where a protein C deficient subject who would, by all medical indicators, be at 100 % risk of experiencing thrombophlebitis, deep vein thrombosis, and or lung emboli, is able to escape all pathologies by using perioperative zymogen protein C (ZPC). This protein C deficient patient has a long history of blood clotting, particularly from surgical procedures. The patient is 81 years old and first experienced clotting due to hernia surgery in 1964, when he was hospitalized for 16 days post-surgery with life threatening complications. It was later determined in 1980, after many episodes, that the patient had hereditary protein C deficiency at the 38 % level. In his hernia surgery, perioperative ZPC was used along with accepted anticoagulation procedures with no blood clots or other related side effects occurring. This procedure can greatly benefit protein C deficient patients, and could potentially find use for non-PC deficient patients in surgeries and a variety of other medical treatments. This particular case helps to validate the importance of ZPC in effecting safer surgery in high-risk patients. It also supports the mechanism of ZPC acting as an anticoagulant without causing bleeding. Most importantly, each clinical case study represents a unique combination of surgeon, hematologist, medical staff, and patient

D.F. Bruley (✉) • K.C. Bruley • E.E. Thiessen • M. White • K.C. Bruley Jr. • S.B. Bruley
Synthesizer Inc., Ellicott City, MD, USA
e-mail: bruley33@verizon.net; kenncbruley@comcast.net; eileen@chemicalgraphics.com; melindabruleyw@comcast.net; kenn.bruley@nelsonmullins.com; bruley34@verizon.net

J.M. Abdallah • T.W. McGuire • M. Duncan • R. Duncan
Vidant Medical Center, East Carolina University, Greenville, NC, USA
e-mail: easternoncology@gmail.com; tmcguire@physicianseast.com; mbduncan@mac.com

M.B. Streiff
Johns Hopkins Medical Institutions, Baltimore, MD, USA
e-mail: mstreif@jhmi.edu

© Springer International Publishing Switzerland 2016

Q. Luo et al. (eds.), *Oxygen Transport to Tissue XXXVIII*, Advances in Experimental Medicine and Biology 923, DOI 10.1007/978-3-319-38810-6_2

functioning as a coordinated team. In this case, smaller amounts of very expensive ZPC achieved safe and efficacious results, which is hugely important for future clinical applications when considering the production cost of ZPC. More studies must be done to establish minimum dosing while achieving safe and efficacious outcomes.

Keywords Zymogen protein C (ZPC) • Surgery • PC deficiency • Patient safety • Optimal dosage

1 Introduction

The National Blood Clot Alliance (NBCA) has recently stated that there are as many as 900,000 cases of deep vein thrombosis (DVT) and pulmonary embolism (PE) diagnosed in the United States each year, resulting in nearly 300,000 deaths annually [1]. A large portion of the blood clots are due to blood coagulation protein surplus/deficiency (*via* hereditary or acquired conditions) or interference with the mechanisms for protein activation/deactivation [2, 3]. This is seen in numerous disease states where Dr. Melvin H. Knisely demonstrated blood sludging in malaria and over 100 other disease conditions [4]. Some examples of inherited thrombophilia (hypercoagulability) include factor II gene mutation, antithrombin III, plasminogen activator inhibitor-1 (PAI-1), protein S deficiency, protein C (PC) deficiency, and Factor V Leiden [5]. Examples of acquired thrombophilia include antiphospholipid syndrome, and hyperhomocysteinemia. Other factors may trigger or cause blood clots, including surgery, trauma, fractures, bed rest, sitting or lying still for several hours at a time, cancer, chemotherapy, intravenous catheters, estrogen use, pregnancy, giving birth, and air/car travel.

PC is the pivotal blood factor anti-coagulant [6–9]. It also serves as an apoptotic, anti-inflammatory and anti-thrombotic agent [10]. Its function, when activated, is to deactivate factor Va and factor VIIIa, thus downscaling the clotting process. Because Zymogen PC (ZPC) is activated only when and where it is needed, and the activated half-life is on order of minutes, ZPC has been coined the "silver bullet" of anticoagulation and has been used successfully perioperatively in major surgeries [11–16]. In the case of hereditary PC deficiency, babies that are born homozygous PC deficient die within weeks without PC concentrate supplements [17]. Those that are heterozygous for the gene typically have their first episode between the ages of 12 and 25 [18] or after 60.

2 The Patient and His Thrombotic History

Patient K is an 81-year old Caucasian male and a retired naval aviator. He was admitted for recurrent left inguinal hernia repair. Table 2.1 represents the history of thrombotic episodes that the patient has suffered from past surgeries or trauma to

Table 2.1 Patient K's thrombotic history

1964	Hernia repair—thrombus found at site of I.V. in left arm
6/24/1969	Hernia repair—saphenous vein thrombus—extended hospitalization
1980	Protein C on family. Patient K's value at 38 %, daughter's value similar, son's 80 %, other daughter at an excess
9/15 –9/28/1983	Left deep vein thrombosis (DVT). Apparent embolus. Heparin for 13 days
1/2/1987	ER visit with clot. Protein C level of 38 %
8/20/1989	ER visit with clot. History of DVTs. Travelling in car with pain in left leg
8/16/1991	Hospital visit with clot—history of DVT 9/83 and several other episodes of superficial thrombus usually after long car ride, as with today
3/9/1993	Fell off ladder; developed clot a month later. Patient K hospitalized and on heparin for 11 days
1995	SVT ablation procedure; evidence of an embolus during the procedure
11/2007	Superficial thrombosis of left calf
12/2/2010	Emergency laparoscopic surgery for appendix. Two (2) units plasma to avoid clotting
9/2012	Cataract surgeries, remained on Coumadin through procedure
2/6/2013	Surgery for left inguinal hernia. Zymogen PC perioperative—NO CLOTS (*subject of this paper*)

different parts of the body, resulting in blood clotting. The patient suffers from protein C deficiency at the 38 % level (heterozygote) and is on chronic anticoagulation therapy (warfarin). From this clotting history and other medical indicators for clotting, the patient was at 100 % risk of developing a superficial thrombophlebitis (STP), a deep vein thrombus (DVT), and/or a pulmonary embolus (PE) during or after surgery. Because of the potential clotting complications in this case, it was decided to use perioperative zymogen protein C (ZPC) along with standard anticoagulation therapy [11–16].

3 Medical Procedure

Major surgery is an environmental thrombotic risk factor that can lead to deep vein thrombosis and pulmonary embolism. These risks are enhanced in patients with underlying thrombophilic defects such as protein C deficiency, particularly for patients with previous thrombotic events. For the purposes of this paper, protein C deficiency refers to the heterozygote type. In preparation for the surgery, the patient's warfarin was discontinued 7 days prior to the surgery and the next day he was started on enoxaparin sodium (Lovenox; Sanofi-AventisUS LLC, Bridgewater, NJ; 1 mg/kg twice daily) until 24 h before the surgery. The patient was admitted to the hospital the morning of surgery on February 6, 2013 and started on intravenous ZPC concentrate (human) (Ceprotin; Baxter International Inc., Deerfield, IL). The night before surgery and before administration of protein C, the patient's protein C activity level was 32 % and his INR was 1.0 with a prothrombin time of 10.6.

The ZPC was ordered at 450 units bolus every 6 h at a rate of 108 cc/h. His morning PC activity level immediately before surgery and before the bolus was 32. This was taken at 8:13 am but was not known until 48 h later, as the analysis had a long processing time. His PC activity level at 2:51 pm was 85 and at 4:54 am the next day was 124. He was maintained on ZPC until his last dose at 5:43 am on 2/8/2013 (POD 2), and then transitioned back to his normal anticoagulation therapy using Lovenox and warfarin according to the following procedure. Coumadin was started on 2/7/13 (POD 1) at 7:45 pm with a first dose of 5 mg. Lovenox was started on 2/7/13 (POD 1) at 8:00 pm, dosing 80 mg SQ every 12 h. He was given instructions to take 5 mg Coumadin every Tuesday, Thursday, Saturday, and Sunday, and 2.5 mg on Monday, Wednesday, and Friday and to continue with the Lovenox until his INR was greater than 2.0.

During the procedure, he received endotracheal general anesthesia. A 15-bladed knife was used to make an 8-cm curvilinear incision over the inguinal canal. The patient had numerous, engorged, collateral veins from chronic venous stasis disease on the left side. After an extensive procedure with a good landing zone, the mesh was placed and it was sutured into place. After sterilization, the patient recovered from general anesthesia and was transported to the post-anesthesia care unit (PACU) in stable condition. Sponge, instrument, and needle counts were reported as correct times two. He was stable throughout the procedure and was released from the hospital for home care on the afternoon of 2/8/13.

4 Results and Discussion

As reported, Patient K was a naval aviator. Therefore, he was often in very cramped, stressful conditions for relatively long periods of time. It is well known that people in thrombophilic circumstances are prone to developing thrombotic episodes. As can be seen from Patient K's history (Table 2.1), his first detected thrombosis was found after hernia repair in 1969. Expanding on his history, he has experienced at least 12 thrombotic events over the course of his lifetime as a result of major and minor interventions and traumas. Because of the high risk of thrombosis in this hernia surgery, it was decided to employ the use of perioperative ZPC to cover the period before, during, and after surgery. Notably, during the time of surgery, ZPC was the only anticoagulant present and it protected him from clotting without increased bleeding.

Throughout the surgery, blood samples were taken and analyzed for ZPC levels in the blood. Unfortunately, the individual sample assays required 48 h or more, so that the results were not immediately available during the procedure and in fact, the last sample taken was never recorded to indicate the ultimate ZPC level in the blood. The highest recorded level was 124 %, which appeared to be sufficient and may have been more than enough. Therefore, we are unable to determine the effective level of ZPC for such a procedure, and more ZPC was probably used than necessary. It has been demonstrated that supraphysiologic levels (238 %) have been used in past studies without increased bleeding or other negative results [12]. Further research must be done to optimize safe dosing and reduce the cost for ZPC.

It has been established that ZPC concentrate has achieved promising results with a very good safety record [19, 20] for treating such conditions as severe sepsis and neonatal purpura fulminans [21, 22]. It has also been used to prevent vascular thrombosis for patients with familial PC deficiency undergoing renal transplantation without noted side effects [23]. Given Patient K's personal and family history of idiopathic PE and PC deficiency, as well as the substantial thrombotic and bleeding risks posed by this surgery, it was decided the off label use of PC concentrate represented the most efficacious approach. The resulting favorable endpoint helps establish the procedure as a treatment strategy for patients who are highly thrombophilic with PC deficiency. There may be other medical indications that could be treated more safely with the protocol used in this case study.

Based on evidence from several major surgeries involving perioperative PC administration [11–14, 16], it is clear that this procedure increases patient safety. In all cases there was no hypersensitivity reaction with Ceprotin administration, and despite the high levels of PC during the perioperative period, there was no increased surgical site bleeding. In our present case, however, a hematoma did occur postoperatively. But this condition presented itself after the patient was started on warfarin and was therapeutic on heparin [Lovenox].

This report presents the use of human protein C concentrate, in an off-label fashion, to safely perform a hernia surgery in a highly thrombophilic patient deficient in protein C. It should be clear that this strategy is not only promising but should be considered in treating thrombophilic individuals with PC deficiency who require major surgery. Patient K has survived and is presently leading a normal life without any consequences from his hernia repair surgery.

5 Economics of ZPC

It is obvious that using perioperative PC (Ceprotin) is very costly. Based on the approximate shelf value of $34.40/unit of Ceprotin, this surgery for ZPC alone cost approximately $134,160. Considering that the patient's ZPC level during that time period may have risen above 124 % (last measured value) of normal, it is important to find the optimal safe dose to minimize the expense of ZPC.

Alternatively, it is important to continue research and development to establish improved bioprocessing strategies that will reduce production costs of ZPC from blood. One approach that shows promise is the replacement of immunoaffinity chromatography (IAC) with immobilized metal affinity chromatography (IMAC) [24–27]. It is estimated that this approach could reduce product costs by a factor of 500–1000. Other possible approaches might include the use of mini-antibodies (mini-Mab) leading to the development of inexpensive ligands to reduce the PC production cost [28]. Additionally, the use of transgenic animals has been demonstrated to produce less expensive blood proteins [29]. Although less attractive from an economic point of view, further investigation of recombinant DNA technology *via* bioreactors is another possibility. Because of the need to reduce cost of important life-saving blood proteins, it is encouraged that research and development be funded and promoted in this arena.

6 Conclusion

This paper presents an important example of safer surgery through the use of ZPC. The procedure has great benefits for protein C deficient patients and could find use in a variety of medical treatments. This particular case helps to validate the importance of ZPC in effecting safer surgery in high risk patients. It also supports the mechanism of ZPC acting as an anticoagulant without causing bleeding. Most importantly, this paper contributes clinical results indicating that smaller amounts of expensive ZPC can be used to achieve the same satisfactory results. More clinical studies must be completed to target the optimum levels of ZPC with respect to cost and effectiveness. These case studies are rare because of the cost of each experiment and the difficulty in getting a willing patient along with a surgeon, hematologist, and medical team to carry out the procedure. Whatever it takes, the world needs a safe anticoagulant that will not result in costly bleeds and mortality.

References

1. National Blood Clot Alliance (n.d.) Blood clot statistics vary – what to do about it? NBCA Stop the Clot News. Web. 23 May 2014
2. Bicher HI, Bruley DF, Knisely MH (1973) Anti-adhesive drugs and tissue oxygenation. In: Bruley DF, Bicher HI (eds) Oxygen transport to tissue, vol 37, Advances in experimental medicine and biology. Plenum Press, New York
3. Esmon CT (1989) The roles of protein C and thrombomodulin in the regulation of blood coagulation. J Biol Chem 264(9):4743–4746
4. Goro FW (1948) Blood sludge. Life Mag 24(22):49–59
5. Walker FJ, Sexton PW, Esmon CT (1979) The inhibition of blood coagulation by activated Protein C through the selective inactivation of activated Factor V. Biochim Biophys Acta 571(2):333–342
6. Bertina RM (1988) Protein C and related proteins: biochemical and clinical aspects, Contemporary issues in haemostasis and thrombosis. Churchill Livingstone, New York
7. Stenflo J (1976) A new vitamin K-dependent protein. J Biol Chem 251:355–363
8. Sharma GR, Grinnell BW et al (2008) Activated protein C modulates chemokine response and tissue injury in experimental sepsis. In: Kang KA, Harrison DK, Bruley DF (eds) Oxygen transport to tissue XXIX, vol 614, Advances in experimental medicine and biology. Springer, New York, pp 83–91
9. Esmon CT (1990) Regulation of coagulation: the nature of the problem. In: Bruley DF, William N (eds) Drohan protein C and related anticoagulants, vol 2, Advances in applied biotechnology series. Gulf Publishing Company, Houston, p 3
10. Bruley DF, Drohan WN (1990) Protein C and related anticoagulants, vol 11, Advances in applied biotechnology series. Gulf Publishing Company, Houston
11. Bruley DF (2009) Zymogen protein C concentrate for safer heterozygote surgery, I am a guinea pig! In: Liss P, Hansell P, Bruley DF (eds) Oxygen transport to tissue XXX, vol 645, Advances in experimental medicine and biology. Springer Publishing, New York, pp 115–21
12. Bruley DF, Mears SC, Streiff MB (2010) Safer surgery using zymogen protein C concentrate. In: Takahashi EJ, Bruley DF (eds) Oxygen transport to tissue XXXI, vol 662, Advances in experimental medicine and biology. Springer Publishing, New York, pp 439–45

13. Bruley DF, Jagannath SB, Streiff MB (2011) Zymogen protein C to prevent clotting without bleeding during invasive medical procedures. In: LaManna JC et al (eds) Oxygen transport to tissue XXXII, vol 701, Advances in experimental medicine and biology. Springer Publishing, New York, pp 91–7
14. Thakkar SC, Streiff MB, Bruley DF et al (2010) Perioperative use of protein c concentrate for protein c deficiency in THA. Clin Orthop Relat Res 468(7):1986–1990
15. Bruley DF, Streiff MB (2013) Nature's "silver bullet" for anticoagulation: mechanism of zymogen protein C to activated protein C. In: Wolf M, Bucher HU, Rudin M, Van Huffel S, Wolf U, Bruley DF, Harrison DK (eds) Oxygen transport to tissue XXXIII, vol 765, Advances in experimental medicine and biology. Springer Publishing, New York, pp 15–21
16. Bruley DF, Schulick RD, Streiff MB (2013) Pancreaticoduodenectomy using perioperative zymogen protein C to help prevent blood clotting: a trilogy on increased patient safety. In: Van Huffel S, Naulaers G, Caicedo A, Bruley DF, Harrison DK (eds) Oxygen transport to tissue XXXV, vol 789, Advances in experimental medicine and biology. Springer Publishing, New York, pp 299–307
17. Marlar RA, Montgomery RR, Broakman AW (1989) Diagnosis and treatment of homozygous protein C deficiency. Report of the Working Party on Homozygous Protein C Deficiency of the Subcommittee on Protein C and Protein S, International Committee on Thrombosis and Haemostasis. J Pediatr 114(4 Pt 1):528–534
18. Mahmoodi BK, Brouwer JL, Veeger NJ et al (2008) Hereditary deficiency of protein C or protein S confers increased risk of arterial thromboembolic events at a young age: results from a large family cohort study. Circulation 118:1659–1667
19. Gatti L, Carnelli V, Rusconi R et al (2003) Heparin-induced thrmobocytopenia and warfarin-induced skin necrosis in a child with severe protein C deficiency: successful treatment with dermatan sulfate and protein C concentrate. J Thromb Haemost 1:387–388
20. Knoebl PN (2008) Human protein C concentrates for replacement therapy in congenital and acquired protein C deficiency. Drugs Today (Barc) 44:429–441
21. Schellongowski P, Bauer E, Holzinger U et al (2006) Treatment of adult patients with sepsis-induced coagulopathy and purpura fulminans using a plasma-derived protein C concentrate (Ceprotin). Vox Sang 90:294–301
22. White B, Livingstone W, Murphy C et al (2000) An open-label study of the role of adjuvant hemostatic support with protein C replacement therapy in purpura fulminans-associated meningococcemia. Blood 96:3719–3724
23. Toupance O, Nguyen P, Brandt B et al (1994) Prevention of vascular thrombosis by human purified protein C concentrate in a patient with familial PC deficiency undergoing renal transplantation. Transpl Int 7:144–145
24. Wu H, Bruley DF (1999) Homologous blood protein separation using immobilized metal affinity chromatography: protein C separation from prothrombin with application to the separation of facto IX and prothrombin. Biotechnol Prog 15(5):928–931
25. Wu H, Bruley DF (2002) Chelator, metal ion and buffer studies for protein c separation. Comp Biochem Physiol A Mol Integr Physiol 132(1):213–220
26. Thiessen EE, Bruley DF (2003) Theoretical studies of IMAC interfacial phenomena for the purification of protein C. In: Thorniley MS, James PE (eds) Oxygen transport to tissue XXV, vol 540, Advances in experimental medicine and biology. Springer, New York, p 183
27. Porath J (1992) Immobilized metal ion affinity chromatography. Protein Expr Purif 3(4):263–281
28. Korah LK, Ahn DG, Kang KA (2003) Mini-antibody production process for the purification of protein C. In: Wilson DF, Evans SM, Biaglow J, Pastuszko A (eds) Oxygen transport to tissue XXIII, vol 510. Kluwer Academic/Plenum Publishers, New York, pp 127–132
29. Velander WH, Lubon H, Drohan WN (1997) Transgenic livestock as drug factories. Sci Am 276(1):70–74

Chapter 3
Clinical Evaluation of MP4CO: A Phase 1b Escalating-Dose, Safety and Tolerability Study in Stable Adult Patients with Sickle Cell Disease

Peter E. Keipert and For the MP4CO-SCD-105 Study Investigators*

Abstract MP4CO, developed by Sangart Inc. (San Diego, CA), is a pegylated human hemoglobin-based carbon monoxide (CO) delivery agent and oxygen therapeutic that has shown potential to prevent and reverse red cell sickling. A double blind, comparator controlled, dose-escalation, Phase 1b study was conducted to assess the safety of MP4CO. Adult sickle cell patients with HbSS or S/β^0 Thal genotype who were not experiencing a painful crisis were randomized to receive either MP4CO or normal saline (NS) in a sequential series of six escalating dose cohorts (A–F). In each cohort, three patients received MP4CO (Treatment group) and one patient received NS (Controls). Single IV doses ranged from 15 mg/kg/dose (0.35 mL/kg infusion) to 172 mg/kg/dose (4 mL/kg infusion). Two cohorts received fractionated doses of 172 or 344 mg/kg (4–8 mL/kg, given as two IV infusions, 24 h apart). Overall, 16/24 patients (66.7 %) reported mild to moderate adverse events (AEs); with 13/18 (72 %) in MP4CO group vs. 3/6 (50 %) in NS Controls. No serious adverse events (SAEs) were experienced and no deaths occurred. Most common AEs (reported by >2 patients) included headaches (mild and transient), fatigue and rash at the application site of the Holter electrodes. No treatment-emergent abnormalities in clinical lab values were noted. Vital signs, ECG readings, and pulmonary pressures remained within normal limits. The maximum increase in blood CO-Hb level was ~2 %, which returned to pre-dosing levels within 8 h after dosing. The mean increase in free plasma Hb (an index of MP4CO dose) ranged from 0.20 to 0.35 g/dL in the two highest dose cohorts, with no significant change in total whole blood hemoglobin level. There was no symptomatic or

*MP4CO-SCD-105 Study Investigators: Jo Howard, MB, BChir, Guy's and St. Thomas' Hospital NHS Foundation Trust, London, UK; Swee Lay Thein, MBBS, DSc, King's College Hospital NHS Foundation Trust, London, UK; Frédéric Galactéros, MD, PhD, Hôpital Henri-Mondor, Créteil, France; Adlette Inati, MD, Lebanese American University Hospital, Beirut, Lebanon; and Marvin Reid, MD, PhD, Sickle Cell Unit, University of the West Indies at Mona, Kingston, Jamaica

P.E. Keipert, Ph.D. (✉) • For the MP4CO-SCD-105 Study Investigators
KEIPERT Corp. Life Sciences Consulting, San Diego, CA 92130, USA
e-mail: peterkeipert@gmail.com; keipertcorpconsulting@gmail.com

© Springer International Publishing Switzerland 2016

Q. Luo et al. (eds.), *Oxygen Transport to Tissue XXXVIII*, Advances in Experimental Medicine and Biology 923, DOI 10.1007/978-3-319-38810-6_3

clinical evidence of renal dysfunction in either group based on serum creatinine and urinary albumin results. Two patients had elevated renal biomarkers (β2M and NAG) at Hour 72, which normalized at follow-up visits. Both patients had documented intercurrent illnesses during the study. Further testing of stored urine samples were within normal limits, which suggested the changes were reflective of a generalized inflammatory state rather than direct tubular injury.

Keywords MP4CO • Pegylated hemoglobin • HBOC • Oxygen therapeutic • Sickle cell disease

1 Introduction

The hallmark of Sickle Cell disease (SCD) remains painful vaso-occlusive crises (VOC), yet to date no agent has been approved to treat these acute ischemic events [1]. MP4CO, developed by Sangart Inc. (San Diego, CA), is a hemoglobin-based carbon monoxide (CO) delivery agent and oxygen therapeutic that has shown potential in non-clinical studies to prevent and reverse red blood cell (RBC) sickling. MP4CO has exhibited anti-adhesive, anti-inflammatory, anti-oxidant, and anti-apoptotic properties at circulating CO-hemoglobin levels <10 % [2]. These protective effects are expected to limit progression of vascular occlusion and mitigate the consequences of ischemic tissue damage and inflammation. The beneficial effects of MP4CO have been ascribed to five mechanisms: (1) down-regulation of ICAM-1, VCAM-1 and NF-kB, (2) upregulation of Heme-Oxygenase-1 and Nrf2 leading to increases in anti-inflammatory mediators, biliverdin and CO, (3) delivery of oxygen to ischemic tissues, (4) intravascular volume expansion and improved perfusion of ischemic tissue, and (5) potential to prevent and reverse polymerization and sickling of RBCs [3, 4].

The investigational product, MP4CO, is pegylated human hemoglobin saturated with CO, and formulated at 4.3 g/dL in physiological acetate electrolyte solution. MP4CO is hyperoncotic (colloid osmotic pressure [COP] ~70 mmHg) with a high affinity for oxygen (P50 ~5 mmHg), resulting in the release of oxygen at low pO_2 to target delivery of oxygen in capillaries and ischemic tissues [5]. The aim of this Phase 1b first-in-man study was to evaluate safety of escalating-doses of MP4CO in adult patients with Sickle Cell disease not experiencing a painful VOC at the time of treatment [6].

2 Methods

We conducted a double blind, comparator controlled, dose-escalation, multi-center Phase 1b study at five sites in four countries [7]. Adult Sickle Cell patients with HbSS or S/β^0 Thal genotype, at least 18 years of age, who were clinically stable

(not experiencing a VOC at the time of testing) and met all eligibility criteria were randomized to receive either MP4CO or normal saline (NS) in a sequential series of six escalating dose cohorts (A–F). In each cohort, three patients received MP4CO (Treatment) and one patient (Control) received normal saline (NS) to maximize the number of treated patients receiving investigational product. Single IV dose cohorts A–D received: (A) 15 or (B) 43 mg/kg (0.35 or 1.0 mL/kg) at 25 mL/min, (C) 86 or (D) 172 mg/kg (2.0 or 4.0 mL/kg) infused over 2 h. Cohorts E and F received fractionated doses totaling 172 or 344 mg/kg (4.0 or 8.0 mL/kg), administered as two IV infusions of 2.0 or 4.0 mL/kg given 24 h apart.

Safety assessments occurred at 24 (±4 h), 48 (±4 h), and 72 h (±1 day) after dosing, followed by visits at Day 7 (±1 day) and a safety follow-up at Day 28 (+5 days). Serious adverse events (SAEs) were monitored until Day 28. Safety evaluations included physical examinations, vital signs, pulse oximetry, Holter ECGs, transesophageal echocardiography (TEE) to measure tricuspid regurgitation jet velocity (TRJV) for estimating pulmonary artery systolic pressures, venous blood co-oximetry, free plasma hemoglobin, pain levels by Visual Analogue Scale (VAS), lab assessments (blood chemistry and hematology), and adverse events (AEs). Laboratory, hematology and chemistry parameters were summarized using descriptive statistics at baseline (BL) and at each post-BL time point. Safety data from baseline through Day 7 for all four patients enrolled within each cohort were reviewed by an unblinded, independent, medical monitor before proceeding to the next higher dose level.

3 Results

In total, 24 patients (of 25 randomized) were dosed, out of 35 screened. Patients were 54 % male, with an average age of 30 years (range: 18–51) and an average weight of 65 kg (range: 53–79). There were no clinically notable changes from BL, and no between-group differences observed in the clinical chemistry parameters evaluated, which included the following: albumin, liver enzymes (alanine aminotransferase [ALT], aspartate aminotransferase [AST], and gamma-glutamyl transferase [GGT]), pancreatic enzymes (amylase, lipase), electrolytes, glucose, serum bilirubin, creatinine, urea levels, and cardiac Troponin-I.

Overall, 16/24 patients (66.7 %) reported mild to moderate AEs; with 13/18 (72 %) in the MP4CO group vs. 3/6 (50 %) in NS Controls. The most frequent AE that appeared to be treatment-emergent was headache (see Table 3.1 for full listing of most common AEs reported in >2 patients). No SAEs were experienced, and no deaths occurred.

Vital signs, ECG readings, standard laboratory values and pulmonary pressures remained within normal limits. There was no evidence of hypertension due to vasoconstriction, based on systolic and diastolic blood pressure data (see Fig. 3.1).

A dose-related increase in venous CO-Hb levels was seen in the higher dose MP4CO cohorts (D–F), where CO-Hb increased by 1–2 % (absolute) after each dose and then normalized to pre-dosing levels by 8 h. There were no notable changes

Table 3.1 Most common adverse events (reported in >2 patients)

Adverse event: preferred term	MP4CO (n = 18)		NS (n = 6)		Total (N = 24)	
	T[a]	n	T[a]	n	T[a]	N
Headache	17	9 (50 %)	1	1 (17 %)	18	10 (42 %)
Fatigue	10	7 (39 %)	2	1 (17 %)	12	8 (33 %)
Rash (Holter application sites)	5	5 (28 %)	0	0	5	5 (21 %)
Back pain	10	3 (17 %)	0	0	10	3 (13 %)
Dizziness	3	3 (17 %)	0	0	3	3 (13 %)
Nausea	3	3 (17 %)	1	1 (17 %)	4	4 (17 %)
Musculoskeletal chest pain	3	3 (17 %)	1	1 (17 %)	4	4 (17 %)
Pain in extremities	2	2 (11 %)	3	2 (33 %)	5	4 (17 %)
Arthralgia	4	2 (11 %)	1	1 (17 %)	5	3 (13 %)
Cough	2	2 (11 %)	1	1 (17 %)	3	3 (13 %)
Infections and Infestations	2	2 (11 %)	1	1 (17 %)	3	3 (13 %)

[a]T = Total # of reported cases for each AE. n = # of patients with at least one report of an AE. Percentages are based on number of patients in Safety Population/treatment group and in total N

observed in methemoglobin levels. Low levels of free plasma hemoglobin were seen at baseline in all MP4CO groups and in NS controls, ranging from 0.08 to 0.13 g/dL. In MP4CO patients in cohorts C and D, plasma hemoglobin doubled at Hour 2, to mean levels of 0.20–0.35 g/dL. Peak plasma hemoglobin at 2 h after Dose 2 in MP4CO patients in cohort F reached a mean level of 0.41 g/dL.

Neither the MP4CO nor the NS group showed evidence of increased hemolysis, based on evaluating markers of hemolysis (i.e., total hemoglobin, reticulocyte count, lactate dehydrogenase [LDH] and total bilirubin). There were no notable between-group differences in mean values or ranges for hematological parameters, including WBCs and differentials (neutrophils, monocytes, lymphocytes, basophils and eosinophils), platelet counts, RBCs, hematocrit, and RBC morphology (MCH, MCHC, MCV).

There were no new treatment-emergent ECG abnormalities observed that were not already present at Baseline prior to dosing. There was no evidence of adverse cardiac effects or arrhythmias, and no exacerbation of any pre-existing abnormalities. TRJV results, assessed by noninvasive TTE, was similar in MP4CO and NS groups (see Fig. 3.2), suggesting the absence of any clinically significant increase in pulmonary artery systolic pressure after administration of MP4CO or NS.

There was no symptomatic or clinical evidence of renal dysfunction in either group based on serum creatinine and urine albumin levels. There were no notable dose effects seen, or any obvious between-group differences in urine albumin, urine β2-Microglobulin (β2M) and *N*-acetyl-β-D-glucosaminidase (NAG) levels during the study (i.e., compared to mean values for all six Control patients combined). Two MP4CO-treated patients exhibited elevated levels of urinary β2M and NAG at Hour 72 that normalized at follow-up visits. Both patients also had intercurrent illnesses; one (cohort E) had an active mild VOC during the study, and one (cohort F) was found to have influenza with pyrexia, rhinorrhea and cough. Both 72-h urine

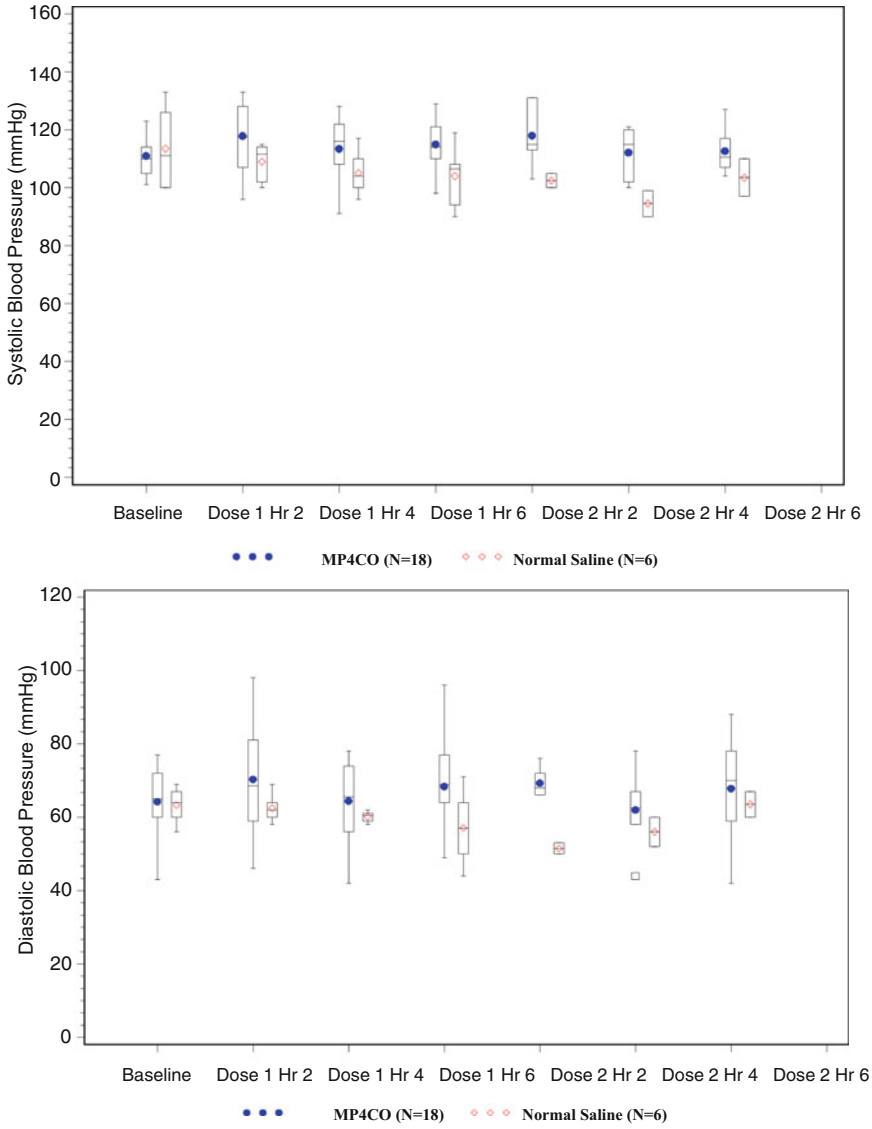

Fig. 3.1 Systolic and Diastolic blood pressure results (Box-and-Whisker plot). **Note**: Single and fractionated doses are combined

samples were analyzed further for Kidney Injury Molecule-1 (KIM-1) and neutrophil gelatinase-associated lipocalin (NGAL) levels, which were found to be normal. This suggests that the elevations of β2M and NAG were likely due to the inflammatory processes (corroborated by elevated C-reactive protein [CRP] levels) and not specifically due to renal tubular injury.

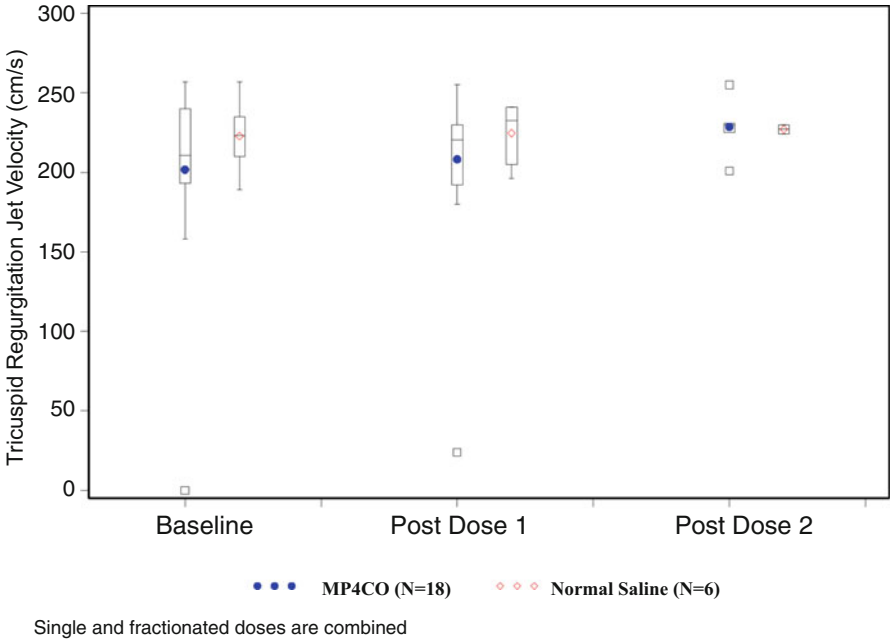

Fig. 3.2 Tricuspid regurgitation jet velocity (TRJV) results (Box-and-Whisker plot). **Note**: Single and fractionated doses are combined

The majority of the VAS measurements collected at screening, BL, post-dosing and daily thereafter were zero (no pain), or only negligibly elevated. Four patients had transiently elevated VAS pain scores. One NS control patient reported a VAS score of 37 mm (on a scale from 0 to 100 mm) at 24 h after dosing. Similarly, one MP4CO-treated patient in cohorts D, E and F had VAS scores that briefly peaked to 30, 20 and 28 mm, respectively, during the study.

4 Discussion and Conclusions

The treatment of acute tissue ischemia associated with VOCs in patients with Sickle Cell disease represents an indication that may benefit from the unique attributes of MP4CO, which include: (1) rapid release of a small therapeutic dose of CO, (2) increased colloidal osmotic pressure to enhance capillary blood flow and tissue perfusion, (3) targeted oxygen delivery in the microcirculation and to ischemic tissues after release of the CO, (4) pegylation to prolong circulating half-life, and (5) lower concentration of hemoglobin to improve safety profile [2].

This study demonstrated minimal evidence of adverse effects of MP4CO on cardiac, pulmonary, hepatic, pancreatic and renal biomarkers, and no clinical evidence of any organ dysfunction or injury. Most AEs reported were consistent with events

that are typically seen in patients with Sickle Cell disease. Unlike earlier generation hemoglobin-based oxygen carriers (HBOCs), neither vasoconstriction nor pulmonary hypertension was observed in this study. Taken together with data from non-clinical mechanism-of-action studies, these encouraging safety results suggest that MP4CO was well tolerated, and support further testing of MP4CO in a larger Phase 2 study for acute therapeutic intervention to treat painful VOCs.

Acknowledgments PEK was employed by Sangart Inc. as VP, Clinical Development, during the conduct of the MP4CO-SCD-105 study.

References

1. Ballas SK, Lusardi M (2005) Hospital readmission for adult acute sickle cell painful episodes: frequency, etiology, and prognostic significance. Am J Hematol 79(1):17–25
2. Belcher JD, Young M, Chen C et al (2013) MP4CO, a pegylated hemoglobin saturated with carbon monoxide, is a modulator of HO-1, inflammation, and vaso-occlusion in transgenic sickle mice. Blood 122(15):2757–2764
3. Belcher JD, Mahaseth H, Welch TE et al (2006) Heme oxygenase-1 is a modulator of inflammation and vaso-occlusion in transgenic sickle mice. J Clin Invest 116:808–816
4. Winslow RM, Lohman J, Malavalli A et al (2004) Comparison of PEG-modified albumin and hemoglobin in extreme hemodilution in the rat. J Appl Physiol 97:1527–1534
5. Vandegriff KD, Young MA, Lohman J (2008) CO-MP4, a polyethylene glycol-conjugated haemoglobin derivative and carbon monoxide carrier that reduces myocardial infarct size in rats. Br J Pharmacol 154(8):1649–1661
6. Howard J, Thein SL, Keipert PE (2013) Poster presentation of MP4CO-SCD-105 study results at the American Society of Hematology (ASH) meeting. New Orleans, LA
7. Howard J, Thein SL, Galactéros F et al (2013) Safety and tolerability of MP4CO: a dose escalation study in stable patients with Sickle Cell disease. Blood 122(21):2205

Chapter 4
Protective Effect of Dl-3-*n*-Butylphthalide on Recovery from Cardiac Arrest and Resuscitation in Rats

Le Zhang, Michelle A. Puchowicz, Joseph C. LaManna, and Kui Xu

Abstract In this study we investigated the effect of Dl-3-*n*-butylphthalide (NBP), a clinically used drug for stroke patients in China, on the recovery following cardiac arrest and resuscitation in rats. Male Wistar rats (3-month old) underwent cardiac arrest (12 min) and resuscitation. Rats were randomly assigned to the following groups: sham non-arrested group, vehicle group (vehicle-treated, 7 days before cardiac arrest and 4 days post-resuscitation), NBP pre-treated group (NBP-treated, 7 days before cardiac arrest), and NBP post-treated group (NBP-treated, 4 days post-resuscitation). Overall survival rates and hippocampal neuronal counts were determined in each group at 4 days post-resuscitation. Results showed that NBP pre-treated group (80 %) and NBP post-treated group (86 %) had significantly higher survival rates compared to that of the vehicle group (50 %). At 4 days of recovery, only about 20 % of hippocampal neurons were preserved in the vehicle group compared to the sham non-arrested group. The hippocampal CA1 cell counts in the NBP pre-treated group and NBP post-treated group were significantly higher than the counts in the vehicle group, about 50–60 % of the counts of non-arrested rats. The data suggest that NBP has both preventive and therapeutic effect on improving outcome following cardiac arrest and resuscitation, and NBP might be a potential early phase treatment for patients recovered from cardiac arrest and resuscitation.

Keywords Transient global ischemia • Ischemia/reperfusion injury • Neuroprotection • Post-resuscitation recovery • Selective neuronal death

L. Zhang
Institute of Neurology, Xiangya Hospital, Central South University, Changsha, Hunan 410008, China

M.A. Puchowicz
Department of Nutrition, Case Western Reserve University, Cleveland, OH, USA

J.C. LaManna • K. Xu (✉)
Department of Physiology and Biophysics, Case Western Reserve University, Robbins Building E732, 10900 Euclid Ave., Cleveland, OH 44139, USA
e-mail: kxx@case.edu

© Springer International Publishing Switzerland 2016

Q. Luo et al. (eds.), *Oxygen Transport to Tissue XXXVIII*, Advances in Experimental Medicine and Biology 923, DOI 10.1007/978-3-319-38810-6_4

1 Introduction

Cardiac arrest is a leading cause of death worldwide, including United States and China, and is also one of the most common diseases that cause disabilities such as permanent coma or permanent brain damage. Most of the mortality and morbidity of cardiac arrest and resuscitation can be attributed to the immediate global ischemia injury and delayed effects of reperfusion damage to the brain [1, 2]. DI-3-*n*-butylphthalide (NBP) was extracted as a pure component from seeds of celery (Apium graveolens Linn) and was synthesized and approved by the State Food and Drug Administration of China for clinical use in stroke patients in 2002. The therapeutic effects of NBP were assessed in a variety of in vivo and in vitro models of stroke; however, there was no report on exploring the effect of NBP on the recovery following cardiac arrest and resuscitation. In this study, we investigated the effect of NBP on the recovery from cardiac arrest and resuscitation in rats. Both pre-treatment and post-treatment of NBP were examined in a rat model of cardiac arrest and resuscitation.

2 Methods

2.1 Animals and Induction of Transient Global Ischemia

The experimental protocol was approved by the Animal Care and Use Committee at Case Western Reserve University. Male Wistar rats (3 months old) were randomly assigned to the following groups: sham non-arrested group, vehicle group (0.5 % Tween 80 was given orally, 400 mg/kg per day 7 days before cardiac arrest and 4 days post-resuscitation), NBP pre-treated group (NBP 80 mg/kg was given orally per day 7 days before cardiac arrest), and NBP post-treated group (NBP 80 mg/kg was given orally per day 4 days post-resuscitation). The concentration for NBP was 8 mg/ml in Tween 80. Transient global brain ischemia was achieved using a rat model of cardiac arrest and resuscitation as described previously [3]. In brief, rats were anesthetized with isoflurane and cannulae were placed in femoral artery and external jugular vein. Cardiac arrest was induced in the conscious rat by the rapid sequential intra-atrial injection of D-tubocurare (0.3 mg) and ice-cold KCl solution (0.5 M; 0.12 ml/100 g of body weight). Resuscitation was initiated at 7 min after arrest. The animal was orotracheally intubated and ventilation was begun simultaneously with chest compressions and the intravenous administration of normal saline. Once a spontaneous heart beat returned, epinephrine (4–10 μg) was administered intravenously, the animal was considered to be resuscitated when mean blood pressure was above 80 % of pre-arrest value. The duration of ischemia was about 12 min. After resuscitation, the oxygen content of the gas mixture was decreased to 25–30 % balanced with nitrogen. Ventilation was adjusted, on the basis of blood gases, to normal ranges until the rats regained their spontaneous

respiration. Non-arrested rats went through the same surgical procedures except cardiac arrest. Overall survival and hippocampal neuronal counts were determined at 4 days after resuscitation.

2.2 Hippocampal Neuronal Counts

Rats surviving 4 days and non-arrested controls were perfusion fixed with paraformaldehyde (4%). The brains were removed and embedded with paraffin and sectioned on a microtome. Neuronal cell counts were made from haematoxylin and eosin (H & E) stained 5 μm coronal sections through the anterior hippocampus. The entire length of the hippocampal pyramidal cell layer (at atlas plate 30 level [4]) was viewed under a high-power light microscope (magnification, 400×). Neurons with rounded cell bodies and clearly visible nucleoli were considered to have survived. The number of neurons surviving was evaluated in the CA1 region of the hippocampus [5].

2.3 Statistical Analysis

Data are expressed as mean ± SD. Statistical analyses were performed using SPSS V20 for Windows. The comparison between any two groups was analyzed with a t-test, and significance was considered at the level of $p < 0.05$.

3 Results

3.1 Physiological Variables

Body weight, mean arterial pressure (MAP), blood gases (pH, PaO_2 and $PaCO_2$) and hematocrit were measured before cardiac arrest and 1 h post-resuscitation (Table 4.1). There was no significant difference in any of the variables between the vehicle, NBP Pre-treated and NBP post-treated groups before arrest or post-resuscitation.

3.2 Overall Survival

Overall survival rates were examined for 4 days following cardiac arrest and resuscitation in resuscitated rats of the vehicle, NBP pre-treated and NBP post-treated groups. The majority of deaths of rats occurred within the first 2 days following

Table 4.1 Physiological variables before cardiac arrest and after resuscitation (mean ± SD)

Variables	Vehicle (n = 12)	NBP pre-treated (n = 10)	NBP post-treated (n = 7)
Body weight (g) pre 4 day post	354 ± 27 344 ± 38 (*n* = 6)	360 ± 22 350 ± 24 (n = 8)	341 ± 28 332 ± 35 (n = 6)
MAP (mmHg) pre 1 h post	114 ± 13 112 ± 19	110 ± 10 109 ± 17	113 ± 13 102 ± 19
pH (unit) pre 1 h post	7.42 ± 0.03 7.37 ± 0.06	7.41 ± 0.02 7.39 ± 0.04	7.41 ± 0.01 7.38 ± 0.05
PaO_2 (mmHg) pre 1 h post	92 ± 6 122 ± 23	93 ± 5 127 ± 31	94 ± 4 125 ± 25
$PaCO_2$ (mmHg) pre 1 h post	43 ± 2 39 ± 6	43 ± 3 38 ± 4	42 ± 2 37 ± 5
Hematocrit (%) pre 1 h post	46 ± 2 47 ± 4	48 ± 3 47 ± 3	47 ± 1 47 ± 4

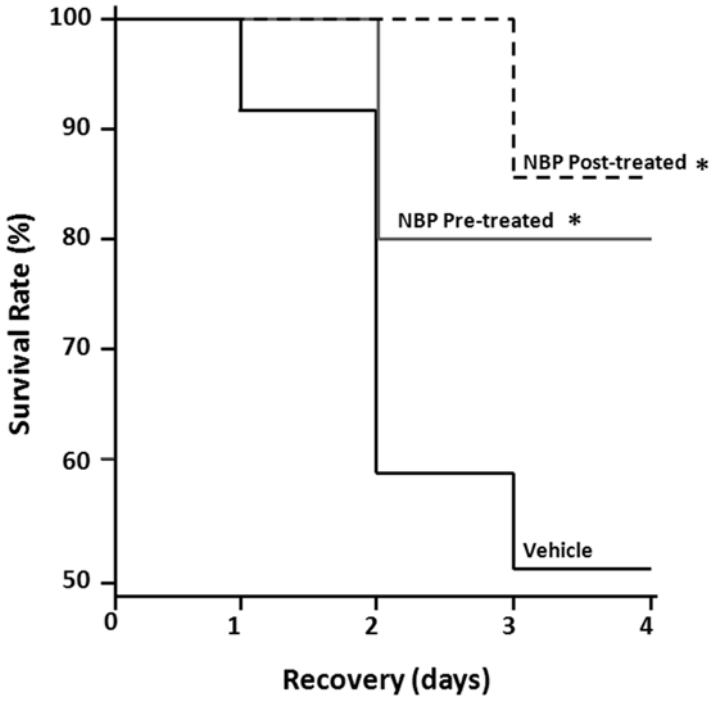

Fig. 4.1 Survival rates at 4 days following cardiac arrest and resuscitation. * indicates significant difference compared to the vehicle group ($p < 0.05$, Wilcoxon survival analysis)

resuscitation. The NBP pre-treated group and NBP post-treated group had a significantly higher survival rate (80 %, 8/10 and 86 %, 6/7, respectively) compared to that of the vehicle group (50 %, 6/12) (Fig. 4.1 and Table 4.2).

Table 4.2 Survival rates (4 days) after cardiac arrest and resuscitation

Experimental group	Number of death				Survival rate
	<1 day	1–2 days	2–3 days	3–4 days	4 days/total
Vehicle	1	4	1	0	50 % (6/12)
NBP pre-treated	0	2	0	0	80 % (8/10)[a]
NBP post-treated	0	0	1	0	86 % (6/7)[a]

[a]Indicates significant difference compared to the vehicle group ($p < 0.05$, Wilcoxon survival analysis)

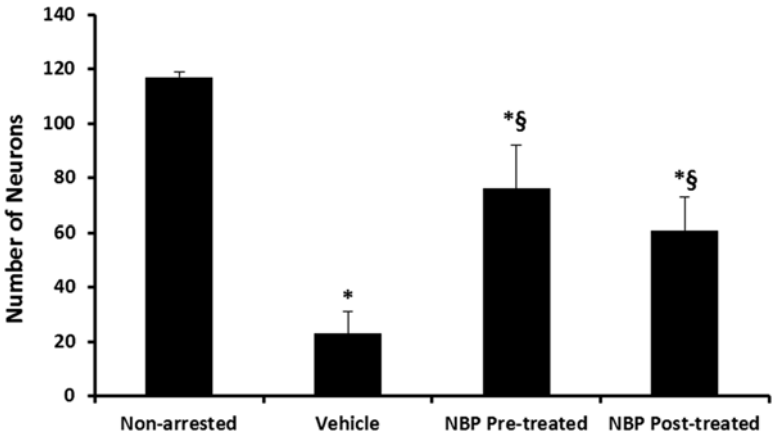

Fig. 4.2 Hippocampal neuronal counts 4 days following cardiac arrest and resuscitation. * indicates significant difference compared to the non-arrested control group ($p < 0.05$, t-test), § indicates significant difference compared to the vehicle group ($p < 0.05$, t-test)

3.3 Hippocampal Neuronal Counts

At 4 days of recovery, only about 20 % of the hippocampal CA1 neurons were preserved in the vehicle group (23 ± 8, $n = 12$) compared to the sham non-arrested group (117 ± 2, $n = 4$). The neuronal counts in the NBP pre-treated group and NBP post-treated group (76 ± 16, $n = 10$ and 61 ± 12, $n = 7$, respectively) were significantly higher than the counts in the vehicle group ($p < 0.05$). There was no difference between the NBP pre-treated group and NBP post-treated group (Fig. 4.2).

4 Discussion

High mortality and morbidity following cardiac arrest and resuscitation remain a globally significant public health problem. Subsequent death and residual neurologic deficit are primarily due to the reperfusion injury associated with oxidative stress caused by cardiac arrest and resuscitation. Long-term survival rates in humans after cardiac arrest and resuscitation are still disappointing and lack pharmaceutical treatment for improving outcome following cardiac arrest and resuscitation.

In this study, we examined the preventive and therapeutic effect of NBP on recovery following cardiac arrest and resuscitation in a rat model. Our data showed that both pre-treatment and post-treatment of NBP significantly improved the overall survival rate and the preservation of hippocampal CA1 neurons following cardiac arrest and resuscitation, suggesting the anti-oxidant properties of NBP and NBP could prevent and protect the brain against oxidative damage following cardiac arrest and resuscitation. The molecular mechanisms of potential protective effects include protecting endothelial cells against oxidative stress, mitochondrial damage and subsequent cell death [6, 7], enhancing angiogenesis associated with upregulation of vascular endothelial growth factor and HIF-1α expression [8], improvement of cerebral microvessels [9], inhibition of the inflammatory response [10] and maintaining the structure and morphology of neurons [11, 12].

In conclusion, NBP has both a preventive and therapeutic effect on improving outcomes following cardiac arrest and resuscitation, and NBP might be a potential treatment strategy for patients recovered from cardiac arrest and resuscitation.

Acknowledgments This study was supported by NIH grant NINDS 1 R01 NS46074. NBP was a gift from Shijiazhuang Pharma Grp NBP Co., LTD, Shijiazhuang, China.

References

1. Crumrine RC, LaManna JC (1991) Regional cerebral metabolites, blood flow, plasma volume, and mean transit time in total cerebral ischemia in the rat. J Cereb Blood Flow Metab 11(2):272–282
2. Xu K, Puchowicz MA, Sun X et al (2010) Decreased brainstem function following cardiac arrest and resuscitation in aged rat. Brain Res 1328:181–189
3. Xu K, LaManna JC (2009) The loss of hypoxic ventilatory responses following resuscitation after cardiac arrest in rats is associated with failure of long-term survival. Brain Res 1258:59–64
4. Paxinos G, Watson C (1998) The rat brain in stereotaxic coordinates, 4th edn. Academic Press, Inc., San Diego
5. Xu K, Puchowicz MA, Lust WD et al (2006) Adenosine treatment delays postischemic hippocampal CA1 loss after cardiac arrest and resuscitation in rats. Brain Res 1071(1):208–217
6. Chang Q, Wang XL (2003) Effects of chiral 3-n-butylphthalide on apoptosis induced by transient focal cerebral ischemia in rats. Acta Pharmacol Sin 24(8):796–804
7. Li L, Zhang B, Tao Y et al (2009) DL-3-n-butylphthalide protects endothelial cells against oxidative/nitrosative stress, mitochondrial damage and subsequent cell death after oxygen glucose deprivation in vitro. Brain Res 1290:91–101
8. Liao SJ, Lin JW, Pei Z et al (2009) Enhanced angiogenesis with dl-3n-butylphthalide treatment after focal cerebral ischemia in RHRSP. Brain Res 1289:69–78
9. Liu CL, Liao SJ, Zeng JS et al (2007) dl-3n-butylphthalide prevents stroke via improvement of cerebral microvessels in RHRSP. J Neurol Sci 260(1-2):106–113
10. Xu HL, Feng YP (2000) Inhibitory effects of chiral 3-n-butylphthalide on inflammation following focal ischemic brain injury in rats. Acta Pharmacol Sin 21(5):433–438
11. Ma S, Xu S, Liu B et al (2009) Long-term treatment of l-3-n-butylphthalide attenuated neurodegenerative changes in aged rats. Naunyn Schmiedebergs Arch Pharmacol 379(6):565–574
12. Peng Y, Xing C, Lemere CA et al (2008) l-3-n-Butylphthalide ameliorates beta-amyloid-induced neuronal toxicity in cultured neuronal cells. Neurosci Lett 434(2):224–229

Chapter 5
Hypoxia-Induced Let-7d Has a Role in Pericyte Differentiation

Nilufer Esen, Anuush Vejalla, Rakhi Sharma, Jesse S. Treuttner, and Paula Dore-Duffy

Abstract The microvascular pericyte is an important regulatory cell that maintains tissue homeostasis. One of the mechanisms by which pericytes maintain tissue homeostasis is through the induction of endogenous adaptative changes to stress signals. These adaptations include migration, differentiation and induction of angiogenesis. We have investigated pericyte responses to hypoxic stress (1 % O_2) and have reported that pericytes adapt to hypoxia, in part, through changes in endogenous and released microRNAs (miRNAs). Of those miRNAs, Let-7d plays an important role. We exposed pericytes to hypoxia with and without basic fibroblast growth factor (bFGF) in stem cell medium. The expression of Let-7d in pericyte-derived neurospheres was determined. Evidence of differentiation was determined by immunocytochemistry. Hypoxia enhanced pericyte spheres were positive for Let-7d. The transcription factor Sox2, a marker of cell differentiation, was also induced in pericytic spheres. Taken together, our results suggest that pericyte expression of Let-7d in response to hypoxia and bFGF is involved in pericyte differentiation. Thus, for the first time, we propose a pathway for induction of pericyte differentiation. Modulation of this pathway in pericytes may be an important target in tissue repair.

Keywords Pericytes • microRNA • Let-7d • Hypoxia • Differentiation

N. Esen, M.D. (✉)
Department of Neurology, Medical School, Wayne State University,
Elliman Building, Rm 3125, 421 E. Canfield Str., Detroit, MI 48201, USA
e-mail: nesenbil@med.wayne.edu

A. Vejalla • R. Sharma • P. Dore-Duffy
Department of Neurology, Wayne State University, Detroit, MI, USA

J.S. Treuttner
Department of Neurological Surgery, Miller School of Medicine, University of Miami,
Miami, FL, USA

© Springer International Publishing Switzerland 2016

Q. Luo et al. (eds.), *Oxygen Transport to Tissue XXXVIII*, Advances in
Experimental Medicine and Biology 923, DOI 10.1007/978-3-319-38810-6_5

1 Introduction

MiRNAs are small noncoding RNAs that repress target gene expression by binding to the 3′-untranslated region or UTRs of mRNA targets [1]. They regulate diverse biological functions including differentiation, proliferation and cell death [2–6]. Many of the identified miRNAs are highly conserved within species. An example of this is the Let-7 family [7, 8] shown to have a central role in the regulation of development, proliferation and differentiation [9]. Let-7 increases during stem cell differentiation and may have a role in regulation of differentiation of the adult stem cell, the microvascular pericyte [10–12].

The pericyte is a regulatory cell that maintains vascular function and tissue homeostasis [10, 11]. One of the mechanisms by which pericytes maintain vascular homeostasis is through the induction of endogenous adaptative changes to stress signals. These adaptations include migration, differentiation and induction of angiogenesis [13–15]. Pericyte differentiation is increased following stress. We reported that pericyte adaptation to hypoxic stress (1 % O_2) included changes in miRNAs [16]. Let-7 family members were significantly increased in response to hypoxia. Pericytes cultured with bFGF differentiate to neurospheres over a 3-week period. Spheres expressed Let-7d and the transcription factor SOX2. Results suggest that pericyte Let-7d is involved in differentiation.

2 Methods

2.1 Isolation of Primary Pericytes

Microvessels were isolated from cortical brain [17]. Tissue was harvested and homogenized in shaved Dounce homogenizers. Fat was removed and vessels collected on micromesh sieves of 80 and 40 μm porosity. Microvessels were enzymatically disrupted and single cell suspensions prepared. Pure pericytes were isolated by differential adhesion or by flow cytometry for platelet derived growth factor β Receptor (PDGFβR) positive cells.

2.2 Induction of Sphere Formation

Pericytes were plated in 35-mm Petri dishes in medium [(DMEM/F12 with N2 supplement, no serum containing 20 ng/mL murine recombinant bFGF (Gibco, Grand Island, NY, USA)]. The number of free-floating spheres was counted after varying days in culture. Spheres were cultured on poly-L-ornithine (Poly-O)-coated glass coverslips for immunocytochemistry.

2.3 In Vitro Exposure to Hypoxia

A GasPak 100 system (Becton Dickinson, Sparks, MD, USA) consisting of hydrogen and carbon dioxide generating envelops and polycarbonate anaerobic jar, disposable methylene blue indicator and catalyst chambers containing palladium catalyst pellets, were used. Cells were incubated in the hypoxia chambers for varying periods of time. Time zero was defined at that time when the methylene blue indicator changed color.

2.4 Isolation of miRNAs and Quantitative RT-PCR

Total RNA was extracted using RNAse easy plus MiRNA isolation kit (Qiagen, Valencia, CA, USA) and analyzed on Paraflow microfluidic chips containing 388 known rat miRNAs (LC Sciences). Expression of Let-7d was confirmed by qRT-PCR. Results are shown as fold change verses control cultures. U6, a small conserved non-coding nucleolar RNA, was used as the endogenous control for all samples.

2.5 Immunohistochemistry

Spheres were fixed in 4 % paraformaldehyde, and permeabilized with 0.01 % Triton X-100 then stained with primary antibodies GFAP, NF200 (both from Sigma, St Louis, MO, USA), O4 (Chemicon International, Temecula, CA, USA) for 30 min at room temperature, washed then incubated with fluorochrome-conjugated secondary antibody as appropriate. Secondary antibody alone and/or isotype control antibody was used as a control.

3 Results

We have investigated the pericyte response to hypoxic stress and have reported that primary pericytes adapt to hypoxia, in part, through changes in endogenous and released microRNAs (miRNAs) [16]. Micro-array analysis was used to examine the expression of 388 rat miRNAs in primary rat cortical pericytes with and without exposure to low oxygen (1 %) after 24 or 48 h. Pericytes subjected to hypoxia showed 27 miRNAs that were higher than control, and 31 that were lower [16]. Among those, Let-7 family members and especially the Let-7d, which were shown to have a role in the regulation of cellular growth and differentiation, were induced significantly as seen in Fig. 5.1, which is the partial presentation of previously published data [16]. Because Let-7 has been shown to have a role in cell differentiation we questioned whether hypoxia induced Let-7 may be involved in increased stem cell activity.

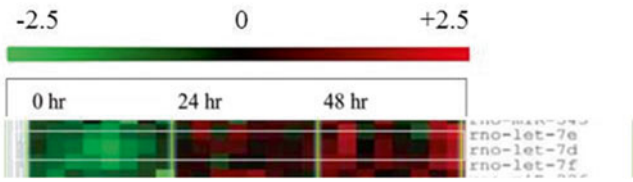

Fig. 5.1 Partial representation of previously published heat map of miRNAs [16] that showed significant ($p<0.01$) differences between control, 24 h hypoxia, and 48 h hypoxia groups. *Red* indicates upregulation over control groups and *green* indicates downregulation

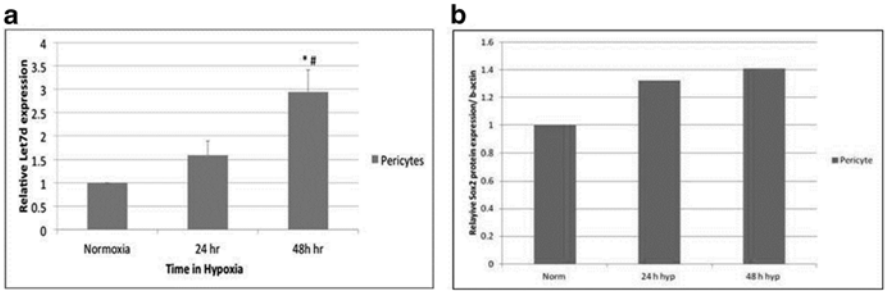

Fig. 5.2 (**a**) Hypoxia induced Let-7d expression was confirmed with qRT-PCR using ABI Assays-on-Demand™ Taqman kits, and the levels of Let-7d were calculated after normalizing cycle thresholds against the "housekeeping" gene U6 and are presented as the fold-induction ($2^{-\Delta\Delta Ct}$) value relative to normoxic pericytes (mean ± SD). *Asterisk* denotes the significant differences between normoxic and the hypoxic cells ($*P<0.05$), while the pound sign denotes difference between 24 h vs. 48 h hypoxia ($\#P<0.05$). (**b**) Bar graphs represent the SOX2 protein expression evaluated by Western blotting, and quantitated by densometric scanning of the films. For quantitation, the pixel intensity of each SOX2 band from pericytes was normalized to the amount of actin included as a "housekeeping" gene

To confirm these microarray findings, we performed qRT-PCR and found that the hypoxia induced expression of Let-7d in mouse pericytes as well, in a time dependent manner (Fig. 5.2a). In addition, when we evaluated the effect of hypoxia on the differentiation antigen SOX2, we found that hypoxia also enhanced the expression of SOX2 protein in pericytes (Fig. 5.2b). These data suggested that hypoxia stimulates pericyte differentiation.

In second series of experiments, we examined Let-7 expression in bFGF stimulated pericyte spheres. In the absence of bFGF, there was no sphere formation. Spheres express neurofilament (NF), glial fibrillary acidic protein (GFAP), and the oligodendrocyte marker 04 confirming (Fig. 5.3) [11] differentiating pericytes towards glial and neuronal lineages. Spheres expressed Let-7d (Fig. 5.4). Results showed that the transcription factor SOX2, another marker of cell differentiation, was induced in pericytes spheres (Fig. 5.5). Taken together, our results suggest that Let-7d is involved in pericyte differentiation.

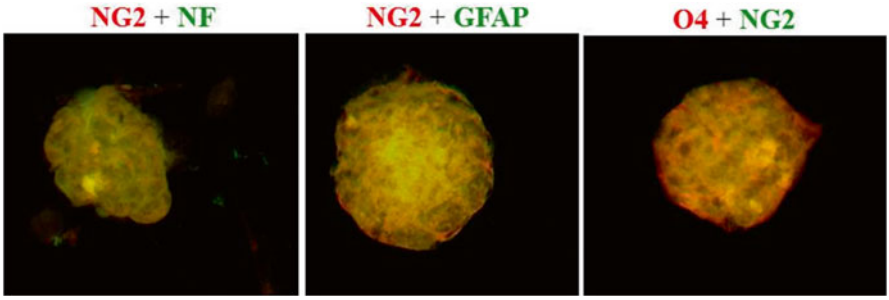

Fig. 5.3 Spheres were stained with PE conjugated NG2 or O4, and FITC conjugated GFAP, NF or NG2 antibodies. Pictures were taken using 40× magnification

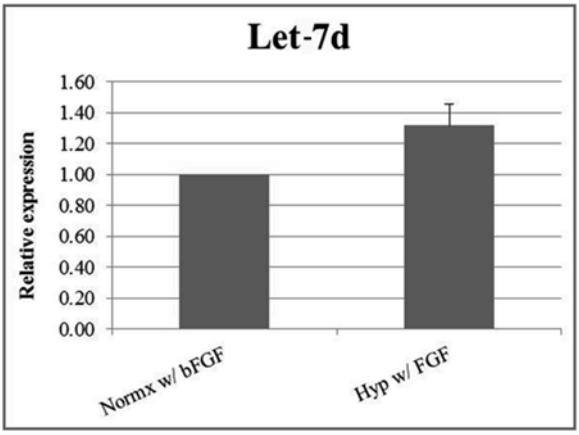

Fig. 5.4 Hypoxia has induced Let-7d in sphere forming microvessels. Let-7d were calculated after normalizing cycle thresholds against the "housekeeping" gene U6 and are presented as the fold-induction ($2^{-\Delta\Delta Ct}$) value relative to normoxic pericytes

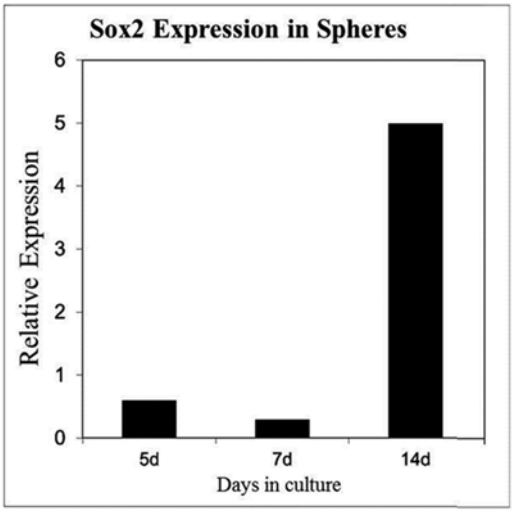

Fig. 5.5 SOX2 expression is induced in sphere forming pericytes as shown by qRT-PCR. The levels of SOX2 gene were calculated after normalizing cycle thresholds against the "housekeeping" gene GAPDH and are presented as the fold-induction ($2^{-\Delta\Delta Ct}$) value

4 Conclusion

In conclusion, for the first time, we propose a pathway for induction of pericyte differentiation in response to hypoxic stress. Modulation of this pathway in the pericyte may be an important target in tissue repair and therapeutics.

Acknowledgments We wish to thank the Eugene Applebaum Foundation, and Wayne State University for funding used to conduct these studies.

References

1. Lee RC, Feinbaum RL, Ambros V (1993) The C. elegans heterochronic gene lin-4 encodes small RNAs with antisense complementarity to lin-14. Cell 75(5):843–854
2. Bussing I, Slack FJ, Grosshans H (2008) let-7 microRNAs in development, stem cells and cancer. Trends Mol Med 14(9):400–409
3. Jovanovic M, Hengartner MO (2006) miRNAs and apoptosis: RNAs to die for. Oncogene 25(46):6176–6187
4. Schickel R, Boyerinas B, Park SM et al (2008) MicroRNAs: key players in the immune system, differentiation, tumorigenesis and cell death. Oncogene 27(45):5959–5974
5. Stefani G, Slack FJ (2008) Small non-coding RNAs in animal development. Nat Rev Mol Cell Biol 9(3):219–230
6. Boyerinas B, Park SM, Hau A et al (2010) The role of let-7 in cell differentiation and cancer. Endocr Relat Cancer 17(1):F19–F36
7. Pasquinelli AE, Reinhart BJ, Slack F et al (2000) Conservation of the sequence and temporal expression of let-7 heterochronic regulatory RNA. Nature 408(6808):86–89
8. Reinhart BJ, Slack FJ, Basson M et al (2000) The 21-nucleotide let-7 RNA regulates developmental timing in Caenorhabditis elegans. Nature 403(6772):901–906
9. Roush S, Slack FJ (2008) The let-7 family of microRNAs. Trends Cell Biol 18(10):505–516
10. Dore-Duffy P (2008) Pericytes: pluripotent cells of the blood brain barrier. Curr Pharm Des 14(16):1581–1593
11. Dore-Duffy P, Katychev A, Wang X et al (2006) CNS microvascular pericytes exhibit multipotential stem cell activity. J Cereb Blood Flow Metab 26(5):613–624
12. Dore-Duffy P, Mehedi A, Wang X et al (2011) Immortalized CNS pericytes are quiescent smooth muscle actin-negative and pluripotent. Microvasc Res 82(1):18–27
13. Dore-Duffy P, LaManna JC (2007) Physiologic angiodynamics in the brain. Antioxid Redox Signal 9(9):1363–1371
14. LaManna JC (1992) Rat brain adaptation to chronic hypobaric hypoxia. Adv Exp Med Biol 317:107–114
15. LaManna JC, Chavez JC, Pichiule P (2004) Structural and functional adaptation to hypoxia in the rat brain. J Exp Biol 207(Pt 18):3163–3169
16. Truettner JS, Katyshev V, Esen-Bilgin N et al (2013) Hypoxia alters MicroRNA expression in rat cortical pericytes. Microrna 2(1):32–44
17. Dore-Duffy P (2003) Isolation and characterization of cerebral microvascular pericytes. Methods Mol Med 893:75–82

Chapter 6
Magnification of Cholesterol-Induced Membrane Resistance on the Tissue Level: Implications for Hypoxia

Ryan Shea, Casey Smith, and Sally C. Pias

Abstract High cellular membrane cholesterol is known to generate membrane resistance and reduce oxygen (O_2) permeability. As such, cholesterol may contribute to the Warburg effect in tumor cells by stimulating intracellular hypoxia that cannot be detected from extracellular oxygen measurements. We probe the tissue-level impact of the phenomenon, asking whether layering of cells can magnify the influence of cholesterol, to modulate hypoxia in relation to capillary proximity. Using molecular dynamics simulations, we affirm that minimally hydrated, adjacent lipid bilayers have independent physical behavior. Combining this insight with published experimental data, we predict linearly increasing impact of membrane cholesterol on oxygen flux across cells layered in tissue.

Keywords Cholesterol • Cancer • Molecular dynamics simulation • Oxygen bioavailability • Kinetics

1 Introduction

Here, we consider intracellular oxygen bioavailability and the potential impact of membrane resistance as a hindrance to oxygen flux. In particular, we examine the kinetics of oxygen transport across a series of several membranes, relevant to cells buried between capillaries, especially within tumors.

R. Shea
Department of Chemistry, New Mexico Institute of Mining and Technology (New Mexico Tech), 801 Leroy Place, Socorro, NM 87801, USA

Department of Mathematics, Chemistry, and Physics, West Texas A&M University, Canyon, TX, USA

C. Smith • S.C. Pias (✉)
Department of Chemistry, New Mexico Institute of Mining and Technology (New Mexico Tech), 801 Leroy Place, Socorro, NM 87801, USA
e-mail: spias@nmt.edu

© Springer International Publishing Switzerland 2016

Q. Luo et al. (eds.), *Oxygen Transport to Tissue XXXVIII*, Advances in Experimental Medicine and Biology 923, DOI 10.1007/978-3-319-38810-6_6

Several investigations provide valuable evidence that oxygen flux is reduced by substantial membrane cholesterol incorporation. Swartz and colleagues [1] demonstrated, using electron paramagnetic resonance (EPR) oximetry, that cultured mammalian cell lines with distinct membrane cholesterol levels differ in intracellular oxygenation. Using a technique that differentiates intra- and extracellular oxygen measurements, the group showed that an oxygen gradient could be observed across the plasma membrane. Assays were performed on three Chinese hamster ovary (CHO) cell lines with phenotypic differences in cholesterol metabolism and plasma membrane cholesterol level. The magnitude of the oxygen gradient increased with the plasma membrane cholesterol concentration. Manipulation of the cholesterol level in the cell lines, likewise, influenced the gradient, with increasing cholesterol content tending to decrease intracellular oxygenation relative to extracellular [1].

Such a gradient could arise if the rate of oxygen consumption exceeded the rate of replenishment. Thus, the work suggests that high-cholesterol plasma membranes can present a measureable barrier to oxygen transport. We especially note from the CHO cell study that plasma membrane cholesterol content can influence intracellular oxygenation in a manner not directly interpretable from extracellular measurements.

The view of high-cholesterol cell membranes as a barrier is further affirmed in studies of red blood cell (RBC) oxygenation by Buchwald and colleagues [2, 3]. Specifically, the rate of oxygen uptake and release declines with the plasma membrane cholesterol content of RBCs [3]. As a result, RBC oxygen saturation is diminished, and oxygen release upon demand is diminished [2]. The authors propose that angina pectoris in patients with hypercholesterolemia may be caused partly by reduced oxygen release from RBCs with elevated membrane cholesterol, contributing to heart muscle hypoxia and painful lactic acid buildup [3].

These studies, together, present compelling evidence that high-cholesterol membranes present a *kinetic* barrier to oxygen transport. Biophysical experiments with EPR oximetry reinforce this view. Subczynski and colleagues have found that cholesterol reduces the membrane oxygen permeability coefficient (a descriptor of flux) by several-fold, compared with phospholipid alone [4, 5]. Given this resistance to oxygen transport, Brown and Galea previously suggested that cholesterol may contribute to the Warburg effect in cancer cells [6]. Indeed, the existing evidence strongly implies that intracellular hypoxia is possible, even when extracellular oxygen is abundant.

We investigate the tissue-level impact of reduced oxygen flux through cholesterol-rich membranes. We do so by examining the structural and functional independence of bilayers placed very close together, representing direct juxtaposition of plasma membrane segments in layered cells. We combine the results with experimentally derived flux information to predict how plasma membrane cholesterol impacts oxygen bioavailability within tissue, given the necessity of crossing multiple membranes to reach mitochondria in cells buried between capillaries.

2 Methods

We have used all-atom molecular dynamics simulations of two adjacent bilayers separated by a thin water layer to calculate electron density and oxygen diffusional free energy profiles. All simulations used the GPU/CUDA-accelerated implementation [7] of the Amber 14 or Amber 12 biomolecular simulation software [8, 9], along with the Lipid14 force field [10] and a cholesterol extension by Ross Walker and Benjamin Madej [11]. We developed O_2 parameters in our laboratory, defining the bond length as 1.21 Å from the CRC Handbook [12], with a vibrational force constant of 849.16 kcal/mol•Å^2 based on Raman spectroscopic measurements [13] and with all other parameters defined the same as the carbonyl oxygen (oC) atom type in Lipid11 [14].

Lipid bilayers were constructed initially using the CHARMM-GUI membrane builder [15, 16]. A bilayer containing 1-palmitoyl-2-oleoylphosphatidylcholine (POPC) and cholesterol in a 1:1 ratio was built with 128 lipids total, including 32 POPC and 32 cholesterol molecules per leaflet and was pre-equilibrated for 500 ns using the GAFFLipid force field [17] with the Lipid11 cholesterol parameters [14]. The Lipid14 force field [10] with a cholesterol extension by Ross Walker and Benjamin Madej [11] was used throughout the remaining simulations. The pre-equilibrated POPC/cholesterol system was further equilibrated for 200 ns with this force-field combination. Its closest 15 water molecules per lipid molecule ("per lipid") were retained using the AmberTools [8] program CPPTRAJ [18], and this minimally hydrated POPC/cholesterol structure was used as the starting configuration for "double bilayer" simulations.

All simulations used the TIP3P water model [19]. Through trial-and-error, we established that bilayers separated by 15 waters per lipid remained structurally distinct, while bilayers separated by only 10 waters per lipid showed physical fusion behavior early in the simulations.

Bonds to hydrogen were constrained using the SHAKE algorithm [20], allowing a 2-fs timestep. A constant temperature of 310 K (37 °C) was maintained using Langevin dynamics with a collision frequency of 1 ps^{-1} during the equilibration phases and using the Berendsen thermostat [21] during the production phase. A constant pressure of 1 atm was maintained using the Berendsen barostat [21] during the pre-equilibration and the Monte Carlo barostat (as implemented in Amber 14) thereafter.

A POPC bilayer was constructed with CHARMM-GUI, including 15 waters per lipid. This bilayer was size-matched with the pre-equilibrated POPC/cholesterol structure described above, based on an expected POPC area per lipid calculated from previous simulations. This surface-area matching called for 82 POPC lipids, with 41 in each leaflet. We used PackMol [22] to place the POPC bilayer close to the pre-equilibrated POPC/cholesterol bilayer. This double bilayer system was minimized over 20,000 steps, heated from 100 to 310 K over 100 ps, then equilibrated for 200 ns prior to adding oxygen.

O_2 molecules were introduced by replacing water molecules between the bilayers, and the double bilayer systems with oxygen were minimized and heated in the same manner as above, while applying a Cartesian restraint on the O_2 molecules with a force constant of 5 kcal/mol•Å^2. An O_2 concentration of 200 mM was used for the entire molecular system (water and lipid). Though higher than the concentration of air-equilibrated water (approximately 200 μM), this concentration allows the O_2 molecules to diffuse independently while facilitating rapid sampling of the O_2 configurational space [see also 23]. Production simulations were run without restraints for 300 ns.

Free energy and electron density profiles were calculated using CPPTRAJ. The free energy was calculated at 1-Å intervals (bins) along the bilayer normal, z, following the approach of Marrink and Berendsen that applies the relationship $G(z) = -\mathrm{RT}\ \ln\{C(z)/C_{\max}\}$, where $C(z)$ is the O_2 population of a given z bin and $C_{\max}$ is the population of the most populated bin [24].

3 Results and Discussion

The constituent POPC and POPC/cholesterol bilayers in the minimally hydrated "double bilayer" system remain structurally independent. As such, the electron density and free energy profiles of both bilayers (Fig. 6.1) closely resemble those calculated in our laboratory for single bilayer systems (data not shown). This observation agrees with prior experimental work demonstrating that the structural distinctness of lipid bilayers is maintained by headgroup-associated hydration repulsion [reviewed in 25]. Thus, we treat each bilayer as having independent oxygen transport behavior in the analysis that follows.

Subczynski and colleagues found in EPR oximetry studies that incorporation of cholesterol in a 1:1 ratio with phospholipid results in a three- to five-fold reduction in the permeability coefficient for oxygen flux [4, 5]. Based on free energy barriers alone and not accounting for the diffusional/collisional behavior of oxygen, we predict a rate reduction of the same order of magnitude as the EPR study (data not shown). We recently have investigated the impact of higher cholesterol concentrations on oxygen transport and have found a consistent decrease in the predicted rate of oxygen transport with modest increases in cholesterol content (publication forthcoming).

Yet, what is the tissue-level impact of membrane resistance? To reach mitochondria, oxygen must diffuse across a minimum of two cholesterol-containing membranes—namely, the plasma membrane of the red blood cell and the plasma membrane of the target cell. Endothelial cell membranes may also intercede, presenting an additional barrier if the cholesterol content is substantial. For cells buried between capillaries, oxygen will then diffuse via the path of least resistance until it reaches its site of consumption. Assuming highly permeable cellular membranes, it seems likely that the most favorable path will normally involve passage from membrane to membrane [26, 27], as the membrane interior provides a low-energy environment for oxygen (observable in Fig. 6.1).

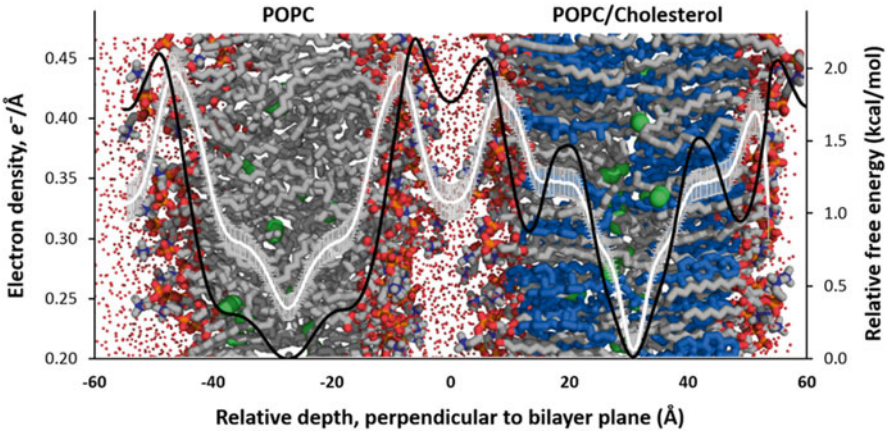

Fig. 6.1 Electron density and free energy profiles are independent for hydrated bilayers in close proximity. The image shows a double bilayer system image overlaid with electron density (*white line*) and relative free energy (*black line*) plotted against relative depth perpendicular to the bilayer plane. The *left* bilayer contains only POPC, and the *right* contains POPC and cholesterol in a 1:1 ratio. The bars on the electron density *curve* indicate the standard deviation. Both curves were calculated from a single trajectory, covering 300 ns of production. The small *red points* indicate the positions of explicit water molecules, simplified for clarity. Bilayers: POPC carbon atoms—*gray*, cholesterol carbon atoms—*blue*, O_2 molecules—*green* spheres. All hydrogen atoms omitted for clarity

If oxygen were required to pass through several membranes, the rate of diffusion would be reduced in proportion to the number of resistant membranes. Supposing a series of equally resistant membranes, we predict the kinetic impact of passing oxygen across several cell layers. Figure 6.2 projects the cumulative effect on oxygen flux when several cholesterol-rich membranes are traversed, assuming a three- or five-fold reduction in permeability per membrane. The overall rate impact is expected to depend linearly on the number of membranes crossed and on the magnitude of resistance presented by each membrane. In the case that an individual membrane reduces oxygen permeability by three-fold, ten sequential membranes are anticipated to decrease oxygen flux by 30-fold, reaching 1/30 or roughly 3 % of the unhindered flux.

The above analysis describes a "worst-case scenario" for oxygen diffusion across cholesterol-rich tissues. In actual tissue, it is likely that oxygen may find alternative, lower-resistance paths for diffusion that avoid some of the large energy barriers presented by cholesterol-rich membranes. For example, oxygen may pass around cells through the extracellular space. Thus, the degree of overall flux reduction may be lower than predicted with our current model. Even if diffusion through extracellular space were possible, the diffusional path-length required for avoiding passage across resistant cells would increase relative to the membrane-to-membrane diffusion scenario, generating a reduction in flux proportional to the path-length. Further modeling that takes the possibility of diffusion through extracellular space into account may be informative.

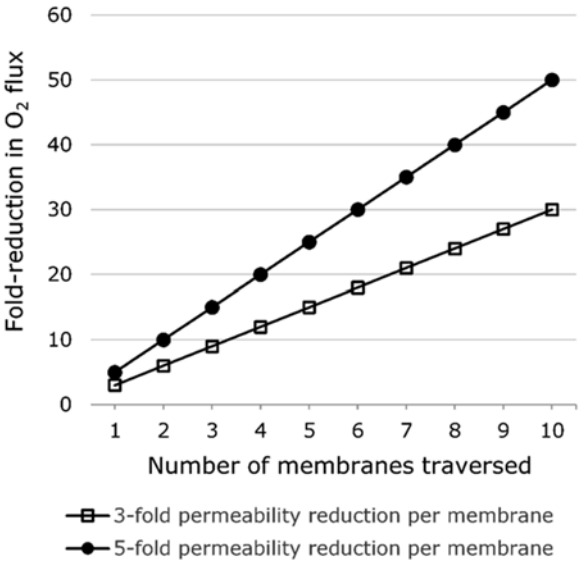

Fig. 6.2 Predicted magnification of flux reduction as O_2 traverses multiple cell layers

It is also important to note that our model greatly simplifies the structure of biological membranes. We have examined membranes incorporating only POPC phospholipid and cholesterol, while actual membranes incorporate many other types of phospholipid, along with substantial amounts of protein. Membrane proteins, like cholesterol, may reduce the permeability of membrane lipids, and the proteins, themselves, may have very low oxygen permeability [4, 28, 29]. Further, we have assumed compositional homogeneity across the leaflets of the bilayer, while plasma membranes are known to differ in the lipid composition of the extracellular and intracellular leaflets. We plan to address such complexities of cellular membrane structure in future modeling work. Moreover, we intend to use our models in conjunction with oxygen measurements in living cells, under conditions predicted by the models to influence intracellular oxygenation.

4 Conclusion

The capacity of cholesterol-rich cellular membranes to hinder oxygen diffusion may result in intracellular hypoxia not discernable from extracellular measurements. Even modest reduction of flux across a single membrane could substantially impact tissue oxygenation, due to magnification of the rate effect when oxygen must traverse several membranes or navigate around intervening cells.

Acknowledgments Financial support for this project was provided by the NM-INBRE program, which is funded by National Institutes of Health grant P20GM103451 through NIGMS. Further financial support was generously provided by the Glendorn Foundation. The project used computing resources of the Extreme Science and Engineering Discovery Environment (XSEDE), which is supported by National Science Foundation grant number ACI-1053575. We thank Snežna Rogelj for her ongoing inspiration and biological insight, Jeff Altig for helpful conversations, and Ryan Bredin for developing our O_2 force field parameters. We gratefully acknowledge Ross Walker and Benjamin Madej for providing advance access to their updated cholesterol force field parameters. Finally, we appreciate the thoughtful review of our manuscript by members of the International Society on Oxygen Transport to Tissue (ISOTT).

References

1. Khan N, Shen J, Chang TY et al (2003) Plasma membrane cholesterol: a possible barrier to intracellular oxygen in normal and mutant CHO cells defective in cholesterol metabolism. Biochemistry 42(1):23–29
2. Steinbach JH, Blackshear PL, Varco RL, Buchwald H (1974) High blood cholesterol reduces in vitro blood oxygen delivery. J Surg Res 16(2):134–139
3. Menchaca HJ, Michalek VN, Rohde TD et al (1998) Decreased blood oxygen diffusion in hypercholesterolemia. Surgery 124(4):692–698
4. Widomska J, Raguz M, Subczynski WK (2007) Oxygen permeability of the lipid bilayer membrane made of calf lens lipids. Biochim Biophys Acta 1768(10):2635–2645
5. Subczynski WK, Hyde JS, Kusumi A (1989) Oxygen permeability of phosphatidylcholine-cholesterol membranes. Proc Natl Acad Sci 86(12):4474–4478
6. Galea AM, Brown AJ (2009) Special relationship between sterols and oxygen: were sterols an adaptation to aerobic life? Free Radic Biol Med 47(6):880–889
7. Salomon-Ferrer R, Götz AW, Poole D et al (2013) Routine microsecond molecular dynamics simulations with AMBER on GPUs. 2. Explicit solvent particle mesh Ewald. J Chem Theory Comput 9(9):3878–3888
8. Case DA, Berryman JT, Betz RM et al (2015) AMBER 2015. University of California, San Francisco
9. Case DA, Darden TA, Cheatham TE III et al (2012) AMBER 12. University of California, San Francisco
10. Dickson CJ, Madej BD, Skjevik AA et al (2014) Lipid14: the Amber lipid force field. J Chem Theory Comput 10(2):865–879
11. Madej B, Gould IR, Walker RC (2015) A parameterization of cholesterol for mixed lipid bilayer simulation within the Amber Lipid14 force field. J Phys Chem B 119(38): 12424–12435
12. Weast RC (ed) (1986) CRC Handbook of Chemistry and Physics, 67th edn. The Chemical Rubber Co., Boca Raton
13. Herzberg G, Spinks JWT (1950) Molecular Spectra and Molecular Structure: Diatomic Molecules, vol 1. van Nostrand, New York
14. Skjevik AA, Madej BD, Walker RC, Teigen K (2012) LIPID11: a modular framework for lipid simulations using Amber. J Phys Chem B 116(36):11124–11136
15. Jo S, Kim T, Iyer VG, Im W (2008) CHARMM-GUI: a web-based graphical user interface for CHARMM. J Comput Chem 29(11):1859–1865
16. Jo S, Lim JB, Klauda JB, Im W (2009) CHARMM-GUI membrane builder for mixed bilayers and its application to yeast membranes. Biophys J 97(1):50–58
17. Dickson CJ, Rosso L, Betz RM et al (2012) GAFFlipid: a General Amber Force Field for the accurate molecular dynamics simulation of phospholipid. Soft Matter 8(37):9617

18. Roe DR, Cheatham TE (2013) PTRAJ and CPPTRAJ: software for processing and analysis of molecular dynamics trajectory data. J Chem Theory Comput 9(7):3084–3095
19. Jorgensen WL, Chandrasekhar J, Madura JD et al (1983) Comparison of simple potential functions for simulating liquid water. J Chem Phys 79(2):926
20. Ryckaert J-P, Ciccotti G, Berendsen HJ (1977) Numerical integration of the Cartesian equations of motion of a system with constraints: molecular dynamics of n-alkanes. J Comput Phys 23(3):327–341
21. Berendsen HJC, Postma JPM, van Gunsteren WF et al (1984) Molecular dynamics with coupling to an external bath. J Chem Phys 81(8):3684
22. Martinez L, Andrade R, Birgin E, Martinez J (2009) Packmol: a package for building initial configurations for molecular dynamics simulations. J Comput Chem 30:2157–2164
23. Wang Y, Cohen J, Boron WF et al (2007) Exploring gas permeability of cellular membranes and membrane channels with molecular dynamics. J Struct Biol 157(3):534–544
24. Marrink S-J, Berendsen HJC (1994) Simulation of water transport through a lipid membrane. J Phys Chem 98(15):4155–4168
25. Schneck E, Sedlmeier F, Netz RR (2012) Hydration repulsion between biomembranes results from an interplay of dehydration and depolarization. Proc Natl Acad Sci 109(36): 14405–14409
26. Dutta A, Popel AS (1995) A theoretical analysis of intracellular oxygen diffusion. J Theor Biol 176(4):433–445
27. Sidell BD (1998) Intracellular oxygen diffusion: the roles of myoglobin and lipid at cold body temperature. J Exp Biol 201(Pt 8):1119–1128
28. Ashikawa I, Yin JJ, Subczynski WK et al (1994) Molecular organization and dynamics in bacteriorhodopsin-rich reconstituted membranes: discrimination of lipid environments by the oxygen transport parameter using a pulse ESR spin-labeling technique. Biochemistry 33(16): 4947–4952
29. Kawasaki K, Yin JJ, Subczynski WK et al (2001) Pulse EPR detection of lipid exchange between protein-rich raft and bulk domains in the membrane: methodology development and its application to studies of influenza viral membrane. Biophys J 80(2):738–748

Chapter 7
Respiratory Pores on Ostrich *Struthio camelus* (Aves: Struthionidae) Eggshells

T. Koyama and A.J.D. Tennyson

Abstract Respiratory pores are essential for the survival of the embryo within the eggshell. Distribution patterns of such pores on ostrich (*Struthio camelus*) eggshells show remarkable variations in bird group. Eggshells preserved in the museum of New Zealand have long, superficial, winding grooves and ridges, with pores distributed densely in the bottom of grooves. Both the grooves and ridges that separate them are twisted. By contrast, the surfaces of eggs from farmed ostriches are mostly smooth, with only occasional, short grooves, and respiratory pores distributed more evenly. The cause of ridging and grooving of the surface of eggs from wild birds is unclear but may be due to the need for stronger shells and effects of environmental stresses. It appears that the arrangement of respiratory pores on ostrich eggshells seems to be changeable by surrounding stresses.

Keywords Ostrich • Eggshell • Respiratory pores • Acclimatization

1 Introduction

All animal species have developed respiratory systems appropriate to their needs. For example, dragonfly (*Oligoaeshna pryeri/Sararaeschna pryeri* (Martin, 1909)) eggs have numerous micro (respiratory) pores through the cuticle wall. These pores, 74 nm in diameter are densely distributed on the inner surface of dragonfly eggshells and occupy 0.17 % of the total surface area [1].

Avian eggs have calcified shells which are perforated by pores that allow gas exchange between the embryo and the atmosphere. The average diameter of a single respiratory pore in an ostrich (*Struthio camelus*) eggshell has been reported to be

T. Koyama (✉)
Hokkaido University, Sapporo, Hokkaido, Japan
e-mail: Tomkoyamajp@yahoo.co.jp

A.J.D. Tennyson
Museum of New Zealand Te Papa Tongarewa, Wellington, New Zealand

© Springer International Publishing Switzerland 2016

Q. Luo et al. (eds.), *Oxygen Transport to Tissue XXXVIII*, Advances in Experimental Medicine and Biology 923, DOI 10.1007/978-3-319-38810-6_7

107 μm and the surface area of the pores in ostrich eggshells has been found to occupy 0.11 % of the total shell surface area [2, 3]. Ostriches evolved in the dry, hot African environment but recently they have been domesticated in farms throughout many parts of the world, sometimes in very different environments. In the present communication we compare surface morphology of the eggshells from presumed wild and farmed ostriches.

2 Materials and Method

Ostrich eggshell surfaces were examined by visual inspection and recorded photographically. Distribution of the respiratory pores was studied on the equators of the eggshells with each external surface pore being counted on five squares of 1×1 cm^2. Three groups of eggs were studied: Group 1: Five eggs that lacked collection data (numbered 25752, 25753, 25754, 25755, 25757) were assumed to be of wild origin in the Museum of New Zealand Te Papa Tongarewa, Wellington; they had been in the collection of the museum for decades so were presumed to have come from wild African birds although the species was farmed in New Zealand as far back as the 1880s (http://www.teara.govt.nz/en/exotic-farm-animals/page-4), website viewed 14 Oct 2014. Group 2: three eggs laid in Japanese ostrich farms in Dacho (= Japanese word for ostrich) kingdom, Ishioka, Ibaraki near Tokyo and Group 3: two eggs from farms in Kagoshima, south Japan. Both the latter groups (2 and 3) were from the domestic black-feathered ostrich strain [4].

3 Results

Long and continuous grooves were present on the eggshells of group 1, although the depth of grooves was variable. These did not stretch linearly and symmetrically along the long axis of the shell but twisted like whorls of hair. Respiratory pores were clustered densely in the bottom of grooves (Figs. 7.1 and 7.2). An impressive cluster of respiratory pores could be seen over the air chamber on the egg (Fig. 7.3). Grooves were separated by ridges. The distance between the neighboring pores along the groove (1.94 ± 0.42 mm) was significantly shorter ($P < 0.01$ $n = 5$ by Students' paired t-test) than that between pores perpendicular to the grooves (4.43 ± 1.02 mm), i.e. beyond the nearest ridge.

The surfaces of eggshells from farmed ostriches of groups 2 and 3 were smooth and ridges and grooves were unclear or absent in most eggshells. Only one or two short, oblique grooves were scattered over two out of the five eggshells. Since pore distances from groups 2 and 3 seemed to be similar, the results in the two groups were combined and presented as one group. Distances between two neighboring pores were calculated together for the test of significant difference. $L\| = 2.66 \pm 0.37$ mm and $L\perp = 2.30 \pm 0.39$ mm (n.s. by Students' t-test) parallel and perpendicular to the long axis of eggshells, respectively.

Fig. 7.1 An example of an eggshell, group 1 (NMNZ OR.25755). Grooves and ridges run alternately and twistingly. Most pores, (*black dots*), are situated in the bottom of grooves. One short groove crosses other grooves obliquely downward

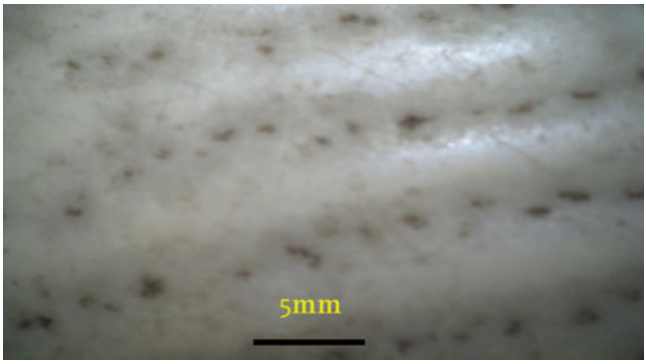

Fig. 7.2 A micrograph of the egg shell (Group 1, NMNZ OR. 25755) at low magnification

4 Discussion

The main structure of the eggshell wall known as the palisade layer (previously referred to as the spongy layer) [5, 6] is composed of columns of packed calcite crystals which extend from the mammillary knobs upward to the cuticle. Spaces between

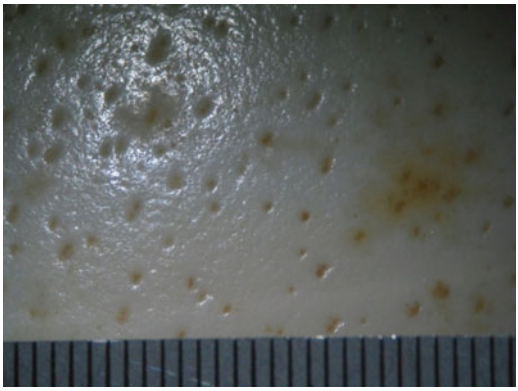

Fig. 7.3 The micrograph shows a cluster of respiratory pores over the air chamber of the egg (NMNZ S. 25755)

the crystal columns form occasional channels. In ostrich eggshells, this structure is less porous than in chicken eggshells [7]. Richards et al. [7] surmised that this reduced porosity made the ostrich eggshell relatively stronger and less likely to be damaged by trauma. Our findings suggest that the calcite crystals in ostrich eggshells may grow in a laminar way, so as to form a twisted pattern on the eggshell surface, with grooves and ridges on their boundaries.

In one eggshell of group 1 (Fig. 7.1) long continuous ridges and grooves were present on the shell surface. Similar structures, though less pronounced, were observed on the other four eggshells in this group. This kind of a surface creates a "corrugated" structure that may strengthen the breakable eggshell in birds like ostriches which are often exposed to dangers in the wild.

The surface of ostrich eggshells from farms had almost no depressions or grooves, nor any clear indication of twisting on the shell surface, although a few short oblique ridges and grooves were found on the eggshells of some of group 2 eggs. The smooth surfaces of farmed eggs showed a uniform distribution of breathing pores. The causes of such differences between groups 1 and 2+3 remain obscure.

However we theorise that these differences might be explained by group 1 birds being from eggs laid in the wild. External environmental stresses on wild-laid eggs might lead to stronger eggshells with more corrugated surfaces. It seems probable that the eggshell structure and pore sites are so arranged as to provide maximum protection to the embryo from adverse environmental factors. If the group 1 eggs were not from wild laid eggs but were from early captive populations, an explanation might be that early captive conditions led to more environmental stress than is found in the modern farmed populations that we obtained eggs from. Finally, it should be mentioned that the ostrich is a widespread running bird. They are divided into five subspecies. The eggshell surface may show some differentiation.

5 Conclusion

Twisting grooves and ridges were seen on ostrich eggshells which were assumed to have been laid in the wild. Respiratory pores were distributed solely in the grooves. No pores were found on ridges. Thus, a remarkably inhomogeneous distribution of respiratory pores was seen on the wild ostrich eggshells. The surfaces of eggshells from farmed, domesticated ostriches were smooth. Respiratory pores were distributed homogeneously over the shell surface. It is surprising that recent domestication of ostriches seems to have caused remarkable changes in the distribution patterns of respiratory pores on ostrich eggshells. This theory needs to be further tested by examination of known wild-sourced eggs.

Acknowledgments The authors wish to express thanks to Professors Drs. Ian Silver and Maria Erecinska for their valuable suggestions. Thanks are also due to Mr Sasao, head manager of Ishioka Ostrich Kingdom for his kind suggestions on ostrich station. At Te Papa, Phil Sirvid, Thomas Schultz, Rick Webber, Ricardo Palma, Susan Waugh and Mike Fitzgerald provided much appreciated assistance during TK's visit. TK wishes to express his thanks also to Dr. Tatsuro Ando, curator of Ashoro fossil Museum, Hokkaido, Japan.

References

1. Koyama T, Takano H, Yokoyama T (2009) In: LaManna JC et al (eds) Oxygen transport to tissue XXXII, vol 701, Advances in experimental medicine and biology., pp 307–310
2. Tulett SG, Board RG (1977) Determinants of avian eggshell porosity. J Zool (London) 183:203–211
3. Ar A, Rahn H (1985) Pores in avian eggshells: gas conductance, gas exchange and embryonic growth rate. Respir Physiol 61:1–20
4. Drenowatz C (1995) Ratite encyclopedia: ostrich, emu, rhea. San Antonio, Ratite Records Inc
5. Toien O, Paganelli CV, Rahn H, Johnson RR (1988) Diffusive resistance of avian eggshell pores. Respir Physiol 74:345–354
6. Taylor TG (1970) How to make eggshells. Sci Am 222:88–95
7. Richards PDG, Richards PA, Lee ME (2000) Ultrastructural characteristics of ostrich eggshell, outer shell membrane and calcified layers. J S Afr Vet Assoc 71(2):97–102

Chapter 8
Evaluation of Both Free Radical Scavenging Capacity and Antioxidative Damage Effect of Polydatin

Ju Jin, Yan Li, Xiuli Zhang, Tongsheng Chen, Yifei Wang, and Zhiping Wang

Abstract Cellular damage such as oxidation and lipid peroxidation, and DNA damage induced by free-radicals like reactive oxygen species, has been implicated in several diseases. Radicals generated by 2,2-azobis (2-amidino-propane) dihydrochloride (AAPH) are similar to physiologically active ones. In this study we found that polydatin, a resveratrol natural precursor derived from many sources, has the capacity of free radical scavenging and antioxidative damage. Using free radical scavenging assays, the IC_{50} values of polydatin were 19.25 and 5.29 μg/ml with the DPPH and the ABTS assay, respectively, and 0.125 mg ferrous sulfate/1 mg polydatin with the FRAP assay. With the AAPH-induced oxidative injury cell model assay, polydatin showed a strong protective effect against the human liver tumor HepG2 cell oxidative stress damage. These results indicate that the antioxidant properties of polydatin have great potential for use as an alternative to more toxic synthetic antioxidants as an additive in food, cosmetics and pharmaceutical preparations for the treatment of oxidative diseases.

Keywords Free radical scavenging • Polydatin • Antioxidation • AAPH

J. Jin • X. Zhang • Z. Wang (✉)
School of Pharmacy, Guangdong Pharmaceutical University, Guangzhou 510006, China
e-mail: wzping_jshb@126.com

Y. Li
School of Chinese Materia Medica, Guangzhou University of Chinese Medicine, Guangzhou, Guangdong 510006, China

T. Chen
MOE Key Laboratory of Laser Life Science & Institute of Laser Life Science, South China Normal University, Guangzhou 510631, China

Y. Wang (✉)
Institute of Biological Medicine, Jinan University, Guangzhou, Guangdong 510632, China
e-mail: twangyf@jnu.edu.cn

© Springer International Publishing Switzerland 2016

Q. Luo et al. (eds.), *Oxygen Transport to Tissue XXXVIII*, Advances in Experimental Medicine and Biology 923, DOI 10.1007/978-3-319-38810-6_8

1 Introduction

Antioxidants are believed to play an important role in the body's defense system against reactive oxygen species (ROS). A marginal dietary intake of antioxidants may lead to an increased production of ROS, which have been demonstrated to induce cellular damage and accelerate the aging process, and are involved in the onset of many diseases, including type 2 diabetes, inflammatory diseases, arteriosclerosis and different types of cancer [1]. Two of the lipid peroxidations are caused by the alkoxy radical ($RO^{\cdot}$) and the peroxy radical ($ROO^{\cdot}$), and can be induced by both physiologically active or a free radical generator, 2,2-azobis(2-amidinopropane) dihydrochloride (AAPH).

Polydatin (or piceid; Fig. 8.1), resveratrol-3-O-β-glucopyranoside, is a precursor of resveratrol isolated from *Polygonumcuspidatum* Sieb.et Zucc. (Chinese name: Huzhang) and glycosylation of resveratrol protects it from enzymic oxidation [2]. Polydatin is reported to exhibit promising pharmacological activities including antiplatelet aggregation, antihemorrhagic shock, and antioxidation activity [3, 4]. Recently, polydatin was found to promote Nrf2-ARE antioxidative pathway through activating Sirt1 [5].

In this report, polydatin antioxidation on free radical scavenging capacity and antioxidative damage effect was investigated. The antioxidative effect was evaluated by the DPPH, FRAP and ABTS free radical scavenging assays. The antioxidative damage effect was determined by AAPH-induced HepG2 cell oxidative injury cell model assays.

2 Materials and Methods

2.1 Analytical Chemicals

All chemicals used were of analytical grade. 2,2′-azino-bis-3-ethylbenzothiazoline-6-sulphonic acid (ABTS), 1,1-diphenyl-2-picryl-hydrazil (DPPH), 2,4,6-tripyridyl-s-triazine(TPTZ), 2,2-azobis(2-amidino-propane) dihydrochloride(AAPH), potassium

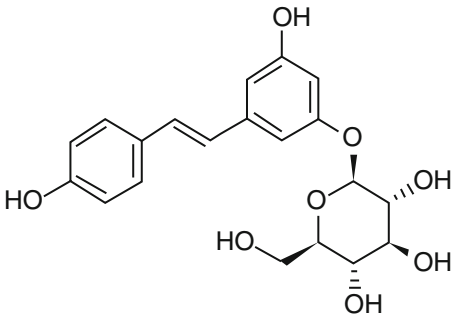

Fig. 8.1 Chemical structure of polydatin

persulfate, iron (III) chloride, 2,6-di-tert-butyl-4-methylphenol(BHT) and polydatin (the contents ≥95 % by HPLC) were purchased from Aladdin Industrial Inc. (Shanghai, China). MTT was purchased from Sigma Chemical (St. Louis, MO, USA).

2.2 Free Radical Scavenging Capacity Determination

The DPPH assay was used to measure radical scavenging activity as reported [6], but with slight modifications. All samples were tested individually at different concentrations by addition to an ethanolic solution of DPPH radical (40 μmol/l). For each measure 100 μl appropriately diluted standards or the sample was added to 3.0 ml of DPPH reagent, the mixtures were stirred and allowed to stand in the dark at room temperature. The same volume ethanol instead of the diluted sample was used as control solution. The absorbance of the resulting solutions was measured at 515 nm after 30 min. Each reaction was performed in triplicate. From this, the radical scavenging activity was determined by the following equation:

$$\text{DPPH scavenging effect (\%)} = [1-(\text{Ac}-\text{As})/\text{Ac}] \times 100$$

where Ac = absorbance of control and As = absorbance of sample.

The ABTS method was carried out as reported [6], but with some modifications. Briefly, $ABTS^{\bullet+}$ was prepared by mixing an ABTS stock solution (7 mmol/l in water) with 2.45 mmol/l potassium persulfate solutions and then incubated in the dark at room temperature for 12 h. This reagent was stable for 2–3 days when stored at 4 °C in the dark. On the day of analysis, the $ABTS^{\bullet+}$ solution was diluted with ethanol to an absorbance of 0.70 (±0.02) at 734 nm. After the addition of 1.0 ml $ABTS^{\bullet+}$ solution to 0.10 ml of sample, the mixture was stirred for 30 s and the absorbance reading was started after another 30 s and finished after 6 min. The readings were performed at 734 nm. The inhibition rate was calculated with the following equation:

$$\text{ABTS scavenging effect (\%)} = [1-(\text{Ac}-\text{As})/\text{Ac}] \times 100$$

where Ac = absorbance of control and As = absorbance of sample.

In the ferric reducing antioxidant power (FRAP) method [6, 7], the yellow Fe^{3+}-TPTZ complex is reduced to the blue Fe^{2+}-TPTZ complex by electron-donating substances under acidic conditions. Any electron donating substances with a half reaction of lower redox potential than Fe^{3+}/Fe^{2+}-TPTZ will drive the reaction and the formation of the blue complex forward. To prepare the FRAP reagent, a mixture of 0.1 mol/l acetate buffer (pH 3.6), 10 mmol/l TPTZ, and 20 mmol/l ferric chloride (10:1:1, v:v:v) was made. To 900 μl reagent, 90 μl water and 30 μl sample were added. The absorbance readings were started immediately after the addition of the sample, and they were performed at 593 nm with readings every 20 s for 10 min. The blank consisted of 120 μl water and 900 μl reagent. The concentrations of polydatin

and $FeSO_4 \cdot 7H_2O$ (used as a standard) were chosen to give an absorbance value not higher than 1.0. The FRAP value represents the ratio between the slope of the linear plot for reducing Fe^{3+}-TPTZ reagent by polydatin compared to the slope of this plot for $FeSO_4$ (expressed in $\triangle A$ per μg).

2.3 Antioxidative Damage Cell Assay

Cell viability was measured using the MTT-based colorimetric assay as described by Mosmann [8]. The cells were seeded in 96-well culture plates at 10^5 cells/ml and allowed to adhere for 24 h. Thereafter, the test sample and/or the radical donor were pretreated with polydatin, with different concentrations, for 24 h and then 1 mmol/l AAPH was added to culture medium, and the plates were incubated under routine conditions for 24 h. Then, 10 μl MTT (1 mg/ml) solution was added to each well. After incubation for 4 h at 37 °C, the medium containing MTT was removed. The resultant formazan crystals in the viable cells were solubilized with 100 μl dimethylsulfoxide (DMSO). An absorbance at 570 nm of each well was then read using a microplate reader (Model 3550-UV, BIO-RAD, Tokyo, Japan).

2.4 Statistical Analysis

All experiments were performed at least in triplicate. Analysis of variance was performed on the data obtained. Significance level was accepted at $p < 0.05$.

3 Results and Discussion

Several features of these results are pertinent for the purpose of this report, which is to demonstrate the polydatin free-radical-scavenging capacity and antioxidative damage effect. One important advantage is the three-assays evaluation. Secondly the antioxidant capacity is determined, which emphasized the contribution of polydatin at the cellular level.

All the results of the three free radial scavenging, DPPH assay, ABTS assay and FRAP assay, are summarized in Fig. 8.2. The free radical DPPH possesses a characteristic absorption at 517 nm (purple color), and the activity observed is in good correlation with the concentration of polydatin with an IC_{50} value of 19.25 ± 1.37 μg/ml at 517 nm (Fig. 8.2a). The anti-oxidant activity of polydatin was calculated from the decolorization of the $ABTS^{\bullet+}$, which was measured at 734 nm. The percentage inhibition was calculated and plotted as concentration of polydatin with an IC_{50} value 0.529 ± 0.064 μg/ml (Fig. 8.2b). In the FRAP assay, a reduction from ferric to ferrous was measured and the result is 0.125 mg ferrous sulfate/1 mg polydatin at 593 nm (Fig. 8.2c).

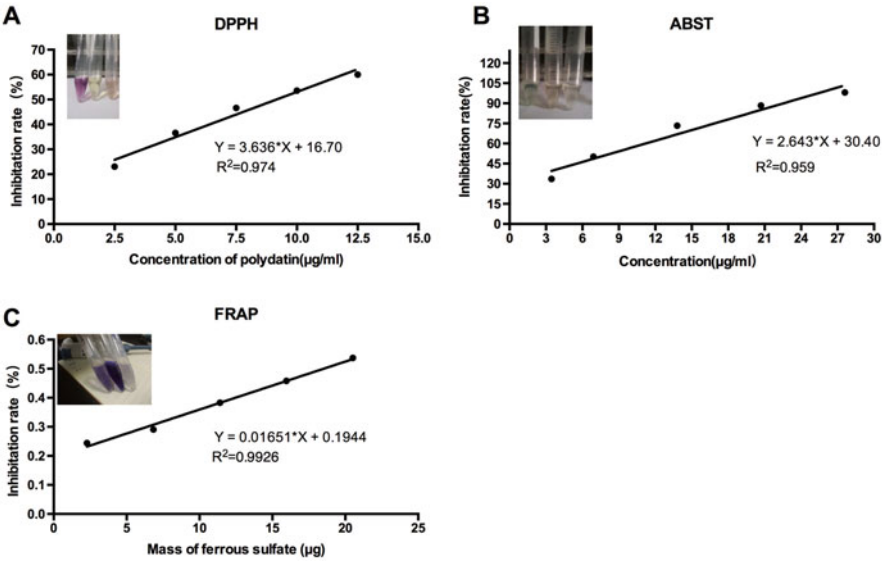

Fig. 8.2 (**a**) DPPH free radical scavenging capacity. The percentage of inhibition is plotted against the concentration of polydatin. (**b**) ABTS free radical scavenging capacity. The inhibition rate is plotted against the concentration of polydatin. (**c**) FRAP free radical scavenging capacity. The absorbance is plotted against the mass of ferrous sulfate. Values are presented as mean ± SD (n = 3)

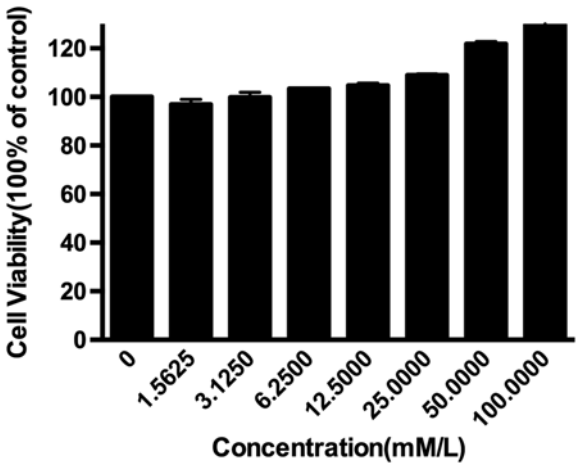

Fig. 8.3 Effects of polydatin on the viability of cells treated with AAPH

At the cellular level, AAPH-induced oxidative stress in HepG2 cells could be ameliorated by polydatin. Polydatin suppressed AAPH-induced oxidative stress in HepG2 cells (Fig. 8.3). And our study will focus more on the cellular level of the effect of polydatin on antioxidants.

These results indicate that the antioxidant properties of polydatin have great potential for use as an alternative to more toxic synthetic antioxidants as an additive in food, cosmetics and pharmaceutical preparations for the treatment of oxidative diseases.

References

1. Lindenmeier M, Burkon A, Somoza V (2007) A novel method to measure both the reductive and the radical scavenging activity in a linoleic acidmodel system. Mol Nutr Food Res 51:1441–1446
2. Regev-Shoshani G, Shoseyov O, Bilkis I et al (2003) Glycosylation of resveratrol protects it from enzymic oxidation. Biochem J 374:157–163
3. Orsini F, Pelizzoni F, Verotta L et al (1997) Isolation, synthesis, and antiplatelet aggregation activity of resveratrol 3-O-beta-Dglucopyranoside and related compounds. J Nat Prod 60:1082–1087
4. Wang XM, Song R, Chen YY et al (2013) Polydatin--a new mitochondria protector for acute severe hemorrhagic shock treatment. Expert Opin Investig Drugs 22(2):169–179
5. Huang KP, Chen C, Hao J et al (2015) Polydatin promotes Nrf2-ARE anti-oxidative pathway through activating Sirt1 to resist AGEs-induced upregulation of fibronetin and transforming growth factor-β1 in rat glomerular messangial cells. Mol Cell Endocrinol 399:178–199
6. Ozgen M, Reese RN, Tulio AZ et al (2006) Modified 2,2'-azino-bis-3-ethylbenzothiazoline-6-sulfonic acid (ABTS) method to measure antioxidant capacity of selected small fruits and comparison to ferric reducing antioxidant power (FRAP) and 2,2'-diphenyl-1-picrylhydrazyl (DPPH) methods. J Agric Food Chem 54:1151–1157
7. Benzie IFF, Strain JJ (1996) The ferric reducing ability of plasma (FRAP) as a measure of "antioxidant power": the FRAP assay. Anal Biochem 239:70–76
8. Mosmann T (1983) Rapid colorimetric assay for cellular growth and survival: application to proliferation and cytotoxicity assays. J Immunol Methods 16(65):55–63

Chapter 9
Spectroscopic Studies on the Interaction of Pyridinoline Cross-Linking in Type 1 Collagen with ZIF8-HB

Yashun Chen, Fangfang He, Wei Liu, and Jucheng Zhang

Abstract Many kinds of fibrosis are related to the content of pyridinoline cross-linking in type 1 collagen. In this study, ZIF-8 (zeolitic imidazolate framework), a metal organic framework (MOF), and ZIF8-hypocrellin B (ZIF8-HB), which combined the merits of hypocrellin B and the properties of ZIF-8, were prepared and applied to the photodegradation of the pyridinoline cross-linking. The effects of O_2 and H_2O_2 in the photodynamic action were investigated. The results indicate that ZIF8-HB is an efficient photosensitizer to decompose pyridinoline cross-linking in collagen.

Keywords Fibrosis • Photosensitizer • ZIF8-HB • Hydroxyl radical • Fluorescence

1 Introduction

Fibrosis is a class of extracellular matrix-related diseases, which is mainly related to the transcriptional regulation of collagen in an organ or tissue. The abnormal accumulation of collagen and little degradation leads to fibrosis, which is related to the formation of pyridinoline cross-linking in the collagen [1]. In a recent study, some measures were taken to reduce the content of pyridinoline cross-linking in collagen in order to suppress the synthesis of the fibrosis [2]. Hypocrellin B (HB) as an effective phototherapeutic agent and natural photosensitizer isolated from the traditional

Y. Chen • W. Liu • J. Zhang (✉)
Key Laboratory of Natural Pharmaceutical & Chemical Biology of Yunnan Province, Honghe University, Mengzi, Yunnan Province, China

College of Science, Honghe University, Mengzi, Yunnan Province, China
e-mail: juchengzhang@163.com

F. He
College of Life Science and Technology, Honghe University, Mengzi, Yunnan Province, China

© Springer International Publishing Switzerland 2016

Q. Luo et al. (eds.), *Oxygen Transport to Tissue XXXVIII*, Advances in Experimental Medicine and Biology 923, DOI 10.1007/978-3-319-38810-6_9

Chinese herb Hypocrella bambuase has attracted considerable attention owing to its low toxicity and potent biological activity [3]. However, the low water solubility and the weak absorption in the phototherapeutic window (600–900 nm) limit its photodynamic therapy application clinically. In recent years, the preparation of a hypocrellin carrier has proved to be an efficient way to facilitate its application [4].

Metal-organic frameworks (MOFs) are a novel class of crystalline porous materials constructed from metal ions connected with organic linkers. Owing to their large surface areas, tuneable pore sizes, numerous structures, as well as catalytic, optical, and electrical properties, MOFs have received a great attention in diverse applications [5]. Among the numerous MOFs reported so far, ZIF-8 was one of the most topical solids, which exhibits higher thermal and chemical stability than other MOFs. Its high specific surface area, photocatalytic property and permanent porosity from its uniformly pore sized cavities make it particularly desirable for many potential applications [6]. In this paper, ZIF8-HB was prepared and used as a highly efficient photosensitizer to decompose the pyridinoline cross-linking in type 1 collagen.

2 Methods

2.1 Materials and Apparatus

Type 1 collagen was purchased from Sigma. HB was prepared by our lab [7]. $Zn(NO_3)_2{\cdot}6H_2O$, *N*,*N*-dimethylformamide (DMF), ethanol and isopropanol were obtained from Concord Fine Chemical Research Institute (Tianjin, China). 2-methylimidazole was purchased from Sinopharm Chemical Reagent Co., (Shanghai, China). Ultrapure water (Wahaha Foods Co. Ltd., Kunming, China) was used throughout this work. All reagents used were analytical grade or above. The fluorescence spectra were recorded by the Hitachi F-7000 fluorospectro- photometer.

ZIF-8 was synthesized according to the work of Yan et al. [8] with a little modification. A solid mixture of $Zn(NO_3)_2{\cdot}6H_2O$ (0.16 g) and 2-methylimidazole (0.04 g) was dissolved in 12 mL DMF in a teflon-lined stainless steel container. The container was sealed and heated to 140 °C for 24 h and then cooled to room temperature. After that, the colorless crystals were washed with DMF and collected by centrifugation at 10,000 rpm (8,720 × *g*) for 10 min. After another two cycles of DMF washing centrifugation, the obtained crystals were washed with ethanol, and dried at room temperature under reduced pressure for 2 h to obtain ZIF-8. ZIF8-HB was prepared as follows: 10 mg of ZIF-8 kept in a desiccator was added into 20 mL of HB aqueous solution having concentration of 25 mg/L, followed by magnetic stirring at 25 °C. After adsorption for 24 h, adsorbent was collected by centrifugation at 12,000 rpm (12,550 × *g*) for 10 min, then washed with ethanol, and dried at room temperature under reduced pressure for 2 h to obtain ZIF8-HB.

2.2 The Degradation Experiments

The activities of ZIF8-HB as photosensitizer were evaluated by photodegradation of the pyridinoline cross-linking in type 1 collagen at the wavelength of 475 nm under 300 W Xe lamp irradiation in open air, under room temperature. The distance between the light source and the cuvette containing the reaction mixture was fixed at 5 cm. The reaction system was prepared as follows: 1 mg of ZIF8-HB was put into 3 mL of collagen aqueous solution (1 mg/mL in PBS buffer solution). Some will be treated with oxygen for 10 min, others will be treated with H_2O_2. The isopropanol was used as the hydroxyl radicals (•OH) scavenger owing to its property to trap hydroxyl radical effectively and selectively [9]. Before the degradation experiments, the mixture was stirred in the shaking table in dark for 180 min to ensure the establishment of an adsorption-desorption equilibrium. A fluorescence emission peak at 395 nm upon excitation at 295 nm was used to detect the content change of pyridinoline cross-linking [7].

3 Results and Discussion

3.1 The Effect of Degradation in the Presence of O_2 and H_2O_2

In a previous study, it was shown that the biological activity of hypocrellin is sensitive to oxygen [10]. Figure 9.1a shows the fluorescence spectra of different photodynamic systems in the presence of H_2O_2 or O_2. It can be seen that the photodynamic systems have a better photodynamic performance than those without O_2 or H_2O_2. The results confirm the conclusions reported previously [10]. Furthermore, H_2O_2 improved the performance of photodynamic action better, compared with the O_2. However, the emission fluorescence spectra of collagen in the presence of H_2O_2 changed a little. The results reveal that H_2O_2 did not degrade the collagen directly.

The fluorescence decay effect of pyridinoline cross-linking in type 1 collagen photodegraded by ZIF-HB and HB were compared under the same experimental conditions. It can be seen from Fig. 9.1b that ZIF8-HB showed a better activity than HB both in the presence and absence of H_2O_2. The reason for this may be that ZIF-8 favored the formation of hydroxyl radicals, which might play a crucial role in the reaction [6].

3.2 Mechanism for Collagen Degradation with ZIF8-HB

As widely accepted, hydroxyl radicals are deemed to be the crucial active species during the photocatalytic process. Usually, a high generation rate of hydroxyl radical results in rapid degradation and short reaction time to achieve specific treatment objectives.

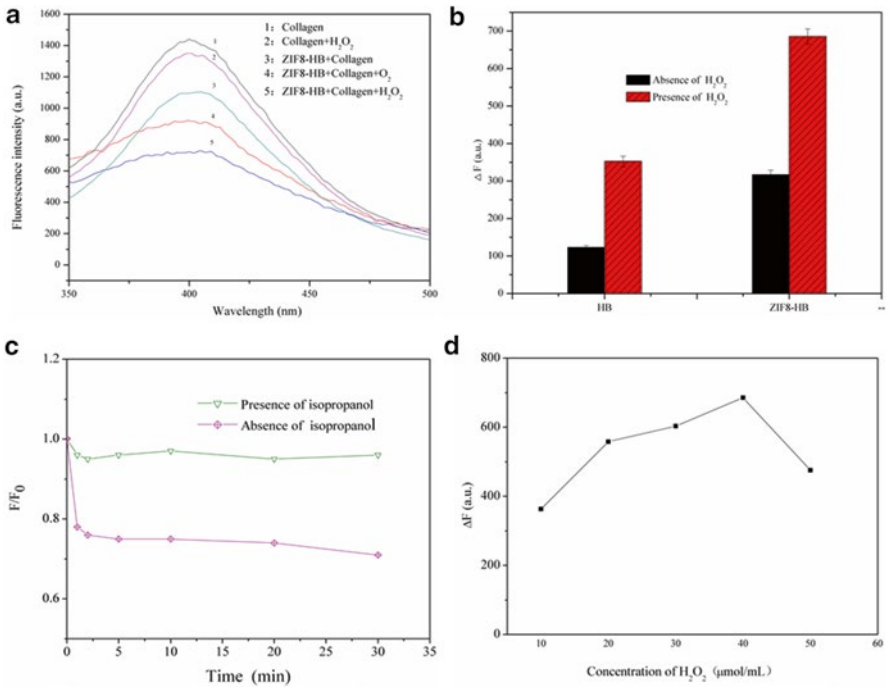

Fig. 9.1 (**a**) Fluorescence spectra of collagen in different reaction systems; (**b**) Comparison fluorescence decay of collagen with ZIF-HB and HB in absence and presence of H_2O_2; (**c**) Comparison fluorescence decay of collagen in absence and presence of isopropanol; (**d**) Fluorescence decay curve of collagen with the increasing concentration of H_2O_2 (emission peak at 395 nm excited at 295 nm)

In this study, a comprehensive investigation of the activity of the ZIF8-HB will necessarily consider the roles of ·OH in the photodynamic action. Hence, isopropanol was used as scavengers of ·OH to decrease its concentration and to investigate its effect on collagen. It can be seen from Fig. 9.1c that the photodegradation of the collagen in the absence of isopropanol is much better than in the presence of it. This result shows that the hydroxyl radical played a main role in the photodegradation of pyridinoline cross-linking in type 1 collagen. As shown in Fig. 9.1d, fluorescence intensity decreased gradually with the increasing concentration of H_2O_2 in a range of 10–40 μmol/mL. However, fluorescence decay became weaker with its concentration increasing to 50 μmol/mL. As reported [11], H_2O_2 could increase the rate of ·OH formation. However, surplus H_2O_2 molecules as scavengers of ·OH would generate H_2O and O_2 (see Eqs. (9.1)–(9.3)) [11]. Hence, we deduced that hydroxyl radicals generated by the ZIF8-HB probably played a crucial role in the reaction.

$$H_2O_2 + e^- \rightarrow {}^{\cdot}OH + OH^- \tag{9.1}$$

$$\cdot OH + H_2O_2 \rightarrow H_2O + HOO\cdot \quad (9.2)$$

$$HOO\cdot + \cdot OH \rightarrow H_2O + O_2 \quad (9.3)$$

4 Conclusions

ZIF8-HB is considered an efficient photosensitizer for degradation of pyridinoline cross-linking in collagen. Furthermore, indicate the effect of the degradation can be enhanced by ZIF8-HB in the presence of H_2O_2. It is expected to be applied in the field of photodynamic therapy for fibrosis.

Acknowledgments This work was supported by the National Nature Science Foundation of China(No.21362010), the Research Foundation of Hong He University (No. XJ14Y07) and the Yunnan Nature Science Foundation (No.2013FD048).

References

1. Trojanowska M, LeRoy EC, Krieg BET (1998) Pathogenesis of fibrosis: type 1 collagen and the skin. J Mol Med 76:266–274
2. Stone PJ (2000) Potential use of collagen and elastin degradation markers for monitoring liver fibrosis in schistosomiasis. Acta Trop 77(1):97–99
3. Xie W, Wei S, Liu J et al (2014) Spectroscopic studies on the interaction of Ga^{3+}-hypocrellin A with myoglobin. Spectrochim Acta A 121:109–115
4. Paramaguru G, Woo T, Renganathan R (2014) Spectroscopic studies on the interaction of Hypocrellin B with $AuTiO_2$ nanoparticles. J Lumin 145:154–159
5. Wang C, Liu DM, Lin WB (2013) Metal-organic frameworks as a tunable platform for designing functional molecular materials. J Am Chem Soc 135:13222–13234
6. Jing HP, Wang CC, Zhang YW et al (2014) Photocatalytic degradation of methylene blue in ZIF-8. RSC Adv 4(97):54454–54462
7. Zhang JC, Liu W, Yi ZZ et al (2009) The molecular mechanism of photodynamic therapy to fibrosis: regulation on the pyridinoline cross-link formation. Chin Sci Bull 54:2230–2234
8. Jiang JQ, Yang CX, Yan XP (2013) Zeolitic imidazolate framework-8 for fast adsorption and removal of benzotriazoles from aqueous solution. ACS Appl Mater Interfaces 5:9837–9842
9. Li GT, Song HY, Liu BT (2012) Production and contribution of hydroxyl radicals in photocatalytic oxidation process. Chin J Environ Eng 6:3388–3892
10. Park JH, English HS, Wannemuehler Y et al (1998) The role of oxygen in the antiviral activity of hypericin and hypocrellin. Photochem Photobiol 68(4):593–597
11. Ai L, Zhang C, Li L et al (2014) Iron terephthalate metal-organic framework: revealing the effective activation of hydrogen peroxide for the degradation of organic dye under visible light irradiation. Appl Catal Environ 148–149:191–200

Chapter 10
The Role of Free Radicals in the Photodynamic Treatment of Fibrotic Skin Diseases

Heping Yan, Yashun Chen, Jucheng Zhang, Wei Liu, and Rui Chen

Abstract The first derivatives of gelatin and type I collagen fluorescence spectra were characterized in order to describe the effect of free radicals on pyridinoline (PYD) cross-links. The different gas saturation conditions were used to investigate the effect of different free radicals. An analysis of first derivative fluorescence spectra suggests that PYD cross-link fluorescence emission is composed of three peaks in gelatin, but only two in type I collagen. The PYD cross-link was photo-degraded more than other gases in the presence of O_2. This suggests that the singlet oxygen ($^1O_2$) plays a key role when using photodynamic therapy to treat skin fibrosis disease with Hypocrellin B (HB).

Keywords Free radical • Photodynamic therapy • Hyporellin B • Fibrotic skin diseases • Pyridinoline cross-link

1 Introduction

Photodynamic therapy (PDT) has been a routine clinical treatment for many diseases, such as cancer, port wine stains, dermatology and Barrett's esophagus (BE) [1–4]. The PDT action depends on photo-generated free radicals and reactive oxygen species (ROS), the ROS including superoxide anion radical ($O_2^{\bullet -}$), hydrogen peroxide (H_2O_2) and hydroxyl radical ($HO^{\bullet}$) [5]. Hypocrellins, mainly including

H. Yan • Y. Chen • J. Zhang (✉) • W. Liu • R. Chen
Key Laboratory of Natural Pharmaceutical & Chemical Biology of Yunnan Province, Honghe University, Mengzi, Yunnan, Province, P. R. China

School of science, Honghe University, Mengzi, Yunnan, Province, P. R. China
e-mail: zhangjucheng@163.com

© Springer International Publishing Switzerland 2016

Q. Luo et al. (eds.), *Oxygen Transport to Tissue XXXVIII*, Advances in Experimental Medicine and Biology 923, DOI 10.1007/978-3-319-38810-6_10

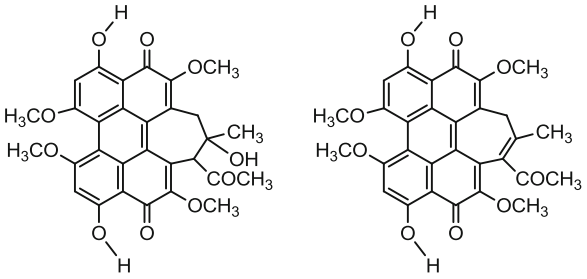

Fig. 10.1 The structure of hypocrellin A (HA) and hypocrellin B (HB)

hypocrellin A (HA) and hypocrellin B (HB), are excellent natural photosensitizers from a fungus *hypocrella bambusae* (Fig. 10.1). The use of hypocrellins for PDT has been reported in many studies [2, 6, 7].

Fibrosis has a common characteristic of an over-accumulation of collagen in the extracellular matrix (ECM), such as type I, type III and type IV collagen [8–11]. The literature indicates that the level of pyridinoline (PYD) cross-links in fibrotic skin, which cross-linked via the hydroxylysine aldehyde, is higher than in normal skin tissues [12]. Also, the metalloproteinase cannot degrade the collagen in fibrotic tissues due to the level of PYD cross-links in collagen. The fluorescence emission peak of PYD cross-links was observed in type I collagen, and in gelatin, which is the denatured collagen protein, and also found in PYD cross-links fluorescence peak at around 392 nm [6]. In the current work, gelatin and type I collagen were used as a model to investigate the photo-degradation by free radicals and ROS which was induced by HB-PDT. The action of the free radicals to degrade PYD cross-links was investigated by the reaction system saturated by different gas conditions. The first derivative fluorescence spectroscopy was used to investigate the model's reaction system.

2 Materials and Methods

2.1 Materials

Collagen (type I, c9879) was purchased from Sigma, terephthalic acid (AR) was obtained from Aladdin, and all the reagents were used as received. Gelatin was obtained from the Institute of Photographic Chemistry, Chinese Academy of Sciences (derived from calf bone). Hypocrellin B (HB) was obtained by the dehydration of HA which was extracted from the fungus *Hypocrella bambusae*. The phosphate-buffered saline (PBS) of pH = 7.4 was prepared by using 50 mmol/L K_2HPO_4 and 50 mmol/L KH_2PO_4. The gelatin solution was 12.5 g/L, and type I collagen solution was 1 g/L. The working solutions were prepared shortly before use.

2.2 Methods

2.2.1 Spectroscopy Measurements

Steady-state absorption and fluorescence spectra were recorded on a TU-1901 UV/Vis spectrophotometer (Beijing Purkinje General Instrument Co., Ltd., China) and an F-7000 spectrophotometer (Hitachi, Japan), respectively. For the fluorescence measurement, gelatin and type I collagen were excited at 295 nm for PYD cross-links. Samples were dark adapted at room temperature for 10 min prior to fluorescence measurement.

2.2.2 Irradiation

The HB-gelatin and HB-collagen solutions were oxygen saturated or bubbled with argon according to the experimental requirements, and then irradiated in a 1 cm × 1 cm quartz cuvette. A 300 W xenon lamp equipped with a filter cutting off the wavelengths shorter than 470 nm and more than 800 nm was used for irradiation. The fluence rate was about 100 mW/cm^2 measured by a UV radiometer.

3 Results and Discussion

3.1 Normal and First Derivative Fluorescence Spectrum of Gelatin and Type I Collagen

The normal fluorescence spectra and first derivative fluorescence spectra of gelatin and type I collagen are shown in Fig. 10.2. This figure shows that the normal fluorescence spectra of gelatin and type I collagen have the same shape which excited at 295 nm, and have a band peak at about 390 nm which is the fluorescence emission peak of PYD cross-links. The normal fluorescence spectra of gelatin and collagen cannot provide more information for us. Numerous papers have indicated the derivative spectrum can provide more information [13, 14]. Therefore, in this work, the first derivative fluorescence spectra of gelatin and type I collagen was used for comparison with the normal spectra.

Figure 10.2 shows the first derivative spectra of PYD cross-links in gelatin and type I collagen. The first derivative spectra for gelatin show a 360 nm peak and two negative peaks around 426 and 475 nm, and those for collagen show a 350 nm peak and a broad negative peak from 377 to 550 nm. The first derivative fluorescence spectra show some differences between gelatin and type I collagen, so the derivative fluorescence can provide more information about the gelatin and type I collagen than normal fluorescence spectroscopy.

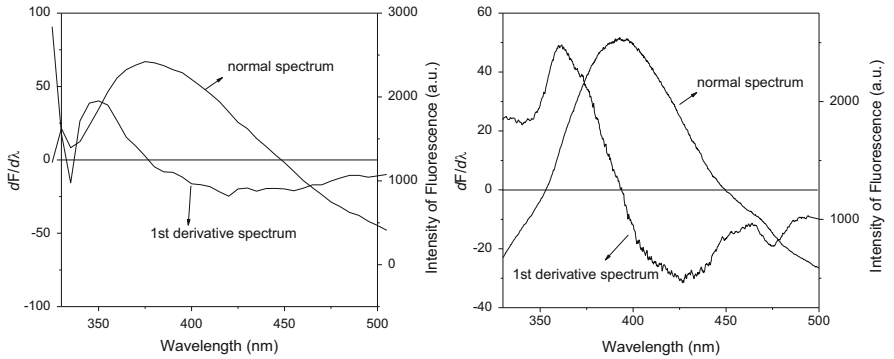

Fig. 10.2 The normal fluorescence spectroscopy and first derivative fluorescence of type I collagen (*left*) and gelatin (*right*)

3.2 Effect of Free Radicals on PYD Cross-Links

The photochemistry path has two reactions, the type I reaction (superoxide anion radical and hydroxyl radical, etc.) and type II reaction (singlet oxygen), in PDT. The two paths generated different free radicals and ROS [15]. To investigate the effect of various free radicals and ROS on PYD cross-links, oxygen, air and argon were used to saturate the reaction solutions to get different free radicals and ROS by PDT. Oxygen can affect the free radical species and oxygen is a critical component in these reactions [1]. The photo-oxidative reaction with the photosensitizer is shown in Fig. 10.3 and the degradation ratio is shown in Fig. 10.4 under different conditions.

Figure 10.3 shows that the first derivative fluorescence peak of gelatin around 360 nm decreased with the irradiation time in all experiments, but the peak decreased more than other conditions in the presence of oxygen saturation. The negative peak at around 426 nm shows the same changes. When oxygen is present in the reaction system, the type II reaction might be the main path, so the singlet oxygen ($^1O_2$) attacks the PYD cross-links in gelatin to cause the reduction of the intensity of fluorescence. These results are in agreement with the literature [1].

3.3 The Fluorescent Probe to Determine Hydroxyl Radical

Because the hydroxyl radical ($HO^{\bullet}$) is generated by type I reaction, determination of this radical can help us to show that the degradation path of PYD cross-links in PDT with HB. Terephthalic acid (THA) was used in many studies as a fluorescent probe to determine $HO^{\bullet}$ [16]. In this experiment, the 1 mmol/L THA was used to determine $HO^{\bullet}$ in HB-gelatin and HB-collagen reaction systems. If the HB-gelatin and HB-collagen generate $HO^{\bullet}$ under irradiation, the $HO^{\bullet}$ can attack THA to generate the THA-OH which has a fluorescence emission peak at 425 nm [16]. However, in

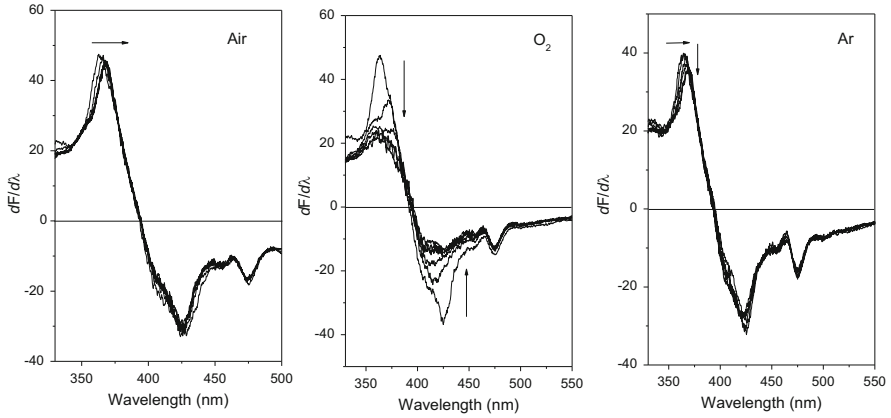

Fig. 10.3 First derivative fluorescence spectra (excited at 295 nm) of gelatin with irradiation of HB for 0–25 min in PBS solution saturated by oxygen, air and Argon, respectively. The *arrows* indicate the change in direction

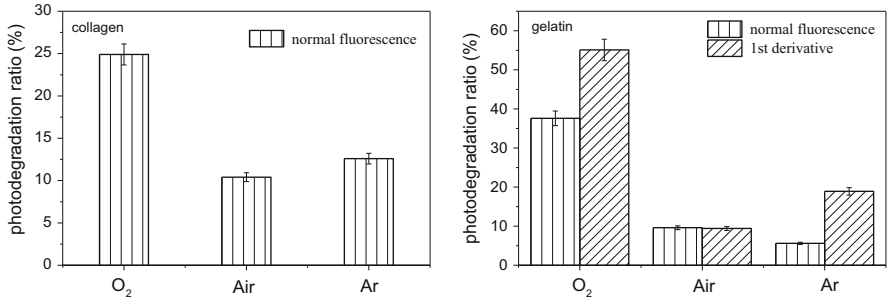

Fig. 10.4 The photo-degradation ratio of collagen and gelatin by HB in different gas saturation conditions

our experiment we did not find the emission peak in an oxygen and air saturated system. This result suggests no hydroxyl radicals were generated in HB-gelatin and HB-collagen reaction systems. This result also confirms that the type II reaction may be the main path to degrade the PYD cross-links in gelatin and collagen by PDT at the molecular level.

4 Conclusions

This work investigated the role of free radicals in photodegradation of PYD cross-links in gelatin and type I collagen by HB-PDT. The different gases, including oxygen, air and argon, were used to obtain different free radical generated conditions.

The results show the PYD cross-links could be degraded by HB-PDT. In this experiment no hydroxyl radical was found in the reaction system using the fluorescent probe THA. This suggests that the type II mechanism might be the main path to degrade the PYD cross-links by HB-PDT.Acknowledgments This work was financially supported by the National Nature Science Foundation of China (21362010), and the Yunnan Natural Science Foundation (2010ZC0153).

References

1. Agostinis P, Berg K, Cengel KA et al (2011) Photodynamic therapy of cancer: an update. CA Cancer J Clin 61(4):250–281
2. Wang K, Gu Y, Liu FG et al (2002) Several questions of Photodynamic Therapy treatment the Port wine stains in clinic (in Chinese). Chin J Laser Med Surg 11:190–192
3. Webber J, Herman M, Kessel D et al (2000) Photodynamic treatment of neoplastic lesions of the gastrointestinal tract. Langenbecks Arch Surg 385:299–304
4. Qumseya BJ, David W, Wolfsen HC (2013) Photodynamic therapy for Barrett's esophagus and esophageal carcinoma. Clin Endosc 46:30–37
5. Singh RP, Sharad S, Kapur S (2004) Free radicals and oxidative stress in neurodegenerative diseases: relevance of dietary antioxidants. Indian Acad Clin Med 5(3):218–225
6. Zhang JC, Liu W, Yi ZZ et al (2009) The molecular mechanism of photodynamic therapy to fibrosis: regulation on the pyridinoline cross-link formation in collagen. Chin Sci Bull 54:2230–2234
7. Huang NY, Liu FG, Gu Y (2007) Animal experiment of the port wine stains' treatment by photodynamic therapy with two dosage form of hypocrellin B (in Chinese). Acta Laser Biol Sin 16:359–363
8. Smith RP (2002) Photodynamic therapy. Curr Probl Cancer 26(2):61–108
9. Dennis AH, David RE (1996) Molecular site specificity of pyridinoline and pyrrole cross-links in type I collagen of human bone. J Biol Chem 271:26508–26516
10. Trojanowska M, LeRoy EC, Krieg BET (1998) Pathogenesis of fibrosis: Type I collagen and the skin. J Mol Med 76:266–274
11. van der Slot AJ, Zuurmond AM, van den Bogaerdt AJ et al (2004) Increased formation of pyridinoline cross-links due to higher telopeptide lysyl hydroxylase levels is a general fibrotic phenomenon. Matrix Biol 23:251–257
12. van der Slot-Verhoeven AJ, van Dura EA, Attema J et al (2005) The type of collagen cross-link determines the reversibility of experimental skin fibrosis. Biochim Biophys Acta 1740:60–67
13. Green GL, O'Haver TC (1974) Derivative luminescence spectrometry. Anal Chem 46(14):2191–2196
14. Mozo-Villarías A (2002) Second derivative fluorescence spectroscopy of tryptophan in proteins. J Biochem Biophys Methods 50:163–178
15. Zhao BZ, He YY (2010) Recent advances in the prevention and treatment of skin cancer using photodynamic therapy. Expert Rev Anticancer Ther 10(11):1797–1809
16. Barreto JC, Smith GS, Strobel NHP et al (1995) Terephthalic acid: a dosimeter for the detection of hydroxyl radicals *in vitro*. Life Sci 56(4):89–96

Part II
Cancer Oxygenation and Metabolism

Chapter 11
Tumor Hypoxia: Causative Mechanisms, Microregional Heterogeneities, and the Role of Tissue-Based Hypoxia Markers

Peter Vaupel and Arnulf Mayer

Abstract Tumor hypoxia is a hallmark of solid malignant tumor growth, profoundly influences malignant progression and contributes to the development of therapeutic resistance. Pathogenesis of tumor hypoxia is multifactorial, with contributions from both acute and chronic factors. Spatial distribution of hypoxia within tumors is markedly heterogeneous and often changes over time, e.g., during a course of radiotherapy. Substantial changes in the oxygenation status can occur within the distance of a few cell layers, explaining the inability of currently used molecular imaging techniques to adequately assess this crucial trait. Due to the possible importance of tumor hypoxia for clinical decision-making, there is a great demand for molecular tools which may provide the necessary resolution down to the single cell level. Exogenous and endogenous markers of tumor hypoxia have been investigated for this purpose. Their potential use may be greatly enhanced by multiparametric *in situ* methods in experimental and human tumor tissue.

Keywords Tumor hypoxia • Malignant progression • Tumor hypoxia, detection • Tumor hypoxia, subtypes • Tumor hypoxia, heterogeneities • Multiparametric immunohistochemistry • Hypoxia markers

1 Introduction

The tumor microenvironment can be distinguished from that of normal tissues by a number of features, among which a key factor is the critically reduced level of oxygenation, i.e., hypoxia, that, at present, is recognized as a principal parameter influencing the disease outcome [1]. For many years, tumor hypoxia has been regarded

P. Vaupel (✉) • A. Mayer
Department of Radiation Oncology and Radiotherapy, Tumor Pathophysiology Section, University Medical Center, Langenbeckstr. 1, 55131 Mainz, Germany
e-mail: vaupel@uni-mainz.de

© Springer International Publishing Switzerland 2016

Q. Luo et al. (eds.), *Oxygen Transport to Tissue XXXVIII*, Advances in Experimental Medicine and Biology 923, DOI 10.1007/978-3-319-38810-6_11

as an obstacle to the local control of solid tumors treated with standard radiotherapy, some chemotherapies and photodynamic therapy. During the last two decades, accumulated evidence demonstrates that hypoxia has a strong negative impact driving cancer cells toward a more aggressive phenotype, resulting from an increased mutagenicity (<0.1 % O_2) and a hypoxia-driven regulation of a plethora of genes promoting changes of the proteome and the metabolome (<1 % O_2), ultimately leading to a poorer patient prognosis [2, 3].

In this chapter, the various pathomechanisms responsible for the development of tumor hypoxia, leading to different subtypes of oxygen deficiency states, the (micro-) regional heterogeneities, and the role of tissue-based markers for hypoxia detection is given special emphasis.

2 Pathogenesis of Tumor Hypoxia

Based on underlying pathogenetic mechanisms and their respective duration, two main types of tumor hypoxia have been identified, coexisting in tumor subvolumes, with complex temporal and spatial heterogeneities: (a) *chronic hypoxia*, most probably the dominant type in solid human malignancies, is mainly caused by diffusion limitations due to enlarged diffusion distances and adverse diffusion geometries (e.g., elongated, U-shaped tumor microvessels with diffusion shunt, glomeruloid microvascular proliferations). Further pathogenetic mechanisms are hypoxemia in anemic patients and elevated interstitial fluid pressure compromising tumor microcirculation by leveling off perfusion pressure gradients (see Fig. 11.1, upper panels) [4–6]; (b) *acute hypoxia* preferentially results from transient perturbations of the microcirculation (e.g., by vascular obstruction) or fluctuations of red blood cell fluxes (see Fig. 11.2, upper panels).

An in-depth characterization of these hypoxia subtypes in the clinical setting is lacking so far, although of great relevance since diagnostic procedures and therapeutic measures may be different when dealing with these subtypes. In addition, chronic and acute hypoxia may foster the development of aggressive phenotypes and treatment resistance in different ways/mechanisms (see Figs. 11.1 and 11.2, lower panels).

3 Microregional Heterogeneities of Tumor Hypoxia

As already mentioned, tumor oxygenation is heterogeneous, both within and (even more pronounced) between tumors. Most solid tumors exhibit spatial and temporal heterogeneities, independent of tumor stage and histological type. There are complex dynamic changes in the degree (level, severity) of hypoxia, in the topographical distribution (tumor center vs. tumor periphery), in the extension of individual hypoxic areas, and in the number of hypoxic subvolumes (single vs. multiple). Hypoxic subvolumes may have spatial dimensions in the submillimeter- range with

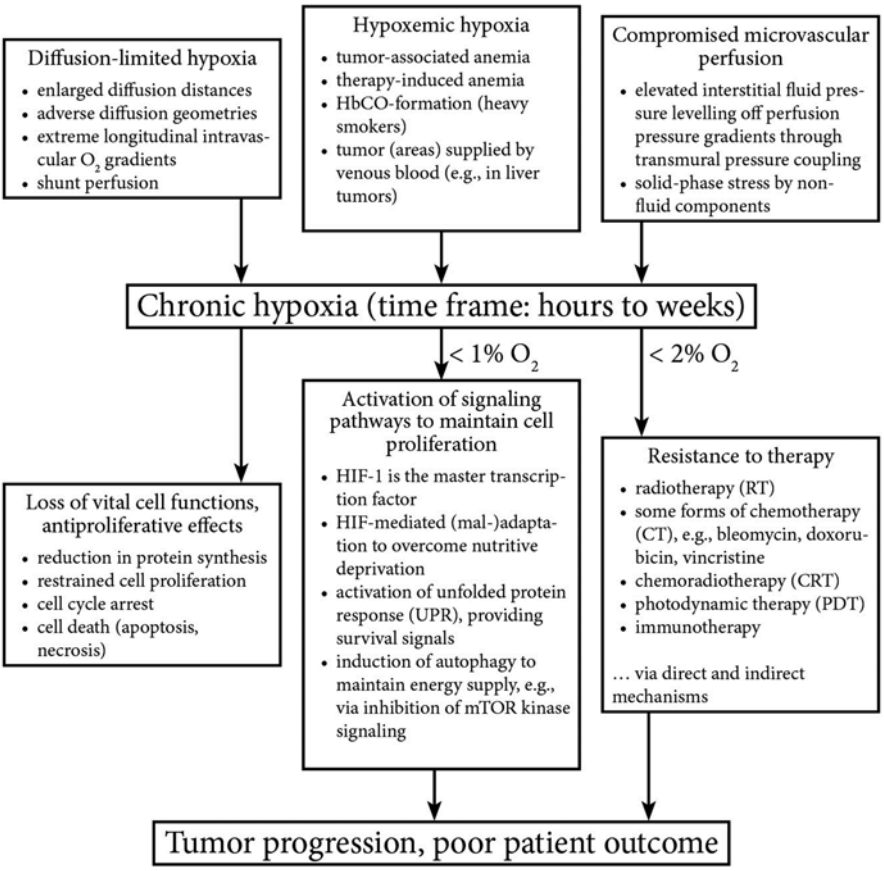

Fig. 11.1 Causative mechanisms for the development of chronic hypoxia (*upper panels*), and biological and clinical consequences leading to the loss of vital cell functions and antiproliferative effects (*lower left panel*). Below 2 % O_2, mechanisms of therapeutic resistance are activated (*lower right panel*). Under moderate hypoxia (<1 % O_2), altered cell signalling may result in survival and maintained cell proliferation (*lower central panel*). The latter two mechanisms contribute to tumor progression and poor patient outcome

very steep pO_2 gradients (up to 60 mmHg/mm). This latter type of hypoxic subregions, despite their clinical importance, cannot be accessed with the currently available PET techniques in the clinical setting due to the averaging problem.

4 Detection of Tumor Hypoxia in the Clinical Setting

Direct detection and exact quantification of hypoxia and its subtypes as a routine procedure within the patient workup is highly desirable due to its diagnostic, therapeutic and prognostic importance. However, this demand has not been met so far.

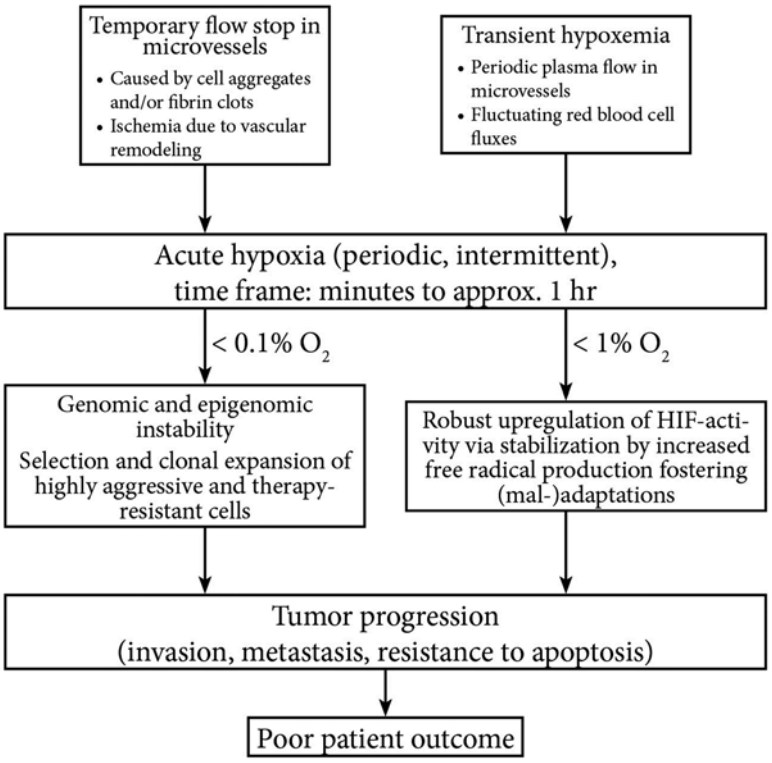

Fig. 11.2 Causative mechanisms for the development of acute hypoxia (*upper panels*). At moderate levels of hypoxia (<1 % O_2), activation of the HIF-system occurs (*central right panel*), while more severe hypoxia (<0.1 % O_2) can cause genomic and epigenomic instability and foster subsequent clonal selection (*central left panel*). Both processes contribute to tumor progression and poor patient outcome

Direct measurements of the tissue oxygenation status using invasive needle electrodes are inter alia laborious and rely on experienced investigators. Despite several limitations, this technique is still considered the "gold standard" [7]. Direct assessment of tumor hypoxia is also possible using the electron paramagnetic resonance (EPR) oxymetry [8]. First clinical EPR oxymetry studies to obtain pre-treatment and intra-treatment measurements have been started to test its clinical feasibility ([9], H.M. Swartz, personal communication).

Current molecular imaging of tumor hypoxia using the PET technique with hypoxia-specific tracers is qualitative rather than quantitative and short-term changes of hypoxia are difficult to detect [10]. Furthermore, the spatial resolution of imaging is too low with regard to the spatial dimensions of microregional heterogeneities, and different biologically relevant levels of hypoxia cannot be discriminated.

5 Tissue-Based Markers of Hypoxia

The existence of hypoxic tissue areas can also be demonstrated in histological sections (e.g., of biopsies, surgical specimens, and experimental tumors), and within them in single cells, using biomarkers. From a biological point of view, this may be the most meaningful way to assess tumor hypoxia, which invariably exerts its effects at the level of the single cell, e.g., by preserving its clonogenicity during a course of radiotherapy. Two primary approaches exist for the assessment of hypoxia in tissue.

5.1 Exogenous Markers

Derivatives of 2-nitroimidazole (azomycin) can be utilized as exogenous (extrinsic) markers which undergo covalent binding to proteins in intact cells under hypoxic conditions, thus creating neoepitopes, which can be detected by immunohistochemistry (IHC) using specific antibodies. Agents currently most widely used are pimonidazole (PIMO), CCI-103F and EF5 [11]. The extent of binding of these drugs in the tissue corresponds to the cumulative extension of the hypoxic areas during the exposure to the drug and, therefore, includes not only areas with chronic, but also with acute hypoxia which has occurred transiently during the time frame starting with the intracellular accumulation of the marker and terminating with the removal of the tissue. Exogenous hypoxia markers may be combined to address specific scientific questions, e.g., hypoxic cell turnover. Different pharmacokinetics of exogenous hypoxia markers must be taken into account: for PIMO, it is necessary to wait for at least 2 h after injection before the tissue can be harvested. In the case of EF5, this delay must be at least 24 h long. For PIMO and CCI-103F, an additional influence of the tissue-pH must be considered [12], while pH does not seem to play a role for EF5. Since chronic hypoxia in solid tumors—as was pointed out—is often caused by greatly increased diffusion distances, the question arises as to whether tissue areas beyond a critical distance from the nearest blood vessel are at all reached by hypoxia markers by diffusion, or whether these areas, due to diffusion limitations of the delivery of the marker in question, would falsely be classified as not being hypoxic. A clear answer cannot be given on the basis of available data. However, no compelling evidence can be found in the literature which indicates that putative diffusion limitations are a relevant obstacle for the delivery of exogenous hypoxia markers to those parts of the tumor, which contain viable tumor cells. In principle, there is also a chance that different levels and activities of nitroreductases in various cell types or tumors could distort the quantitative relationship between pO_2 and intensity of marker binding. Due to the redundancy of the enzymes that act as nitroreductases, though, a great importance of this mechanism appears to be relatively unlikely. In conclusion, exogenous hypoxia markers offer some excellent properties for studies of tumor biology. In fact, using these markers, some fundamental insights have been gained. These relate to, e.g., the relationship between hypoxia and cell

proliferation, and the dynamics of hypoxic tissue areas during the course of (fractionated) radiotherapy [13, 14]. Arguably the biggest drawback of exogenous hypoxia markers (which explains why data obtained with them are derived mainly from studies of experimental tumors) is the fact that the injection of a drug in humans is invasive, requires informed consent from the patient and is also associated with a significant logistical effort on behalf of the treating physician and other medical staff (e.g., coordination between the application of the marker, and diagnostic biopsy extraction or surgery).

5.2 Endogenous Biomarkers

The latter difficulties could be avoided if hypoxia would consistently lead to qualitative and, ideally, quantitative changes in the proteome in human cells, particularly in tumor cells: such proteome changes could be used as endogenous hypoxia biomarkers. With the discovery of hypoxia inducible factor (HIF)-1 by Semenza and Wang at the beginning of the 1990s [15], such a vision seemed to become tangible. Studies showed *in vitro* that the α-subunit of this heterodimeric transcription factor, HIF-1α, is very stringently regulated by hypoxia [16, 17]. Furthermore, immunohistochemical studies demonstrated the expression of the protein in precancerous lesions, numerous invasive tumors of different entities and their metastases [18, 19]. Investigations of this kind also revealed expression patterns at least partially compatible with triggering of the expression of the protein by diffusion limitations of oxygen [20]. However, it also quickly became evident that the inducibility of HIF-1α is strikingly cell type dependent. In some cell types, HIF-1α signals could be detected by western blot even under normoxic conditions [21]. In addition to mutations in the von Hippel Lindau gene, which is directly involved in the regulation of HIF-1α, activation of oncogenes, the effect of growth factors and cytokines, among others, were recognized as hypoxia-independent influences on the quantitative level of protein expression of HIF-1α.

The regulation of gene expression by hypoxia via HIF-1 is not restricted solely to the regulation of the protein abundance of the α-subunit, but also involves other, complex post-translational modifications [22]. For example, hypoxia inhibits asparagine hydroxylation of HIF-1α by the protein Factor Inhibiting HIF (FIH), which would otherwise lead to a reduction of the binding of the transcriptional cofactors CBP/p300 and a consecutive attenuation of the transactivation of a subgroup of HIF-1 target genes [23]. Hence, it was considered that certain target genes of HIF-1 could be better endogenous hypoxia markers than HIF-1 itself since their protein abundance reflects additional steps of hypoxia-dependent regulation of gene expression. Requirements for such marker proteins include a robust and quantitative induction by hypoxia via HIF-1 and at the same time, ideally, a lack of interference with regard to their protein abundance by other mechanisms. Glucose transporter (GLUT)-1 and carbonic anhydrase (CA) IX were the two HIF-1 target genes that were the most prominent candidates in this respect and have thus been investigated most intensively.

Both HIF-1α and its target proteins GLUT-1 and CA IX have been studied as endogenous hypoxia markers using IHC of human tumors with varying results. In some early publications, weak correlations between the intensity of their expression and data obtained with the Eppendorf oxygen electrode were described [20, 24, 25]. The latter method (see above) is considered to be the gold standard for determining the oxygenation status by many authors. It was, however, evident that these correlations were unable to assign individual patients to groups of hypoxic or better oxygenated tumors with sufficient certainty, particularly on the basis of a single reading in a clinical specimen. The weakness of the correlations found was partially attributed to the sampling error arising from the fact that IHC and electrode measurements were carried out in different parts of the tumor tissue.

Therefore, we and others carried out comparisons of the expression of these markers in precisely those micro-regions of the tumor, in which the oxygenation status had previously been determined [26–29]. As a surprisingly persistent result of these studies, no statistically significant correlation between the two methods was found anymore. These data were frequently interpreted as proof for the dominance of non-hypoxic stimuli over total HIF-1α protein abundance *in vivo*. Indeed, studies from different institutions have repeatedly demonstrated expression patterns of HIF-1α and its target genes GLUT-1 and CA IX in selected specimens that appear to be compatible with such an interpretation [20]. Additionally, we were able to show in severely hypoxic leiomyomas that these tumors do not activate the HIF-system at all, whereas the HIF-system was invariably active in their malignant counterparts, leiomyosarcomas [30]. On the one hand, these findings are compatible with a concept of modulation of the pure pO_2 signal by different activity states of intracellular signal transduction cascades. On the other hand, it should also be noted that the spatial resolution of electrode and IHC differ considerably. While endogenous hypoxia markers indicate the oxygenation status of each individual cell, data from the Eppendorf electrode represent the average oxygenation of hundreds of cells at each step of its path through the tissue. In uniformly hypoxic or well-oxygenated tissues, these considerations would have little impact on the intermodal comparability. The pattern of hypoxic and well-oxygenated tumor areas actually found *in vivo*, however, is characterized by proximity of these two extremes in confined spaces. Because of this methodological "mismatch", assessment of the suitability of endogenous hypoxia markers should not be based solely on the comparison with the Eppendorf electrode data.

6 Perspectives

In the meantime, a large number of studies have shown that a high level of expression of proteins of the HIF-mediated transcriptional response reaction—whether they are caused by hypoxia or not—is accompanied by a worsening of the patients' prognosis and that these proteins are also causally involved in tumor progression and resistance to therapy [31]. Thus, there is now a primary motivation to

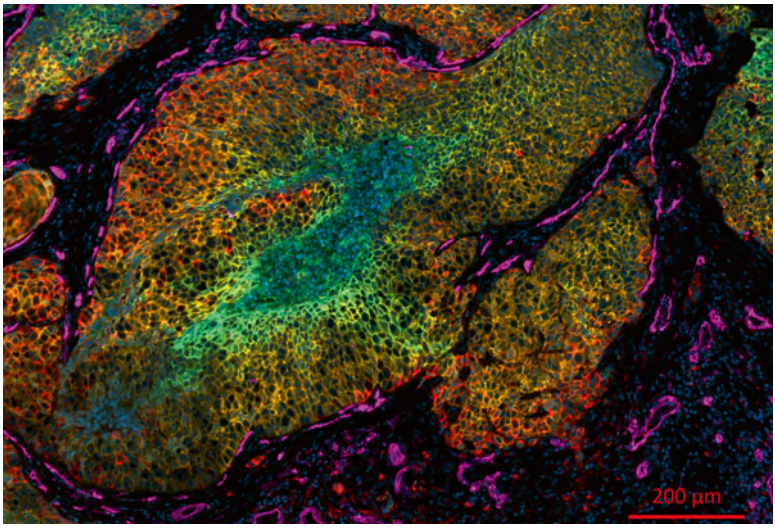

Fig. 11.3 5-plex immunofluorescence staining of a squamous cell carcinoma of the head and neck region. Shown are hypoxic regions (CA IX, *green*), mTOR activation (phosphorylated ribosomal protein S6, *red*), epidermal growth factor receptor (*orange*), microvascular endothelium (*purple*) and cell nuclei (DAPI, *blue*). Using single cell-based quantitative analysis methods, relationships between fundamental pathophysiological processes can be investigated

investigate components of the HIF system in tumors. Ideally, this should be done in a multiparametric approach, which investigates endogenous hypoxia markers in the pathophysiological context of tumor vascularization, proliferation and activation of specific signal transduction cascades (Fig. 11.3).

References

1. Vaupel P (2004) Tumor microenvironmental physiology and its implications for radiation oncology. Semin Radiat Oncol 14(3):198–206
2. Vaupel P (2008) Hypoxia and aggressive tumor phenotype: implications for therapy and prognosis. Oncologist 13(Suppl 3):21–26
3. Vaupel P, Mayer A (2007) Hypoxia in cancer: significance and impact on clinical outcome. Cancer Metastasis Rev 26(2):225–239
4. Vaupel P, Mayer A (2014) Hypoxia in tumors: pathogenesis-related classification, characterization of hypoxia subtypes, and associated biological and clinical implications. Adv Exp Med Biol 812:19–24
5. Bayer C, Shi K, Astner ST et al (2011) Acute versus chronic hypoxia: why a simplified classification is simply not enough. Int J Radiat Oncol Biol Phys 80(4):965–968
6. Vaupel P, Mayer A (2014) Imaging tumor hypoxia: blood-borne delivery of imaging agents is fundamentally different in hypoxia subtypes. J Innov Opt Health Sci 07(02):1330005
7. Vaupel P, Höckel M, Mayer A (2007) Detection and characterization of tumor hypoxia using pO_2 histography. Antioxid Redox Signal 9(8):1221–1236

8. Epel B, Redler G, Halpern H (2014) How in vivo EPR measures and images oxygen. Adv Exp Med Biol 812:113–119
9. Swartz HM, Williams BB, Zaki BI et al (2014) Clinical EPR: unique opportunities and some challenges. Acad Radiol 21(2):197–206
10. Horsman MR, Mortensen LS, Petersen JB et al (2012) Imaging hypoxia to improve radiotherapy outcome. Nat Rev Clin Oncol 9(12):674–687
11. Ljungkvist AS, Bussink J, Kaanders JH et al (2007) Dynamics of tumor hypoxia measured with bioreductive hypoxic cell markers. Radiat Res 167(2):127–145
12. Kleiter MM, Thrall DE, Malarkey DE et al (2006) A comparison of oral and intravenous pimonidazole in canine tumors using intravenous CCI-103F as a control hypoxia marker. Int J Radiat Oncol Biol Phys 64(2):592–602
13. Ljungkvist AS, Bussink J, Kaanders JH et al (2006) Dynamics of hypoxia, proliferation and apoptosis after irradiation in a murine tumor model. Radiat Res 165(3):326–336
14. Yaromina A, Kroeber T, Meinzer A et al (2011) Exploratory study of the prognostic value of microenvironmental parameters during fractionated irradiation in human squamous cell carcinoma xenografts. Int J Radiat Oncol Biol Phys 80(4):1205–1213
15. Semenza GL, Wang GL (1992) A nuclear factor induced by hypoxia via de novo protein synthesis binds to the human erythropoietin gene enhancer at a site required for transcriptional activation. Mol Cell Biol 12(12):5447–5454
16. Jiang BH, Semenza GL, Bauer C et al (1996) Hypoxia-inducible factor 1 levels vary exponentially over a physiologically relevant range of O_2 tension. Am J Physiol 271(4 Pt 1): C1172–C1180
17. Jewell UR, Kvietikova I, Scheid A et al (2001) Induction of HIF-1α in response to hypoxia is instantaneous. FASEB J 15(7):1312–1314
18. Zhong H, De Marzo AM, Laughner E et al (1999) Overexpression of hypoxia-inducible factor 1α in common human cancers and their metastases. Cancer Res 59(22):5830–5835
19. Talks KL, Turley H, Gatter KC et al (2000) The expression and distribution of the hypoxia-inducible factors HIF-1α and HIF-2α in normal human tissues, cancers, and tumor-associated macrophages. Am J Pathol 157(2):411–421
20. Haugland HK, Vukovic V, Pintilie M et al (2002) Expression of hypoxia-inducible factor-1α in cervical carcinomas: correlation with tumor oxygenation. Int J Radiat Oncol Biol Phys 53(4):854–861
21. Zhong H, Mabjeesh N, Willard M et al (2002) Nuclear expression of hypoxia-inducible factor 1alpha protein is heterogeneous in human malignant cells under normoxic conditions. Cancer Lett 181(2):233–238
22. Dengler VL, Galbraith MD, Espinosa JM (2014) Transcriptional regulation by hypoxia inducible factors. Crit Rev Biochem Mol Biol 49(1):1–15
23. Mahon PC, Hirota K, Semenza GL (2001) FIH-1: a novel protein that interacts with HIF-1α and VHL to mediate repression of HIF-1 transcriptional activity. Genes Dev 15(20):2675–2686
24. Airley R, Loncaster J, Davidson S et al (2001) Glucose transporter glut-1 expression correlates with tumor hypoxia and predicts metastasis-free survival in advanced carcinoma of the cervix. Clin Cancer Res 7(4):928–934
25. Loncaster JA, Harris AL, Davidson SE et al (2001) Carbonic anhydrase (CA IX) expression, a potential new intrinsic marker of hypoxia: correlations with tumor oxygen measurements and prognosis in locally advanced carcinoma of the cervix. Cancer Res 61(17):6394–6399
26. Mayer A, Wree A, Höckel M et al (2004) Lack of correlation between expression of HIF-1α protein and oxygenation status in identical tissue areas of squamous cell carcinomas of the uterine cervix. Cancer Res 64(16):5876–5881
27. Mayer A, Höckel M, Vaupel P (2005) Carbonic anhydrase IX expression and tumor oxygenation status do not correlate at the microregional level in locally advanced cancers of the uterine cervix. Clin Cancer Res 11(20):7220–7225
28. Mayer A, Höckel M, Wree A et al (2005) Microregional expression of glucose transporter-1 and oxygenation status: lack of correlation in locally advanced cervical cancers. Clin Cancer Res 11(7):2768–2773

29. Dellas K, Bache M, Pigorsch SU et al (2008) Prognostic impact of HIF-1α expression in patients with definitive radiotherapy for cervical cancer. Strahlenther Onkol 184(3):169–174
30. Mayer A, Höckel M, Wree A et al (2008) Lack of hypoxic response in uterine leiomyomas despite severe tissue hypoxia. Cancer Res 68(12):4719–4726
31. Mayer A, Vaupel P (2011) Hypoxia markers and their clinical relevance. In: Osinsky S, Friess H, Vaupel P (eds) Tumor hypoxia in the clinical setting. Akademperiodyka, Kiev, Ukraine, pp 187–202

Chapter 12
Molecular Imaging of Tumor Hypoxia: Existing Problems and Their Potential Model-Based Solutions

Kuangyu Shi, Sibylle I. Ziegler, and Peter Vaupel

Abstract Molecular imaging of tissue hypoxia generates contrast in hypoxic areas by applying hypoxia-specific tracers in organisms. In cancer tissue, the injected tracer needs to be transported over relatively long distances and accumulates slowly in hypoxic regions. Thus, the signal-to-background ratio of hypoxia imaging is very small and a non-specific accumulation may suppress the real hypoxia-specific signals. In addition, the heterogeneous tumor microenvironment makes the assessment of the tissue oxygenation status more challenging. In this study, the diffusion potential of oxygen and of a hypoxia tracer for 4 different hypoxia subtypes: ischemic acute hypoxia, hypoxemic acute hypoxia, diffusion-limited chronic hypoxia and anemic chronic hypoxia are theoretically assessed. In particular, a reaction-diffusion equation is introduced to quantitatively analyze the interstitial diffusion of the hypoxia tracer [^{18}F]FMISO. Imaging analysis strategies are explored based on reaction-diffusion simulations. For hypoxia imaging of low signal-to-background ratio, pharmacokinetic modelling has advantages to extract underlying specific binding signals from non-specific background signals and to improve the assessment of tumor oxygenation. Different pharmacokinetic models are evaluated for the analysis of the hypoxia tracer [^{18}F]FMISO and optimal analysis model were identified accordingly. The improvements by model-based methods for the estimation of tumor oxygenation are in agreement with experimental data. The computational modelling offers a tool to explore molecular imaging of hypoxia and pharmacokinetic modelling is encouraged to be employed in the corresponding data analysis.

Keywords Tumor hypoxia • Molecular imaging • Simulation of hypoxia imaging • Pharmacokinetic modelling

K. Shi (✉) • S.I. Ziegler
Department of Nuclear Medicine, Klinikum rechts der Isar, Technical University Munich, Ismaningerstr. 22, 81675 Munich, Germany
e-mail: k.shi@tum.de

P. Vaupel
Department Radiooncology and Radiotherapy, Klinikum rechts der Isar, Technical University Munich, Ismaningerstr. 22, 81675 Munich, Germany

© Springer International Publishing Switzerland 2016

Q. Luo et al. (eds.), *Oxygen Transport to Tissue XXXVIII*, Advances in Experimental Medicine and Biology 923, DOI 10.1007/978-3-319-38810-6_12

1 Introduction

Tumor hypoxia is considered a major resistance factor of standard radiotherapy and some chemotherapy, and can trigger tumor aggressiveness. It occurs mainly due to insufficient supply of oxygen [1] and can be characterized by different subtypes including ischemic hypoxia, hypoxemic hypoxia, diffusion-limited hypoxia and anemic hypoxia [2]. Molecular imaging provides a non-invasive method to assess the tissue oxygenation status upon systemic application of hypoxia-specific tracers such as [^{18}F]FMISO [3, 4], [^{18}F]FAZA [5] or [$^{60/61/64Cu}$]ATSM [6]. However, the amount of hypoxia-specific tracer accumulated depends on the microenvironment within tumor tissues. For the different hypoxia subtypes shown in Fig. 12.1, the less diffusible tracer needs to be transported over relatively longer distances than oxygen to reach hypoxic regions usually far away from functional blood vessels. It accumulates slowly in hypoxic regions [7]. Thus, the signal-to-background ratio of hypoxia imaging is very small and the non-specific accumulation of the tracers during transport may suppress the real hypoxia-specific signals. In addition, the heterogeneous tumor microenvironment makes the estimation of the tissue oxygenation status from the integrated signals of non-uniform tracer distribution more challenging.

The diffusion limitation of the hypoxia-specific molecule can be assessed by immunohistochemistry. Figure 12.2 shows the staining image of an example cryosection of a CAL-33 xenograft tumor in nude mice [8]. The tissue section is stained using CD31 for vascular endothelium, Hoechst 33342 for perfusion and pimonidazole (PIMO) for hypoxia. PIMO is a typical molecular marker for tumor hypoxia and the functional mechanism is similar to the PET tracer [^{18}F]FMISO. The intensity profiles between two example vessels (marked as yellow line in Fig. 12.2a) of PIMO and Hoechst are plotted in Fig. 12.2b. It is shown that in the middle of the two vessels, the Hoechst intensity stays constant but the PIMO intensity drops substantially.

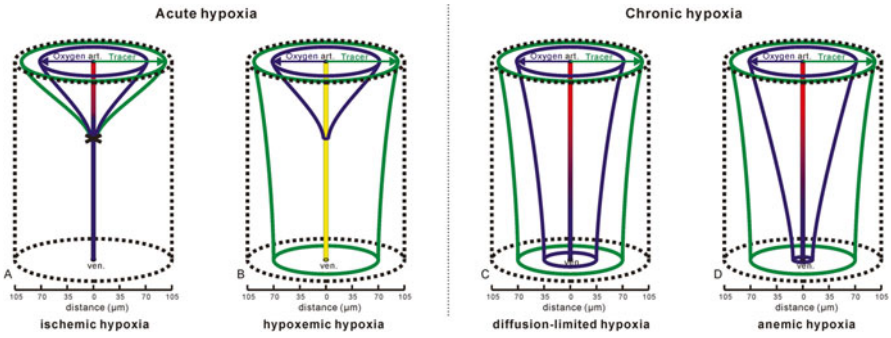

Fig. 12.1 Diffusion limitations of O_2 ('maximal O_2 diffusion front') and of a hypoxia-specific tracer for different subtypes of hypoxia in a tumor tissue cylinder (*broken line*)

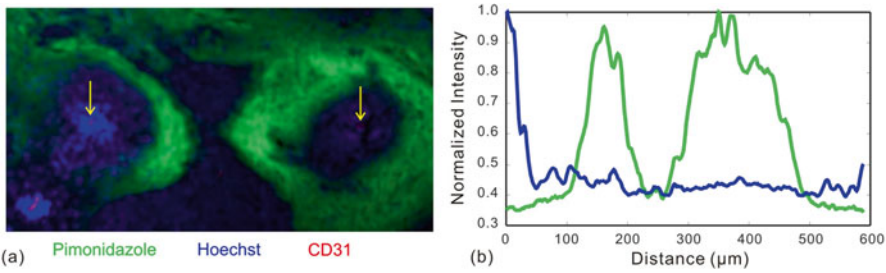

Fig. 12.2 Example of diffusion limitation for pimonidazole: (**a**) staining image; (**b**) intensity profile of Hoechst and PIMO along a line connecting the two microvessels indicated in *yellow arrows* as shown in (**a**)

Understanding the diffusion behavior of the hypoxia-specific tracer is important for the development of imaging strategies of hypoxia. The diffusion potential of a molecule depends on both the transport and the reaction within the tissue. Reaction-diffusion models were employed to investigate the diffusion of hypoxia tracer in tissues. They have advantages in exploring the diffusion properties of molecules in tissues and revealing the quantitative relation between *in vivo* imaging and the tumor microenvironment [9, 10]. In order to model the oxygen distribution within the tumor, the distribution of the microvasculature has been incorporated into the model and the reaction-diffusion equations were solved under certain boundary conditions on this geometry [11–14]. Kelly and Brady put forward a model to simulate the spatio-temporal distribution of [^{18}F]FMISO in tumors and generated meaningful time courses of imaging [9]. Histology-derived microvessel maps have been integrated for the simulation of realistic dynamic [^{18}F]FMISO PET imaging [15].

For hypoxia imaging with low signal-to-noise ratio due to diffusion limitations, special analysis strategies need to be considered to extract real hypoxia-related uptake from background signals. Pharmacokinetic modelling is an advanced method to compensate for the influence of confounding factors and to reduce the deviation between estimation and underlying physiology [16]. Compartmental models define physiologically different pools of the tracer substance as compartments and set up the relation between these compartments using linear differential equations [17]. Casciari et al. attempted (using a four-compartment model based on the pharmacodynamics of misonidazole) to determine the cellular reaction rate of [^{18}F]FMISO [18]. Thorwarth et al. proposed a specific model to identify the tumor oxygen status by decomposing the time-activity curve (TAC) into perfusion, diffusion and hypoxia-induced retention components based on the two-compartment model [7]. An empirical model was proposed to assess hypoxia by the slope of the late phase of dynamic activities [19]. The performance of the pharmacokinetic models depends on the description of the uptake procedure of the hypoxia tracer as well as the numerical stability. Computational simulation using a reaction-diffusion tool offered a measure to explore quantitative strategies of hypoxia imaging. The

present study evaluated the existing pharmacokinetic modelling methods for a typical hypoxia imaging tracer [^{18}F]FMISO based on reaction-diffusion simulations and identified an optimal analysis method accordingly.

2 Methods

To understand the transport of a hypoxia-specific tracer, a reaction-diffusion model is established to simulate the supply and accumulation of the tracer in hypoxic tissue. In this study, we focus on the hypoxia tracer [^{18}F]FMISO. A 2D-vascular map of different vessel densities is randomly generated to mimic tumor tissues of different oxygen levels and heterogeneities. Tissue oxygenation status is simulated by modelling oxygen diffusion from the microvasculature and metabolism according to Michaelis-Menten kinetics [9, 10]. The transport and metabolism of [^{18}F]FMISO is described by a reaction-diffusion equation [9, 10], and the uptake in tissue is calculated based on the microvasculature and oxygen level.

Digital phantoms (2D, 1×1 mm, pixel: 10×10 μm) of various microvasculatures and hypoxia distributions are constructed by simulating the transport and consumption of oxygen, as well as the delivery and the accumulation of [^{18}F]FMISO using the described reaction-diffusion equations. The phantoms are generated according to the pO_2 distribution. The tracer uptake signal is integrated spatially over the phantom and a TAC is generated, respectively. Noise is simulated according to Gaussian distribution. The simulated noisy TACs are fitted by each pharmacokinetic model investigated (Casciari, Irreversible & Reversible two-tissue compartmental, Thorwarth, Cho). The modelling results are compared to the features of each phantom. The prognostic capability of a model depends on the relation between relevant model-estimated kinetic parameters and underlying oxygen tensions. A monotonic correlation is expected and we define the hypoxia-sensitivity as the Spearman correlation to pO_2. Here we expect a negative value for hypoxia-sensitivity.

3 Results and Discussion

Figure 12.3 shows an example of three selected phantoms with different vascular maps corresponding to severe hypoxia, mild hypoxia and normoxia. The mean pO_2 increases as the vascular density (VD) raises. The hypoxia fraction (HF) is described as the proportion of hypoxic areas with a threshold of 7.5 mmHg (approx. 1 % O_2). The corresponding simulated TAC of each phantom is displayed on the bottom. The first 5 min of TAC corresponding to perfusion bolus increases from severe hypoxia to normoxia. In contrast, the last frames of TAC corresponding to [^{18}F]FMISO uptake decreases as HF decreases. The fitting results of the Casciari model, irreversible

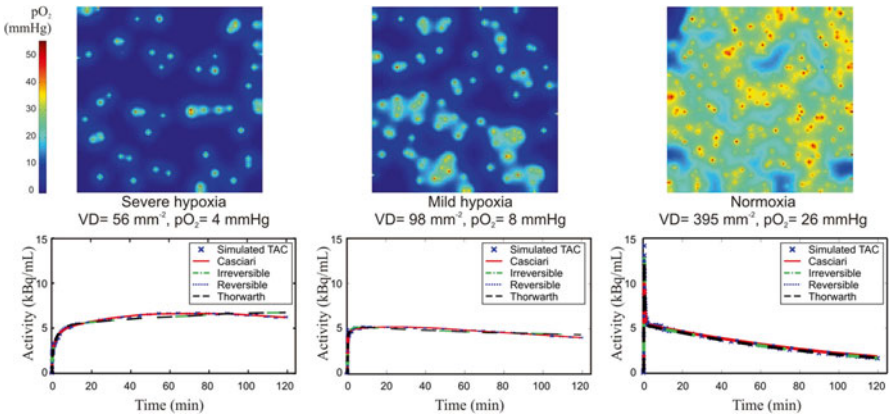

Fig. 12.3 Three phantoms of various vascular maps corresponding to severe hypoxia, mild hypoxia and normoxia: the *upper panels* display the distributions of the oxygen tension (pO_2) in the phantoms; the *bottom panels* show simulated TACs and corresponding modelling results of the investigated models. *VD* vascular density

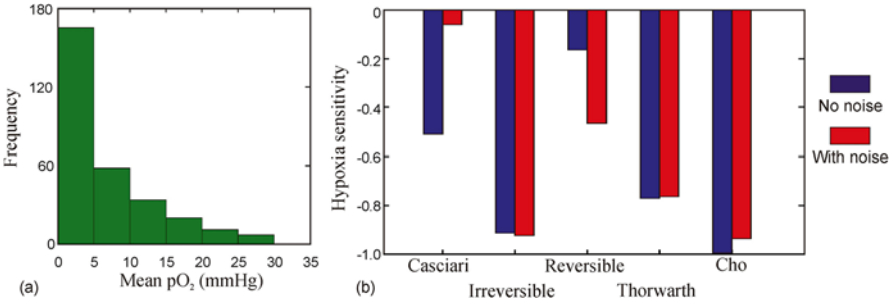

Fig. 12.4 Model sensitivity to hypoxia: (**a**) the simulated pO_2 distribution of 300 phantoms; (**b**) the sensitivity of different models to oxygen for ideal TAC (no noise) and TAC with noise, which is the Spearman correlation coefficient between the estimated hypoxia-related parameter and corresponding oxygen tension of 300 phantoms in (**a**)

two-tissue compartmental model (Irreversible), reversible two-tissue compartmental model (Reversible) and Thorwarth model are illustrated. All four models allow to produce a suitable fitting by setting proper initial values and fitting boundaries.

Figure 12.4 shows the sensitivity of each investigated model to hypoxia which is calculated as the Spearman correlation coefficient between the estimated hypoxia-related parameter and corresponding oxygen tension of 300 phantoms. The phantoms are selected according to an experimental pO_2 distribution based on polarographic measurements of oxygen tensions in C3H mouse mammary adenocarcinomas [20]. The hypoxia-related parameters were estimated on both ideal TAC and

TAC with added Gaussian noise for each model. The results show that both the irreversible two-tissue compartmental model and the Cho model have the highest sensitivity to underlying oxygen tensions and the irreversible two-tissue compartmental model is less sensitive to noise. The irreversible two-tissue compartmental model has been reported by various experimental studies as an appropriate model to analyze [^{18}F]FMISO imaging [21]. This is consistent with our (so far unpublished) experimental results.

4 Conclusions

The diffusion of hypoxia-specific tracers within tissues is complicated according to various subtypes of tumor hypoxia. Although reaction-diffusion simulation could not cover all the aspects of the pathophysiological procedure, it provides a tool to get quantitative insight into the hypoxia tracer uptake and can assist the development of imaging protocols. For the analysis of hypoxia PET imaging, pharmacokinetic modeling is encouraged to extract the low hypoxia signals from high perfusion backgrounds. Clinical studies of pharmacokinetic modeling of [^{18}F]FMISO PET in glioma patients are currently performed with stereotactic biopsy validations.

Acknowledgments This study was supported by the German Research Foundation (DFG), Collaborative Research Centre (SFB) 824.

References

1. Vaupel P, Kallinowski F, Okunieff P (1989) Blood flow, oxygen and nutrient supply, and metabolic microenvironment of human tumors: a review. Cancer Res 49:6449–6465
2. Bayer C, Shi K, Astner ST et al (2011) Acute versus chronic hypoxia: why a simplified classification is simply not enough. Int J Radiat Oncol Biol Phys 80:965–968
3. Koh WJ, Rasey JS, Evans ML et al (1992) Imaging of hypoxia in human tumors with [^{18}F] Fluoromisonidazole. Int J Radiat Oncol Biol Phys 22:199–212
4. Rasey JS, Koh WJ, Evans ML et al (1996) Quantifying regional hypoxia in human tumors with positron emission tomography of [^{18}F]Fluoromisonidazole: a pretherapy study of 37 patients. Int J Radiat Oncol Biol Phys 36:417–428
5. Souvatzoglou M, Grosu AL, Röper B et al (2007) Tumour hypoxia imaging with [^{18}F]FAZA PET in head and neck cancer patients: a pilot study. Eur J Nucl Med Mol Imaging 34:1566–1575
6. Lewis JS, Herrero P, Sharp TL et al (2002) Delineation of hypoxia in canine myocardium using PET and copper(II)-diacetyl-bis(N(4)-methylthiosemicarbazone). J Nucl Med 43:1557–1569
7. Thorwarth D, Eschmann SM, Paulsen F et al (2005) A kinetic model for dynamic [^{18}F]FMISO PET data to analyse tumour hypoxia. Phys Med Biol 50:2209–2224
8. Maftei CA, Bayer C, Shi K et al (2011) Changes in the fraction of total hypoxia and hypoxia subtypes in human squamous cell carcinomas upon fractionated irradiation: evaluation using pattern recognition in microcirculatory supply units. Radiother Oncol 101:209–216
9. Kelly CJ, Brady M (2006) A model to simulate tumour oxygenation and dynamic [^{18}F]FMISO PET data. Phys Med Biol 51:5859–5873

10. Wang Q, Vaupel P, Ziegler SI et al (2015) Exploring the quantitative relationship between metabolism and enzymatic phenotype by physiological modeling of glucose metabolism and lactate oxidation in solid tumors. Phys Med Biol 60:2547–2571
11. Secomb TW, Hsu R, Dewhirst MW et al (1993) Analysis of oxygen transport to tumor tissue by microvascular networks. Int J Radiat Oncol Biol Phys 25:481–489
12. Pogue BW, Paulsen KD, O'Hara JA et al (2001) Estimation of oxygen distribution in RIF-1 tumors by diffusion model-based interpretation of pimonidazole hypoxia and Eppendorf measurements. Radiat Res 155:15–25
13. Dasu A, Toma-Dasu I, Karlsson M (2003) Theoretical simulation of tumour oxygenation and results from acute and chronic hypoxia. Phys Med Biol 48:2829–2842
14. Petit SF, Dekker AL, Seigneuric R et al (2009) Intra-voxel heterogeneity influences the dose prescription for dose-painting with radiotherapy: a modelling study. Phys Med Biol 54:2179–2196
15. Mönnich D, Troost EG, Kaanders JH et al (2011) Modelling and simulation of [^{18}F] Fluoromisonidazole dynamics based on histology-derived microvessel maps. Phys Med Biol 56:2045–2057
16. Huang SC (2008) Role of kinetic modeling in biomedical imaging. J Med Sci 28:57–63
17. Gunn RN, Gunn SR, Cunningham VJ (2001) Positron emission tomography compartmental models. J Cereb Blood Flow Metab 21:635–652
18. Casciari JJ, Graham MM, Rasey JS (1995) A modeling approach for quantifying tumor hypoxia with [^{18}F]fluoromisonidazole PET time-activity data. Med Phys 22:1127–1139
19. Cho H, Ackerstaff E, Carlin S et al (2009) Noninvasive multimodality imaging of the tumor microenvironment: registered dynamic magnetic resonance imaging and positron emission tomography studies of a preclinical tumor model of tumor hypoxia. Neoplasia 11:247–259
20. Vaupel PW, Frinak S, Bicher HI (1981) Heterogeneous oxygen partial pressure and pH distribution in C3H mouse mammary adenocarcinoma. Cancer Res 41:2008–2013
21. Bartlett RM, Beattie BJ, Naryanan M et al (2012) Image-guided pO_2 probe measurements correlated with parametric images derived from [^{18}F]Fluoromisonidazole small-animal PET data in rats. J Nucl Med 53:1608–1615

Chapter 13
Direct and Repeated Clinical Measurements of pO_2 for Enhancing Cancer Therapy and Other Applications

Harold M. Swartz, Benjamin B. Williams, Huagang Hou, Nadeem Khan, Lesley A. Jarvis, Eunice Y. Chen, Philip E. Schaner, Arif Ali, Bernard Gallez, Periannan Kuppusamy, and Ann B. Flood

Abstract The first systematic multi-center study of the clinical use of EPR oximetry has begun, with funding as a PPG from the NCI. Using particulate oxygen sensitive EPR, materials in three complementary forms (India Ink, "OxyChips", and implantable resonators) the clinical value of the technique will be evaluated. The aims include using repeated measurement of tumor pO_2 to monitor the effects of treatments on tumor pO_2, to use the measurements to select suitable subjects for the type of treatment including the use of hyperoxic techniques, and to provide data that will enable existing clinical techniques which provide data relevant to tumor pO_2 but which cannot directly measure it to be enhanced by determining circumstances where they can give dependable information about tumor pO_2.

H.M. Swartz (✉) • B.B. Williams • P. Kuppusamy
Department of Radiology, Geisel School of Medicine at Dartmouth, One Medical Center Drive Lebanon, Lebanon, NH, USA

Department of Medicine, Geisel School of Medicine at Dartmouth, One Medical Center Drive Lebanon, Lebanon, NH, USA
e-mail: Harold.Swartz@Dartmouth.edu

H. Hou • N. Khan • A.B. Flood
Department of Radiology, Geisel School of Medicine at Dartmouth, One Medical Center Drive Lebanon, Lebanon, NH, USA

L.A. Jarvis • P.E. Schaner
Department of Medicine, Geisel School of Medicine at Dartmouth, One Medical Center Drive Lebanon, Lebanon, NH, USA

E.Y. Chen
Department of Surgery, Geisel School of Medicine at Dartmouth, One Medical Center Drive Lebanon, Lebanon, NH, USA

A. Ali
Department of Radiation Oncology, Emory Medical School, Atlanta, GA, USA

B. Gallez
Louvain Drug Research Institute, Université Catholique de Louvain, Brussels, Belgium

© Springer International Publishing Switzerland 2016

Q. Luo et al. (eds.), *Oxygen Transport to Tissue XXXVIII*, Advances in Experimental Medicine and Biology 923, DOI 10.1007/978-3-319-38810-6_13

Keywords Tumor pO_2 • Oximetry • EPR • Hypoxia

1 Introduction

It is widely recognized that hypoxia has a profound effect on the radiosensitivity of tissue and that hypoxic cells can be as much as three times less sensitive to radiation than well oxygenated cells [1–5]. A practical consequence of this fact is that tumors with significant hypoxia that are treated with radiation therapy have decreased probabilities for complete tumor control and reduced patient survival rates [1]. Despite the fundamental importance of tumor oxygenation during radiation therapy, measurements of the partial pressure of oxygen (pO_2) are not routinely performed in the clinical setting because of a lack of available quantitative measurement techniques that are noninvasive.

Electron Paramagnetic Resonance (EPR) oximetry based on particulates is a technique that is capable of providing repeated, direct, and noninvasive measurements of pO_2, following one-time implantation of a paramagnetic oxygen reporter [6]. These capabilities contrast with other techniques currently clinically available to measure oxygenation, which provide indirect measurements and/or are invasive at the time of measurement [7]. Based on the unique capabilities of EPR oximetry, the National Cancer Institute of US National Institutes of Health has funded a 5-year program project grant at Dartmouth (Dartmouth PPG) whose primary aim is to demonstrate the clinical capabilities of EPR oximetry for cancer. An additional goal is to relate EPR measurements to existing clinically available techniques, in order to understand under what circumstances those less direct techniques can give clinically useful information about tumor pO_2.

The clinical utility of repeated measurements of tumor oxygen is based on well-established observations of the effects of hypoxia on outcomes, the variability of oxygen levels in apparently similar tumors in different patients, the variation of oxygen levels as a function of growth of the tumor and in response to therapy, and the potential to modify oxygen levels by treatments such as breathing oxygen-rich mixtures [8–10]. Therefore, repeated measurements of tumor oxygen would enable the selection of subjects for various therapeutic approaches, evaluation of the effectiveness of methods to modify a patient's oxygen level, and guidance of the timing of treatments to ensure more optimal oxygen levels at the time of irradiation.

The PPG, while centered at Dartmouth, collaborates with two other academic radiation oncology centers (Emory University in Atlanta, Georgia and the Université catholique de Louvain in Brussels) to evaluate EPR oximetry using three different types of paramagnetic oxygen sensitive materials with complementary properties.

2 Methods

All measurements utilize clinical EPR in vivo oximetry, which has previously been described in some detail in reference [6]. The organizing principle for the PPG is the use of three different methods, which provide complementary capabilities to make the measurements in patients with tumors, These are described in some detail in the following.

The first method uses India ink whose oxygen-dependent broadening of the EPR linewidth reports the pO_2 of the tissue. India ink has already been used successfully in a wide array of animal studies [11–13] and in human subjects [6, 14–16]. India ink, because of its extensive prior use in human subjects including its current use for marking boundaries in surgery and radiation therapy, does not require approval by the US Food and Drug Administration (FDA) as a new drug. Consequently, early results for EPR oximetry focused on this sensor and were a major factor in the decision to fund the Dartmouth PPG (discussed in results below, Table 13.1). However, because India ink has a large linewidth, the sensor needs to be placed within 10 mm of the surface to get adequate signal to noise and therefore, while very useful for superficial tumors, it is not suitable for deeper tumors. It is placed in one or more sites in the tumor at depths from 1 to 5 mm, by a simple injection through a small needle (about 23 gauge).

The second method uses a paramagnetic material that is a derivative of lithium pthalocyanine, lithium octa-n-butoxynaphthalocyanine (LiNc-BuO) (see Fig. 13.1a, b [A]). Because of its very narrow linewidth and high spin density, it can be detected at deeper depths than India ink (discussed further in results below, Fig. 13.3),

Table 13.1 EPR oximetry using injected India ink to assess pO_2 measurements in tumors measured in vivo while patient breathes room air and enriched oxygen[a]

	Tumor		Tumor pO_2 as mmHg	
Type	Site	Breathing room air	Breathing enriched oxygen	Effect of breathing enriched oxygen
Lymphoma	Post. thigh	<5	>100	Increased
Lymphoma	Post. thigh	<3	>10	Increased
Lymphoma	Post. thigh	~1	>5	Increased
Melanoma	Knee	<10	>50	Increased
Melanoma	Foot	Anoxic	Anoxic	No change
Melanoma	Scalp	Anoxic	Anoxic	No change
Melanoma	Scalp and neck	~6	~12	Increased
Melanoma	Scapula	<1	<5	Increased
Melanoma	Chest	~10	~10	No change
Melanoma	Calf	Anoxic	~3	Increased
Sarcoma	Nose	~10	~10	No change

[a]Adapted from a table in Swartz et al. [6]; reproduced with permission.

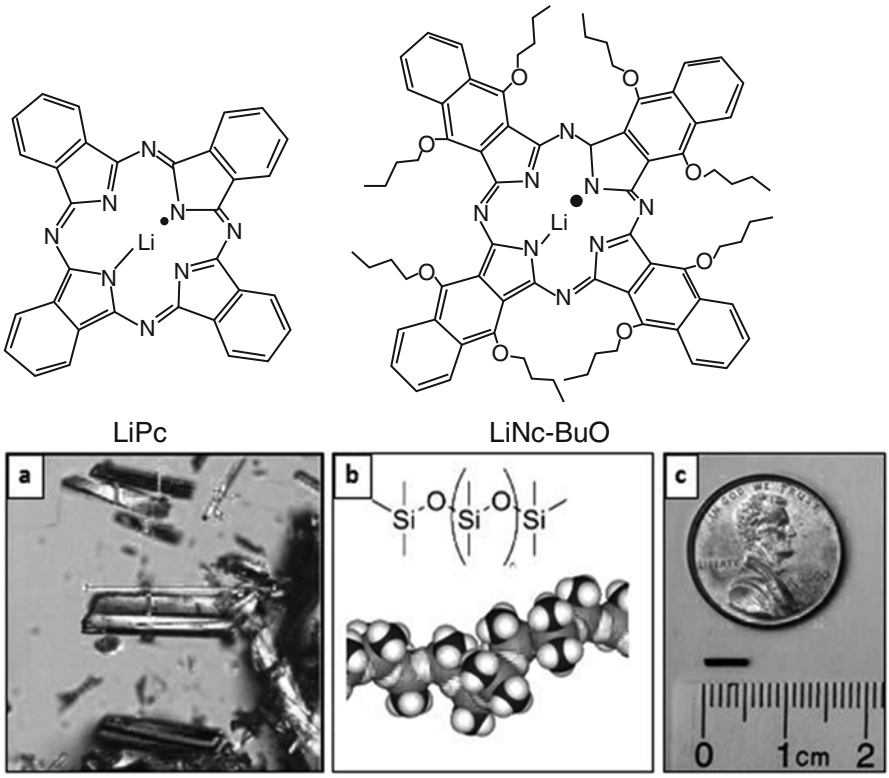

Fig. 13.1 (**a**) Molecular structure of lithium phthalocyanine (LiPc) and lithium octa-n-butoxynaphthalocyanine (LiNc-BuO) oximetry probes. The probes are prepared in the form of fine crystals which are paramagnetic and biologically inert. The crystals exhibit high spin density (~10^{20} spins/g), single sharp EPR peak (peak-to-peak width <50 mG under anoxic conditions), and are sensitive to oxygen partial pressure of oxygen (5–9 mG/mmHg pO_2). (**b**) LiNc-BuO crystals, PDMS coating, and the OxyChip. (*A*) Microcrystals of LiNc-BuO are encapsulated into (*B*) polydimethylsiloxane (PDMS), a biocompatible and oxygen-permeable polymer, to obtain (*C*) small pieces of probes (OxyChip) for implantation in tissues. The OxyChip is 0.6 mm in diameter and 5 mm in length and can be conveniently loaded into the tip of an 18-G angio-catheter to be implanted in tumors. (**b** [B] is reproduced from Courtney 2015 [23])

making it potentially a more effective oximetric material for deeper tumors. Like India ink, it also is very unreactive and very stable, both of which are very desirable characteristics for substances placed into tumors. However, because, unlike India ink, lithium phthalocyanine derivatives have not been commonly used in humans, they would require the very time-consuming and very expensive regulatory processes to get approval from the FDA for direct implantation, even though they are inert. To reduce the regulatory requirements for direct implantation of the crystals, we have developed a method to package them in a widely accepted biocompatible material that is permeable to oxygen, polydimethylsiloxane (PDMS) (Fig. 13.1b

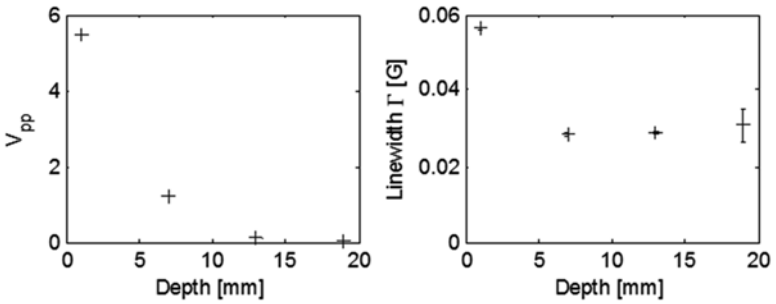

Fig. 13.3 OxyChips were measured at depths of 1, 7, 13, and 19 mm in lossy material. The peak-to-peak amplitude [V_{pp}] (*left*) and estimated linewidth (*right*) are shown. Consistent linewidths, regardless of depth, establish the capability to measure pO_2 at 2 cm depth in as little as 5 s per measurement. (Error bars are estimated uncertainty in fit parameter, where the oxygen response is ~7 mG/mmHg)

[B]). This packaging has enabled us to get an approved Investigation Device Exemption (IDE) from the FDA to conduct an initial Phase 1 safety study in human subjects. The packaged sensor currently in use is 5 mm in length, 0.6 mm in diameter and consists of 40 % of the sensor to 60 % of PDMS; this packaged sensor, called an OxyChip, has been extensively studied in preclinical studies (Fig. 13.1b [C]) [17–19].

When this early Phase 1 study using OxyChips is successfully completed, we anticipate not only expanding our clinical studies in humans using the OxyChip but also using this demonstration of the safety of the coated material to receive an IDE to conduct clinical studies using the third method in the PPG, an implantable resonator.

The implantable resonator contains multiple tips, each of which contains an oxygen sensitive material (based on the OxyChip) which is then connected to a loop under the skin by means of a very thin wire. We then can magnetically couple a surface component to the implanted part of the resonant circuit (Fig. 13.2). The FDA has already reviewed preliminary documentation for an IDE for the implantable resonator and, based on these discussions, we anticipate receiving approval once the OxyChip passes the criteria for Phase 1 safety (expected in 2016). The resonator is put in place either through a large biopsy needle or directly at the time of an open biopsy or other procedure that exposures the tumor.

3 Results

Table 13.1 shows clinical measurements of pO_2 made in 11 patients with three types of tumors located in several different anatomical sites, all measured using India ink. All patients were measured initially while breathing room air and then again while

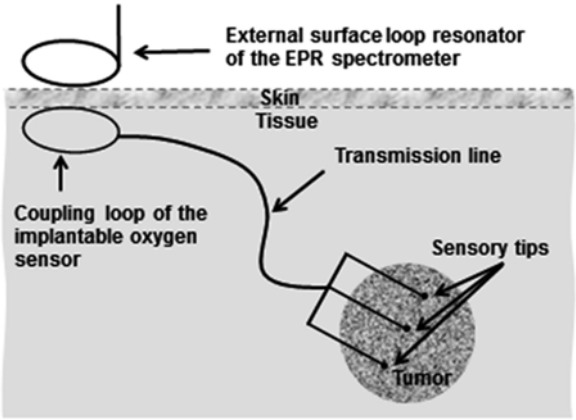

Fig. 13.2 Implantable resonators for deep-tissue EPR oximetry. The implantable sensors can be made with different length of the transmission line (i.e., depth) that can vary from 1 to >10 cm. Multiple implantable deep-tissue oxygen sensors can be implanted with sensory tips inserted into the tissue of interest and coupling loops positioned under the skin. The external surface loop resonator of the EPR spectrometer is used for inductive coupling to acquire EPR spectra

breathing 100 % oxygen through a face mask. These results show that EPR oximetry can be used to make measurements in tumors under clinically applicable

OxyChip to be reliably equilibrated with the test gas (100 % N_2). Single 5 s scans of the spectrum were carried out with constant non-saturating RF power and low modulation amplitude that did not distort the spectrum.

Figure 13.3 shows the peak-to-peak amplitude and estimated linewidth, as the depth was increased from conditions.

Perhaps most importantly, the results also show that not all tumors respond to breathing enriched oxygen. Only seven of the eleven patients had an increase in oxygen after breathing gas mixtures enriched with oxygen. Of the four patients who showed no change after breathing enriched oxygen, two had tumors that were initially assessed as anoxic, and the other two tumors had the highest observed initial levels of oxygen (~10 mmHg).

The finding of tumor variability in response to breathing oxygen has very important implications. The failure of a substantial number of tumors to respond to the increased oxygen in the breathing gas provides an explanation for why previous attempts to improve outcomes by the use of hyperoxic approaches have had at best marginal success [3, 8, 20]. Without monitoring tumor hypoxia directly and repeatedly in response to breathing enriched oxygen (or in some cases without controlling the timing of hypoxic therapy relative to treatment), they could not differentiate between tumors that did and did not respond to the hyperoxic therapy. Therefore, before separating the data into the appropriate subpopulations, they concluded that the procedure did not significantly improved outcomes.

Our results, showing the ability to determine which tumors are responsive to hyperoxic therapy, i.e., which will have increased pO_2 after breathing enriched oxygen, support the conclusion that it is possible to assess which tumors respond to hyperoxic therapy so that these patients could be selected to receive concurrent hyperoxic therapy with their standard treatments. Alternatively, some have suggested that treatment could be delivered more aggressively knowing that the tumor is hypoxic and unresponsive to hyperoxic therapy [21] and so oximetry would provide clinically useful information in such cases as well.

In vitro measurements were performed to establish depth sensitivity profiles for oximetry using the second type of sensor, the OxyChip (Fig. 13.3). The non-resonant losses of microwaves which occurs in tissue was modeled using slices of bologna sausage, which allowed the OxyChips to be placed at well-defined depths while maintaining a regular geometry and constant non-resonant losses such as that which occurs in tissues in vivo. Within the block of bologna at four different depths, a single OxyChip was placed within Teflon tubing inside a microcapillary tube that allowed the 1 mm to ~2 cm. Of importance for clinical oximetry, consistent, valid data continued to be obtained throughout the full range of depth. Additional averaging of multiple 5 s scans can be used to increase precision of the measurement and/or provide the capability to get measurements deeper than 20 mm.

These data support the conclusion that the OxyChip can be used to make measurements directly from the surface up to 20 mm, which would significantly enhance the applications using surface resonators. (The implantable resonator would allow assessment at any depth.)

4 Discussion and Conclusions

The results to date in preclinical and clinical studies indicate that clinical applications of EPR oximetry based on particulates may provide valuable additional capabilities to the current state for measuring hypoxia in tumors and, using that knowledge, to improve clinical care. Furthering this evidence for EPR oximetry and our understanding of the mechanisms involved is the primary aim of the Dartmouth PPG.

There are several existing options available to clinicians to measure hypoxia. While providing much useful information, other current methods cannot provide the quantitative data on tumor pO_2 that can be obtained with EPR oximetry with particulates. Therefore, a second but very important goal of the Dartmouth PPG is to systematically gather data using existing methods in current use to characterize hypoxia, in conjunction with EPR oximetry. For a brief listing of the clinically available techniques to measure oxygen in tumors, see the companion paper in this volume by Flood et al. which discusses methods in the context of comparative effectiveness [22]. Here we briefly discuss how the clinical uses of these methods relate to and could be augmented by measurements of EPR oximetry.

The oxygen electrode (which is no longer made for clinical use) while providing very important data, is too invasive for repeated use and is limited to relatively superficial tumors. Other limitations are due to local perturbations when used. Nevertheless, the data from EPR oximetry could delineate where the data obtained with its one time use might provide a better basis for its use for patient selection.

There are several MRI techniques that are widely available clinically. They provide information that, while not directly measuring pO_2, is related indirectly to tumor hypoxia, e.g., by providing evidence of poor rates of diffusion of oxygen to the tumor. Techniques that are especially clinically promising include blood oxygen level dependent (BOLD), diffusion-weighted imaging, perfusion weighted imaging, and magnetic resonance spectroscopy. The parameters that they measure can be significant factors in hypoxia. Changes they measure may already be clinically significant, but their effective use could be significantly enhanced if EPR oximetry was used either as an important second source of data or to delineate the circumstances where these techniques would most likely reflect clinically important information on hypoxia in a patient.

The use of optical methods such as near infrared to measure the saturation and volume of hemoglobin are also becoming more widely available. While this information can give pO_2 in the vascular system, it cannot then be directly used to estimate pO_2 in the tumor. However, coupled with data from EPR, its clinical value could be enhanced if used under conditions when EPR oximetry has shown that the optical method is a reasonable indicator of tumor oxygenation.

The positron emission tomography (PET) tracers of hypoxia localizing drugs are increasing available, providing qualitative indication of the presence of hypoxic areas at the time that the drugs were given. Again, while the information is limited to qualitative indications and describes one point in time, EPR oximetry could help to delineate those circumstances in which the information from hypoxic localizing drugs could be useful in the clinical management of therapy to overcome the effects of tumor hypoxia.

In summary, the translation from preclinical to clinical use of EPR oximetry based on particulates is proceeding effectively with measurements initiated in human subjects. In the near future it should be feasible to test the clinical impact of these measurements. That impact is anticipated to include: improved selection of patients for hyperoxic therapy, enhanced effectiveness of radiation therapy (including optimizing combinations with chemotherapy) by delineating the windows when the radiation will be most effective, and improved clinical utility of existing but indirect methods to characterize tumor hypoxia. If the goals of the PPG are fully achieved the result would be a very significant enhancement of the ability to effectively treat many solid cancers.

Acknowledgments This work was supported by grants from the National Institutes of Health [P01 CA190193 (the Dartmouth PPG) and R01 EB004031] and pilot project funding from the Prouty Fund of the Norris Cotton Cancer Center at Geisel Medical School.

References

1. Vaupel P, Mayer A (2007) Hypoxia in cancer: significance and impact on clinical outcome. Cancer Metastasis Rev 26:225–239. doi:10.1007/s10555-007-9055-1
2. Vaupel P, Mayer A (2015) The clinical importance of assessing tumor hypoxia: relationship of tumor hypoxia to prognosis and therapeutic opportunities. Antioxid Redox Signal 10:878–879. doi:10.1089/ars.2014.6155
3. Walsh JC, Lebedev A, Aten E et al (2014) The clinical importance of assessing tumor hypoxia: Relationship of tumor hypoxia to prognosis and therapeutic opportunities. Antioxid Redox Signal 21:1516–1554. doi:10.1089/ars.2013.5378
4. Menon C, Fraker DL (2005) Tumor oxygenation status as a prognostic marker. Cancer Lett 221:225–235. doi:10.1016/j.canlet.2004.06.029
5. Dhani N, Fyles A, Hedley D et al (2015) The clinical significance of hypoxia in human cancers. Semin Nucl Med 45:110–121. doi:10.1053/j.semnuclmed.2014.11.002
6. Swartz HM, Williams BB, Zaki BI et al (2014) Clinical EPR: unique opportunities and some challenges. Acad Radiol 21:197–206. doi:10.1016/j.acra.2013.10.011
7. Springett R, Swartz HM (2007) Measurements of oxygen in vivo: overview and perspectives on methods to measure oxygen within cells and tissues. Antioxid Redox Signal 9:1295–1301. doi:10.1089/ars.2007.1620
8. Wilson WR, Hay MP (2011) Targeting hypoxia in cancer therapy. Nat Rev Cancer 11:393–410. doi:10.1038/nrc3064
9. Vaupel P (2009) Prognostic potential of the pre-therapeutic tumor oxygenation status. Adv Exp Med Biol 645:241–246. doi:10.1007/978-0-387-85998-9_36
10. Hoogsteen IJ, Marresy HAM, van der Kogel AJ et al (2007) The hypoxic tumour microenvironment, patient selection and hypoxia-modifying treatments. Clin Oncol (R Coll Radiol) 19:385–396. doi:10.1016/j.clon.2007.03.001
11. Goda F, O'Hara JA, Rhodes ES et al (1995) Changes of oxygen tension in experimental tumors after a single dose of X-ray irradiation. Cancer Res 55:2249–2252
12. O'Hara JA, Goda F, Demidenko E et al (1998) Effect on regrowth delay in a murine tumor of scheduling split-dose irradiation based on direct pO_2 measurements by electron paramagnetic resonance oximetry. Radiat Res 150:549–556. doi:10.2307/3579872
13. O'Hara JA, Goda F, Liu KJ et al (1995) The pO_2 in a murine tumor after irradiation: an in vivo electron paramagnetic resonance oximetry study. Radiat Res 144:222–229. doi:10.2307/3579262
14. Khan N, Hou H, Hein P et al (2005) Black magic and EPR oximetry: from lab to initial clinical trials. In: Okunieff P, Williams J, Chen Y (eds) Advances in experimental medicine and biology: Oxygen transport to tissues XXVI. 31st annual meeting of the International Society on Oxygen Transport to Tissue, Rochester, NY, 16–20 August 2003
15. Khan N, Williams BB, Swartz HM (2006) Clinical applications of in vivo EPR: rationale and initial results. Appl Magn Reson 30:185–199. doi:10.1007/BF03166718
16. Swartz HM, Khan N, Buckey J et al (2004) Clinical applications of EPR: overview and perspectives. NMR Biomed 17:335–351. doi:10.1002/nbm.911
17. Meenakshisundaram G, Eteshola E, Pandian RP et al (2009) Oxygen sensitivity and biocompatibility of an implantable paramagnetic probe for repeated measurements of tissue oxygenation. Biomed Microdevices 11:817–826. doi:10.1007/s10544-009-9298-4
18. Dinguizli M, Jeumont S, Beghein N et al (2006) Development and evaluation of biocompatible films of polytetrafluoroethylene polymers holding lithium phthalocyanine crystals for their use in EPR oximetry. Biosens Bioelectron 21:1015–1022. doi:10.1016/j.bios.2005.03.009
19. Hou H, Dong R, Li H et al (2012) Dynamic changes in oxygenation of intracranial tumor and contralateral brain during tumor growth and carbogen breathing: a multisite EPR oximetry with implantable resonators. J Magn Reson 214:22–28. doi:10.1016/j.jmr.2011.09.043

20. Janssens GO, Rademakers SE, Terhaard CH et al (2012) Accelerated radiotherapy with carbogen and nicotinamide for laryngeal cancer: results of a phase III randomized trial. J Clin Oncol 30:1777–1783. doi:10.1200/JCO.2011.35.9315
21. Gallez B, Baudelet C, Jordan BF (2004) Assessment of tumor oxygenation by electron paramagnetic resonance: principles and applications. NMR Biomed 17:240–262. doi:10.1002/nbm.900
22. Flood AB, Satinsky VA, Swartz HM (2015) Comparing the effectiveness of methods to measure oxygen in tissues for prognosis and treatment of cancer. In: Advances in experimental medicine and biology: oxygen transport to tissues XXXVIII. 43rd annual meeting of the International Society on Oxygen Transport to Tissue, Wu-han, China, 11–16 July 2015 (submitted to same volume)
23. Courtney A (2015) The synthesis of bouncing putty: a cross-linked silicone polymer. [image in Fig. 1b [B] from https://www.wou.edu/las/physci/ch462/BouncingPutty.htm. Accessed 20 August 2015]

Chapter 14
Impact of the Tumor Microenvironment on the Expression of Inflammatory Mediators in Cancer Cells

A. Riemann, A. Ihling, S. Reime, M. Gekle, and O. Thews

Abstract Hypoxia and extracellular acidosis are common features of solid malignant tumors. The aim of the study was to analyze whether these pathophysiological parameters affect the expression of inflammatory mediators in tumor cells. Therefore the mRNA expression of MCP-1 (monocyte chemotactic protein 1), iNOS and osteopontin was measured under hypoxic (pO_2 1 mmHg) and acidotic (pH 6.6) conditions by qPCR in AT1 R-3327 prostate cancer cells. In addition, the underlying signaling cascades were analyzed by using inhibitors of the p38 and ERK1/2 MAP kinase pathways.

Hypoxia led to a significant decrease of the expression of MCP-1 and osteopontin over the complete observation period of 24 h, whereas the iNOS expression after an initial reduction slightly increased. Acidotic conditions for up to 6 h increased the iNOS expression significantly which was functional as indicated by an elevated level of nitrate/nitrite formation by 30 %. Acidosis had almost no impact on the MCP-1 expression of tumor cells, whereas the osteopontin level tended to increase leading to a significantly elevated level after 24 h at pH 6.6. Inhibiting the p38 and ERK1/2 under control conditions revealed that the MAPKs play a significant role for the regulation of the expression of inflammatory mediators. MCP-1 expression could be lowered by inhibiting ERK1/2 whereas iNOS expression was dependent on both p38 and ERK1/2 MAPK. These results indicate that the adverse tumor microenvironment affects the expression of inflammatory mediators by tumors cells and may therefore modulate the immune response within the tumor tissue.

Keywords Acidosis • Hypoxia • Tumor • Inflammatory mediators • ERK1/2

A. Riemann • A. Ihling • S. Reime • M. Gekle • O. Thews (✉)
Julius-Bernstein-Institute of Physiology, University of Halle,
Magdeburger Str. 6, 06114 Halle, Germany
e-mail: oliver.thews@medizin.uni-halle.de

© Springer International Publishing Switzerland 2016

Q. Luo et al. (eds.), *Oxygen Transport to Tissue XXXVIII*, Advances in Experimental Medicine and Biology 923, DOI 10.1007/978-3-319-38810-6_14

1 Introduction

The tumor microenvironment is characterized by an insufficient oxygen supply resulting in a forced glycolytic metabolism. For this reason pronounced hypoxia (with pO_2 values below 5 mmHg) is commonly found in experimental as well as in human tumors [1, 2]. This adverse milieu can limit the efficacy of non-surgical treatment modalities, but can also affect the malignant progression of tumors (reduced apoptotic potential, increased invasiveness or formation of far-distance metastasis). The inflammatory response in the tumor tissue, for instance the activity of tumor-associated macrophages (TAM) or the release of inflammatory mediators [3, 4], is an important aspect for local tumor progression or control. The sources of cytokine secretion could be TAMs, fibroblasts but also the tumor cells themselves [4]. Previous studies indicated that the expression of different inflammatory mediators (TNF-α, COX-2, MCP-1 and iNOS) in normal tissue fibroblasts is modulated by the extracellular pH [5]. For this reason, the aim of the present study was to analyze whether the expression of cytokines by tumor cells is also dependent on parameters of the metabolic microenvironment. Therefore, the expression of the monocyte chemotactic protein 1 (MCP-1), the inducible NO synthase (iNOS) and osteopontin (OPN) was studied in tumor cells during hypoxia and extracellular acidosis.

Since previous studies clearly revealed that extracellular acidosis activates MAP kinases p38 and ERK1/2 in different tumor cells as well as in fibroblasts [5–7] the question arises whether these signaling pathways are involved in the modulation of the expression of inflammatory mediators in tumor cells. Therefore, the expression during acidosis was assessed while these MAPK were inhibited.

2 Methods

2.1 Cell Culture

The subline AT-1 of the rat R-3327 Dunning prostate carcinoma was used in all experiments. Cells were grown in RPMI medium supplemented with 10 % fetal calf serum (FCS). Twenty-four hours before the experiments, cells were serum-depleted. Afterwards they were incubated for 3, 6 or 24 h in bicarbonate-HEPES- (pH 7.4) or MES- (pH 6.6) buffered Ringer solutions in room air supplemented with 5 % CO_2. For hypoxia experiments cells were incubated for 3, 6 or 24 h in room air (+5 % CO_2) or a gas mixture containing 0.1 % O_2, 94.9 % N_2 and 5 % CO_2 resulting in a pO_2 of approximately 1 mmHg.

For assessing the role of the MAP kinases, inhibitors of p38 (SB203580) or ERK1/2 (U0126) were added to the medium during acidotic or hypoxic incubation,

2.2 Measurements

Expression of MCP-1 (CCL2), iNOS and OPN (SPP1) were assessed after acidotic or hypoxic incubation by quantitative PCR. In brief, total RNA was isolated using the InviTrap Spin Tissue RNA Mini Kit (Stratec, Berlin, Germany). 1 µg RNA was subjected to reverse transcription with SuperScript II reverse transcriptase (Invitrogen, Carlsbad, CA, USA) and analyzed by qPCR using the Platinum SYBR Green qPCR Supermix (Invitrogen, Carlsbad, CA, USA). For data analysis qPCR data were normalized to the results at pH 7.4 under normoxic conditions.

Production of nitrite and nitrate was studied using nitrate/nitrite fluorometric assay kit (Cayman Chemical, Ann Arbor, MI, USA). Data were normalized to overall protein content in µg before calculating relative hypoxia/ acidosis-induced effects.

3 Results

Incubating AT1 cells at 1 mmHg pO_2 led to a significant decrease in **MCP-1** expression. After 3 h expression was more than halved (Fig. 14.1a) further continuously decreasing over the whole observation period of 24 h finally reaching a value ten-times lower than under normoxic conditions. In contrast, incubating the cells at an acidotic pH of 6.6 (under normoxic conditions) had no effect on the MCP-1 expression (Fig. 14.1b).

Inducible NO-synthase (**iNOS**) showed only minor dependency on the environmental pO_2. During the first 3 h of hypoxia the expression was initially lowered, however, afterwards iNOS mRNA constantly increased up to 24 h (Fig. 14.1c). Exposing the cells to an acidic environment for 3–6 h the iNOS expression was significantly increased by a factor of 2–4 (Fig. 14.1d). Keeping the cells at pH 6.6 for 24 h had no effect on the mRNA level.

The expression of **osteopontin** showed both, hypoxia- and pH-dependency. Under hypoxic conditions the OPN mRNA level was constantly reduced by a factor of 2–4 (Fig. 14.1e). However, keeping the cells under normoxia but at pH 6.6 led to an increase in the OPN expression after 24 h (Fig. 14.1f).

Since acidosis had a strong impact on the iNOS expression it was tested whether this change in expression is reflected functionally by an increased formation of nitrite and nitrate. After 3 h iNOS expression was increased by a factor of 1.8 (1.5–2.1) but the nitrite/nitrate remained almost unchanged ($101 \pm 10\,\%$ of control at pH 7.4). However, after 6 h, where the iNOS expression increased to a factor of 3.6 (2.5–5.4), the nitrite/nitrate production increased significantly to $129 \pm 6\,\%$ ($p < 0.01$) indicating that the acidosis-induced change in iNOS expression has a functional impact.

Since previous data showed that extracellular acidosis strongly activates p38- and ERK1/2-MAP kinases [6] further experiments should test whether the acidosis-induced changes in inflammatory mediator expression (Fig. 14.1) was facilitated by

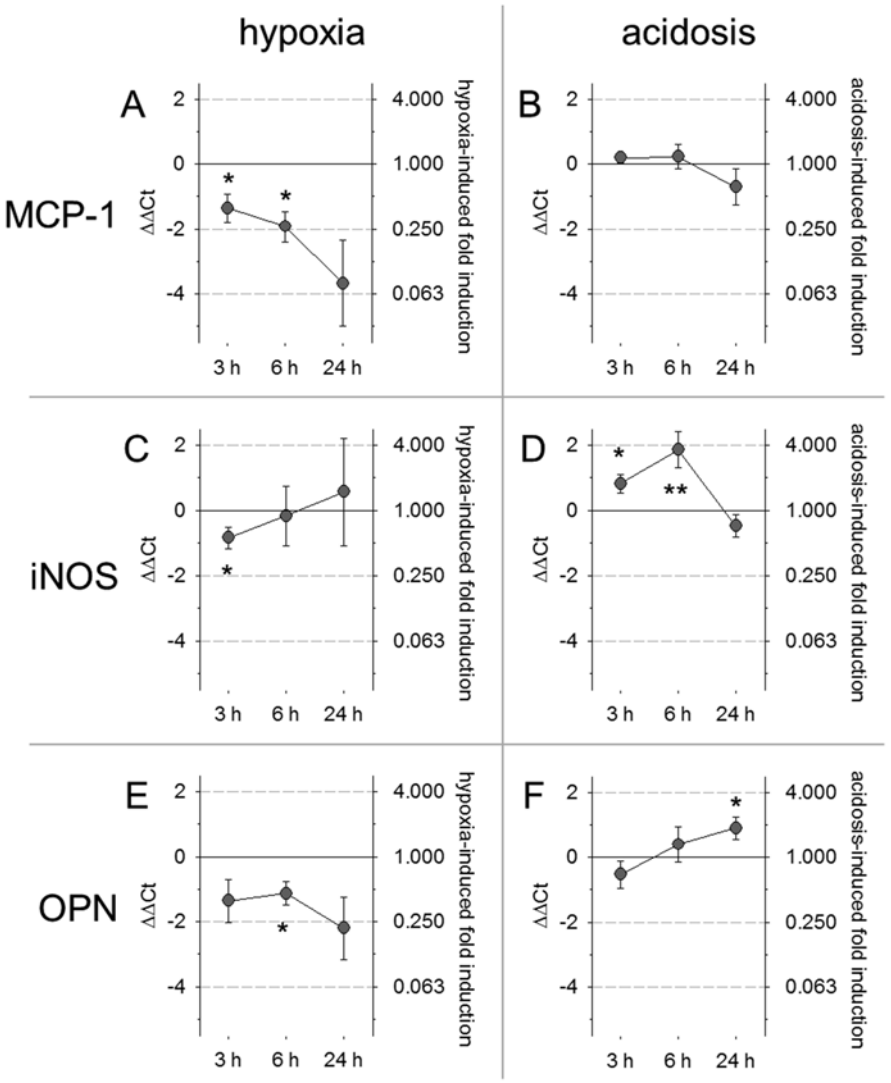

Fig. 14.1 Change of expression of MCP-1 (**a**, **b**), iNOS (**c**, **d**) and OPN (**e**, **f**) either by hypoxia (**a**, **c**, **d**) or extracellular acidosis (**b**, **d**, **f**) measured by qPCR. Cells were incubated at pH 7.4 and pO_2 1 mmHg or at pH 6.6 and pO_2 150 mmHg for up to 24 h. Data show the fold induction and ΔΔCt values of the respective mRNA induced by hypoxia or acidosis. n = 4–15; (*) $p < 0.05$ vs. control; (**) $p < 0.01$ vs. control

the MAPK signalling pathways. Therefore, the acidosis-induced change in mRNA expression was assessed after inhibiting p38 or ERK1/2. Incubating AT-1 cells with the p38 inhibitor SB203580 for 3 h had almost no impact on the expression of MCP-1, either at pH 7.4 or at pH 6.6 (Fig. 14.2a, b). However, interrupting the ERK1/2 pathway (by inhibiting the upstream kinases MEK1/2 by U0126) significantly

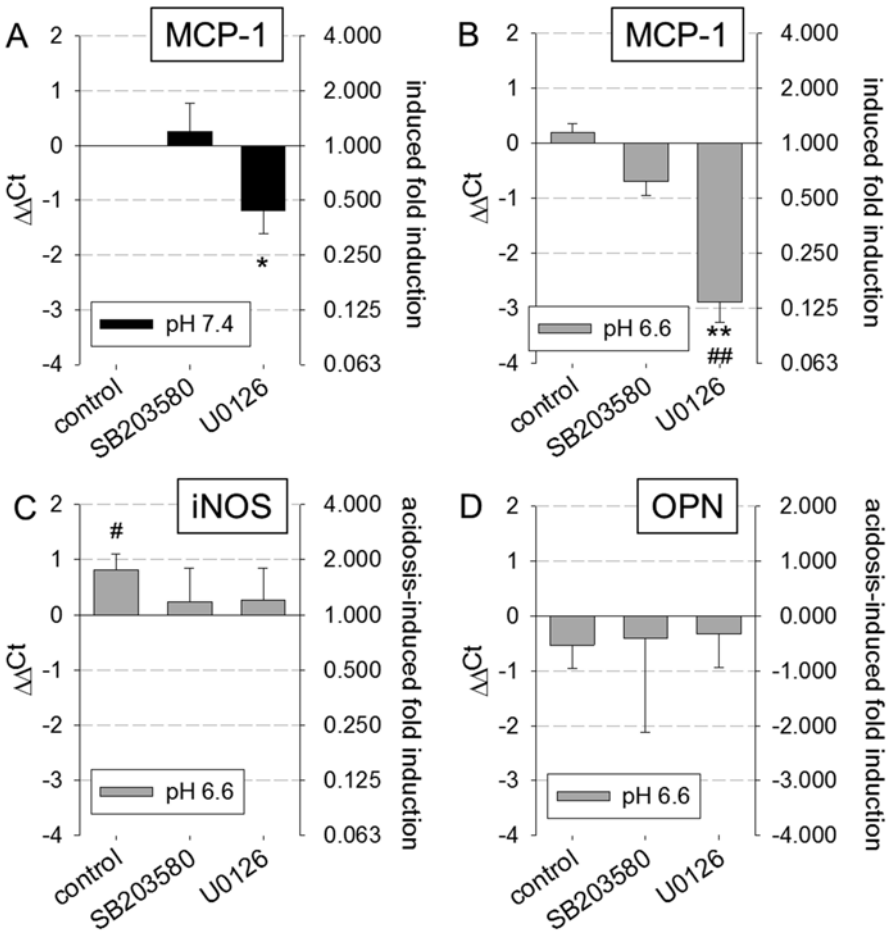

Fig. 14.2 Impact of inhibition the MAP kinase signaling pathways p38 and ERK1/2 on the change in expression of the inflammatory mediators (**a**, **b**) MCP-1, (**c**) iNOS and (**d**) OPN at pH 7.4 or pH 6.6. Cells were incubated in an acidotic medium (pH 6.6) for 3 h. MAP kinases were inhibited by specific blockers (SB2013580: p38-inhibitor; U0126: ERK1/2-inhibitor). n = 3–15; (*) $p < 0.05$ vs. w/o inhibitor; (**) $p < 0.01$ vs. w/o inhibitor; (#) $p < 0.05$ pH 6.6 vs. pH 7.4; (##) $p < 0.01$ pH 6.6 vs. pH 7.4

reduced the expression of MCP-1. Even at pH 7.4 U0126 reduced the expression by a factor of 2 (Fig. 14.2a), indicating that MCP-1 expression depends on ERK1/2. Under acidotic conditions U0126 reduced the MCP-1 expression by a larger factor (8×) (Fig. 14.2b) which shows that at low pH the impact of ERK1/2 is more pronounced. The iNOS expression was significantly increased by the acidic environment (Fig. 14.1d). When blocking the MAP kinase pathways the expression was markedly reduced to approximately the same level as at pH 7.4 (Fig. 14.2c). This reduction was reached either with p38 inhibition (SB203580) or ERK1/2 inhibition (U0126). The osteopontin expression was independent of MAPK signalling (Fig. 14.2d).

4 Conclusion

Inflammatory mediators in tumor tissues can affect the progression or the local control of tumors [4]. MCP-1 regulates the migration and infiltration of monocytes, memory T- and NK-cells in tumors and, therefore, plays a role in anti-tumoral immunity [8, 9], iNOS is a major source of reactive nitrogen species (e.g., peroxynitrite formation) relevant for cytotoxic effects and immune modulation [10], and osteopontin (OPN) is a chemoattractant and acts as an anti-apoptotic factor [11]. Hypoxia (pO_2 1 mmHg) as well as acidosis (pH 6.6) had an impact on the mRNA expression of these inflammatory mediators in AT1 prostate carcinoma cells. Hypoxia led to a decreased expression of MCP-1 and OPN (Fig. 14.1). Since MCP-1 and OPN are responsible for immune cell recruitment, hypoxia might hamper the immunological response in the tumor tissue. These functional aspects of altered expression of inflammatory mediators on the immunological response should be addressed in further studies.

In contrast to hypoxia, acidosis increased the iNOS as well as osteopontin expression. As indicated by the increased nitrite/nitrate formation under acidotic conditions, the modulation of inflammatory mediators seems to be functionally relevant. These results reveal that the acidotic extracellular environment could support the cytotoxic effect of irradiation or some chemotherapeutic agents acting by the formation of radicals. Concerning MCP-1 expression, acidosis led to only a slight reduction. The results of iNOS and MCP-1 are in good accordance with the observations on the effect of acidosis in normal tissue fibroblasts [5] which are part of the tumor stroma as well as in tumor-associated macrophages [12]. These data indicate that the response to acidosis is cell line independent. In fibroblasts the acidosis-induced up-regulation of iNOS was p38-dependent [5] a finding which was described for other cell lines and other stimuli as well [13, 14]. In AT1 tumor cells both signaling pathways play a relevant role (Fig. 14.2b). The MCP-1 expression in AT1 cells was predominantly ERK1/2-dependent (Fig. 14.2a) which was described in fibroblasts in a similar manner [5].

The results of the present study indicate that hypoxia as well as acidosis affect the secretion of inflammatory mediators in tumor cells which could modulate the response to immune cells within the tumor tissue (e.g., tumor-associated macrophages) as well as therapeutic cytotoxicity. Since hypoxia and/or acidosis have opposing effects on different mediators, the net effect cannot be predicted. Additionally, the interaction of other cells integrated into the tumor mass (fibroblasts, macrophages), which also react to low pH or pO_2, has to be taken into account.

Acknowledgments This study was supported by the BMBF (ProNet-T^3 Ta-04) and the Wilhelm-Roux program of the Medical School, University Halle-Wittenberg, Germany.

References

1. Thews O, Vaupel P (2015) Spatial oxygenation profiles in tumors during normo- and hyperbaric hyperoxia. Strahlenther Onkol 191:875–882
2. Vaupel P, Kallinowski F, Okunieff P (1989) Blood flow, oxygen and nutrient supply, and metabolic microenvironment of human tumors: a review. Cancer Res 49:6449–6465
3. Mao Y, Poschke I, Kiessling R (2014) Tumour-induced immune suppression: role of inflammatory mediators released by myelomonocytic cells. J Intern Med 276:154–170
4. Seruga B, Zhang H, Bernstein LJ et al (2008) Cytokines and their relationship to the symptoms and outcome of cancer. Nat Rev Cancer 8:887–899
5. Riemann A, Ihling A, Thomas J et al (2015) Acidic environment activates inflammatory programs in fibroblasts via a cAMP-MAPK pathway. Biochim Biophys Acta 1853:299–307
6. Riemann A, Schneider B, Ihling A et al (2011) Acidic environment leads to ROS-induced MAPK signaling in cancer cells. PLoS One 6:e22445
7. Sauvant C, Nowak M, Wirth C et al (2008) Acidosis induces multi-drug resistance in rat prostate cancer cells (AT1) in vitro and in vivo by increasing the activity of the p-glycoprotein via activation of p38. Int J Cancer 123:2532–2542
8. McClellan JL, Davis JM, Steiner JL et al (2012) Linking tumor-associated macrophages, inflammation, and intestinal tumorigenesis: role of MCP-1. Am J Physiol Gastrointest Liver Physiol 303:G1087–G1095
9. Deshmane SL, Kremlev S, Amini S et al (2009) Monocyte chemoattractant protein-1 (MCP-1): an overview. J Interferon Cytokine Res 29:313–326
10. Lala PK, Chakraborty C (2001) Role of nitric oxide in carcinogenesis and tumour progression. Lancet Oncol 2:149–156
11. Shevde LA, Samant RS (2014) Role of osteopontin in the pathophysiology of cancer. Matrix Biol 37:131–141
12. Riemann A, Wußling H, Loppnow H et al (2016) Acidosis differently modulates the inflammatory program in monocytes and macrophages. Biochim Biophys Acta 1862:72–81
13. Pedoto A, Nandi J, Oler A et al (2001) Role of nitric oxide in acidosis-induced intestinal injury in anesthetized rats. J Lab Clin Med 138:270–276
14. Campo GM, Avenoso A, D'Ascola A et al (2013) 4-mer hyaluronan oligosaccharides stimulate inflammation response in synovial fibroblasts in part via TAK-1 and in part via p38-MAPK. Curr Med Chem 20:1162–1172

Chapter 15
Comparing the Effectiveness of Methods to Measure Oxygen in Tissues for Prognosis and Treatment of Cancer

Ann Barry Flood, Victoria A. Satinsky, and Harold M. Swartz

Abstract Given the clinical evidence that hypoxic tumors are more resistant to standard therapy and that adjusting therapies can improve the outcomes for the subpopulation with hypoxic tumors, in vivo methods to measure oxygen in tissue have important clinical potential. This paper provides the rationale for and methodological strategies to use comparative effectiveness research to evaluate oximetry for cancer care. Nine oximetry methods that have been used *in vivo* to measure oxygen in human tumors are evaluated on several clinically relevant criteria to illustrate the value of applying comparative effectiveness to oximetry.

Keywords Comparative effectiveness • Clinical oximetry • EPR (electron paramagnetic resonance) • Tumor hypoxia • Cost effectiveness

1 Introduction

There is a considerable body of evidence to support the observation that solid tumors, especially malignant tumors, exhibit a very low oxygen concentration compared to normal tissue of a comparable type [1]. Hypoxia in tissues develops from a variety of factors, including the well-described poor vascularization and structural abnormalities in malignant tumors, which result in poor perfusion and diffusion of oxygen in the tumor [2, 3]. Likewise, the evidence is strong that hypoxia in cancer has very important clinical implications for predicting long-term patient outcomes, i.e., hypoxia is associated with poorer outcomes irrespective of type of treatment. Perhaps more importantly, for the subpopulation of patients whose tumors respond, there is strong evidence that the therapeutic ratio can be improved when radio-or

A.B. Flood (✉) • V.A. Satinsky • H.M. Swartz
EPR Center for the Study of Viable Systems, Department of Radiology, HB 7785, Geisel School of Medicine at Dartmouth, Hanover, NH, USA
e-mail: ann.b.flood@dartmouth.edu; Victoria.A.Satinsky@Dartmouth.edu; Harold.Swartz@Dartmouth.edu

© Springer International Publishing Switzerland 2016

Q. Luo et al. (eds.), *Oxygen Transport to Tissue XXXVIII*, Advances in Experimental Medicine and Biology 923, DOI 10.1007/978-3-319-38810-6_15

chemotherapy is augmented by appropriately timed administration of hyperoxic therapy (such as breathing enriched oxygen or carbogen) and/or vasoactive agents (such as nicotinamide) or cytotoxic agents that function in the presence of hypoxia (such as tirapazamine) [2, 4–7].

The scientific evidence about the mechanisms leading to hypoxia, the biological consequences of its presence (such as increased insensitivity to radiotherapy or chemotherapy, the proliferation of aggressive malignancies that can thrive in low oxygen), and the clinical importance of reducing hypoxia during therapy are all substantial and highly relevant to the importance of our thesis. However, these topics per se are not reviewed in depth here. Instead, the focus of this paper is how the clinical implications of these factors can be enhanced by greater application of comparative effectiveness methodology to meaningfully compare and contrast available methods to assess hypoxia for practical applications to improve cancer care.

Comparative effectiveness research is broadly defined as research into the relative effectiveness of two or more health care practices which can be used in a 'real world' clinical setting to treat a specific disease or condition [11]. Three primary strategies are used to compare effectiveness, based on assessing the risks and benefits of each treatment being evaluated: by synthesis of the literature and modeling, by observational studies, and by head-to-head trials [11, 12].

Comparative effectiveness methodology is an outgrowth of clinical studies designed to establish the effectiveness of a new clinical approach ranging from screening to diagnostics to therapeutics [8–10]. The term efficacy, in contrast to effectiveness, is generally used to differentiate outcomes of a treatment when performed under an idealized, highly controlled protocol for care in contrast to what can be achieved in conditions of usual clinical practice. Since their introduction in the 1940s, randomized controlled trials (RCTs), which typically compare a new therapeutic approach to a standard therapy or placebo, have been the 'gold standard' for determining the efficacy of a new strategy. Because RCT designs randomly assign eligible subjects to treatment arms, follow strict protocols, and have the potential for blinding the analysis, they eliminate selection bias and have strong internal validity.

However, while RCTs are well suited for assessing whether an individual method represents an improvement over random chance or the standard therapy, they do not address several important pragmatic issues regarding the generalizability of the results when used in usual care. In other words, because RCTs use strictly defined and controlled protocols for care, the results may only apply to idealized (i.e., ultra-controlled) clinical practices and may only be feasible to carry out in large medical centers with strict oversight of trials rather than in usual care settings such as in community hospitals or clinics. Moreover, intrinsic to the statistical designs governing RCTs, the analyses of outcomes in RCTs focus on assessing the average effect on patients. As a result, they cannot examine whether only certain subpopulations may have benefitted, without changing the underlying statistical assumptions. In addition, RCTs are not well suited to compare several widely disparate approaches to treatment of the same disease such as comparing prostate cancer treatments as varied as surgical intervention, radiation therapy, hormonal therapy or watchful waiting.

They also ignore such practical issues as cost differences in the expenditures on resources to achieve any improvements in outcomes and ignore aspects that might lead patients or their doctors to prefer one strategy over another. Indeed, the rise of patient-centered care, with its emphasis on including patient preferences and/or in individualizing care based on biological variations in the patient's tumor or its response to treatment, is arguably not well-suited to RCTs because they use a priori assignment of all eligible patients to treatment arms and do not permit deviation related to patient responses. Finally, RCTs are not designed to evaluate multiple methods, all of which are still at an investigational development stage, i.e., they are not designed to assess the relative effectiveness or to compare the practical feasibility of methods still being developed for use in standard clinical care.

For all these reasons, alternative methodological approaches have emerged as important tools for clinical research to be able to answer these more complex and practical problems when assessing the clinical feasibility and other practical implications of alternative strategies. While several approaches have been proposed to assess the clinical implications, politically motivated concerns have led to the recent focus on *comparative* effectiveness to address these issues, especially in contrast to *cost* effectiveness research. For example, in the US, the federal stimulus bill of 2009 explicitly targeted that clinical studies use comparative effectiveness methodology. Subsequently, as a part of the 2010 major healthcare reform law informally called "Obamacare", a new federal initiative called the Patent-Centered Outcomes Research Institute (PCORI) was established to conduct comparative effectiveness research. Included in this legislative mandate was an explicit prohibition that PCORI **not** include cost effectiveness thresholds in its studies. For example, policy-makers raised concerns that third party payers of health care might emphasize research that supported paying 'only' for less costly alternatives.

While some have argued that comparative effectiveness research, like RCTs, neglects patient-centered care, others argue that, because comparative effectiveness studies typically enroll a heterogeneous population, they are well-positioned to uncover subpopulations that can benefit most from particular treatments [13]. Likewise, effectiveness research can help identify treatments or services with essentially equivalent effectiveness, e.g., the likelihood of achieving 5-year disease-free status or survival. Where there is such equipoise in outcomes, i.e., where there is no dominant reason related to outcomes to choose one treatment over another, patient preferences for choosing one treatment over the other can be incorporated, thereby usually improving patient satisfaction with care, compliance with the treatment regimen and sometimes improving outcomes as well [14].

Yet, while there has been an important shift in emphasis to promote pragmatic clinical studies, the scientific body of clinical studies of outcomes remains overwhelmingly focused on RCTs. For example, Holve and Pittman [11] examined all of the clinical studies reported in a US federally mandated registry of clinical trials, Clinicaltrials.gov [15]. Out of approximately 53,000 records on Clinicaltrials.gov (with ~13,000 added annually), the overwhelming percent (~85 %) are RCTs, most of which are early Phase 1 or 2 studies, i.e., are preclinical studies or early safety trials. Of the approximately 1700 active Phase 3 or 4 studies (the majority involving

cancer), fewer than one-third were designated as comparative effectiveness research. This provides evidence that, despite attempts to promote pragmatic and comparative studies of the clinical implications of alternative strategies, there is a general need for greater application of these methods to evaluate clinical care across the board.

2 Methods

More specifically on the topic of assessing tumor hypoxia and attempts to alter it during treatment, we found only one clinical study that attempted to directly compare the effectiveness of different methods for assessing hypoxia [21]

Nonetheless, we argue that the current status of technology and research supports turning to comparative effectiveness methods to help address some very important questions about when and whether to use oximetry, and about which oximetry method to use. Namely, there is evidence that methods to assess hypoxia in tumors have the potential to be clinically meaningful in at least three scenarios: (1) because hypoxia is associated with important long-term patient outcomes including death, it has prognostic value for physicians and patients and their families; (2) if treating physicians could identify the subset of patients whose tumor is resistant to radio- or chemotherapy, they could adapt their treatment to be most effective; and (3) if physicians knew both that a patient's tumor was hypoxic and that it responds to hyperoxic treatment, oximetry could help with the timing to administer care to improve outcomes. Secondly, there is an important need to compile evidence about the comparative effectiveness of oximetry methods. While about two dozen oximetry methods to assess hypoxia have been proposed, many have not been successfully applied to humans *in vivo* and most, if not all, have yet to establish their effectiveness in clinical settings [2].

Another reason that comparative effectiveness methods need to be applied to oximetry is because they are better suited than RCTs to address whether and when subpopulations of patients may experience better outcomes. Many have argued that hypoxia and individualized responsiveness to hyperoxic therapy are the major explanation as to why standard therapies or new variants appear to fail when their effectiveness is evaluated for the 'average' patient. It is because the subpopulation with hypoxic tumors require a different approach [2–5, 7, 16]. Oximetry could help establish when hypoxia is present, in order to validate these hypotheses in subpopulations.

Finally, oximetry methods need to be compared on the basis of practical considerations, such as the capability of the oximetry method to measure tumors at various depths, the sensitivity of the method to assess hypoxia at the most clinically sensitive levels of partial pressure of oxygen (pO_2), and the practicality of using the method during cancer therapy or during application of concurrent hyperoxic therapy (such as the rapidity with which measurements can be repeated or the degree to which specialized facilities and equipment would be needed to carry out oximetry). Comparative effectiveness can address all these important pragmatic questions as well as considering patient oriented preferences—such as the relative discomfort and invasiveness of oximetry methods.

3 Results

The first comparative effectiveness strategy to compare oximetry methods consists of a synthesis of publications, including prior reviews. While there are several excellent reviews related to oximetry methods, most focus on the evidence and mechanisms of how tumors become hypoxic, why hypoxia leads to complex responsiveness to primary therapy, and evidence from cancer treatment studies [2, 3, 17, 18]. A few reviews include or focus on the potential of various types of oximetry to be used in clinical care [2, 4, 19].

In synthesizing the literature two guiding principles are key: (1) determine the methods that are most appropriate to compare for the same type of disease or condition and (2) decide on key criteria to evaluate. For purposes of this paper, we began with the list of 23 oximetry methods in Walsh and colleagues' "Table 4: existing techniques for *in vivo* assessment in tissue oxygenation" ([2], p 1525]). We selected the nine methods that have been or are being currently used in humans with tumors. Table 15.1 presents these nine methods, organized by whether the method directly assesses hypoxia or uses qualitative or indirect methods, such as those that evaluate the expression of endogenous markers in the presence of hypoxia. (See Swartz et al. in this same volume for further description of these methods [20].)

Table 15.1 compares these methods based on four criteria. Two criteria describe the capacity of the method to assess hypoxia (how deep below the surface the method can measure a tumor and how well the method can quantify the extent of hypoxia—the latter is especially needed to assess change in hypoxia in the presence of hyperoxic therapy). The third criterion, invasiveness of the method, is both a patient-centered indicator as well as a potential source for side effects. The last criterion is whether the measurement can be repeated, with the assumption that this capacity is more conducive to monitoring the effects of treatments.

Table 15.1 shows that three of the nine methods currently are limited as to the depth of the tumor they can assess and, while five assess the amount of hypoxia, only three are precise. The Eppendorf electrode probe is the only method labeled as significantly invasive in this table. Others, however, are minimally invasive. For example, the carbon-based EPR particulates leave a permanent tattoo, and all EPR particulates require being injected or implanted into the tumor initially but thereafter are noninvasive. Likewise, several imaging technologies require administering a tracer, usually intravenously, for each measurement session.

Repeatability in this table applies to all but one method. However, more subtle descriptions of repeatability, such as the ease and rapidity with which measurements can be repeated for monitoring during treatment, are not noted here. A practical consideration, such as how specialized the facility is or how cumbersome the device would be to co-locate during radiation therapy, may also preclude making rapidly repeated measurements in usual clinical care.

While observational studies, the second strategy of comparative research, are not detailed here, the practical considerations as well as strengths and limitations of a given oximetry method are not easy to discern in the literature to date. The third strategy, head-to-head comparisons of different oximetry methods to assess the

Table 15.1 Methods of oximetry used in vivo in humans and criteria for effectiveness research

Criteria: Oximetry method:	Depth	Quantitative/ Qualitative	Invasive?	Repeatable?
A. Direct assessment of hypoxia (O_2 concentration or pO_2)				
Polarographic oxygen electrode (Eppendorf)	3–4 cm	Quantitative	Yes	No
EPR oximetry (spectroscopy with particulates):				
Carbon- or phthalocyanine-based paramagnetic sensors	1–2 cm[a]	Quantitative	No[b]	Yes
Implantable wires with phthalocyanine-based sensors	Any	Quantitative	No[b]	Yes
B. Other assessment of hypoxia				
MRI/MRS techniques:				
DCE-MRI	Any	Indirect: not applicable	No	Yes
BOLD	Any	Indirect: not applicable	No	Yes
Diffusion and perfusion assessment	Any	Indirect: not applicable	No	Yes
Near-infrared (NIR) spectroscopy (multiple modalities)	1–6 cm	Indirect: not applicable	No[b]	Yes
PET:				
^{18}F tracers: FMISO, etc.	Any	Qualitative	No[b]	Yes
^{64}Cu-ATSM	Any	Qualitative	No[b]	Yes

Acronyms: *BOLD* blood oxygen level dependent, *DCE* dynamic contrast enhanced, *EPR* electron paramagnetic resonance, *PET* positron emission tomography, *MRI/MRS* magnetic resonance imaging/^{19}F-magnetic resonance spectroscopy, *FMISO* fluoro-misonidazole, *Cu-ATSM* Cu(II)-diacetyl-bis(N^4-methylthiosemicarbazone)

[a]EPR Probes can be placed intra-cavity so that depth can apply to oral cancer, uterine or cervical cancer, or colorectal cancers as well as at same depth below skin

[b]Method is minimally invasive. EPR carbon-based particulates produce a permanent tattoo. EPR particulates need to be injected or implanted initially but thereafter are measured noninvasively. Tracers need to be injected intravenously prior to each measurement session

same set of patients with the same condition, has seldom been carried out. A notable exception is a head-to-head comparison of five marker assays regarding their ability to predict local-regional control [21]. The authors reported diversity and little correlation among the markers within individual tumors of 67 head and neck patients in their study.

4 Conclusions and Implications

There is strong evidence that hypoxia in tumors is prognostic of poorer outcomes and can influence clinical treatment decisions, including the decision to use hyperoxic therapy concurrently with standard treatment to improve responsiveness to

radio- and chemotherapy. Indeed tumor hypoxia is a powerful and independent prognostic factor, even when stage, tumor size and treatment type are considered [22]. More importantly for this paper, not all tumors of the same type exhibit hypoxia and not all respond to hyperoxic therapy. Consequently, there is an important need for practical, effective oximetry methods. While about two dozen oximetry methods have been proposed, not all are equally available or well suited for all types and depths of tumors, and some may not be practical in standard clinical practice. Comparative effectiveness strategies and methodologies offer an important means to rigorously compare and contrast oximetry methods, even at the stage of early clinical phases of research.

Besides the obvious implications of guiding treatment of cancer, a systematic evaluation of oximetry methods could result in some methods being invaluable in preclinical studies to understand the mechanisms of how hypoxia influences tumors even though not well suited for clinical studies or standard care. If one type of oximetry method is clearly more efficient and effective in predicting success in treatment, then there would be a 'dominated' oximetry winner—at least for some types of cancer. If instead there are several oximetry methods comparable in their effectiveness, other reasons to choose among them may begin to predominate, e.g., based on patient-based preferences such as the convenience or time to undergo oximetry measurements or based on physician or health care system related reasons, including having sufficient patient volume to justify the purchase of equipment or appropriate expertise available to administer the method.

Head-to-head clinical studies for comparative effectiveness research, like RCTs, can be very expensive to carry out [11] and so there is an imperative to use systematic and rigorous methods to evaluate the evidence already available in the literature wherever feasible. These other strategies developed for comparative effectiveness research can help provide the needed insights while avoiding the biases in observational studies carried out independently. Especially in complex situations where the underlying scientific and medical mechanisms are themselves evolving and there is no real 'gold standard' for assessing hypoxia, comparative effectiveness research needs to include the insights and perspectives of researchers who are cognizant of the problems with measuring oximetry as well as with the complexity of intervening on biological mechanisms.

So the challenges to apply comparative effectiveness to evaluate oximetry methods in cancer care are great, but so is the importance of the task to identify subpopulations with hypoxia in order to improve their outcomes.

Acknowledgments This work was funded in part by a grant from the US National Cancer Institute, National Institutes of Health (PO1CA190193).

References

1. Vaupel P, Höckel M, Mayer A (2007) Detection and characterization of tumor hypoxia using pO_2 histography. Antioxid Redox Signal 9:1221–1236. doi:10.1089/ars.2007.1628
2. Walsh JC, Lebedev A, Aten E et al (2014) The clinical importance of assessing tumor hypoxia: relationship of tumor hypoxia to prognosis and therapeutic opportunities. Antioxid Redox Signal 21:1516–1554. doi:10.1089/ars.2013.5378

3. Vaupel P, Mayer A (2007) Hypoxia in cancer: significance and impact on clinical outcome. Cancer Metastasis Rev 26:225–239. doi:10.1007/s10555-007-9055-1
4. Wilson WR, Hay MP (2011) Targeting hypoxia in cancer therapy. Nat Rev Cancer 11:393–410. doi:10.1038/nrc3064
5. Menon C, Fraker DL (2005) Tumor oxygenation status as a prognostic marker. Cancer Lett 221:225–235. doi:10.1016/j.canlet.2004.06.029
6. Bussink J, Kaanders JH, von der Kogel AJ (2002) Tumor hypoxia at the micro-regional level: clinical relevance and predictive value of exogenous and endogenous hypoxic cell markers. Radiother Oncol 67:3–15. doi:10.1016/S0167-8140(03)00011-2
7. Janssens GO, Rademakers SE, Terhaard CH et al (2012) Accelerated radiotherapy with carbogen and nicotinamide for laryngeal cancer: results of a phase III randomized trial. J Clin Oncol 30:1777–1783. doi:10.1200/JCO.2011.35.9315
8. Gatsonis C (2010) The promise and realities of comparative effectiveness research. Stat Med 29:1977–1981. doi:10.1002/sim.3936
9. Goss CH, Tefft N (2013) Comparative effectiveness research—what is it and how does one do it? Paediatr Respir Rev 14:152–156. doi:10.1016/j.prrv.2013.06.006
10. Amstrong K (2012) Methods in comparative effectiveness research. J Clin Oncol 30:4208–4214. doi:10.1200/JCO.2012.42.2659
11. Holve E, Pittman P (2009) A first look at the volume and cost of comparative effectiveness research in the United States. Academy health. http://www.academyhealth.org/files/filedownloads/ah_monograph_09final7.pdf. Accessed 30 Aug 2015
12. Tunis SR, Stryer DB, Clancy CM (2003) Practical clinical trials: increasing the value of clinical research for decision making in clinical and health policy. JAMA 290:1624–1632. doi:10.1001/jama.290.12.1624
13. Epstein R, Teagarden JR (2010) Comparative effectiveness and personalized medicine: evolving together or apart? Health Aff (Millwood) 29:1783–1787. doi:10.1377/hlthaff.2010.0642
14. O'Connor AM, Llewellyn-Thomas HA, Flood AB (2004) Modifying unwarranted variations in health care: shared decision making using patient decision aids. Health Aff (Millwood) Suppl Variation: VAR63–72. doi:10.1377/hlthaff.var.63
15. Clinicaltrials.gov (2015) U.S. National Institutes of Health, Rockville. http://www. clinicaltrials.gov. Accessed 25 Aug 2015
16. Dhani N, Fyles A, Hedley D et al (2015) The clinical significance of hypoxia in human cancers. Semin Nucl Med 45:110–121. doi:10.1053/j.semnuclmed.2014.11.002
17. Koch CJ, Evans SM (2015) Optimizing hypoxia detection and treatment strategies. Semin Nucl Med 45:163–176. doi:10.1053/j.semnuclmed.2014.10.004
18. Overgaard J (2011) Hypoxic modification of radiotherapy in squamous cell carcinoma of the head and neck—a systematic review and meta-analysis. Radiother Oncol 100:22–32. doi:10.1016/j.radonc.2011.03.004
19. Springett R, Swartz HM (2007) Measurements of oxygen in vivo: overview and perspectives on methods to measure oxygen within cells and tissues. Antioxid Redox Signal 9:1295–1301. doi:10.1089/ars.2007.1620
20. Swartz HM, Williams BB, Hou H et al. (2015) Direct and repeated clinical measurements of p02 for enhancing cancer therapy and other applications [submitted same issue]. In: Advances in experimental medicine and biology: oxygen transport to tissues XXXVIII. 43rd annual meeting of the International Society on Oxygen Transport to Tissue, Wuhan, China, 11–16 July 2015 (in press)
21. Nordsmark M, Eriksen JG, Gebski V et al (2007) Differential risk assessments from five hypoxia specific assays: the basis for biologically adapted individualized radiotherapy in advanced head and neck cancer patients. Radiother Oncol 83:389–397. doi:10.1016/j.radonc.2007.04.021
22. Vaupel P (2004) Tumor microenvironmental physiology and its implications for radiation oncology. Semin Radiat Oncol 14(3):198–206, doi:http://dx.doi.org/10.1016/j.semradonc.2004.04.008

Chapter 16
Potential Indexing of the Invasiveness of Breast Cancer Cells by Mitochondrial Redox Ratios

Nannan Sun, He N. Xu, Qingming Luo, and Lin Z. Li

Abstract The invasive/metastatic potential of cancer cells is an important factor in tumor progression. The redox ratios obtained from ratios of the endogenous fluorescent signals of NADH and FAD, can effectively respond to the alteration of cancer cells in its mitochondrial energy metabolism. It has been shown previously that the redox ratios may predict the metastatic potential of cancer mouse xenografts. In this report, we aimed to investigate the metabolic state represented by the redox ratios of cancer cells in vitro. Fluorescence microscopic imaging technology was used to

N. Sun
Department of Radiology, Perelman School of Medicine, University of Pennsylvania, Philadelphia, PA, USA

Britton Chance Laboratory of Redox Imaging, Johnson Research Foundation, Perelman School of Medicine, University of Pennsylvania, Philadelphia, PA, USA

Department of Biomedical Engineering, MoE Key Laboratory for Biomedical Photonics, Huazhong University of Science and Technology, Wuhan, Hubei, China

Britton Chance Center for Biomedical Photonics, Wuhan National Laboratory for Optoelectronics, Wuhan, Hubei, China

H.N. Xu
Department of Radiology, Perelman School of Medicine, University of Pennsylvania, Philadelphia, PA, USA

Britton Chance Laboratory of Redox Imaging, Johnson Research Foundation, Perelman School of Medicine, University of Pennsylvania, Philadelphia, PA, USA

Q. Luo
Britton Chance Center for Biomedical Photonics, Wuhan National Laboratory for Optoelectronics, Huazhong University of Science and Technology, Wuhan, Hubei, China

L.Z. Li (✉)
Molecular Imaging Laboratory, Department of Radiology, Britton Chance Laboratory of Redox Imaging, Johnson Research Foundation, Department of Biochemistry and Biophysics, Perelman School of Medicine, University of Pennsylvania, Philadelphia, PA, USA
e-mail: linli@mail.med.upenn.edu

© Springer International Publishing Switzerland 2016

Q. Luo et al. (eds.), *Oxygen Transport to Tissue XXXVIII*, Advances in Experimental Medicine and Biology 923, DOI 10.1007/978-3-319-38810-6_16

observe the changes of the endogenous fluorescence signals of NADH and FAD in the energy metabolism pathways. We measured the redox ratios (FAD/NADH) of breast cancer cell lines MDA-MB-231, MDA-MB-468, MCF-7, and SKBR3. We found that the more invasive cancer cells have higher FAD/NADH ratios, largely consistent with previous studies on breast cancer xenografts. Furthermore, by comparing the fluorescence signals of the breast cancer cells under different nutritional environments including starvation and addition of glutamine, pyruvate and lactate, we found that the redox ratios still effectively distinguished the highly invasive MDA-MB-231 cells from less invasive MCF-7 cells. These preliminary data suggest that the redox ratio may potentially provide a new index to stratefy breast cancer with different degrees of aggressiveness, which could have significance for the diagnosis and treatment of breast cancer.

Keywords Invasive potential • Redox ratio • Breast cancer • NADH • FAD

1 Introduction

Although in the past few decades the 5-year survival rate of breast cancer patient has increased significantly in the USA, about 23 % of the surviving patients have a metastatic disease that will kill about 40,000 people each year [1, 2]. It is estimated that 20–30 % of patients with node-negative breast cancer will eventually develop a metastatic disease [3]. Thus, cancer metastasis is the key determinant of cancer prognosis. The invasion of surrounding tissue is the first step of the metastasis and the highly metastatic cancer cells generally have a higher invasive potential. Studying the invasive potential of cancer cells may help us understand cancer metastasis and develop methods to inhibit metastasis and reduce the mortality rate of cancer patients.

NADH and FAD are two coenzymes with endogenous fluorescence and play key roles in the mitochondrial bioenergetics. NADH and $FADH_2$ pass their hydrogen atoms to oxygen to generate ATP and water in the electron transport chain. NADH and $FADH_2$ are oxidized to NAD^+ and FAD, respectively. Chance et al. demonstrated that the redox ratio, calculated by the fluorescence intensities of NADH and FAD, could be used to represent the metabolic redox state of mitochondria [4, 5].

In this study, we used the endogenous fluorescence signals from NADH and FAD, to study the energy state of breast cancer cells. Previously, our group has used the low-temperature fluorescence imaging method, i.e., the Chance redox scanner, to study the metabolic state of the melanoma xenografts in nude mice [6]. It was found that the tumors with different degrees of metastatic potential exhibited different redox ratios and their normalized FAD redox ratios, FAD/(FAD+NADH), correlate positively with the increase of invasive potential of cell lines. It has also been found that MDA-MB-231 xenografts with a higher metastatic potential presented a more oxidized state in the localized tumor regions than MCF-7 xenografts with a lower metastatic potential [7]. Based on these results, we aimed to investigate the correlation between the redox state and the invasive potential of cultured breast cancer cells in vitro. We also measured the

redox state of breast cancer cell lines after adding nutrients (e.g. glucose, glutamine, pyruvate and lactate) to cell culture environment, in order to test whether cellular environment may affect the relationship between redox state and invasive potential.

2 Methods

NADH and FAD fluorescence signals were obtained by DeltaVision Deconvolution Microscope System which has a xenon lamp as an excitation light source, a 12-bit CCD, and an objective of 40X/0.95 NA. The imaging system (except the eyepiece) is covered by a thermally controlled chamber to maintain the samples under 37 °C. The excitation wavelengths of NADH and FAD channels are 360/40 nm and 470/40 nm, respectively. The emission wavelengths of NADH and FAD channels are 455/50 nm and 520/40 nm, respectively. Typically for each cell culture dish, three to five fields of views (FOVs) were alternatively taken with an exposure time of 3 s for each channel. In order to decrease the fluorescence background, the culture medium RPMI 1640 was replaced with Live Cell Imaging Solution (LCIS, Life Technologies) 1 h before imaging. LCIS can keep cells healthy for up to 4 hours at ambient atmosphere and temperature. To make sure light exposure did not cause photobleaching in living cells, ten images were acquired consecutively at exposure time of 1 s. The fluorescence intensity of the tenth image did not show a significant difference from that of the first image.

To validate that the fluorescence signals came from NADH and FAD, rotenone (a mitochondrial inhibitor) dissolved in DMSO was added to MCF-7 cells (final concentration 10 μM, treatment time 5 min before imaging) to test the responses of NADH and FAD signals in the presence of 10 mM glucose in the imaging solution. We also measured the redox ratios of four breast cancer cell lines (MDA-MB-231, MDA-MB-468, MCF-7, and SKBr3 cells). The microenvironmental changes of MDA-MB-231 and MCF-7 cells were achieved by adding no glucose to the media (starvation) or adding glutamine, lactate, or pyruvate (final concentration 20 mM for each nutrient in the presence of 10 mM glucose) 1 h before imaging. The reference condition was 10 mM glucose in the media.

For data analysis, we calibrated the excitation light intensity according to the photosensor readings that was automatically recorded for each channel as the intensity of illumination on the samples each time before acquiring images. The FAD/NADH ratio images were constructed from FAD and NADH images pixel by pixel. The background intensity of each channel was obtained from a randomly selected cell-free area. FAD and NADH intensities were calculated by first subtracting their background intensity, respectively, then thresholding at the three times of the standard deviation of the background. For individual FOVs, the mean values for both FAD and NADH were calculated, and the mean value of FAD/NADH was calculated by the FAD mean value divided by the NADH mean value. The FAD, NADH, and FAD/NADH were finally reported as averages across all FOVs. For the experiments where four lines were imaged, the MDA-MB-231 cancer cell line was used as a reference, and the mean values of FAD, NADH, and FAD/NADH of other cell lines were normalized by dividing the respective reference values of MAD-MB-231.

The standard errors of the means (SEM) and the p-values of Student's t test were reported based on the number of FOVs.

3 Results

Figure 16.1 shows the effect of rotenone treatment on MCF-7 cells. Rotenone, as a mitochondrial inhibitor, can disrupt the electron transport chain in the mitochondria, and lead to a decreased production of ATP and cell death. Since DMSO was used as the solvent for rotenone, we also studied its effects on the metabolic states of the cells. From Fig. 16.1 we can see that, after adding 8 μl DMSO to the imaging solution (1 ml), NADH, FAD, and FAD/NADH did not present statistical differences from the controls ($p > 0.05$). The small dose of DMSO did not have a significant effect on cellular redox state. Compared with the control or DMSO group, the rotenone treatment group (DMSO&Rote) had a significantly decreased FAD, increased NADH, and decreased FAD/NADH. Therefore, we demonstrated that rote that none treatment did lead to an accumulation of NADH and a decrease of FAD, and the cellular redox state became more reduced. These results were consistent with the reported effects of rotenone on mitochondrial energy pathways.

The imaging results comparing four breast cancer cell lines are shown in Fig. 16.2. The FAD of the MDA-MB-468 cells had the lowest intensity and was

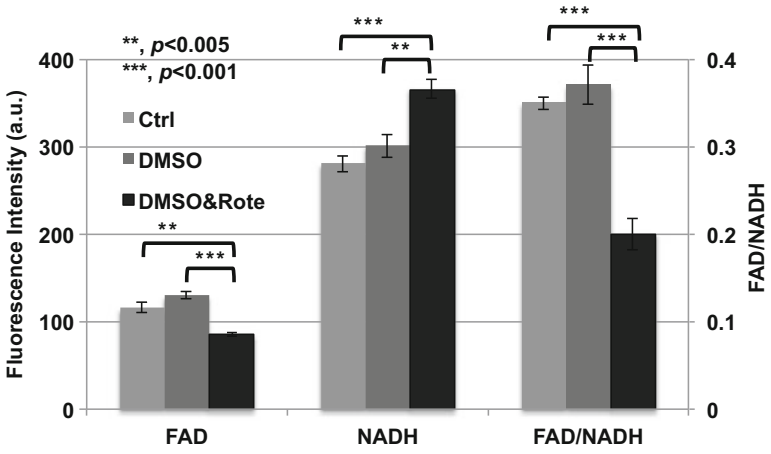

Fig. 16.1 The addition of rotenone to MCF-7 cells (number of FOVs = 6 from two dishes at one experimental session) results in an increase in NADH fluorescence, a decrease in FAD fluorescence, and a decrease in FAD/NADH ratio. *Left Y-axis* is for NADH and FAD, and the *right Y-axis* for FAD/NADH ratio. *Bar height* represents the mean and *error bar* represents the standard error (SE). *Ctrl* represents the control group. There was 10 mM glucose in the imaging solution as the basic supply of nutrient for each of the three groups. For the *DMSO* group, 8 μl DMSO was added into 1 ml imaging solution. *DMSO&Rote* represents the group in which 8 μl DMSO with rotenone was added into 1 ml imaging solution. The final concentration of rotenone was 10 μM

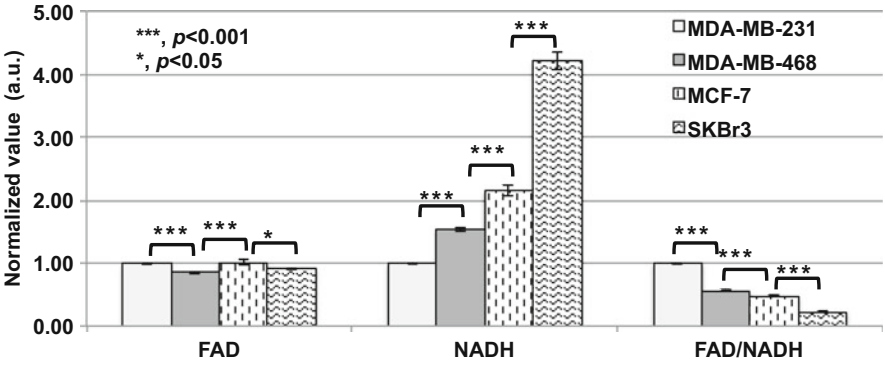

Fig. 16.2 Normalized FAD, NADH, and FAD/NADH values of MDA-MB-231, MDA-MB-468, MCF-7, and SKBr3 breast cancer cell lines (three experiments at different days, duplicated dishes each time, with total number of FOVs = 24). There was 10 mM glucose in the imaging solutions of all groups. *Bar height* represents the mean and the *error bar* represents the SE

significantly lower than that of the MDA-MB-231 cells ($p < 0.001$). FAD of the MDA-MB-231 cells was not statistically different from that of the MCF-7 cells or the SKBr3 cells. However, NADH signals showed a very different rank order from that of FAD signals. NADH signals of these four cell lines followed the rank order: MDA-MB-231<MDA-MB-468<MCF-7<SKBr3. Therefore, FAD/NADH ratio falls in the following rank order: MDA-MB-231>MDA-MB-468>MCF-7>SKBr3. This rank order is identical to the order of the invasive potential measured by Boyden chamber method as reported in literature [8, 9], i.e., when the invasive potential is higher, the FAD/NADH ratio is also consistently higher.

From the above results we postulated that metabolic fluorescence signals effectively differentiate between breast cancer cells with different invasive potential in the case of a sufficient supply of glucose (10 mM glucose in the imaging solution). When cells were under starvation, by comparing the MDA-MB-231 cells with higher invasive potential and MCF-7 cells with lower invasive potential, we still found significant differences in the metabolic fluorescence signals of two cell lines. Despite that redox ratio difference between the two lines was mitigated compared to the control condition with high glucose (Fig. 16.2), FAD/NADH of the more invasive MDA-MB-231 cells was significantly larger than that of the less invasive MCF-7 cells (Fig. 16.3). We came to the same conclusion for redox ratios when cells with glucose were additionally supplied with 20 mM glutamine, lactate, or pyruvate, respectively (Fig. 16.3). Therefore, even though the redox state was dependent on the nutrition supplies or micro-environmental conditions, the relative correlation between the redox ratio and invasive potential was maintained for these two breast tumor cell lines.

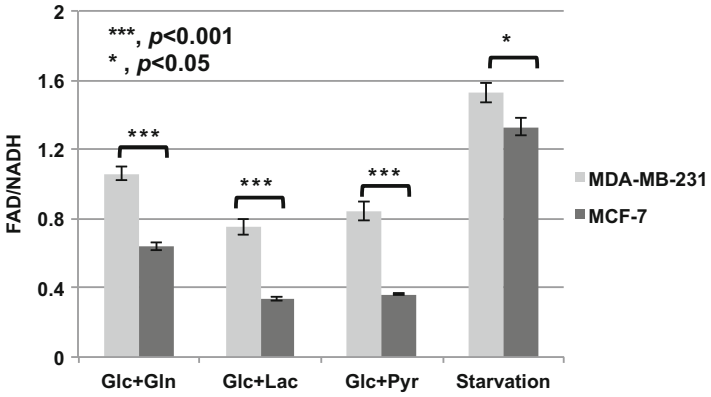

Fig. 16.3 Comparison of FAD/NADH ratios of MDA-MB-231 and MCF-7 when the microenvironments were changed (three experiments at different days, duplicated dishes each time, with total number of FOVs = 24). Starvation indicates there was no nutrition in the media. Glc+Gln, Glc+Lac, and Glc+Pyr represent 10 mM glucose + 20 mM glutamine, 10 mM glucose + 20 mM lactate, and 10 mM glucose + 20 mM pyruvate in the media, respectively

4 Discussions and Conclusions

In this study, the endogenous fluorescence signals of four breast cancer cell lines measured *in vitro* demonstrated a correlation between the higher redox ratios and their rank order of invasive potentials using reported results in the literature. We acknowledge that the rank order of invasive potential between some breast cancer lines (e.g. MCF7 vs. SKBR3) might not be consistent among the literature reports [8–11]. In our future study, we should measure the invasive potential of cancer cell lines via Boyden chamber and directly test the correlation between the invasiveness and redox ratios. Even though the redox states of the cancer cells changed when their microenvironments were changed, the endogenous fluorescent metabolic signals still effectively distinguished between the highly invasive cells and the slightly invasive ones; furthermore, the positive correlation between the rank order of invasive potentials and the redox ratio was maintained. The results from this study are consistent with our previous results obtained with cancer mouse xenografts [5, 6]. These results suggest the potential value of optical redox imaging for predicting tumor invasive/metastatic potential in clinical practice so that physicians may tailor therapy based on redox indices. Indeed we have applied the method to imaging clinical specimens of breast cancer patients [12–14]. Work is in progress to test whether optical redox imaging indices have any prognostic values.

Lastly we note that our experiments did not measure and control the pH and pO_2 in cell cultures, which may affect redox state as well. In the future we will investigate whether these factors will affect the correlation between the redox ratio and invasive potential of cancer cells.

Acknowledgements The work was financially supported in part by grants from the US National Institute of Health (R01-CA155348 and CA191207). This work was also supported and funded by

the China's Program of Introducing Talents to Universities on Photonics and Optoelectronics Science & Technology (111 Plan Program No. B07038).

References

1. Roth BJ, Krilov L, Adams S et al (2013) Clinical cancer advances 2012: annual report on progress against cancer from the american society of clinical oncology. J Clin Oncol 31(1):131–161
2. DeSantis C, Siegel R, Bandi P et al (2011) Breast cancer statistics, 2011. CA Cancer J Clin 61(6):409–418
3. Cianfrocca M, Goldstein LJ (2004) Prognostic and predictive factors in early-stage breast cancer. Oncologist 9:606–616
4. Chance B, Schoener B, Oshino R et al (1979) Oxidation-reduction ratio studies of mitochondria in freeze-trapped samples. NADH and flavoprotein fluorescence signals. J Biol Chem 254(11):4764–4771
5. Li LZ, Xu HN, Ranji M et al (2009) Mitochondrial redox imaging for cancer diagnostic and therapeutic studies. J Innov Opt Health Sci 2(4):325–341
6. Li LZ, Zhou R, Xu HN et al (2009) Quantitative magnetic resonance and optical imaging biomarkers of melanoma metastatic potential. Proc Natl Acad Sci USA 106:6608–6613
7. Xu HN, Nioka S, Glickson J et al (2010) Quantitative mitochondrial redox imaging of breast cancer metastatic potential. J Biomed Opt 15:036010
8. Thompson EW, Paik S, Brunner N et al (1992) Association of increased basement membrane invasiveness with absence of estrogen receptor and expression of vimentin in human breast cancer cell lines. J Cell Physiol 150:534–544
9. Freund A, Chauveau C, Brouillet JP et al (2003) IL-8 expression and its possible relationship with estrogen-receptor-negative status of breast cancer cells. Oncogene 22(2):256–265
10. Neve RM, Chin K, Fridlyand J et al (2006) A collection of breast cancer cell lines for the study of functionally distinct cancer subtypes. Cancer Cell 10(6):515–527
11. Gordon LA, Mulligan KT, Maxwell-Jones H et al (2003) Breast cell invasive potential relates to the myoepithelial phenotype. Int J Cancer 106(1):8–16
12. Xu HN, Tchou J, Chance B et al (2013) Imaging the redox states of human breast cancer core biopsies. Adv Exp Med Biol 765:343–349
13. Xu HN, Tchou J, Li LZ (2013) Redox imaging of human breast cancer core biopsies: a preliminary investigation. Acad Radiol 20:764–768
14. Xu HN, Li LZ (2016). Redox subpopulations and the risk of cancer progression: A new method for characterizing redox heterogeneity. Proc SPIE 9689:96893Z-1-7

Chapter 17
Directional Migration of MDA-MB-231 Cells Under Oxygen Concentration Gradients

D. Yahara, T. Yoshida, Y. Enokida, and E. Takahashi

Abstract To elucidate the initial mechanism of hematogenous metastasis of cancer cells, we hypothesized that cancer cells migrate toward regions with higher oxygen concentration such as intratumor micro vessels along the oxygen concentration gradient. To produce gradients of oxygen concentration *in vitro*, we devised the gap cover glass (GCG). After placing a GCG onto cultured MDA-MB-231 cells (a metastatic breast cancer cell line), the migration of individual cells under the GCG was tracked up to 12 h at 3 % oxygen in the micro incubator. We quantified the migration of individual cells using forward migration index (FMI). The cell migration perpendicular to the oxygen gradients was random in the direction whereas FMIs of the cell located at 300, 500, 700, and 1500 μm from the oxygen inlet were positive ($p < 0.05$) indicating a unidirectional migration toward the oxygen inlet. Present results are consistent with our hypothesis that MDA-MB-231 cells migrate toward regions with higher oxygen concentration.

Keywords Metastasis • Oxygen gradient • Migration • Cancer cell

1 Introduction

Hematogenous metastasis of tumor begins with local invasion of tumor cells followed by intravasation. It has not been determined whether tumor cells reach micro vessels as a result of directionally random migration or whether they are somehow directed to micro vessels. Here, we hypothesized that tumor cells in a hypoxic microenvironment preferentially migrate toward higher oxygen regions such as intratumor micro vessels along the oxygen concentration gradient. To test this hypothesis, we have established an *in vitro* model for hypoxic microenvironment in

D. Yahara • T. Yoshida • Y. Enokida • E. Takahashi (✉)
Advanced Technology Fusion, Graduate School of Science and Engineering, Saga University, Saga, Japan
e-mail: eiji@cc.saga-u.ac.jp

© Springer International Publishing Switzerland 2016

Q. Luo et al. (eds.), *Oxygen Transport to Tissue XXXVIII*, Advances in Experimental Medicine and Biology 923, DOI 10.1007/978-3-319-38810-6_17

cultured MDA-MB-231 metastatic breast cancer cell line using the gap cover glass (GCG). We tracked the migration of individual cells in oxygen concentration gradients for 12 h.

2 Methods

2.1 Gap Cover Glass (GCG)

We devised the GCG by combining two thin (150 μm) rectangular glass slips (9×18 mm) to a 25×18 mm microscopy cover glass (the roof) in such a way that the glass slips are placed at an interval of 2 mm beneath the roof cover glass (Fig. 17.1). When the GCG is placed on cultured cells in a culture dish, supply of oxygen to the cell is limited only from both open ends of the GCG (Fig. 17.1). Thus, oxygen consumption by cells gradually reduces oxygen concentration under the GCG as it diffuses from the open ends to the center.

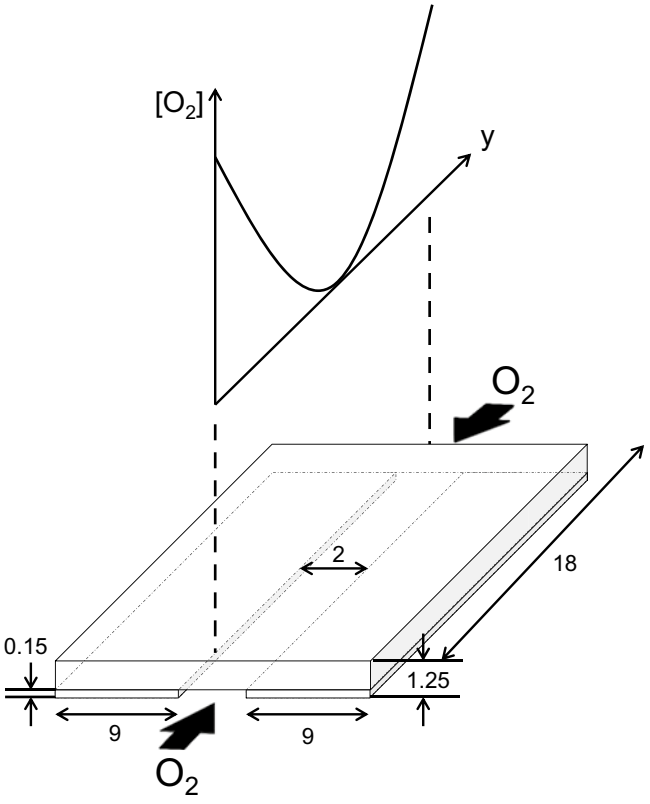

Fig. 17.1 Structure of the gap cover glass (GCG). Supply of oxygen to the cell is limited only from both open ends. Cellular consumption of oxygen produces oxygen concentration gradients under the GCG as indicated in the figure. Dimensions in mm

2.2 Cell Tracking

MDA-MB-231 cells were cultured in 35 mm type I collagen coated culture dishes (Corning). Cell density was 1.5–2.5 × 10^6 cells/ml. After replacing the culture medium (DMEM, high glucose) with Lavobitz's L-15 medium that had been exposed to 3 % oxygen overnight, the culture dish was placed in the micro incubator on the stage of inverted microscope. Oxygen concentration in the micro incubator was regulated at 3 % and the temperature was kept at 37 °C. Two hours later, a GCG was placed onto the cultured cells. Phase contrast images were taken every 1 h up to 12 h using 16-bit CCD camera (SV-512, SpectraVision).

Tracking of individual cells was performed offline. First, we defined 120 × 740 μm rectangular regions of interest (ROIs) at 100, 300, 500, 700, 900, and 1500 μm inside from an open end of the GCG (GCG edge). In addition, a ROI at -300 μm (*i.e.*, outside the GCG) served as the control. We arbitrarily picked up four cells with the normal spindle shape in the respective ROIs. Finally, we determined, using Image-J software, the coordinates of individual cells.

Migration of individual cells was classified according to the initial position (distance from the GCG edge) of the cell. We calculated the forward migration index, *FMIx* and *FMIy*, representing the efficiency of the forward migration of cells along the *x*- and *y*-axis, respectively,

$$FMIx = \frac{1}{n}\sum_{i=1}^{n}\frac{x_i^E}{D_i}$$

$$FMIy = \frac{1}{n}\sum_{i=1}^{n}\frac{y_i^E}{D_i}$$

where D_i, x_i^E, and y_i^E denote total length of the track (accumulated distance), *x*-end point, *y*-end point, for cell *i*, respectively.

3 Results

3.1 GCG Effects

GCG appeared to successfully produce gradients of oxygen concentration in monolayer cultured MDA-MB-231 cells. The cells (under the GCG) locating approximately <700 μm from the GCG edge showed normal spindle-like morphology while those located beyond this boundary were round-shaped. Because majority of the round cells was intact (LIVE/DEAD cell viability kit, Life Technologies), we interpret that these changes in the cell shape indicate the presence of significant hypoxic stress in these regions. These results are consistent with our previous data in which intracellular oxygen concentration under the cover glass was determined by the red shift of GFP fluorescence [1]. Number of cells outside the GCG increased to 116 % at 12 h after placing the GCG.

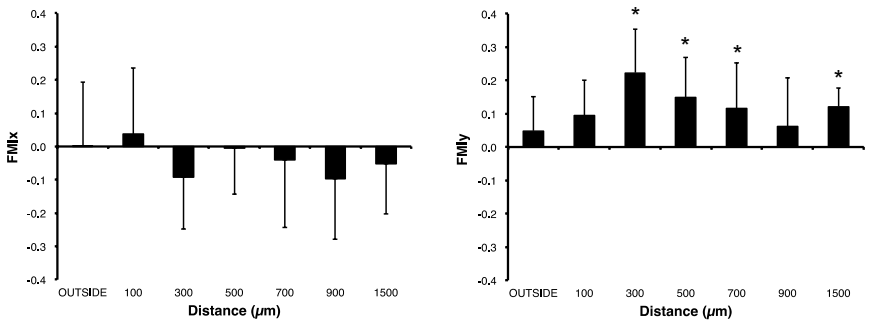

Fig. 17.2 Forward migration index (FMI) in cells at different distance from the edge of GCG. Data are presented as mean ± SD. *, $p < 0.05$ (comparisons with hypothetical value of 0)

3.2 Cell Tracking

Total length of the track (accumulated distance) during 12 h in the cell initially located in the ROI at −300 μm (control) was 188 ± 76 μm (mean ± SD, n = 32). The accumulated distance in cells in each ROIs was not different from the control.

FMIy was significantly different from the hypothesized value (=0) in cells at 300, 500, 700, and 1500 μm ROIs while *FMIx* was not significantly different from zero (*t*-test, Fig. 17.2). From these results, we conclude that MDA-MB-231 cells under the GCG demonstrated directional migration toward the GCG edge.

4 Discussion

Control of hematogenous metastasis has a significant clinical implication. For this ultimate end, we investigated *in vitro* the basic mechanism how cancer cells in hypoxic microenvironment reach the intratumor micro vessels. We hypothesized that tumor cells in a hypoxic microenvironment preferentially migrate toward higher oxygen regions.

To our knowledge, only two papers have been published that experimentally address the "aerotactic" behavior of mammalian cells *in vitro*. Using the micro-fluidic device, Chang et al. [2] produced gradients of oxygen in the miniature cell culture chamber in which oxygen concentration varied from 16 to 1 % along the 3 mm flow path. In the A549 carcinoma cell line, they demonstrated directional migrations of the cell toward the lower oxygen concentration region (negative "aerotaxis"). Mosadegh et al. [3] devised the unique paper-based 3-D invasion assay system. Oxygen gradients were generated between the top and the bottom layers (320 μm apart), although the magnitude of the oxygen gradients was not determined. Subpopulations of the A549 cell line in this device underwent directed movement toward higher oxygen concentrations indicating a positive "aerotaxis".

In the present study, we introduced the GCG to produce stable oxygen gradients in monolayer cultured cells. Unlike the microfluidic device, GCG utilizes cellular consumption of oxygen to produce oxygen gradients. Thus, the distribution of oxygen under the GCG is somewhat less precisely defined; it is affected by the spatial distribution of the cell and the cellular respiration. Although we did not directly measure the oxygen concentration distribution in the present study, previous studies from our laboratory [4] demonstrated in cultured Hep3B cells approximately 0.045 mmHg/μm gradients of oxygen concentration under the GCG. If these values are applicable to the present study, then, at 3 % oxygen in the micro incubator, oxygen would be depleted approximately 500 μm away from the GCG edge. The oxygen diffusion length calculated above appeared to be consistent with the appearance of the round-shaped cell in the present study.

In the present study, we demonstrated significant directional migrations toward the edge of GCG (positive *y*-direction) in the cell initially located at 300, 500, 700, and 1500 μm from the edge of the GCG. We also found that the cell migrations parallel to the *x*-axis were random in direction. Ideally, under the GCG, oxygen concentration reduces in proportion to the distance from the oxygen inlet. Therefore, the present result indicates that directionality in cell migration depends on the oxygen level to which the cell is exposed.

In the present GCG, not only gradients of oxygen but also gradients of nutrient (glucose), metabolites (for example, H^+), and autocrine factors should be produced under the GCG. Paradise et al. [5] demonstrated using the Dunn chamber that α(ν) β(3) CHO-B2 cells showed preferential migration toward acid in extracellular pH gradients. In the present study, gradients of pH are also established under the GCG where the medium pH decreased proportionally to the distance from the GCG edge (pH imaging by BCECF, data not shown). Thus, the cell migration demonstrated in the present study was toward alkaline. These data suggest a complex interaction among various factors in the microenvironment including oxygen concentration, pH, metabolites, nutrients, extracellular signal molecules and so on. We think that particularly the pH gradient might affect oxygen dependent cell migration because enhanced lactate output in cancer cells (Warburg effect) should produce steep pH gradients in the extracellular space. Therefore, it still remains to be determined whether the direction of cell migration is predominantly determined by the gradient of oxygen or not.

Acknowledgments This study was supported by JSPS KAKENHI Grant Number 26430117 to ET.

COI: The authors declare no conflict of interest.

References

1. Takahashi E, Sato M (2010) Imaging of oxygen gradients in monolayer cells using green fluorescent protein. Am J Physiol Cell Physiol 299:C1318–C1323
2. Chang CW, Cheng YJ, Tu M et al (2014) A polydimethylsiloxane-polycarbonate hybrid microfluidic device capable of generating perpendicular chemical and oxygen gradients for cell culture studies. Lab Chip 14:3462–3472

3. Mosadegh B, Lockett MR, Minn KT et al (2015) A paper-based invasion assay: assessing chemotaxis of cancer cells in gradients of oxygen. Biomaterials 52:262–271
4. Takahashi E, Sato M (2014) Anaerobic respiration sustains mitochondrial membrane potential in a hypoxic microenvironment. Am J Physiol Cell Physiol 306:C334–C342
5. Paradise RK, Whitfield MJ, Lauffenburger DA et al (2013) Directional cell migration in an extracellular pH gradient: a model study with an engineered cell line and primary microvascular endothelial cells. Exp Cell Res 319:487–497

Chapter 18
Stress-Induced Stroke and Stomach Cancer: Sex Differences in Oxygen Saturation

Maria Ulanova, Artem Gekalyuk, Ilana Agranovich, Alexander Khorovodov, Victoria Rezunbaeva, Ekaterina Borisova, Aly Esmat Sharif, Nikita Navolokin, Ekaterina Shuvalova, and Oxana Semyachkina-Glushkovskaya

Abstract Sex differences in stress-related diseases such as stroke and stomach cancer are well established, but the mechanisms underlying this phenomenon remain unknown. Despite the fact that sexual hormones play an important role in the high resistance of females to harmful effects of stress compared with males, the regulation of oxygenation status can be a potential factor, which might explain sex differences in stress-induced cerebrovascular catastrophes in newborn rats and in mutagens activation in adult rats with stomach cancer.

Keywords Sex differences • Haemorrhagic stroke • Oxygen saturation

1 Introduction

The phenomenon of sex differences in stress-related diseases is an actual and actively debated problem in medicine [1]. There are many theories explaining why this happens. The sexual hormones are the most obvious mechanism underlying sex differences to stress. However, using this concept it is difficult to explain sex differences in stress-related vascular catastrophes in newborns who have no active sexual status, or in old people who have a significant reduction in the level of sexual hormones [2].

There is a hypothesis that a general biological process, such as effectiveness of the regulation of oxygenation status, can be an important mechanism responsible for sex differences in stress-related pathological processes, independent of the age.

M. Ulanova • A. Gekalyuk • I. Agranovich • A. Khorovodov • V. Rezunbaeva • A.E. Sharif • N. Navolokin • E. Shuvalova • O. Semyachkina-Glushkovskaya (✉)
Saratov State University, Astrakhanskaya Str. 83, Saratov 410012, Russia
e-mail: glushkovskaya@mail.ru

E. Borisova
Institute of Electronics, Bulgarian Academy of Sciences,
Tsarigradsko Chaussee 72, Sofia 1784, Bulgaria

© Springer International Publishing Switzerland 2016

Q. Luo et al. (eds.), *Oxygen Transport to Tissue XXXVIII*, Advances in Experimental Medicine and Biology 923, DOI 10.1007/978-3-319-38810-6_18

Stroke and cancer are two examples in which there are significant sex differences predominantly in the first days of life and in advanced age, i.e. in newborns and old people in whom metabolic factors play a rather more important role in these processes than sexual hormones [3–5]. Changes in oxygen status are strongly associated with stress-related pathological processes during neonatal stroke development, as well as with stomach cancer in old people [6, 7].

Taking these data into account, we studied the role of effectiveness of the regulation of oxygenation status as a possible age-independent mechanism underlying sex differences in stress-related cerebrovascular catastrophes and mutagenic processes in the gastrointestinal tract, using two models of stress-induced diseases, i.e. stroke in newborn rats and stomach cancer in old rats.

2 Methods and Materials

Investigations on stress-related strokes were carried out in newborn rats, both sexes, 3-days old: (1) intact, unstressed newborn rats (control group, n = 10); (2) stressed rats 4 h after stress (pre-stroke group, rats with initial pathological changes in the brain tissues and cerebral circulation, n = 12); stressed rats 24 h after stress-off (post-stroke group, rats with intracranial hemorrhage, n = 12).

To induce hemorrhagic stroke, the following protocol of sound stress impact was used (120 dB, 17 Hz): 10 s of sound followed by a 60-s pause; this cycle was repeated during 2 h [8]. To analyze brain injury induced by stress and to confirm the development of stroke, all newborn rats were decapitated for histological study of brain tissue. The samples were fixed in 10 % buffered neutral formalin. The formalin fixed specimens were then embedded in paraffin, sectioned (4 μm) and stained with hematoxylin and eosin.

To induce stomach cancer we used a model of stress + nitrosamine. With this aim, old female rats (n = 15) and male rats (n = 15) lived for 9 months under chronic social stress (overpopulation) and received external nitrosamine (*N*-methyl alanine, 2 g/kg, with meat and preserved fish and nitrite (1 g/L) with drinking water).

Levels of blood oxygen saturation (SpO_2) in brain tissue were monitored using a pulse oximeter (model CMS60D; Contec Medical Systems Co. Ltd., Qinhuangdao, China). The optical sensor was based on a dual wavelength pulse oximetry approach, using 660 nm and 880 nm for SpO_2 detection. Oxy-hemoglobin saturation (SpO_2) is given as a percentage of HbO_2 vs. the total Hb in blood. The gastric tissue hemoglobin oxygen saturation (Hb-SpO_2) (%) was measured using a commercial optical diagnostic system LAKK (SPE "LASMA", Russia).

The results are reported as mean ± standard error of the mean (SEM). Differences from the initial level in the same group were evaluated with the Wilcoxon test. Intergroup differences were evaluated with the Mann-Whitney test and ANOVA-2 (post-hoc analysis with the Duncan's rank test). Significance level was set at $p < 0.05$ for all analyses.

3 Results and Discussion

3.1 Sex Differences in Stress-Induced Hemorrhagic Stroke and Cerebral Oxygenation in Newborn Rats

Our results showed that female newborn rats demonstrated high resistance to the harmful effects of stress on the brain, compared with males in all stages of stroke development. Indeed, the pre-stroke was characterized by progressive relaxation of cerebral veins. These changes were accompanied by perivascular edema, i.e. fluid pathway from the vessels. The relaxation of cerebral veins and the perivascular edema are markers of an accumulation of extensive blood in the venous system and suppression of blood outflow from the brain leading to venous insufficiency [9]. The males had more pronounced pre-stroke-related changes in the cerebral vessels than females. Figure 18.1 shows perivascular edema, which is more severe in males vs. females.

The accumulation of blood in the cerebral venous system and the suppression of blood outflow from the brain were associated with mild hypoxia; this has also been shown in other our investigations [8, 10]. The oxygen saturation level was lower in males compared with females (Table 18.1).

The sound stress caused brain bleeding in the cortex. The severity of stress-induced cortical bleeding was higher in males than in females. Figure 18.2 shows a typical example of sex differences in the size of the brain hemorrhage. More males

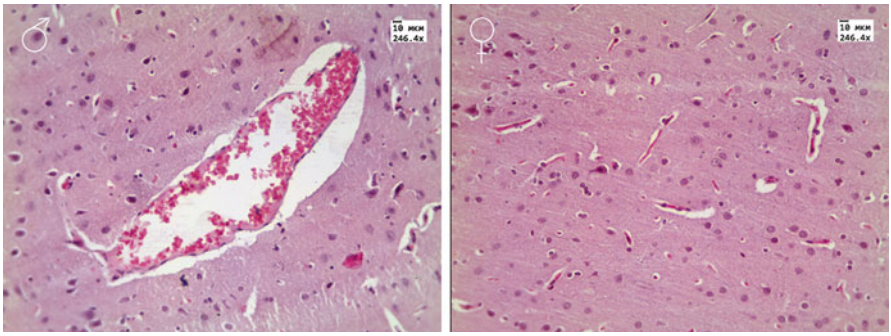

Fig. 18.1 The typical example of sex differences in the severity of perivascular edema in newborn rats

Table 18.1 Changes in SpO_2 level in brain tissues in the different stages of stress-induced stroke in male and female newborn rats

Gender of rats	Control group	Pre-stroke	Post-stroke
Female	97 ± 2 %	83 ± 3 %*	67 ± 2 %*
Male	95 ± 3 %	70 ± 4 %*†	48 ± 2 %*†

P < 0.05: * — vs. controls; † — between sexes

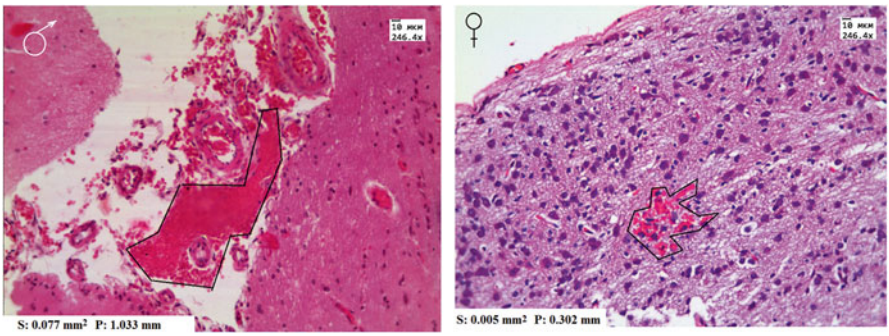

Fig. 18.2 Typical example of sex differences in the size of stress-induced intracranial hemorrhage in newborn rats

(10 of 12 in males, and 8 of 12 in females) demonstrated more pronounced brain hemorrhage (average size 0.079 ± 0.003 mm^2 for males and 0.009 ± 0.001 mm^2 for females). The mortality rate was 40 % (4 of 10) in males and 25 % (2 of 8) in females.

Our results present clear sex difference in stress-related stroke and in cerebral vascular and hypoxic changes associated with this pathological condition in newborn rats. Thus, in the early stages of ontogeny, when sex hormones are not functionally active, sex differences in the development of cerebral vascular catastrophes (such as stroke) is associated with significant gender-related differences in oxygen saturation of the brain tissues. This fact allows us to assume that in newborn rats the metabolic mechanisms are a potential factor responsible for sex differences in resistance to stress-related stroke.

3.2 Sex Differences in the Development of Stress-Induced Gastric Cancer and Oxygenation of Gastric Mucosa in Old Rats

There are sex differences in the mutagens processes, which are related to cancer development [5]. Stomach cancer is one example [11]. There is much debate about why this is happening, but our knowledge on metabolic mechanisms, such as oxygen saturation, in these processes remain poorly understood.

Here we studied the role of oxygen saturation of gastric mucosa in sex differences in stomach cancer with gastric ulcers (model of stress + nitrosamine).

Our results demonstrate that chronic social stress (housing of 15 females and 15 males during 9 months in conditions of overpopulation) with an additional factor—external nitrosamine (*N*-methyl alanine, 2 g/kg, with meat and preserved fish and nitrite (1 g/L) with drinking water) was accompanied by formation of stomach cancer with gastric ulcers (small = 1 × 1 mm, and large = 3–7 mm) in 73 % (11 of 15) of

Fig. 18.3 Typical example of development of gastric ulcers in females (small size) and in males (large size) in old rats

females and in 93 % (14 of 15) of males. Note, that more than half of females demonstrated small ulcers (9 of 11), while most number of males had large ulcers (12 of 14). Figure 18.3 shows a typical example of the different size of gastric ulcers in male and female rats.

We found low oxygen saturation levels of tumor tissues in stomach compared with the normal mucosa, which was more pronounced in males than in females. Thus, the reduction of Hb SpO_2 in males was from 80 %-46 %, while in females it was from 85 to 61 %. The decrease in oxygenation of gastrointestinal mucosa was reported by Wending et al. in 1984 [12]. Additional clinical investigations have also shown poor oxygenation of tumor tissues in gastrointestinal tract [13, 14].

Thus, the results of this experimental series suggest that sex differences in stomach cancer are largely realized by regulation of the oxygenation status of the gastrointestinal mucosa.

4 Conclusions

In general, using two models of stress-related diseases (hemorrhagic stroke and stomach cancer) we clearly show sex differences in resistance to the harmful effects of stress on the cerebral vessels in newborn rats and on gastrointestinal mucosa in adult animals. Effectiveness of the regulation of the oxygenation status is independent of the age mechanism underlying sex differences in stress-related alterations of homeostasis.

Acknowledgments M. U., A. G., I. A., V. R., E. B., O. S.-G. acknowledge support by Grant of Russia Foundation of Basic Research (№NK 14-02-00526/14), Grant of Ministry of Education and Science of the Russian Federation No. 17.488.2014/K; E. B. acknowledges support by Grant DFNI-B02/9/2014 of Bulgarian National Science Fund, E. Sh. acknowledges support by the RF Ministry of Education and Sciences within the basic part (project code 1287).

References

1. Becker JB, Monteggia LM, Perrot-Sinal TS et al (2007) Stress and disease: is being female a predisposing factor? J Neurosci 27(44):11851–11855
2. Haast RA, Gustafson DR, Kiliaan AJ (2012) Sex differences in stroke. J Cerebral Blood Flow Metab 32:2100–2107
3. Fullerton HJ, Wu YW, Zhao S (2003) Risk of stroke in children: ethnic and gender disparities. Neurology 61:189–194
4. Ellekjaer H, Holmen J, Indredavik B et al (1997) Epidemiology of stroke in innherred, Norway, 1994 to 1996: incidence and 30-day case-fatality rate. Stroke 28(11):2180–2184
5. Dorak MT, Karpuzoglu E (2012) Gender differences in cancer susceptibility: an inadequately addressed issue. Front Genet 3:1–11
6. Luo L, Chen D, Qu Y et al (2014) Association between hypoxia and perinatal arterial ischemic stroke: a meta-analysis. PLoS One 9(2), e90106
7. Wolf M, Bucher HU, Rudin M et al (2012) Oxygen transport to tissue XXXIII (Advances in Experimental Medicine and Biology). Springer Science+Business Media LLC, New York, p 233
8. Pavlov AN, Semyachkina-Glushkovskaya OV, Zhang Y et al (2014) Multiresolution analysis of pathological changes in cerebral venous dynamics in newborn mice with intracranial hemorrhage: adreno-related vasorelaxation. Physiol Meas 35:1983–1999
9. Valdueza JM, Doepp F, Schreiber SJ et al (2013) What went wrong? The flawed concept of cerebrospinal venous insufficiency. J Cereb Blood Flow Metab 33:657–668
10. Semyachkina-Glushkovskaya O, Pavlov A, Kurth J et al (2015) Optical monitoring of stress-related changes in the brain tissues and vessels associated with hemorrhagic stroke in newborn rats. Biomed Opt Express 6(10):2015. doi:10.1364/BOE.6.004088
11. Song HJ, Kim HJ, Choi N-K (2008) Gender differences in gastric cancer incidence in elderly former drinkers. Alcohol 42(5):363–368
12. Wendling P, Manz S, Thews G et al (1984) Heterogeneous oxygenation of rectal carcinomas in humans: a critical parameter for preoperative irradiation. Adv Exp Med Biol 180:293–300
13. Graffman S, Bjoerk P, Ederoth T et al (2001) Polarographic pO_2 measurements of intra-abdominal adenocarcinoma in connection with intraoperative radiotherapy before and after change of oxygen concentration of anesthetic gases. Acta Oncol 40:105–107
14. Mattern J, Kallinowski F, Herfarth C et al (1996) Association of resistance-related protein expression with poor vascularization and low level of oxygen in human rectal cancer. Int J Cancer 67:20–23

Part III
Brain Oxygenation and Function

Chapter 19
Changes in Oxygenation Levels Precede Changes in Amplitude of the EEG in Premature Infants

Alexander Caicedo, Liesbeth Thewissen, Anne Smits, Gunnar Naulaers, Karel Allegaert, and Sabine Van Huffel

Abstract Brain function is supported by an appropriate balance between the metabolic demand and the supply of nutrients and oxygen. However, the physiological principles behind the regulation of brain metabolism and demand in premature infants are unknown. Some studies found that changes in hemodynamic variables in this population precede changes in EEG activity; however, these studies only used descriptive statistics. This paper describes the relationship between changes in cerebral oxygenation, assessed by means of near-infrared spectroscopy (NIRS), and changes in EEG, using mathematical methods taken from information dynamics. In a cohort of 35 neonates subjected to sedation by propofol, we quantified the direction of information transfer between brain oxygenation and EEG. The results obtained indicate that, as reported in other studies, changes in NIRS are likely to precede changes in EEG activity.

Keywords aEEG • NIRS • Premature infants • Transfer entropy

A. Caicedo (✉) • S. Van Huffel
Department of Electrical Engineering (ESAT), STADIUS, KU Leuven, Leuven, Belgium

iMinds, Medical IT, Leuven, Belgium
e-mail: alexander.caicedodorado@esat.kuleuven.be

L. Thewissen • G. Naulaers • K. Allegaert
Department of Development and Regeneration, KU Leuven, Leuven, Belgium

Department of Neonatology, University Hospitals Leuven, Leuven, Belgium

A. Smits
Department of Pediatrics, University Hospitals Leuven, Leuven, Belgium

© Springer International Publishing Switzerland 2016

Q. Luo et al. (eds.), *Oxygen Transport to Tissue XXXVIII*, Advances in Experimental Medicine and Biology 923, DOI 10.1007/978-3-319-38810-6_19

1 Introduction

Brain metabolism is supported by adequate cerebral hemodynamic regulation, which provides the necessary substrates and is reflected in appropriate brain functioning. Oxygen is one of the most important substrates that is needed in order to meet the energy demand of the brain. For monitoring purposes, brain oxygenation levels can be assessed by means of near-infrared spectroscopy (NIRS), while brain function can be assessed by means of EEG [1]. Several studies have shown that EEG is a very good predictor of early neonatal outcome, especially in asphyxiated infants [2]; however, its prognostic value is decreased in cooled neonates [3]. Changes in brain oxygenation probably relate to changes in brain function. Consequently, combining the information provided by brain oxygenation levels and brain function enables to assess the coupling of the cerebral metabolic demand and oxygen delivery to the brain. This coupling was shown to be lost in case of pathological conditions such as hypoxic-ischemic encephalopathy [4, 5]. However, these studies are only a description of observations and lack metrics that are able to adequately measure the link between the dynamics of cerebral hemodynamics regulation and EEG.

In this paper we attempt to identify whether changes in brain oxygenation precede changes in EEG in premature infants, as shown in [5], but using a quantitative method based on information dynamics instead of descriptive statistics.

2 Methods

Data were acquired from 35 neonates undergoing an intubation procedure in the Neonatal Intensive Care Unit. The data were recorded as part of a study to identify the optimal dose of propofol for procedural sedation in neonates (ClinicalTrials.gov NCT01621373). Concomitant measurements of brain oxygenation, measured by NIRS (INVOS 5100, Covidien, neonatal probe) with the optode located left frontoparietal, and raw EEG, from channels C3-C4, were obtained from the patients (Olympic CFM 6000, Natus). NIRS signals were measured at 1 Hz, while EEG signals were acquired at 100 Hz. The measurements were carried out before administration of propofol and lasted up to 12 h. In this study we analysed data from 2 min before up to 10 h after protocol administration in order to have a homogeneous dataset. All data were pre-processed by detecting artefacts manually and replacing them by NaN (Not a Number) in the data stream. For the EEG measurements, segments of data with an impedance higher than 10 KΩ were identified and replaced by NaN, since the measurement is unreliable.

Due to the different temporal characteristics between the NIRS signals and EEG, we used a continuous estimate of the power contained in the EEG signal, by computing a running root mean squared (RMS) value of the EEG. For this purpose we used a window length of 60 s, with an overlapping of 59 s, producing one new value every second. In this way both signals, NIRS and the power contained in the EEG,

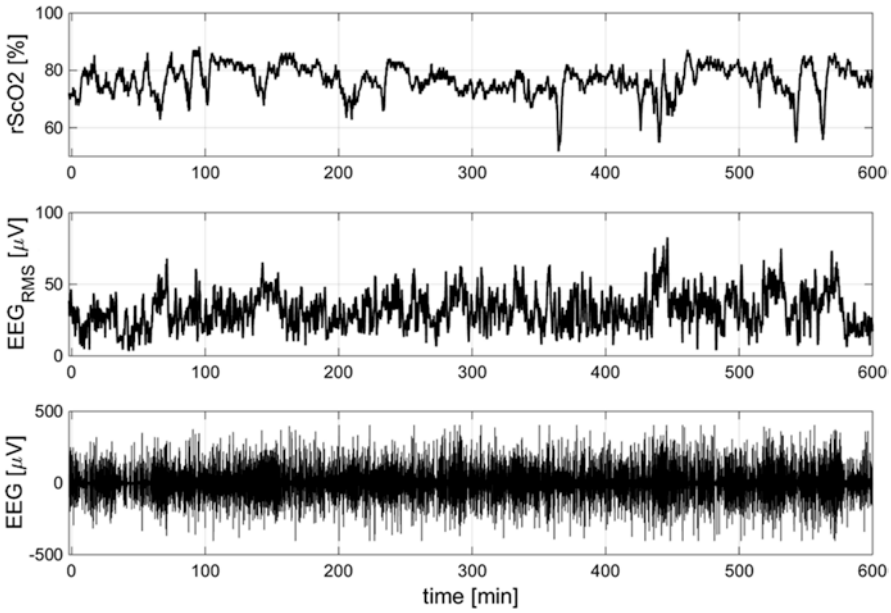

Fig. 19.1 Representative set of measurements for one subject. The $rScO_2$, preprocessed EEG and raw EEG measurements are shown

have a common temporal scale and sampling frequency. The 60-s window for the RMS computation was selected since the spectral decomposition of the NIRS signal indicates that most of its power is located below 0.16 Hz. Therefore, to keep the power of this component, a window of around 1-min length was needed; shorter windows will introduce components at a higher frequency, while longer windows will filter components that we would like to keep. Figure 19.1 is a representative sample of the recordings.

In order to identify the directionality of the relation between brain oxygenation levels and EEG power, we use transfer entropy. Transfer entropy is a measure for the amount of information transferred from one signal (process) to another [6]. A transfer entropy equal to zero indicates no transfer of information in the established direction, whilst any other value indicates a link between the processes. Higher values of transfer entropy indicate a higher transfer of information and, hence, a stronger directional coupling [7]. The transfer entropy computes the rate of information transfer between two different signals, namely X and Y. This computation starts from an autoregressive model between X and Y, using L delays in X and K delays in Y as follows:

$$y_n = \sum_{r=1}^{L} a_r x_{n-r+1} - \sum_{q=1}^{K} b_p y_{n-p}$$

where a_r and b_q represent the coefficients for this model, and can be simplified in the following form $y_n = a^{(L)}x_n^{(L)} - b^{(K)}y_n^{(K)}$, where the upper script (.) represents a set of ensemble, K or L, samples that form a vector of the past instances of the respective signals. Transfer entropy is then computed as follows:

$$T_{X\to Y} = \sum p\left(y_{n+1}, y_n^{(K)}, x_n^{(L)}\right)\log\frac{p\left(y_{n+1}\middle| y_n^{(K)}, x_n^{(L)}\right)}{p\left(y_{n+1}\middle| y_n^{(K)}\right)}$$

where X and Y represent the two time series, $p\left(y_{n+1}, y_n^{(K)}, x_n^{(L)}\right)$ represents the joint probability distribution, and $p\left(y_{n+1}\middle| y_n^{(K)}, x_n^{(L)}\right)$ and $p\left(y_{n+1}\middle| y_n^{(K)}\right)$ represents the conditional probability distributions.

In order to identify the direction of information transfer, and whether changes in oxygenation levels precede the changes in EEG activity, we computed $T_{NIRS\to EEG}$ and $T_{EEG\to NIRS}$.

To compute the transfer entropy values we proceed as follows:

1. The systemic and EEG signals were preprocessed as indicated before.
2. The time at which the propofol was applied was indicated. The signals were segmented from 2 min before propofol administration up to 10 h.
3. The transfer entropy values were computed for the first 2 min prior to propofol administration in order to generate a reference value for the baseline.
4. The remaining part of the signal was segmented in non-overlapping windows of 5 min. For each window, $T_{NIRS\to EEG}$ and $T_{EEG\to NIRS}$ were computed.
5. For each window the method evaluates the order of the model, specifically K and L, we have imposed as the maximum model order 20 samples. This is done to guarantee that there are enough samples to compute the probability distributions.
6. The results were analyzed using a Kruskal–Wallis test in order to indicate whether the differences between the two values are significant.

3 Results

Figure 19.2 shows the values of $TE_{NIRS\to EEG}$ and $TE_{EEG\to NIRS}$ for the 35 neonates, during the 10 h of measurements. The figure presents the median as a solid line, and the 25–75 percentiles as a shaded area; also presented are the values for $TE_{NIRS\to EEG}$ in blue and the values for $TE_{EEG\to NIRS}$ in red.

For the statistical analysis, all data were collected in two variables, each one representing each TE measurement. The values were dispersed as follows: $TE_{NIRS\to EEG}$ [0.0036, 0.0062, 0.0202] and $TE_{EEG\to NIRS}$ [0.0007, 0.0019, 0. 0128]; where the numbers within square brackets represent the 25, 50 and 75 percentiles respectively.

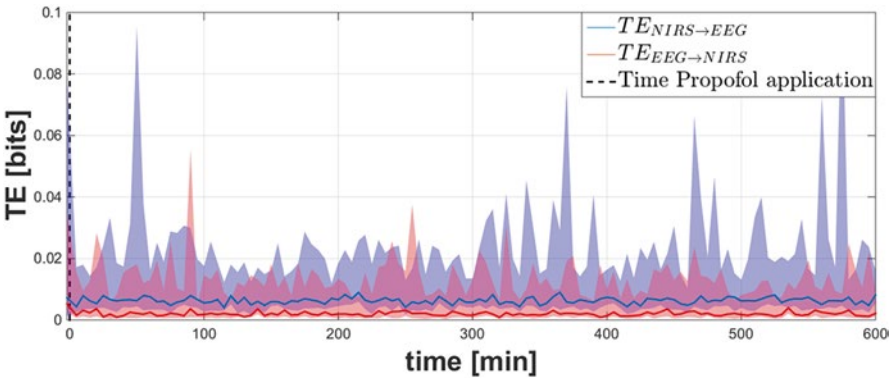

Fig. 19.2 Transfer entropy values. The *solid line* represents the median over the different epochs across time, the *shaded areas* represent the 25 and 75 % percentiles for the TE values across the group, the *blue* values represent $TE_{NIRS \to EEG}$, while the *red* ones represent $TE_{EEG \to NIRS}$

Results from the Kruskal–Wallis test indicated that $TE_{NIRS \to EEG}$ values were significantly higher than $TE_{EEG \to NIRS}$ values, with $p < 0.001$.

4 Discussion and Conclusions

In this study, we found that the transfer of information, measured by means of transfer entropy, is larger in the direction of NIRS → EEG than in the direction from EEG → NIRS. This indicates that the changes in NIRS are likely to precede the changes in EEG. These results are in agreement with the findings of Roche-Labarbe et al., who describe that the changes in NIRS precede the changes observed in EEG [5]. In their study they investigated whether bursts of EEG activity were coupled to a hemodynamic response in premature infants. They found that changes in hemodynamic parameters were sometimes observed a few seconds before onset of the EEG activity. They hypothesize that these observations might be due mainly to the fact that the neural activity might have started before it was observed in the EEG. The cause for this phenomenon can be multifactorial and may be due to the fact that EEG measures only the superficial changes in the electrical activity of the brain and not more internal layers, where many processes might occur and not be reflected in the EEG; this is further discussed in [5]. We would like to stress that in our study we only indicate that, according to the values provided by transfer entropy, changes in NIRS are more likely to precede the changes in EEG, than otherwise. To the best of our knowledge, this is the first study that quantifies the direction of information transfer between NIRS and EEG in general.

Since the transfer of information EEG → NIRS is not zero, this indicates that there is a flow of information in this direction. This can be attributed to the feedback mechanisms that are in charge of the regulation of brain hemodynamics, and which are in charge of delivering nutrients and oxygen to meet the metabolic demand. These results indicate that the analysis of EEG–NIRS, using transfer entropy, can be used to assess the status of these regulatory mechanisms in the premature brain.

Additionally, we expected some effect of the application of propofol in the coupling between the signals. However, this was not observed in the present results. We hypothesized that this might be due to the fact that propofol not only affects the hemodynamic regulatory mechanisms due to its vasodilator action, but also produces a depression in the EEG, via other mechanisms. These two responses might have been equally affected, producing no change in the transfer entropy values.

It is important to note that transfer entropy assumes that, in the selected window, the processes under analysis are stationary. In addition, the processes are assumed to be linearly related and to have a Gaussian distribution. We are aware that these conditions might not be fulfilled in the selected window of 5 min. However, even though by selecting shorter windows these conditions are more likely to be met, the number of samples in the window under analysis then becomes too small to provide reliable probability distribution, as well as estimation of model parameters which are, afterwards used for the estimation of the transfer entropy values.

In conclusion, the results presented in this study confirm the observations of Roche-Labarbe et al., by providing a quantification for the directionality of information transfer between NIRS and EEG measurements. The physiological mechanism of this phenomena is still unclear and requires more studies.

Acknowledgments Alexander Caicedo is a postdoctoral fellow of the research foundation Flanders (FWO). Bijzonder Onderzoeksfonds KU Leuven (BOF). This research was also supported by: Center of Excellence (CoE) #: PFV/10/002 (OPTEC). Fonds voor Wetenschappelijk Onderzoek-Vlaanderen (FWO), project #: G.0427.10N (Integrated EEG-fMRI), G.0108.11 (Compressed Sensing), G.0869.12N (Tumor imaging), G.0A5513N (Deep brain stimulation). Agentschap voor Innovatie door Wetenschap en Technologie (IWT), project #: TBM 080658-MRI (EEG-fMRI), TBM 110697-NeoGuard. iMinds Medical Information Technologies.. Dotatie-Strategisch basis onderzoek (SBO- 2015). ICON: NXT_Sleep. Belgian Federal Science Policy Office. IUAP #P7/19/ (DYSCO, 'Dynamical systems, control and optimization', 2012–2017). Belgian Foreign Affairs-Development Cooperation. VLIR UOS programs (2013–2019). EU: European Union's Seventh Framework Programme (FP7/2007–2013): EU MC ITN TRANSACT 2012, #316679, ERASMUS EQR: Community service engineer, #539642-LLP-1-2013. Other EU: INTERREG IVB NWE programme #RECAP 209G. European Research Council: ERC Advanced Grant, #339804 BIOTENSORS. This paper reflects only the authors' views and the Union is not liable for any use that may be made of the contained information.

References

1. Prior PF, Maynard DE (1986) Monitoring cerebral function. Long-term recordings of cerebral electrical activity and evoked potentials. Elsevier, Amsterdam, pp 1–441

2. Hallberg B, Grossmann K, Bartocci M et al (2010) The prognostic value of early aEEG in asphyxiated infants undergoing systemic hypothermia treatment. Acta Paediatr 99(4):531–536
3. Ancora G, Maranella E, Grandi S et al (2013) Early predictors of short term neurodevelopmental outcome in asphyxiated cooled infants. A combined brain amplitude integrated electroencephalography and near infrared spectroscopy study. Brain Dev 35(1):26–31
4. Pichler G, Avian A, Binder C et al (2013) aEEG and NIRS during transition and resuscitation after birth: promising additional tools; an observational study. Resuscitation 84(7):974–978
5. Roche-Labarbe N, Wallois F, Ponchel E et al (2007) Coupled oxygenation oscillation measured by NIRS and intermittent cerebral activation on EEG in premature infants. Neuroimage 36(3):718–727
6. Schreiber T (2000) Measuring information transfer. Phys Rev Lett 85:461. doi:10.1103/physrevlett.85.461
7. Faes L, Marinazzo D, Montalto A et al (2014) Lag-specific transfer entropy as a tool to assess cardiovascular and cardiorespiratory information transfer. IEEE Trans Biomed Eng 61(10):2556–2568

Chapter 20
Effects of Positive and Negative Mood Induction on the Prefrontal Cortex Activity Measured by Near Infrared Spectroscopy

A. Compare, Agostino Brugnera, R. Adorni, and K. Sakatani

Abstract The neurophysiological mechanism of positive versus negative emotions is insufficiently understood. In the present study, we examined the effect of event recall tasks on the prefrontal cortex (PFC) activity using near infrared spectroscopy (NIRS). Nine healthy adults were instructed to recall episodes of their life associated with positive (happiness) and negative (anger) emotion, both silently and verbally. Heart rate (HR) changes were simultaneously measured. NIRS showed an increased oxyhemoglobin (oxy-Hb) in the bilateral PFC during silent and verbal recall of both positive and negative episodes. The changes of oxy-Hb in the bilateral PFC during silent recall of negative episodes were significantly larger than those during silent recall of positive episodes ($p<0.01$). There was no difference in average changes of oxy-Hb between silent and verbal recall of negative episodes ($p>0.95$), while changes of oxy-Hb during verbal recall of positive episodes were larger than those during silent recall of positive episodes ($p<0.05$). Both verbal and silent recall of positive and negative episodes increased HR; however, verbal recall caused larger increases of HR than silent recall ($p<0.01$). The present results suggest that recall of negative episodes affect the PFC activity, which plays a key role in cognitive control of emotions, more than positive episodes.

Keywords NIRS • Emotional recall • HR • Anger • Happiness

A. Compare
Department of Human & Social Sciences, University of Bergamo, Bergamo, Italy
Human Factors and Technology in Healthcare, University of Bergamo, Bergamo, Italy

A. Brugnera (✉) • R. Adorni
Department of Human & Social Science, University of Bergamo, Bergamo, Italy
e-mail: agostino.brugnera@unibg.it

K. Sakatani
NEWCAT Research Institute, Department of Electrical and Electronic Engineering, College of Engineering, Nihon University, Tokyo, Japan

© Springer International Publishing Switzerland 2016

Q. Luo et al. (eds.), *Oxygen Transport to Tissue XXXVIII*, Advances in Experimental Medicine and Biology 923, DOI 10.1007/978-3-319-38810-6_20

1 Introduction

The prefrontal cortex (PFC) is a cerebral region involved in a number of high-level functions. Indeed, it supports cognitive functions that are necessary to organize behavior in time and in context, as social behavior [1], and it has a key role in cognitive control of emotions [2].

In the past 40 years, the branch of affective neuroscience extensively studied the bond between emotions and the brain, leading to various hypotheses about the role of specific brain regions in regulating and experiencing emotions [3]. Rohr and colleagues [4] reviewed four major emotion processing hypotheses: (a) the right hemisphere hypothesis (emotions are processed only by right hemisphere); (b) the valence hypothesis (right hemisphere has a major role in negative emotion processing, while the left one in positive emotion processing); (c) the one-network hypothesis (all emotions are processed by a specific set of brain regions); and finally (d) the localist hypothesis (specific emotions are processed by specific brain regions). The valence hypothesis has been recently studied with near-infrared spectroscopy (NIRS), which has been established as a useful tool for evaluating the association between right/left asymmetry of PFC activity and psychological stress/emotional responses [5–7]. Importantly, NIRS is suitable for studies focused on emotion because it offers some advantages as compared with other neuroimaging techniques. In particular, NIRS is less sensitive to external noise sources (e.g. movements), and requires less time and burden (both physical and psychological) for the preparation of the subjects and the application of the probes [6–8]. For example, unlike the other neuroimaging techniques, individuals can undergo NIRS recording while speaking and interacting with another person, an important condition for the evaluation of emotions. Indeed, personally relevant recall tasks are known to induce stronger physiological arousal than tasks that are not personally relevant [9–11].

Several studies investigated the relationship between the autonomic nervous system (ANS) activation and the experiencing of emotions [12]. One common result is that positive emotions evoke differential heart rate (HR) acute responses as compared to negative ones, with the latter being associated with a major acute sympathetic activity (or reduced parasympathetic activity), which results in higher HR [10]. By contrast, positive emotions seem to be associated with an increased acute parasympathetic activity (or reduced sympathetic activity), resulting in a reduced HR [10]. Some studies also explored the use of both central and autonomic nervous system indexes, revealing an association between the activation of the PFC and that of the ANS in response to emotional experiencing [10, 13, 14].

The purpose of the present study was to investigate simultaneously the physiological and neural underpinnings of emotion experiencing. Using high-ecological validity recall tasks designed to induce positive and negative emotions, we aimed to examine the role of mood induction in NIRS responses and ANS reactivity. In particular, we tested the hypotheses that emotion valence (positive vs. negative) may differently affect (i) the lateralization of the PFC activity, (ii) the HR, and (iii) the association between the PFC and ANS pattern of activation.

2 Methods

We studied nine healthy university students. All participants were right-handed; they were matched for gender (four males); the mean age was 25 (SD = 3.9) years. The study was conducted in accordance with APA (American Psychological Association, 1992) ethical standards for the treatment of human experimental volunteers (see also the Declaration of Helsinki, BMJ, 1991; 302, 1194).

Participants were seated in a comfortable chair, in a silent room. During psychophysiological recording, they were instructed to limit any movement of the body and to minimize those of the head.

A 5-min rest period (baseline) was followed by completion of two personally relevant recall tasks, designed to evoke positive (happiness) or negative (anger) affects. Both the happiness and anger recall tasks involved a 2-min silent and a subsequent 3-min verbal recall phase, during which NIRS and psychophysiological measures were recorded. The order of the two tasks was randomized across participants.

Regarding the Anger Recall task, the participants were asked to talk about an incident that made them feel angry, frustrated, or irritated—as described previously—[for a full description of the procedure see for example 9, 10]. They were asked to recreate the incident from the beginning to the end relaying what was said and done and describing associated thoughts and feelings. During the silent phase (2 min), the participants were asked to think about this situation, focusing on visualizing different aspects of it (e.g., location, people involved). During the verbal phase (3 min), the participants were invited to tell the experimenter about the situation. As the experimenter listened, he/she prompted the participants for details.

Regarding the Happiness Recall task, the participants were asked to discuss an event that made them feel happy, glad, or cheerful [10]. The procedure was the same as for the Anger Recall task.

We used a Bluetooth® CW NIRS system (Pocket NIRS, Hamamatsu Photonics K.K., Japan) for measurements of the concentration changes of oxy-Hb, deoxy-Hb, and total-Hb in the PFC. It uses light emitting diodes of three different wavelengths (735, 810, and 850 nm) as light sources and one photo-diode as a detector, and has two channels, one left and one right. The sampling rate was 61.3 Hz. The concentration changes of hemoglobin are expressed in arbitrary units (a.u.). Statistical analyses were performed considering the differences between experimental conditions and the baseline due to fact that CW NIRS devices provides only relative hemoglobin concentration changes.

Regarding the physiological measurements, we used the Pulse sensor, a wearable Bluetooth® designed by STMicroelectronics and manufactured by MR&D (Italy). It monitors continuously different physiological parameters, among which heart's activity. In the present study, only data on HR are reported. The device was attached to the person's chest using an adhesive patch; the ECG of each subject was visually inspected in order to correct missing beats and artifacts.

For each experimental condition, we analyzed HR in terms of the difference from the mean baseline value. As regards the NIRS signal, the concentration changes

were averaged to a single mean for each condition (baseline, silent 1 and 2, verbal 1 and 2). The baseline mean was therefore subtracted from the mean computed for every experimental condition (e.g., silent recall 1—baseline).

The resulting mean Δoxy-Hb, Δdeoxy-Hb, and Δtotal-Hb and mean ΔHR were finally subjected to multifactorial repeated-measures ANOVAs. As for NIRS, the ANOVA factors were Task (happiness vs. anger), Condition (silent vs. verbal recall), and hemisphere (right vs. left). As for HR, the ANOVA factors were Task and Condition. Multiple Post-Hoc mean comparisons were performed using the Fisher test.

3 Results

NIRS showed an increase of Δoxy-Hb and Δtotal-Hb associated with a decrease of Δdeoxy-Hb, in the bilateral PFC during silent and verbal recall of both positive and negative episodes (see Fig. 20.1 for a typical NIRS signal during the experiment).

The analyses performed on Δdeoxy-Hb and Δtotal-Hb evidenced no statistical significant effects. The analyses performed on Δoxy-Hb evidenced a significant interaction between Task and Condition ($F1,8 = 5.32$; $p < 0.05$). In particular, Δoxy-Hb in the bilateral PFC during silent recall of negative episodes was larger than that recorded during silent recall of positive episodes ($p < 0.01$). There was no difference in Δoxy-Hb between silent and verbal recall of negative episodes ($p > 0.95$), while Δoxy-Hb during verbal recall of positive episodes was larger than that recorded during silent recall of positive episodes ($p < 0.05$). Figure 20.2 reports all the means of Δoxy-Hb.

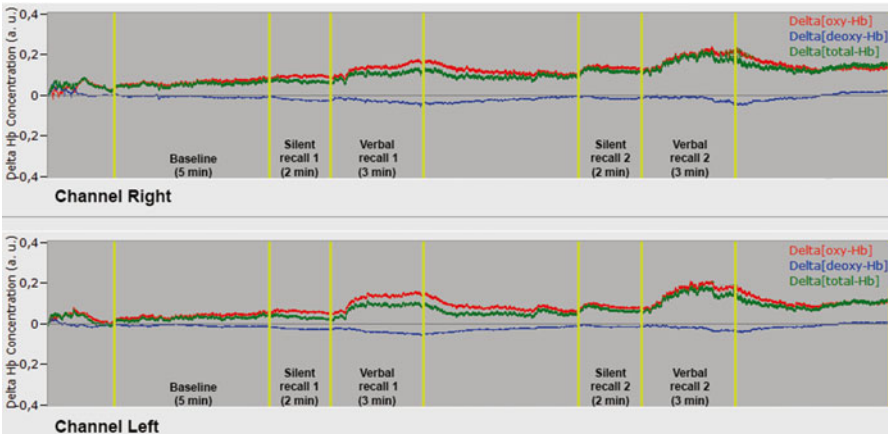

Fig. 20.1 Typical oxy, deoxy and total hemoglobin concentration changes during the experimental conditions recorded in one participant

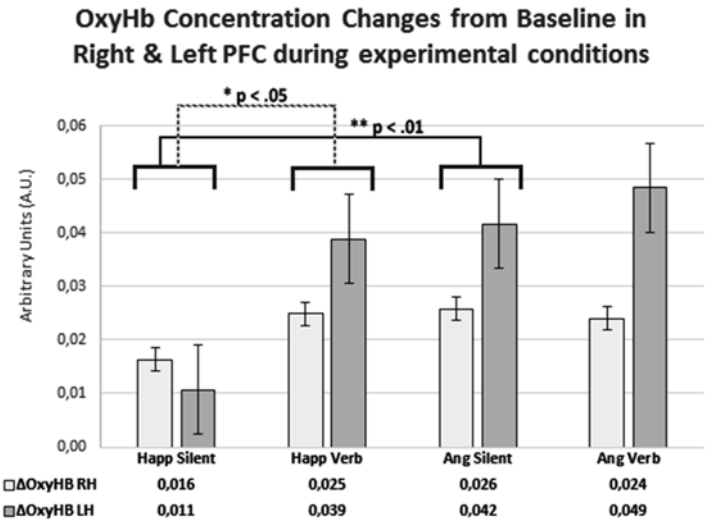

Fig. 20.2 Mean Δoxy-Hb among all subjects (n = 9) in the bilateral PFC during the experimental conditions. Below each condition are reported the related means, expressed in arbitrary units (a.u.). The lines between conditions represent the significant interactions (with the corresponding p-value) found in ANOVA

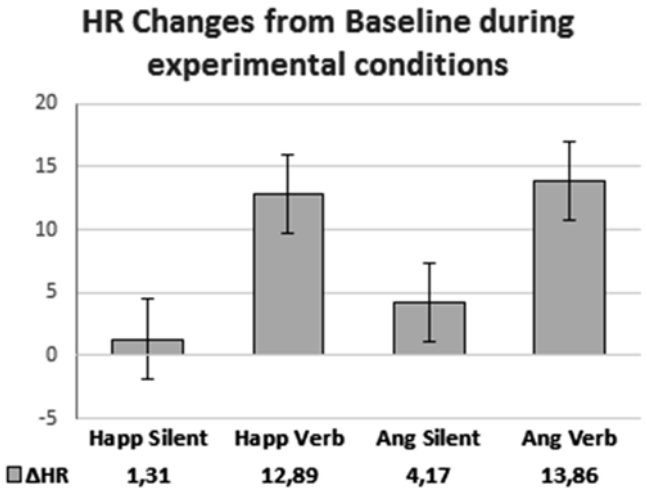

Fig. 20.3 Mean ΔHR among all subjects (n = 9). Below each condition are reported the related means

Overall, both verbal and silent recall of positive and negative episodes increased HR (Fig. 20.3). The effect of the Condition ($F1,8 = 9.80$; $p < 0.05$) suggested that verbal recall was associated with a larger increase of HR than silent recall. HR changes recorded during negative episodes (Mean = 9.4; SE = 2.21) were slightly larger than those recorded during positive episodes (Mean = 7.04; SE = 2.36); however, there was no statistical significance.

4 Discussion

The NIRS data evidenced an increase of the PFC activation in all task conditions with respect to the baseline. The hypothesis that emotion valence may differently affect the lateralization of the PFC activity [4–7] is not supported by the present results, as we observed an increase of oxy-Hb concentration changes over the PFC bilaterally. Interestingly, our results evidenced an increase of the PFC activation during both conditions (silent and verbal), when the participants were asked to recall negative episodes. Conversely, during the recall of positive episodes, significant increase of the PFC activation was observed only during the verbal condition (and not the silent one). That is, negative emotions increased neuronal activity of the PFC both when the participants were silently recalling the events and when they were narrating them. These findings suggest that the recall of negative episodes may affect neuronal activity of the PFC, which plays a key role in cognitive control of emotions [2], more extensively (i.e. across different experimental conditions) than positive episodes. This observation suggests some caution when using passive tasks (i.e. passive viewing of emotional images or video clips) in cognitive neuroscience studies: indeed, passive "induction" of positive emotions could not be directly comparable to the passive induction of negative emotions [10, 11].

Regarding the autonomic data, interestingly the inferior limit of the participants' standard error during silent happiness recall is negative (see Fig. 20.3). This suggests that some participants experienced a HR decrease, due to a reduced sympathetic activity or an increased parasympathetic activity. Anger recall is instead constantly associated with a slight—even if not significant—increase of cardiac frequency when compared to happiness one, according to the hypothesis of a major activation of sympathetic system (or reduced parasympathetic activity) during experiencing negative emotions [10].

Examined all together, these data suggest that autonomic responses to emotional tasks have a "linear" trend, while hemodynamic cerebral responses show a "more complex" activation pattern than one may expect according, for example, to the valence hypothesis [4]. This may be due to the high number of factors affecting the PFC activation. Concluding, neurophysiological correlates of emotions remain one of the most promising neuropsychological research fields, in which NIRS could provide—in the near future—a valuable help in understanding the underpinning factors of emotional experiences and (dys)regulation.

This study has some limits. First, it is a preliminary study, therefore all the data should be re-examined in the light of an increase of the sample size. Secondly, the open nature of the task allowed the participants to recall any memories, thus not permitting control of the exact type and the intensity of emotion described and experienced by participants.

Finally, the data's lack of support to the valence hypothesis could be partly explained by the high ecological validity of the task. When compared to more widespread and standardized paradigms (i.e. passive viewing of pictures or video clips) the free recall of personally relevant emotional episodes is similar to a realistic social

interaction. As such, it does not allow the researcher to control for a large number of experimental factors that could vary between individuals. Therefore, the recall task could be influenced by spurious variables (e.g. social interaction, self-regulation and narrative discourse production) known to be connected with prefrontal activity [1, 2]. Otherwise, these limits are strictly connected to the ecological validity of the protocol, which represents its strong point.

Acknowledgments This research was supported in part by the Strategic Research Foundation Grant-aided Project for Private Universities (S1411017) and a Grant-in-Aid for Exploratory Research (25560356) from the Ministry of Education, Culture, Sports, Sciences, and Technology of Japan. Furthermore, this research was supported through grants from Iing Co., Ltd. (Tokyo, Japan), Alpha Electron Co., Ltd. (Fukushima, Japan), NJI Co., Ltd. (Fukushima, Japan), and Southern Tohoku General Hospital (Fukushima, Japan). Finally, the present investigation was funded by the project Smart Aging (MIUR, Smart Cities Nazionale progetto n. 00442, Italy).

References

1. Kolb B et al (2012) Experience and the developing prefrontal cortex. Proc Natl Acad Sci U S A 109(Supplement 2):17186–17193
2. Ochsner KN, Gross JJ (2005) The cognitive control of emotion. Trends Cogn Sci 9(5):242–249
3. Dalgleish T (2004) The emotional brain. Nat Rev Neurosci 5(7):583–589
4. Rohr CS et al (2013) Affect and the brain's functional organization: a resting-state connectivity approach. PLoS One 8(7):e68015
5. Ishikawa W et al (2014) Correlation between asymmetry of spontaneous oscillation of hemodynamic changes in the prefrontal cortex and anxiety levels: a near-infrared spectroscopy study. J Biomed Opt 19(2):027005
6. Tanida M et al (2004) Relation between asymmetry of prefrontal cortex activities and the autonomic nervous system during a mental arithmetic task: near infrared spectroscopy study. Neurosci Lett 369(1):69–74
7. Sakatani K (2012) Optical diagnosis of mental stress: review. Adv Exp Med Biol 737:89–95
8. Tuscan L-A et al (2013) Exploring frontal asymmetry using functional near-infrared spectroscopy: a preliminary study of the effects of social anxiety during interaction and performance tasks. Brain Imaging Behav 7(2):140–153
9. Ironson G et al (1992) Effects of anger on left ventricular ejection fraction in coronary artery disease. Am J Cardiol 70(3):281–285
10. Kop WJ et al (2011) Autonomic nervous system reactivity to positive and negative mood induction: the role of acute psychological responses and frontal electrocortical activity. Biol Psychol 86(3):230–238
11. Bond CVA (1998) Personal relevance is an important dimension for visceral reactivity in emotional imagery. Cogn Emot 12(2):231–242
12. Norman GJ, Berntson GG, Cacioppo JT (2014) Emotion, somatovisceral afference, and autonomic regulation. Emot Rev 6(2):113–123
13. Waldstein SR et al (2000) Frontal electrocortical and cardiovascular reactivity during happiness and anger. Biol Psychol 55(1):3–23
14. Balconi M, Grippa E, Vanutelli ME (2015) What hemodynamic (fNIRS), electrophysiological (EEG) and autonomic integrated measures can tell us about emotional processing. Brain Cogn 95:67–76

Chapter 21
Correlation Between the Cerebral Oxyhaemoglobin Signal and Physiological Signals During Cycling Exercise: A Near-Infrared Spectroscopy Study

Atsuhiro Tsubaki, Haruna Takai, Keiichi Oyanagi, Sho Kojima, Yuta Tokunaga, Shota Miyaguchi, Kazuhiro Sugawara, Daisuke Sato, Hiroyuki Tamaki, and Hideaki Onishi

Abstract Near-infrared spectroscopy (NIRS) is a widely used noninvasive method for measuring human brain activation based on the cerebral haemodynamic response. However, systemic changes can influence the signal's parameters. Our study aimed to investigate the relationships between NIRS signals and skin blood flow (SBF) or blood pressure during dynamic movement. Nine healthy volunteers (mean age, 21.3 ± 0.7 years; 6 women) participated in this study. The oxyhaemoglobin (O_2Hb) signal, SBF, and mean arterial pressure (MAP) were measured while the volunteers performed multi-step incremental exercise on a bicycle ergometer, at workloads corresponding to 30, 50, and 70 % of peak oxygen consumption (VO_2peak) for 5 min. The Pearson's correlation coefficients for the O_2Hb signal and SBF at 50 and 70 % VO_2peak were 0.877 ($P<0.01$) and –0.707 ($P<0.01$), respectively. The correlation coefficients for O_2Hb and MAP during warm-up, 30 % VO_2peak, and 50 % VO_2peak were 0.725 ($P<0.01$), 0.472 ($P<0.01$), and 0.939 ($P<0.01$), respectively. Changes in the state of the cardiovascular system influenced O_2Hb signals positively during low and moderate-intensity exercise, whereas a negative relationship was observed during high-intensity exercise. These results suggest that the relationship between the O_2Hb signal and systemic changes is affected by exercise intensity.

A. Tsubaki (✉) • H. Takai • S. Kojima • S. Miyaguchi • K. Sugawara • D. Sato • H. Tamaki • H. Onishi
Institute for Human Movement and Medical Sciences, Niigata University of Health and Welfare, 1398 Shimami-cho, Kita-ku, Niigata-shi, Niigata 950-3198, Japan
e-mail: tsubaki@nuhw.ac.jp

K. Oyanagi
Kobe City Medical Center General Hospital, 2-2-1 Minatojimaminamimachi, Chuo-ku, Kobe-city, Hyogo, 650-0047, Japan

Y. Tokunaga
Niigata Rehabilitation Hospital, 761 Kizaki, Kita-ku, Niigata-shi, Niigata 950-3304, Japan

© Springer International Publishing Switzerland 2016

Q. Luo et al. (eds.), *Oxygen Transport to Tissue XXXVIII*, Advances in Experimental Medicine and Biology 923, DOI 10.1007/978-3-319-38810-6_21

Keywords Near-infrared spectroscopy • Multistep incremental exercise • Oxyhaemoglobin • Skin blood flow • Mean arterial pressure

1 Introduction

Near-infrared spectroscopy (NIRS) is widely used to monitor real-time haemodynamic changes related to cortical neural activation during gross motor tasks. Studies have investigated cortical oxygenation during the human gait [1] and cycling exercise [2, 3].

NIRS measures the concentrations of oxyhaemoglobin (O_2Hb) and deoxyhaemoglobin (HHb) in tissues, based on their differential absorption at multiple wavelengths, using the modified Beer-Lambert law [4]. Thus, experimental tasks that induce physiological signals can block the detection of cortical activation by NIRS, as the near-infrared beams are transmitted through the scalp and skull and the resultant O_2Hb signals might represent task-related cardiovascular responses occurring during the perfusion of the extracranial layers.

Our study aimed to determine the relationship between NIRS signals and skin blood flow (SBF) or blood pressure during such gross motor tasks. To investigate the effect of exercise intensity on the relationship between NIRS signals and the cardiovascular control system, an incremental multistep cycle ergometer exercise protocol was used.

2 Methods

Nine healthy volunteers ([mean ± standard deviation] age, 21.3 ± 0.7 years; height, 161.6 ± 9.2 cm; weight, 54.5 ± 8.0 kg; 6 women) participated in this study. The subjects did not exhibit symptoms of neurological, medical, or cardiovascular disease and were not taking any medications. Each subject provided written consent after receiving information regarding the potential risks, study objectives, measurement techniques, and benefits associated with the study. This study was approved by the Ethics Committee of Niigata University of Health and Welfare and conformed to the standards set out by the Declaration of Helsinki.

To detect the exercise workload individually, the peak oxygen consumption (VO_2peak) was determined using an incremental protocol on a cycle ergometer (Aerobike 75XLII; Combi, Japan) before the main experiments. Exhaustion was defined as described previously [3].

In the main experiment, subjects performed multi-step incremental exercise on a cycle ergometer. After a 4-min rest and a 4-min warm-up, exercise began at workloads corresponding to 30, 50, and 70 % of the VO_2peak, with each phase lasting 5 min. A 4-min cool-down followed the 70 % VO_2peak workload. During this experiment, the NIRS signals, mean arterial pressure (MAP) and SBF were measured continuously.

A multichannel NIRS imaging system (OMM-3000; Shimadzu Co., Kyoto, Japan) with three wavelengths (780, 805, and 830 nm) was used to detect changes in O_2Hb at a sampling rate of 190 ms. NIRS optodes, consisting of 12 light-source fibres and 12 detectors providing 34-channel simultaneous recording, were set in a 3×8 multichannel probe holder, as described in our previous study [5]. The NIRS array map covered the right central, left central, and parietal areas of the scalp to measure cortical tissue oxygenation in motor-related areas.

Beat-to-beat MAP was recorded by volume clamping the finger pulse with a finger photoplethysmograph (Finometer; Finapres Medical Systems, Amsterdam, The Netherlands) on the left middle finger. Changes in SBF were measured at the forehead using a laser Doppler blood flow meter (Omegaflow FLO-CI; Omegawave Inc., Osaka, Japan), which collected data from the scalp layer within 1 mm from the probe. Analogue data were converted to digital data using an A/D converter (PowerLab; AD Instruments, Australia) at a 1000-Hz sampling rate.

To detect the effect of systemic changes on NIRS signals, the average of the O_2Hb values from all 34 channels was calculated for each subject as the global average of O_2Hb. MAP and SBF were down-sampled by adopting the sampling rate for NIRS monitoring. The global averages of the O_2Hb concentration, MAP, and SBF were expressed as the change from the average rest phase value and were calculated every 10 s. The relationships between O_2Hb and SBF and between O_2Hb and MAP were assessed during rest, warm-up, 30 % VO_2peak, 50 % VO_2peak, 70 % VO_2peak, and cool-down. Pearson's correlation coefficients were calculated, with the significance level set at $P < 0.05$.

3 Results

During the main experiment, the average O_2Hb began increasing above the baseline value following the 30 % VO_2peak phase. During the 50 % VO_2peak phase, the average O_2Hb increased to 0.029 mM·cm (Fig. 21.1) and subsequently increased to its peak value of 0.045 mM·cm during the first minute of the 70 % VO_2peak phase. From that point, O_2Hb decreased to 0.020 mM·cm at the end of the 70 % VO_2peak phase and decreased even further during the first 30 s of the cool-down phase, with lower values at this point than those detected during the initial rest phase. Finally, O_2Hb rebounded during the cool-down phase to 0.027 mM·cm. HHb increased from the middle part of the 50 % VO_2peak phase to the first 30 s of the cool-down phase, with a peak value of 0.042 mM·cm.

During the warm-up and 30 % VO_2peak phases, SBF remained below the resting value (Fig. 21.2). Following the increase in exercise intensity, SBF increased to 2.74 a.u. at the end of the 50 % VO_2peak phase and to 7.59 a.u. at the end of the 70 % VO_2peak phase. During the 70 % VO_2peak phase, SBF increased from 3.75 to 7.59 a.u. in 5 min. Following the high-intensity exercise, SBF declined gradually during the cool-down phase.

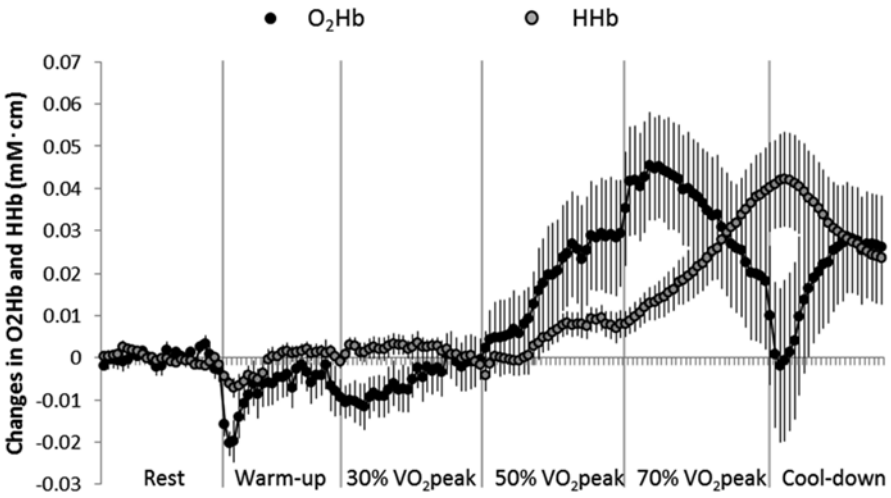

Fig. 21.1 Temporal changes in the average global oxyhaemoglobin (O_2Hb, *black circle*) and deoxyhaemoglobin (HHb, *grey circle*) values. Values are presented as the mean ± standard error of the mean (SEM)

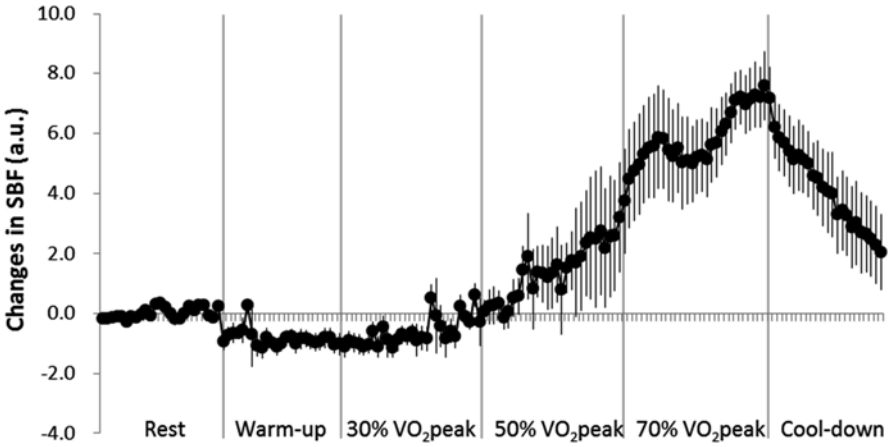

Fig. 21.2 Temporal changes in the average skin blood flow (SBF) value. Values are presented as the mean ± standard error of the mean (SEM)

We observed a slight increase in MAP from the warm-up phase to the end of the 30 % VO_2peak phase (Fig. 21.3). MAP increased gradually to 18.8 mmHg during the 50 % VO_2peak phase and to 30.0 mmHg during the 70 % VO_2peak phase, and then it rapidly returned to resting levels during the cool-down phase.

The relationship between O_2Hb and SBF varied according to the exercise phase (Figs. 21.4 and 21.5). A moderate positive correlation was observed during the 30 % VO_2peak phase, and a strong positive correlation was observed during the 50 %

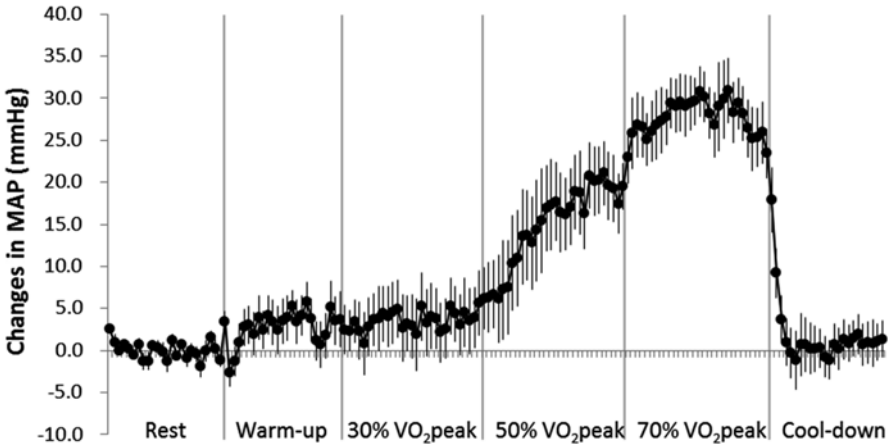

Fig. 21.3 Temporal changes in the average mean arterial pressure (MAP). Values are presented as the mean ± standard error of the mean (SEM)

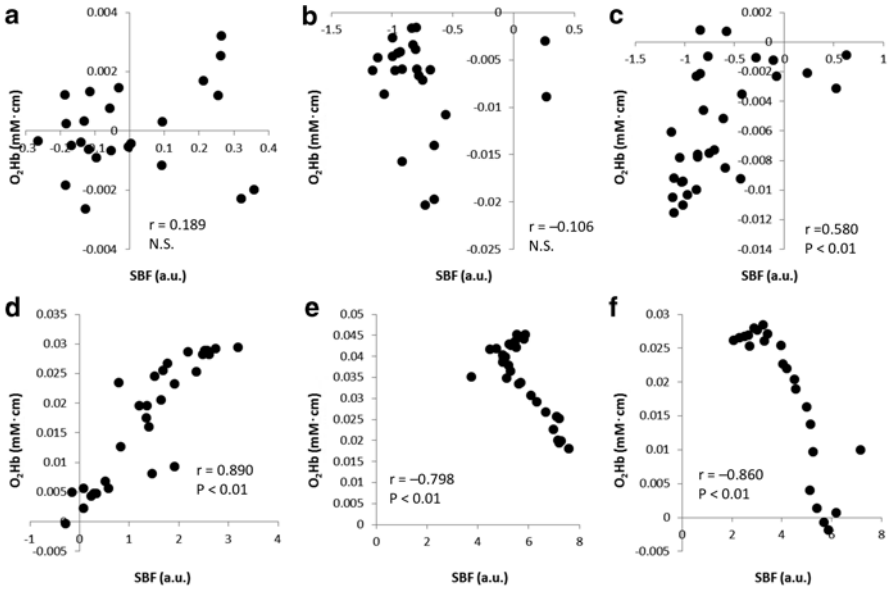

Fig. 21.4 Scatter plots for the skin blood flow (SBF) and O_2Hb during the rest (**a**), warm-up (**b**), 30 % VO_2peak (**c**), 50 % VO_2peak (**d**), 70 % VO_2peak (**e**) and cool-down (**f**) phases

VO_2peak phase. In contrast, a strong negative correlation was observed during the 70 % VO_2peak and cool-down phases. A moderate positive correlation was observed between O_2Hb and MAP during the warm-up and 30 % VO_2peak phases, and a strong positive correlation was observed during the 50 % VO_2peak phase.

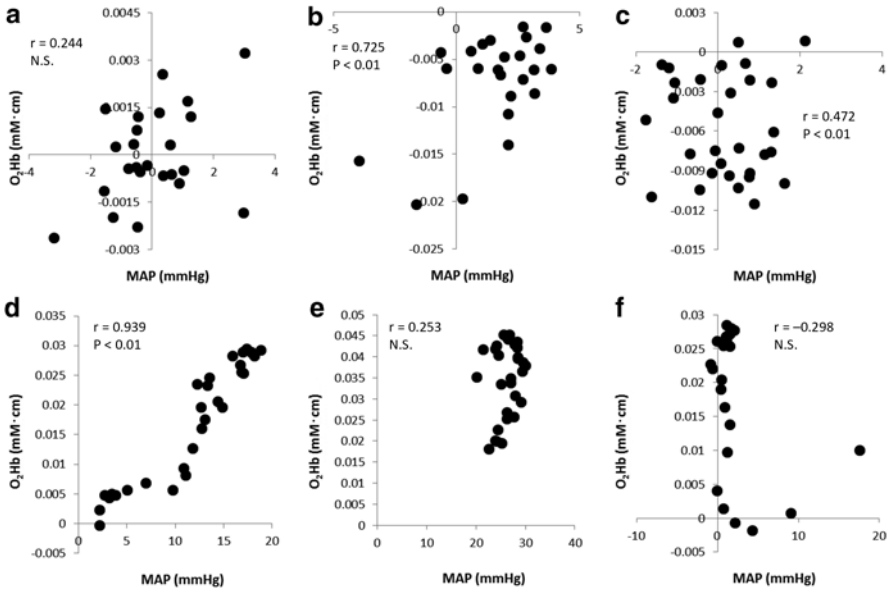

Fig. 21.5 Scatter plots for the mean arterial pressure (MAP) and O_2Hb during the rest (**a**), warm-up (**b**), 30 % VO_2peak (**c**), 50 % VO_2peak (**d**), 70 % VO_2peak (**e**) and cool-down (**f**) phases

4 Discussion

In the present study, the relationships between O_2Hb and MAP and between O_2Hb and SBF varied by exercise intensity. O_2Hb was moderately positively correlated with both SBF and MAP during the 30 % VO_2peak phase and strongly correlated during the 50 % VO_2peak phase. A strong negative correlation between O_2Hb and SBF was observed during the 70 % VO_2peak and cool-down phases.

NIRS can be used to measure changes in cerebral haemodynamics and metabolism, thus allowing for the use of multichannel NIRS recording for functional optical imaging of human brain activity [6]. Many studies have reported that changes in O_2Hb reflect changes in cortical neural activation [1, 7, 8], although none have discussed the relationship between O_2Hb changes and systemic circulatory changes during gross motor tasks. Our results indicate that brain activation can be monitored during motor tasks, such as cycling on an ergometer.

SBF, MAP, and O_2Hb all increased between 30 % VO_2peak and 50 % VO_2peak and were strongly correlated during the 50 % VO_2peak phase. These results suggest that cortical neural activation, blood pressure changes, and SBF changes affected the changes in O_2Hb during low and moderate-intensity exercise. Some studies have reported that an increase in cerebral oxygenation occurs with increased exercise intensity [2, 3], which is consistent with our results. The reason for the strong positive relationship between SBF and O_2Hb is because SBF affects the O_2Hb concentration, and these parameters have been found to be closely correlated ($R^2 = 0.94$) in

the frontal cortex [9]. Another study has shown that O_2Hb and forehead SBF were significantly increased during exercise, and the correlation between O_2Hb and forehead SBF was strong (R = 0.71–0.99) [10]. The strong positive relationship between MAP and O_2Hb is likely due to the effect of blood pressure on O_2Hb. Minati et al. [11] reported correlation coefficients of 0.93–0.95 between O_2Hb and MAP during visual stimulation combined with motor activity.

During the 70 % VO_2peak phase, SBF increased from 3.75 to 7.59 a.u. over 5 min, while O_2Hb decreased from 0.045 to 0.020 mM · cm, resulting in a strong negative correlation. Following exhaustive exercise, decreases in O_2Hb have also been observed in the prefrontal cortex [3, 12] and in the prefrontal and motor cortices [13]. Cortical oxygenation, measured using NIRS in healthy subjects, has shown a quadratic response to incremental exercise, increasing during moderate and high intensities, then falling at very high intensities [14]. In contrast, SBF increases during exhaustive exercise, and these contrasting phenomena create a strong negative correlation during the 70 % VO_2peak phase, suggesting that O_2Hb accurately reflects cortical haemodynamic changes during cycle ergometer exercise.

This study has some limitations. First, the measurement locations differed for SBF and O_2Hb. SBF was recorded at the forehead to prevent interference from the near-infrared and laser light emitted from the laser Doppler flow meter. Second, we could not clarify the relationship between O_2Hb and exercise duration; our results only examined changes in O_2Hb during 15 min of continuous exercise. Thus, future studies are needed to clarify the relationship between O_2Hb and exercise time.

In conclusion, we found that the relationships between O_2Hb and SBF and between O_2Hb and MAP varied according to exercise intensity during cycling. The relationships during the 70 % VO_2peak and cool-down phases suggest that O_2Hb signals reflect cortical haemodynamic changes other than SBF or MAP. The relationship between O_2Hb and systemic factors during motor tasks must be confirmed in order to detect cortical activation during gross motor tasks, and the findings of the present study serve as the basis for further investigation.

Acknowledgments This study was supported by a Grant-in-Aid for Young Scientists (B) from the Japan Society for the Promotion of Science and a Grant-in-Aid for Exploratory Research from the Niigata University of Health and Welfare.

References

1. Miyai I, Tanabe HC, Sase I et al (2001) Cortical mapping of gait in humans: a near-infrared spectroscopic topography study. Neuroimage 14:1186–1192
2. Bhambhani Y, Malik R, Mookerjee S (2007) Cerebral oxygenation declines at exercise intensities above the respiratory compensation threshold. Respir Physiol Neurobiol 156:196–202
3. Rupp T, Perrey S (2008) Prefrontal cortex oxygenation and neuromuscular responses to exhaustive exercise. Eur J Appl Physiol 102:153–163
4. Boas DA, Gaudette T, Strangman G et al (2001) The accuracy of near infrared spectroscopy and imaging during focal changes in cerebral hemodynamics. Neuroimage 13:76–90

5. Tsubaki A, Takai H, Kojima S et al (2016) Changes in cortical oxyhaemoglobin signal during low-intensity cycle ergometer activity: a near-infrared spectroscopy study. Adv Exp Med Biol 876:79–85
6. Tamura M, Hoshi Y, Okada F (1997) Localized near-infrared spectroscopy and functional optical imaging of brain activity. Philos Trans R Soc Lond B Biol Sci 352:737–742
7. Obrig H, Wolf T, Doge C et al (1996) Cerebral oxygenation changes during motor and somatosensory stimulation in humans, as measured by near-infrared spectroscopy. Adv Exp Med Biol 388:219–224
8. Niederhauser BD, Rosenbaum BP, Gore JC et al (2008) A functional near-infrared spectroscopy study to detect activation of somatosensory cortex by peripheral nerve stimulation. Neurocrit Care 9:31–36
9. Takahashi T, Takikawa Y, Kawagoe R et al (2011) Influence of skin blood flow on near-infrared spectroscopy signals measured on the forehead during a verbal fluency task. Neuroimage 57:991–1002
10. Miyazawa T, Horiuchi M, Komine H et al (2013) Skin blood flow influences cerebral oxygenation measured by near-infrared spectroscopy during dynamic exercise. Eur J Appl Physiol 113:2841–2848
11. Minati L, Kress IU, Visani E et al (2011) Intra- and extra-cranial effects of transient blood pressure changes on brain near-infrared spectroscopy (NIRS) measurements. J Neurosci Methods 197:283–288
12. Subudhi AW, Dimmen AC, Roach RC (2007) Effects of acute hypoxia on cerebral and muscle oxygenation during incremental exercise. J Appl Physiol 103:177–183
13. Subudhi AW, Miramon BR, Granger ME et al (2009) Frontal and motor cortex oxygenation during maximal exercise in normoxia and hypoxia. J Appl Physiol 106:1153–1158
14. Rooks CR, Thom NJ, McCully KK et al (2010) Effects of incremental exercise on cerebral oxygenation measured by near-infrared spectroscopy: a systematic review. Prog Neurobiol 92:134–135

Chapter 22
Effect of Locomotor Respiratory Coupling Induced by Cortical Oxygenated Hemoglobin Levels During Cycle Ergometer Exercise of Light Intensity

Keiichi Oyanagi, Atsuhiro Tsubaki, Yuichi Yasufuku, Haruna Takai, Takeshi Kera, Akira Tamaki, Kentaro Iwata, and Hideaki Onishi

Abstract This study aimed to clarify the effects of locomotor-respiratory coupling (LRC) induced by light load cycle ergometer exercise on oxygenated hemoglobin (O_2Hb) in the dorsolateral prefrontal cortex (DLPFC), supplementary motor area (SMA), and sensorimotor cortex (SMC). The participants were 15 young healthy adults (9 men and 6 women, mean age: 23.1 ± 1.8 (SEM) years). We conducted a task in both LRC-inducing and LRC-non-inducing conditions for all participants. O_2Hb was measured using near-infrared spectroscopy. The LRC frequency ratio during induction was 2:1; pedaling rate, 50 rpm; and intensity of load, 30 % peak

K. Oyanagi (✉) • K. Iwata
Kobe City Medical Center General Hospital,
2-2-1 Minatojimaminamimachi, Chuo-ku, Kobe City, Hyogo 650-0047, Japan
e-mail: k_oyanagi_0731@yahoo.co.jp; iwaken@kcho.jp

A. Tsubaki • H. Onishi
Institute for Human Movement and Medical Sciences, Niigata University of Health and Welfare, 1398 Shimami-cho, Kita-ku, Niigata 950-3198, Japan
e-mail: tsubaki@nuhw.ac.jp; onishi@nuhw.ac.jp

Y. Yasufuku
Medical Research Institute, Kitano Hospital, Tazuke Kofukai Foundation,
2-4-20 Ohgimachi, Kita-ku, Osaka, Japan
e-mail: barronn66whtq-pti@yahoo.co.jp

H. Takai
Marukawa Hospital, 962 Asahimachidoge, Shimoniikawa-gun, Toyama, Japan
e-mail: hpm13005@nuhw.ac.jp

T. Kera
Tokyo Metropolitan Institute of Gerontology,
35-2 Sakae-cho, Itabashi-ku, Tokyo 173-0015, Japan
e-mail: okerasanjp@gmail.com

A. Tamaki
Hyogo University of Health Sciences, 1-3-6 Minatojima, Chuo-ku, Kobe 650-8530, Japan
e-mail: a-tamaki@huhs.ac.jp

© Springer International Publishing Switzerland 2016

Q. Luo et al. (eds.), *Oxygen Transport to Tissue XXXVIII*, Advances in Experimental Medicine and Biology 923, DOI 10.1007/978-3-319-38810-6_22

volume of oxygen uptake. The test protocol included a 3-min rest prior to exercise, steady loading motion for 10 min, and 10-min rest post exercise (a total of 23 min). In the measurement of O_2Hb, we focused on the DLPFC, SMA, and SMC. The LRC frequency was significantly higher in the LRC-inducing condition ($p < 0.05$). O_2Hb during exercise was significantly lower in the DLPFC and SMA, under the LRC-inducing condition ($p < 0.05$). The study revealed that even light load could induce LRC and that O_2Hb in the DLPFC and SMA decreases during exercise via LRC induction.

Keywords O_2Hb • LRC • 30 % VO_2peak • DLPFC • SMA

1 Introduction

Locomotor-respiratory coupling (LRC) is a phenomenon in which locomotor and respiratory rhythms coordinate rhythmically during rhythmical exercise [1]. Relief of respiratory distress and breathing effort, and prolonged exercise time have been reported as physiological benefits of LRC [2, 3].

Various reports on the generation mechanism of LRC have been published, suggesting that LRC occurs via the interplay between the promotion of expiration caused by the contraction of trunk muscles at pedaling and the nerve center of respiratory rhythm through the input of proprioceptive sensations from the extremities caused by motion [4]. In addition, the fact that motion results from brain activity suggests that some brain activities occur during LRC. However, the exact brain activity during LRC remains unclear.

Therefore, this study aimed to clarify the effects of LRC induced by light load during bicycle ergometer exercise on oxygenated hemoglobin (O_2Hb) in the dorsolateral prefrontal cortex (DLPFC), supplementary motor area (SMA), and sensorimotor cortex (SMC).

2 Methods

The participants were 15 young healthy adults (9 men and 6 women, mean age: 23.1 ± 1.8 (SEM) years). We used cycle ergometer for the exercise task. Before testing, the peak volume of oxygen uptake (VO_2peak) of each participant was measured in a submaximal exercise-load test in order to determine the light load (30 % VO_2peak). The exercise was performed under the induction and non-induction conditions for LRC. The LRC was induced by providing visual and auditory stimulations using an LRC induction system. For the induction stimulation, the directions for inhalation or exhalation were provided by pedaling on the right side. The LRC frequency ratio was one breathing cycle per two pedaling cycles. The pedaling rate was fixed at 50 rpm. The test protocol included a 3-min rest prior to exercise, steady loading motion for 10 min, and a 10-min rest post exercise. In the measurement of brain activity, O_2Hb

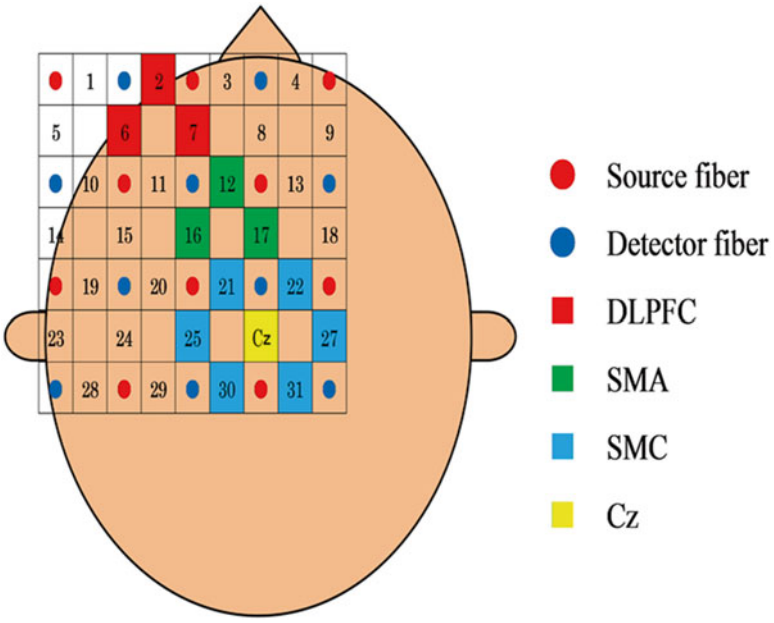

Fig. 22.1 Schematic diagram of the location of the optodes. The channels covering the DLPFC are shaded *red*; those covering the SMA, *green*; and those covering the SMC, *light blue*

was measured during the task and at rest, using near-infrared spectroscopy. In this study, we focused on the DLPFC, SMA, and SMC [5]. The distance between each optode was 30 mm, and the measurement was conducted at all 31 channels using 10 light-emitting and 10 light-receiving optodes (Fig. 22.1). This study was conducted with approval of the ethics committee of Niigata University of Health and Welfare.

3 Analysis

The occurrence of LRC was judged based on the phase difference between the cycles of pedaling and exhalation initiation timing. We decided the occurrence of LRC when the phase difference between the consecutive cycles was within ±0.1 s, four times or more consecutively. The LRC frequency was calculated using the following formula [6]:

The frequency of LRC = (the number of synchronous respiratory cycles)/(the total number of respiratory cycles)

The variations of O_2Hb from the reference value, which was the mean O_2Hb value during the 3-min rest prior to exercise, were calculated for each minute to obtain the peak value during the steady loading motion. The frequencies of LRC and peak values of O_2Hb variations during the steady loading motion were compared between the exercise conditions using an applicable *t*-test. The level of significance was set at $p < 0.05$.

4 Results

The frequency of LRC was significantly higher in the LRC-inducing condition (53.7 % ± 11.6 %) than in the LRC-non-inducing condition (21.8 % ± 17.6 %; $p < 0.001$). The time course of the O_2Hb levels in each condition is shown in Fig. 22.2. In the DLPFC, the peak values of the O_2Hb variations during the steady loading motion in the LRC-non-inducing and LRC-inducing conditions were 0.038 ± 0.008 and 0.015 ± 0.006 mM · cm, respectively. In the SMA, these values were 0.0368 ± 0.005 and 0.019 ± 0.001 mM · cm, respectively, showing significantly lower values in the LRC-inducing condition ($p < 0.05$). In the SMC, these values were 0.043 ± 0.007 and 0.040 ± 0.007 mM · cm, respectively, showing no significant difference.

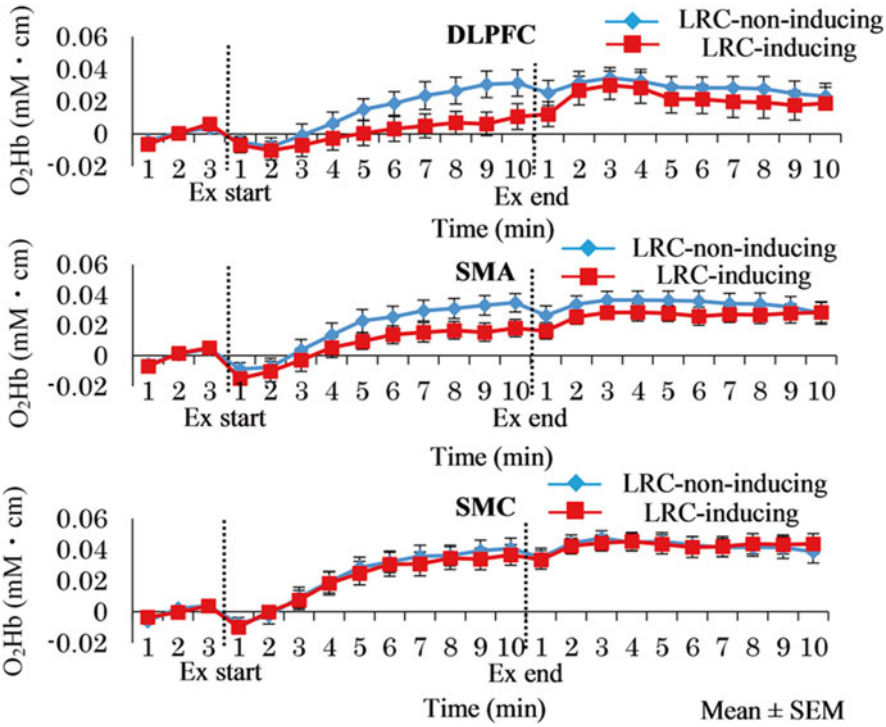

Fig. 22.2 Temporal changes in the oxygenated hemoglobin (O_2Hb) levels in the dorsolateral prefrontal cortex (DLPFC), supplementary motor area (SMA), and sensory motor area (SMC). The *dotted lines* represent the exercise start (Ex start) and exercise end (Ex end), respectively. *$p < 0.05$

5 Discussion

This study revealed that even light load can induce LRC and that the O_2Hb levels in the DLPFC and SMA were significantly decreased by LRC induction. LRC is known to occur because of various factors, including the interplay between the mechanical and nervous systems. In particular, LRC during bicycle ergometer exercise was reported to be caused by the interplay between the input of proprioceptive sensations from the peripheral locomotor nerves and the nerve center of the respiratory rhythm [7]. In addition to the previous findings, our study suggests that clarifying the change in brain activity depending on the occurrence of LRC induction is useful for developing an exercise therapy that takes into consideration brain activity.

In this study, the frequency of LRC was 53.7 % ± 11.6 % in the LRC-inducing condition and 21.8 % ± 17.6 % in the LRC-non-inducing condition, showing a significantly higher frequency in the LRC-inducing condition. LRC is highly inducible by visual and acoustic stimulations [8]. Therefore, we induced LRC using an LRC induction system, in which visual and auditory stimulations for inhalation and exhalation were provided, synchronizing with the participant's pedaling. The spontaneous occurrence rate of LRC with light load was reported to be approximately 20 % [9], and we observed a similar tendency.

The O_2Hb peak values in the DLPFC and SMC during the steady loading motion were significantly lower in the LRC-inducing condition. Decreased O_2Hb levels were reported in the DLPFC during the task of synchronizing motion with a rhythmical stimulation [10]. Brain activity in the SMA decreases during steady rhythmical motion [11]. The pedaling rate of 50 rpm was more easily maintained by induction stimulation under the LRC-inducing condition than that under the LRC-non-inducing condition [8]. Owing to the lack of rhythmical stimulation, the LRC-non-inducing condition may require greater voluntary motion control than the LRC-inducing condition. Taken together, the significantly lower O_2Hb levels in the DLPFC and SMA in the LRC-inducing condition may be due to the synchronization with a steady rhythmical stimulation. By contrast, in the SMC, no significant changes were observed in the O_2Hb levels in the LRC-inducing or LRC-non-inducing condition in this study. This may be because the cerebral blood flow in the SMC presumably reflects the motion output and the load intensity was the same (30 % VO_2peak) in both conditions.

The limitation of this study is that only light load was used. Further analysis of the effects of LRC induction on the cerebral blood at mild and heavy loads will allow the expansion of the LRC application as a means of exercise therapy.

6 Conclusion

This study clarified the effects of intentional LRC induction on O_2Hb levels during bicycle ergometer exercise at light load. The LRC frequency was significantly higher in the LRC-inducing condition. The peak values of O_2Hb variations during the steady loading exercise were significantly lower in the DLPFC and SMA in the LRC-inducing condition.

References

1. Garlando F, Kohl J et al (1985) Effect of coupling the breathing and cycling rhythms on oxygen uptake during bicycle ergometry. Eur J Appl Physiol Occup Physiol 54(5):497–501
2. Takano N, Inaishi S et al (1997) Individual differences in breathlessness during exercise, as related to ventilatory chemosensitivities in humans. J Physiol 499(Pt 3):843–848
3. Tamaki A, Hasegawa S et al (2005) Study of locomotor respiratory coupling during pedaling. Acta Med Hyogo 30(2):161–166
4. Iwamoto E, Taito S et al (2010) The neural influence on the occurrence of locomotor-respiratory coordination. Respir Physiol Neurobiol 173(1):23–28
5. Suzuki M, Miyai I et al (2004) Prefrontal and premotor cortices are involved in adapting walking and running speed on the treadmill: an optical imaging study. Neuroimage 23(3):1020–1026
6. Hill AR, Adams JM et al (1985) Short-term entrainment of ventilation to the walking cycle in humans. J Appl Physiol 65(2):570–578
7. Viala D, Freton E (1983) Evidence for respiratory and locomotor pattern generators in the rabbit cervico-thoracic cord and for their interactions. Exp Brain Res 49(2):247–256
8. Hoffmann CP, Torregrosa G et al (2013) Sound stabilizes locomotor-respiratory coupling and reduces energy cost. PLoS One 7(9):e45206
9. Bernasconi P, Bürki P et al (1995) Running training and co-ordination between breathing and running rhythms during aerobic and anaerobic conditions in humans. Eur J Appl Physiol Occup Physiol 70(5):387–393
10. Thaut MH, Stephan KM et al (2009) Distinct cortico-cerebellar activations in rhythmic auditory motor synchronization. Cortex 45(1):44–53
11. Thickbroom GW, Byrnes ML et al (2000) The role of the supplementary motor area in externally timed movement: the influence of predictability of movement timing. Brain Res 874(2):233–241

Chapter 23
Hypoxia and Neonatal Haemorrhagic Stroke: Experimental Study of Mechanisms

Oxana Semyachkina-Glushkovskaya, Ekaterina Borisova, Anton Namikin, Ivan Fedosov, Arkady Abdurashitov, Ekaterina Zhinchenko, Artem Gekalyuk, Maria Ulanova, Victoria Rezunbaeva, Latchezar Avramov, Dan Zhu, Qingming Luo, and Valery Tuchin

Abstract We studied the level of blood oxygen saturation (SpO_2) in the brain in newborn rats in the pre- and post-stroke periods, as well as the changes in cerebral blood flow and beta-arrestin-1 as a marker of hypoxic stress. Our results show that mild hypoxia precedes the stroke development and is associated with venous relaxation and decrease blood outflow from the brain resulting in the elevation of synthesis of beta-arrestin-1 in the brain. The incidence of stroke is characterized by severe hypoxia, which is accompanied by the progression of pathological changes in cerebral veins and the high level of beta-arrestin-1.

O. Semyachkina-Glushkovskaya (✉)
Saratov State University, Astrakhanskaya Str. 83, Saratov 410012, Russia

Britton Chance Center for Biomedical Photonics, Huazhong University of Science and Technology, Wuhan 430074, China
e-mail: glushkovskaya@mail.ru

E. Borisova • L. Avramov
Institute of Electronics, Bulgarian Academy of Sciences, Tsarigradsko Chaussee 72, Sofia 1784, Bulgaria

A. Namikin • I. Fedosov • A. Abdurashitov • E. Zhinchenko • A. Gekalyuk • M. Ulanova • V. Rezunbaeva
Saratov State University, Astrakhanskaya Str. 83, Saratov 410012, Russia

D. Zhu
Britton Chance Center for Biomedical Photonics, Huazhong University of Science and Technology, Wuhan 430074, China

Q. Luo
Britton Chance Center for Biomedical Photonics, Wuhan National Laboratory for Optoelectronics, Huazhong University of Science and Technology, Wuhan 430074, China

V. Tuchin
Saratov State University, Astrakhanskaya Str. 83, Saratov 410012, Russia

Britton Chance Center for Biomedical Photonics, Huazhong University of Science and Technology, Wuhan 430074, China

Laboratory of Biophotonics, Tomsk State University, Tomsk 634050, Russia

© Springer International Publishing Switzerland 2016

Q. Luo et al. (eds.), *Oxygen Transport to Tissue XXXVIII*, Advances in Experimental Medicine and Biology 923, DOI 10.1007/978-3-319-38810-6_23

Keywords Hypoxia • Neonatal haemorrhagic stroke • Cerebral blood flow • Beta-arrestin-1

1 Introduction

Hemorrhagic stroke in human neonates, defined as a cerebrovascular event occurring during 28 days after birth, is among the top ten causes of death (mortality rate is up to 25 %) and cognitive disability (about 45–85 %) in newborns [1]. Pathogenesis of neonatal hemorrhagic stroke (NHS) is multifactorial but there is strong evidence that cerebral hypoxia is one of the most frequent causes of mortality and morbidity in babies with NHS [2]. Indeed, most cases of NHS occur in the context of hypoxia. For example, in a prospective cohort study of 250 neonates, 35 % of neonatal stroke was associated with severe hypoxia [3]. Despite being relatively small for the body's mass, the brain receives 15 % of total cardiac output and 20 % of the body's oxygen supply. As such, the brain is extraordinary vulnerable to changes to oxygen content. So, hypoxia in the perinatal period is an important cause of cerebral palsy and associated disabilities in children [4].

Hypoxia is one of main reasons for pathological changes in the cerebral blood flow (CBF) and production of beta-arrestin-1, which is marker of vascular stress-reactivity [5–7]. However, the correlation between time-dependent changes in cerebral oxygenation and the CBF during the stroke development is still unknown.

Although investigators have implicated hypoxia as a potential risk factor for NHS, the role of hypoxia in NHS remains controversial because brain bleeding itself may cause respiratory distress. Therefore, it is difficult to ascertain if cerebral hypoxia is a key factor in NHS, or if it is a consequence of intracerebral hemorrhage [8].

Since the reduction of level of SpO_2 in the brain can be a reason for NHS [1–3, 8], we assume that the values of SpO_2 might be a marker of pre-stroke period.

For better understanding of the role of hypoxia in NHS and changes in vascular stress-reactivity, we studied the level of blood oxygen saturation (SpO_2) in the brain in newborn rats with a model of stress-induced hemorrhagic stroke in the pre- and post-stroke periods, as well as the changes in CBF and beta-arrestin-1.

2 Methods

Experiments were carried out in newborn mongrel rats, 3 days old using three groups: (1) stressed rats in the pre-stroke groups: i.e. at 0 h (immediately), 1, 2, 3, 4, 5, 6, 7 and 8 h after stress-termination (n = 10 in each groups); (2) stressed rats 24 h after stress termination (post-stroke group, rats with intracranial hemorrhage, n = 10); (3) intact, unstressed newborn rats (control group, n = 10).

Note, that the rat is a good animal subject for the study of development of cerebrovascular catastrophes during the first days of life due to similar dynamics of the brain maturation with human [9].

To induce hemorrhagic stroke, the following protocol of sound stress's impact was used (120 dB, 17 Hz): 10 s of sound followed by a 60-s pause; this cycle was repeated throughout a 2 h period [10, 11].

To analyze the CBF we used a commercial swept-source Doppler optical computed tomography (DOCT) system OCS1300SS (Thorlabs Inc., USA).

The level of blood oxygen saturation (SpO_2) in the brain was monitored using a cerebrovascular catastrophes during the first days of life due to similar dynamics of the brain matpulse oximeter (model CMS60D; Contec Medical Systems Co., Ltd., Qinhuangdao, China).

Beta-arrestin level was measured in the brain and blood serum in newborn rats by enzyme immunoassay (Beta-arrestin-1 (ARRB1) ELISA) according to a standardprotocol[http://www.uscnk.com/manual/ELISA-Kit-for-Arrestin-Beta-1-ARRb1-SEB993Mu.pdf].

The results are reported as mean ± standard error of the mean (SEM). Differences from the initial level in the same group were evaluated by the Wilcoxon test. Intergroup differences were evaluated using the Mann-Whitney test and ANOVA-2 (post-hoc analysis with Duncan's rank test). The significance level was set at $p<0.05$ for all analyses.

3 Results and Discussion

3.1 Changes in Blood Oxygen Saturation of the Brain Tissues in the Pre- and Post-stroke Period

Figure 23.1 shows that the pre-stroke period was characterized by a gradual reduction of the SpO_2 level. Indeed, the decrease in SpO_2 was observed immediately (0 h, by 13 %, $p<0.05$) after stress termination with maximal reduction of oxygen delivery at 7 and 8 h of the pre-stroke time (by 26 %, $p<0.05$ and 24 %, $p<0.05$, respectively). In the post-stroke period, the SpO_2 level was decreased by 23 % ($p<0.05$), i.e. it remained low.

Thus, our results demonstrate that the stroke-related changes in the brain are characterized by development of a time-dependent reduction of oxygen supply from moderate to severe cerebral hypoxia. The results of this series of experiments clearly show that cerebral hypoxia precedes NHS. Our conclusion is consistent with other experimental and clinical data. Thoresen et al. in experiments on newborn pigs showed that severe hypoxia itself can induce spontaneous brain hemorrhage in newborn pigs [12]. Alderliesten et al. in clinical observations show a lower cerebral fraction tissue oxygen extraction in newborns before severe stroke [13]. Taking into account these facts we suppose that hypoxia in the pre-stroke period might be a causative factor provoking critical changes in the brain, associated with cerebral hemorrhage in newborn rats.

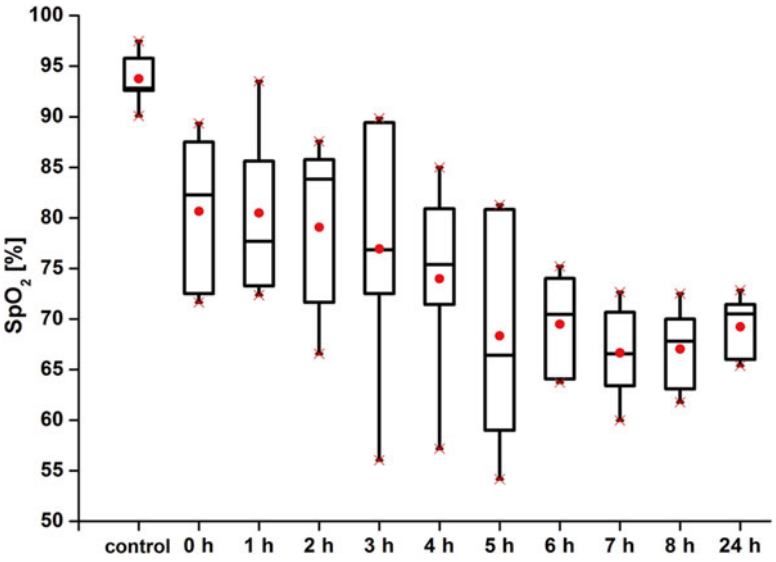

Fig. 23.1 Time-dependent changes in blood oxygen saturation in the neonatal brain in the pre- and post-stroke periods

3.2 Changes in Cerebral Venous Blood Flow in the Pre- and Post-stroke Period

Figure 23.2 shows the time-dependent changes in the diameter of the sagittal sinus and the blood flow velocity in the pre- and post-stroke episodes. During the pre-stroke period, we observed a gradual increase in the size of the sagittal sinus and a decrease in blood flow velocity. The maximal changes of these hemodynamic parameters were observed in the post-stroke stage. Thus, the diameter of the sagittal sinus was increased maximally 3.7 times in the post-stroke period, compared with control group (1.11 ± 0.02 vs. 0.30 ± 0.03 mm, $p < 0.05$). The blood flow velocity in the dilated sagittal sinus was decreased maximally by 65 % ($p < 0.05$) in the post-stroke group versus normal animals (2.09 ± 0.03 vs. 6.00 ± 0.09 mm/s, $p < 0.05$).

3.3 Changes in the Level of Beta-Arrestin-1 in the Bran in the Pre- and Post-stroke Period

In a third series of experiments, we analyzed the time-dependent changes in the production of beta-arrestin-1 in the brain, as an important factor of vascular reactivity to hypoxic stress [7]. Figure 23.3 shows that the pre-stroke period was accompanied by increase in the level of beta-arrestin-1 in the brain tissues. The similar intensity of beta-arrestin production we observed in newborn rats with brain hemorrhages.

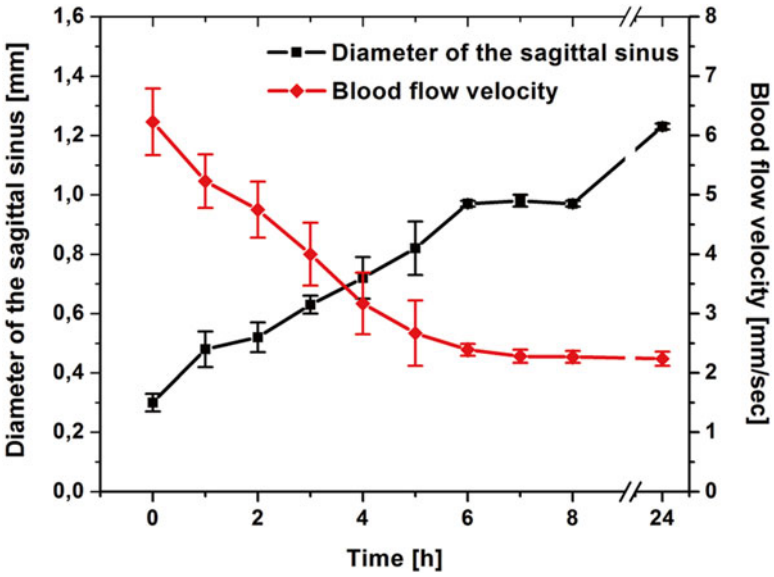

Fig. 23.2 Time-dependent changes in the sagittal sinus (diameter, mm and blood flow velocity, mm/s) in the pre- and post-stroke periods

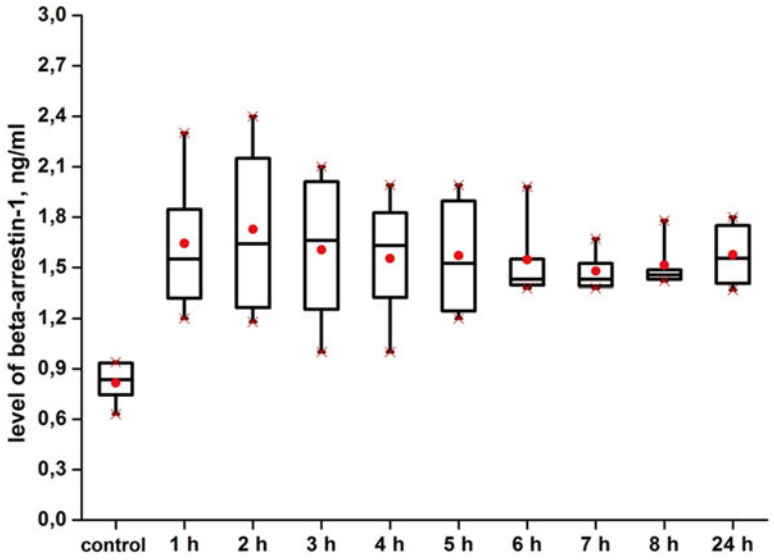

Fig. 23.3 Time-dependent changes in beta-arrestin-1 in brain tissues in the pre- and post-stroke

Collectively, our results suggest that stroke-related changes in the brain of newborn rats are associated with increase in diameter of the sagittal sinus with reduction of blood flow velocity in this vessel and level of SpO_2 in the brain tissues. The relaxing effect of hypoxia on the brain vasculature is described also in other studies [6].

A normal physiological response to reduction of oxygen delivery is relaxation of cerebral vessels that activates metabolism in the brain tissues via the increasing of CBF. The particularities of cerebral veins are no muscles and valves in their thin walls, therefore, they have low resistance to critical stretching occurring during blood accumulation in them. The immature brain vessels of newborns have limitation in vasorelaxation capabilities (increase of vessel size). The hypoxia-induced vasorelaxation of cerebral veins causes increasing of cerebral venous pressure [14]. This high pressure can induce easily the rupture of thin walls of immature cerebral veins of newborns [15].

Hypoxia causes the vascular stress due to critical relaxation of cerebral vessels via modulating of synthesis of beta-arrestin [7]. The beta-arrestin is marker of stress-reactivity of vessels and vascular homeostasis [16]. We found the increased synthesis of this vascular stress factor in the brain and blood of newborn rats in all stages of stroke development. Thus, the activation of higher expression of beta-arrestin reflects the increase in stress-response in the brain and peripheral circulatory system associated with the stroke-related changes in the cerebral tissues and vessels.

4 Conclusions

In general, our results suggest that the pre-stroke period is associated with progressive reduction of cerebral oxygenation that is accompanied by relaxation of cerebral veins with an increase in synthesis of the marker of hypoxic stress (beta-arrestin-1). The post-stroke period is characterized by severe hypoxia, which is associated with more pronounced changes in the venous system as well as with high production of beta-arrestin-1.

Acknowledgments Fedosov I, Namykin A., Abdurashitov A., Zinchenko E., Gekaluyk A., Ulanova M., Razunbaeva V., Tuchin V. in preparation of this original article, discussion of obtained results, all experimental works was supported by Grant of Russian Science Foundation no. 14-15-00128. The work of Borisova E., Avramov L. in the partly performing of pulse oximetry was supported by Grant DFNI-B02/9/2014 of Bulgarian National Science Fund.

The work of Zhu D., Luo Q. related to discussion was supported by National Nature Science Foundation of China under Grants 81171376 and 91232710, the Science Fund for Creative Research Group of China under Grant 61421064, and the Program of Introducing Talents of Discipline to Universities in China under Grant B07038**.**

References

1. van der Aa NE, Benders MJHL, Groenendaal F, de Vries LS (2014) Neonatal stroke: a review of the current evidence on epidemiology, pathogenesis, diagnostics and therapeutic options. Acta Paediatr 103:356–364
2. Luo L, Chen D, Qu Y et al (2014) Association between hypoxia and perinatal arterial ischemic stroke: a meta-analysis. PLoS One 9(2):e90106

3. Michoulas A, Basheer SN, Roland EH et al (2001) The role of hypoxia-ischemia in term newborns with arterial stroke. Pediatr Neurol 44(4):254–258
4. Fatemi A, Wilson MA, Johnston MV (2009) Hypoxic ischemic encephalopathy in the term infant. Clin Perinatol 36(4):835–vii
5. Bodin P, Burnstock G (1995) Synergistic effect of acute hypoxia on flow-induced release of ATP from cultured endothelial cells. Experientia 51:256–259
6. Tomiyama Y, Brian JE, Todd MM (1999) Cerebral blood flow during hemodilution and hypoxia in rats. The role of ATP-sensitive potassium channels. Stroke 30(9):1942–1947
7. Lombardi MS, van den Tweel E, Kavelaars A et al (2004) Hypoxia/ischemia modulates G protein-coupled receptor kinase 2 and β-arrestin-1 levels in the neonatal rat brain. Stroke 35:981–986
8. Jhawar BS, Ranger A, Steven D et al (2003) Risk factors for intracranial hemorrhage among full-term infants: a case-control study. Neurosurgery 52:581–590
9. Coyle JT (1977) Biochemical aspects of neurotransmission in the developing brain. Int Rev Neurobiol 20:65–103
10. Pavlov AN, Semyachkina-Glushkovskaya OV, Zhang Y et al (2014) Multiresolution analysis of pathological changes in cerebral venous dynamics in newborn mice with intracranial hemorrhage: adrenorelated vasorelaxation. Physiol Meas 35:1983–1999
11. Semyachkina-Glushkovskaya O, Lychagov V, Bibikova O et al (2013) The experimental study of stress-related pathological changes in cerebral venous blood flow in newborn rats assessed by DOCT. JIOHS 3(3):1350023 (10 pages).
12. Thoresen M, Satas S, Løberg EM et al (2001) Twenty-four hours of mild hypothermia in unsedated newborn pigs starting after a severe global hypoxic-ischemic insult is not neuroprotective. Pediatr Res 50(3):405–411
13. Alderliesten T, Lemmers PM, Smarius JJ et al (2013) Cerebral oxygenation, extraction, and autoregulation in very preterm infants who develop peri-intraventricular hemorrhage. J Pediatr 162(4):698–704
14. Volpe JJ (1995) Intracranial hemorrhage: germinal matrix-intraventricular hemorrhage of the premature infant. In: Neurology of the newborn. Philadelphia: W.B. Saunders, pp 403–62.
15. Hambleton G, Wigglesworth JS (1976) Origin of intraventricular haemorrhage in the preterm infant. Arch Dis Child 51(9):651–659
16. Hara MR, Kovacs JJ, Whalen EK et al (2011) A stress response pathway regulates DNA damage through β2-adrenoreceptors and β-arrestin-1. Nature 477(7364):349–353

Chapter 24
Interrelationship Between Broadband NIRS Measurements of Cerebral Cytochrome C Oxidase and Systemic Changes Indicates Injury Severity in Neonatal Encephalopathy

Gemma Bale, Subhabrata Mitra, Isabel de Roever, Marcus Chan, Alexander Caicedo-Dorado, Judith Meek, Nicola Robertson, and Ilias Tachtsidis

Abstract Perinatal hypoxic ischaemic encephalopathy (HIE) is associated with severe neurodevelopmental problems and mortality. There is a clinical need for techniques to provide cotside assessment of the injury extent. This study aims to use non-invasive cerebral broadband near-infrared spectroscopy (NIRS) in combination with systemic physiology to assess the severity of HIE injury. Broadband NIRS is used to measure the changes in haemodynamics, oxygenation and the oxidation state of cytochrome c oxidase (oxCCO). We used canonical correlation analysis (CCA), a multivariate statistical technique, to measure the relationship between cerebral broadband NIRS measurements and systemic physiology. A strong relationship between the metabolic marker, oxCCO, and systemic changes indicated severe brain injury; if more than 60 % of the oxCCO signal could be explained by the systemic variations, then the neurodevelopmental outcome was poor. This boundary has high sensitivity and specificity (100 and 83 %, respectively). Broadband NIRS measured concentration changes of the oxidation state of cytochrome c oxidase has the potential to become a useful cotside tool for assessment of injury severity following hypoxic ischaemic brain injury.

Keywords Near-infrared spectroscopy • Cytochrome c oxidase • Hypoxic ischaemic encephalopathy • Neonatal • Oxygen metabolism

---

The original version of this chapter was revised. An erratum to this chapter can be found at DOI 10.1007/978-3-319-38810-6_59

G. Bale (✉) • I. de Roever • M. Chan • I. Tachtsidis
Biomedical Optics Research Laboratory, University College London, London, UK
e-mail: gemma.bale.11@ucl.ac.uk

S. Mitra • J. Meek • N. Robertson
Institute for Women's Health, University College London, London, UK

A. Caicedo-Dorado
Department of Electrical Engineering ESTA, Katholieke Universiteit Leuven, Leuven, Belgium

© The Author(s) 2016

Q. Luo et al. (eds.), *Oxygen Transport to Tissue XXXVIII*, Advances in Experimental Medicine and Biology 923, DOI 10.1007/978-3-319-38810-6_24

1 Introduction

Hypoxic ischaemic encephalopathy (HIE) resulting from hypoxic ischemic (HI) brain injury affects 1–2 live births per 1000 and is associated with severe neurodevelopmental problems and mortality [1]. Diminished supply of oxygen (hypoxia) and blood (ischaemia) to the newborn brain in the perinatal period causes neuronal injury. HIE is an evolving process; after the initial period of energy failure during the injury, the cerebral metabolism recovers to normal for the first few hours of life but then can deteriorate, leading to a secondary energy failure (SEF) [2]. Strategies to treat HIE focus on preventing the cascade of events leading to SEF and, currently, therapeutic hypothermia (TH) has been the only successful treatment that is in routine clinical use [3]. The current gold standard assessment of the injury is the magnetic resonance spectroscopy (MRS) measured lactate to N acetyl aspartate ratio (Lac/NAA) which is the most sensitive predictor of outcome in the first 30 days of life [4]. However the magnetic resonance (MR) scan is generally performed at the end of the first week of life and a real-time, cotside measurement of cerebral metabolism that can assess the progression of cerebral injury would be helpful in the immediate stages following HI brain injury.

Our group has previously presented a broadband NIRS device called CYRIL (CYtochrome Research Instrument and appLication) to monitor cerebral hemodynamics and metabolism in the newborn brain [5]. CYRIL measures the changes in concentration of oxygenated- and deoxygenated-haemoglobin ($\Delta[HbO_2]$ and Δ[HHb], respectively) and the oxidation state of cytochrome c oxidase (Δ[oxCCO]). Cytochrome c oxidase (CCO) is the terminal electron acceptor in the electron transport chain in mitochondria. It is responsible for more than 95 % of oxygen metabolism in the body as it is essential for the efficient generation of ATP [2]. The enzyme contains four redox centers, one of which—copper A (CuA)—has a broad absorption peak in the near-infrared (NIR) spectrum which changes depending on its redox state. As the total concentration of CCO is assumed constant, the changes in the NIRS-measured oxCCO concentration are indicative of the CCO redox state and, therefore, provide a representation of oxygen utilization in the tissue. Detection of CCO using NIRS is more difficult than other chromophores as its in-vivo concentration is less than 10 % of that of haemoglobin and has a broad spectral signature. We use broadband (multi-wavelength) NIRS and the UCLn algorithm to accurately resolve spectral changes due to oxCCO without cross-talk from haemoglobin chromophores [6].

We hypothesize that the dynamic changes in the cerebral metabolism, as monitored by broadband NIRS measured Δ[oxCCO], in response to systemic changes will indicate brain injury severity. To test this, we use canonical correlation analysis (CCA), a multivariate statistical technique that measures the relationship between two groups of variables [7]. CCA can be seen as an extension to normal correlation analysis where the relation between two multidimensional datasets (or group of signals) is analysed instead of two individual signals. In this way CCA can estimate the strength of the relationship between systemic changes and cerebral metabolism.

2 Methods

Ethical approval for the Baby Brain Study at University College London Hospitals Trust (UCLH), London was obtained from the North West Research Ethics Centre (REC reference: 13/LO/0106). Term infants born at or transferred to UCLH for treatment of acute brain injury were eligible for investigation; only babies without congenital malformations were considered. Each subject was monitored continuously with EEG and treated with TH which was initiated within 6 h of birth; body temperature was lowered to 33.5 °C for 72 h.

Broadband NIRS measurements were collected continuously over a period of 3 h on the third day of life during TH. We used a custom-built two-channel broadband NIRS system called CYRIL that has been described previously [5]. All measurements were taken bilaterally on the forehead over the frontal lobe at a sampling frequency of 1 Hz. The changes in chromophore concentrations (oxCCO, HbO_2 and HHb) were calculated from the measured changes in broadband near-infrared light attenuation using the modified Beer-Lambert law as applied with the UCLn algorithm across 136 wavelengths (770–906 nm) with a fixed differential pathlength factor of 4.99 and 2.5 cm optode separation.

Systemic data from the Intellivue Monitors (Philips Healthcare, UK) were collected using an application called ixTrend (ixellence GmbH, Germany). Signals recorded include oxygen saturation (SpO_2) measured by pulse oximetry on the foot or hand, heart rate (HR) by electrocardiograph (ECG), respiratory rate (RR), mean arterial blood pressure (MABP) from an intra-arterial catheter, and transcutaneous carbon dioxide ($PaCO_2$) and oxygen (PaO_2) tension.

The babies spent 1 h in the MR scanner after rewarming, this occurred on average on day 7 of life (range: day 5–15). MR scans included a measurement of thalamic Lac/NAA with proton (^1H) MRS; Lac/NAA score ≥ 0.3 has been shown to be associated with worse neurodevelopmental outcome.

Data analysis was carried out in MATLAB (Mathworks, USA) and Excel (Microsoft, USA). Systemic data were down-sampled and interpolated to the NIRS data timeframe (1 Hz). Both NIRS and systemic data were processed with an automatic wavelet de-noising function which reduces the high frequency noise but maintains the trend information. Artefacts in the NIRS signals from movement or changes in ambient lighting were removed using the method suggested by Scholkmann et al. [8] which is based on moving standard deviation and spline interpolation. This method also corrects shifts in the baseline due to artefact.

For the CCA analysis, the signals were grouped into ‘cerebral’ (HbO_2, HHb and oxCCO) and ‘systemic’ sets (MABP, SpO_2, HR, RR, $PaCO_2$ and PaO_2). The first step of CCA is to form linear combinations of the variables in each data set. Then the correlation between each group of variables is used to assess the dependency of the cerebral signals on the systemic signals. This gives a score that ranges from 0 to 1, where 0 indicates no dependency and 1 indicates total dependency. CCA results

were compared with the severity of the injury which was assessed by MRS measured Lac/NAA on days 5–15 of life; the subjects were grouped into severe brain injury (Lac/NAA $\geq$ 0.3) and mild brain injury (Lac/NAA < 0.3). The median of the CCA scores for the dependency of each chromophore on the systemic changes, also known as cross-loading coefficients, were found for each injury group as the data were not normally distributed. A Kruskal–Wallis test was used to assess the significance of the difference between the groups; the level of statistical significance was set at $p < 0.05$. The sensitivity and specificity of the CCA scores for injury classification are evaluated.

3 Results

Data were recorded from 11 subjects (6 female) with HIE: severe injury n = 6, mild injury n = 5. One of the severely injured neonates died a few months after birth. All infants were born at term gestation (mean 39 ± 1 weeks), and were of normal birth weight (mean 3.1 ± 0.6 kg). The CCA analysis showed that each of the cerebral signals could (in part) be explained by the systemic physiological variations; the HbO_2 signal had a mean CCA score of 0.55 ± 0.20 which means that 55 % of the HbO_2 signal could be explained by systemic variations, the HHb and oxCCO mean CCA scores were 0.59 ± 0.23 and 0.58 ± 0.18, respectively. The CCA scores for each cerebral variable were grouped into mild and severe injury categories and are shown in Fig. 24.1. There is no significant difference between the mild and severely injured groups in the dependency of either HbO_2 or HHb on the systemic signals ($p = 0.36$ and 0.72, respectively). However, the infants with severe injury showed a significantly

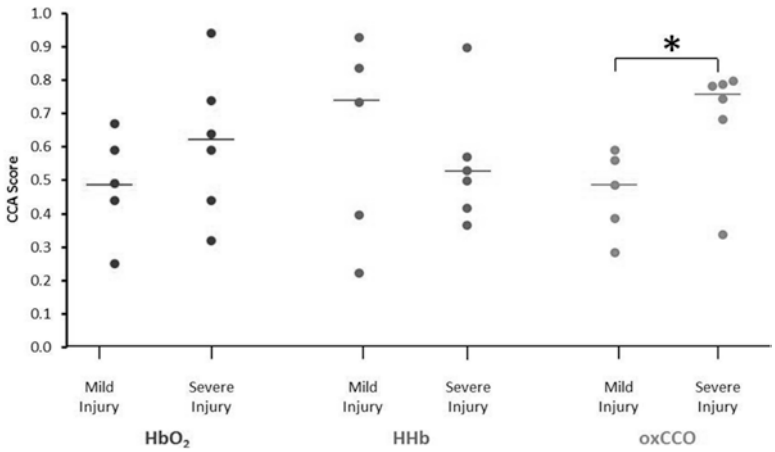

Fig. 24.1 CCA scores for mild (n = 5) and severe (n = 6) groups for each chromophore. Median score for each group is displayed as a line. The Kruskal–Wallis test found a significant difference between the groups for oxCCO only: HbO_2 $p = 0.36$, HHb $p = 0.72$ and oxCCO $p = 0.04$

($p=0.04$) higher oxCCO dependency (median: 0.74) than those with mild injury (median: 0.49). The infants with severe injury were identified by an oxCCO CCA score ≥ 0.6 (sensitivity 100 %, specificity 83 %).

4 Discussion

CCA showed that broadband NIRS measured cerebral signals could be explained, in part, by changes in the systemic physiology which is expected because the systemic physiology should influence the cerebral haemodynamics and metabolism. Although the relationship between changes in the haemoglobin signals (HbO_2 and HHb) and systemic signals varied between the infants, their relationship was not indicative of injury as measured by Lac/NAA. The relationship between Δ[oxCCO] and systemic physiology was able to predict injury; a high oxCCO dependency on the systemic signals indicated a negative outcome. This means that although the cerebral vascular response to systemic events was not significantly different between the mild and severe injuries, the cerebral metabolic response was. This could be explained by lower cellular energetics in the more injured brain which would mean that CCO has less capacity to buffer changes in oxygenation from systemic variations. It is possible that the differences in the metabolic responses are due to changes in the brain leading to, or after, SEF in the severely injured brain.

We have previously found a strong linear correlation between changes in oxCCO and NIRS measured cerebral oxygenation during systemic desaturation events in infants with severe HIE [5]. This relationship supports the findings in this study; in the more injured brain CCO is more readily affected by changes in oxygen delivery and therefore would be more disturbed by systemic variations.

There are many limitations to this study to discuss. Firstly, this is a small sample size. Secondly, the Lac/NAA is measured in the thalamus whereas the NIRS measurements are over the frontal lobe, and the Lac/NAA is only a surrogate for patient outcome; a neurodevelopmental outcome will be a more robust indicator. Finally, the CCA technique assumes a linear and stationary relationship between all of the variables which may not be true in this complex system; in this study CCA examines the relationship over a long window of time (3 h) during which the relationship between the variables might change; in future, we could use temporal CCA to investigate the relationship between cerebral and systemic variables over time.

5 Conclusions

We identified severe HIE from mild HIE with an early cotside biomarker of metabolism. A strong relationship between oxCCO and systemic physiology, assessed with CCA, on day 3 of life indicated severe injury. The broadband NIRS measured oxCCO is more sensitive to brain injury than HbO_2 or HHb.

Acknowledgments The authors would like to thank the parents who gave consent for their children to participate in this study. This research was funded by The Wellcome Trust, grants 088429/Z/09/Z and 104580/Z/14/Z, and the UCL-Cambridge Centre for Doctoral Training in Photonic Systems Development, Engineering and Physical Sciences Research Council, grant EP/G037256/1. N.R., S.M. and J.M. acknowledge the support of the UCL/UCLH Biomedical Research Centre. A.C.-D. is a Postdoctoral Fellow of the Research Foundation Flanders (FWO).

References

1. Finer NN et al (1981) Hypoxic-ischemic encephalopathy in term neonates: perinatal factors and outcome. J Pediatr 98:112–117
2. Lorek A et al (1994) Delayed ('secondary') cerebral energy failure after acute hypoxia-ischemia in the newborn piglet: continuous 48-hour studies by phosphorus magnetic resonance spectroscopy. Pediatr Res 36(6):699–706
3. Shah PS et al (2007) Hypothermia to treat neonatal hypoxic ischemic encephalopathy: systematic review. Arch Pediatr Adolesc Med 161:951–958
4. Thayyil S et al (2010) Cerebral magnetic resonance biomarkers in neonatal encephalopathy: a meta-analysis. Pediatrics 125(2):382–395
5. Bale G et al (2014) A new broadband near-infrared spectroscopy system for in-vivo measurements of cerebral cytochrome-c-oxidase changes in neonatal brain injury. Biomed Opt Express 5(10):3450–3466
6. Matcher SJ et al (1995) Performance comparison of several published tissue near-infrared spectroscopy algorithms. Anal Biochem 227:54–68
7. Caicedo A et al (2013) Canonical correlation analysis in the study of cerebral and peripheral haemodynamics interrelations with systemic variables in neonates supported on ECMO. Adv Exp Med Biol 765:23–29
8. Scholkmann F et al (2010) How to detect and reduce movement artifacts in near-infrared imaging using moving standard deviation and spline interpolation. Physiol Meas 31(5):649–662

Open Access This chapter is licensed under the terms of the Creative Commons Attribution 4.0 International License (http://creativecommons.org/licenses/by/4.0/), which permits use, sharing, adaptation, distribution and reproduction in any medium or format, as long as you give appropriate credit to the original author(s) and the source, provide a link to the Creative Commons license and indicate if changes were made.
The images or other third party material in this chapter are included in the chapter's Creative Commons license, unless indicated otherwise in a credit line to the material. If material is not included in the chapter's Creative Commons license and your intended use is not permitted by statutory regulation or exceeds the permitted use, you will need to obtain permission directly from the copyright holder.

Chapter 25
PFC Activity Pattern During Verbal WM Task in Healthy Male and Female Subjects: A NIRS Study

Chenyang Gao, Lei Zhang, Dewu Luo, Dan Liu, and Hui Gong

Abstract Near-infrared spectroscopy (NIRS), as a non-invasive optical imaging method, has been widely used in psychology research. Working memory (WM) is an extensively researched psychological concept related to the temporary storage and processing of information. Many neuropsychological studies demonstrate that several brain areas of prefrontal cortex (PFC) are engaged during verbal WM tasks. The gender-based differences in WM remains under dispute. To better understand the active module and gender differences in PFC activity patterns during verbal WM tasks, we investigated the blood oxygenation changes of the PFC in 15 healthy subjects using a homemade multichannel continuous-wave NIRS instrument, while performing a verbal n-back task. We employed traditional activation and novel connectivity analyses simultaneously. Males had a higher level of oxygenation activity and connectivity in PFC than females. Only the results of females revealed a leftward lateralization in the 2-back task.

Keywords NIRS • Hemodynamic • Verbal working memory • Gender difference • Functional connectivity

1 Introduction

NIRS is a developing technology that monitors brain activity noninvasively by measuring cerebral hemodynamic responses [1]. NIRS can provide high temporal resolution and reasonable spatial resolution in comparison to other traditional neuroimaging methods [2] and can help reveal more about brain function related to human cognitive.

C. Gao • L. Zhang • D. Luo • D. Liu • H. Gong (✉)
Wuhan National Laboratory for Optoelectronics, Huazhong University of Science and Technology, Wuhan, People's Republic of China

Key Laboratory of Biomedical Photonics of Ministry of Education, Huazhong University of Science and Technology, Wuhan, People's Republic of China
e-mail: huigong@mail.hust.edu.cn

© Springer International Publishing Switzerland 2016

Q. Luo et al. (eds.), *Oxygen Transport to Tissue XXXVIII*, Advances in Experimental Medicine and Biology 923, DOI 10.1007/978-3-319-38810-6_25

Working memory (WM) is a core component of human cognition, being an essential part of the mnemonic processes, and fundamental for many cognitive activities [3]. The study of WM will help us learn more about human cognition. There are many studies on WM which mainly engaged the VLPFC and DLPFC. As a classical and effective working memory paradigm [4], we utilized the n-back task for our experiment.

Recently, increasing evidence has been provided that functional differences in brain activity may underlie gender differences in cognitive performance [5]. As is known, females surpass males in some areas of verbal ability, but gender differences in brain activation remain controversial [6, 7]. Our view is that gender differences are related to differences in the cerebral organization of verbal function and in the structure of the verbal-related cortex.

There is also dispute about gender-based hemispheric lateralization during verbal WM tasks [8, 9]. Some studies report that there is no significant gender difference in lateralization in verbal-related tasks, whereas others state that females are more leftward lateral than males [10]. Knowing whether males or females tend to overly activate one side of their brain in response to a task could help better define how to acquire and interpret signals from a system user, depending on the gender.

We analyzed brain activation in a traditional way and brain connectivity using wavelet transform coherence (WTC). NIRS-based connectivity is a novel analysis tool for NIRS data from the perspective of functional integration [11] which could be complementary to NIRS activation analysis. There were different types of connectivity used in NIRS study previously [12], and we assessed functional connectivity during task. It was expected that gender-related differences would be observed in both brain activation and connectivity.

2 Methods

Fifteen right-handed, paid volunteers (7 females, aged 20–26 years, mean 22.9 years), recruited from the university, participated in this study. All participants were in good health, right-handed, with normal or corrected-to-normal vision. Informed consent was collected from each subject before the experiment and all had a short practice before the formal experiment to ensure that they could perform it. The study was approved by the Human Subjects Institutional Review Board of Huazhong University of Science and Technology.

A block design verbal n-back task was employed in this study (Fig. 25.1a). In the task, subjects were presented with a sequence of 30 letters. Each letter was presented for 500 ms and there was a 2.5-s interval during which the screen was blank. As each letter was presented, subjects were to decide whether it matched with the letter that had been presented n items back in the sequence. Subjects gave their responses by pressing a keyboard to indicate a match or mismatch. The experiment included 2-back and 0-back tasks. The 0-back task was set to compare with the 2-back task. There were six blocks in the experiment, each block lasted 90 s,

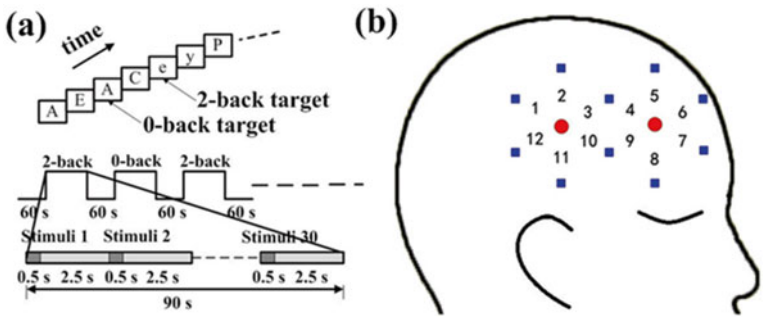

Fig. 25.1 **(a)** Examples of a sequence of letters (*top*) and experimental design (*bottom*). (**b**) Position of the two NIRS probes on the head. The probe distribution on the other side of the brain is the same as shown in this figure. *Red circles* represents light source and *blue squares* indicate detector

including 30 trails. The 2-back task and 0-back tasks were shown alternately. In each task block, ten letters were set as yes cases. The rest period lasted 60 s between the blocks.

The NIRS data were recorded using a homemade continuous-wave NIRS instrument. The probe was supported by a piece of thermoplastic and held 4 sources (850 and 785 nm) and 20 detectors, forming 24 NIRS channels that covered the PFC (Fig. 25.1b). The distance between the detector and the source of the same probe was 3 cm, and the acquisition rate was 100 Hz.

3 Data Analysis

The raw NIRS data were filtered at <3 Hz to remove instrument noise, downsampled to ten samples per second, and converted to change in optical density (ΔOD).

Accuracy rate and response time of each subject were recorded by a computer. The ΔOD data were bandpass filtered between 0.015 and 0.5 Hz to eliminate slow signal drift and arterial pulsation. The modified Beer-Lambert law (MBLL) method was used to convert the ΔOD data into hemoglobin signals, with a 6.0 differential pathlength factor (DPF) value of 785 nm, and a 5.2 DPF value of 850 nm [13]. Finally, the hemoglobin signals were block averaged. The mean value of concentration change in oxy-Hb for the 60 in each task was calculated, and then the value for the control task (0-back) was subtracted from those for test. The average task hemodynamic response across channels of the same hemisphere was obtained to indicate brain activation for each hemisphere.

WTC measures the cross-correlation of two data series as a function of time and frequency, with the ability to detect locally phase-locked behavior, which might not be detectable using traditional time series analysis methods. The WTC MATLAB package was employed to evaluate functional connectivity of interhemispheric and intrahemispheric in PFC.

To analyze the difference between the beginning and end of the task, we divided the 90-s task time course into two parts of equal length (the first 45 s and later 45 s) and analyzed gender differences in activity and connectivity of the two parts separately.

4 Results

The accuracy of all subjects in the 2-back task was lower and the response time was longer than the 0-back task. There was no significant gender difference in behavior.

All the subjects' VLPFC, nine subjects' DLPFC and three subjects' rostral PFC were engaged during the 2-back task. HbO_2 activity of males was significantly higher ($p<0.05$) than that of females on both sides, especially in the right cortex (Fig. 25.2a). Only results of females showed evidence of leftward dominance. Results of Hb show the same gender difference, but with less significance. Before all the t-tests applied in this study, the data were tested as being normally distributed using the Lilliefors test.

Gender differences also exist in functional connectivity. The interhemispheric connectivity of HbO_2 and Hb in males during the 2-back task was significantly higher ($p<0.05$ in HbO_2 and $p<0.1$ in Hb) than in females, which implies that the PFC of males was engaged more balanced by the verbal WM task. In addition, bilateral intrahemispheric connectivity increased in males compared to females, which is consistent with the results of activity (Table 25.1).

Functional activation analysis and time courses (Fig. 25.2b) showed that gender differences in HbO_2 were present in the beginning part (Fig. 25.3a). Lateralization analysis indicated that female left dominance in HbO_2 only existed in the second part. Functional interhemispheric connectivity results showed significant gender differences ($p<0.05$) in both Hb and HbO_2 that were only present in the beginning (Fig. 25.3b), which is correlated with the high functional activity in males.

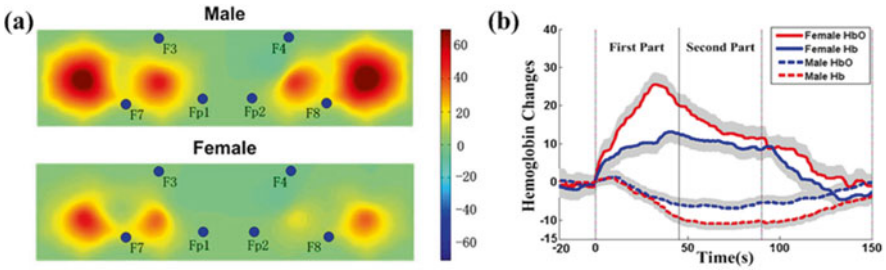

Fig. 25.2 (**a**) Pseudo-color maps made by all channels of average activity of HbO_2 during the 2-back task using interpolation. EEG electrode position is presented for each location. (**b**) Grand average all channels' time courses of HbO_2 and Hb in the 2-back task, artificially divided into two parts for analysis. The *gray area* indicates standard error (SE). The *gray vertical lines* at 0 and 90 s indicate the start and end of the task

Table 25.1 Activation and WTC value of 2-back and 0-back

	Male		Female	
	Left	Right	Left	Right
0-back activation	4.51	2.93	2.41	1.21
2-back activation	17.77	17.56	14.47	9.88
0-back WTC	0.516		0.472	
2-back WTC	0.674		0.542	

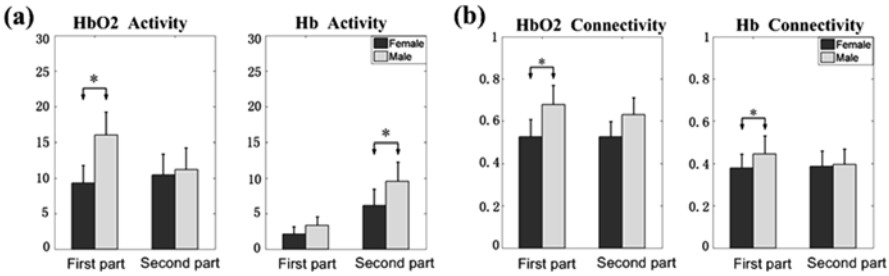

Fig. 25.3 (**a**) Results of brain activity during different task period. (**b**) Results of functional connectivity during different task period

5 Discussion

We have studied gender differences of brain functions in verbal WM tasks on the prefrontal cortical area, which controls working memory and executive brain function, with NIRS. We also propose our conclusion for the ongoing dispute regarding WM.

The significant differences found in behavioral and brain activation between the 2-back and 0-back tasks, together with the activated cortex, are consistent with a previous study, implying that our experiment design is appropriate. The activated area indicated that the verbal WM task is related to both maintenance and manipulation of information, and maintenance surpasses manipulation during this task. Rostral PFC is thought to represent a more abstract higher level content [3], this may be why this area was hardly engaged.

Results of both functional activity and connectivity demonstrated that gender-specific hemodynamics exist in PFC during verbal WM tasks. The findings of the gender-specific brain activation, in line with the inverse intelligence-activation relationship [10] provides hemodynamic evidence for the neural efficiency hypothesis. Considering the results of behavior, we can conclude that females are good at the verbal WM task. Gender-based difference in intrahemispheric and interhemispheric functional connectivity are consist with brain activation. This may reveal the mechanisms of gender differences in the other side, that males need more brain functional

integration during verbal WM. Gender-based lateralization may be interpreted as environmental and cultural factors. Such lateralization preferences may increase the processing speed by avoiding longer pathways mainly via the corpus callosum, that would otherwise be needed to connect regions on opposite sides of the brain [9].

The brain activation of PFC changed during the different task periods. This indicates that, for studies that did not find a significant gender difference or found a difference only in HbO_2 [10], a separated task period analysis may help to understand gender-based difference more accurately and comprehensively. In the separate task period analysis, brain activation and functional connectivity of HbO_2 are more consistent compared to Hb. This may be interpreted that the HbO_2 signal had a better signal to noise ratio (SNR), and was a more sensitive indicator of changes in regional cerebral blood flow. The HbO_2 of males increased fast at the beginning of task, then decreased and then came closer to that of females in the later period. The reason for this may be that males need more time to get used to the verbal WM task than females; as soon as both males and females were used to this task, the gender-based difference reduced.

Although there were significant gender differences in PFC activity, we did not find any gender-based behavioral difference in this study, thereby supporting the viewpoint that differences in brain activation were not reflected in cognitive performance [5]. Some gender differences may not be apparent in behavior, so we should utilize brain functional imaging methods, such as NIRS, fMRI etc., to study gender differences during tasks. Due to fewer limitations on the subjects and the environment [14], NIRS may be a better choice.

6 Conclusion

Results of both brain activation and functional connectivity revealed significant gender differences and provide evidence that females do a better job than males during verbal WM tasks. In addition, gender-based PFC mechanism changed during different task period.

Acknowledgments This study was supported by the Science Fund for Creative Research Group (Grant No. 61421064).

References

1. Medvedev AV (2014) Does the resting state connectivity have hemispheric asymmetry? A near-infrared spectroscopy study. NeuroImage 85(Pt 1):400–407
2. Strangman G, Boas DA, Sutton JP (2002) Non-invasive neuroimaging using near-infrared light. Biol Psychiatry 52:679–693
3. Nee DE, Brown JW, Askren MK et al (2013) A meta-analysis of executive components of working memory. Cereb Cortex 23:264–282

4. Owen AM, McMillan KM, Laird AR et al (2005) N-back working memory paradigm: a meta-analysis of normative functional neuroimaging studies. Hum Brain Mapp 25:46–59
5. Bell EC, Willson MC, Wilman AH et al (2006) Males and females differ in brain activation during cognitive tasks. NeuroImage 30:529–538
6. Goldstein JM, Jerram M, Poldrack R et al (2005) Sex differences in prefrontal cortical brain activity during fMRI of auditory verbal working memory. Neuropsychology 19:509–519
7. Jausovec N, Jausovec K (2009) Gender related differences in visual and auditory processing of verbal and figural tasks. Brain Res 1300:135–145
8. Phillips V, Kim E, Kim JG (2014) Gender-based brain lateralization using multichannel near infrared spectroscopy. Brain-Computer Interface (BCI), 2014 International Winter Workshop, pp 1–4
9. Peng G, Wang WS (2011) Hemisphere lateralization is influenced by bilingual status and composition of words. Neuropsychologia 49:1981–1986
10. Li T, Luo Q, Gong H (2010) Gender-specific hemodynamics in prefrontal cortex during a verbal working memory task by near-infrared spectroscopy. Behav Brain Res 209:148–153
11. Friston KJ (2011) Functional and effective connectivity: a review. Brain Connect 1:13–36
12. Wolf U, Toronov V, Choi JH et al (2011) Correlation of functional and resting state connectivity of cerebral oxy-, deoxy-, and total hemoglobin concentration changes measured by near-infrared spectrophotometry. J Biomed Opt 16:087013
13. Duncan A, Meek JH, Clemence M et al (1996) Measurement of cranial optical path length as a function of age using phase resolved near infrared spectroscopy. Pediatr Res 39:889–894
14. Villringer A, Chance B (1997) Non-invasive optical spectroscopy and imaging of human brain function. Trends Neurosci 20(10):435–442

Chapter 26
Spatial Distribution of Changes in Oxidised Cytochrome C Oxidase During Visual Stimulation Using Broadband Near Infrared Spectroscopy Imaging

P. Phan, D. Highton, S. Brigadoi, I. Tachtsidis, M. Smith, and C.E. Elwell

Abstract Functional hyperaemia, characterised as an increase in concentration of oxyhaemoglobin [HbO_2] and a decrease in concentration of deoxyhaemoglobin [HHb] in response to neuronal activity, can be precisely mapped using diffuse optical spectroscopy. However, such techniques do not directly measure changes in metabolic activity during neuronal activation. Changes in the redox state of cerebral oxidised cytochrome c oxidase Δ[oxCCO] measured by broadband spectroscopy may be a more specific marker of neuronal metabolic activity. This study aims to investigate the spatial distribution of Δ[oxCCO] responses during the activation of the visual cortex in the healthy adult human brain, and reconstruct images of these changes.

Multi-channel broadband NIRS measurements were collected from the left visual cortex of four healthy volunteers using an in-house broadband spectrometer during an inverting checkerboard visual stimulation paradigm. Δ[HbO_2], Δ[HHb] and Δ[oxCCO] were calculated by fitting the broadband spectra between 780 and 900 nm using the UCLn algorithm. Centre of gravity analysis was applied to the concentration data to determine the centres of activation for [HbO_2], [HHb] and [oxCCO].

All four subjects showed similar changes in [oxCCO] in the presence of a typical visual-evoked haemodynamic response in channels overlying the visual cortex.

The original version of this chapter was revised. An erratum to this chapter can be found at DOI 10.1007/978-3-319-38810-6_59

P. Phan (✉) • S. Brigadoi • I. Tachtsidis • C.E. Elwell
Department of Medical Physics and Biomedical Engineering, University College London, London, UK
e-mail: thanh.phan.11@ucl.ac.uk

D. Highton
Neurocritical Care, National Hospital for Neurology and Neurosurgery, London, UK

M. Smith
Department of Medical Physics and Biomedical Engineering, University College London, London, UK

Neurocritical Care, National Hospital for Neurology and Neurosurgery, London, UK

NIHR University College London Hospitals Biomedical Research Centre, London, UK

© The Author(s) 2016

Q. Luo et al. (eds.), *Oxygen Transport to Tissue XXXVIII*, Advances in Experimental Medicine and Biology 923, DOI 10.1007/978-3-319-38810-6_26

Image reconstruction of the optical data showed a clear and spatially localized activation for all three chromophores. Centre of gravity analysis showed different localisation of the changes in each of the three chromophores across the visual cortex with the x-y coordinates of the mean centres of gravity (across 4 subjects) of HbO_2, HHb and oxCCO at (63.1 mm; 24.8 mm), (56.2 mm; 21.0 mm) and (63.7 mm; 23.8 mm), respectively.

The spatial distribution of Δ[oxCCO] response appears distinct from the haemodynamic response in the human visual cortex. Image reconstruction of Δ[oxCCO] shows considerable promise as a technique to visualise regional variation in [oxCCO] in a range of scenarios.

Keywords Near infrared spectroscopy • Functional imaging • Cytochrome coxidase • Diffuse optical imaging • Visual cortex

1 Introduction

Near-infrared spectroscopy (NIRS) is a non-invasive optical technique that characterises cerebral haemodynamics and metabolism using the attenuation of near infrared light (700–1000 nm) to derive concentration changes in oxyhaemoglobin Δ[HbO_2], deoxyhaemoglobin Δ[HHb] and the oxidation status of cytochrome c oxidase Δ[oxCCO].

[HbO_2] and [HHb] are popular targets for functional brain investigation. Several studies using diffuse optical imaging have been able to produce detailed [HbO_2] and/or [HHb] maps of various functional regions [1, 2]. However, it is notable that changes in [HbO_2] and [HHb] provide information only on the haemodynamic responses to neuronal activity and do not inform directly on the changes in cellular metabolism associated with functional activation.

Cytochrome c oxidase is the terminal electron acceptor in the mitochondrial electron transport chain and directly responsible for more than 95 % of oxygen metabolism [3]. Δ[oxCCO] is therefore a direct and reliable marker of changes in cellular oxygen metabolism, but its measurement requires an optimised broadband spectroscopic technique [4]. There are no published data on the spatial distribution of cytochrome c oxidase or imaging of changes of cytochrome c oxidase redox state across the human cerebral cortex. As [oxCCO] is directly related to cellular oxygen metabolism, the ability to measure the spatial distribution of the signal and image these changes may facilitate opportunities to investigate regional cerebral metabolism across a wide range of scenarios.

This study aims to utilise visual stimulation to (1) assess the spatial distribution of [oxCCO] responses resulting from functional brain activation, and (2) evaluate the possibility of reconstructing images of these responses. A visual stimulation paradigm was chosen given its capability to produce a highly repeatable and well-characterised functional activation response that has been corroborated across multiple imaging modalities, including broadband spectroscopy and functional magnetic resonance imaging [1, 5].

2 Methods

A detailed description of the broadband system used in this study can be found elsewhere [6]. In summary, it utilises a 50 W halogen light source and two CCD cameras (Pixis 512, Princeton Instruments, Trenton, NJ, USA) each connected to four detectors. Figure 26.1 shows the optical array which incorporates four source locations 2 cm apart. This results in source detector separations of 2.5 cm and 3.78 cm. The optode positions were digitised using a Patriot™ Digitizer (Polhemus, Colchester, Vermont, USA).

Visual functional activation was achieved with a 4Hz inverting checkerboard delivering 20 s stimulation and 20 s black screen repeating over 10 epochs. The optode array was fixed horizontally with the fourth source location positioned over Oz (10/20 EEG position).

Intensity data were continuously collected during the 10 epochs using eight detector fibres arranged symmetrically around one broadband light source. This was repeated for each of the four source locations by translating the fibres over the fixed optode array, yielding an aggregate of 32 measurement channels. $\Delta[HbO_2]$, $\Delta[HHb]$ and $\Delta[oxCCO]$ were derived using the UCLn algorithm over the wavelength range 780 nm to 900 nm. The wavelength dependence of the differential pathlength factor (DPF) was taken into account when resolving concentration changes, as described by Matcher et al. [4]. The specific requirements for applying this method for measuring changes in chromophore concentrations in the adult head have been described in detail elsewhere [6].

There were 32 time-series datasets of concentration changes for each of the four subjects. Concentration changes were averaged across epochs producing 32 40 s traces corresponding to 20 s of stimulation and 20 s of rest.

Centre of gravity analysis [7] was applied on the time-course datasets to investigate the localisation of changes in the three chromophores using the 2.5 cm source-detector separation channels. The location of detector 8 was taken as the origin and

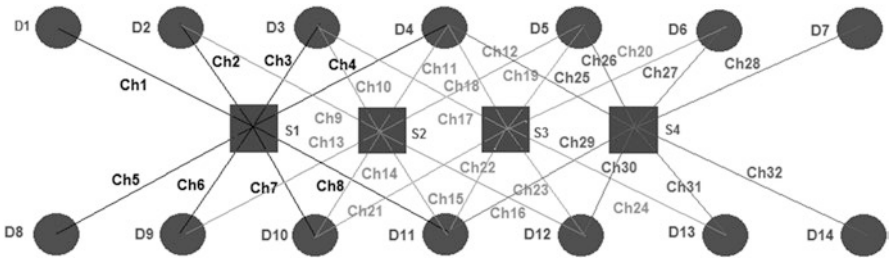

Fig. 26.1 Array of source (*square*) and detector (*circle*) locations. Measurement channels between different source-detector pairs are labelled from Ch1 to Ch32. For example source location S1 resulted in measurement channels Ch1–Ch8

all units are in mm. The centres of gravity were determined using the mean response amplitudes of the changes occurring during time $t = 15–20$ s of the each individual stimulation and the coordinates of the channels [7]. Ten epochs produced ten centres of gravity for each chromophore. Mean coordinates of the ten repeats were calculated for the three chromophores to produce the final centres of gravity with 95 % CI.

A multispectral approach, which directly reconstructs images of concentration changes from attenuation data, was employed to reconstruct $\Delta[HbO_2]$, Δ[HHb] and Δ[oxCCO]. Data at seventeen wavelengths were selected from the measured broadband spectrum (every 10 nm from 740 to 900 nm) to perform the reconstruction [8]. TOAST++ software [9] was used to run the forward model on the registered adult volumetric mesh and the Tikhonov regularized least-square solution was used to solve the inverse problem. The volumetric images were then projected on the cortical surface mesh.

3 Results

Following ethics approval and volunteer consent, four healthy adults were studied. Figure 26.2 shows the average changes of $[HbO_2]$, [HHb] and [oxCCO] in all 32 channels over the left visual cortex of a single subject which is representative of the data acquired from all four subjects. A typical haemodynamic response to functional activation (increase in $[HbO_2]$ and decrease in [HHb]) was seen across different channels.

Figure 26.3 shows the result of centre of gravity analysis for the same subject There is no overlap between 95 % CI in x and y directions between centres of gravity

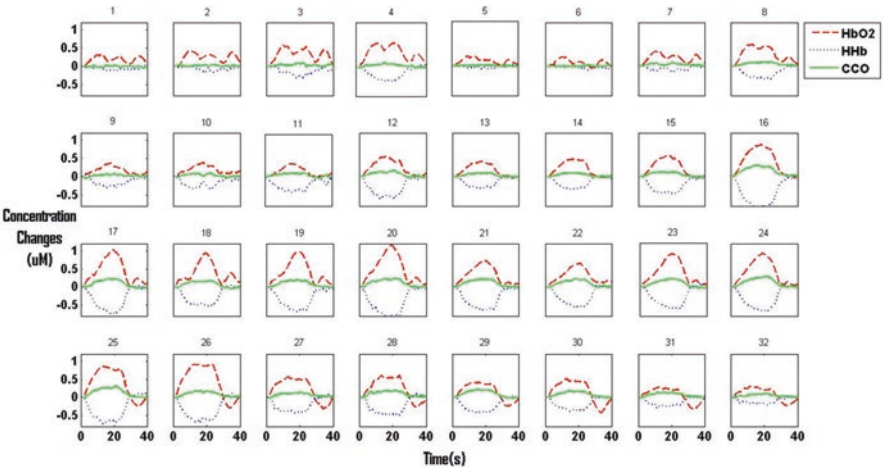

Fig. 26.2 Averaged $\Delta[HbO_2]$, Δ[HHb] and Δ[oxCCO] from a single subject. Stimulation occurred between 0 and 20 s and rest between 20 and 40 s

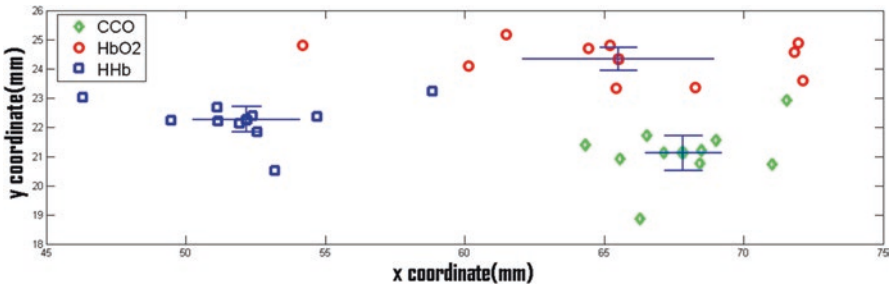

Fig. 26.3 Centres of gravity of the three chromophores for individual repeats. Overall centres of gravity are the intersection between the two 95 % CI lines for each chromophore

Table 26.1 Mean *X Y* coordinates ± SD of centres of gravity for three chromophores in four subjects

	HbO_2		HHb		oxCCO	
Subject	*X* (mm)	*Y* (mm)	*X* (mm)	*Y* (mm)	*X* (mm)	*Y* (mm)
1	62.2 ± 5.5	24.4 ± 1.4	59.6 ± 3.6	20.4 ± 1.0	59.7 ± 2.6	25.1 ± 1.6
2	65.5 ± 5.5	24.3 ± 0.6	52.2 ± 3.1	22.3 ± 0.7	67.8 ± 2.2	21.1 ± 1.0
3	62.6 ± 6.4	24.0 ± 1.5	55.4 ± 2.2	21.2 ± 0.9	64.9 ± 2.0	24.1 ± 0.9
4	62.1 ± 4.5	26.6 ± 1.3	57.7 ± 1.3	20.1 ± 0.8	62.5 ± 2.7	24.9 ± 1.5
Mean	63.1 ± 0.8	24.8 ± 0.6	56.2 ± 1.6	21.0 ± 0.5	63.7 ± 1.7	23.8 ± 0.9

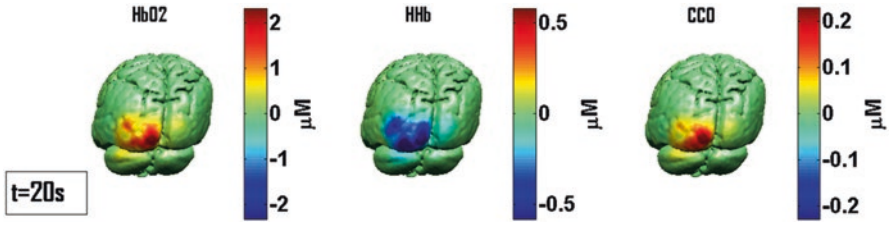

Fig. 26.4 Images of concentration changes of three chromophores for the same subject shown for time point $t = 20$ s demonstrating spatial distribution of responses

of [oxCCO] and [HHb] and between [HHb] and [HbO_2], suggesting that they have distinctly separate locations. In the case of [oxCCO] and [HbO_2], there is no overlap in the *y* direction but some in the *x* direction, suggesting a less distinct spatial separation than that seen for [HHb]. The centres of gravity for all subjects are summarised in Table 26.1.

Figure 26.4 shows cortical images of reconstructed concentration changes for the subject shown in Figs. 26.2 and 26.3. Time point $t = 20$ s shows the maximal changes during the stimulation period. These images show different localisations between [HbO_2]/[oxCCO] and [HHb] changes, whereas a similar region is active for [HbO_2] and [oxCCO], consistent with the centres of gravity analysis results.

4 Discussion

We have demonstrated focal localisation of Δ[oxCCO] that is discrete from the haemodynamic signal ([HbO_2], [HHb]) during activation of the visual cortex. The regional separation of changes in each chromophore may reflect the effect of surrounding/overlying vasculature versus regions of direct metabolic activity. The distinct spatial localisation of HbO_2 and HHb might be explained by the fact that the HbO_2 signal is derived from arteries, capillaries and veins whereas the HHb signal is derived mostly from capillaries and veins within the region of interest and therefore affected by the difference in distribution of arteries and veins in the field of view. Such separation in the centres of gravity for HbO_2 and HHb has previously been demonstrated by Koenraadt et al. [7]. Furthermore we have illustrated, for the first time, the feasibility of reconstructing Δ[oxCCO] images from a broadband NIRS array. Previous authors have simulated broadband NIRS image reconstruction for [HbO_2] and [HHb] [10], but in vivo investigation has been limited by the lack of easily accessible and appropriate hardware. We have used an experimental paradigm with a robustly reproducible response and multiple changes in source position to provide multichannel, multiwavelength data required for image reconstruction of [oxCCO], but this approach does have practical limitations. Further work is required to develop optimised hardware to deliver a multispectral NIRS multichannel array capable of real-time recordings. The delivery of Δ[oxCCO] topography and image reconstruction will allow investigation of regional changes in cerebral metabolism in the healthy and injured brain.

Acknowledgments This work was undertaken at University College London Hospitals and partially funded by the Department of Health's National Institute for Health Research Centres funding scheme via UCLH/UCL Biomedical Research Centre and by the EPSRC (EP/K020315/1). IT is supported by the Wellcome Trust (088429/Z/09/Z and 104580/Z/14/Z).

References

1. Zeff BW, White BR, Dehghani H, Schlaggar BL et al (2007) Retinotopic mapping of adult human visual cortex with high-density diffuse optical tomography. Proc Natl Acad Sci U S A 104(29):12169–12174
2. Gibson AP, Austin T, Everdell NL et al (2006) Three-dimensional whole-head optical tomography of passive motor evoked responses in the neonate. Neuroimage 30(2):521–528
3. Richter OM, Ludwig B (2003) Cytochrome oxidase structure, function and physiology of a redox driven molecular machine. Rev Physiol Biochem Pharmacol 147:47–74
4. Matcher SJ, Elwell CE, Cooper CE et al (1995) Performance comparison of several published tissue near-infrared spectroscopy algorithms. Anal Biochem 227(1):54–68
5. Heekeren HR, Kohl M, Obrig H et al (1999) Noninvasive assessment of changes in cytochrome c oxidase oxidation in human subjects during visual stimulation. J Cereb Blood Flow Metab 19(6):592–603
6. Kolyva C, Tachtsidis I, Ghosh A, Moroz T et al (2012) Systematic investigation of changes in oxidized cerebral cytochrome c oxidase concentration during frontal lobe activation in healthy adults. Biomed Opt Express 3(10):2550–2566

7. Koenraadt KLM, Duysens J, Smeenk M et al (2012) Multi-channel NIRS of the primary motor cortex to discriminate hand from foot activity. J Neural Eng 9(4):046010
8. Corlu A, Choe R, Durduran T et al (2005) Diffuse optical tomography with spectral constraints and wavelength optimization. Appl Opt 44:2082–2093
9. Schweiger M, Arridge S (2014) The Toast++ software suite for forward and inverse modeling in optical tomography. J Biomed Opt 19:040801
10. Larusson F, Fantini S, Miller EL (2011) Hyperspectral image reconstruction for diffuse optical tomography. Biomed Opt Express 2(4):946–965

Open Access This chapter is licensed under the terms of the Creative Commons Attribution 4.0 International License (http://creativecommons.org/licenses/by/4.0/), which permits use, sharing, adaptation, distribution and reproduction in any medium or format, as long as you give appropriate credit to the original author(s) and the source, provide a link to the Creative Commons license and indicate if changes were made.
The images or other third party material in this chapter are included in the chapter's Creative Commons license, unless indicated otherwise in a credit line to the material. If material is not included in the chapter's Creative Commons license and your intended use is not permitted by statutory regulation or exceeds the permitted use, you will need to obtain permission directly from the copyright holder.

Chapter 27
Effects of Physical Exercise on Working Memory and Prefrontal Cortex Function in Post-Stroke Patients

M. Moriya, C. Aoki, and K. Sakatani

Abstract Physical exercise enhances prefrontal cortex activity and improves working memory performance in healthy older adults, but it is not clear whether this remains the case in post-stroke patients. Therefore, the aim of this study was to examine the acute effect of physical exercise on prefrontal cortex activity in post-stroke patients using near-infrared spectroscopy (NIRS). We studied 11 post-stroke patients. The patients performed Sternberg-type working memory tasks before and after moderate intensity aerobic exercise (40 % of maximal oxygen uptake) with a cycling ergometer for 15 min. We measured the NIRS response at the prefrontal cortex during the working memory task. We evaluated behavioral performance (response time and accuracy) of the working memory task. It was found that physical exercise improved behavioral performance of the working memory task compared with the control condition ($p < 0.01$). In addition, NIRS analysis indicated that physical exercise enhanced prefrontal cortex activation, particularly in the right prefrontal cortex ($p < 0.05$), during the working memory task compared with the control condition. These findings suggest that the moderate-intensity aerobic exercise enhances prefrontal cortex activity and improves working memory performance in post-stroke patients.

Keywords Cognitive function • Exercise • Rehabilitation • NIRS • Prefrontal cortex

M. Moriya
Department of Rehabilitation, Nihon University Itabashi Hospital, Tokyo, Japan

Graduate School of Health Sciences Research, Major of Physical Therapy, Teikyo Heisei University, Tokyo, Japan

C. Aoki
Graduate School of Health Sciences Research, Major of Physical Therapy, Teikyo Heisei University, Tokyo, Japan

K. Sakatani (✉)
Department of Electrical and Electronic Engineering, NEWCAT Research Institute, College of Engineering, Nihon University, Tokyo, Japan
e-mail: sakatani.kaoru@nihon-u.ac.jp

© Springer International Publishing Switzerland 2016

Q. Luo et al. (eds.), *Oxygen Transport to Tissue XXXVIII*, Advances in Experimental Medicine and Biology 923, DOI 10.1007/978-3-319-38810-6_27

1 Introduction

It has been reported that physical exercise ameliorates age-related cognitive decline [1, 2]. Acute effects of physical exercise on the performance of higher-order cognitive tasks have been demonstrated in aged people [2]. Recently, a study using near-infrared spectroscopy (NIRS) indicated that acute moderate exercise elicits increased activation of the prefrontal cortex (PFC) and improves cognitive performance in the Stroop test in normal young adults [3]. In addition, moderate exercise enhances PFC activity concomitantly with improved working memory performance in older subjects [2, 4]. However, the effect of physical exercise on PFC activity and working memory performance in patients with brain disorders, such as stroke, is not known.

In order to clarify this issue, we evaluated the acute effect of physical exercise on PFC activity in post-stroke patients using NIRS.

2 Methods

2.1 Subjects

We studied 11 post-stroke patients (seven males, four females, aged 69.6 ± 12.0 years). Six patients had suffered cerebral hemorrhage while five had suffered cerebral infarction. Three patients exhibited right hemiparesis and eight patients exhibited left hemiparesis. None of the patients had apparent cognitive dysfunction or heart diseases such as arrhythmia and ischemic heart diseases. The ethical committee of Teikyo Heisei University approved this study (No. 25-053). All subjects provided written informed consent as required by the ethical committee.

2.2 Working Memory Task and Physical Exercise

We employed the modified Sternberg test as a working memory task [4–6]. In the Sternberg test, subjects were asked to remember one digit and six digits successively. There were eight 1-digit trials and eight 6-digit trials. Each trial began with the presentation of one digit or a set of six digits to be encoded for 1 s on a display. Then a blank display was shown for 2 s, followed by the test digit until a response was obtained within 2 s. Subjects held a small box with two buttons side by side. They were required to press the right button if they thought the test digit was contained within the encoded stimulus and to press the left one if not, as quickly and accurately as possible. Similar tasks have been used previously in NIRS experiments and have been demonstrated to activate the PFC [4–6].

The patients performed Sternberg-type working memory tasks before and after moderate intensity aerobic exercise (40 % of maximal oxygen uptake) with an ergometer for 15 min. The subjects performed the Sternberg test 15 min after the end of exercise.

2.3 NIRS Measurements of PFC Activity

We measured concentration changes of oxyhemoglobin (oxy-Hb), deoxyhemoglobin (deoxy-Hb) and total Hb (t-Hb) in the bilateral PFC during the working memory task using a two-channel NIRS (PNIRS-10, Hamamatsu Photonics K.K., Hamamatsu, Japan). The NIRS probes were set symmetrically on the forehead; the positioning is similar to the midpoint between electrode positions Fp1/Fp3 (left) and Fp2/Fp4 (right) of the international 10–20 system [7]. The sensor part (weighing approximately 100 g, which imposes only a minimal burden on the subject) communicated with a PC via Bluetooth™ (class 2).

2.4 Data Analysis

We analyzed the changes in NIRS parameters (oxy-Hb and deoxy-Hb) by subtracting the mean control values from the mean activation values (during the whole task period). We evaluated behavioral performance (response time and accuracy) of the working memory task. The oxy-Hb concentration changes and behavioral performance before and after the exercise were compared using Student's *t*-test.

3 Results

Performance of the Sternberg test increased NIRS-evaluated concentrations of oxy-Hb and total-Hb, concomitantly with a decrease of deoxy-Hb, in the bilateral PFC (Fig. 27.1). These NIRS parameter changes indicate activation of the bilateral PFC in the post-stroke patients. Similar NIRS parameter changes were observed after physical exercise.

The effects of physical exercise on behavioral performance of the Sternberg test are summarized in Table 27.1. Interestingly, both accuracy and reaction time in the Sternberg test were improved after physical exercise ($p<0.01$). In addition, NIRS analysis revealed that physical exercise enhanced PFC activation, particularly the right PFC ($p<0.05$), during the working memory task compared with before the physical exercise.

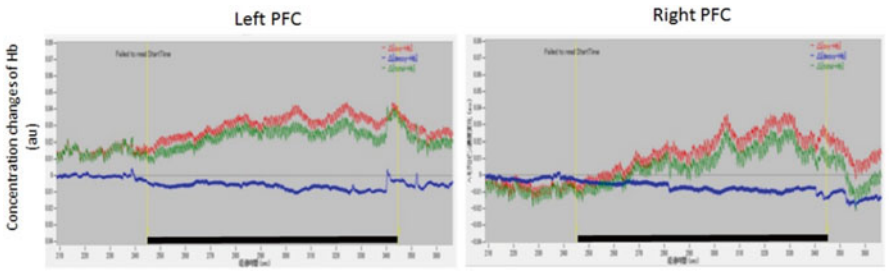

Fig. 27.1 Typical example of Hb changes in the right/left PFC in a post-stroke patient. The red, green and blue lines indicate oxy-Hb, total-Hb and deoxy-Hb respectively. The vertical axis indicates Hb concentration expressed in an arbitrary unit (au). Thick bars indicate the period of performance of the Sternberg test

Table 27.1 Effects of physical exercise on behavioral performance of Sternberg test and changes of oxy-Hb during the test

		Before	After
Sternberg test	Accuracy (number)	3.18 ± 2.0	4.54 ± 1.6**
	Reaction time (ms)	2051 ± 356	1833 ± 293**
Changes of oxy-Hb	R-PFC (au)	0.018 ± 0.02	0.026 ± 0.02*
	L-PFC (au)	0.017 ± 0.02	0.022 ± 0.02

**$p < 0.01$, *$p < 0.05$

4 Discussion

This is the first study to evaluate the effect of physical exercise on cognitive function in post-stroke patients. Our results show that moderate-intensity aerobic exercise improved performance of the working memory task compared with the control condition. The post-stroke patients could respond more quickly after exercise, and also answered correctly more often after exercise.

In addition, NIRS showed that physical exercise increased the concentration changes of oxy-Hb in the PFC during the working memory task compared with the control condition, indicating that the improved performance of the working memory task was not caused by habituation. We believe that moderate-intensity exercise enhanced the PFC activity concomitantly with the improvement of working memory performance. These findings indicate that physical exercise has beneficial effects on cognitive function in not only normal adults [2–4], but also in post-stroke patients.

It should be noted that oxy-Hb concentrations increased in the bilateral PFC, but statistical significance was achieved only in the right PFC. This asymmetry of PFC activity could not be explained by the laterality of the lesion in the post-stroke patients, since three out of eleven patients had right-side lesion. A possible explanation is that hemispheric asymmetry of PFC activity is associated with working

memory function [8–10]. For example, young subjects showed activation of the right-lateralized PFC in a logical reasoning task, though no hemispheric asymmetry was observed in older subjects during the same task [10]. Interestingly, administration of *Ginkgo biloba* (EGb), which is well known to improve cognitive functions in healthy subjects and patients with dementia, to older subjects improves working memory function by counteracting the aging-related hemispheric asymmetry reduction [5]. These observations are consistent with the present findings that right-dominant PFC activity is associated with enhanced working memory performance after physical exercise.

Physical therapy has been shown to improve motor function of post-stroke patients. Neuroimaging studies, including NIRS, demonstrated that physical therapy could enhance neuronal activation during motor tasks associated with improvement of motor function in post-stroke patients [11].

In conclusion, our results indicate that introduction of moderate-intensity aerobic exercise into physical therapy improves not only motor ability, but also cognitive performance in post-stroke patients by enhancing PFC activity during cognitive function.

Acknowledgements This research was supported in part by Strategic Research Foundation Grant-aided Project for Private Universities (S1411017) from the Ministry of Education, Culture, Sports, Sciences and Technology of Japan, and grants from Iing Co., Ltd. (Tokyo, Japan) and Southern Tohoku General Hospital (Fukushima, Japan).

References

1. Kramer AF, Erickson KI, Colcombe SJ (2006) Exercise, cognition, and the aging brain. J Appl Physiol 101:1237–1242
2. Kamijo K, Hayashi Y, Sakai T et al (2009) Acute effects of aerobic exercise on cognitive function in older adults. J Gerontol 64B:356–363
3. Yanagisawa H, Dan I, Tsuzuki D et al (2010) Acute moderate exercise elicits increased dorsolateral prefrontal activation and improves cognitive performance with Stroop test. Neuroimage 50:1702–1710
4. Tsujii T, Komatsu K, Sakatani K (2013) Acute effects of physical exercise on prefrontal cortex activity in older adults: a functional near-infrared spectroscopy study. Adv Exp Med Biol 765:293–298
5. Sakatani K, Tanida M, Hirao N et al (2014) Ginko biloba extract improves working memory performance in middle-aged women: role of asymmetry of prefrontal cortex activity during a working memory task. Adv Exp Med Biol 812:295–301
6. Tanida M, Sakatani K, Tsujii T (2012) Relation between working memory performance and evoked cerebral blood oxygenation changes in the prefrontal cortex evaluated by quantitative time-resolved near-infrared spectroscopy. Neurol Res 34:114–119
7. Tanida M, Katsuyama M, Sakatani K (2007) Relation between mental stress-induced prefrontal cortex activity and skin conditions: a near-infrared spectroscopy study. Brain Res 1184: 210–216
8. Cabeza R (2002) Hemispheric asymmetry reduction in older adults: the HAROLD model. Psychol Aging 17:85–100

9. Cabeza R, Daselaar SM, Dolcos F et al (2004) Task-independent and task-specific age effects on brain activity during working memory, visual attention and episodic retrieval. Cereb Cortex 14:364–375
10. Tsujii T, Okada M, Watanabe S (2010) Effects of aging on hemispheric asymmetry in inferior frontal cortex activity during belief-bias syllogistic reasoning: a near-infrared spectroscopy study. Behav Brain Res 210:178–183
11. Miyai I, Yagura H, Hatakenaka M et al (2003) Longitudinal optical imaging study for locomotor recovery after stroke. Stroke 34:2866–2870

Chapter 28
Relation Between Prefrontal Cortex Activity and Respiratory Rate During Mental Stress Tasks: A Near-Infrared Spectroscopic Study

Yuta Murayama, Lizhen Hu, and Kaoru Sakatani

Abstract In order to clarify the central mechanism controlling respiratory rate during mental stress, we examined the relation between prefrontal cortex (PFC) activity and respiratory rate during mental arithmetic (MA) tasks. Employing two-channel near-infrared spectroscopy (NIRS), we measured hemoglobin (Hb) concentration changes in the bilateral PFC during MA tasks in normal adults. To evaluate asymmetry of the PFC activity, we calculated the laterality index (LI); (R-L)/(R + L) of oxy-Hb concentration changes (R = right, L = left); positive LI scores indicate right-dominant activity, while negative scores indicate left-dominant activity. For measurements of respiratory rate, we employed a Kinect motion sensor (Microsoft). The MA tasks increased both oxy-Hb in the bilateral PFC and respiratory rate ($p < 0.001$). In addition, there was a significant correlation between LI and respiratory rate ($r = 0.582$, $p < 0.02$). These results indicate that the MA-induced activity in the right PFC was greater than that in the left PFC in subjects with large increases of respiratory rate, suggesting that the right PFC has a greater role in cerebral regulation of respiratory rate during mental stress.

Keywords Autonomic nervous system • NIRS • Prefrontal cortex • Respiration • Stress

Y. Murayama • L. Hu
Department of Electrical and Electronic Engineering, NEWCAT Research Institute, College of Engineering, Nihon University, Tokyo, Japan

K. Sakatani (✉)
Department of Electrical and Electronic Engineering, NEWCAT Research Institute, College of Engineering, Nihon University, Tokyo, Japan

Department of Neurological Surgery, School of Medicine, Nihon University, Tokyo, Japan
e-mail: sakatani.kaoru@nihon-u.ac.jp

© Springer International Publishing Switzerland 2016

Q. Luo et al. (eds.), *Oxygen Transport to Tissue XXXVIII*, Advances in Experimental Medicine and Biology 923, DOI 10.1007/978-3-319-38810-6_28

1 Introduction

The prefrontal cortex (PFC) plays an important role in mediating behavioral and somatic responses to stress via projections to the neuroendocrine and autonomic centers in the medial hypothalamus [1]. Interestingly, a number of studies have found that the right PFC dominates regulation of the hypothalamic-pituitary-adrenal (HPA) axis and autonomic nervous system (ANS) during mental stress. Electroencephalographic studies have shown that a greater right-frontal activation is associated with increased heart rate during unpleasant emotional stimuli [2]. Functional magnetic resonance imaging (fMRI) revealed that right dominance of PFC activity during mental stress tasks is correlated with changes in salivary cortisol levels and heart rate [3]. In addition, our near-infrared spectroscopy (NIRS) studies have shown that subjects with right-dominant activity of the PFC exhibit larger increases of heart rate compared to those with left-dominant activity [4–8].

The ANS regulates not only heart rate, but also respiratory rate. However, the central mechanism of respiratory control during mental stress remains unclear. Here, we used NIRS to examine the relation between the PFC activity and respiratory rate during mental stress tasks.

2 Methods

2.1 Experimental Settings

We studied 20 young adult males (mean age 21.4±0.8 years). All subjects were healthy, with no history of psychiatric or neurological disorders. To avoid the influence of environmental stress, subjects were seated in a comfortable chair in a normal room with good air conditioning throughout the experiments. Written informed consent was obtained on forms approved by the ethical committee of Nihon University School of Medicine.

We measured concentration changes of oxyhemoglobin (oxy-Hb), deoxyhemoglobin (deoxy-Hb) and total Hb (t-Hb) in the bilateral PFC using two-channel NIRS (PNIRS-10, Hamamatsu Photonics K.K., Hamamatsu, Japan). The NIRS probes were set symmetrically on the forehead; the positioning was similar to the midpoint between electrode positions Fp1/Fp3 (left) and Fp2/Fp4 (right) of the international 10–20 system [5]. The sensor (weighing approximately 100 g, which imposes only a minimal burden on the subject) communicated with a PC via Bluetooth™ (class 2).

We employed a mental arithmetic (MA) task to induce mental stress [4–8]. The subjects were asked to subtract serially a 2-digit number from a 4-digit number (e.g. 1022–13) as quickly as possible for 60 s. One trial consisted of the following steps. First, control conditions for 60 s. Second, the MA task for 60 s. Third, the recovery phase for 60 s.

Employing a Kinect motion-sensing input device (Microsoft Co., Washington, USA), we continuously monitored chest movements induced by respiration during the experiment. The sensor was placed 180 cm from the subject's chest wall. The results obtained with Kinect were highly correlated to those obtained with a clinically used strain gauge respiratory gating system, suggesting that the Kinect is useful for respiratory motion tracking in clinical experiments [9].

2.2 Data Analysis

We analyzed the changes in NIRS parameters (oxy-Hb and deoxy-Hb) by subtracting the mean control values from the mean activation values (during the whole task period). To evaluate the asymmetry of the oxy-Hb changes in the right and left PFC, we calculated the laterality index (LI) as follows:

$$LI = (R\Delta oxy - L\Delta oxy)/(\Delta oxyRt + \Delta oxyLt)$$

where $R\Delta oxy$ and $L\Delta oxy$ denote oxy-Hb concentration changes of the right and the left PFC during the MA task [4–8]. Positive LI indicate that the increase of Oxy-Hb in the right PFC is larger than that in the left PFC, while negative LI indicates a reverse relationship. The LI and respiratory rate changes were compared using Pearson's correlation coefficient and Student's *t*-test.

3 Results

The MA task led to elevation of oxy-Hb and total-Hb concentrations and a decrease in deoxy-Hb concentration in the bilateral PFC of all subjects, indicating that activity was enhanced in this brain region. Figure 28.1a shows a typical example of NIRS parameter changes in the bilateral PFC.

The baseline respiratory rate varied among the subjects, with values in the range of 16.4 ± 4.3 respirations/min. After the subjects had begun to perform the MA task, respiratory rate generally increased and peaked within 30 s, and then returned to the baseline after the MA task. Figure 28.1b shows an example of chest movements detected by Kinect.

Regression analysis was used to investigate the relationship between left/right asymmetry in PFC activity during the MA task and respiratory rate changes induced by the task. There was a significant positive correlation between the LI of changes in oxy-Hb concentration and the respiratory rate changes ($r = +0582$, $p < 0.02$) (Fig. 28.2).

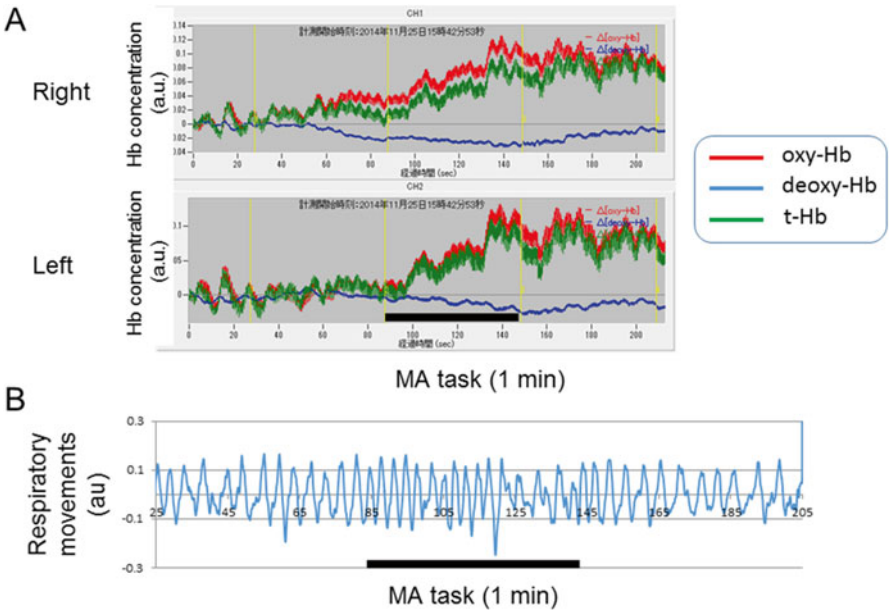

Fig. 28.1 (**a**) Typical example of NIRS parameter changes in the bilateral PFC during a mental arithmetic (MA) task. (**b**) an example of chest movements detected by Kinect. Thick bars indicate the MA task for 1 min

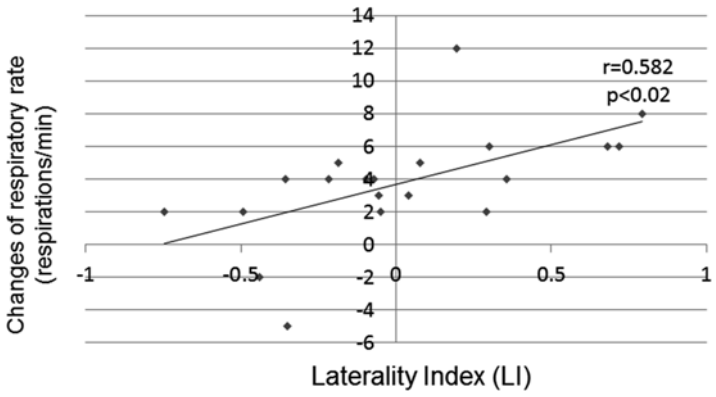

Fig. 28.2 Relation between laterality index (LI) and changes of respiratory rate during mental arithmetic task

4 Discussion

The present study is the first to examine the relationship between right/left asymmetry of PFC activity and change of respiratory rate during mental stress. We found a significant positive correlation between LI and change of respiratory rate during mental arithmetic tasks, indicating that right-dominant PFC activity was associated with a greater increase of respiratory rate during the task. In our previous studies, we found that right-dominant PFC activity was associated with a greater increase of heart rate during the task [4–8]. These results suggest that left/right asymmetry of PFC activity during mental stress tasks may be involved in the neuronal mechanism which controls heart rate and respiratory rate during mental stress.

The anatomic basis of the relation between right/left asymmetry of PFC activity and changes of respiratory rate may be the extensive direct projections from the PFC to the nucleus tractus solitarius (NTS) [10]. The NTS is the center of vagal afferents that conduct viscerosensory information from various viscera, including lungs, and a number of autonomic reflexes, including Hering-Breuer reflexes, all of which are integrated within the NTS [11].

The PFC may influence transmission through the various reflex pathways that start with vagal afferents and are switched in the NTS to neurons of the dorsal respiratory group. Our results suggest that respiratory control by the PFC may be regulated by the balance of neuronal activity between right and left PFC.

Finally, the following limitations of NIRS need to be discussed. First, NIRS measures blood oxygenation changes within the illuminated area, which includes both intracranial and extracranial tissues [12]. NIRS parameter changes could therefore be elicited by changes in blood flow in the scalp; however, the changes induced by neuronal activation are believed to reflect the changes in cerebral blood oxygenation (CBO) and hemodynamics within the activated cortices [4–9]. Second, NIRS reflects the average changes of CBO within the illuminated area; thus, the evoked CBO changes in the present study indicate the average CBO changes in that part of the prefrontal cortex through which the NIR light passes. Finally, continuous-wave NIRS, such as PNIRS, does not yield absolute values for the hemoglobin concentration changes without information concerning the optical pathlength in each subject [13]. However, we did not find any significant differences in optical pathlength between the right and left frontal regions of five subjects. Zhao et al. reported that the optical pathlength was relatively homogeneous in the forehead as compared to other regions of the head, such as the frontal-temporal junction [14]. These observations support the validity of the data analysis in the present study.

Acknowledgments This research was supported in part by the Strategic Research Foundation Grant-aided Project for Private Universities (S1411017) and a Grant-in-Aid for Exploratory Research (25560356) from the Ministry of Education, Culture, Sports, Sciences, and Technology of Japan. It was also supported through grants from Iing Co., Ltd. (Tokyo, Japan), Alpha Electron Co., Ltd. (Fukushima, Japan), NJI Co., Ltd. (Fukushima, Japan), and Southern Tohoku General Hospital (Fukushima, Japan).

References

1. Buijs RM, van Eden CG (2000) The integration of stress by the hypothalamus, amygdale and prefrontal cortex: balance between the autonomic nervous system and the neuroendocrine system. Prog Brain Res 126:117–132
2. Waldstein SR, Kop WJ, Schmidt LA et al (2000) Frontal electrocortical and cardiovascular reactivity during happiness and anger. Biol Psychol 55:3–23
3. Wang J, Rao H, Wetmore GS et al (2005) Perfusion functional MRI reveals cerebral blood flow pattern under psychological stress. Proc Natl Acad Sci U S A 102:17804–17809
4. Tanida M, Sakatani K, Takano R, Tagai K (2004) Relation between asymmetry of prefrontal cortex activities and the autonomic nervous system during a mental arithmetic task: near infrared spectroscopy study. Neurosci Lett 369:69–74
5. Tanida M, Katsuyama M, Sakatani K (2007) Relation between mental stress-induced prefrontal cortex activity and skin conditions: a near infrared spectroscopy study. Brain Res 1184: 210–216
6. Tanida M, Katsuyama M, Sakatani K (2008) Effects of fragrance administration on stress-induced prefrontal cortex activity and sebum secretion in the facial skin. Neurosci Lett 432:157–161
7. Sakatani K, Tanida M, Katsuyama M (2010) Effects of aging on activity of the prefrontal cortex and autonomic nervous system during mental stress task. Adv Exp Med Biol 662: 473–478
8. Sakatani K (2012) Optical diagnosis of mental stress: review. Adv Exp Med Biol 737:89–95
9. Xia J, Siochi RA (2012) A real-time respiratory motion monitoring system using KINECT: proof of concept. Med Phys 39:2682–2685
10. Hurley KM, Herbert H, Moga MM et al (1991) Efferent projections of the infralimbic cortex of the rat. J Comp Neurol 308:249–276
11. Lipski J, Ezure K, Wong She RB (1991) Identification of neurons receiving input from pulmonary rapidly adapting receptors in the cat. J Physiol 443:55–77
12. Van der Zee P, Cope M, Arridge SR et al (1992) Experimentally measured optical pathlengths for the adult head, calf and forearm and the head of the newborn infants as a function of inter optode spacing. Adv Exp Med Biol 316:143–153
13. Delpy DT, Cope M, van der Zee P et al (1988) Estimation of optical pathlength through tissue from direct time of flight measurement. Phys Med Biol 33:1433–1442
14. Zhao H, Tanikawa Y, Gao F et al (2002) Maps of optical differential pathlength factor of human forehead, somatosensory motor and occipital regions at multi-wavelengths in NIR. Phys Med Biol 47:2075–2093

Chapter 29
Effects of Antioxidant Supplements (BioPQQ™) on Cerebral Blood Flow and Oxygen Metabolism in the Prefrontal Cortex

Masahiko Nakano, Yuta Murayama, Lizhen Hu, Kazuto Ikemoto, Tatsuo Uetake, and Kaoru Sakatani

Abstract Pyrroloquinoline quinone (PQQ) is a quinone compound originally identified in methanol-utilizing bacteria and is a cofactor for redox enzymes. At the Meeting of the International Society on Oxygen Transport to Tissue (ISOTT) 2014, we reported that PQQ disodium salt (BioPQQ™) improved cognitive function in humans, as assessed by the Stroop test. However, the physiological mechanism of PQQ remains unclear. In the present study, we measured regional cerebral blood flow (rCBF) and oxygen metabolism in prefrontal cortex (PFC), before and after administration of PQQ, using time-resolved near-infrared spectroscopy (tNIRS). A total of 20 healthy subjects between 50 and 70 years of age were administered BioPQQ™ (20 mg) or placebo orally once daily for 12 weeks. Hemoglobin (Hb) concentration and absolute tissue oxygen saturation (SO_2) in the bilateral PFC were evaluated under resting conditions using tNIRS. We found that baseline concentrations of hemoglobin and total hemoglobin in the right PFC significantly increased after administration of PQQ ($p<0.05$). In addition, decreases in SO_2 level in the PFC were more pronounced in the PQQ group than in the placebo group ($p<0.05$).

M. Nakano • K. Ikemoto
Niigata Research Laboratory, Mitsubishi Gas Chemical Co., Inc., Tokyo, Japan

Y. Murayama • L. Hu
Department of Electrical and Electronic Engineering, NEWCAT Research Institute, College of Engineering, Nihon University,
1 Nakagawara, Tokusada, Tamuramachi, Koriyama, Fukushima Prefecture 963-8642, Japan

T. Uetake
CX Medical Japan Co., Inc., Tokyo, Japan

K. Sakatani (✉)
Department of Electrical and Electronic Engineering, NEWCAT Research Institute, College of Engineering, Nihon University,
1 Nakagawara, Tokusada, Tamuramachi, Koriyama, Fukushima Prefecture 963-8642, Japan

Department of Neurological Surgery, School of Medicine, Nihon University, Tokyo, Japan
e-mail: sakatani.kaoru@nihon-u.ac.jp

© Springer International Publishing Switzerland 2016

Q. Luo et al. (eds.), *Oxygen Transport to Tissue XXXVIII*, Advances in Experimental Medicine and Biology 923, DOI 10.1007/978-3-319-38810-6_29

These results suggest that PQQ causes increased activity in the right PFC associated with increases in rCBF and oxygen metabolism, resulting in enhanced cognitive function.

Keywords NIRS • Prefrontal cortex • Pyrroloquinoline quinone • Stroop test • Working memory

1 Introduction

Pyrroloquinoline quinone (PQQ) is a water-soluble quinone compound first identified in 1979 and is a cofactor found in bacterial redox enzyme [1, 2]. PQQ is present in a variety of everyday foods and beverages, such as parsley, green tea, and fermented soybeans [3]. PQQ is also found in various organs and tissues [4] and is abundant in human breast milk [5]. The estimated daily intake of PQQ from typical foods and beverages are 0.01–0.4 mg/day [6]. PQQ is an anti-oxidant and promotes mitochondrial biogenesis [7]. Reduced PQQ exhibits a high anti-oxidant capacity that is 7.5-fold greater than that of ascorbic acid [8]. It has been reported that PQQ induces dose-dependent inhibition of cell death in neuroblastoma cultures [9] and upregulates the expression of nerve growth factor in fibroblast cultures [10]. Improved learning has been demonstrated in rats fed PQQ supplements at the early stage of the Morris water maze test [11]. These results suggest that PQQ has potential for prevention of neurodegeneration caused by oxidative stress, and may improve memory. In our previous human study, significant improvements were observed in Stroop selective attention, reverse Stroop test, and visual-spatial cognitive function in the laptop tablet Touch M evaluation after administration of PQQ for 12 weeks [12]. However, the physiological mechanism underlying these results remains unclear. In the present study, we measured regional cerebral blood flow (rCBF) and oxygen metabolism in the prefrontal cortex (PFC) using time-resolved near-infrared spectroscopy (tNIRS) before and after administration of PQQ.

2 Methods

2.1 Study Design, Subjects, and Test Substance

The study was designed as a randomized, placebo-controlled, double-blinded, two-group parallel study, conducted in compliance with the Declaration of Helsinki (2008) and the Ethical Guidelines for Epidemiological Studies (issued in 2004 by the Ministry of Education, Culture, Sports, Science and Technology, and the Ministry of Health, Labor and Welfare). The study protocol (#201408-14-MGC01)

was approved by the ethical committee of Ikuseikai Yamaguchi Hospital (Tokyo, Japan) on October 31, 2014 (Approved #2014-8). The study recruited healthy Japanese adults between 50 and 70 years of age with Mini Mental Status Examination (MMSE) scores greater than 27, regarded as cognitively normal. The following individuals were excluded: (a) those with a medical history of mental illness or brain disease, (b) those with medical symptoms of cerebrovascular disorder, and (c) those taking drugs or supplements for improvement of brain function or blood flow within 3 months prior to the study. Participants were recruited by CX Medical Japan (Tokyo, Japan), and had no relationships with the Mitsubishi Gas Chemical Co., Inc. (Tokyo, Japan). The 20 volunteers were randomly assigned to two groups for treatment with either PQQ ($n=10$) or placebo ($n=10$). All participants underwent internal and physical examinations, and peripheral blood tests at baseline (before dosing, 0 weeks) and 12 weeks. The test substance was provided in the form of a two-piece hard capsule, containing 10 mg of the active dietary ingredient, PQQ disodium salt (BioPQQ™), manufactured by the Mitsubishi Gas Chemical Co., Inc. Two capsules each were swallowed with a cup of water once daily after breakfast for 12 weeks. The dose of PQQ disodium salt (20 mg/day) was chosen based on the results of our previous study [12].

2.2 Evaluations

A two-channel, three-wavelength (760, 800 and 830 nm), time-resolved spectroscopy monitor TRS-20 (Hamamatsu Photonics K.K., Japan) was employed to evaluate baseline cerebral tissue hemoglobin oxygenation under resting conditions [13]. The State Trait Anxiety Inventory (STAI) was carried out to evaluate mental stress [14]. All measurements were expressed as mean ± standard deviation. Statistical analyses were performed using two-tailed paired Student's *t*-test or one-factor ANOVA employing a post hoc Turkey-Kramer test. Values of $p<0.05$ were considered significant. Data analysis and statistical analysis were performed using Excel 2013 (Microsoft) with the add-in software Statcel3 (OMS Publishing Inc., Saitama, Japan).

3 Results

3.1 Subjects

All 20 volunteers completed the study. The placebo group contained ten subjects (4 male, 6 female) with a mean age of 60.9 ± 4.5 years. The PQQ group contained ten subjects (4 male, 6 female) with a mean age of 59.5 ± 3.7 years. Measurements of physiological parameters indicated there were no adverse events related to blood, nor were there adverse internal or physical examination findings at any point in the study.

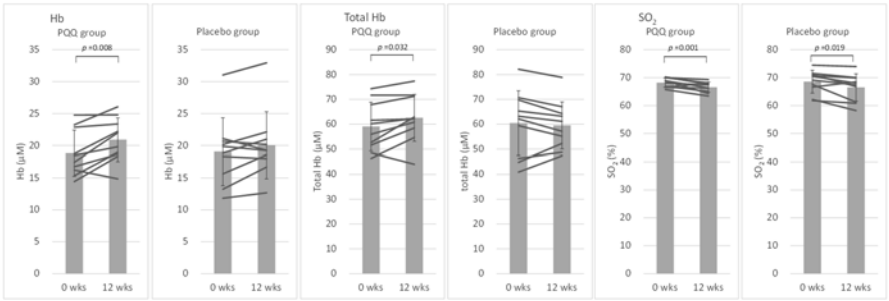

Fig. 29.1 tNIRS measurements of Ch1. Thin lines represent data from individual volunteers; Shaded columns and error bars indicate mean and standard deviation, respectively. The significant *p* values of paired Student's *t*-test are also shown.

3.2 Time-Resolved Near-Infrared Spectroscopy (tNIRS)

In channel 1 (Ch1, right lateral) for the PQQ group, oxyhemoglobin (HbO_2) concentrations did not change between 0 weeks and 12 weeks (Table 29.1; Fig. 29.1). However, deoxyhemoglobin (Hb) and total Hb (= HbO_2 + Hb) increased significantly ($p = 0.008$ and 0.032, respectively). In addition, absolute tissue oxygen saturation ($SO_2 = (HbO_2/\text{total Hb}) \times 100$) decreased significantly after 12 weeks compared to baseline ($p = 0.001$). Although the placebo group likewise showed a statistically significant decrease in SO_2, the individual changes in HbO_2, Hb and Total Hb did not themselves reach statistical significance. In channel 2 (Ch2, left lateral), SO_2 decreased significantly in the PQQ group ($p = 0.008$), whereas Hb concentration increased significantly in the placebo group ($p = 0.024$). There were no significant changes in the Ch2/Ch1 ratios for all of the measurements.

3.3 State-Trait Anxiety Inventory (STAI)

The total scores for state anxiety and trait anxiety in the PQQ and placebo groups did not change between 0 and 12 weeks (Table 29.2). When each group was subdivided based upon the score at baseline, the average state anxiety score decreased significantly between the weeks in the high subgroup of the PQQ group from 42.6 ± 5.7 (ranging from 38 to 52) to 34.0 ± 6.6 (ranging from 27 to 41) ($p = 0.028$).

4 Discussion

In a randomized, placebo-controlled, double-blinded, two-group parallel study with healthy middle-aged volunteers, it was found that Hb and total Hb increased significantly in right PFC after administration of PQQ for 12 weeks. In addition, oxygen saturation (SO_2) significantly decreased, indicating increased O_2 consumption in

Table 29.1 tNIRS determination of HbO_2, Hb, total Hb, and SO_2

			PQQ group			P lacebo group		
			0 Weeks	12 Weeks	*p*	0 Weeks	12 Weeks	*p*
Ch1 (right lateral)	HbO_2	μM	40.25±6.40	41.66±6.40	0.154	41.42±8.63	39.47±5.82	0.147
	Hb	μM	18.83±3.58	20.91±3.40	0.008	19.07±5.28	20.07±5.22	0.104
	TotalHb	μM	59.08±9.75	62.57±9.45	0.032	60.48±13.00	59.53±9.48	0.540
	SO_2	%	68.21±1.65	66.58±1.85	0.001	68.57±4.10	66.50±4.90	0.019
Ch 2 (left lateral)	HbO_2	μM	41.42±7.12	40.85±7.12	0.676	40.52±7.42	41.43±6.54	0.441
	Hb	μM	17.58±3.30	18.50±3.17	0.080	17.40±3.82	18.65±4.29	0.024
	TotalHb	μM	58.99±10.09	59.35±9.96	0.843	57.92±10.39	60.38±9.74	0.107
	SO_2	%	70.20±1.98	68.77±1.91	0.008	69.95±3.74	68.72±3.91	0.172
Ch2/Ch1	HbO_2		1.03±0.09	0.98±0.10	0.173	0.99±0.11	1.05±0.08	0.118
	Hb		0.94±0.07	0.89±0.07	0.084	0.93±0.12	0.95±0.07	0.0543
	TotalHb		1.00±0.08	0.95±0.08	0.098	0.97±0.11	1.02±0.07	0.210
	SO_2		1.03±0.01	1.03±0.03	0.656	1.02±0.02	1.03±0.03	0.064

Table 29.2 STAI scores

			PQQ group			Placebo group		
		n	0 Weeks	12 Weeks	*p*	0 Weeks	12 Weeks	*p*
State anxiety	Total	10	35.9±9.0	32.3±6.1	0.131	39.2±7.6	38.2±6.5	0.733
	Low subgroup	5	29.2±6.3	30.6±5.6	0.404	32.8±2.6	36.0±8.8	0.537
	High subgroup	5	42.6±5.7	34.0±6.6	0.028	45.6±4.4	40.4±2.6	0.086
Trait anxiety	Total	10	37.0±13.0	35.5±7.9	0.588	40.8±6.0	38.6±7.9	0.269
	Low subgroup	5	28.4±5.3	30.8 ±4.5	0.472	36.4±5.1	34.8±9.4	0.675
	High subgroup	5	45.6±13.3	40.2±8.0	0.239	45.2±2.6	42.4±4.1	0.178

PFC. It is reported that total Hb reflects cerebral blood volume change and neuronal activation is coupled with increases in rCBF, which is thought to be accompanied by increases in cerebral blood volume [15]. Therefore, total Hb is closely link to rCBF. Our results suggest that increases in rCBF and oxygen metabolism are associated with the enhancement of brain activity including cognitive function after administration of PQQ, providing an important clue for further clarification of the underlying mechanisms. There were no significant differences in the optical path lengths, peripheral blood Hb concentrations and hematocrit levels between 0 and 12 weeks between PQQ-treated or placebo group (paired *t*-test and Tukey-Kramer test). These observations indicate that the optical characteristics and systemic Hb conditions did not affect cerebral blood oxygenation during the study. In addition, the STAI state anxiety score decreased significantly in the PQQ subgroup with high initial STAI scores. This was in agreement with previous results showing that mental stress was significantly improved by PQQ administration in volunteers with high levels of mental stress [16]. Meanwhile, it has been reported that subjects with right-dominant brain activity under resting conditions showed higher anxiety scores in STAI [14]. The different outcome in this study may be partly due to the NIRS method. The previous study employed continuous wave NIRS, which measures relative values, while tNIRS in this study measured baseline blood flow under resting conditions. Administration of *Ginkgo biloba* extract for 6 weeks has been reported to alter the PFC activation pattern to right-dominant, in both middle-aged and young subjects [17]. In aged subjects, increased left lateral blood flow is a mechanism that can compensate for decline in right lateral activity of the PFC. Right-dominant activity was observed in this study after the administration of PQQ, which is very similar to the results of the *G. biloba* study mentioned above. Two mechanisms of improved brain blood flow can be hypothesized; a mechanism involving blood vessels or that involving the nervous system. In the former, bilateral improvement would be expected. However, in this study, only right lateral blood flow significantly improved. Therefore, PQQ and *G. biloba* extract may act on the nervous

system in similar ways. Further studies are needed to elucidate the mechanism in more detail.

Acknowledgments This research was supported in part by the Strategic Research Foundation Grant-aided Project for Private Universities (S1411017) and a Grant-in-Aid for Exploratory Research (25560356) from the Ministry of Education, Culture, Sports, Sciences, and Technology of Japan. Furthermore, this research was supported through grants from Iing Co., Ltd. (Tokyo, Japan), Alpha Electron Co., Ltd. (Fukushima, Japan), NJI Co., Ltd. (Fukushima, Japan), and Southern Tohoku General Hospital (Fukushima, Japan).

References

1. Salisbury SA, Forrest HS, Cruse WBT et al (1979) A novel coenzyme from bacterial primary alcohol dehydrogenase. Nature 280:843–844
2. Duine JA, Frank J, Van Zeeland JK (1979) Glucose dehydrogenase from Acinetobacter calcoaceticus: a quinoprotein. FEBS Lett 108:443–446
3. Kumazawa T, Sato K, Seno H et al (1995) Levels of pyrroloquinoline quinone in various foods. Biochem J 307:331–333
4. Kumazawa T, Seno H, Urakami T et al (1992) Trace levels of pyrroloquinoline quinone in human and rat samples detected by gas chromatography/mass spectrometry. Biochem Biophys Acta 1156:62–66
5. Mitchell AE, Johnes AD, Mercer RS et al (1999) Characterization of pyrroloquinoline quinone amino acid derivatives by electrospray ionization mass spectrometry and detection in human milk. Anal Biochem 269:317–325
6. Harris CB, Chowanadisai W, Mishchuk DO et al (2013) Dietary pyrroloquinoline quinone (PQQ) alters indicators of inflammation and mitochondrial-related metabolism in human subjects. J Nutr Biochem 24:2076–2084
7. Rucker R, Chowanadisai W, Nakano M (2009) Potential physiological importance of pyrroloquinoline quinone. Altern Med Rev 14:268–277
8. Mukai K, Ouchi A, Nakano M (2011) Kinetic study of the quenching reaction of singlet oxygen by pyrroloquinolinequinol ($PQQH_2$, a reduced form of pyrroloquinolinequinone) in micellar solution. J Agric Food Chem 59:1705–1712
9. Nunome K, Miyazaki S, Nakano M et al (2008) Pyrroloquinoline quinone prevents oxidative stress-induced neuronal death probably through changes in oxidative status of DJ-1. Biol Pharma Bull 31:1321–1326
10. Yamaguchi K, Sasano A, Urakami T et al (1993) Stimulation of nerve growth factor production by pyrroloquinoline quinone and its derivatives in vitro and in vivo. Biosci Biotech Biochem 57:1231–1233
11. Ohwada K, Takeda H, Yamazaki M et al (2008) Pyrroloquinoline quinone (PQQ) prevents cognitive deficit caused by oxidative stress in rats. J Clin Biochem Nutr 42:29–34
12. Itoh Y, Hine K, Miura H et al (in press) Effect of the antioxidant supplement pyrroloquinoline quinone disodium salt (BioPQQ™) on cognitive functions. Adv Exp Med Biol 876:319–326
13. Tanida M, Sakatani K, Tsujii T (2012) Relation between working memory performance and evoked cerebral blood oxygenation changes in the prefrontal cortex evaluated by quantitative time-resolved near-infrared spectroscopy. Neurol Res 34:114–119
14. Ishikawa W, Sato M, Fukuda Y et al (2014) Correlation between asymmetry of spontaneous oscillation of hemodynamic changes in the prefrontal cortex and anxiety levels: a near-infrared spectroscopy study. J Biomed Optics 19:027005
15. Hoshi Y, Kobayashi N, Tamura M (2001) Interpretation of near-infrared spectroscopy signals: a study with a newly developed perfused rat brain model. J Appl Physiol 90:1657–1662

16. Nakano M, Yamamoto T, Okumura H et al (2012) Effects of oral supplementation with pyrroloquinoline quinone on stress, fatigue, and sleep. Funct Foods Health Dis 2:307–324
17. Sakatani K, Tanida M, Hirano N, Takemura N (2014) *Ginkgo biloba* extract improves working memory performance in middle-aged women: role of asymmetry of prefrontal cortex activity during a working memory task. Adv Exp Med Biol 12:295–301

Chapter 30
Temporal Comparison Between NIRS and EEG Signals During a Mental Arithmetic Task Evaluated with Self-Organizing Maps

Katsunori Oyama and Kaoru Sakatani

Abstract Simultaneous monitoring of brain activity with near-infrared spectroscopy and electroencephalography allows spatiotemporal reconstruction of the hemodynamic response regarding the concentration changes in oxyhemoglobin and deoxyhemoglobin that are associated with recorded brain activity such as cognitive functions. However, the accuracy of state estimation during mental arithmetic tasks is often different depending on the length of the segment for sampling of NIRS and EEG signals. This study compared the results of a self-organizing map and ANOVA, which were both used to assess the accuracy of state estimation. We conducted an experiment with a mental arithmetic task performed by 10 participants. The lengths of the segment in each time frame for observation of NIRS and EEG signals were compared with the 30-s, 1-min, and 2-min segment lengths. The optimal segment lengths were different for NIRS and EEG signals in the case of classification of feature vectors into the states of performing a mental arithmetic task and being at rest.

Keywords NIRS • EEG • Self-organizing map • Laterality index

1 Introduction

Simultaneous monitoring of brain activity with near-infrared spectroscopy (NIRS) and electroencephalography (EEG) has been studied to investigate cognitive and emotional processing [1]. Recent findings show that EEG activity is intrinsically

K. Oyama (✉)
Department of Computer Science, College of Engineering, Nihon University, Koriyama, Japan
e-mail: oyama@cs.ce.nihon-u.ac.jp

K. Sakatani
Department of Electrical and Electronics Engineering, College of Engineering, Nihon University, Koriyama, Japan

Department of Neurological Surgery, Nihon University School of Medicine, Tokyo, Japan
e-mail: sakatani.kaoru@nihon-u.ac.jp

© Springer International Publishing Switzerland 2016

Q. Luo et al. (eds.), *Oxygen Transport to Tissue XXXVIII*, Advances in Experimental Medicine and Biology 923, DOI 10.1007/978-3-319-38810-6_30

associated with cortical hemodynamic responsiveness to the negative valence on the right side [2], which may provide an important context for early detection of various types of illnesses during telehealth or remote patient monitoring.

Recent studies have identified the prefrontal cortex (PFC) as a key region for the experience and regulation of emotional responses, and NIRS is a well-suited technique for investigation of PFC activity [2]. Tanida, Katsuyama, and Sakatani [4] reported that the degree of right-lateralized asymmetry in the PFC activation patterns is positively correlated with heart rate changes during a mental arithmetic task. On the other hand, EEG records brain activity that is produced by the firing of neurons directly within the brain. Brain activity is recorded noninvasively by placing electrodes on the scalp. Both event-related desynchronization (ERD) and event-related potential (ERP) have been used to measure mental work or memory load with statistical significance [5]. In particular, the ERD-based approach decomposes EEG signals into power spectra, such as theta (4–6 Hz), low alpha (6–8 Hz), middle alpha (8–10 Hz), high alpha (10–12 Hz), and beta (12–30 Hz), to find desynchronization, i.e., a reduction in band power of particular frequencies in response to an event such as initiation of a mental arithmetic task. ERD-based approaches have recently shown that theta band power responds to prolonged visual emotional stimulation [6, 7]. In addition, desynchronization in low alpha band power correlates to a presented warning stimulus [8]. Researchers have found affective state changes related to negative valence typically trigger anterior asymmetry in alpha reduction [5, 9, 10].

However, affective states or states related to mental tasks can vary in length during observation [3]. One emerging issue with data-mining techniques is that the accuracy of state estimation during mental arithmetic tasks is often different depending on the length of the segment for sampling of NIRS and EEG signals. In the present study, the results of a self-organizing map (SOM) and analysis of variance (ANOVA) were compared to determine the optimal length of the segment.

2 Methods

2.1 NIRS Recordings

Feature values of the concentration changes in oxyhemoglobin in the left and right PFCs at time t are assigned $h_l(t)$ and $h_r(t)$, respectively. These feature values are discretized into $h_l(t_n)$ and $h_r(t_n)$ with the length of the segment $t_n - t_{n-1}$.

$$h_l\left(t_n\right) = \frac{\int_{t_{n-1}}^{t_n} h_l\left(t\right) dt}{t_n - t_{n-1}}$$
$$h_r\left(t_n\right) = \frac{\int_{t_{n-1}}^{t_n} h_r\left(t\right) dt}{t_n - t_{n-1}} \tag{30.1}$$

Then, the laterality index (LI) is introduced to measure the valence on the PFC that is related to the stress level [4, 11]. Laterality $l(t_n)$ for input of the SOM is defined as the difference between hemodynamic responses on both sides of the PFC during time frame t_n as below:

$$l\left(t_n\right) = \frac{h_r\left(t_n\right) - h_l\left(t_n\right)}{h_r\left(t_n\right) + h_l\left(t_n\right)} \tag{30.2}$$

2.2 EEG Recordings

The feature value of the EEG index $w(t)$ is defined as the ratio of $s_i(t)$ to $d_i(t)$ for chosen electrodes at position i, where the spectral power between 8 and 12 Hz is assigned $s_i(t)$, and the spectral power between 13 and 30 Hz is assigned $d_i(t)$, which is sensitive to changes in the mental tasks that are related to working memory.

$$w\left(t\right) = \frac{\sum_{i=1}^{I} s_i\left(t\right)}{\sum_{i=1}^{I} d_i\left(t\right)} \tag{30.3}$$

In particular, let $w_l(t_n)$ be the average of $w(t)$ for four channels in the left PFC (AF3, F3, F7, T3) during time frame t_n. Likewise, $w_r(t_n)$ is the average of $w(t)$ for four channels in the right PFC (AF4, F4, F8, T4). Thus, these feature values for both the left and right PFCs can be compared within time frame t_n as below:

$$\begin{aligned} w_l\left(t_n\right) &= \frac{\int_{t_{n-1}}^{t_n} w_l\left(t\right) dt}{t_n - t_{n-1}} \\ w_r\left(t_n\right) &= \frac{\int_{t_{n-1}}^{t_n} w_r\left(t\right) dt}{t_n - t_{n-1}} \end{aligned} \tag{30.4}$$

2.3 Cluster Analysis by SOM

The feature values discussed in the previous sections form feature vectors for generation of an SOM, which allows visualization and exploration of a high-dimensional data space by nonlinearly projecting it onto a 2-D plane. NIRS and EEG signals may involve outliers and unknown patterns of waveforms, whereas SOM provides

more robust learning compared to other types of cluster analyses such as k-means [12]. Each feature vector for SOM includes $l(t_n)$, $w_l(t_n)$, and $w_r(t_n)$ in a segment length of 30 s, 1 min, or 2 min. For assessment of the experimental result, the quantization error (QE) explains reliability of measurement of SOM by calculating the average distance of the feature vectors to the cluster centroids; in other words, the higher QE is taken from the SOM, the more errors in classification of feature vectors can be found.

An experiment of a mental arithmetic task performed by 10 participants (young males) was conducted to observe the state transition between the mental arithmetic task (2 min) and being at rest (2 min). Each participant performed the mental arithmetic task in three cycles (12 min total). NIRS sensors (PocketNIRS; DynaSense Inc., Japan) and EEG sensors (Emotiv EPOC system; Emotiv Inc., U.S.A.) were equipped to monitor brain activity in the PFC. Body movements were prohibited during the experiment except those required for reading the arithmetic problems. NIRS and EEG signals were first verified with video data each second to look for the appearance of artifacts caused by body movement, and the corresponding feature vectors were sampled for cluster analysis using the SOM. Because the artifacts in this experiment had a smaller impact on SOM than 5 % of QE, no major artifact removal was performed from the NIRS and EEG signals.

3 Results

Figure 30.1 shows an example of $l(t)$ and $w_l(t)$ from the first participant, which are continuous values before discretization into $l(t_n)$ and $w_l(t_n)$. The states of performing a mental arithmetic task (**a**) and being at rest (**r**) were periodically changed every 2 min. For most participants, the value of $l(t)$ increased as the mental arithmetic task was performed, and the value of $w_l(t)$ changed periodically.

Each feature vector after sampling from the example in Fig. 30.1 is composed of feature values of $l(t_n)$, $w_l(t_n)$, and $w_r(t_n)$ as shown in Table 30.1. Then, these were normalized so that all the feature values were assigned a value of 0 to 1 for input to the SOM.

SOMs (training length: 300 iterations, map size: 40×40) were created with the feature vectors obtained from all ten participants. From the results shown in Fig. 30.2, compared to the 30-s segment, the feature vectors of the 1-min segment were well separated into the **a** and **r** states. QE was the smallest if the 1-min segment was chosen, whereas QE was the largest with the 30-s segment. The difference between the results according to the length of the segment was considerably larger because each value in the feature vectors does not exceed 1. Other SOMs (training length: 500 iterations, map size: 100×100) were also created, and the results were the same, with a 1 % difference in QE.

One-way ANOVA was performed to compare the effect of the feature values on the two states as shown in Table 30.2. We found a significant effect of $l(t_n)$ on the two states except $l(t_n)$ with the 30-s segment ($F(1, 118) > 1.38$, $p < 0.3$). In contrast,

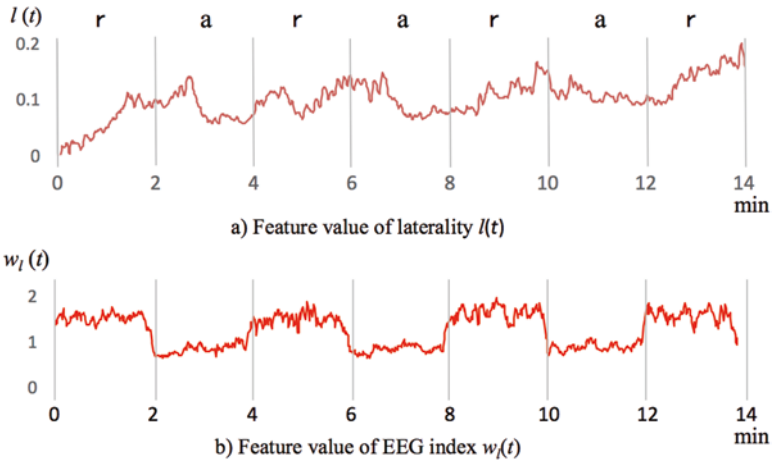

Fig. 30.1 Plotted values obtained from NIRS and EEG signals. The states of performing mental arithmetic task and being at rest are labeled with **a** and **r**, respectively

Table 30.1 Feature vectors (length of the 1-min segment) sampled from the example in Fig. 30.1

t_n	$l(t_n)$	$w_l(t_n)$	$w_r(t_n)$
1	0.375	0.617	0.577
2	0.253	0.387	0.399
3	0.418	0.239	0.276
4	0.568	0.446	0.454
5	0.507	0.576	0.559
6	0.546	0.478	0.520
7	0.678	0.249	0.332
8	0.702	0.521	0.544
9	0.538	0.692	0.681
10	0.397	0.445	0.496
11	0.581	0.273	0.381
12	0.759	0.485	0.565

F-values of both $w_l(t_n)$ and $w_r(t_n)$ were higher than the others if the 30-s segment was applied; i.e., for both $w_l(t_n)$ and $w_r(t_n)$, mean values in the **a** state and mean values in the **r** state were clearly separated from each other.

4 Discussion

From the experimental results, the optimal lengths of segments for mental arithmetic tasks were different between NIRS and EEG signals. The NIRS signal may have required a segment of more than 1 min for sampling, whereas the EEG signal took

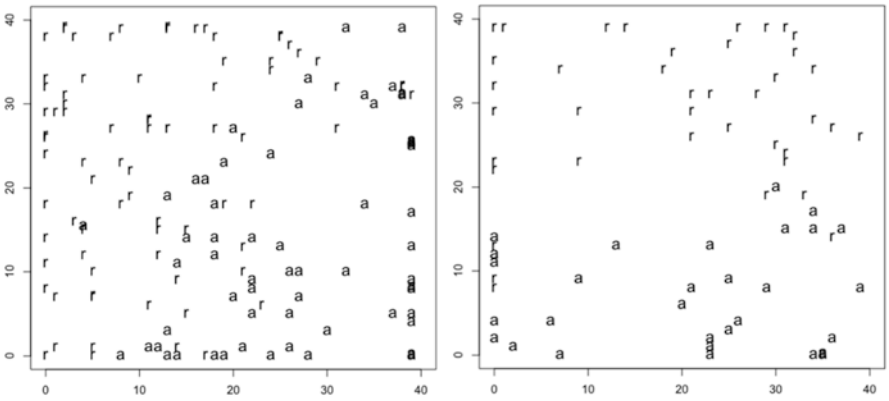

Fig. 30.2 SOMs with feature vectors in the 30-s and 1-min segments. Each feature vector is labeled with the state. Similar feature vectors are clustered by competitive learning

Table 30.2 Results of ANOVA

Feature value	Segment length	*F*-value	*p*-value
$l(t_n)$	30 s	1.38	$p<0.3$
	1 min	3.75	$p<0.1$
	2 min	7.19	$p<0.01$
$w_l(t_n)$	30 s	83.34	$p<0.001$
	1 min	45.49	$p<0.001$
	2 min	36.73	$p<0.001$
$w_r(t_n)$	30 s	45.29	$p<0.001$
	1 min	22.88	$p<0.001$
	2 min	9.446	$p<0.01$

a segment of less than 30 s; in other words, the reaction time for the concentration change in oxyhemoglobin during the transition between the states was longer than the EEG power spectra.

The results of SOM and ANOVA suggested a relationship between QE and the *F*-value. The combination of SOM and ANOVA may contribute to instant monitoring of parameters such as the optimal length of a segment for state estimation. However, more experimental parameters (e.g., different types of feature values and tasks) must be further validated to determine the comprehensive relationship between QE and the *F*-value.

In this paper, the lengths of the segments in each time frame for observation of NIRS and EEG signals were compared using SOMs and ANOVA. Our experimental results suggested that the optimal segment lengths were different for NIRS and EEG signals. Further works will involve application of SOM and ANOVA to real-world case studies. Development of an algorithm for real-time monitoring of the mental state may eventually provide a potential for early detection of illness and healthcare support to service users.

Acknowledgments This work was supported in part by JSPS Grant-in-Aid for Young Scientists (B) Grant Number 26730079, the Strategic Research Foundation Grant-aided Project for Private Universities (S1411017) from the Ministry of Education, Culture, Sports, Sciences and Technology of Japan, and grants from Iing Co., Ltd. (Tokyo, Japan).

References

1. Biallas M, Trajkovic I, Haensse D et al (2012) Reproducibility and sensitivity of detecting brain activity by simultaneous electroencephalography and near-infrared spectroscopy. Exp Brain Res 222(3):255–264
2. Balconi M, Grippa E, Vanutelli ME (2015) What hemodynamic (fNIRS), electrophysiological (EEG) and autonomic integrated measures can tell us about emotional processing. Brain Cogn 95:67–76
3. Oyama K, Takeuchi A, Chang CK (2013) Brain lattice: concept lattice based causal analysis of changes in mental workload. IEEE international multi-disciplinary conference on cognitive methods in situation awareness and decision support (CogSIMA). pp 59–66
4. Tanida M, Katsuyama M, Sakatani K (2007) Relation between mental stress-induced prefrontal cortex activity and skin conditions: a near-infrared spectroscopy study. Brain Res 1184: 210–216
5. Ishikawa W, Sato M, Fukuda Y et al (2014) Correlation between asymmetry of spontaneous oscillation of hemodynamic changes in the prefrontal cortex and anxiety levels: a near-infrared spectroscopy study. J Biomed Opt 19(2):027005
6. Brouwer AM, Hogervorst MA, van Erp JBF et al (2012) Estimating workload using EEG spectral power and ERPs in the n-back task. J Neural Eng 9(4):045008
7. Knyazev GG (2007) Motivation, emotion, and their inhibitory control mirrored in brain oscillations. Neurosci Biobehav Rev 31:377–395
8. Krause CM, Viemerö V, Rosenqvist A et al (2000) Relative electroencephalographic desynchronization and synchronization in humans to emotional film content: an analysis of the 4–6, 6–8, 8–10 and 10–12 Hz frequency bands. Neurosci Lett 286:9–12
9. Klimesch W, Russegger H, Doppelmayr M et al (1998) A method for the calculation of induced band power: implications for the significance of brain oscillations. Electroencephalogr Clin Neurophysiol 108(2):123–130
10. Davidson RJ (1998) Anterior electrophysiological asymmetries, emotion, and depression: conceptual and methodological conundrums. Psychophysiology 35:607–614
11. Dimberg U, Petterson M (2000) Facial reactions to happy and angry facial expressions: evidence for right hemisphere dominance. Psychophysiology 37:693–696
12. Bação F, Lobo V, Painho M (2005) Self-organizing maps as substitutes for K-means clustering. In: Computational science—ICCS 2005, Pt. 3, Lecture Notes in Computer Science, vol 3516, pp 209–217

Chapter 31
The Role of Phonological Processing in Semantic Access of Chinese Characters: A Near-Infrared Spectroscopy Study

Jinyan Sun, Linshang Rao, Chenyang Gao, Lei Zhang, Lan Liang, and Hui Gong

Abstract The Stroop task was used to investigate the role of phonological processing in semantic access for written Chinese language. Fourteen children were recruited to perform the Stroop task, using color characters, their homophones and neutral characters as stimuli. Near-infrared spectroscopy (NIRS) was used to measure the brain activation in the prefrontal cortex (PFC) during the task. In view of better sensitivity, oxy-hemoglobin was chosen to indicate the task activation. In behavioral performance, there was a significant classical Stroop interference effect as indexed by longer response time and higher error rate for the color task than the neutral task, whereas there was no evident interference effect for the color homophones. The NIRS data agreed with the behavioral data, and showed a significant Stroop effect only for the color characters in the bilateral PFC. These results suggested that phonology may not play an important role in semantic activation of Chinese characters for children.

Keywords Near-infrared spectroscopy • Stroop • Phonological processing • Semantic access • Chinese

J. Sun • L. Rao • L. Liang
Department of Biomedical Engineering, Guangdong Medical University, Dongguan 523808, People's Republic of China

C. Gao • L. Zhang • H. Gong (✉)
Wuhan National Laboratory for Optoelectronics, Britton Chance Center for Biomedical Photonics, Huazhong University of Science and Technology, Wuhan 430074, People's Republic of China
e-mail: huigong@mail.hust.edu.cn

© Springer International Publishing Switzerland 2016

Q. Luo et al. (eds.), *Oxygen Transport to Tissue XXXVIII*, Advances in Experimental Medicine and Biology 923, DOI 10.1007/978-3-319-38810-6_31

1 Introduction

The role of phonology in semantic access is a key issue in studies about reading, which has been investigated in different languages. The Dual Route Theory is the most influential, and assumes that semantics is accessed either directly via orthography or indirectly via phonology [1]. Written Chinese is a logographic system. Research on Chinese suggests that there are also two pathways in accessing semantics of Chinese characters. Many studies found that orthographic information plays a stronger role in semantic retrieval for Chinese and phonological information plays a limited role [2, 3], while other studies suggest that phonological information plays an essential role in semantic activation of Chinese [4].

The Stroop task was often used in language studies given its linguistic nature [4, 5]. The homophonic Stroop effect (SE) in behavioral performance is regarded as evidence for automatic involvement of phonology in Chinese character recognition, indicating an essential role of phonology in semantic activation [4, 6]. However, the color characters and their homophones appeared alternately in most previous studies [4, 6]. The semantic activation of the color characters might have an influence on the semantic retrieval of their homophones, which would affect the homophonic SE. Additionally, some event-related potential (ERP) studies suggested that the homophonic SE in the behavioral performance might arise from the later stage, but not the initial stage of the semantic activation for Chinese characters [5]. Thus, it is necessary to further investigate the homophonic SE to better understand the role of phonology in semantic access.

Most previous studies investigated the homophonic SE with behavioral [4, 6] or electrophysiological measures [5], while little is known about the hemodynamic activation for this effect. In the present study, the role of phonology in semantic activation of Chinese characters was studied using the Stroop task, and near-infrared spectroscopy (NIRS) was used to measure the activation of the prefrontal cortex (PFC) during the task. A block design was used in our study. The color characters appeared in one task block and their homophones appeared in another task block. Since the Stroop facilitation effect is mainly due to the inadvertent reading of words, especially when the congruent stimuli are shown in a blocked manner [7], only incongruent stimuli were used to indicate the role of the phonology.

2 Methods

Fourteen (4 girls) Chinese primary school children (age range, 8.67-11.31 years; mean age, 9.9 years; standard deviation (SD), 0.99 years) participated in this study. All subjects were right-handed, had normal or corrected-to-normal vision and normal color vision. All subjects were healthy without neurological or psychiatric disorders. Informed consent was received from each subject and their parents before the experiment. This study was approved by the Human Subjects Institutional Review Board at Huazhong University of Science and Technology.

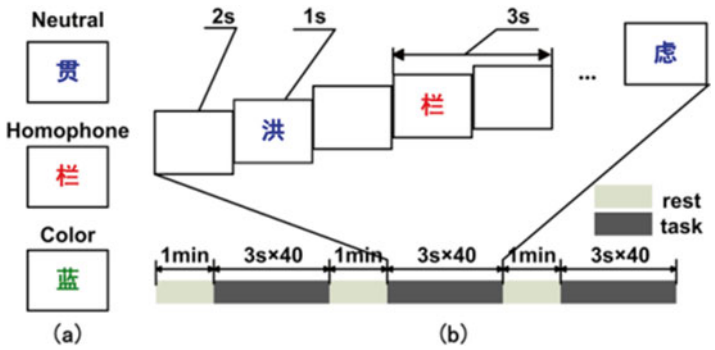

Fig. 31.1 Examples of the three types of stimuli (**a**) and the experimental procedures of the Stroop task (**b**)

There were three types of stimuli: four color characters (红, 黄, 蓝, 绿 mean "red", "yellow", "blue", and "green"), their corresponding homophones (洪, 皇, 栏, 虑 mean "flood", "emperor", "fence" and "ponder") and four neutral (color-irrelevant) characters (涂, 贯, 奖, 球 mean "scrawl", "pass through", "prize" and "ball"). Characters were displayed in four colors: red, yellow, blue and green. To investigate the interference effect, color characters and their corresponding homophones showed only in the incongruent color. The subjects were instructed to judge the color of the stimulus as fast and accurately as possible. They pressed "D", "F", "J" and "K" for characters shown in "red", "yellow", "blue" and "green", respectively.

The experiment consisted of three rest blocks and three task blocks (neutral, homophone and color task block for each kind of stimuli). In each rest block, a white cross was shown in the centre of the screen for 1 min. In each task block, 40 stimulus trials were presented in a pseudorandom order. In each trial, an empty screen remained for 2 s, followed by a stimulus showing for 1 s (Fig. 31.1). Before the formal experiment, there was a practice session to ensure that subjects were familiar with the task. The task block order was counterbalanced across subjects.

A portable, continuous-wave NIRS system [8], developed by the Britton Chance Center for Biomedical Photonics, was used to detect the concentration changes of oxy-hemoglobin (Δ[HbO2]), deoxy-hemoglobin (Δ[Hb]) and tot-hemoglobin (Δ[tHb]). The NIRS system consists of a personal computer, a measuring and controlling module, and a probe [8]. The probe held four sources and ten detectors, providing 16 detector channels (Ch1–16, Fig. 31.2). The distance between the source and the detector was about 2.45 cm. The probe covered almost the whole forehead of the subject during the experiment.

For behavioral data, trials with response time (RT) greater than 3 SD above the mean values were excluded from the analysis (<1 %). Since the SE decreases with practice [9], only the first 20 stimuli in each task block were included in the behavioral and NIRS data analyses.

The raw optical data were converted to change in optical density (ΔOD) values, then converted to hemodynamic parameters (Δ[HbO2], Δ[Hb] and Δ[tHb]), and

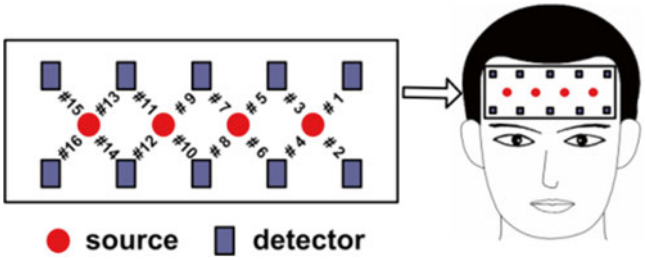

Fig. 31.2 The NIRS probe and the schematic of NIRS measurement channel locations on the head

finally bandpass filtered with a frequency range from 0.001 to 0.1 Hz to remove the slow baseline drifts and other physiological noise. Because Δ[HbO2] has a higher amplitude and a better signal-to-noise ratio than the other two parameters [10], Δ[HbO2] was used for the statistical analyses. The mean values of Δ[HbO2] for the baseline (the last 30-s rest before the task) and the task (the first 60 s of the task) were calculated for each channel, task and subject. The difference in the mean values of Δ[HbO2] between the task and the baseline was taken as the task activation. The activation was compared between tasks using paired t-tests in a channel-wise manner. The results reached significant level if $p<0.05$. The t value maps were constructed by using the inverse distance weighting method [11].

3 Results

Behavioral results: Figure 31.3 displays the average RT and error rate for each task. The repeated-measures ANOVA revealed a significant task effect for RT [$F(2,26)=6.102$; $p=0.007$]. Follow-up multiple comparisons showed that RT for the color task was evidently longer than the neutral ($p=0.019$) and homophone tasks ($p=0.022$), while the RT for the homophone task did not differ significantly from the RT for the neutral task ($p=0.888$). For error rate, although the task effect was not significant [$F(2,26)=2.443$; $p=0.107$], further multiple comparisons showed that the error rate for the color task was significantly higher than the neutral task ($p=0.008$).

NIRS results: Fig. 31.4 shows the temporal responses of Δ[HbO2], Δ[tHb] and Δ[Hb] to each task at Ch5 from one representative subject, and the group-averaged homophonic and color SE at each channel represented by Δ[HbO2]. The classical (color) SE was significant in the bilateral PFC (left: Ch4/5/7; right Ch11/13/16) ($p<0.05$), while the homophonic SE was not evident ($p>0.05$). Figure 31.5 show the t value maps from the homophonic and classical SE tests, respectively. The activation for the color task was also significantly stronger than the homophone task in the bilateral PFC (left: Ch1/3/5/7; right: Ch11/13/16) ($p<0.05$.

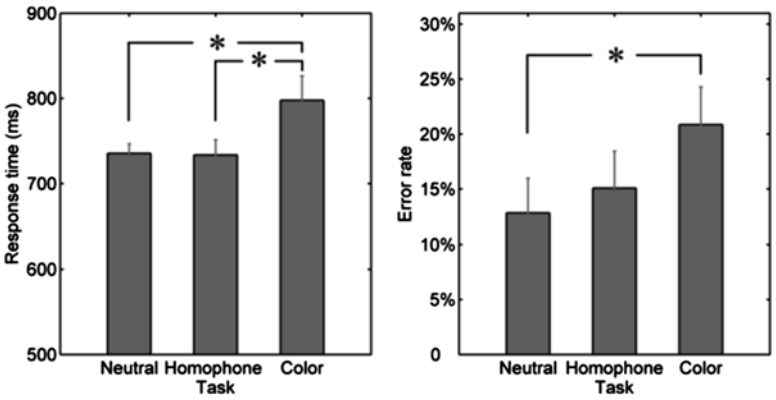

Fig. 31.3 The response time (*left*) and error rate (*right*) for each task. The data are shown as mean ± standard error (SE). "*" indicates a significant difference between tasks ($p < 0.05$)

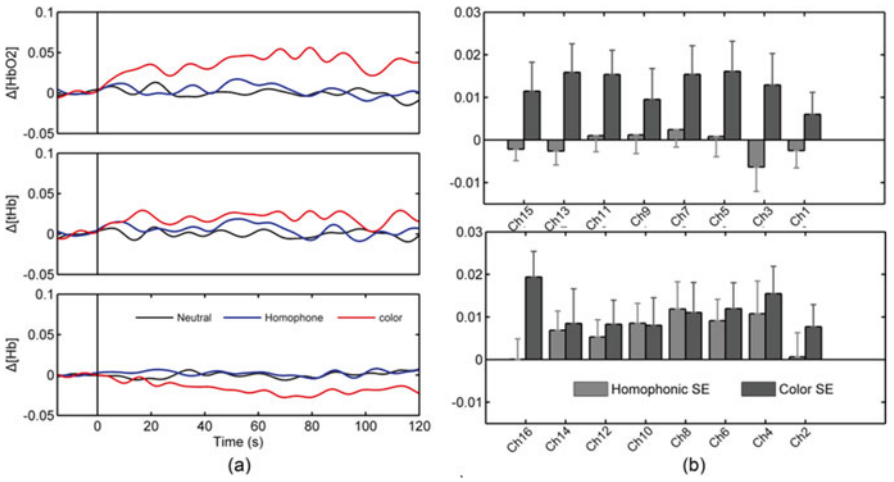

Fig. 31.4 (**a**) Time courses of measured parameters to each task at Ch5 from one representative subject. The line at time zero indicates start of the task. (**b**) Mean homophonic SE and color SE represented by Δ[HbO2] at each channel (mean ± SE)

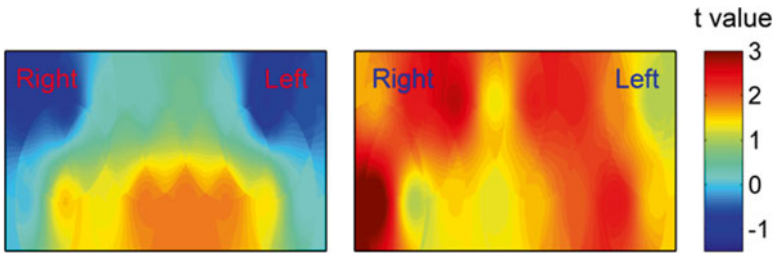

Fig. 31.5 2D maps for the *t* values from the homophonic (*left*) and classical SE (*right*) tests

4 Discussion

In this study, there was a significant classic SE in behavioral performance (RT and error rate) and in prefrontal activation, which was consistent with previous studies [4, 12]. The involvement of the bilateral PFC in the Stroop task agreed with previous studies [13], which proved the validity of our data.

The homophonic SE was not significant either in the behavioral performance or in prefrontal activation. These results differ from the research of Spinks et al. and Guo et al. [4, 6]. The reason for this might be the difference in the task design. In our study, the block design was used. The color characters appeared in one task block and their homophones appeared in another task block, which could decrease the influence of the color characters on the semantic retrieval of their homophones. Additionally, congruent stimuli were not included, which prevented the inadvertent word reading to some extent [7]. This design can better investigate whether the phonology is automatically involved in semantic access. Since the Stroop interference effect was produced by the conflict between the word's meaning and color naming, the absence of the evident homophonic SE indicates that phonological codes of the color homophones have not been effectively activated. In fact, the absence of the homophonic SE was consistent with some studies [14, 15]. Our study improves understanding of neural correlates of homophonic SE, and suggests that the phonology does not play an essential role in semantic activation of Chinese characters, which agrees with some previous ERP studies [5].

The longer response time and stronger activation in the PFC of the color task compared with the homophone task indicates that the semantic activation is stronger by combining the phonological and orthographic information than using only the phonological information. Together with the absence of the homophonic SE, our results support that orthography dominates over phonology in access to semantics of Chinese characters for children, which is consistent with many previous studies [2, 3].

Our study indicates that phonology does not play an important role in the initial semantic activation of Chinese character for children. Studies have also identified that dorsolateral PFC and some language areas (such as Broca's area) are importantly involved in the classic Stroop task [16–18], showing significant Stroop effect in these areas. In the future, we can use a fiber-based NIRS [19] system to measure more brain areas involved in the Stroop task to better understand the role of the phonology in semantic access of Chinese.

Acknowledgments The authors would like to acknowledge the support from the PhD research startup foundation of Guangdong Medical University (2XB14006).

References

1. Coltheart M, Rastle K, Perry C et al (2001) DRC: a dual route cascaded model of visual word recognition and reading aloud. Psychol Rev 108:204–256
2. Meng XZ, Jian J, Shu H et al (2008) ERP correlates of the development of orthographical and phonological processing during Chinese sentence reading. Brain Res 1219:91–102

3. Zhou X, Ye Z, Cheung H et al (2009) Processing the Chinese language: an introduction. Lang Cogn Process 24:929–946
4. Guo T, Peng D, Liu Y (2005) The role of phonological activation in the visual semantic retrieval of Chinese characters. Cognition 98:B21–B34
5. Wang K, Mecklinger A, Hofmann J et al (2010) From orthography to meaning: an electrophysiological investigation of the role of phonology in accessing meaning of Chinese single-character words. Neuroscience 165:101–106
6. Spinks JA, Liu Y, Perfetti CA et al (2000) Reading Chinese characters for meaning: the role of phonological information. Cognition 76:B1–B11
7. MacLeod CM, MacDonald PA (2000) Interdimensional interference in the Stroop effect: uncovering the cognitive and neural anatomy of attention. Trends Cogn Sci 4:383–391
8. Lv X, Zheng Y, Li T et al (2008) A portable functional imaging instrument for psychology research based on near-infrared spectroscopy. Front Optoelectron China 1:279–284
9. Milham MP, Banich MT, Claus ED et al (2003) Practice-related effects demonstrate complementary roles of anterior cingulate and prefrontal cortices in attentional control. Neuroimage 18:483–493
10. Strangman G, Culver JP, Thompson JH et al (2002) A quantitative comparison of simultaneous BOLD fMRI and NIRS recordings during functional brain activation. Neuroimage 17: 719–731
11. Aihara T, Takeda Y, Takeda K et al (2012) Cortical current source estimation from electroencephalography in combination with near-infrared spectroscopy as a hierarchical prior. Neuroimage 59:4006–4021
12. Sun J, Zhai J, Song R et al (2011) Reduced prefrontal cortex activation in the color-word Stroop task for Chinese dyslexic children: a near-infrared spectroscopy study. J Phys Conf Ser 277:012034
13. Schroeter ML, Zysset S, Wahl M et al (2004) Prefrontal activation due to Stroop interference increases during development—an event-related fNIRS study. Neuroimage 23:1317–1325
14. Zhang X, Hu C (2011) The deaf college students' phonological facilitation effects in the Stroop paradigm. J Chongqing Normal Univ (Nat Sci) 1:021
15. Chen X, Zhang J (2004) The automatic activation of morphological, phonological, semantic information of Chinese words in color word interference. Psychol Sci 27:1112–1115
16. January D, Trueswell JC, Thompson-Schill SL (2009) Co-localization of stroop and syntactic ambiguity resolution in Broca's area: implications for the neural basis of sentence processing. J Cogn Neurosci 21:2434–2444
17. Sun J, Sun B, Zhang L et al (2013) Correlation between hemodynamic and electrophysiological signals dissociates neural correlates of conflict detection and resolution in a Stroop task: a simultaneous near-infrared spectroscopy and event-related potential study. J Biomed Opt 18:096014
18. Jourdan Moser S, Cutini S, Weber P et al (2009) Right prefrontal brain activation due to Stroop interference is altered in attention-deficit hyperactivity disorder—a functional near-infrared spectroscopy study. Psychiatry Res 173:190–195
19. Zhang Z, Sun B, Gong H et al (2012) A fast neuronal signal-sensitive continuous-wave near-infrared imaging system. Rev Sci Instrum 83:094301

Chapter 32
Improvement of Impaired Cerebral Microcirculation Using Rheological Modulation by Drag-Reducing Polymers

D.E. Bragin, Z. Peng, O.A. Bragina, G.L. Statom, M.V. Kameneva, and E.M. Nemoto

Abstract Nanomolar intravascular concentrations of drag-reducing polymers (DRP) have been shown to improve hemodynamics and survival in animal models of ischemic myocardium and limb, but the effects of DRP on the cerebral microcirculation have not yet been studied. We recently demonstrated that DRP enhance microvascular flow in normal rat brain and hypothesized that it would restore impaired microvascular perfusion and improve outcomes after focal ischemia and traumatic brain injury (TBI). We studied the effects of DRP (high molecular weight polyethylene oxide, 4000 kDa, *i.v.* at 2 μg/mL of blood) on microcirculation of the rat brain: (1) after permanent middle cerebral artery occlusion (pMCAO); and (2) after TBI induced by fluid percussion. Using in vivo two-photon laser scanning microscopy (2PLSM) over the parietal cortex of anesthetized rats we showed that both pMCAO and TBI resulted in progressive decrease in microvascular circulation, leading to tissue hypoxia (NADH increase) and increased blood brain barrier (BBB) degradation. DRP, injected post insult, increased blood volume flow in arterioles and red blood cell (RBC) flow velocity in capillaries mitigating capillary stasis, tissue hypoxia and BBB degradation, which improved neuronal survival (Fluoro-Jade B, 24 h) and neurologic outcome (Rotarod, 1 week). Improved microvascular perfusion by DRP may be effective in the treatment of ischemic stroke and TBI.

Keywords Cerebral blood flow • Drag reducing polymers • Ischemia • Rheological modulation • Traumatic brain injury

D.E. Bragin (✉) • O.A. Bragina • G.L. Statom • E.M. Nemoto
Department of Neurosurgery, University of New Mexico, Albuquerque, NM, USA
e-mail: dbragin@salud.unm.edu

Z. Peng
Department of Neurosurgery, Central South University, Changsha, China

M.V. Kameneva
McGowan Institute for Regenerative Medicine, University of Pittsburgh, Pittsburgh, PA, USA

© Springer International Publishing Switzerland 2016

Q. Luo et al. (eds.), *Oxygen Transport to Tissue XXXVIII*, Advances in Experimental Medicine and Biology 923, DOI 10.1007/978-3-319-38810-6_32

1 Introduction

Although ischemic stroke and traumatic brain injury (TBI) arise from very different initial insults, the mechanisms involved in the injury process have many similarities [1]. Among them is a reduction in cerebral blood flow (CBF) leading to microvascular circulation impairment and deprivation of oxygen and glucose delivery to tissue.

Currently, there are no approved therapies targeting impaired CBF after TBI and only one targeting impaired CBF after ischemic stroke, but that one is limited by a short treatment window.

Rheological modulation of the blood circulation by minute quantities of drag reducing polymers (DRP) was demonstrated to improve circulation and survival in animal models of hemorrhagic shock, ischemic myocardium and limbs. However, except for one qualitative study [2], the effects of DRP on the impaired cerebral circulation have not yet been studied. We recently showed that DRP enhanced microvascular flow and tissue oxygenation in a healthy rat brain. Here, we examine the acute effects of DRP on impaired cerebral microcirculation and oxygen delivery after TBI induced by fluid percussion, and ischemic stroke induced by permanent middle cerebral artery occlusion (pMCAO), and the translation of these effects into long-term neurologic outcome and function.

2 Methods

2.1 Study Paradigm

Most of the procedures used in these studies were previously described [3, 4]. The fluid percussion was used as a model of TBI and was induced by 1.5 ATA 50 ms pulse from a custom-built Pneumatic Impactor connected to the brain through a pressure transducer filled with artificial cerebrospinal fluid [5]. The suture pMCAO was used as a model of ischemic injury [6].

The acute effects of DRP on microvascular blood flow velocity, tissue oxygenation (NADH) and blood brain barrier (BBB) permeability were measured on laboratory acclimated, male, Sprague–Dawley rats weighing 250–300 g by two-photon laser scanning microscopy (2PLSM) under 2 % isoflurane/69%nitrous oxide/28 % oxygen anesthesia via a cranial window over the left parietal cortex. After baseline imaging, TBI or pMCAO was induced and, after post-insult imaging and DRP (2 μg/mL in blood) or saline *i.v.* injection, the consequent imaging was followed during 4 h. Doppler flux was measured via a lateral temporal window using a 0.9 mm diameter probe (DRT4, Moor Inst., Axminster, UK) in the same region of the brain studied by 2PLSM. Brain and rectal temperatures were monitored and controlled at 38 ± 0.5 °C. Arterial blood gases, electrolytes, hematocrit and pH were measured hourly.

Neurodegeneration was examined by Fluoro-Jade B staining at 24 h after insult [7]. Coordination and motor deficits were evaluated by Rotarod at 1 week after insults [8]. Time to dismount with increasing speed of rotation was used as a measure of deficit.

2.2 Two-Photon Laser Scanning Microscopy

Fluorescent serum (tetramethylrhodamine isothiocyanate (TAMRA) dextran, 500 kDa in physiological saline, 5 % wt/vol) was visualized using an Olympus BX 51WI upright microscope and water-immersion LUMPlan FL/IR 20X/0.50 W objective. Excitation was provided by a PrairieView Ultima multiphoton microscopy laser scan unit powered by a Millennia Prime 10 W diode laser source pumping a Tsunami Ti:Sapphire laser (Spectra-Physics, Mountain View, CA, USA) tuned to 750 nm center wavelength. Band-pass-filtered epifluorescence (560–660 nm for TAMRA and 425–475 nm for NADH) was collected by photomultiplier tubes of the Prairie View Ultima system. Images (512 × 512 pixels, 0.15 μm/pixel in the *x*- and *y*-axes) or line scans were acquired using Prairie View software. Red blood cell flow velocity was measured in microvessels ranging from 3 to 50 μm diameter up to 500 μm below the surface of the parietal cortex as previously described [3, 4]. Tissue hypoxia was assessed by measurement of NADH autofluorescence and BBB permeability by TAMRA transcapillary extravasation. In offline analyses using NIH ImageJ software, three-dimensional anatomy of the vasculature in areas of interest were reconstructed from two-dimensional (planar) scans of the fluorescence intensity obtained at successive focal depths in the cortex (XYZ stack).

Statistical analyses were done by Student's *t*-test or Kolgomorov-Smirnov test where appropriate. Differences between groups were determined using two-way analysis of variance (ANOVA) for multiple comparisons and post hoc testing using the Mann–Whitney *U*-test. Statistical significance level was set at $p < 0.05$.

3 Results

3.1 Acute Effects on Cerebral Blood Flow and Metabolism

Both TBI and pMCAO progressively decreased microvascular circulation with development of tissue hypoxia and BBB damage in peri-injury or penumbra zones of the rat brain, respectively. DRP injection significantly increased arteriolar blood volume flow in both, TBI (from 71.3 ± 10.5 to 84.3 ± 9.4 %) and pMCAO (from 67.3 ± 11.3 to 81.8 ± 10.2 %) that was not observed in saline-treated animals (Fig. 32.1a, $p < 0.05$). The increase in arteriolar blood volume flow restored circulation in collapsed capillaries by 24 ± 6.7 % and 31.0 ± 7.1 % compared to saline after

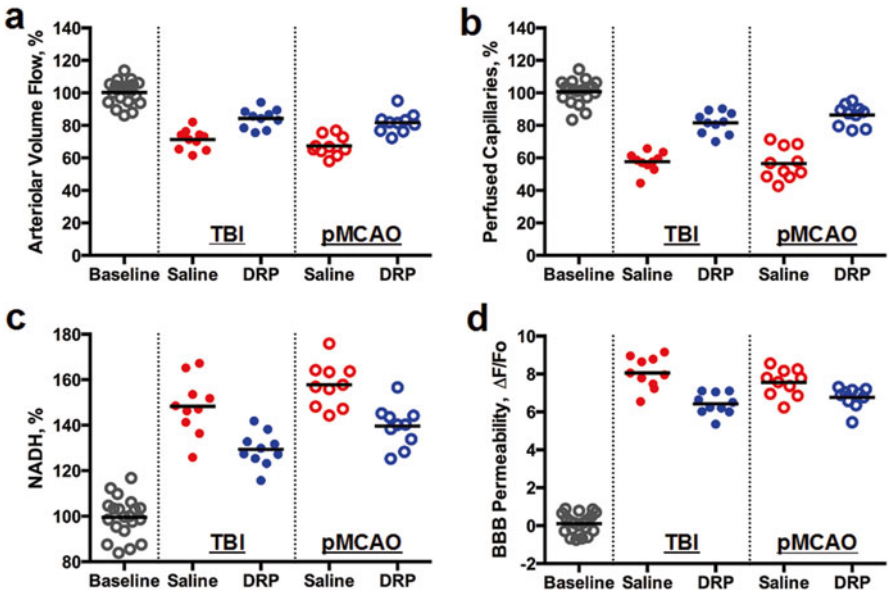

Fig. 32.1 Intravenous injection of DRP in acute period of TBI or pMCAO: (**a**) increases arteriolar volume flow; (**b**) increases number of perfused capillaries; (**c**) improves tissue oxygenation (NADH); and (**d**) attenuates BBB damage ($N = 10$ rats per group)

TBI and pMCAO, respectively (Fig. 32.1b, $p < 0.05$). The improved capillary perfusion increased tissue oxygenation reflected by a decrease of NADH autofluorescence by $18 \pm 4.6\,\%$ and $17.0 \pm 6.5\,\%$ comparing saline after TBI and pMCAO, respectively (Fig. 32.1c, $p < 0.05$). DRP also reduced BBB damage in microvessels, as quantified by measurement of perivascular tissue fluorescence reflecting the rate of TAMRA dextran extravasation. The fluorescence ratios ($\Delta F/Fo_{[pre\text{-}injury]}$) were 8.7 ± 0.8 vs. 7.1 ± 0.9 for TBI saline vs. DRP and 8.3 ± 0.9 vs. 7.2 ± 0.6 for pMCAO saline vs. DRP, respectively (Fig. 32.1d, $p < 0.05$).

3.2 Long-Term Outcome

The microvascular flow and tissue oxygenation improved by DRP reduced neurodegeneration by $37.6 \pm 11.2\,\%$ (TBI) and $44.2 \pm 12.6\,\%$ (pMCAO) compared to saline as measured 24 h post-insult by Fluoro-Jade B staining (Fig. 32.2a, $p < 0.05$). Evaluation of neurological motor deficits by Rotarod tests at 1 week after insults revealed that DRP-treated rats performed significantly better than saline-treated animals. Rotarod latency times were $75.6 \pm 16.0\,\%$ vs. $47.3 \pm 15.2\,\%$, for TBI-DRP vs. TBI-saline rats and $78.2 \pm 19.0\,\%$ vs. $51.4 \pm 17.3\,\%$, for pMCAO-DRP vs. pMCAO-saline from a baseline, respectively (Fig. 32.2b, $p < 0.05$).

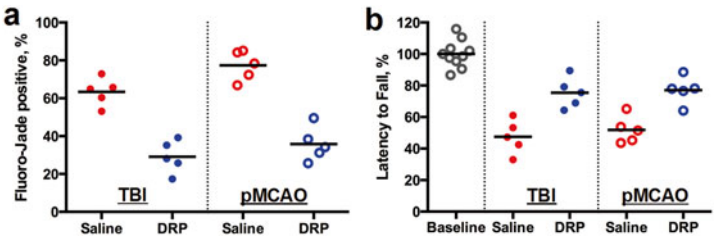

Fig. 32.2 (**a**) Intravenous injection of DRP reduces neurodegeneration as measured 24 h post-insult by Fluoro-Jade B staining and (**b**) improves neurologic outcome as measured by Rotarod test for motor and coordination deficits 1 week after TBI or pMCAO ($N=5$ rats per group)

4 Discussion

After TBI or ischemic stroke, DRP improve impaired cerebral microvascular perfusion thereby reducing tissue hypoxia and BBB degradation and protecting neurons from death, which translates into improved neurologic outcome. Based on our data and previous in vitro [9, 10] and in vivo [11] studies, we could speculate that the mechanisms of increasing the arteriolar blood volume flow include an increase of flow velocity by reduction of flow separations and vortices at vessel bifurcations and increasing a pressure gradient across the arterial vessel network due to the viscoelastic properties of DRP. This leads to a rise in the pre-capillary blood pressure thus enhancing capillary perfusion and countering capillary stasis.

DRP also reduce the near-wall cell-free layer increasing wall shear stress and decreasing plasma skimming at vessel bifurcations (i.e., lowering hematocrit in daughter branches of microvessels), described in vitro [12, 13] and in vivo [14] which could explain protection of the BBB. Recent studies reported that increased wall shear stress restrains expression of proinflammatory cytokines that initiate a signaling cascade leading to activation of BBB damage [15, 16].

Due to the absence of effective therapies for impaired cerebral microcirculation leading to tissue hypoxia, despite the numerous pharmacological treatments successfully tested in animals that failed clinically, the use of DRP is a promising approach for the treatment of TBI, ischemic stroke and other low CBF pathologic conditions.

Acknowledgments This work was supported by AHA 14GRNT20380496 and NIH 8P30GM103400 and R21NS091600.

References

1. Bramlett HM, Dietrich WD (2004) Pathophysiology of cerebral ischemia and brain trauma: similarities and differences. J Cereb Blood Flow Metab 24(2):133–150
2. Gannushkina IV, Grigorian SS, Kameneva MV et al (1982) Possibility of restoring the cerebral blood flow in cerebral ischemia by injecting special polymers into the blood. Pat Fiz Eksp Ter 3:58–59

3. Bragin DE, Bush RC, Muller WS et al (2011) High intracranial pressure effects on cerebral cortical microvascular flow in rats. J Neurotrauma 28(5):775–785
4. Bragin DE, Bush RC, Nemoto EM (2013) Effect of cerebral perfusion pressure on cerebral cortical microvascular shunting at high intracranial pressure in rats. Stroke 44(1):177–181
5. Dixon CE, Lyeth BG, Povlishock JT et al (1987) A fluid percussion model of experimental brain injury in the rat. J Neurosurg 67(1):110–119
6. Foley LM, Hitchens TK et al (2010) Quantitative temporal profiles of penumbra and infarction during permanent middle cerebral artery occlusion in rats. Transl Stroke Res 1(3):220–229
7. Schmued LC, Hopkins KJ (2000) Fluoro-Jade B: a high affinity fluorescent marker for the localization of neuronal degeneration. Brain Res 874(2):123–130
8. Hamm RJ, Pike BR, O'Dell DM et al (1994) The rotarod test: an evaluation of its effectiveness in assessing motor deficits following traumatic brain injury. J Neurotrauma 11(2):187–196
9. Kameneva MV, Polyakova MS, Fedoseeva EV (1990) Effect of drag-reducing polymers on the structure of the stagnant zones and eddies in models of constricted and branching blood vessels. Fluid Dynamics 25:956–959
10. Kameneva MV, Poliakova MS, Gvozdkova IA (1988) The nature of the effect of polymers reducing hydrodynamic resistance on blood circulation. Dokl Akad Nauk SSSR 298(5): 1253–1256
11. Pacella JJ, Kameneva MV, Brands J et al (2012) Modulation of pre-capillary arteriolar pressure with drag-reducing polymers: a novel method for enhancing microvascular perfusion. Microcirculation 19(7):580–585
12. Kameneva MV, Wu ZJ, Uraysh A et al (2004) Blood soluble drag-reducing polymers prevent lethality from hemorrhagic shock in acute animal experiments. Biorheology 41(1):53–64
13. Zhao R, Marhefka JN, Antaki JF et al (2010) Drag-reducing polymers diminish near-wall concentration of platelets in microchannel blood flow. Biorheology 47(3–4):193–203
14. Brands J, Kliner D, Lipowsky HH, Kameneva MV et al (2013) New insights into the microvascular mechanisms of drag reducing polymers: effect on the cell-free layer. PLoS One 8(10):e77252
15. Walsh TG, Murphy RP, Fitzpatrick P et al (2011) Stabilization of brain microvascular endothelial barrier function by shear stress involves VE-cadherin signaling leading to modulation of pTyr-occludin levels. J Cell Physiol 226(11):3053–3063
16. Rochfort KD, Collins LE, McLoughlin A et al (2015) Shear-dependent attenuation of cellular ROS levels can suppress proinflammatory cytokine injury to human brain microvascular endothelial barrier properties. J Cereb Blood Flow Metab. doi: 10.1038/jcbfm.2015.102

Chapter 33
Relationship Between Cerebral Oxygenation and Metabolism During Rewarming in Newborn Infants After Therapeutic Hypothermia Following Hypoxic-Ischemic Brain Injury

Subhabrata Mitra, Gemma Bale, Judith Meek, Cristina Uria-Avellanal, Nicola J. Robertson, and Ilias Tachtsidis

Abstract Therapeutic hypothermia (TH) has become a standard of care following hypoxic ischemic encephalopathy (HIE). After TH, body temperature is brought back to 37 °C over 14 h. Lactate/N-acetylasperatate (Lac/NAA) peak area ratio on proton magnetic resonance spectroscopy (^{1}H MRS) is the best available outcome biomarker following HIE. We hypothesized that broadband near infrared spectroscopy (NIRS) measured changes in the oxidation state of cytochrome-c-oxidase concentration (Δ[oxCCO]) and cerebral hemodynamics during rewarming would relate to Lac/NAA. Broadband NIRS and systemic data were collected during rewarming from 14 infants following HIE over a mean period of 12.5 h. ^{1}H MRS was performed on day 5–9. Heart rate increased by 20/min during rewarming while blood pressure and peripheral oxygen saturation (SpO_2) remained stable. The relationship between mitochondrial metabolism and oxygenation (measured as Δ[oxCCO] and Δ[HbD], respectively) was calculated by linear regression analysis. This was reviewed in three groups: Lac/NAA values <0.5, 0.5–1, >1. Mean regression coefficient (r^2) values in these groups were 0.41 (±0.27), 0.22 (±0.21) and 0.01, respectively. The relationship between mitochondrial metabolism and oxygenation became impaired with rising Lac/NAA. Cardiovascular parameters remained stable during rewarming.

The original version of this chapter was revised. An erratum to this chapter can be found at DOI 10.1007/978-3-319-38810-6_59

S. Mitra (✉) • J. Meek • C. Uria-Avellanal • N.J. Robertson
Institute for Women's Health, University College London and Neonatal Unit, University College London Hospitals Trust, London, UK
e-mail: subhabratamitra@hotmail.com

G. Bale • I. Tachtsidis
Biomedical Optics Research Laboratory, Department of Medical Physics and Biomedical Engineering, University College London, London, UK

© The Author(s) 2016

Q. Luo et al. (eds.), *Oxygen Transport to Tissue XXXVIII*, Advances in Experimental Medicine and Biology 923, DOI 10.1007/978-3-319-38810-6_33

Keywords Hypoxic-ischaemic brain injury • Cerebral oxygenation • Cerebral metabolism • Cytochrome-c-oxidase • Newborn infant

1 Introduction

Perinatal hypoxic-ischaemic (HI) brain injury causes significant morbidity and mortality. Therapeutic hypothermia (TH) is beneficial following hypoxic ischemic encephalopathy (HIE) and has become the standard of care in recent years [1, 2]. During TH, body temperature is maintained at 33.5 °C followed by a slow rewarming that brings body temperature back to 37 °C. Rewarming early from TH induces cortical neuron apoptosis in a piglet model following HIE [3]. Rebound seizures have been noted during the rewarming period both in animal models [4] and neonatal intensive care [5] and further 'cooling' with slower rewarming has been suggested. Changes in cerebral metabolism and hemodynamics have been investigated in both preclinical models and clinical studies during and after HI, but the dynamic effects of rewarming on newborn cerebral metabolism and hemodynamics have not yet been fully investigated.

NIRS is a non-invasive tool that has been widely used for continuous bedside monitoring of cerebral oxygenation and hemodynamic changes. We have recently developed a new broadband NIRS system to monitor Δ[oxCCO] as well as the concentration changes of oxy- and deoxy hemoglobin (Δ[HbO_2] and Δ[HHb], respectively) in neonatal brain [6]. Cytochrome-c-oxidase (CCO) plays a crucial role in mitochondrial oxidative metabolism and ATP synthesis and is responsible for more than 95 % of oxygen metabolism in the body [7]. Changes in total hemoglobin ($HbT = HbO_2 + HHb$) and hemoglobin difference ($HbD = HbO_2 - HHb$) were calculated. Changes in HbD and HbT reflect changes in cerebral oxygenation and changes in cerebral blood volume, respectively.

Following HIE, Lac/NAA peak area ratio obtained from ^{1}H MRS is the best available MR biomarker for prediction of neurodevelopmental outcome [8].

The aim of this study was to assess the cerebral metabolic and hemodynamic changes during the rewarming period in a cohort of term infants following perinatal hypoxic-ischemic brain injury. We hypothesized that the dynamic changes in cerebral oxygenation and metabolism during the rewarming period would relate to the severity of the injury as assessed by Lac/NAA.

2 Methods

Ethical approval for the study at University College London Hospitals NHS Foundation Trust (UCLH) was obtained from the NREC (reference: 13/LO/0225). Hypothermia and subsequent rewarming were instituted with a servo-controlled cooling machine Tecotherm Neo, Inspiration Healthcare, UK. Using a cooling mattress and a rectal temperature probe, it maintains a constant core temperature during hypothermia and

increases the temperature as programmed during the rewarming period. Normally, the core temperature is increased by 0.5 °C over every 2-h period so that the temperature is increased from 33.5 to 37 °C over 14 h. Rewarming data were collected from a cohort of 14 infants. NIRS monitoring was commenced as early as possible in the rewarming phase and was continued for the maximum possible time. One NIRS channel was placed on either side of the forehead and data were collected at 1 Hz. The optode source-detector distance of 2.5 cm was chosen to ensure a good depth penetration [9]. The differential path length (DPF) was chosen as 4.99 [10]. Changes in chromophore concentrations were calculated from the measured changes in broadband NIR light attenuation using the modified Beer-Lambert law as applied with the UCLn algorithm [11] across 136 wavelengths (770–906 nm). Systemic data were collected using ixTrend software (ixellence GmbH, Germany) and were synchronised with the NIRS data. Brain magnetic resonance imaging (MRI) and MRS were performed between day 5–9 using a 3T Philips MRI scanner (Philips Healthcare, UK).

3 Data Analysis

Initial data analysis was carried out in MATLAB (Mathworks, USA). Systemic data were down-sampled and interpolated to the NIRS data timeframe (1 Hz). Artefacts from movement or changes in external lighting were removed and baseline shifts were corrected using the method suggested by Scholkmann et al. [12]. Linear regression analysis was performed to assess the relationship between Δ[oxCCO] and Δ[HbD] and an averaged regression coefficient (r^2) was created to compare this relationship between groups. All statistical analyses were performed using GraphPad Prism 6 (GraphPad Software, USA).

4 Results

NIRS and systemic data were collected over a mean period of 12.5 h (5–14 h). Active cooling was started at a mean of 3 h of age. All infants were ventilated during rewarming. Clinical characteristics of the cohort are presented in Table 33.1. During rewarming the heart rate gradually increased from a mean of 108/min (range 75–130/min) to 128/min (121–135/min). The peripheral oxygen saturation (SpO_2) fell briefly at the start of rewarming, but was mostly over 95 %. Mean blood pressure (BP) was stable throughout the rewarming (45–55 mmHg) (Fig. 33.1). Transcutaneous CO_2 dropped by mean 1.3 kPa. Changes in oxCCO concentration from both left and right side are shown in Fig. 33.2. No significant difference was noted between the two sides. The averaged regression coefficients (r^2) between Δ[oxCCO] and Δ[HbD] were plotted against Lac/NAA values obtained from ^{1}H MRS. Although in clinical practice a Lac/NAA peak area ratio >0.3 has been associated with poor neurodevelopmental outcome following HIE [8], we divided the current cohort into three groups (Lac/NAA <0.5, 0.5–1 and >1) to more explicitly demonstrate the

Table 33.1 Characteristics of the infants: data are presented as mean (range)

Infant characteristics	Mean (range)
Birth weight (g)	3161 (1770–3800)
Gestational age (weeks)	39 (38–41)
Male:female	1.3:1
Apgar score at 1 min	1 (0–4)
Apgar score at 5 min	3 (0–7)
Apgar score at 10 min	3 (0–8)
Umbilical cord pH (arterial)	6.9 (6.56–7.28)
Base excess (arterial)	−15 (9.7–24)
Serum lactate	12 (9–17)
Age at start of active cooling (min)	178 (55–284)

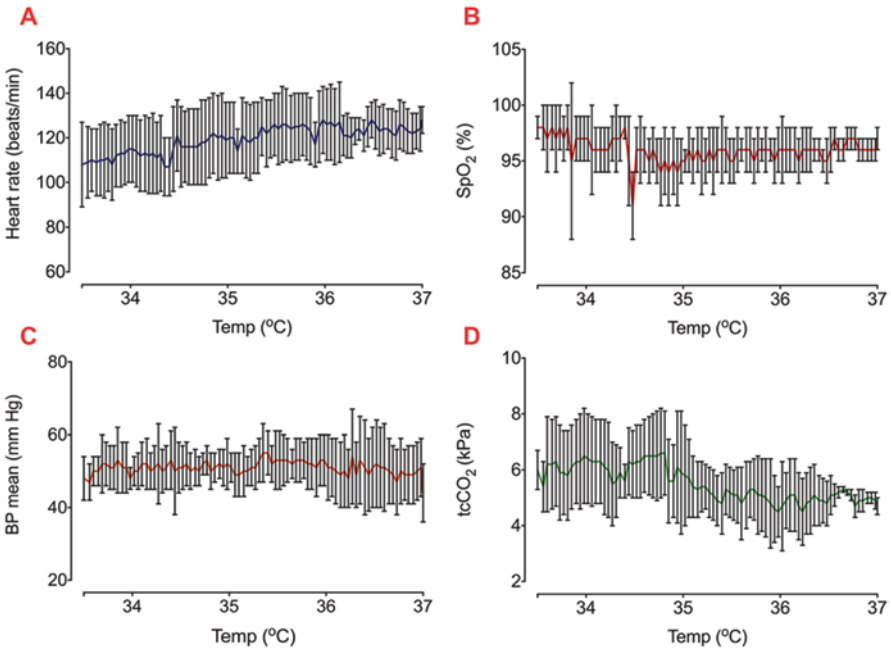

Fig. 33.1 Systemic changes (heart rate (**a**), SpO_2 (**b**), mean blood pressure (**c**) and transcutaneous CO_2 (**d**)) among all infants during rewarming (mean ± s.d.)

relationship between the average regression coefficient between Δ[oxCCO] and Δ[HbD] with Lac/NAA. Lac/NAA peak area ratio ranged from 0.08 to 1.32 in this cohort, and four infants had a value of ≥0.3. Eleven infants had Lac/NAA <0.5, 2 had Lac/NAA 0.5–1 and 1 had Lac/NAA>1. Mean r^2 values between Δ[oxCCO] and Δ[HbD] in these groups were 0.41 (±0.27), 0.22 (±0.21) and 0.01, respectively (Fig. 33.3).

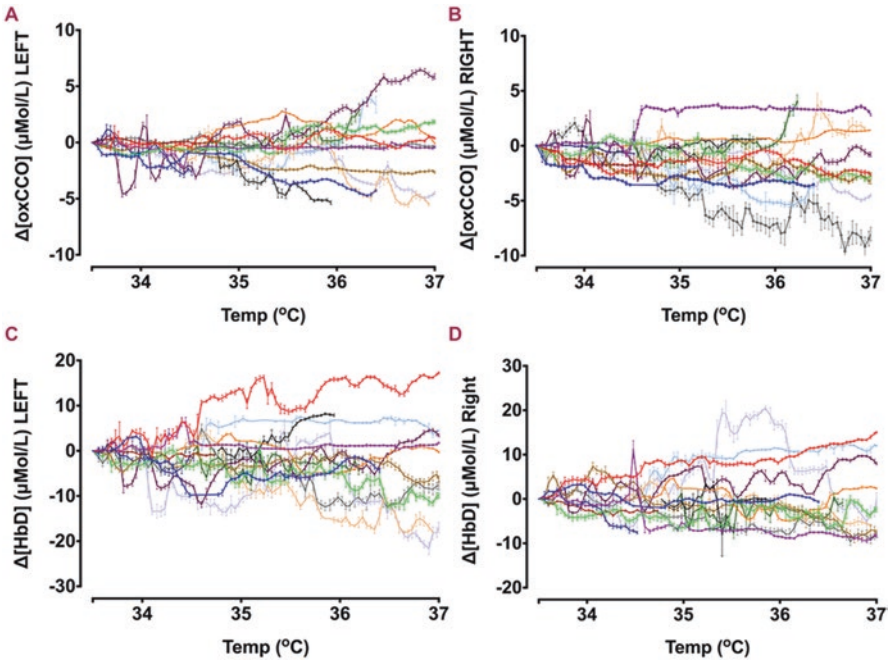

Fig. 33.2 Δ[oxCCO] (**a**, **b**) and Δ[HbD] (**c**, **d**) from both left and right sides during rewarming. Each individual color represents data from one infant

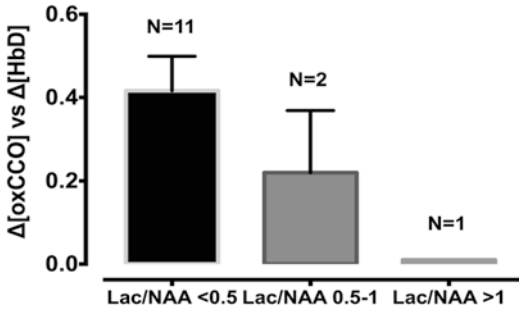

Fig. 33.3 Averaged regression coefficient (r^2) between oxCCO and HbD presented in three groups: Lac/NAA <0.5, 0.5–1 and >1

5 Discussion

The relationship between cerebral metabolism and oxygenation measured during rewarming following TH in a group of infants with HIE became more disturbed with an increasing degree of brain injury. Rewarming is a complex process; it has the potential to significantly influence cardiovascular function and stimulate the activity of excitatory amino acids suppressed during hypothermia [13].

Gebaur et al. reported that during hypothermia left ventricular output remains low due to decreased heart rate and a decreased stroke volume. During rewarming both stroke volume and cardiac output increases as the core temperature increases [14]. In

our study, heart rate increased steadily throughout rewarming but mean BP remained stable, no hypotensive episodes were noted. Our findings were similar to those of Gebauer et al. but were different from those reported by Thoresen and Whitlaw [15]. They noted changes in cardiovascular indices in 9 infants with HIE during mild hypothermia and rewarming. Mean arterial BP fell during rewarming while the heart rate increased. This difference is probably related to the process of rewarming. In the study described by Thoresen et al. rewarming was performed over a minimum of 5 h by removing the cooling cap and adjusting the overhead heater to control the rise of temperature no more than per hour. We used a servo controlled cooling machine, which increased the core temperature in a more stable way, and the rewarming was done over a much longer period. A rapid and unstable increase in core temperature most likely induces a reduced peripheral vascular tone with increased cardiac work. Rewarming at a rate of 0.5–1 °C/h did not influence the beneficial effects of therapeutic hypothermia in a rat model, but a higher rewarming rate of 2 °C/h abolished those beneficial effects on both cardiac and cerebral function (reduced severity of myocardial and cerebral functions abnormalities and attenuated release of IL-6 and TNF-α) [16].

Availability of oxygen has a significant influence on the oxidation of CCO. The relationship between mitochondrial metabolism and oxygenation became more impaired with increasing severity of injury, measured as rising Lac/NAA on ^{1}H MRS. This probably indicates that following severe HIE and cell death, cerebral metabolism failed to improve in spite of oxygen availability. We did not notice any significant pattern of changes in Δ[oxCCO] with a change in temperature, nor did we notice any specific cut-off temperature point which indicated any change in the trend of cerebral metabolism during rewarming. In near-term fetal sheep, carotid artery blood flow (CaBF) and mean arterial blood pressure (MABP) changed only transiently during rewarming. No significant difference was noted from 6 h onwards [3]. In a recent study, asphyxiated newborn infants had stable regional cerebral oxygenation during rewarming [17].

The limitation of the present study is the small number of infants enrolled and, in particular, the number of infants with severe brain injury.

We noted that the mitochondrial metabolism-oxygenation coupling during rewarming was influenced by the severity of hypoxic ischemic brain injury. Servo-controlled slow rewarming process had no significant influence on the stability of cerebrovascular hemodynamics and metabolism.

Acknowledgments We thank all the families and neonatal staff in UCLH for their support. This project was supported by EPSRC (EP/G037256/1), The Wellcome Trust (088429/Z/09/Z and 104580/Z/14/Z) and UK Department of Health's NIHR BRC funding scheme.

References

1. NICE (2010) Therapeutic hypothermia with intracorporeal temperature monitoring for hypoxic perinatal brain injury. (http://www.nice.org.uk/guidance/ipg347/chapter/1-guidance)
2. Committee on Fetus and Newborn. American Academy of Pediatrics (2014) Hypothermia and neonatal encephalopathy. Pediatrics 133(6):1146–1150

3. Wang B, Armstrong JS, Lee JH et al (2015) Rewarming from therapeutic hypothermia induces cortical neuron apoptosis in a swine model of neonatal hypoxic-ischemic encephalopathy. J Cereb Blood Flow Metab 35(5):781–793
4. Gerrits LC, Battin MR, Bennet L et al (2005) Epileptiform activity during rewarming from moderate cerebral hypothermia in the near-term fetal sheep. Pediatr Res 57(3):342–346
5. Kendall GS, Mathieson S, Meek J et al (2012) Recooling for rebound seizures after rewarming in neonatal encephalopathy. Pediatrics 130(2):e451–e455
6. Bale G, Mitra S, Meek J et al (2014) A new broadband near-infrared spectroscopy system for in-vivo measurements of cerebral cytochrome-c-oxidase changes in neonatal brain injury. Biomed Optics Express 5(10):3450–3466
7. Richter OM, Ludwig B (2003) Cytochrome c oxidase—structure, function, and physiology of a redox-driven molecular machine. Rev Physiol Biochem Pharmacol 147:47–74
8. Thayyil S, Chandrasekaran M, Taylor A et al (2010) Cerebral magnetic resonance biomarkers in neonatal encephalopathy: a meta-analysis. Pediatrics 125(2):e382–e395
9. Grant PE, Roche-Labarbe N, Surova A et al (2009) Increased cerebral blood volume and oxygen consumption in neonatal brain injury. J Cereb Blood Flow Metab 29(10):1704–1713
10. Duncan A, Meek JH, Clemence M et al (1996) Measurement of cranial optical path length as a function of age using phase resolved near infrared spectroscopy. Pediatr Res 39:889–894
11. Matcher S, Elwell C, Cooper C (1995) Performance comparison of several published tissue near-infrared spectroscopy algorithms. Anal Biochem 227(1):54–68
12. Scholkmann F, Spichtig S, Muehlemann T et al (2010) How to detect and reduce movement artifacts in near-infrared imaging using moving standard deviation and spline interpolation. Physiol Meas 31(5):649–662
13. Nakashima K, Todd MM (1996) Effects of hypothermia on the rate of excitatory amino acid release after ischemic depolarization. Stroke 27(5):913–918
14. Gebauer CM, Knuepfer M, Robel-Tillig E, Pulzer F, Vogtmann C (2006) Hemodynamics among neonates with hypoxic-ischemic encephalopathy during whole-body hypothermia and passive rewarming. Pediatrics 117(3):843–850
15. Thoresen M, Whitelaw A (2000) Cardiovascular changes during mild therapeutic hypothermia and rewarming in infants with hypoxic-ischemic encephalopathy. Pediatrics 106(1 Pt 1):92–99
16. Lu X, Ma L, Sun S et al (2014) The effects of the rate of postresuscitation rewarming following hypothermia on outcomes of cardiopulmonary resuscitation in a rat model. Crit Care Med 42(2):e106–e113
17. Peng S, Boudes E, Tan X et al (2015) Does near-infrared spectroscopy identify asphyxiated newborns at risk of developing brain injury during hypothermia treatment? Am J Perinatol 32(6):555–564

Open Access This chapter is licensed under the terms of the Creative Commons Attribution 4.0 International License (http://creativecommons.org/licenses/by/4.0/), which permits use, sharing, adaptation, distribution and reproduction in any medium or format, as long as you give appropriate credit to the original author(s) and the source, provide a link to the Creative Commons license and indicate if changes were made.

The images or other third party material in this chapter are included in the chapter's Creative Commons license, unless indicated otherwise in a credit line to the material. If material is not included in the chapter's Creative Commons license and your intended use is not permitted by statutory regulation or exceeds the permitted use, you will need to obtain permission directly from the copyright holder.

Part IV
Muscle Oxygenation and Sport Medicine

Chapter 34
Low Volume Aerobic Training Heightens Muscle Deoxygenation in Early Post-Angina Pectoris Patients

Shun Takagi, Norio Murase, Ryotaro Kime, Masatsugu Niwayama, Takuya Osada, and Toshihito Katsumura

Abstract The aim of this study was to investigate the effect of low volume aerobic exercise training on muscle O_2 dynamics during exercise in early post-angina pectoris (AP) patients, as a pilot study. Seven AP patients (age: 72 ± 6 years) participated in aerobic exercise training for 12 weeks. Training consisted of continuous cycling exercise for 30 min at the individual's estimated lactate threshold, and the subjects trained for 15 ± 5 exercise sessions over 12 weeks. Before and after training, the subjects performed ramp cycling exercise until exhaustion. Muscle O_2 saturation (SmO_2) and relative changes from rest in deoxygenated hemoglobin concentration (ΔDeoxy-Hb) and total hemoglobin concentration (ΔTotal-Hb) were monitored at the vastus lateralis by near infrared spatial resolved spectroscopy during exercise. The SmO_2 was significantly lower and ΔDeoxy-Hb was significantly higher after training than before training, while there were no significant changes in ΔTotal-Hb. These results indicated that muscle deoxygenation and muscle O_2 extraction were potentially heightened by aerobic exercise training in AP patients, even though the exercise training volume was low.

Keywords Cycling training • Ischemic heart disease • Muscle O_2 dynamics • Near infrared spectroscopy • Peak aerobic capacity

S. Takagi (✉)
Faculty of Sport Sciences, Waseda University, Tokorozawa, Saitama, Japan

Department of Sports Medicine for Health Promotion, Tokyo Medical University, Shinjuku, Tokyo, Japan
e-mail: stakagi@aoni.waseda.jp

N. Murase • R. Kime • T. Osada • T. Katsumura
Department of Sports Medicine for Health Promotion, Tokyo Medical University, Shinjuku, Tokyo, Japan

M. Niwayama
Department of Electrical and Electronic Engineering, Shizuoka University, Hamamatsu, Shizuoka, Japan

© Springer International Publishing Switzerland 2016

Q. Luo et al. (eds.), *Oxygen Transport to Tissue XXXVIII*, Advances in Experimental Medicine and Biology 923, DOI 10.1007/978-3-319-38810-6_34

1 Introduction

Heart disease patients have not only potentially impaired muscle O_2 supply due to reduced heart pump function, but also impaired muscle O_2 utilization due to muscle deconditioning. Muscle deoxygenation in heart disease patients has been reported using the near infrared spectroscopy (NIRS) technique [1, 2]. A previous study demonstrated that early after ischemic heart disease (IHD) patients, especially ones who had a relatively preserved left ventricular ejection fraction (LVEF), showed an absence of muscle deoxygenation during exercise, and the absence of muscle deoxygenation was related to low peak aerobic capacity [2].

Adequate volume of aerobic training enhances aerobic capacity and skeletal muscle deoxygenation during graded exercise in healthy young subjects [3]. In early post-IHD patients, although the traditional guideline for aerobic training frequency is 3 sessions/week, low volume aerobic training (1 or 2 sessions/week) also improves aerobic capacity [4]. However, to date, it is unclear whether muscle deoxygenation is heightened by low volume aerobic training in IHD, such as angina pectoris (AP) patients. The aim of this study was to investigate the effect of low volume aerobic exercise training on muscle O_2 dynamics during exercise in early post-AP patients.

2 Methods

2.1 Subjects

Seven AP patients were recruited 27 ± 10 (range 18–42) days after receiving coronary artery bypass grafting. At baseline, the mean left ventricular ejection fraction (LVEF) was 62 ± 7 %, as assessed by echocardiography. All medication dosages remained stable during the study. This study protocol was approved by the institutional ethics committee. All subjects were informed of the purpose of the study and written informed consent was obtained.

2.2 Experimental Design

The subjects trained for 12 weeks at the individual's estimated lactate threshold (LT), using an upright cycling ergometer. The estimated LT was determined as in previous studies [5, 6]. Training frequency was set in advance at two exercise sessions/week for 12 weeks; however, the subjects exercised at 15 ± 5 sessions over the 12 weeks' training, as their schedules permitted.

Before and after training, the subjects performed 10 W/min ramp bicycle exercise, after a 3-min warm-up at 10 W, until exhaustion (Strength Ergo 8, Fukuda-Denshi, Japan). No subjects reported chest pain during exercise. Pulmonary O_2 uptake (VO_2)

was monitored continuously throughout the exercise (AE310S, Minato Medical Science, Japan) to evaluate peak VO_2. Muscle O_2 saturation (SmO2) and relative changes from rest in oxygenated hemoglobin concentration (ΔOxy-Hb), deoxygenated hemoglobin concentration (ΔDeoxy-Hb), and total hemoglobin concentration (ΔTotal-Hb) were monitored at the vastus lateralis (VL) in the left leg by near infrared spatial resolved spectroscopy (NIR_{SRS}). The NIR_{SRS} data were averaged over the last 10 s at rest, every 10 W, and peak exercise. The measurement site in the VL was defined as 30 % of the length between the patella and the greater trochanter above the patella, as defined in previous studies [2].

We used a two-wavelength (770 and 830 nm) light-emitting diode NIR_{SRS} (Astem Co., Japan). The probe consisted of one light source and two photodiode detectors, and the optode distances were 20 and 30 mm, as were used in previous studies [2, 7]. The data sampling rate was 1 Hz. We measured fat layer thickness at the measurement site using an ultrasound device (LogiQ3, GE-Yokokawa Medical Systems, Japan), and subsequently, as applied in previous studies [2, 7], the light scattering effect of the fat layer was corrected by normalizing measurement sensitivity [8, 9]. The specifications of correction for the influence of fat layer thickness have been fully described [8, 9].

2.3 Statistics

All data are given as means ± standard deviation (SD). To compare changes in oxygen dynamics and pulmonary VO_2 during submaximal exercise (i.e. 20–50 W) between groups, a 2-way repeated-measures analysis of variance was used, with training and power output (PO) as factors. Where appropriate, the Bonferroni post-hoc test was performed to determine specific significant differences. Differences in physical variables, peak VO_2, and peak workload were compared between groups using paired t tests. For all statistical analyses, significance was accepted at $p<0.05$.

3 Results

While VO_2 during submaximal exercise (from 20 to 50 W) was not significantly changed by exercise training, exercise training significantly increased peak VO_2 (before: 15.0 ± 3.9 ml/kg/min, after: 19.2 ± 5.1 ml/kg/min, $p<0.05$), peak workloads (before: 73 ± 20 W, after: 88 ± 28 W, $p<0.05$), estimated LT (before: 10.2 ± 1.5 ml/kg/min, after: 12.6 ± 2.9 ml/kg/min, $p<0.05$), and workload at estimated LT (before: 39 ± 12 W, after: 48 ± 13 W, $p<0.05$) in AP patients. Body weight ($p=0.50$) and fat layer thickness ($p=0.66$) were not significantly altered by exercise training (Table 34.1).

Figure 34.1 presents muscle O_2 dynamics before and after exercise training in AP patients. During submaximal exercise, there was a significant training × PO interaction for SmO_2 ($p<0.05$) and ΔDeoxy-Hb ($p<0.01$). As a result, SmO_2 was

Table 34.1 Demographic and clinical information ($n=7$)

	Before	After
Age (years)	72±6	–
Height (cm)	161.2±8.5	–
Weight (kg)	62.1±11.7	61.0±13.6
Men/women	5/2	–
Fat layer thickness at VL (mm)	5.14±1.56	4.92±1.13
Medication (%)		
ACE inhibitor	14	–
Angiotensin II receptor antagonist	29	–
Antiplatelet agent	29	–
Beta blockers	57	–
Calcium channel antagonist	43	–

ACE angiotensin converting enzyme, *VL* vastus lateralis. Values are means ± standard deviation

significantly lower, and ΔDeoxy-Hb was significantly higher at a given absolute workload after training, compared with before training. We did not observe significant main effects of training in ΔOxy-Hb ($p=0.55$) or ΔTotal-Hb ($p=0.90$), nor interactions (ΔOxy-Hb: $p=0.48$, ΔTotal-Hb: $p=0.80$). In addition, at peak exercise, SmO_2 was significantly lower ($p<0.01$) and ΔDeoxy-Hb was significantly higher ($p<0.05$) after training than before training. ΔOxy-Hb at peak exercise tended to be lower after training ($p=0.09$), and no significant change was observed in ΔTotal-Hb at peak exercise ($p=0.75$). Change in ΔSmO_2 (values at peak exercise minus values at resting) by training tended to be negatively associated with change in peak VO_2 ($r=-0.69$, $p=0.09$).

4 Discussion

After exercise training, we observed lower SmO_2 and higher ΔDeoxy-Hb during exercise, while Δtotal-Hb, which is an indicator of blood volume, did not change in AP patients. Moreover, changes in ΔSmO_2 by exercise training may be related to increase in peak VO_2 in AP patients. Unfortunately, we did not have a control group (i.e. a non-training AP group or healthy elderly group). However, we confirmed that muscle deoxygenation was blunted in early post-AP patients compared to age-matched healthy subjects, and in early post-IHD patients in the non-training group no significant changes were observed before and after 12 weeks training in muscle O_2 dynamics (unpublished data). These data suggest that low volume of aerobic training heightens muscle deoxygenation and O_2 extraction in AP patients, and the change in peripheral factors may be related to increase in peak aerobic capacity. NIRS data reflect the balance between O_2 utilization and supply. Therefore, enhancement of muscle deoxygenation by exercise training implies increased muscle O_2 utilization, partly due to increased oxidative enzyme activity [10] and/or reduced muscle O_2 supply [11]. However, in this study, submaximal pulmonary VO_2 was not

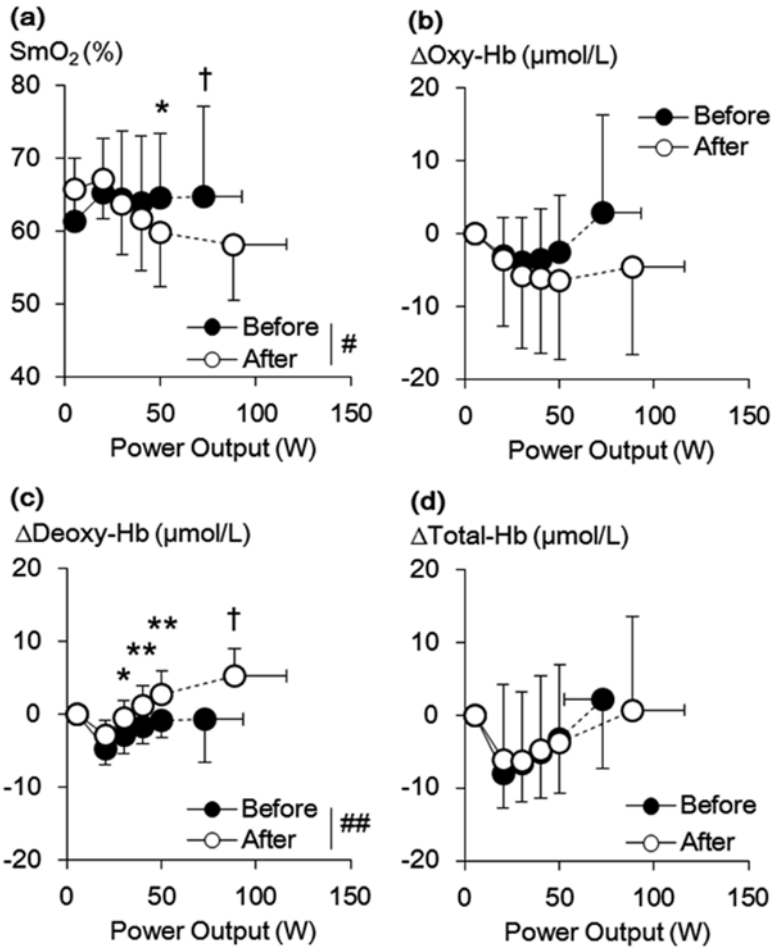

Fig. 34.1 Change in muscle O_2 saturation (SmO_2: **a**), oxygenated hemoglobin (Δoxy-Hb: **b**), deoxygenated hemoglobin (Δdeoxy-Hb: **c**), and total hemoglobin (Δtotal-Hb: **d**) responses during ramp cycling exercise before (closed circles) and after (open circles) exercise training. Significant difference between groups at a given absolute workload (*: $p<0.05$, **: $p<0.01$). Significant difference between groups at peak exercise (†: $p<0.05$). There was a significant training and power output interaction (#: $p<0.05$, ##: $p<0.01$). Symbols indicating a significant difference between power output in both groups have been omitted for the sake of clarity

significantly improved by training. Therefore, a change in blood distribution may have occurred in this study, as a training adaptation, as seen in rat experiments [12].

In elderly subjects, low volume aerobic exercise training (15 ± 6 sessions) at estimated LT for 30 min did not enhance muscle desaturation response during exercise [7]. In the present study, muscle desaturation response was enhanced by a similar volume of exercise training to the previous study [7]. One possible explanation for disparities in training effects may be the initial level of the subject's peak aerobic

capacity. In general, if the same volume of exercise training is conducted, a gain of peak aerobic capacity is higher in an individual who has low aerobic capacity than an individual with higher aerobic capacity [13]. In fact, a greater increase in ΔDeoxy-Hb at peak exercise by exercise training tends to be related to a lower initial level of peak aerobic capacity ($r=-0.69$, $p=0.09$). In addition, these disparities in the effects of exercise training between studies may be partly explained by pump functions of heart (i.e. convective O_2 supply) before training.

Remarkably, SmO_2 at rest seemed to be lower in AP before training, compared to previous values of elderly subjects ($69.1 \pm 3.6\%$) [7], even though the difference in SmO_2 at rest before and after training did not reach statistical significance ($p=0.18$). These results lead us to speculate that non-essential circulation at rest may already be sacrificed in some AP patients.

In conclusion, muscle deoxygenation and O_2 extraction were potentially heightened by aerobic exercise training in AP patients, even though the exercise training volume was low.

Acknowledgments The authors are grateful for revision of this manuscript by Andrea Hope. We also thank Dr. Shoko Nioka for her helpful suggestions. This work was supported in part by JSPS KAKENHI Grant Number 26882044 to S.T.

References

1. Wilson JR, Mancini DM, McCully K et al (1989) Noninvasive detection of skeletal muscle underperfusion with near-infrared spectroscopy in patients with heart failure. Circulation 80(6):1668–1674
2. Takagi S, Murase N, Kime R et al (2014) Skeletal muscle deoxygenation abnormalities in early post-myocardial infarction. Med Sci Sports Exerc 46(11):2062–2069
3. Kime R, Niwayama M, Fujioka M et al (2010) Unchanged muscle deoxygenation heterogeneity during bicycle exercise after 6 weeks of endurance training. Adv Exp Med Biol 662:353–358
4. Dressendorfer RH, Franklin BA, Cameron JL et al (1995) Exercise training frequency in early post-infarction cardiac rehabilitation. Influence on aerobic conditioning. J Cardiopulm Rehabil 15(4):269–276
5. Beaver WL, Wasserman K, Whipp BJ (1986) A new method for detecting anaerobic threshold by gas exchange. J Appl Physiol 60(6):2020–2027
6. Wasserman K, Whipp BJ, Koyl SN (1973) Anaerobic threshold and respiratory gas exchange during exercise. J Appl Physiol 35(2):236–243
7. Takagi S, Kime R, Murase N et al (2016) Effects of low volume aerobic training on muscle desaturation during exercise in elderly subjects. Adv Exp Med Biol 876:63–70
8. Niwayama M, Suzuki H, Yamashita T et al (2012) Error factors in oxygenation measurement using continuous wave and spatially resolved near-infrared spectroscopy. J Jpn Coll Angiol 52:211–215
9. Niwayama M, Lin L, Shao J et al (2000) Quantitative measurement of muscle hemoglobin oxygenation using near-infrared spectroscopy with correction for the influence of a subcutaneous fat layer. Rev Sci Instrum 71(12):4571–4575
10. Ades PA, Waldmann ML, Meyer WL et al (1996) Skeletal muscle and cardiovascular adaptations to exercise conditioning in older coronary patients. Circulation 94(3):323–330

11. Clausen JP, Trap-Jensen J (1970) Effects of training on the distribution of cardiac output in patients with coronary artery disease. Circulation 42(4):611–624
12. Armstrong RB, Laughlin MH (1984) Exercise blood flow patterns within and among rat muscles after training. Am J Physiol 246(1 Pt 2):H59–H68
13. Wenger HA, Bell GJ (1986) The interactions of intensity, frequency and duration of exercise training in altering cardiorespiratory fitness. Sports Med 3(5):346–356

Chapter 35
The Effects of Passive Cycling Exercise for 30 min on Cardiorespiratory Dynamics in Healthy Men

Sayuri Fuse, Ryotaro Kime, Takuya Osada, Norio Murase, and Toshihito Katsumura

Abstract An increase in the incidence rate of cardiovascular disease is attributed to high daily sitting time, while a drop in risk of cardiovascular disease comes from a decrease in daily sitting time, rather than an increase in physical activity levels. Although short-duration passive exercise increases energy expenditure and blood flow, few studies have reported on the responses of cardiorespiratory dynamics to long-duration passive exercise. The purpose of this study was to consider the effect of long-duration passive exercise for 20 min on cardiorespiratory and muscle oxygen dynamics. Eight healthy men continuously performed passive exercise using a cycle ergometer for 20 min at 50 rpm. Changes in oxygen uptake, cardiac output and muscle oxygenation were measured during passive cycling exercise. The oxygen uptake at 1 min after the start of passive exercise was significantly increased, compared to resting level, but subsequently returned to the same as resting level. Cardiac output showed no change during passive cycling exercise. Tissue oxygen saturation increased after the start of passive exercise and subsequently maintained steady state. These results suggest that the effect of increases in energy expenditure was not maintained by passive exercise for 20 min. In addition, it is likely that passive cycling exercise for 20 min has an effect on peripheral circulation, although the exercise seems to have no effect on central circulation.

Keywords Passive leg movement • Oxygen uptake • Cardiac output • Near infrared spectroscopy • Muscle oxygen dynamics

S. Fuse (✉) • R. Kime • T. Osada • N. Murase • T. Katsumura
Department of Sports Medicine for Health Promotion, Tokyo Medical University, Tokyo, Japan
e-mail: fuse@tokyo-med.ac.jp

© Springer International Publishing Switzerland 2016

Q. Luo et al. (eds.), *Oxygen Transport to Tissue XXXVIII*, Advances in Experimental Medicine and Biology 923, DOI 10.1007/978-3-319-38810-6_35

1 Introduction

Over the past few decades, the way in which we conduct our everyday lives has changed dramatically [1]. Technological advances, societal influences and environmental attributes have caused us to increase the proportion of the day spent in sedentary pursuits, or sitting [2]. A recent study has reported that even among adults reporting high levels of moderate-vigorous physical activity (>7 h per week (h/wk)), a high amount of television viewing (≧7 h per day (h/d)) remained associated with increased risk of cardiovascular mortality, compared with those reporting the least television viewing (<1 h/d) [3]. Therefore, a drop in risk of cardiovascular disease comes from a decrease in daily sitting time, rather than an increase in physical activity levels [1, 3].

Previous studies have reported passive leg cycle exercise increased cardiovascular responses [4], energy expenditure [5] and femoral arterial blood flow [6] and promoted venous return [7, 8]. Consequently, passive cycling has lately attracted attention as a method to reduce sedentary time [5]. However, these studies employed short-duration passive exercise. Few studies have reported the effects of long-duration passive exercise on cardiorespiratory dynamics. If long-duration passive cycling exercise increases energy expenditure and muscle blood flow, it may be useful for preventing arteriosclerosis and metabolic disease, especially for the sedentary. Therefore, the purpose of this study was to determine the effect of passive leg cycle exercise for 20 min on cardiorespiratory and muscle oxygen dynamics.

2 Methods

2.1 Subjects

Eight healthy men (age: 20.8 ± 0.3 years; height: 174.2 ± 2.2 cm; weight: 64.9 ± 2.2 kg; mean ± SE) participated in the study. They were over the age of 20 years and were physically active, but not participating in any formal training or organized sports. All of the subjects were informed of the purpose and nature of the study, and their written informed consent was given. The study was approved by the Tokyo Medical University Local Research Ethics Committee, Japan.

2.2 Experimental Design

All subjects were asked to fast for 6 h, abstain from alcohol and caffeine for 8 h, and not to perform any vigorous exercise for 24 h before the exercise protocol. After arriving at the laboratory, subjects rested quietly in a temperature controlled room (23–25 °C) for at least 20 min. Participants continuously performed passive exercise using a cycle ergometer (Strength Ergo 8, Fukuda-Denshi, Tokyo, Japan) for 20 min following a rest in sitting position for 3 min. Passive cycling exercise was conducted

automatically by a minus load setting, which was equipped with a cycle ergometer. The minus load setting specifies the maximum power at which the machine moves the pedals. In this study, passive cycling was set to −50 W at 50 rpm. The position during exercise was upright, like a normal bicycle.

2.3 Measurement Parameters

Pulmonary oxygen uptake (VO_2) was continuously assessed breath-by-breath with an online metabolic system (AE310S, Minato Medical Science, Japan) from the start of rest in sitting position to the end of passive cycling exercise. Cardiac output (CO) was simultaneously monitored using transthoracic impedance cardiography (PhysioFlow, Manatec Biomedical, France).

Relative changes from rest in tissue oxygen saturation (ΔStO_2), oxygenated hemoglobin concentration (ΔoxHb), deoxygenated hemoglobin concentration (ΔdxHb) and total hemoglobin concentration (ΔtoHb) were measured at the left vastus lateralis muscle by near infrared spatial resolved spectroscopy (NIRS oximeter, Astem, Japan). The probe position was defined as a distal point of 30 % of the length between the patella and the greater trochanter. We used a probe which consisted of one light source and two photodiode detectors, and the optode distances were 2.0 and 3.0 cm, respectively. The measurement site was irradiated with two-wavelength (770 and 830 nm) near infrared lights from a light source, and the light hit both detectors [9]. The sampling rate was 1 Hz. To correct for the scatter factor of fat layer thickness, we measured fat layer thickness at the measurement site using an ultrasound device (LOGIQ 3, GE Yokogawa Medical Systems, Japan) by placing the ultrasound probe at the same site as the NIRS oxymeter probe had been placed [9].

2.4 Statistics

All data were averaged every 60 s and expressed as means ± standard error (SE). The statistical differences between values were tested using one-way repeated-measures analysis of variance. When a significant difference was present, a multiple comparison test was conducted using the Bonferroni method to compare values at rest and each exercise time. All the statistical analyses were performed using IBM SPSS Statics 22 and $p < 0.05$ was considered statistically significant.

3 Results

VO_2 was significantly increased at 1 min after the start of passive cycling exercise compared to resting level (rest; 4.2 ± 0.2 ml/kg/min, 1 min; 6.1 ± 0.3 ml/kg/min, $p < 0.05$), and then returned to resting level within a few minutes (3 min; 4.9 ± 0.2 ml/kg/min, $p > 0.05$) (Fig. 35.1A). Minute ventilation indicated the same change as VO_2,

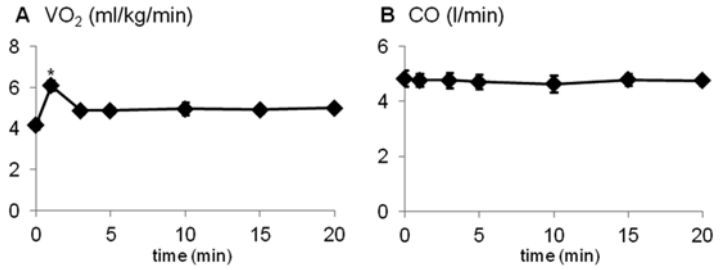

Fig. 35.1 Changes in oxygen uptake (VO_2; **A**) and cardiac output (CO; **B**) during passive cycling exercise. There was a significant difference from resting level (*$p<0.05$)

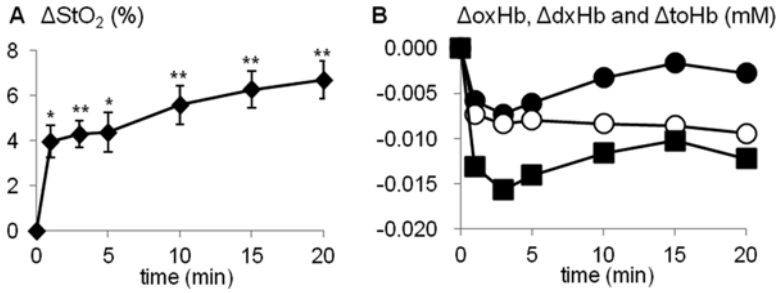

Fig. 35.2 Changes in muscle oxygen saturation (ΔStO_2; **A**) and oxygenated hemoglobin (ΔoxHb, *closed circles*; **B**), deoxygenated hemoglobin (ΔdxHb, *open circles*; **B**) and total hemoglobin (ΔtoHb, *closed squares*; **B**) in the vastus lateralis muscle during passive cycling exercise. There was a significant difference from resting level (*$p<0.05$, **$p<0.01$)

but showed no significant differences from resting level. CO showed no change during exercise (Fig. 35.1B).

ΔStO_2 was significantly increased during passive exercise (1 min; 3.9±0.7 %, $p<0.05$, 3 min; 4.3±0.6 %, $p<0.01$, 5 min; 4.3±0.9 %, $p<0.05$, 10 min; 5.6±0.9 %, 15 min; 6.3±0.8 %, 20 min; 6.7±0.8 %, $p<0.01$) (Fig. 35.2A). Additionally, both ΔoxHb and ΔtoHb were drastically decreased immediately after the start of exercise, and then both parameters showed progressive increase until the end of exercise (Fig. 35.2B). In contrast, ΔdxHb were maintained until the end of exercise, after the initial drop at the start of exercise (Fig. 35.2B). There were no significant differences for ΔoxHb, ΔdxHb and ΔtoHb between rest and any exercise times.

4 Discussion

Previous studies have reported that passive cycling exercise increased both CO and VO_2 [4, 8]. In this study, however, VO_2 was significantly increased at 1 min after the start of exercise compared to resting level, and then returned to resting level

(Fig. 35.1A). In addition, CO showed no change during exercise (Fig. 35.1B). In passive exercise, where voluntary activation of the muscles is minimal, central command is also minimized and so the fast exercise drive to breathe should result only from the activation of limb afferents [10]. It is suggested that an increase in VO_2 at 1 min after the start of exercise contributed to an adaptation of the afferent feedback from the moving limbs, especially mechanoreceptors [10]. During passive cycling at 40 and 60 rpm, CO was significantly elevated compared to rest [4, 8]. In contrast, CO was not augmented during passive exercise at 50 rpm, in spite of different exercise times, which were adopted by recent studies [7, 11], including this study. Some investigations [4, 5, 8] suggested that the pedaling frequency during passive cycling exercise influenced changes in CO and energy expenditure. Therefore, it is unlikely that exercise time during passive exercise is associated with cardiorespiratory responses.

It is suggested that the mechanical lengthening and shortening of the muscles during passive leg cycling promotes circulation within the lower limbs of able-bodied individuals [4, 8]. Research using an NIRS device indicated that the increase in Δtotal-Hb during exercise at a constant work rate was attributed to a dilation of peripheral blood vessels [12] and the increase in ΔStO_2 was matched by rises in muscle blood flow and venous return [13]. In this study, ΔStO_2 was significantly increased during passive exercise. Additionally, both ΔoxHb and ΔtoHb showed a progressive increase from 10 min to the end of exercise. In contrast, ΔdxHb were maintained until the end of exercise, after the initial drop at the start. These results suggest that passive cycling exercise may induce increases in venous return and oxygen supply to muscle tissue.

In conclusion, oxygen uptake was significantly increased at the start of passive cycling exercise compared to resting level, and then returned to resting level within a few minutes. The oxygen supply to the muscle tissue may have been increased by passive cycling exercise, even though cardiac output was not significantly increased during exercise. It is therefore likely that passive cycling exercise at 50 rpm for 20 min has an effect on lower leg circulation, although the exercise seems to have no effect on cardiorespiratory dynamics.

Acknowledgments The authors are grateful to Andrea Hope for revision of this manuscript. We also thank Mikiko Anjo and Ayaka Kime for their helpful technical assistance.

References

1. Mansoubi M, Pearson N, Clemes SA et al (2015) Energy expenditure during common sitting and standing tasks: examining the 1.5 MET definition of sedentary behavior. BMC Public Health 15:516–523
2. Clemes SA, O'Connell SE, Edwardson CE (2014) Office workers objectively measured sedentary behavior and physical activity during and OutsideWorking hours. J Occup Environ Med 56(3):298–303
3. Matthews CE, George SM, Moore SC et al (2012) Amount of time spent in sedentary behaviors and cause-specific mortality in US adults. Am J Clin Nutr 95:437–445
4. Nobrega ACL, Williamson JW, Friedman DB et al (1994) Cardiovascular responses to active and passive cycling movements. Med Sci Sports Exerc 26(6):709–714

5. Peterman JE, Kram R, Byrnes WC (2012) Factors affecting the increased energy expenditure during passive cycling. Eur J Appl Physiol 112:3341–3348
6. Mortensen SP, Askew CD, Walker M et al (2012) The hyperaemic response to passive leg movement is dependent on nitric oxide: a new tool to evaluate endothelial nitric oxide function. J Physiol 590(17):4391–4400
7. Muraki S, Fornusek C, Raymond J et al (2007) Muscle oxygenation during prolonged electrical stimulation-evoked cycling in paraplegics. Appl Physiol Nutr Metab 32:463–472
8. Muraki S, Yamasaki M, Ehara Y et al (1996) Cardiovascular and respiratory responses to passive leg cycle exercise in people with spinal cord injuries. Eur J Appl Physiol 74:23–28
9. Niwayama M, Sone S, Murata H et al (2007) Errors in muscle oxygenation measurement using spatially-resolved NIRS and its correction. J Jpn Coll Angiol 47:17–20
10. Bell HJ, Ramsaroop DM, Duffin J (2003) The respiratory effects of two modes of passive exercise. Eur J Appl Physiol 88:544–552
11. Krzeminski K, Kruk B, Nazar K et al (2000) Cardiovascular, metabolic and plasma catecholamine responses to passive and active exercise. J Physiol Pharmacol 51:267–278
12. Kime R, Im J, Moser D et al (2009) Noninvasive determination of exercise-induced vasodilation during bicycle exercise using near infrared spectroscopy. Med Sci Monit 15(3):CR89–CR94
13. Kime R, Niwayama M, Sone S et al (2008) Muscle deoxygenation distribution in a single muscle during bicycle exercise using multi-channel near-infrared spatial resolved spectroscopy. J Jpn Coll Angiol 48:383–388

Chapter 36
Regional Differences of Metabolic Response During Dynamic Incremental Exercise by ^{31}P-CSI

Yasuhisa Kaneko, Ryotaro Kime, Yoshinori Hongo, Yusuke Ohno, Ayumi Sakamoto, and Toshihito Katsumura

Abstract The aim of this study was to detect the differences in muscle metabolic response of the quadriceps during incremental dynamic knee exercise using regional ^{31}Phosphorus Chemical Shift Imaging (^{31}P-CSI). Sixteen healthy men participated in this study (age 28 ± 5 years, height 171.4 ± 3.9 cm, weight 67.1 ± 9.8 kg). The experiments were carried out with a 1.5-T superconducting magnet with a 5-in. diameter circular surface coil. The subjects performed isometric unilateral knee extension exercise to detect their maximum voluntary contraction (MVC) in prone position. Then they performed dynamic unilateral knee extension exercise in the magnet at 10, 20, 30 and 40 % of their MVC with the transmit-receive coil placed under the right quadriceps. The subjects pulled down a rope with the adjusted weight attached to the ankle at a frequency of 0.5 Hz for 380 s. Intracellular pH (pHi) was calculated from the median chemical shift of the inorganic phosphate (Pi) peak relative to phosphocreatine (PCr). The quadriceps were divided into three regions, (1) medial, (2) anterior, (3) lateral, and in comparison, there was no significant difference in Pi/PCr nor in pHi between regions, except Pi/PCr of the medial

Y. Kaneko (✉)
Department of Sports Medicine for Health Promotion, Tokyo Medical University, Tokyo, Japan

Department of Oriental Medicine, Kuretake College of Medical Arts and Sciences, Tokyo, Japan
e-mail: ykaneko@tokyo-med.ac.jp

R. Kime • T. Katsumura
Department of Sports Medicine for Health Promotion, Tokyo Medical University, Tokyo, Japan

Y. Hongo • Y. Ohno
Kuretake Medical Clinic, Kuretake College of Medical Arts and Sciences, Tokyo, Japan

A. Sakamoto
Department of Oriental Medicine, Kuretake College of Medical Arts and Sciences, Tokyo, Japan

Kuretake Medical Clinic, Kuretake College of Medical Arts and Sciences, Tokyo, Japan

© Springer International Publishing Switzerland 2016

Q. Luo et al. (eds.), *Oxygen Transport to Tissue XXXVIII*, Advances in Experimental Medicine and Biology 923, DOI 10.1007/978-3-319-38810-6_36

region was significantly higher than the anterior region at maximum intensity ($p<0.05$). These results suggest that regional muscle metabolic response is similar in the quadriceps except at maximum intensity.

Keywords Magnetic resonance spectroscopy • Dynamic exercise • Quadriceps • pH

1 Introduction

Imbalanced activity of vastus medialis (VM) and vastus lateralis (VL) has been found in patients with patellofemoral joint pain (PFP) through electromyographic investigation. Facilitating balanced use of these muscles is considered to be a key point of therapy for recovery and prevention of further injuries [1, 2]. It is essential to evaluate various aspects of the activities of knee extensor muscles to improve patient diagnosis, and to confirm whether appropriate rehabilitation or training was provided. We have focused on the aspect of muscle metabolism as a form of evaluation. The aim of this study was to detect the differences in muscle metabolism response at the lateral, anterior and medial regions of the quadriceps of healthy subjects during dynamic incremental knee extension exercise using two-dimensional ^{31}Phosphorus Chemical Shift Imaging (^{31}P-CSI).

2 Methods

Sixteen healthy male subjects (age 28±5 years, height 171.4±3.9 cm, weight 67.1±9.8 kg) participated in this study. All subjects were briefed about the experimental protocol and written informed consent was obtained before the experiment. The institutional review board of the Tokyo Medical University approved the research protocol.

The experiments were carried out with a 1.5-T superconducting magnet (GE Healthcare, Milwaukee, WI, USA) with a 5-in. diameter circular surface coil (GE Healthcare, Milwaukee, WI, USA) double-tuned to ^{1}H at 63.5 MHz and ^{31}P at 25.8 MHz. First, subjects performed isometric unilateral knee extension of the right leg in prone position to measure their maximum voluntary contraction (MVC) and determine the intensity of the following exercise. Then, they lay prone in the bore to obtain T_2-weighted ^{1}H images, followed by acquisition of regional differences in phosphorus signals by ^{31}P-CSI. The magnetic field homogeneity was optimized using the localized water signal from the quadriceps muscles prior to the ^{31}P-CSI acquisitions.

A one-pulse ^{31}P-CSI acquisition was carried out with a circular surface coil placed under the quadriceps muscles of the right leg. Spatially resolved acquisition relied on ^{31}P-CSI with 3-cm slice thickness, and a 108 cm^2 field of view. The volume of each voxel was 3×3×3 cm, or 27 cm^3. A TR of 1000 ms was used, and a

two-dimensional ^{31}P metabolite map was generated every 380 s. This acquisition procedure followed that of a previous study [3] to obtain good spectral data and represents an optimal compromise among signal-to-noise, temporal resolution, and spatial resolution. Mnova software (Mestrelab Research, Spain) was used for ^{31}P-CSI post processing. Baseline correction was performed semi-automatically by setting the peak ranges of Pi and PCr as references, and phase correction was applied semi-automatically using Pi and PCr as reference peaks. Supplementary manual phase or baseline correction was performed, if necessary. The peak areas and peak positions of PCr and Pi were fitted in the frequency domain. The intracellular pH (pHi) was calculated from the median chemical shift of the Pi peak relative to PCr [3]. T_2-weighted ^{1}H images were obtained through the whole body imaging coil with TR = 3200 ms and TE = 95 ms. Scanning time for the T_2 image was 39 s.

The subjects performed dynamic unilateral knee extension of right leg. The subjects pulled down a rope with the adjusted weight attached to the ankle at a frequency of 0.5 Hz for 380 s at 10, 20, 30 and 40 % of their MVC in prone position. The exercise was ceased when the subject was not able to keep up the frequency. The range of motion (ROM) of knee extension exercise was 0–30° due to the diameter of the scanner bore.

The changes in Pi/PCr and pHi during the experiments were analyzed by two-way ANOVA for repeated measurements. The significance level was set to 0.05. Statistics were completed using the Statistical Package for the Social Sciences (SPSS) Statics (IBM, Chicago, IL, USA).

3 Results

A representative view of ^{31}P-CSI spectra is shown in Fig. 36.1. To compare the regional metabolic differences, eight voxels were selected. Two voxels in the medial side were defined as the medial region, and two in the lateral side were defined as the lateral region. Voxels between the medial and lateral regions were defined as the anterior region. The anterior region had twice the thickness of the other regions, and was divided further into two regions, d (deep)-anterior and s (superficial)-anterior, to evaluate the metabolic differences in depth. Pi/PCr increased at 30 % MVC in lateral region ($p < 0.05$), d-anterior region ($p < 0.01$), and s-anterior region ($p < 0.01$), and in every region at 40 % MVC ($p < 0.01$) compared to at rest. Although pHi in medial region started increasing from 20 % MVC ($p < 0.05$), statistical increases in pHi were observed in every region at 40 % MVC ($p < 0.05$) (Table 36.1). There were no statistical differences between regions in Pi/PCr nor pHi. Because the tolerance of exercise varied between subjects, Pi/PCr and pHi at the maximum intensity (the intensity of exercise each subject managed to complete) was compiled and compared in each region. Although no significant difference was observed in Pi/PCr and pHi between regions at rest, the Pi/PCr in the medial region was significantly higher than the anterior region ($p < 0.05$) and tended to be higher than the lateral region ($p = 0.073$) (Fig. 36.2). pHi at maximum intensity showed no significant difference between the regions.

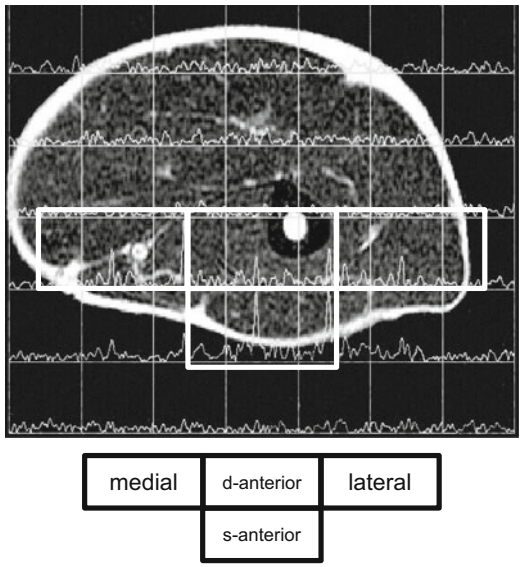

Fig. 36.1 Representative view of ^{31}P-CSI spectra and two-dimensional ^{1}H magnetic resonance image in thigh muscles. Each voxel (*thin-line square*) was 3 × 3 × 3 cm, or 27 cm^3. The four regions were defined as medial, lateral, s-anterior, and d-anterior regions (*thick-line squares*) to evaluate the regional metabolic differences in quadriceps during dynamic incremental knee extension exercise

Table 36.1 Changes in Pi/PCr and pHi of each region at rest and during incremental exercise

	Region	Rest	10 % MVC	20 % MVC	30 % MVC	40 % MVC	*p*
Pi/PCr	Medial	0.16 ± 0.05	0.21 ± 0.10	0.27 ± 0.10	0.36 ± 0.16	0.48 ± 0.19**	n.s.
	Lateral	0.17 ± 0.07	0.16 ± 0.07	0.23 ± 0.10	0.26 ± 0.12*	0.35 ± 0.17**	
	d-Anterior	0.13 ± 0.05	0.14 ± 0.05	0.15 ± 0.06	0.28 ± 0.14**	0.33 ± 0.16**	
	s-Anterior	0.12 ± 0.04	0.16 ± 0.05	0.22 ± 0.11	0.25 ± 0.14**	0.36 ± 0.13**	
pHi	Medial	7.15 ± 0.07	7.12 ± 0.07	7.12 ± 0.09*	7.07 ± 0.13*	6.96 ± 0.09**	n.s.
	Lateral	7.16 ± 0.10	7.18 ± 0.13	7.13 ± 0.10	7.05 ± 0.07	6.97 ± 0.06**	
	d-Anterior	7.12 ± 0.12	7.10 ± 0.10	7.13 ± 0.10	7.04 ± 0.12	7.01 ± 0.09*	
	s-Anterior	7.14 ± 0.10	7.10 ± 0.11	7.09 ± 0.12	7.00 ± 0.20	6.99 ± 0.07*	

Both Pi/PCr and pHi were increased at greater intensity in every region compared to rest ($p < 0.05$). There were no significant differences between the regions
Mean ± S.D. *$p < 0.05$ vs. rest **$p < 0.01$ vs. rest

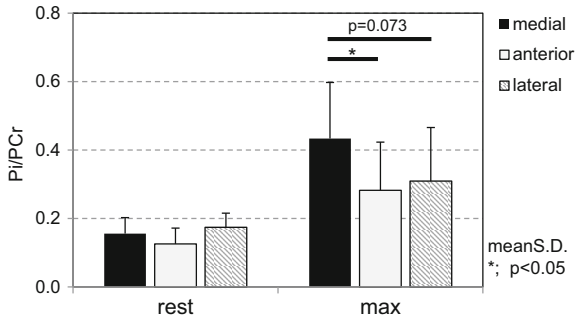

Fig. 36.2 Pi/PCr of each region at rest and at the maximum intensity (max). No significant difference was observed at rest while the medial region showed a significantly higher ratio than the anterior region ($p < 0.05$) and tended to be higher than the lateral region ($p = 0.073$) at the maximum intensity

4 Discussion

The present study shows that regional difference in metabolic response of the quadriceps was observed only at maximum intensity during knee extension exercise in healthy subjects. Each region: medial, lateral, d-anterior and s-anterior, as defined in the study, may anatomically represent each knee extensor: vastus medialis (VM), vastus lateralis (VL), vastus intermedius (VI), and rectus femoris (RF), respectively. In this study, the Pi/PCr ratio was higher in VM than VI and RF at maximum intensity, while Pesta et al. [4] found that the PCr changes were uniform across the different components of the quadriceps in sprint and endurance athletes. Other studies [5, 6] also reported heterogenic muscle metabolism, although the response patterns were different. The reason for this contradiction is not well understood, but may be caused by different exercise protocols and length of exercise time. The present study set a fixed workload based on MVC with weights at each session, while the others used a rubber band for workload [5], or ramp increment [6], and the length of exercise ranged from 2 to 12 min.

Differences in muscle metabolism may relate to the range of motion since ROM affects electromyography activation and a low range is the optimal ROM to activate the VM muscle, while a different range is recommended for other extensors [7, 8]. Kalliokoski et al. [9] reported on the spatial heterogeneity of muscle blood flow, which revealed the greatest increase in VM and VI, compared to the two other muscles, during isometric exercise at 50°. In the present study, subjects performed knee extension exercise at 0–30° which is the preferable range to enhance VM activity. From a clinical point of view, further study is required in PFP subjects with the same protocol.

5 Conclusion

We found that most muscle regions of the quadriceps are metabolically similar except at maximum intensity in the medial region exhibiting a higher Pi/PCr compared to the anterior region in healthy subjects.

References

1. Souza DR, Gross MT (1991) Comparison of vastus medialis obliquus: vastus lateralis muscle integrated electromyographic ratios between healthy subjects and patients with patellofemoral pain. Phys Ther 71(4):310–316
2. Pal S, Besier TF, Draper CE et al (2011) Patellar tilt correlates with vastus lateralis: vastus medialis activation ratio in maltracking patellofemoral pain patients. J Orthop Res 30:927–933
3. Petroff OA, Prichard JW, Behar KL et al (1985) Cerebral intracellular pH by 31P nuclear magnetic resonance spectroscopy. Neurology 35:781–788

4. Pesta D, Paschke V, Hoppel F et al (2013) Different metabolic responses during incremental exercise assessed by localized 31P MRS in sprint and endurance athletes and untrained individuals. Int J Sports Med 34(8):669–675
5. Kime R, Kaneko Y, Hongo Y et al. (2016) Regional Differences in Muscle Energy Metabolism in Human Muscle by ^{31}P-Chemical Shift Imaging. Adv Exp Med Biol 876:49–54
6. Cannon DT, Howe FA, Whipp BJ et al (2013) Muscle metabolism and activation heterogeneity by combined 31P chemical shift and T2 imaging, and pulmonary O2 uptake during incremental knee-extensor exercise. J Appl Physiol 115(6):839–849
7. Signorile JF, Lew KM, Stoutenberg M et al (2014) Range of motion and leg rotation affect electromyography activation levels of the superficial quadriceps muscles during leg extension. J Strength Cond Res 28(9):2536–2545
8. Escamilla RF, Fleisig GS, Zheng N et al (1998) Biomechanics of the knee during closed kinetic chain and open kinetic chain exercises. Med Sci Sports Exerc 30(4):556–569
9. Kalliokoski KK, Kemppainen J, Larmola K et al (2000) Muscle blood flow and flow heterogeneity during exercise studied with positron emission tomography in humans. Eur J Appl Physiol 83(4–5):395–401

Chapter 37
Muscle Deoxygenation and Its Heterogeneity Changes After Endurance Training

Ryotaro Kime, Masatsugu Niwayama, Yasuhisa Kaneko, Shun Takagi, Sayuri Fuse, Takuya Osada, Norio Murase, and Toshihito Katsumura

Abstract The purpose of this study was to elucidate the time course of muscle deoxygenation and its heterogeneity changes through endurance training. Nine healthy untrained male participated in this study. The subjects performed a ramp incremental cycle exercise protocol to estimate VO_{2peak} and muscle tissue oxygen saturation (SmO_2) distribution in the VL muscle before and after 3 (3 wk-T) and 6 weeks of endurance training (6 wk-T). The probe of multi-channel near infrared spatially resolved spectroscopy was attached to the left vastus lateralis muscle along the direction of the long axis. The subjects performed cycle exercise at 60 % of VO_{2peak} for 30 min/day, 3 days/week as the endurance training. After the training, VO_{2peak} at 3 wk-T and 6 wk-T were significantly increased compared to pre-training (Pre-T) and VO_{2peak} at 6 wk-T was significantly increased compared to 3 wk-T. Mean SmO_2 within measurement sites at VO_{2peak} was significantly decreased after 3 wk-T and 6 wk-T compared to Pre-T, but mean SmO_2 was not significantly different between 3 wk-T and 6 wk-T. Conversely, the heterogeneity of the SmO_2 during exercise was not significantly changed through endurance training. A significantly negative correlation was found between ΔVO_2 and ΔSmO_2 after the first 3 weeks of

R. Kime (✉) • S. Fuse • T. Osada • N. Murase • T. Katsumura
Department of Sports Medicine for Health Promotion, Tokyo Medical University, Tokyo, Japan
e-mail: kime@tokyo-med.ac.jp

M. Niwayama
Department of Electrical and Electronic Engineering, Shizuoka University, Shizuoka, Japan

Y. Kaneko
Department of Sports Medicine for Health Promotion, Tokyo Medical University, Tokyo, Japan

Department of Oriental Medicine, Kuretake College of Medical Arts and Sciences, Tokyo, Japan

S. Takagi
Department of Sports Medicine for Health Promotion, Tokyo Medical University, Tokyo, Japan

Faculty of Sport Sciences, Waseda University, Saitama, Japan

© Springer International Publishing Switzerland 2016

Q. Luo et al. (eds.), *Oxygen Transport to Tissue XXXVIII*, Advances in Experimental Medicine and Biology 923, DOI 10.1007/978-3-319-38810-6_37

endurance training. In contrast, no correlation was found betweenΔVO_2 and ΔSmO_2 after the last 3 weeks of endurance training. These results suggest that the enhanced muscle O_2 availability may be one of the primary factors in increasing VO_{2peak} after the first 3 weeks of endurance training.

Keywords Cycle exercise • Near infrared spectroscopy • Tissue oxygen saturation • Oxygen uptake • Vastus lateralis

1 Introduction

Typically, blood flow increases in relation to local metabolic rate, and the dynamic O_2 balance is distributed heterogeneously not only in a single muscle, but also in other activating muscles [1–3]. Near-infrared spectroscopy (NIRS) has been widely used in measuring muscle deoxygenation during exercise. We have previously reported that the muscle deoxygenation level at exhaustion was negatively correlated with peak oxygen uptake (VO_{2peak}), and the results suggest that O_2 availability may be enhanced in higher oxidative capacity muscles [4]. In addition, we have reported on muscle deoxygenation and its heterogeneity changes in an exercising muscle from endurance training [5]. However, the training period was 6 weeks, which was longer than usual endurance training period, as 3 weeks of endurance training is enough to obtain performance benefit through some physiological adaptation [6]. Therefore, the purpose of this study was to elucidate the time course of muscle deoxygenation and its heterogeneity changes through endurance training. In addition, we evaluated whether the increased oxidative capacity from endurance training may be caused by enhanced muscle O_2 extraction.

2 Methods

2.1 Subjects

Nine healthy untrained males (age: 27±7 years height: 169.4±4.1 cm, weight: 65.9±8.4 kg) participated in this study. All subjects were briefed about the experimental protocol, and written informed consent was obtained before the experiment. The institutional review board of Tokyo Medical University approved the research protocol.

2.2 Experimental Design

Peak oxygen uptake (VO_{2peak}) and muscle tissue oxygen saturation (SmO_2) distribution in the vastus lateralis (VL) muscle were determined before and after 3 and 6 weeks of endurance training. For the endurance training, the subjects performed cycle exercise for 30 min/day, 3 days/wk. The work rate during training was set at

60 % VO_{2peak} and increased every 5 % VO_{2peak} when the subjects could maintain the work rate three times easily. The incremental ramp exercise protocol proceeded by 3-min unloaded cycling was performed in an upright position to estimate VO_{2peak} and SmO_2 distribution in the VL muscle. During the test, pulmonary VO_2 and carbon dioxide production (VCO_2) were assessed breath-by-breath with an online metabolic system (AE-310 Minato, Japan). Pedal frequency of 60 rpm was maintained by keeping time with a metronome.

2.3 Measurement Parameters

We used two wavelength light-emitting diode NIR_{SRS} (Astem Co., Japan). The probe of the system consisted of two light sources and one photodiode detector, and the optode distance was 20 and 30 mm, respectively. The measurement probes were attached to the left VL muscle along the direction of the long axis. The eight measurement probes were arranged vertically, with the most distal site being channel 1 and the most proximal site was channel 8. SmO_2 was derived from the relative absorption coefficients obtained from the slope of light attenuation over a distance measured at two focal points from the light emission. A previous study reported that fat layer thickness affects SmO_2 [7]. In contrast, Niwayama et al. [8] recently reported that the SmO_2 can be quantified by the correction of fat layer thickness effects, and the specifications of the NIR_{SRS} were fully described. In this study, we measured fat layer thickness on each measurement site in VL muscle to correct for these effects using an ultrasound device (LogiQ3, GE-Yokokawa Medical Systems, Japan) by placing an ultrasound probe on the same sites as the NIR_{SRS} probes had been placed. SmO_2 at rest and at VO_{2peak} were defined as the SmO_2 averaged over the last 5 s of each period. Relative dispersion (RD) of SmO_2 was calculated as $RD = (SD/Mean) \times 100$ (%) as an index of heterogeneity.

2.4 Statistics

All data were averaged every 60 s and are expressed as means ± standard error (SE). The statistical differences between values were tested using one-way repeated measures analysis of variance. When a significant difference was present, multiple comparisons were conducted using the Bonferroni method to compare values within each training status. All statistical analyses were performed using IBM SPSS Statistics 22 and $p < 0.05$ was considered statistically significant.

3 Results

The VO_{2peak} was significantly enhanced after 3 and 6 weeks of endurance training. In addition, VO_{2peak} was significantly increased at 6-wk compared to 3-wk of endurance training (Pre-T: 42.7 ± 9.9 ml/kg/min, 3-wk: 51.7 ± 11.3 ml/kg/min, 6-wk:

55.0±9.1 ml/kg/min) (Fig. 37.1). SmO_2 at VO_{2peak} was significantly decreased after endurance training at the proximal sites, but not at the distal sites. Further, mean SmO_2 within measurement sites was significantly decreased after 3 wk-T and 6 wk-T compared with Pre-T, but mean SmO_2 was not significantly different between 3 wk-T and 6 wk-T (Fig. 37.2). RD of SmO_2 was not significantly different before and after endurance training at VO_{2peak} (Pre-T: 10.2±3.1 %, 3 wk-T: 10.5±3.9 %, 6 wk-T: 11.4±4.8 %). A significantly negative correlation was found between ΔVO_2 and ΔSmO_2 after the 3 weeks of endurance training. In contrast, no correlation was

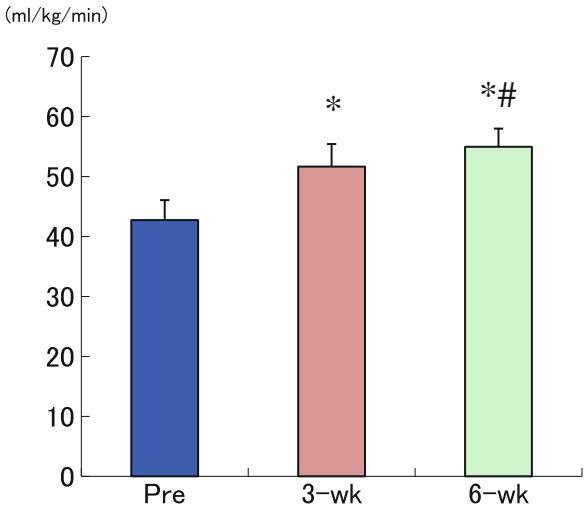

Fig. 37.1 Peak oxygen uptake during cycle exercise before and after 3 and 6 weeks of endurance training. Significant difference from Pre-T (* $p<0.05$). Significant difference from 3 wk-T (# $p<0.05$)

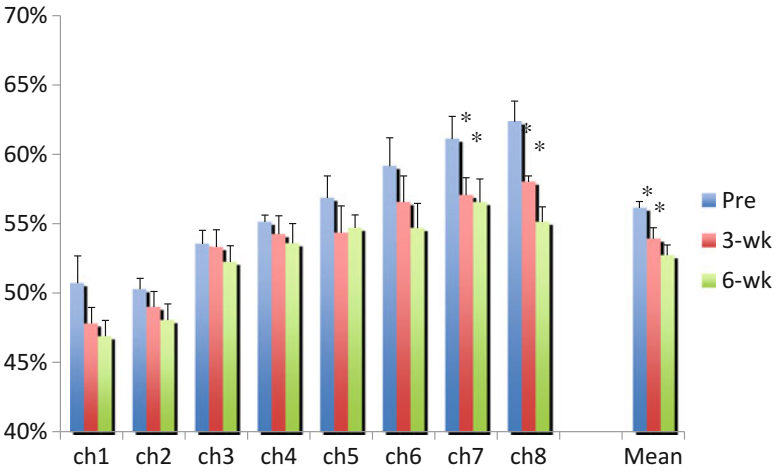

Fig. 37.2 SmO_2 in VL muscle at VO_{2peak} before and after 3 and 6 weeks of endurance training. The eight measurement probes were arranged vertically, with the most distal site being channel 1 and the most proximal site was channel 8. Significant difference from Pre-T (* $p<0.05$)

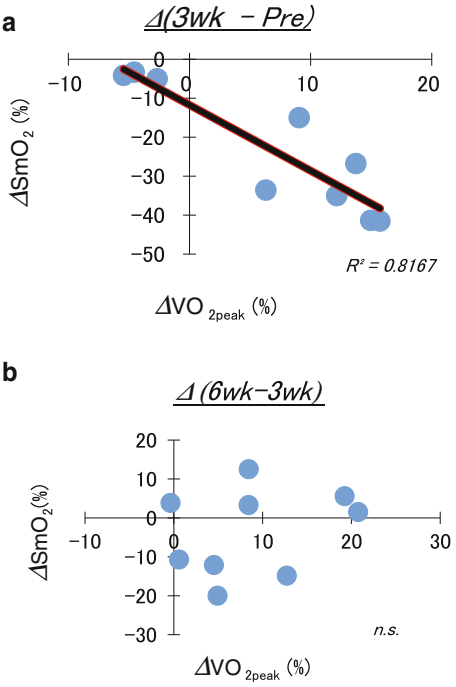

Fig. 37.3 Relationship betweenΔVO_2 and ΔSmO_2 after the first 3 weeks (*upper*) and the last 3 weeks of endurance training (*lower*)

found after the last 3 weeks of endurance training (Fig. 37.3). Fat layer thickness showed no significant difference after the 6 weeks of endurance training (Pre-T: 3.62 ± 1.22 cm, 6-wk T: 3.56 ± 1.28 cm).

4 Discussion

We investigated changes in SmO_2 and its distribution in VL muscle during cycle exercise at VO_{2peak} after 3 and 6 weeks of endurance training. This study reveals that muscle deoxygenation was greatly enhanced at VO_{2peak}, but muscle deoxygenation heterogeneity was unchanged by the endurance training. Recently, some PET studies have demonstrated that muscle O_2 extraction was higher and muscle blood flow heterogeneity in the exercising muscle was lower in endurance-trained men [1, 2]. In addition, some classical studies have reported that muscle O_2 extraction was enhanced after endurance training as demonstrated by a lower venous femoral PO_2 during exercise [9]. It is therefore suggested that muscle O_2 extraction may be improved in the activating muscle by endurance training. In this study, mean SmO_2 in VL was significantly enhanced after endurance training.

We hypothesized that SmO_2 distribution in the activating muscle would be more homogeneous at higher work rates after endurance training [10]. However, the RD of SmO_2 was not significantly different between pre-T, 3 wk-T and 6 wk-T, even

though a previous study demonstrated that the muscle blood flow heterogeneity in the exercising muscle was lower in endurance-trained men [1]. The differing results in these studies may be explained by the variations in muscle group measurement, measurement depth and measurement devices.

There was a significantly negative correlation between ΔVO_2 and ΔSmO_2 after the first 3 weeks of endurance training. In contrast, no correlation was found between these parameters after the last 3 weeks of endurance training. These results suggest that the enhanced muscle O_2 availability may be one of the primary factors in increasing VO_{2peak} after the first 3 weeks of endurance training. In contrast, the primary factors in increasing VO_{2peak} after the last 3 weeks of endurance training may be caused by increase in both muscle O_2 availability and muscle O_2 supply to the activating muscles. We recognize that there was an absence of cardiac output measurement in our study. Further research is needed to clarify the time course of changes in central and local O_2 dynamics during endurance training.

In conclusion, muscle deoxygenation was significantly enhanced by 3 wk-T and 6 wk-T, but the muscle deoxygenation was not significantly different between 3 wk-T and 6 wk-T. In contrast, functional heterogeneity of O_2 balance did not change by the endurance training. Although there was a significantly negative correlation between ΔVO_2 and ΔSmO_2 after the first 3 weeks of the training, no correlation was found between these parameters after the last 3 weeks of the training.

Acknowledgments The authors are grateful for revision of this manuscript by Andrea Hope. We also thank Mikiko Anjo and Ayaka Kime for their helpful technical assistance. This study was supported in part by Grant-in-Aid for scientific research from the Japan Society for Promotion of Science (24500799) to R. K.

References

1. Kalliokoski KK, Oikonen V, Takala TO et al (2001) Enhanced oxygen extraction and reduced flow heterogeneity in exercising muscle in endurance-trained men. Am J Physiol Endocrinol Metab 280:E1015–E1021
2. Kalliokoski KK, Knuuti J, Nuutila P (2005) Relationship between muscle blood flow and oxygen uptake during exercise in endurance-trained and untrained men. J Appl Physiol 98:380–383
3. Mizuno M, Kimura Y, Iwakawa T et al (2003) Regional differences in blood flow and oxygen consumption in resting muscle and their relationship during recovery from exhaustive exercise. J Appl Physiol 95:2204–2210
4. Kime R, Osada T, Shiroishi K et al (2006) Muscle oxygenation heterogeneity in a single muscle at rest and during bicycle exercise. Jpn J Phys Fitness Sports Med 55(Suppl):S19–S22
5. Kime R, Niwayama M, Fujioka M et al (2010) Unchanged muscle deoxygenation heterogeneity during bicycle exercise after 6 weeks of endurance training. Adv Exp Med Biol 662:353–358
6. Kime R, Karlsen T, Nioka S et al (2003) Discrepancy between cardiorespiratory system and skeletal muscle in elite cyclists after hypoxic training. Dyn Med 2:4, online journal
7. Komiyama T, Quaresima V, Shigematsu H et al (2001) Comparison of two spatially resolved near-infrared photometers in the detection of tissue oxygen saturation: poor reliability at very low oxygen saturation. Cli Sci (Lond) 101(6):715–718

8. Niwayama M, Sone S, Murata H et al (2007) Errors in muscle oxygenation measurement using spatially-resolved NIRS and its correction (abstract in English). J Jpn Coll Angiol 47(1):17–20
9. Roca J, Agusti AGN, Alonso A et al (1992) Effects of training on muscle O2 transport at VO2max. J Appl Physiol 73(3):1067–1076
10. Kime R, Im J, Moser D et al (2005) Reduced heterogeneity of muscle deoxygenation during heavy bicycle exercise. Med Sci Sports Exer 37(3):412–417

Chapter 38
Response of BAX, Bcl-2 Proteins, and SIRT1/PGC-1α mRNA Expression to 8-Week Treadmill Running in the Aging Rat Skeletal Muscle

Fang-Hui Li, Hai-Tao Yu, Lin Xiao, and Yan-Ying Liu

Abstract The aim of this study was to analyze the effects of exercise training on Bax and Bcl-2 protein content and sirtuin1 (SIRT1) mRNA expression levels to prevent sarcopenia in aging rats. Eight 18 months old male Sprague–Dawley rats were trained 5 days weekly for 8 weeks on a treadmill, and eight sedentary rats served as controls. Gastrocnemius muscles were dissected 2 days after the last training session. The mRNA content of PGC-1α, caspase-3, NRF1, TFAM, SOD2, and SIRT1 was estimated by RT-PCR with GAPDH used as an internal control. The protein expression of BAX and Bcl-2 was assessed by Western immunoblot. After training, significant ($p < 0.05$) increases were noted for the gastrocnemius muscle weights, the gastrocnemius mass/body mass ratio, the bcl-2/BAX ratio, the Bcl-2 protein and the SIRT1, PGC-1α, NRF1, TFAM, SOD2 mRNA content in the trained gastrocnemius, relative to the control samples. No difference was found in the BAX protein between control and trained muscles, whereas the caspase-3 mRNA content decreased by 50 %, in the gastrocnemius muscle of trained animals. Exercise training may inhibit age-induced myonuclear apoptosis by stimulating SIRT1/PGC-1α mRNA expression, thereby preventing sarcopenia in aging rat.

Keywords Sarcopenia • Exercise training • Sirtuin1 • Aging rat • Mitochondrial

1 Introduction

Sarcopenia, the age-related decline in muscle mass and function, represents a significant health issue due to its associated high prevalence of frailty and disability [1]. Studies in animal models [2] and humans [1] have shown that the severity of skeletal

Author contributed equally with all other contributors.

F.-H. Li (✉) • H.-T. Yu • L. Xiao • Y.-Y. Liu
School of Physical Education and Health, Zhaoqing University, Zhaoqing 526061, China
e-mail: fanghuili2007@163.com

© Springer International Publishing Switzerland 2016

Q. Luo et al. (eds.), *Oxygen Transport to Tissue XXXVIII*, Advances in Experimental Medicine and Biology 923, DOI 10.1007/978-3-319-38810-6_38

muscle cell apoptosis increases over the course of aging and correlates with the degree of muscle mass and strength decline. Sirtuin 1 (SIRT1), a nicotinamide adenine dinucleotide (NAD^+)-dependent histone deacetylase, is implicated in the prevention of many age-related diseases such as sarcopenia, Alzheimer's disease, and type 2 diabetes by maintaining mitochondrial homeostasis [3]. SIRT1/PGC-1α (peroxisome proliferator-activated receptor-γ coactivator 1α) pathway plays a vital role in regulating oxidative stress, mitochondrial biogenesis, apoptosis, thereby contributing to maintain skeletal muscle homeostasis and human longevity [3]. Disruption of the SIRT1/PGC-1α pathway contributes to age-related loss of muscle function and sarcopenia. Enhanced transcriptional activity and protein content of PGC-1α in skeletal muscle prevent muscle wasting by reducing myocyte apoptosis and proteasome degradation [4].

Non-damaging habitual exercise using resistive or endurance regime provides some protection against age-related sarcopenia and impaired contractile function. Song et al. [5] found that 12 weeks of treadmill exercise training resulted in adaptations in Bcl-2 family apoptotic signaling and related stress proteins in skeletal muscle of aged rats. Regular exercise and its mechanism of preventing sarcopenia in aged rats led us to hypothesize that exercise training might be effective with respect to reducing myocyte apoptosis, especially in type II fiber containing skeletal muscles that may be more susceptible to muscle mass losses via the intrinsic apoptotic pathway. Ziaaldini et al. [6] found that exercise training alleviated the deleterious effects of the aging process via SIRT1-dependent pathways through the stimulation of NAD^+ biosynthesis by NAMPT. If exercises can elevate the SIRT1/PGC-1α axis messenger ribonucleic acid (mRNA) expression in skeletal muscle of aged rats in vivo, age-related loss of muscle mass and myocyte apoptosis would be delayed. Therefore, this study aimed to investigate the alterations in BAX and Bcl-2 protein expression after 8 weeks of treadmill exercise training. Alterations in SIRT1/PGC-1α axis mRNA expression in skeletal muscle from an aged rat model after exercise training were also studied.

2 Materials and Methods

2.1 Animals and Training Protocol

Adult male Sprague–Dawley rats aged 18 months were studied. Sixteen rats with similar body weights (range of 340–260 g) were randomly assigned to control ($n = 8$) or training ($n = 8$) groups. The training intensity increased progressively. For the first 4 weeks, the speed of the treadmill and duration of the training sessions gradually increased from a speed of 10 m/min for 10 min to a running speed of 15 m/min for 10 min by the end of week 4. For the next 4 weeks, a 5-min warm-up session at a speed of 10 m/min was followed by the 10-min training session at a speed of 15 m/min [7]. Training animals were killed 6 h after the last training session and the control animals were euthanized at the same time as training animals. The gastrocnemius muscle were quickly removed and frozen immediately in liquid nitrogen and stored at −80 °C environment for further analysis.

2.2 RT-PCR for mRNA Expression

Total RNA from skeletal muscle samples (~30 mg) was extracted with TRIzol (Invitrogen, Singapore) according to the manufacturer's protocol. Analyses of the real-time quantitative PCR data were performed by using the comparative threshold cycle [Ct] method. The primer sequences are shown in Refs. [4, 5].

2.3 Bax and Bcl-2 Protein Content

Protein content for BAX, Bcl-2 was determined by Western blot (WB). Separating gel and stacking gel solutions were made, polymerization then initiated by TEMED and ammonium persulfate. Separating and stacking gels were then quickly poured into a Bio-Rad Protein III gel-box. Eighty micrograms of protein from gastrocnemius muscle homogenates in sample buffer were then loaded into the wells of the 10 % polyacrylamide gels, and electrophoresed at 150 V. The gels were then transferred at 30 V overnight onto a nitrocellulose membrane (Bio-Rad). After blocking, membranes were incubated at room temperature in PBS and the appropriate primary antibodies for 12 h: rabbit polyclonal BAX and mousemonoclonal Bcl-2 (Santa Cruz Biotechnology, USA). Following membranes incubated with horseradish peroxidase-conjugated secondary antibodies in PBS for 90 min, densitometry was performed using a Kodak film cartridge and film, a scanner interfaced with a microcomputer, and the NIH Image J Analysis program.

2.4 Statistical Analysis

All data were presented as mean ± SE. All differences were analyzed with the Student's *t*-test. For all analyses, $P < 0.05$ was considered statistically significant.

3 Results

3.1 Gastrocnemius Wet Weight and Gastrocnemius Index

Although the animal body mass was similar in the control (CON) and exercise training (ET) gastrocnemius muscles, the gastrocnemius muscle weights and gastrocnemius mass/body mass ratio elevated by 29 % and 37.5 % ($p < 0.05$), respectively, relative to the control gastrocnemius muscle (Table 38.1).

Table 38.1 Weight, gastrocnemius weight and gastrocnemius mass/body mass after training

Groups	Body mass (g)	Gastrocnemius weight (g)	Gastrocnemius mass/body mass
CON	378.8 ± 65.7	0.61 ± 0.16	1.60 ± 0.20
ET	378.0 ± 27.6	0.79 ± 0.13*	2.20 ± 0.11**

* p <0.05, ** p <0.01 vs. the CON groups

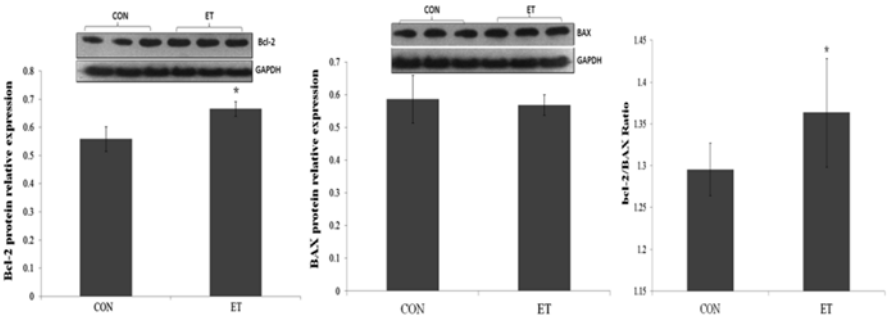

Fig. 38.1 Western blot analysis and densitometric ratios of BAX and Bcl-2 in gastrocnemius. Western blot analysis was used to determine the level of proteins extracted from gastrocnemius, relative to the endogenous control GAPDH

3.2 Protein Level of BAX and Bcl-2 Protein

According to the WB analysis, Bcl-2 protein content and Bcl-2/BAX ratio in gastrocnemius of the trained animals was 18 % higher (p <0.05) than that of the control animals, whereas the protein content of BAX was similar in gastrocnemius muscle obtained from the ET and CON animals (Fig. 38.1).

3.3 Expression of SIRT1-PGC-1α Axis mRNA

After ET, we found that the SIRT1, PGC-1α, mitochondrial transcription factor A (TFAM), nuclear respiratory factors 1 (NRF1) and superoxide dismutase 2 (SOD2) mRNA content had significantly elevated in gastrocnemius compared with the CON, whereas the caspase-3 mRNA content decreased by 50 % in the gastrocnemius muscle of trained animals (Table 38.2).

4 Discussion

To our knowledge, exercise training partly wiped out this age difference. The gastrocnemius muscle weight and gastrocnemius mass/body mass ratio from the trained animals were 29 and 37.5 % significantly higher than those of CON animals,

Table 38.2 Comparisons of SIRT1-PGC-1α axis gene mRNA expression of skeletal muscle

Groups	SIRT1	PGC-1a	NRF1	TFAM	Caspase-3	SOD2
CON	1.02±0.12	1.23±0.32	1.08±0.67	0.98±0.33	0.96±0.13	1.06±0.2
ET	2.41±0.63*	2.51±0.11*	5.16±0.40**	2.52±0.13*	0.48±0.06*	2.09±0.4*

Data are presented as means±SE. *$p<0.05$ and **$p<0.01$ indicated significant differences compared to control animals

respectively. A critical event in mitochondrial-driven apoptosis is the formation of permeable membrane pores, regulated by the balance between competing anti-apoptotic Bcl-2 family proteins such as Bcl-2 and proapoptotic proteins including BAX [2]. Previously, elevation of BAX and caspase-3 protein expression in aging skeletal muscle was reported by Alway et al. [8]. Song et al. found that the bcl-2 protein levels reduced by 20 % in aged rats compared to young rats and the BAX protein levels was 11 % higher in aged rat compared to young rats. Moreover, bcl-2/Bax ratio in the white gastrocnemius increased by 98 % with aging [5]. In addition, caspase-3 mRNA content in aged rats was 72 % higher than that in young rats [9]. We found that exercise training resulted in a marked elevation of Bcl-2 protein expression and the Bcl-2/Bax ratio in the white gastrocnemius from old rats (Fig. 38.1). Remarkably, exercise training diminished caspase-3 mRNA levels by over 95 %, indicative of a robust effect of exercise training on key integrative regulator of apoptosis. But the change of the protein content of BAX was not significant statistically,which is in accordance with those presented in the study by Narashimhan M et al.[10], who reported that moderate training on a treadmill for 2 weeks did not decrease the protein content of BAX. However, Song et al. [5] demonstrated that 12 weeks of treadmill exercise training markedly reduced protein content of BAX in the white gastrocnemius and soleus muscles of old rats. There is possibility that moderate training on a treadmill for 2 weeks and 8 weeks was insufficient to decrease the protein content of BAX in the white gastrocnemius from old rats. Our results suggest that a contributing mechanism by which exercise training may protect muscle from deteriorating in aging populations involves elevated bcl-2/BAX ratio by increasing bcl-2 protein expression.

Moreover, atrophied aging human skeletal muscle demonstrates a sensitized mitochondrial permeability transition pore (mPTP) and an associated increase in myonuclear localization of the mitochondrial-derived proapoptotic factor [11]. Furthermore, we hypothesized that exercise can prevent opening of mPTP through alterations in Bcl-2 and BAX. Our further study will be designed to investigate whether alterations in Bcl-2 and BAX due to moderate training would be positively related to the prevention of mPTP opening.

Alterations in mitochondrial function and low mitochondriogenesis are considered major factors underlying sarcopenia [3, 4]. Skeletal muscle aging was associated with a downregulation of the SIRT1-mediated transcriptional pathway of mitochondrial biogenesis that impinged on multiple aspects of mitochondrial homeostasis [12]. SIRT1 has been shown to increase the transcription of PGC-1α and activate PGC-1α by deacetylation. The mRNA expression of PGC-1α decreased significantly by 35 % in skeletal muscles of old rats compared to young rats as previously described [13]. In the present study we found that exercise training increased by 2.1-fold the

SIRT1 mRNA content from the white gastrocnemius in old rats (Table 38.2). As expected, the mRNA expression of PGC-1α and SIRT1 was significantly correlated [14]. Interestingly, the expression of mitochondrial biogenesis genes is known to be under the control of the PGC-1α and their activator SIRT1. Increased PGC-1α activity can enhance its DNA binding, thus inducing expression of genes involved in antioxidative enzyme SOD2 and NRF1. NRF1 can promote the expression of TFAM that directly stimulates mitochondrial DNA replication and transcription. Thus, our study reveals that exercise training increases transcription of NRF1 and TFAM, probably through upregulating transcription of SIRT1 and PGC-1α. In conclusion, our results found elevated SIRT1/PGC-1α axis genes expression levels, and suggest that regular exercises increase protection against the pro-apoptotic process in skeletal muscle, and hold back changes in muscle mitochondrial function with advanced age. However, we understand that even though this study provides correlative evidence it still has its own limitation, and our further study will be designed to investigate the effect of moderate training on mitochondrial regulation and apoptosis through SIRT1-null rat model.

Acknowledgments This study was supported by the National Natural Science Foundation of China (NSFC) Grant (31500961), the Guangdong Scientific Project (2014A020220015&2015A020219015), and Distinguished Young Talents in Higher Education of Guangdong, China (2014KQNCX225).

References

1. Marzetti E, Lees HA, Manini TM et al (2012) Skeletal muscle apoptotic signaling predicts thigh muscle volume and gait speed in community-dwelling older persons: an exploratory study. PLoS One 2:e32829
2. Dirks A, Leeuwenburgh C (2002) Apoptosis in skeletal muscle with aging. Am J Physiol Regul Integr Comp Physiol 2:R519–R527
3. Westerheide SD, Anckar J, Stevens SM Jr et al (2012) Stress-inducible regulation of heat shock factor 1 by the deacetylase SIRT1. Science 5917:1063–1066
4. Wenz T, Rossi SG, Rotundo RL et al (2012) Increased muscle PGC-1alpha expression protects from sarcopenia and metabolic disease during aging. Proc Natl Acad Sci U S A 48:20405–20410
5. Song W, Kwak HB, Lawler JM (2012) Exercise training attenuates age-induced changes in apoptotic signaling in rat skeletal muscle. Antioxid Redox Signal 3–4:517–528
6. Ziaaldini MM, Koltai E, Csende Z et al (2015) Exercise training increases anabolic and attenuates catabolic and apoptotic processes in aged skeletal muscle of male rats. Exp Gerontol 67:9–14
7. Li FH, Yang HP, Qing F (2013) Effects of eight weeks low volume moderate intensity exercise on the differential proteome expression in aged rat skeletal muscles. China Sport Sci 8:64–72
8. Alway SE, Degens H, Krishnamurthy G et al (2002) Potential role for Id myogenic repressors in apoptosis and attenuation of hypertrophy in muscles of aged rats. Am J Physiol Cell Physiol 1:C66–C76
9. Kang C, Chung E, Diffee G et al (2013) Exercise training attenuates aging-associated mitochondrial dysfunction in rat skeletal muscle: role of PGC-1α. Exp Gerontol 11:1343–1350
10. Narasimhan M, Hong J, Atieno N et al (2014) Nrf2 deficiency promotes apoptosis and impairs PAX7/MyoD expression in aging skeletal muscle cells. Free Radic Biol Med 71:402–414

11. Gouspillou G, Sgarioto N, Kapchinsky S et al (2014) Increased sensitivity to mitochondrial permeability transition and myonuclear translocation of endonuclease G in atrophied muscle of physically active older humans. FASEB J 4:1621–1633
12. Gomes AP, Price NL, Ling AJ et al (2013) Declining NAD(+) induces a pseudohypoxic state disrupting nuclear-mitochondrial communication during aging. Cell 7:1624–1638
13. Nemoto S, Fergusson MM, Finkel T (2013) SIRT1 functionally interacts with the metabolic regulator and transcriptional coactivator PGC-1{alpha}. J Biol Chem 16:16456–16460
14. Charles AL, Meyer A, Dal-Ros S et al (2013) Polyphenols prevent ageing-related impairment in skeletal muscle mitochondrial function through decreased reactive oxygen species production. Exp Physiol 2:536–545

Chapter 39
Muscle Oxygen Dynamics During Cycling Exercise in Angina Pectoris Patients

Shun Takagi, Norio Murase, Ryotaro Kime, Masatsugu Niwayama, Takuya Osada, and Toshihito Katsumura

Abstract Muscle O_2 dynamics during ramp cycling exercise were compared between angina pectoris patients (AP; $n=7$, age: 73 ± 6 years) after coronary artery bypass grafting and age-, height-, and body weight-matched elderly control subjects (CON; $n=7$, age: 74 ± 8 years). Muscle O_2 saturation (SmO_2) and relative change in deoxygenated (Δdeoxy-Hb) and total hemoglobin concentration (Δtotal-Hb) were measured continuously during exercise in the vastus lateralis (VL) by near infrared spatial resolved spectroscopy. Pulmonary O_2 uptake (VO_2) was also monitored throughout exercise to determine peak VO_2. In AP, SmO_2 was significantly higher, and Δdeoxy-Hb was significantly lower during exercise, compared to CON. In all subjects, ΔSmO_2 (values at peak exercise minus values at resting) was negatively correlated to peak VO_2 ($r=-0.52$, $p<0.05$), and Δdeoxy-Hb at peak exercise tended to be negatively associated with peak VO_2 ($r=0.48$, $p=0.07$). Blunted skeletal muscle deoxygenation response was observed in AP patients, which may be related to lower aerobic capacity in AP patients.

Keywords Aerobic capacity • Blood volume • Ischemic heart disease • Muscle oxygen saturation • Near infrared spectroscopy

S. Takagi (✉)
Faculty of Sport Sciences, Waseda University, Tokorozawa, Saitama, Japan

Department of Sports Medicine for Health Promotion, Tokyo Medical University, Shinjuku, Tokyo, Japan
e-mail: stakagi@aoni.waseda.jp

N. Murase • R. Kime • T. Osada • T. Katsumura
Department of Sports Medicine for Health Promotion, Tokyo Medical University, Shinjuku, Tokyo, Japan

M. Niwayama
Department of Electrical and Electronic Engineering, Shizuoka University, Hamamatsu, Shizuoka, Japan

© Springer International Publishing Switzerland 2016

Q. Luo et al. (eds.), *Oxygen Transport to Tissue XXXVIII*, Advances in Experimental Medicine and Biology 923, DOI 10.1007/978-3-319-38810-6_39

1 Introduction

The near infrared spectroscopy (NIRS) technique can serve as an indicator of muscle oxygen dynamics in the arterioles, capillaries, and venules noninvasively during whole body exercise. Recently, we reported the absence of muscle deoxygenation response during incremental cycling exercise in ischemic heart disease, such as post-myocardial infarction (MI) patients, using the NIRS technique, and the abnormalities in muscle deoxygenation were related to their peak aerobic capacities [1]. However, to date, muscle oxygen dynamics have not been fully established in angina pectoris (AP) patients. In AP patients, heart pump function, as well as muscle oxidative enzyme activity [2] may be potentially impaired, and it is unclear whether the absence of muscle deoxygenation is particular to MI patients. The aim of this study was to investigate the muscle deoxygenation response during cycling exercise in AP patients.

2 Methods

2.1 Subjects

AP patients ($n=7$) and age-, height-, and weight-matched control subjects (CON; $n=7$) participated in the study (Table 39.1); the study protocol was approved by the Institutional Ethics Committee. The AP patients were recruited 30 ± 10 days (range 18–42 days) after receiving coronary artery bypass grafting, and the mean left ventricular ejection fraction (EF) was 62 ± 7 %, as assessed by echocardiography. All subjects were informed of the purpose of the study and written informed consent was given.

Table 39.1 Demographic and clinical information

	AP ($n=7$)	CON ($n=7$)
Age (years)	75 ± 6	74 ± 8
Height (cm)	159.4 ± 9.9	160.7 ± 8.3
Weight (kg)	61.1 ± 11.9	60.9 ± 12.0
Men/women	5/2	5/2
Fat layer thickness at VL (mm)	5.04 ± 1.67	4.46 ± 2.71
Medication (%)		
ACE inhibitor	14	0
Angiotensin II receptor antagonist	29	14
Antiplatelet agent	29	0
Beta blockers	57	0
Calcium channel antagonist	43	14
Diabetes (%)	14	14
Dyslipidemia (%)	43	43
Hypertension (%)	71	43

All data are given as mean ± SD. *ACE* angiotensin converting enzyme, *VL* vastus lateralis

2.2 Experimental Design

The subjects performed 10 W/min (AP and CON) or 15 W/min (CON) ramp bicycle exercise, after a three-minute warm up at 10 W, until exhaustion (Strength Ergo 8, Fukuda-Denshi, Japan). None of the AP patients had chest pain, showed ST-segment depression, or severe arrhythmia during or after exercise. Pulmonary O_2 uptake (VO_2) was recorded continuously throughout the exercise (AE310S, Minato Medical Science, Japan), and consequently, peak VO_2 was determined. Muscle oxygen dynamics, i.e., muscle O_2 saturation (SmO_2) and relative changes from rest in oxygenated hemoglobin concentration (Δoxy-Hb), deoxygenated hemoglobin concentration (Δdeoxy-Hb), and total hemoglobin concentration (Δtotal-Hb) were monitored in the vastus lateralis (VL) in the left leg by near infrared spatial resolved spectroscopy (NIR_{SRS}). The NIR_{SRS} data were averaged over the last 10 s at rest, every 10 W, and peak exercise. The measurement site in the VL was defined as 30 % of the length between the patella and the greater trochanter above the patella, as defined in previous studies [1].

We used a two-wavelength (770 and 830 nm) light-emitting diode NIR_{SRS} (Astem Co., Japan). The probe consisted of one light source and two photodiode detectors, and the optode distances were 20 and 30 mm, as used in previous studies [1]. The data sampling rate was 1 Hz. Even though fat layer thickness affects NIRS data because of light scattering, Niwayama et al. recently reported that the effects of fat layer thickness can be corrected through relative changes in Hb and absolute value of SmO_2 by normalized measurement sensitivity [3]. In this study, we measured fat layer thickness at each measurement site in the muscles to correct for these effects using an ultrasound device (LogiQ3, GE-Yokokawa Medical Systems, Japan), as applied in previous studies [1].

2.3 Statistics

All data are presented as means ± standard deviation (SD). To compare changes in oxygen dynamics and pulmonary VO_2 during submaximal exercise (i.e. 20–50 W) between groups (AP vs. CON), a 2-way repeated-measures analysis of variance was used with group and power output as factors. Where appropriate, the Bonferroni post-hoc test was performed to determine specific significant differences. Differences in fat layer thickness, peak VO_2, and peak workload were compared between AP and CON using unpaired t-tests. For all statistical analyses, significance was accepted at $p < 0.05$.

3 Results

Figure 39.1 represents muscle oxygen dynamics, (i.e. the change in SmO_2 (**a**), Δoxy-Hb (**b**), Δdeoxy-Hb (**c**), and Δtotal-Hb (**d**)) for AP and CON, with power output increasing. During submaximal exercise, no significant group × power output

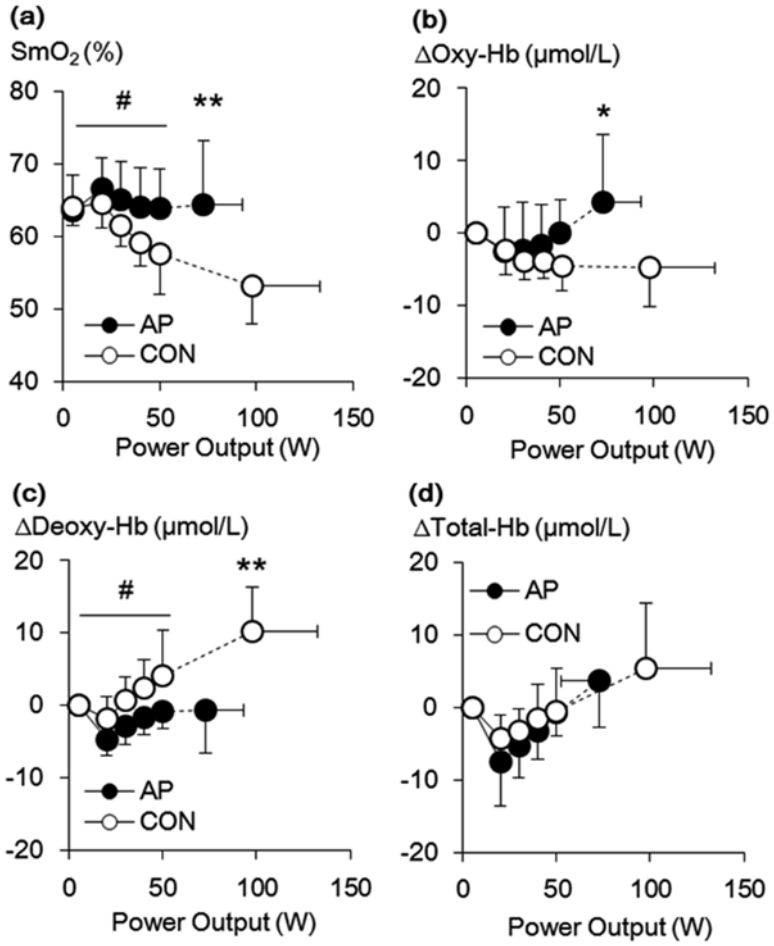

Fig. 39.1 Change in muscle O_2 saturation (SmO_2: **a**), oxygenated hemoglobin (Δoxy-Hb: **b**), deoxygenated hemoglobin (Δdeoxy-Hb: **c**), and total hemoglobin (Δtotal-Hb: **d**) responses during ramp cycling exercise. The closed circles show NIRS data in AP patients and the open circles show NIRS data in control subjects. There was a significant difference between AP and CON at peak exercise (*: $p<0.05$, **: $p<0.01$), and a significant main effect of groups (AP vs. CON) (#: $p<0.05$). Symbols indicating a significant difference between power output in AP and CON have been omitted for the sake of clarity

interaction was observed in changes in SmO_2 ($p=0.12$), Δoxy-Hb ($p=0.19$), Δdeoxy-Hb ($p=0.11$), or Δtotal-Hb ($p=0.43$). However, there was a significant main effect of groups (AP vs. CON) in SmO_2 ($p<0.05$) and Δdeoxy-Hb ($p<0.05$), but not in Δoxy-Hb ($p=0.38$) or Δtotal-Hb ($p=0.41$). At peak exercise in AP, SmO_2 ($p<0.01$) and Δoxy-Hb ($p<0.05$) were significantly higher, and Δdeoxy-Hb ($p<0.01$) was significantly lower, compared to CON. There was no significant difference in Δtotal-Hb at peak exercise ($p=0.68$).

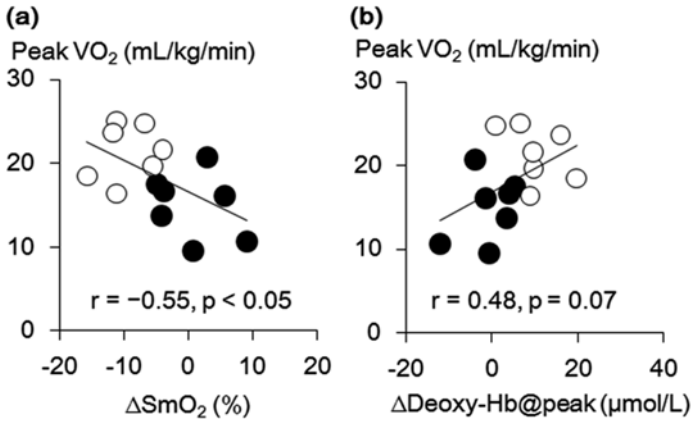

Fig. 39.2 Relationship between muscle deoxygenation and aerobic capacity in AP (*closed circles*) and CON (*open circles*). **a**, change in muscle O_2 saturation from rest to peak exercise (ΔSmO_2) and peak VO_2. **b**, change in deoxygenated hemoglobin from rest to peak exercise (ΔDeoxy-Hb@peak) and peak VO_2

While VO_2 was similar between AP and CON during submaximal exercise (from 20 to 50 W), peak VO_2 was significantly lower in AP than CON (15.0 ± 3.9 vs. 20.4 ± 5.0 ml/kg/min, $p < 0.05$). Similarly, peak power output tended to be lower in AP (72 ± 20 vs. 97 ± 35 W, $p = 0.09$). Because both height and body weight were matched between AP and CON, fat layer thickness was not significantly different between them ($p = 0.53$, Table 39.1).

Figure 39.2 demonstrates the relationship between muscle deoxygenation and aerobic capacity. ΔSmO_2 (values at peak exercise minus values at resting) was negatively correlated to peak VO_2 ($r = -0.55$, $p < 0.05$) (Fig. 39.2a). Similarly, Δdeoxy-Hb at peak exercise tended to be negatively associated with peak VO_2 ($r = 0.48$, $p = 0.07$) (Fig. 39.2b). In contrast, peak workload was not significantly related to ΔSmO_2 ($p = 0.66$) or Δdeoxy-Hb at peak exercise ($p = 0.79$).

4 Discussion

A low number of subjects probably accounts for the lack of significant interaction for any variables in muscle O_2 dynamics. However, at submaximal and peak exercise, higher Δdeoxy-Hb and lower SmO_2 were found in AP patients, while Δtotal-Hb, which is an indicator of blood volume, was similar between AP and CON. These data suggest that both muscle deoxygenation and muscle O_2 extraction may be lower in AP patients than age- and body size-matched elderly control subjects, as seen in MI patients [1].

The absence of muscle deoxygenation and muscle O_2 extraction implies that muscle O_2 supply is higher compared to muscle O_2 utilization. One reason for this

may be that O_2 utilization was lower in activating muscle of AP patients. Karlsson et al. reported that AP patients have a lower composition of oxidative muscle fibers and oxidative enzyme activity (such as citrate synthase activity), compared with age-matched healthy subjects [2]. These data partly suggest that lower muscle O_2 utilization may cause the absence of muscle deoxygenation response. Another possibility to explain the absence of muscle deoxygenation was increased O_2 supply compared to CON. In contrast to MI patients [1], lower pulmonary VO_2, which reflects low muscle O_2 supply or muscle oxidative capacity [4], was not observed in AP patients. Therefore, a possibility remains that blood distribution may be altered in AP patients. However, to our knowledge, no study has reported on higher muscle O_2 supply in AP patients. These areas require further examination.

In this study, muscle O_2 extraction was impaired in AP patients, similar to the reports on post-MI patients in a previous study [1]. In contrast, in heart failure patients, muscle O_2 extraction was enhanced during incremental exercise [5], compared to controls. Potential reasons for the disparities among studies may be the difference in heart pump function. EF in both AP patients of this study ($62 \pm 7\,\%$) and in MI patients of a previous study ($55 \pm 8\,\%$) [1] was relatively preserved, compared to heart failure patients ($22 \pm 2\,\%$) [5]. Impairment of muscle O_2 supply due to reduced pump function of the heart may cause a compensatory enhancement of muscle O_2 extraction [5]. Therefore, the lower muscle O_2 extraction in AP patients of this study may be partly caused by preserved EF, which means impaired muscle O_2 extraction may not be particular to MI patients.

We also found a relationship between muscle deoxygenation and peak VO_2 in AP patients, similar to that seen in MI patients [1]. These findings suggest that blunted muscle deoxygenation response may be related to lower peak aerobic capacity in AP patients. In this study, we did not match the peak workload between AP and CON, and peak workload was not significantly associated with ΔSmO_2 or Δdeoxy-Hb at peak exercise. We therefore believe that the relationships are not significantly affected by peak workload. However, the number of subjects was limited and future studies are needed with a larger number of subjects.

In conclusion, abnormalities in muscle O_2 dynamics were found in AP patients, similar to those seen in MI patients. Blunted muscle deoxygenation may be related to lower peak aerobic capacity in AP patients.

Acknowledgments The authors are grateful for revision of this manuscript by Andrea Hope. This study was supported in part by Grant-in-Aid for scientific research from the Japan Society for the Promotion of Science (12J06298, 26882044) to S.T.

References

1. Takagi S, Murase N, Kime R et al (2014) Skeletal muscle deoxygenation abnormalities in early post-myocardial infarction. Med Sci Sports Exerc 46(11):2062–2069
2. Karlsson J (1988) Onset of blood lactate accumulation exercise capacity, skeletal muscle fibers and metabolism before and after coronary artery bypass grafting. Am J Cardiol 62(8):108E–114E

3. Niwayama M, Suzuki H, Yamashita T et al (2012) Error factors in oxygenation measurement using continuous wave and spatially resolved near-infrared spectroscopy. J Jpn Coll Angiol 52:211–215
4. Meyer K, Schwaibold M, Hajric R et al (1998) Delayed VO_2 kinetics during ramp exercise: a criterion for cardiopulmonary exercise capacity in chronic heart failure. Med Sci Sports Exerc 30(5):643–648
5. Wilson JR, Mancini DM, McCully K et al (1989) Noninvasive detection of skeletal muscle underperfusion with near-infrared spectroscopy in patients with heart failure. Circulation 80(6):1668–1674

Part V
Acupuncture, Meridians, and Primo Vascular System

Chapter 40
Chronological Review on Scientific Findings of Bonghan System and Primo Vascular System

Kyung A. Kang

Abstract In 1962, Bonghan Kim in North Korea published a report on a new vascular system in mammals, which he claimed as the acupuncture meridian. He soon named it the Bonghan System. Between 1962 and 1965, he published five reports, with detailed descriptions on the system. Kim also described the self-regenerating nature of a unique cell type Sanals in the system and these cells are now confirmed to be a type of stem cells. According to his findings, the system appears to have vital roles in maintaining mammalian lives. Kim disappeared in around 1965 and the research on this system also completely stopped. In 2002, Kwang-Sup Soh reported re-discovery of the system and, since then, his team has been leading the research on the system. The Soh team has confirmed many of Kim's findings to be valid, although so many of Kim's results are still to be verified. In 2010, the system was renamed the Primo Vascular System (PVS). Soh and researchers trained by Soh have also been reporting new scientific facts on the system. The PVS exists throughout the entire body, including inside the blood and lymphatic vessels. Recent reports revealed more evidence for it to be the acupuncture meridian, where some acupuncture therapies are applied for the blood pressure control. Thus, the PVS is expected to have roles in the oxygen transport in tissues. Many study results also suggest that the PVS may have roles in body homeostasis and regeneration. This article chronologically reviews Kim's scientific findings on the Bonghan System, which were verified by the PVS scientists (after 2000), and also the new findings reported by the PVS scientists.

Keywords Bonghan system • Primo vascular system • Acupuncture meridian • Regeneration • Homeostasis

K.A. Kang (✉)
Department of Chemical Engineering, University of Louisville, Louisville, KY 40292, USA
e-mail: kyung.kang@louisville.edu

© Springer International Publishing Switzerland 2016

Q. Luo et al. (eds.), *Oxygen Transport to Tissue XXXVIII*, Advances in Experimental Medicine and Biology 923, DOI 10.1007/978-3-319-38810-6_40

1 Introduction

Bonghn Kim, an M.D. in North Korea, published a report in 1962, describing a new vascular system as the entity of the acupuncture meridian [1], which had been a mysterious entity associated with Chinese medicine for thousands of years. At that time, there were serious debates among the international scientists on whether it was in fact the acupuncture meridian and even whether this system existed. The doubts about Kim's discovery may have stemmed from the fact that this system was very difficult to identify by scientists other than Kim, because the system was very small in size and optically transparent and Kim did not reveal the method for identifying the system in detail. Kim and his colleagues published four more reports on the system [2–5] and it was soon named the Bonghan System (BHS). His reports were translated in several languages and sent out to many countries. The novelty and the extent of Kim's findings were impressive and they implied the significance of the system in animal physiology. However, because Kim's publications were reports of a governmental institute, not journal publications, the validity of his findings needed to be verified before they were taken as scientific facts.

Due to the unexpected and unclear situations in North Korea at that time, Kim suddenly disappeared in around 1965, and the research activity on the system completely stopped [6]. Between 1965 and 2000, Fujiwara in Japan [7] might have been the only one who was known to successfully identify it. In 2002, the first article on the system since Fujiwara's, was published by Kwang-Sup Soh in South Korea [8]. Since then, numerous articles on the system were published in various journals, mainly by the Soh team, until recently. In 2010, the Bonghan System (BHS) was renamed as the Primo Vascular System (PVS). Most scientists who have known and/or have studied the system now fully agree that the BHS is the PVS. Many findings of Kim and his colleagues were studied and confirmed to be valid, but there are still many scientifically important contents to be verified. Meanwhile, several new and important findings on the system were also revealed.

This article chronologically reviews what Kim reported; what and when findings were scientifically validated *(Kim's findings validated by others after 2000 are italicized in the text)*; what are still to be confirmed; and what have been the new findings that were not in Kim's reports. *This article includes only limited scientific content and references, to fit them to the allowed space for the volume.*

2 The Bonghan System

2.1 Kim's First Report (1962), Great Discovery in Biology and Medicine: Substance of Kyungrak

In August 1961, Bonghan Kim made a presentation on a new vascular system, which he claimed as the real entity ('substance' in Kim's word) of the acupuncture meridian, at a scientific conference of the Pyongyang Medical College (North Korea). Its content was published in 1962 [1]. 'Kyungrak' is the acupuncture meridian in Korean.

2.1.1 Kim's Study Results Confirmed or Partially Confirmed by Others

The animals that Kim used for his study were mainly the rabbit and, sometimes, dog, guinea pig, and frog. He stated that he also made observations in humans. *After 2000, the system was identified in the rabbit, dog, cow, rat, mouse, pig, chick embryo, and human* [9, 10]. This new system (i.e., the acupuncture meridian) was beneath the epidermis, and composed of the small, oval-shaped 'Kyunghyul' (acupoint in Korean), and bundles of tubular 'Kyungmaik' (meridian channel, in Korean). Kim stated that the system was also inside the body, implying the possibility of the existence of other sub-types, which were described in his later reports more in detail.

2.1.2 Kim's Results Not Studied or Not Yet Sufficiently Confirmed

Kim also reported the electrical induction and conductivity (electrogram) at the Kyunghyul of the system, and the changes in the wave form with changes in physiological conditions and also when stimuli were applied, which were not studied yet.

2.2 Kim's Second Report (1964), On the Kyungrak System

2.2.1 Kim's Study Results Confirmed or Partially Confirmed by Others

In this report [2] Kim described the system in detail and introduced new terms for the system and its sub-elements. The system was named the Bonghan System (BHS); the three main sub-units were BH corpuscle ('*Corpusculum Bonghan'* in his words; BHC); BH duct (BHD) and BH ductules inside the BHD; and BH liquor (BHL) for the liquid flowing inside the BHS.

He classified the system mainly into two sub-types, the Superficial (in the skin) and Profound (inside the body) BHS. He then sub-classified the Profound BHS further into the Intravascular and Extravascular systems. The two sub-types were reported to have the same histological structure but with different surrounding tissues. More detailed classifications were later presented in his third report.

Morphological properties of multiple ductules inside a single BHD and rod-shaped nuclei of ductules were reported, which *Ogay et al. confirmed later* [11].

2.2.2 Kim's Results Not Studied or Not Yet Sufficiently Confirmed

The Superficial and Profound BHS were characterized, in detail, morphologically and histologically, with schematic diagrams and actual images of optical microscopy. BHS paths in legs and abdominal areas were traced using radioactive-isotope P^{32}. Communication between the subtypes was described. Unique movements of needles placed in the superficial BHCs were reported. Extensive results on the bioelectrical signals via BHCs were also reported. Kim claimed that this system was also present in animals of evolutionary lower levels, such as hydra, and also even in the plant.

2.3 The Third Report (1965), Kyungrak System

In the third report [3], the BHS was described in even more detail, showing the rapid progress in his research. Out of five reports, this report may be the most helpful document for the people who would like to learn about the BHS.

2.3.1 Kim's Study Results Confirmed or Partially Confirmed by Others

Kim made further classifications for the BHS, by its location in the animal body: The **Superficial BHS** is in the corium or subcutaneous tissue, surrounded by dense blood vessels, and its corpuscles are said to be acupoints. **Internal (Intra-vascular) BHS** floats inside blood and lymphatic vessels; **External (Extra-vascular) BHS**, usually runs along the large-sized blood vessels and nerves, or independently; **Intra-External (organ surface)** sub-type is freely laid on the surface of internal organs in the thoracic and abdominal cavities; **Neural**, in the central and peripheral nervous systems; and **Intra-organic**, inner surface of organs. *The internal and intra-external subtypes were first confirmed by Fujiwara in 1967* [7]*, and most subtypes were confirmed by the Soh team, one by one over the years. The superficial BHS was confirmed in 2014, by the Ryu Team* [12].

The report contains detailed characterizations on the system and sub-systems. *The composition of the BHL was later confirmed by the Kwon team* [13].

Kim also briefly discussed the BHS in terms of the embryonic and comparative biology. The time course of the BHD premordium in chick embryos was reported, in detail: The BHD was found to form earlier than the blood or lymphatic vessel in the embryo, which was implied in its new name the Primo Vascular System. *A study by Lee* et al. *confirmed Kim's findings in the chick embryo* [14].

2.3.2 Kim's Results Not Studied or Not Yet Sufficiently Confirmed

The content of the report is so extensive that only a portion has so far been studied/confirmed by the PVS scientists. The report describes detailed characterizations of the system and the sub-systems, including their chemical, mechanical (particularly their autonomic movements), and electrical properties with and without stimuli. The report included high-quality images of the system and sub-systems. It also describes various stages of BHC; the inter-relationships between the BHS sub-types, and between the BHS and organs; the composition, circulation paths and directions of BHL, using the isotope P^{32}; and observing the tracer signal after cutting BHDs. Kim believed that the BHS was tied up to the individual cell.

2.4 The Fourth Report (1965), Theory of Sanal

The fourth report [4] was in the same volume with the third one. 'Sanal' is a Korean word, meaning the live ('San') egg ('Al'), with a similar feel of the stem cell, and it has the self-regenerating property as 'a live egg.' Considering that the concept of

stem cells was clearly recognized only in the 2000s, Kim's discovery and his study results of Sanals are remarkable.

2.4.1 Kim's Study Results Confirmed or Partially Confirmed by Others

Kim reported that the form and size of Sanals were similar for various animal species (rabbit, birds, amphibian, fish, and man), and also for the ones in the plant. The usual size of Sanals was reported to be 1.2–1.5 μm. *The sanal as the stem cell (possessing self-regenerating nature) was confirmed by the Soh* [15] *and Kwon teams* [16, 17]. Lately, more researchers are attracted to this aspect of the BHS.

In this report, new terminologies on the BH Sanal were first introduced: The solid content with large amount of nucleic acid in the Sanal became Sanalosom; the liquid, Sanaloplasm; and the membrane, Sanal membrane.

2.4.2 Kim's Results Not Studied or Not Yet Sufficiently Confirmed

Kim hypothesized the nature of the Sanal and organism self-renovation as follows, while suggesting them to be re-examined:

(1) All morphological constituent parts of the organism are incessantly renewed.
(2) The self-renovation of organisms takes the 'BH Sanal Cell Cycle' process.
(3) The self-renovation of the organism is performed by the BHS.

For the Sanal study, as in the study of the BHS path, Kim and his team injected P^{32} into Sanals and traced their paths inside the animal body. The circulation course of the BHL was found not unitary as in the blood circulation, each organ part was linked to a relevant circulation route, and the routes were inter-related. Some of the characteristics of the Sanal reported were: In the BHL there were many small, DNA-rich granules and they grew to be Bonghan Sanals; The Sanal is composed of Sanlosome, Sanaloplasm, and Sanal membrane. Kim also described the composition of the Sanal in detail, its structure and movement in various environments, and the method for culturing Sanals.

A very interesting study result/concept described in the report is that normal cells would be sanalized and these sanalized cells would be regenerated to be cells. He used liver tissues to show this sanalization/regeneration processes.

2.5 The Fifth Report (1965), Cell Cycle of Blood Bonghan Sanal

The content of Kim's firth report [5] was barely studied or confirmed by other scientists, except the *non-marrow haematopoiesis study done by the Kwon team* [17]. This volume describes the cell cycles and chemical composition of blood Bonghan Sanal, particularly red blood cells, granulocytes, and lymphocytes. It also reports the meridians in the blood-cell producing organ (e.g., bone marrow, lymph nodes).

3 Scientific Activities After 2000

The study on the BHS re-started in 2000 by Kwang-Sup Soh, and the publications on this system started to come out in 2002, first confirming Kim's study results. In addition, there were new scientific discoveries on the system, including developing several new methods for identifying/imaging the BHS; identification of the system in the adipose tissue; possible roles of the system in the cancer metastasis [18]; positively confirming Sanals as stem cells [15–17]; PVS presence in the human body, for the first time, by identifying it in the human umbilical cord and placenta [10]; etc.

In 2010, Soh and other scientists involved in the research renamed the BHS the 'Primo Vascular System' to give the system a more scientifically relevant meaning. Its sub-systems were also renamed, accordingly.

BHS: Primo Vascular System (PVS) BHD: Primo Vessel (PV)
Bonhan Ductule: sub-Primo Vessel (sub-PV) BHC: Primo Node (PN)
BHL: Primo Fluid Sanal: Primo-microcell (P-microcell)
Sanalsome, Sanaloplasm, Sanal membrane: *not re-named yet.*

A term 'Primogenesis' was created for the phenomenon of forming PVS, in 2013, by the Kang team.

4 Current Status of PVS Research Activity

Most research on the PVS has been and is still being done in Korea. Currently, there are at least six active research teams in Korea and two appear to have research funds from the government. It is not clear whether there are any privately funded teams, but the rest of the Korean teams appear to study the PVS on a voluntary basis.

In the U.S., there are four known teams, all of which were trained by the Soh team. Up to now, no team is known to be federally funded and the research is done on a voluntary basis. The PVS is recently recognized more, particularly by the scientific societies associated with complementary medicine. Research proposals submitted to the federal agencies have been receiving more positive responses.

5 ISOTT and PVS

The PVS is now confirmed to be a new vascular system, distributed in the entire body including inside blood and lymphatic systems; to store unique stem cells; and to produce blood cells [2–5, 17]. One of the acupuncture therapies, which are to be via the nodes of the superficial PVS, is known to regulate the blood pressure [19–21], implying that the PVS may be directly/indirectly involved in transporting oxygen, various biochemicals, and cells.

In terms of direct association between the PVS and ISOTT, the first ISOTT experience of this author (Kang; a PVS scientist) was at the Ruston meeting (Louisiana, USA; in 1983) as a graduate student of the ISOTT founder D. F. Bruley. She was then exposed to the knowledge of the BHS/PVS in 2007 when she first met Dr. Soh, currently world leading PVS scientist. With this author's suggestion, Dr. Soh became an ISOTT member, made the first ISOTT presentation on the PVS during the Cleveland meeting (Ohio, USA; in 2009) and the second one, during the Ascona meeting (Switzerland; in 2010). He did not submit manuscripts for these presentations, but he did invite several ISOTT members for the first International Symposium on the PVS (ISPV). The first paper about the PVS published in ISOTT proceedings dealt with the cancer associated PVS by the Kang team [22], which was presented during the Bruges meeting (Belgium, in 2012).

In August 2010, the International Society of Primo Vascular System (ISPVS) was founded by Soh and Kang, with its constitution and Bylaws based on those of the ISOTT, with the permission of the ISOTT founder D. F. Bruley. The first International Symposium of Primo Vascular System (ISPS) was organized by Soh and held in Jaechon, Korea, during September 17–18, 2010, and ISOTT members Vaupel, Harrison, and the author (and Soh) attended the symposium. Dr. Bruley was also invited but decided not attend due to his poor health at that time. During the symposium preparation, the author contacted Springer Publishing (the ISOTT proceeding publisher) for the possibility of publishing the ISPV proceedings. After receiving a very positive survey, Springer agreed to publish the proceedings "The Primo Vascular System: Its Role in Cancer and Regeneration [9]," and it was published in 2012. During the symposium, 13 international scientists from nine countries were invited as founding members of the ISPVS and Soh, Vaupel, and Kang are three of the 13 members. In 2012, the website for the ISPVS (www.ispvs.org) was established and it is currently maintained by Soh and Kang. By 2014, English versions of Kim's first four reports were located and they were placed in the ISPVS website for scientists to be able to freely access (note that the reports were published before the copyright was enforced).

The ISOTT became the first international society to have PVS content in an official session, entitled 'Acupuncture, Meridians, and Primo Vascular System,' during the 2015 annual conference in Wuhan, China.

Conclusions

The BHS/PVS is a newly recognized vascular system, distributed throughout the entire mammalian body, and scientific evidences have shown this system as the acupuncture meridian. The system appears to have roles/functions in keeping the body's homeostasis and regeneration, i.e., fundamental to maintaining mammalian lives. In a cancerous local environment, PVS appears to have role in metastasis.

The system is very small and optically translucent and, therefore, the urgent needs for effectively performing PVS research are techniques for identifying and

harvesting it, in an accurate and user-friendly manner, to further characterize it. There is still so much to learn about various aspects of the system and, therefore, a focused, multi-disciplinary approach is highly desired.

References

1. Kim BH (1962) Great discovery in biology and medicine—substance of Kyungrak—Foreign Language Publishing House, Pyongyang, DPRK. www.ispvs.org
2. Kim BH (1964) On the Kyungrak system The Kyungrak Institute, Pyongyang, DPRK. www.ispvs.org
3. Kim BH (1965) Kyungrak system. Proc Acad Kyungrak DPRK, Pyongyang, 1965(2):9–67. Medical Science Press, Pyongyang, DPRK. www.ispvs.org
4. Kim BH (1965) Sanal theory. Proc Acad Kyungrak DPRK, Pyungyang, 1965(2):69–104. Medical Science Press, Pyongyang, DPRK. www.ispvs.org
5. Kyungrak Institute of DPRK (1965) Blood Bonghan Sanal-cell cycle. J Acad Med Sci Democratic People's Republic of Korea 12:1–7, Medical Science Press, Pyongyang, DPRK [in Korean]
6. Kang KA (2013) Historical observations on the half-century freeze in research between the bonghan system and the primo vascular system. J Acupunct Meridian Stud 6(6):285–292
7. Fujiwara S, Yu SB (1967) Bonghan theory, morphological studies. Igaku no Ayumi 60:567–577 [in Japanese]
8. Shin HS, Soh KS (2002) Electrical method to detect a Bong-Han Duct inside blood vessels. Sae Mulli 45(6):376–378
9. Soh K-S, Kang KA, Harrison DR (2012) The primo vascular system: its role in cancer and regeneration. Springer Publisher, New York
10. Lee B-S, Lee BC, Park JE, Choi H-K, Choi S-J, Soh K-S (2014) Primo vascular system in human umbilical cord and placenta. J Acupunct Meridian Stud 7(6):291–297
11. Ogay V, Bae KH, Kim KW, Soh K-S (2009) Comparison of the characteristic features of Bonghan Ducts, blood and lymphatic capillaries. J Acupunct Meridian Stud 2(2):107–1179
12. Lim CJ, Yoo JH, Kim YB, Lee SY, Ryu PD (2013) Gross morphological features of the organ surface primo-vascular system revealed by hemacolor staining. Evid-Based Compl Alter Med. Article ID 350815
13. Kwon BS, Ha CM, Yu SS, Lee BC, Ro JY, Hwang SH (2012) Microscopic nodes and ducts inside lymphatics and on the surface of internal organs are rich in granulocytes and secretory granules. Cytokine 60:587–592
14. Lee S-Y, Lee B-C, Soh K-S, Jhon G-J (2012) Development of the putative primo vascular system before the formation of vitelline vessels in chick embryos. In: Soh K-S, Kang KA, Harrison DR (eds) The primo vascular system: its role in cancer and regeneration. Springer, New York, pp 77–82
15. Ogay V, Soh K-S (2012) Identification and characterization of small stem-like cells in the primo-vascular system of adult animals. In: Soh K-S, Kang KA, Harrison DR (eds) The primo vascular system: its role in cancer and regeneration. Springer, New York, pp 149–155
16. Lee SJ, Park SH, Kim YI, Hwang S, Kwon PM, Han IS, Kwon BS (2014) Adult stem cells from the hyaluronic acid-rich node and duct system differentiate into neuronal cells and repair brain injury. Stem Cells Dev 23(23):2831–2840
17. Hwang S, Lee SJ, Park SH, Chitteti BR, Srour EF, Cooper S, Hangoc G, Broxmeyer HE, Kwon BS (2014) Nonmarrow hematopoiesis occurs in a hyaluronic-acid-rich node and duct system in mice. Stem Cells Dev 23(21):2661–2671
18. Soh K-S, Yoo JS (2014) A transformative approach to cancer metastasis: primo vascular system as a novel microenvironment for cancer stem cells. Cancer Cell Microenviron 1:e142

19. Li P, Tjen-A-Looi SC, Cheng L, Liu D, Painovich J, Vinjamury S, Longhurst JC (2015) Long-lasting reduction of blood pressure by electroacupuncture in patients with hypertension: randomized controlled trial. Med Acupuncture 27(4):253–264
20. Flachskampf FA, Gallasch J, Gefeller O, Gan J, Mao J, Pfahlberg AB, Wortmann A, Klinghammer L, Pflederer W, Daniel WG (2007) Randomized trial of acupuncture to lower blood pressure. Circulation 115(24):3121–3129
21. Tam K-C, Yiu H-H (1975) The effect of acupuncture on essential hypertension. Am J Chin Med 3(4):369–375
22. Kang KA, Maldonado C, Perez-Aradia G, An P, Soh K-S (2013) Primo vascular system and its role in cancer. Adv Exp Med Biol 789:289–296

Chapter 41
Temporal Change of Alcian Blue-Stained Primo Vascular System in Lymph Vessels of Rats

Jungdae Kim, Dong-Hyun Kim, Sharon Jiyoon Jung, and Kwang-Sup Soh

Abstract This study aims to investigate the temporal change of a vascular system now known as the primo vascular system (PVS). We used Alcian blue (AB) dye for imaging the distribution of the PVS in lymphatic vessels. The target lymph vessels were chosen as they are easily accessible from the skin, and long-term observation is possible with intact physiological conditions due to a minimal surgical procedure. AB solution was injected into the inguinal lymph node and the target lymph vessels were located along the superficial epigastric vessels. The imaging system allowed processing for extraction of images showing changes in the AB intensity of the visualized PVS components. This newly developed procedure can be used for further study on various dynamic processes of PVS in lymph vessels.

Keywords Primo vascular system • Acupuncture • Meridians • Lymph • Alcian blue

1 Introduction

In traditional oriental medicine, acupuncture has been used for treatment of various diseases for several thousand years. The first anatomical and biological study on the reality of acupuncture points and meridians was started by Bong-Han Kim just half a century ago [1, 2]. He reported that new anatomical node and ductule structures

J. Kim • D.-H. Kim • K.-S. Soh (✉)
Nano Primo Research Center, Advanced Institute of Convergence Technology, Seoul National University, Suwon 443-270, South Korea
e-mail: kssoh1@gmail.com

S.J. Jung
Nano Primo Research Center, Advanced Institute of Convergence Technology, Seoul National University, Suwon 443-270, South Korea

Department of Transdisciplinary Studies, Graduate School of Convergence Science and Technology, Seoul National University, Suwon 443-270, South Korea

© Springer International Publishing Switzerland 2016

Q. Luo et al. (eds.), *Oxygen Transport to Tissue XXXVIII*, Advances in Experimental Medicine and Biology 923, DOI 10.1007/978-3-319-38810-6_41

were discovered through a series of experimental animal studies and that the structures may correspond to the acupuncture points and acupuncture meridians. The structure was distributed not only in the skin tissue, following the meridian lines, but also inside the blood vessels and even inside the lymphatic vessels throughout the body. He reported that this ductule structure is distinct from the lymphatic vessels in the pattern of distributions and histological properties [1].

During the last decade, this Bonghan system, also known as the Primo Vascular System (PVS), has been confirmed using various methods with more modern technology [3]. The PVS inside the lymph vessel was first observed by injecting the staining dye of Janus Green B into the lymph nodes and vessels around the inferior vena cava of rabbits [4]. The staining dyes such as Alcian blue (AB) [5], fluorescent magnetic nanoparticles [6], DiI (1.1′-dioctadecyl-3,3,3′,3′-tetramethyl indocarbocyanine perchlorate) [7], and methylene blue [8] were employed for visualization of the PVS in lymphatics of rabbit, rat and mouse. Because the PVS was known to have a high concentration of hyaluronic acid, the most frequently used dye is AB which stains surface mucopolysaccharides to identify the structure [5]. The observation positions for target lymph vessels were also extended, starting from the inferior vena cava to the thoracic lymph vessels [9] and those around the superficial epigastric vein [10].

Until now, the PVS in lymph vessels was studied only for the purpose of harvesting the tissues for analysis. Monitoring of the PVS to study its dynamic changes over time has not yet been performed, although this is necessary for a deeper understanding of the physiological roles of the PVS.

In this study we focus on the temporal change of the PVS in lymph vessels near the superficial epigastric vessels of rats. The condition of long-term monitoring requires minimal surgery for injecting the staining dye and imaging the observations. Compared to observations of the PVS near the caudal vena cava, this newly developed procedure will provide a useful method for further study on the dynamic process of the PVS in the lymph vessels, under more intact conditions.

2 Materials and Methods

Nine-week-old Sprague–Dawley male rats (weight 260–300 g) were purchased from DooYeol Laboratory Animal Company (Seoul, Korea). The animals were housed in a constant temperature-controlled environment (23 °C) with 60 % relative humidity. All animals were exposed to a 12-h light–dark cycle and allowed access to water, but not to food for 1 day prior to experiments. Procedures involving the animals and their care conformed to institutional guidelines (Approval No. WJIACUC 20140807-03-07). The rats were anesthetized by intramuscular injection of Zoletil (0.7 mL/kg, Virbac Laboratories, Carros, France) and xylazine (0.3 mL/kg, Bayer, Korea) in the hind limb. Hair on the lateral side of the body was removed using a hair clipper and a depilatory (thioglycolic acid 80 %, Niclean cream, Ildong Pharm., Seoul, Korea). As shown in Fig. 41.1a, the lateral side of abdominal skin was shaved and the position of the inguinal node and superficial epigastric vessels were identified through the skin with a bright backlight.

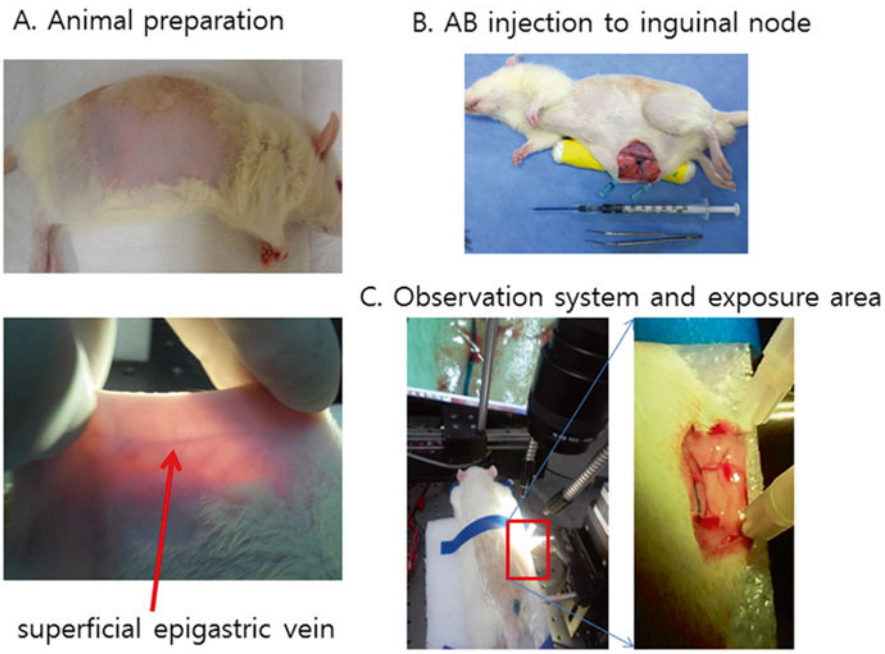

Fig. 41.1 Photographs showing the protocol of Alcian blue (AB) injection into the inguinal node and the observation system

The AB powder 8GX (Sigma, St. Louis, MO, USA) was dissolved in phosphate-buffered saline (PBS) solution pH 7.2 (Life Technology Corp, Waltham, MA, USA) to make 1 % AB staining dye solution. An apparatus called the vortex machine was used to process the dye. The solution was applied to the vortex machine for 10 s and filtered with a 0.22-μm syringe filter (Merck Millipore, Darmstadt, Germany). The AB solution was loaded in a 1-mL syringe with a glass capillary needle and kept at a constant temperature of 37 °C in a warm bath before injecting it into the inguinal lymph node. The homemade injector was composed of a disposable 1-mL Kovax-Syringe (26G × 1/2 in.) and a luer lock from a scalp vein set (24G 3/4, Becton, Dickinson and Company, East Rutherford, NJ, USA). The original needle tip of sterile hypodermic syringe was removed and replaced with the luer connector [11]. Thin-walled glass capillaries (World Precision Instruments, Inc., FL, USA; outer and inner diameters of 1.5 and 1.12 mm, respectively) were pulled by a micropipette puller (PP-830, Narishige Inc., East Meadow, NY, USA) to have a 20-μm average tip size. The pulled capillary was inserted into the luer connector to have an injection needle for injection of AB dye solution. Figure 41.1b shows that AB was injected with the injection tools.

At two places on the skin of the rat's body, two surgical procedures were performed for AB injection into the inguinal node and observation along the superficial epigastric vessel. The first was an incision of the subcutaneous layer of the skin along the linea alba at the navel of the rat lying in supine position. With further incisions (as shown in Fig. 41.1b), the skin flap was folded back to expose the left- or right-side

inguinal lymph nodes with the prepared 1 % AB staining dye solution. The second was another incision of the subcutaneous layer of the skin just above the superficial epigastric vessel at the corresponding lateral side of the rat lying in prone position. The skin was stretched in such a way that the superficial epigastric vessels could be seen under the stereomicroscope (SZX10, Olympus, Japan). As shown in Fig. 41.1c, the rat was lying in a prone position on a pad of Styrofoam, and part of the skin tissue was exposed for observation of the PVS in the lymphatic vessels near the superficial epigastric vein. The stretched skin tissue was pinned to the Styrofoam pad for better observation with reduced movement of the imaging part. The imaging system was composed of the stereomicroscope and two light sources (a 100-W metal halide lamp and a light emitting diode) for illumination. Depending on the condition, images were taken in the reflective mode above the target area, or in the transmit mode through the skin. About 0.2-mL of the AB solution was loaded in the syringe. The AB injection with glass capillary into the inguinal node was made until the lymph node became fully stretched. Image acquisitions were made just after the injection every hour. For isolation of the AB-stained region with RGB color images, the imaging software facility known as ImageJ enabled the RGB 24-bit channels to be split into three 8-bit images of Red, Green, and Blue components. Of the three components, the Red component predominantly isolates the AB-stained region. The intensity of AB staining dye concentration is related linearly to the intensity of brightness in the inverted image of the Red component. This image processing provides a method for systematic comparison of AB-staining intensities at different times.

3 Results

Just after the AB injections at the inguinal lymph node, the lymph vessels were filled with the AB solution and the staining solution in these lymph vessels gradually disappeared by a natural washing process. The washing process always goes with lymph circulations through peristalsis in the lymph vessels. The PVS in the lymph vessels still remained AB-stained even if the lymph vessels were cleared up within 1 h. By touching the PVS with forceps, we confirmed that the AB-stained PVS floated and freely moved inside the lymph vessels. When stretched, the PVS seemed to produce an elastic force like a rubber band.

Figure 41.2 shows a measured time-lapse sequence of AB-stained PVS inside the lymph vessel near the superficial epigastric vessel. Figure 41.2a shows the inguinal node just after the AB injection. In Fig. 41.2b, the exposed area is shown along the superficial epigastric vessel with AB flow just after the injection (0 h). The left and right side of the superficial epigastric vessels in Fig. 41.2b are associated with the inguinal and axillary lymph nodes, respectively. In Fig. 41.2c, the exposed area was subdivided into four different regions with more magnified views after 1 and 2 h in the upper and lower panels, respectively. A disconnected PVS can be seen in Region 4 at 2 h after the injection.

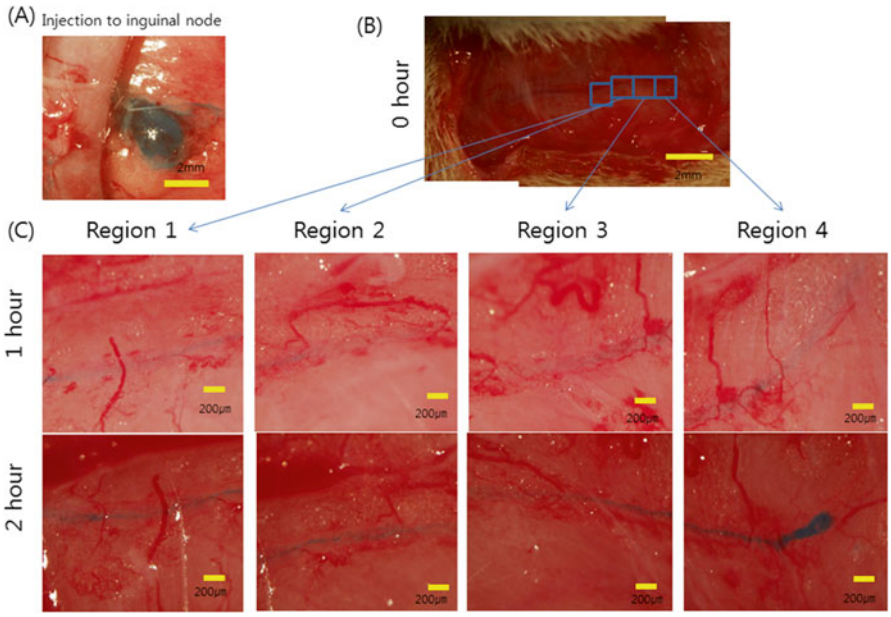

Fig. 41.2 Time-lapse sequences of AB-stained PVS inside the lymph vessel near the superficial epigastric vessel

Figure 41.3 shows an in vivo image taken from a different rat in the same way as in the previous example. The area (the squared region in the upper panel) is isolated on the in vivo sample image and shows magnified views at different times. With the image processing described in the Methods section, only the red components of the colored images are shown for more clear identification of AB-stained PVS in the area (the sequence of gray images in the lower left panel). In the selected area, the profile plots crossing the PVS in the lymph vessel along the dotted lines are shown for the AB concentration changes in the PVS compared to those in the lumen of the lymph vessel. The profile plots display two-dimensional graphs of the intensities of pixels along the line within the image.

4 Discussion

The medical significance of the PVS has only recently been explored, such as immune function due to innate immune cells like mast cells [12], and a regeneration function suggested by the enriched small adult stem cells with properties similar to those of very small embryonic-like stem cells. Recent study shows that injection of cells from the PVS partially repaired ischemic brain damage in mice, and the PVS may be a pathway for delivering stem cells to regenerate the target tissues [13].

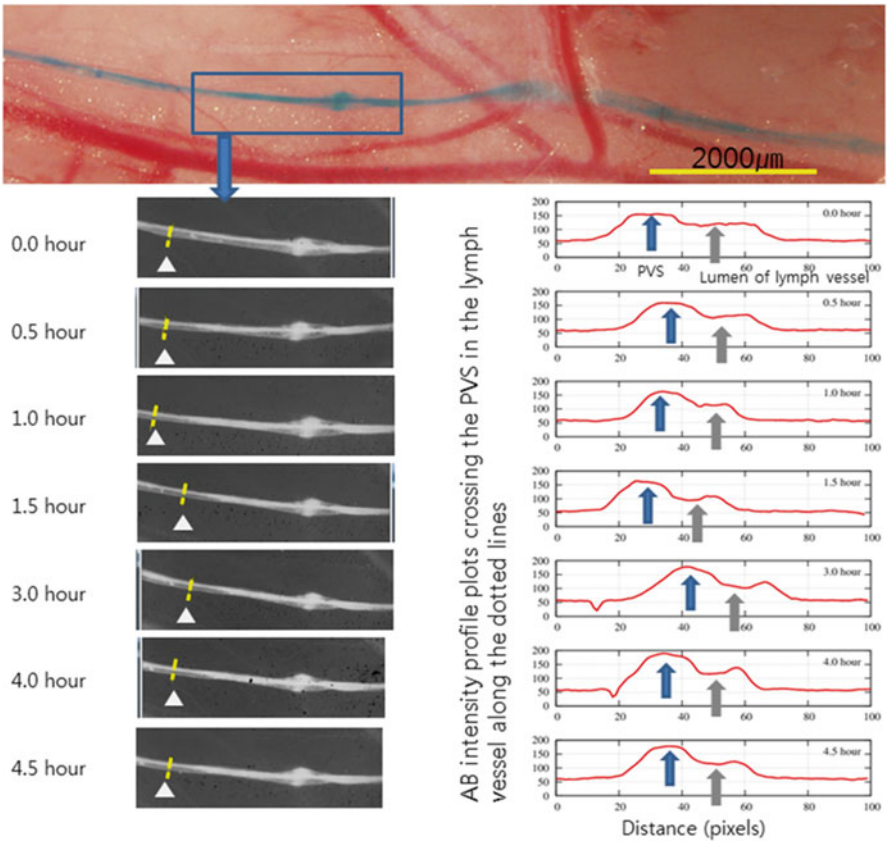

Fig. 41.3 Time dependence of the intensity of AB dye stained the PVS at two different regions. The *dotted lines* pointed by the *arrow* heads are shown in the series of *gray* images at the *lower left panels*. The profile plots for AB concentration intensity come along the *dotted lines*. The AB intensity of the PVS and lumen of lymph vessel changes as indicated by the *arrows* (The *left arrows* correspond to the PVS and the right ones to the lumen of lymph vessel)

The PVS is known to be a hyaluronic acid-rich node and duct system, and for this reason Alcian blue was mainly used for visualization. The success rate of Alcian blue depends on fine uncontrollable conditions and the experimenter's skill. Recently, a more stable high success rate was achieved with use of hollow gold nanoparticles [14]. This new material might be tested in the future for monitoring purposes.

In this study, the imaging system and image process technique were developed for measuring the temporal change of AB-stained PVS in lymphatic vessels near the superficial epigastric vessels of rats. This preliminary study is a significant step toward more systematic studies on monitoring the dynamic changes of the PVS.

Acknowledgements This work was supported in part by the Basic Science Research Program through the National Research Foundation of Korea (NRF) funded by the Ministry of Science, ICT & Future Planning (grant number: 2013R1A1A2008343).

References

1. Kim BH (1963) On the Kyungrak system. J Acad Med Sci DPRK 90:1–35
2. Kang KA (2013) Historical observations on the half-century freeze in research between the Bonghan system and the primo vascular system. J Acupunct Meridian Stud 6(6):285–292
3. Soh KS (2009) Bonghan circulatory system as an extension of acupuncture meridians. J Acupunct Meridian Stud 2(6):93–106
4. Lee BC, Yoo JS, Baik KY et al (2005) Novel threadlike structures (Bonghan ducts) inside lymphatic vessels of rabbits visualized with a Janus Green B staining method. Anat Rec B New Anat 286B:1–7
5. Lee C, Seol SK, Lee BC et al (2006) Alcian blue staining method to visualize Bonghan threads inside large caliber lymphatic vessels and X-ray microtomography to reveal their microchannels. Lymphat Res Biol 4:181–189. doi:10.1089/lrb.2006.4402
6. Johng HM, Yoo JS, Yoon TJ et al (2007) Use of magnetic nanoparticles to visualize threadlike structures inside lymphatic vessels of rats. eCAM 4(1):77–82. doi:10.1093/ecam/nel057
7. Lee BC, Soh KS (2008) Contrast-enhancing optical method to observe a Bonghan duct floating inside a lymph vessel of a rabbit. Lymphology 41:178–185
8. Ogay V, Bae KH, Kim KW, Soh KS (2009) Comparison of the characteristic features of Bonghan ducts, blood and lymphatic capillaries. J Acupunct Meridian Stud 2(2):107–117
9. Choi IH, Jeong HK, Hong YK (2011) Detection of the primo vessels in the rodent thoracic lymphatic ducts. In: Soh KS, Kang KA, Harrison D (eds) The primo vascular system: its role in cancer and regeneration. Springer, New York, pp 25–40
10. Lee SH, Bae KH, Kim GO et al (2013) Primo vascular system in the lymph vessel from the inguinal to the axillary nodes. Evid Based Complement Alternat Med 2013:472704, Article ID 472704. http://dx.doi.org/10.1155/2013/472704
11. Jung SJ, Bae KH, Nam MH et al (2013) Primo vascular system floating in lymph ducts of rats. J Acupunct Meridian Stud 6(6):306–318
12. Kwon BS, Ha CM, Yu S, Lee BC, Ro JY, Hwang S (2012) Microscopic nodes and ducts inside lymphatics and on the surface of internal organs are rich in granulocytes and secretory granules. Cytokine 60:587–592
13. Lee SJ, Park SH, Kim YI et al (2014) Adult stem cells from the hyaluronic acid-rich node and duct system (HAR-NDS) differentiate into neuronal cells and repair brain injury. Stem Cells Dev 23(23):2831–2840. doi:10.1089/scd.2014.0142
14. Kang KA (2015) Personal communication

Chapter 42
Ultrastructure of the Subcutaneous Primo-Vascular System in Rat Abdomen

Chae Jeong Lim, So Yeong Lee, and Pan Dong Ryu

Abstract Recently, we identified the primo-vascular system (PVS), a novel vascular network, in rat subcutaneous tissues. Little is known about the subcutaneous PVS (sc-PVS). Here, we examined the ultrastructure of the sc-PVS in the hypodermis at the rat abdominal midline by electron microscopy. On the surface of sc-PVS, we observed three types of cells: microcells (5–6 μm), large elliptical cells (>20 μm), and erythrocyte (3–4 μm). The inside of the sc-PVS was filled with numerous cells, which can be classified into three major groups: leucocytes, mast cells, and erythrocytes. The dense leucocytes and mast cells were easily noticed. The extracellular matrix of the sc-PVS was mainly composed of extensive fibers (79 ± 6.5 nm) tightly covered by micro- (0.5–1 μm) and nanoparticles (10–100 nm). In conclusion, the ultrastructural features, such as the resident cells on and in the sc-PVS and fiber meshwork covered by particles, indicate that sc-PVS might act as a circulatory channel for the flow and delivery of numerous cells and particles. Our findings will help understand the nature of various sc-PVS beneath-the-skin layers and how they relate to acupuncture meridians.

Keywords Primo-vascular system (PVS) • Subcutaneous PVS • Resident cells • Fibrous structure • Electron microscopy

C.J. Lim • S.Y. Lee • P.D. Ryu (✉)
Department of Veterinary Pharmacology, College of Veterinary Medicine and Research Institute for Veterinary Science, Seoul National University, Seoul 151-742, Republic of Korea
e-mail: pdryu@snu.ac.kr

© Springer International Publishing Switzerland 2016

Q. Luo et al. (eds.), *Oxygen Transport to Tissue XXXVIII*, Advances in Experimental Medicine and Biology 923, DOI 10.1007/978-3-319-38810-6_42

1 Introduction

The primo-vascular system (PVS), which consists of primo-vessel (PV) and primo-node (PN), is a novel vascular tissue reported by Kim in the 1960s to be the acupuncture meridians [1]. However, Kim's findings have not been reproduced until recently, mainly because the detailed experimental methods were not available. In the early 2000s, Dr. Soh's group rediscovered the part of the findings using dyes, such as alcian blue and trypan blue, to visualize the PVS [2].

The organ-surface PVS (os-PVS) in the abdominal cavity of rats has been most extensively studied. The os-PVS has a bundle structure of several subducts, different from that of an lymph vessel (LV) with a single tube [3]. In addition, it has a unique cellular composition, high density of leucocytes and mast cells (MCs) [4].

A recent study revealed that the PVS also exists in the hypodermis [5]. This observation corresponds to Kim's initial report that the PVS in the skin is the anatomical entity of the meridians [6]. However, our understanding of the structure and function of the subcutaneous PVS (sc-PVS) is limited. Thus, in this study, we examined the resident cells and extracellular matrix (ECM) of sc-PVS identified in the ventral midline of the hypodermis of rats by electron microscopy.

2 Materials and Methods

Male Sprague–Dawley rats (5–7 weeks; $n = 12$, Orient Bio, Korea) were used and kept in an isolator at a constant temperature (22–26 °C) under a 12:12-h light–dark cycle. All the experiments were performed in accordance with the Guide for the Laboratory Animal Care Advisory Committee of Seoul National University and approved by the Institute of Laboratory Animal Resource of Seoul National University (SNU-140926-2). With the rats under deep anesthesia (Zoletil, 25 mg/kg; Xylazine, 10 mg/kg), the abdominal skin layer of each rat was incised. three kinds of samples, sc-PVS, os-PVS, and LVs were harvested as follows: (1) sc-PVS was revealed on the hypodermal layer by Hemacolor staining [5]; (2) os-PVS was observed on the organs in the abdominal cavity [4]; and (3) LVs were collected around the caudal vena cava [7].

For scanning electron microscopy (SEM), samples were primary-fixed with Karnovsky's fixative for 2 h and were post-fixed with 2 % osmium tetroxide for 2 h. The samples were dehydrated with graded ethanol, critical point-dried in liquid CO_2 (CPD 030 BAL-TEC) for 1 h, gold coated by a sputter coater (EM ACE 200, Leica), and then examined with SEM (Sigma, Carl Zeiss, UK).

For transmission electron microscopy (TEM), samples were treated in the same manner until the post-fixation, then underwent *en bloc* staining with 0.5 % uranyl acetate for 30 min, and were then dehydrated with an ethanol series. The samples were kept in propylene oxide for 20 min, infiltrated with Spurr's resin overnight on a rotator, and observed with TEM (JEOL, JEM 1010, Japan) at 80 kV of accelera-

tion voltage. The diameters of cells, fibers, and particles of the sc-PVS were measured by ImageJ software (developed at the US National Institute of Health). All data values are presented as mean ± standard error.

3 Results

SEM revealed the cytomorphology of the surface of the sc-PVS. The sc-PVS consisted of a PN (Fig. 42.1a) and a PV (Fig. 42.1d) part comprised of a bundle of subducts. The most abundant cells on the sc-PVs were round microcells of 5–6 μm (Fig. 42.1b, e; asterisks), which were also located on the os-PVs (Fig. 42.1h; asterisks). Most of the surface cells belonged to one of three types: microcells, large elliptical cells (>20 μm, Fig. 42.1c), or erythrocytes (3–4 μm). The surface texture of the sc-PV microcells was generally smooth (Fig. 42.1f), but the os-PV microcells were rough (Fig. 42.1i). The fibers and fluidic structures were well developed at the bottom of the microcells in the ECM of the PVs (Fig. 42.1f, i).

TEM further revealed the composition of resident cells inside the sc-PVS. There were three major cell groups inside the sc-PVs (Fig. 42.1j): MCs, erythrocytes (Fig. 42.1m), and leucocytes. The most abundant was the latter, including neutrophils (Fig. 42.1n), eosinophils (Fig. 42.1o), and lymphocytes (Fig. 42.1p). MCs were also rich, although less abundant than leucocytes. The sc-PV MCs were elliptical or elongated as are those observed in skin layers [8]. Most MCs appeared degranulated (Fig. 42.1j, l), but normal MCs were also observed (Fig. 42.1k).

To identify the ECM of the sc-PVS, we conducted high-magnified SEM. The ECM (Fig. 42.2a) of sc-PVs consists of extensive and winding fibers and microparticles (0.5–1 μm). The latter appeared to sprout from inside the sc-/os-PVs (Fig. 42.2a, b, d; asterisks). The surface of the fibers and microparticles was tightly covered by nanoparticles (10–100 nm, Fig. 42.2c, e; asterisks). There were round or triangular openings (~300 nm) in fiber meshwork. LVs also showed dense fibers and openings, but the micro-/nanoparticles were not well developed. The fibers of LVs were smaller than those of PVs (sc-PVs, 79 ± 6.5 nm; os-PVs, 83 ± 7.0 nm vs. LVs, 48 ± 2.3 nm; $n = 3$; $p < 0.001$), and showed a periodic striped pattern (Fig. 42.2g, arrows), but such a pattern was much less evident in PVs.

4 Discussion

The major findings of this study are as follows: (1) the cells on the surface of the sc-PVS were mainly composed of microcells (the majority), elliptical cells, and erythrocytes; (2) the cells inside the sc-PVS could be grouped into three types: leucocytes, MCs, and erythrocytes; and (3) the ECM of the sc-PVS showed the fibers and microparticles covered with nanoparticles, different from that of LVs.

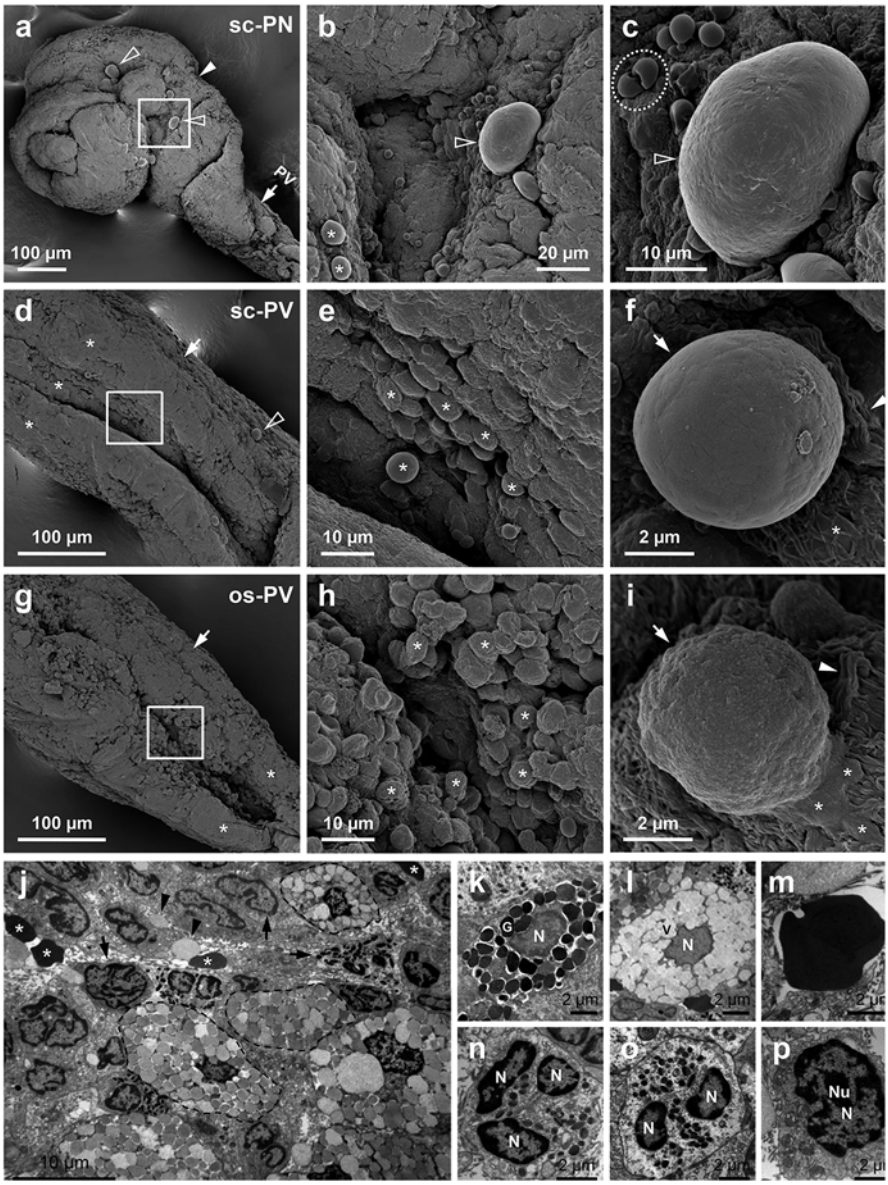

Fig. 42.1 Electron micrographs of cells on the surface and inside the sc-PVS. (**a**, **d**, **g**) SEM images of macroscopic structure of sc-PN ((**a**), 489.3×429.5 μm), sc-PV ((**d**), 212.1 μm), and os-PV ((**g**), 207.6 μm). Note the bundle composed of subducts (*asterisks*) and large cells (*open arrowheads*). (**b**, **e**, **h**) Magnified views (*squares* in (**a**), (**d**), and (**g**)) of sc-PN (**b**), sc-PV (**e**), and os-PV (**h**). Note the microcells (the majority, *asterisks*) and large elliptical cell (*open arrowhead*). (**c**, **f**, **i**) PVS cells including an elliptical cell ((**c**), *open arrowhead*, 28.1×19.2 μm), erythrocytes ((**c**), *circle*), and microcells ((**f**), *arrow*, 6.2 μm; (**i**), *arrow*, 5.1 μm). Note the fibers (*arrowheads*) and fluidic structures (*asterisks*). (**j**) TEM image of cells inside sc-PVs. Note the leucocytes (*arrows*), MCs (*dotted lines*), erythrocytes (*asterisks*), and secreted vesicles (*arrowheads*). (**k**) Normal MC with central nucleus (N) and surrounding dense granules (G). (**l**) Degranulated MC. Note that vesicles (V) swelled and became grainy. (**m**) Normal erythrocyte without a nucleus. (**n**) Neutrophil with three lobes of nucleus (N). (**o**) Eosinophil with two lobes of nucleus (N). (**p**) Lymphocyte with a nucleus (N) and nucleolus (Nu)

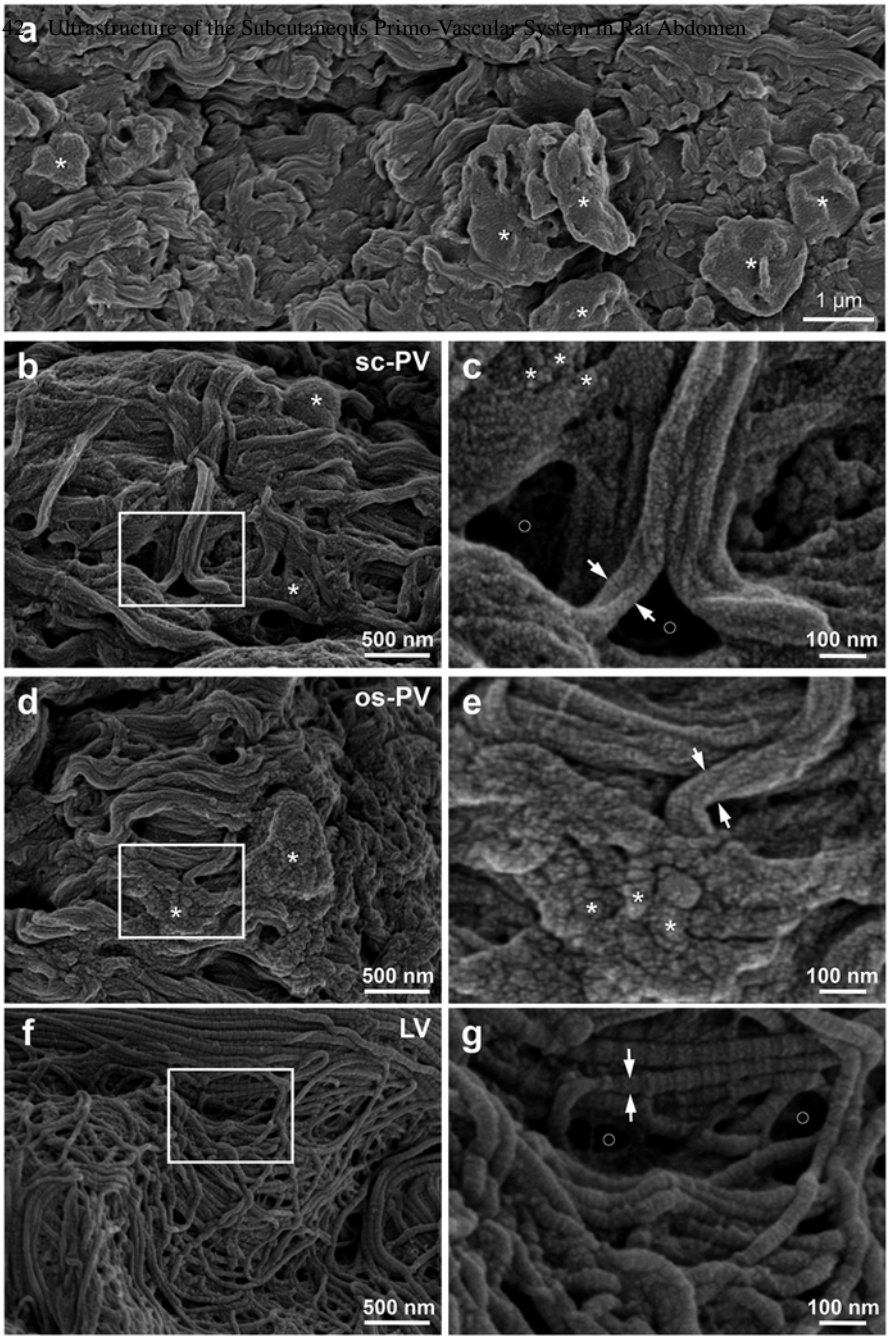

Fig. 42.2 SEM micrographs of the extracellular matrix of sc-PV, os-PV, and lymph vessel. (**a**) A low magnification view of the surface of an sc-PV. Note the dense fibrous structures that are randomly oriented in multiple directions and microparticles (0.5–1 μm; *asterisks*) covering the surface on the sc-PV. (**b**, **d**, **f**) Comparison of fibers on the sc-PV (**b**), os-PV (**d**), and lymph vessel **Fig. 42.2** (continued) (LV, (**f**)). (**c**, **e**, **g**) Magnified views (*squares* in (**b**), (**d**), and (**f**)) of the fiber appearance on the sc-PV (**c**), os-PV (**e**), and LV (**g**). Note that the diameters of the ECM fibers in the sc-PV ((**c**), *arrows*, 76.4 nm) and the os-PV ((**e**), *arrows*, 81.4 nm) are thicker than those of the LV ((**g**), *arrows*, 46.5 nm). Note also the regular stripes on the fibers in the LV. The fibers of the sc-PV and the os-PV have irregular surfaces containing nanoparticles (10–100 nm, (**c**) and (**e**), *asterisks*). There are openings in the fiber meshwork. ((**c**) and (**g**), *circles*)

Our study newly revealed that there are at least three types of resident cells on the sc-PVS, and the cells are attached on the surface of the fibrous structure of the ECM. Among these, erythrocytes were easily identified by their size (3–4 μm) and concave form [9]. Some microcells are likely to be stem cells, because similar microcells (3–5 μm) of the PVS inside the LVs were recently identified as adult stem cells [10]. The detailed properties of other microcells remain to be studied further. The nature of the elliptical cells is presently unknown, although they are similar to MCs in elliptical shape and size (>20 μm) [4].

The cell composition in the sc-PVS is in good agreement with previous reports [4, 5]. The presence of rich leucocytes and MCs indicates that the sc-PVS may play an important role in immune reaction. In addition, the sc-PVS seems to be related to a conception vessel meridian, the acupuncture meridian on the ventral hypodermal region, in terms of the location and resident cells. They are both linearly distributed along the ventral midline in the hypodermis and contain high-density MCs [5, 8, 11].

Other novel findings of the sc-PVS are the extensive fibers and micro-/nanoparticles that appeared to have 'sprouted' from the ECM of sc-PVs. These features were markedly different from those of LVs, which are part of another circulating system. For example, the LVs did not present the microparticles, and were less variable in the fiber diameter and more prominent in the fiber stripes. In this study, the sc-PVS was visible only after Hemacolor staining, which was successful in ~20 % of the rats tested. Further study is needed to improve the reproducibility of sampling of sc-PVS tissue.

Taken together, our results demonstrate that ultrastructural features of the sc-PVS are similar to those of the os-PVS, but different from LVs. Our findings indicate that the sc-PVS can function as a circulatory channel for the flow and delivery of various cells and particles to the body.

Acknowledgments This study was supported by the National Research Foundation of Korea funded by the Ministry of Education, Science and Technology (2015-061732).

References

1. Kim BH (1963) On the kyungrak system. J Acad Med Sci of Democratic People's Republic of Korea 90:1–41
2. Soh KS (2009) Bonghan circulatory system as an extension of acupuncture meridians. J Acupunct Meridian Stud 2:93–106
3. Lee BC, Yoo JS, Ogay V et al (2007) Electron microscopic study of novel threadlike structures on the surfaces of mammalian organs. Microsc Res Tech 70:34–43
4. Lim CJ, Yoo JH, Kim Y et al (2013) Gross morphological features of the organ surface primovascular system revealed by hemacolor staining. Evid Based Complement Alternat Med 2013:12 p, Article ID 350815
5. Lim CJ, Lee SY, Ryu PD (2014) Identification of primo-vascular system in abdominal subcutaneous tissue layer of rats. Evid Based Complement Alternat Med 2015:13 p, Article ID 751937

6. Soh KS, Kang KA, Ryu YH (2013) 50 Years of Bong-Han theory and 10 years of primo vascular system. Evid Based Complement Alternat Med 2013:12 p, Article ID 587827
7. Lee BC, Soh KS (2008) Contrast-enhancing optical method to observe a Bonghan duct floating inside a lymph vessel of a rabbit. Lymphology 41:178–185
8. Zhang D, Ding G, Shen X et al (2008) Role of the mast cell in acupuncture effect: a pilot study. Explore 4:170–177
9. Potter MD, Shinpock SG, Popp RA et al (1997) Mutations in the murine fitness 1 gene result in defective hematopoiesis. Blood 90:1850–1857
10. Lee SJ, Park SH, Kim YI et al (2014) Adult stem cells from the hyaluronic acid-rich node and duct system differentiate into neuronal cells and repair brain injury. Stem Cells Dev 23:2831–2840
11. Yin CS, Jeong HS, Park HJ et al (2007) A proposed transpositional acupoint system in a mouse and rat model. Res Vet Sci 84:159–165

Chapter 43
Effects of Acupuncture Stimulation on Muscle Tissue Oxygenation at Different Points

Yasuhisa Kaneko, Ryotaro Kime, Eiji Furuya, Ayumi Sakamoto, and Toshihito Katsumura

Abstract Muscle tissue oxygenation is a critical issue in muscle complications such as pain, exhaustion, stiffness, or fatigue during and after exercise. The aim of this study was to investigate whether the changes of muscle tissue oxygenation could be observed at both erector spinae muscle at S1 level and gastrocnemius during and after acupuncture stimulation to ipsilateral erector spinae at S1 level. The subjects were ten healthy males. Muscle oxygenation was monitored by near infrared spectroscopy (NIRS), and the probes were placed on the right side of the erector spinae muscle at S1 level (Guanyuanshu, BL26) and the belly of the gastrocnemius on the right (Chengjin, BL56). The subjects lay on the bed in prone position for 10 min, followed by acupuncture insertion into the right side of BL26. The needle was left for 10 min and subjects were kept still for 10 min after removal. At BL26, oxygenated-hemoglobin (oxy-Hb) was significantly increased compared to the baseline at 10 min after insertion ($p<0.05$), then continued increasing. Total hemoglobin (t-Hb) was increased at 2 min after removal ($p<0.05$). Tissue-oxygen saturation (StO_2) was increased at 7 min after insertion ($p<0.05$). At BL56, oxy-Hb and t-Hb were increased at 6 and 2 min after removal, respectively ($p<0.05$). StO_2 showed no significant change. The acupuncture stimulation affected muscle tissue oxygenation differently at both stimulated and non-stimulated points in the same innervation.

Y. Kaneko (✉)
Department of Sports Medicine for Health Promotion, Tokyo Medical University, Tokyo, Japan

Department of Oriental Medicine, Kuretake College of Medical Arts and Sciences, Tokyo, Japan
e-mail: ykaneko@tokyo-med.ac.jp

R. Kime • T. Katsumura
Department of Sports Medicine for Health Promotion, Tokyo Medical University, Tokyo, Japan

E. Furuya • A. Sakamoto
Department of Oriental Medicine, Kuretake College of Medical Arts and Sciences, Tokyo, Japan

© Springer International Publishing Switzerland 2016

Q. Luo et al. (eds.), *Oxygen Transport to Tissue XXXVIII*, Advances in Experimental Medicine and Biology 923, DOI 10.1007/978-3-319-38810-6_43

Keywords Acupuncture • Muscle blood flow • Oxygenation • Near infrared spectroscopy

1 Introduction

Muscle complications such as pain, exhaustion, stiffness or fatigue are frequently observed during and after exercise. These can be caused by multiple factors such as limitation of energy supply, deoxygenation, intramuscular accumulation of metabolic by-products, impairment of Ca^{2+} kinetics or ion shifts [1, 2] Appropriate delivery of oxygen by blood flow to deoxygenated muscle is a critical issue, from an elite athlete after severe exercise to a patient with peripheral artery disease. One of the physiological effects of acupuncture is that it increases tissue blood flow at the point stimulated by acupuncture [3, 4]. One previous animal study has demonstrated the change of blood flow in biceps femoris by repetitive acupuncture-like electrical stimulation at ipsilateral dorsal roots at the 3rd-5th lumbar segments [5]. To our knowledge, there have been no human studies investigating the change of blood flow at the non-stimulated point during and after stimulating lumbar segments with acupuncture using near infrared spectroscopy (NIRS). The aim of this study was to investigate whether the changes of muscle tissue oxygenation could be observed at both erector spinae muscle at S1 level and gastrocnemius, which are both innervated by the S1 segment, during and after acupuncture stimulation to ipsilateral erector spinae at S1 level in healthy human subjects. Our hypothesis is that the changes of muscle tissue oxygenation affected by acupuncture can be observed simultaneously in both points because these are in the same innervation.

2 Methods

Ten healthy male subjects (age 29 ± 4 years, height 173.7 ± 2.7 cm, weight 69.0 ± 5.2 kg) participated in this study. All subjects were briefed about the experimental protocol and written informed consent was obtained before the experiment. The institutional ethics committee of Kuretake College of Medical Arts & Sciences approved the research protocol.

Muscle tissue oxygenation of each point and the surrounding area was monitored by near infrared spectroscopy (NIRS, HB-14, Astem Co., Japan) throughout the study. The optode distance between the LED as a light source and the photodiode detector was 30 mm. The NIRS probes were placed on the right side of the lumbar region, at the same level as the inferior border of the spinous process of the fifth lumbar vertebra, 1.5 B-cun lateral to the posterior median line, or the right side of the erector spinae muscle at S1 level (Guanyuanshu, BL26) and on the posterior aspect of

the right leg, between the two muscles bellies of the gastrocnemius muscle, 5 B-cum distal to the popliteal crease (Chengjin, BL56). BL26 and BL56 are both innervated by the S1 segment. The subjects lay on the bed in prone position for 10 min, followed by acupuncture needle (diameter 0.20 mm, length 50 mm, manufactured by Seirin Co. Ltd., Japan) stimulation at a depth of 15 mm into the right side of BL26. The depth was determined as the same as the measurement range with the NIRS device in the hemisphere of 1/2 of the distance as half of the optode distance described above [6]. The needle was twisted for manipulation for 1 min at 1Hz and left for 9 min. The technique of twisting the needle is regularly used as a clinical technique in acupuncture therapy to add a certain amount of stimulation to elicit the effects of stimulation. The acupuncture therapist who performed the procedures in this study has 14 years of clinical experience, so that subjects were given a steady amount of stimulation without any painful sensation. Subjects were kept resting for 10 min after the removal of the needle to observe the effect after stimulation. Oxygenated-hemoglobin (oxy-Hb), deoxygenated-hemoglobin (deoxy-Hb), total hemoglobin (t-Hb), and tissue-O_2 saturation (StO_2) at BL26 and BL56 were detected at 1 Hz. To correct the effects of the fat layer thickness on StO_2 quantification, the fat layer thickness was measured prior to needle insertion at each point, using an ultrasound device (LogiQ3, GE-Yokokawa Medical Systems, Japan). The specifications of correction for the influence of fat layer thickness have been fully described by Niwayama et al. [7]. Data detected after correction was averaged over every 1 min. The last minute of resting before the stimulation was defined as baseline. At the end of the examination, subjects were asked if they felt any sensation (e.g. pain, dullness, numbness) during needling.

The changes in oxy-Hb, deoxy-Hb, t-Hb, and StO_2 at BL26 and BL56 during the experiments were analyzed by one-way ANOVA for repeated measurements and by Tukey-Kramer test for a multiple comparisons test. The significance level was set to 0.05. Statistics were completed using JSTAT 13.0 for Windows.

3 Results

At BL26, where the needle was inserted, oxy-Hb was significantly increased compared to the baseline at 10 min after insertion ($p<0.05$), then continued increasing until the end of the experiment. Deoxy-Hb did not show any significant difference throughout the observation. t-Hb was increased at 2 min after removal ($p<0.05$) and continued increasing. StO_2 started increasing at 7 min after insertion ($p<0.05$) and continued until the end of the examination. At BL56, spatially away from stimulation but in the same innervation as BL26, oxy-Hb and t-Hb were increased at 6 and 2 min after removal, respectively, ($p<0.05$) and continued increasing. No changes were observed in deoxy-Hb or StO_2 (Figs. 43.1 and 43.2). No subjects reported feeling any painful sensation during needling.

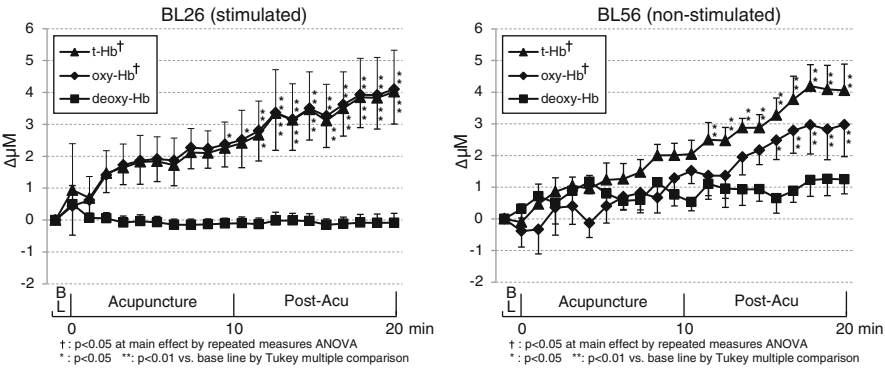

Fig. 43.1 Changes in oxy-Hb, deoxy-Hb, and t-Hb at BL26 (stimulated), and BL56 (non-stimulated) by acupuncture. Oxy-Hb started increasing significantly at 10 min after insertion ($p < 0.05$) at BL26, and 6 min after the removal ($p < 0.05$) at BL56 compared to baseline. t-Hb started increasing at 2 min after the removal ($p < 0.01$) and there was no change in deoxy-Hb at both points

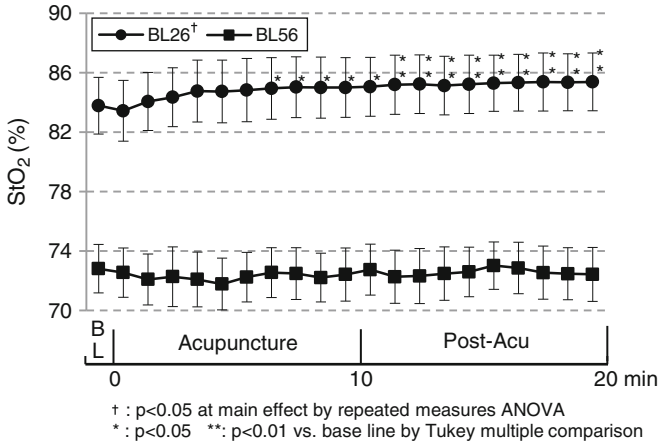

Fig. 43.2 Changes in StO_2. StO_2 started increasing significantly at 7 min after insertion at BL26 compared to baseline ($p < 0.05$), and continued increasing until the end of the examination, while no change was observed at BL56

4 Discussion

This study provides evidence of changes in muscle tissue oxygenation at different points in the same innervation during and after acupuncture stimulation in healthy human subjects. Oxy-Hb and t-Hb were increased after acupuncture stimulation at BL26, as StO_2 also showed a significant difference from baseline. Sandberg et al. [3] and Ohkubo et al. [4] described similar results for the stimulated point in different muscles from those in the present study, although in those studies the change in

oxygenation appeared at different times after stimulation. The physiological response to acupuncture stimulation may vary due to the total amount of stimulation (e.g. diameter of needle, depth of insertion, way of manipulation) or sensitivity of the muscles where stimulated, although these effects are uncertain. The mechanism of increasing muscle blood flow around stimulated area can be explained by axon reflex, which produces calcitonin gene-related peptide (CGRP) induced by somatic afferent stimulation [8]. It is suggested that a similar response might have occurred in this study with acupuncture stimulation at BL26. However, Kimura et al. indicated that acupuncture stimulation released nitric oxide (NO), which played a role in cutaneous vasodilation at the stimulated area, and which appeared to be independent of the axon reflex in humans [9]. In this study, we were not able to eliminate the effects of cutaneous blood flow during this procedure, and the results at BL26 might contain the change of both cutaneous oxygenation and muscle oxygenation mediated by CGRP and NO production, respectively.

The changes of muscle tissue oxygenation at BL56 innervated by the S1 segment were also observed, but oxy-Hb increased 6 min later than that at BL26. The change of t-Hb appeared simultaneously to BL26. StO_2 did not change throughout the examination. Previous studies reported that dorsal roots stimulation excited type IV afferent fibers and released CGRP from afferent nerve terminals in anesthetized rats [5, 10]. This vasodilative substance then produced antidromic vasodilation, and subsequent increases in the blood flow of biceps femoris muscles, and this response was totally abolished by a CGRP receptor antagonist [5]. Interestingly, this vasodilation is independent of systemic blood pressure [5]. Another study showed the effects of electroacupuncture stimulation of the hind paw on blood flow of the bicep femoris, and concluded that the increase in muscle blood flow was due to a passive response to a systemic reflex pressor response [11]. Excitement of sympathetic nerve system followed by invasive acupuncture stimulation is considered to be the cause of blood flow change. However, changes in the sympathetic nerve system should appear quickly after needle insertion, while the significant change in StO_2 was observed 7 min after the insertion, at the earliest. It is suggested that the changes in muscle tissue oxygenation at BL56 might be led gradually by vasodilative substances, induced by acupuncture stimulation. Additionally, BL26 might be affected by the same mechanism as BL56 because BL26 is also innervated by the S1 segment.

As we described above, a multiple reflex might be affected in BL26; (1) axon reflex, (2) NO production and (3) antidromic vasodilation via somatic afferent nerves, while only (3) antidromic vasodilation was suggested to be affected in BL56. It could possibly lead to the spatial differences of muscle tissue oxygenation in response to the acupuncture stimulation, although in the same innervation.

It can be assumed that the increase of oxy-Hb with acupuncture stimulation lead more arterial blood into the muscle tissues. It may increase regional O_2, as an assumption regarding the equation made by Nioka et al. [12], and possibly be helpful in reoxygenation from deoxygenated muscle conditions, such as post exercise or peripheral disease. It is remarkable that this application can affect areas indirectly, especially in cases where direct application is inhibited, e.g. scars, ulcers by ischemia, immobilization by cast. Nevertheless, subjects in this study were healthy men, and it is uncer-

tain whether similar responses would be observed in injured patients. Further studies are needed to confirm this.

In Chinese medicine, Guanyanshu (BL26) is frequently used in the treatment of lumbar pain, which is a common problem among athletes following excess exercise during practice. Chengjin (BL56) belongs to the same meridian as Guanyanshu and should be affected by the stimulation at Guanyanshu through the meridian. The physiological phenomena observed in the present study might partly relate to its clinical effect as described in Chinese medicine.

There are limitations in this study. We were unable to confirm if the changes in muscle tissue oxygenation were influenced by systemic response. We would need to monitor heart rate or blood pressure in future studies to identify any unique effects of acupuncture. Psychological effects, such as subjects' thoughts or beliefs in acupuncture, might have influenced the results in this study. We selected an experienced acupuncture therapist for the intervention in order to minimize anxiety associated with pain from needling, and no subjects reported feeling any painful sensations, but it was still uncertain if we thoroughly eliminated any anxiety which could possibly have affected the results. We were also unable to exclude placebo effects because we did not use any placebo acupuncture (e.g. a blunted needle which subjects would feel penetrated the skin, but there would be no penetration).

5 Conclusions

Changes in muscle tissue oxygenation by acupuncture stimulation were detected at both the stimulated point and non-stimulated point. Although each point was located in the same innervation, the oxygenation patterns at each point were different.

References

1. Allen DG, Lamb GD, Westerblad H (2008) Skeletal muscle fatigue: cellular mechanisms. Physiol Rev 88(1):287–332
2. Katayama K, Amann M, Pegelow DF et al (2007) Effect of arterial oxygenation on quadriceps fatigability during isolated muscle exercise. Am J Physiol Regul Integr Comp Physiol 292(3): R1279–R1286
3. Sandberg M, Lundeberg T, Lindberg LG et al (2003) Effects of acupuncture on skin and muscle blood flow in healthy subjects. Eur J Appl Physiol 90:114–119
4. Ohkubo M, Hamaoka T, Niwayama M et al (2009) Local increase in trapezius muscle oxygenation during and after acupuncture. Dyn Med 8:2
5. Sato A, Sato Y, Shimura M et al (2000) Calcitonin gene-related peptide produces skeletal muscle vasodilation following antidromic stimulation of unmyelinated afferents in the dorsal root in rats. Neurosci Lett 283(2):137–140
6. Chance B, Dait MT, Zhang C et al (1992) Recovery from exercise-induced desaturation in the quadriceps muscles of elite competitive rowers. Am J Physiol 262:C766–C775

7. Niwayama M, Suzuki H, Yamashita T et al (2012) Error factors in oxygenation measurement using continuous wave and spatially resolved near-infrared spectroscopy. J Jpn Coll Angiol 52:211–215
8. Loaiza LA, Yamaguchi S, Ito M et al (2002) Vasodilatation of muscle microvessels induced by somatic afferent stimulation is mediated by calcitonin gene-related peptide release in the rat. Neurosci Lett 333(2):136–140
9. Kimura K, Takeuchi H, Yuri K et al (2013) Effects of nitric oxide synthase inhibition on cutaneous vasodilation in response to acupuncture stimulation in humans. Acupunct Med 31(1):74–80
10. Sakaguchi M, Inaishi Y, Kashihara Y et al (1991) Release of calcitonin gene-related peptide from nerve terminals in rat skeletal muscle. J Physiol 434:257–270
11. Noguchi E, Ohsawa H, Kobayashi S et al (1999) The effect of electro-acupuncture stimulation on the muscle blood flow of the hindlimb in anesthetized rats. J Auton Nerv Syst 75(2–3):78–86
12. Nioka S, Kime R, Sunar U et al (2006) A novel method to measure regional muscle blood flow continuously using NIRS kinetics information. Dyn Med 16(5):5

Part VI
Technologies and Modeling

Chapter 44
Continuous Wave Spectroscopy with Diffusion Theory for Quantification of Optical Properties: Comparison Between Multi-distance and Multi-wavelength Data Fitting Methods

Yung-Chi Lin, Zhi-Fong Lin, Shoko Nioka, Li-Hsin Chen, Sheng-Hao Tseng, and Pau-Choo Chung

Abstract Typically, continuous wave spectroscopy (CWS) can be used to accurately quantify biological tissue optical properties (μ_a and μ_s') by employing the diffuse reflectance information acquired at multiple source-detector separations (multi-distance). On the other hand, sample optical properties can also be obtained by fitting multi-wavelength light reflectance acquired at a single source detector separation to the diffusion theory equation. To date, multi-wavelength and multi-distance methods have not yet been rigorously compared for their accuracy in quantification of the sample optical properties. In this investigation, we compared the accuracy of the two above-mentioned quantifying methods in the optical properties recovery. The liquid phantoms had μ_a between 0.004 and 0.011 mm^{-1} and μ_s' between 0.55 and 1.07 mm^{-1} whose optical properties mimic the human breast. Multi-distance data and multi-wavelength data were fitted to the same diffusion equation for consistency. The difference between benchmark μ_a and μ_s' and the fitted results, ΔError (ΔE) was used to evaluate the accuracy of the two methods. The results showed that either method yielded ΔE within 15–30 % when values were within certain limits to standard values applicable to μ_s' and μ_a for human adipose tissue. Both methods showed no significant differences in ΔE values. Our results suggest that both multi-distance and multi-wavelength methods can yield similar reasonable optical properties in biological tissue with a proper calibration.

Y.-C. Lin • L.-H. Chen • P.-C. Chung (✉)
Institute of Computer and Communication Engineering, National Cheng Kung University, Tainan, Taiwan
e-mail: pcchung@ee.ncku.edu.tw

Z.-F. Lin • S.-H. Tseng
Department of Photonics, National Cheng Kung University, Tainan, Taiwan

S. Nioka
Department of Radiology, Medical School of University of Pennsylvania, Philadelphia, PA, USA

© Springer International Publishing Switzerland 2016

Q. Luo et al. (eds.), *Oxygen Transport to Tissue XXXVIII*, Advances in Experimental Medicine and Biology 923, DOI 10.1007/978-3-319-38810-6_44

Keywords Near-infrared spectroscopy • Diffuse reflectance • Optical property • Curve fitting • Simulating phantom

1 Introduction

Continuous wave spectroscopy (CWS) is well established over the centuries as an accurate method of chemical analysis. Continuous light features that photon fluence or energy is greater and more cost effective compared to time domain spectroscopy (TRS) and frequency domain spectroscopy (FDS). However, until now, because of biological tissue scattering property, CWS has not been well established or confirmed for its use as an accurate quantitative method of tissue optical property measurement. Instead, TRS and FDS are most commonly used to quantitate optical properties of biological tissues, with reduced scattering coefficient (μ_s') and absorption coefficient (μ_a). In recent years, the light diffusion theory was adapted with time domain and frequency domain spectroscopes to solve both μ_s' and μ_a information, because they produced their specific parameters, particularly time and phase information, respectively. Thus, the optical properties of human tissues have been reported using TRS and FDS measurements [1–3]. However, CWS has not been used for quantitation because of the lack of light pathlength information or the scattering features of tissue.

Attempts have been made to use a diffusion equation for CWS to determine the optical properties. Basically, they used multi-distance [4] or multi-wavelength data [5] from CWS to fit the diffusion theory with a minimum square algorithm. Most of the cases used a multi-distance method for fitting the diffusion theory and came up with reasonable accuracy, adequate for machine calibration purposes [6, 7]. However, there only a few studies used the multi-wavelength fitting method and they have not tested its accuracy compared to the more common multi-distance method. In this paper, we attempt to test the accuracy of the multi-wavelength method in comparison to the multi-distance method. In the Monte Carlo simulation, we found that the two methods exhibited a similar performance, also experimentally.

2 Material and Methods

By mixing a known amount of nigrosin and intralipid, we created an array of liquid phantoms that had similar optical properties to those in adipose tissues. The phantoms were carefully designed to have various optical properties so that we could compare the experimentally derived μ_a and μ_s' to the theoretical values at various conditions. In the setup of the measurement system, the architecture included a tungsten halogen light source and an optical spectrometer to detect the returned photon counts in a specific range of wavelengths through the optic fiber. Subsequently, the reflection of light received from the sensors can be obtained by the diffusion theory

and depends on the absorption, the scattering coefficients of the subject, and the span between the source and detector [8].

2.1 Multi-distance CW Method

The multi-distance method is a spatially resolved measure based on the information of various source-detector separations to estimate the optical parameters. When the photons enter the medium the reflected photons received by detector will decay as the distance between the source and detector (SD) increases. Multi-Distance Fitting utilizes the degree of decay of the reflectance in distinct positions to calculate μ_a and μ_s'. The signal received from the sample divided by the signal received from the standard phantom in different SD was used to compare the reflectance of the standard phantom to find the optimized reflectance of the sample.

2.2 Multi-wavelength CW Method

The multi-wavelength (MW) method relative to the multi-distance (MD) method is to measure the spectrum of the phantoms and apply the spectral fitting to adapt the reflectance spectrum of the subject. We employ different ingredients to mimic the absorption and scattering in tissue, and the total absorption coefficient can be the amount of volume fraction of nigrosin, intralipid and water in the liquid phantom based on their extinction coefficients. Besides, in order to compensate the response of the instrument from measurement, a calibration procedure can be implemented by employing the simulating phantoms with known optical properties.

2.3 The Curve-Fitting Algorithm

For the sake of conjecturing the phantom's optical properties, the minimization inverse procedure is performed and the algorithm is described as follows. The diffusion theory was used to investigate the optical properties and as the forward model in MD/MW CWS system due to the reduced scattering coefficient is much larger than the absorption coefficient that satisfied the diffusion approximation. A series of optical parameters were substituted for the forward model to calculate the estimated reflectance (R_i^{est}) with minimum divergence against the measured reflectance (R_i^{mea}). Subsequently, the inverse procedure is used to extract the optical parameters from the measured reflectance. Further, an iterative nonlinear least-squares method was used to minimize the residual between the reflectance from measured experimentally and the reflectance calculated with the adding-doubling method estimated by diffusion theory over the spectral range or spatially resolved measurements. The curve fitting techniques can be used to obtain appropriate values of absorption and scattering under optimization options.

2.4 *Monte Carlo Simulation*

To understand the theoretical performance of our measurement setup, we carried out Monte Carlo simulations to mimic the homogeneous tissue [9]. In the simulations, the sample was modeled as a $80 \times 80 \times 80$ mm^3 cube, and the light source that injected photon packets perpendicularly into the sample was located at the center of the surfaces of the cube. There were four circular detectors (each of diameter 1 mm) placed on the same surface with the light source.

The curve-fitting was done wavelength-by-wavelength or distinct SDs using the phantom with the five sets of nigrosin concentrations mixed with a uniform concentration of intraplipid in fixed absorption but varied scattering case (Experiment I). In contrast, another experiment was performed using the phantom with the six sets of intralipid concentrations and a constant concentration of nigrosin in the case of fixed scattering but varied absorption (Experiment II). Simultaneously, we selected one of them to be the standard phantom.

3 Simulation and Experimental Results

In the following, Monte Carlo simulation is launched by importing the two groups of optical properties designed for Experiment I and II and the simulated results are analyzed by multi-wavelength and multi-distance methods.

From the results of the simulation, six wavelengths were chosen to show in Fig. 44.1; it can be seen that as the samples' μ_s' are fixed and μ_a are varied, the optical properties recovery errors of the MD method and MW method are both below 15 % when phantom 3 was chosen as standard.

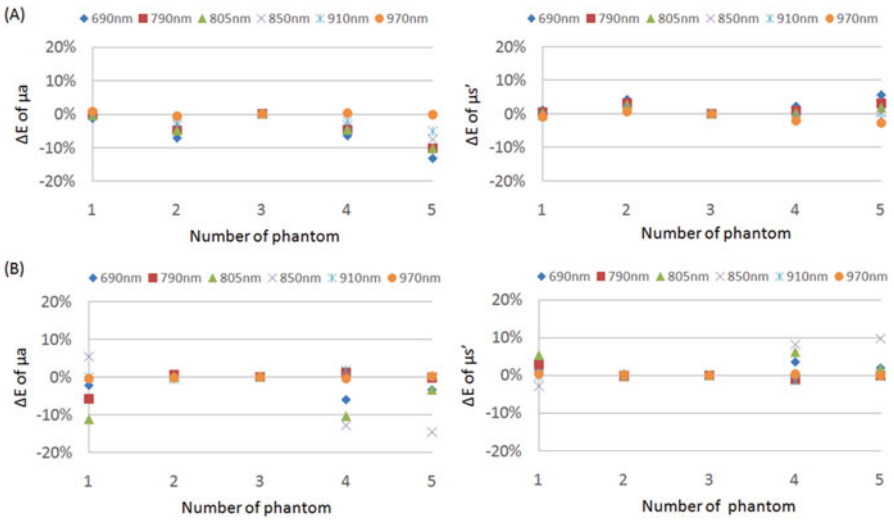

Fig. 44.1 The error (ΔE) of estimated μ_a and μ_s' by (**a**) the multi-wavelength and (**b**) the multi-distance method from Monte Carlo simulation in the case of Experiment I

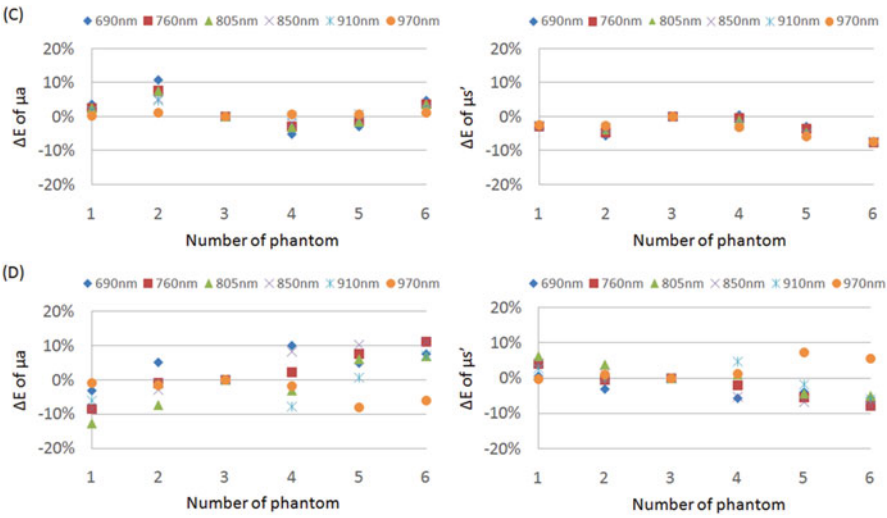

Fig. 44.2 The error (ΔE) of estimated μ_a and μ_s' by (**c**) the multi-wavelength and (**d**) the multi-distance method from Monte Carlo simulation in the case of Experiment II

Similarly, as the samples' μ_a are fixed and μ_s' are varied, the optical properties recovery errors of the MD method and MW method are both below 15 %, as shown in Fig. 44.2. The Monte Carlo simulation results indicated that the two methods have comparable measurement accuracy, as the sample optical properties are close to those of human adipose tissues.

Subsequently, the simulating phantoms prepared by the design from Experiment I and II were measured by our measurement system.

The analysis results are shown in Figs. 44.3 and 44.4. The error size of μ_a and μ_s' are below 20 and 30 %, respectively with the MW method, and are below 35 and 30 %, respectively with the MD method, when sample #3 was chosen as standard in Experiment I and II.

4 Conclusions and Discussion

In this study, we compared the performance of analytic spectra acquired from distinct source-detector separation to that of analyzing the reflectance spectrum collected by multi-wavelength at a single separation. We also presented a methodology to calibrate the reflectance spectrum of liquid diffusive and absorbing media at NIR wavelengths. The methodology evaluates optical properties via the standard phantom and requires only a simple experimental setup. The MD-CWS method can evaluate optical properties directly through spatially-resolved measurements in specific wavelengths. However, the MW-CWS method can get the volumes of the phantom composition to further compute absorption and scattering coefficients by means of spectra fitting in a constant source-detector separation. It is noteworthy to prudently decide on the standards because the estimation accuracy depends on how close the

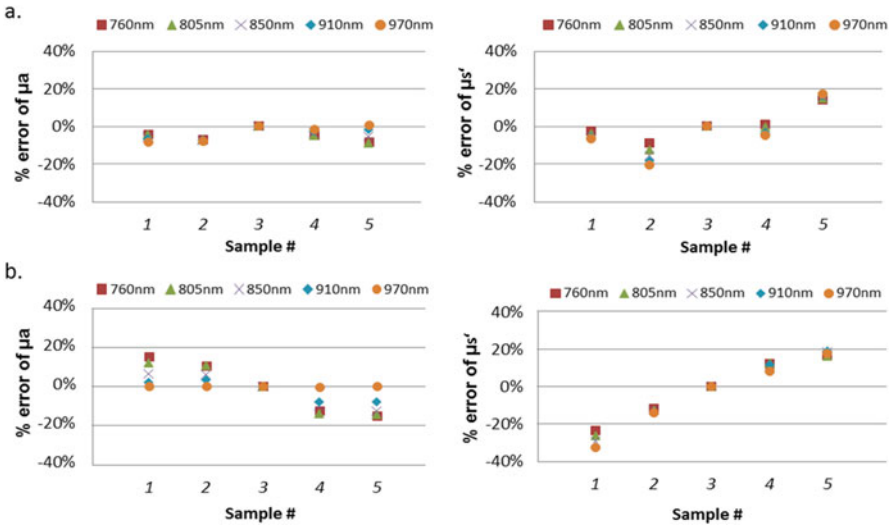

Fig. 44.3 The percentage error of μ_a and μ_s' on phantoms (**a**) using the Multi-wavelength (MW) method and (**b**) using the Multi-distance (MD) method in the case of Experiment I

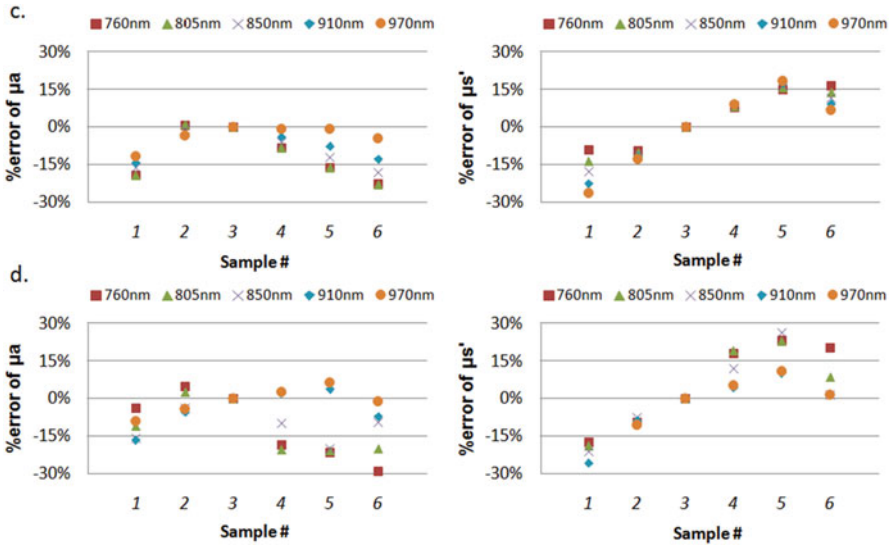

Fig. 44.4 The percentage error of μ_a and μ_s' on phantoms (**c**) using the Multi-wavelength (MW) method and (**d**) using the Multi-distance (MD) method in the case of Experiment II

phantom reflects the real condition. Afterwards, the absorption and the reduced scattering coefficients can be obtained from multi-distance and multi-wavelength CW measurements of the fluence rate by using least square fitting optimization.

Accordingly, this pre-feasibility study will help us to make a prototype of the measuring instrument using CWS. In this paper we evaluated the capability of the MW-CWS method, i.e., how accurately we can reduce data by comparison to MD-CWS as well as verification using Monte Carlo simulation. Moreover, in our experiments, we found that both methods can produce similar results and using the MW-CWS method is able to respond to the change of the concentration more sensitively than using the MD-CWS method in homogeneous media. The quantification of optical properties by the MW/MD CWS method can be validated and used to estimate the tissue components for further tumor detection.

References

1. Nissilä I, Hebden JC, Jennionsr D et al (2006) Comparison between a time-domain and a frequency-domain system for optical tomography. J Biomed Opt 11:064015
2. Contini D, Torricelli A, Pifferi A et al (2006) Multi-channel time-resolved system for functional near infrared spectroscopy. Opt Express 14(12):5418–5432
3. Patterson MS, Moulton JD et al (1991) Frequency-domain reflectance for the determination of the scattering and absorption properties of tissue. Appl Opt 30(31):4474–4476
4. Mourant JR, Bigio IJ et al (1997) Predictions and measurements of scattering and absorption over broad wavelength ranges in tissue phantoms. Appl Opt 36(4):949–957
5. Jacques SL (2009) Spectral imaging and analysis to yield tissue optical properties. J Innov Opt Health Sci 2:123–129
6. Dimofte A, Finlay JC, Zhu TC (2005) A method for determination of the absorption and scattering properties interstitially in turbid media. Phys Med Biol 50(10):2291–2311
7. Martelli F et al (2007) Calibration of scattering and absorption properties of a liquid diffusive medium at NIR wavelengths. CW method. Opt Express 15(2):486–500
8. Farrell TJ, Patterson MS, Wilson B (1992) A diffusion theory model of spatially resolved, steady state diffuse reflectance for the noninvasive determination of tissue optical properties in vivo. Med Phys 19(4):879–888
9. Fang Q (2010) Mesh-based Monte Carlo method using fast ray tracing in Plücker coordinates. Biomed Optic Express 1(1):165–175

Chapter 45
Multi-modality Optical Imaging of Rat Kidney Dysfunction: In Vivo Response to Various Ischemia Times

Zhenyang Ding, Lily Jin, Hsing-Wen Wang, Qinggong Tang, Hengchang Guo, and Yu Chen

Abstract We observed in vivo kidney dysfunction with various ischemia times at 30, 75, 90, and 120 min using multi-modality optical imaging: optical coherence tomography (OCT), Doppler OCT (DOCT), and two-photon microscopy (TPM). We imaged the renal tubule lumens and glomerulus at several areas of each kidney before, during, and after ischemia of 5-month-old female Munich-Wistar rats. For animals with 30 and 75 min ischemia times, we observed that all areas were recovered after ischemia, that tubule lumens were re-opened and the blood flow of the glomerulus was re-established. For animals with 90 and 120 min ischemia times, we observed unrecovered areas, and that tubule lumens remained close after ischemia. TPM imaging verified the results of OCT and provided higher resolution images than OCT to visualize renal tubule lumens and glomerulus blood flow at the cellular level.

Keywords Optical coherence tomography • Doppler optical coherence tomography • Two-photon microscopy • Kidney dysfunction • Ischemia

1 Introduction

Ischemic insults are common in renal surgery such as kidney transplantation or partial nephrectomy. Ischemia leads to various degrees of kidney dysfunction or delayed graft function. Real-time monitoring of ischemic insults helps to improve the

Z. Ding
College of Precision Instrument and Opto-Electronics Engineering, Tianjin University, Tianjin 300072, China

Fischell Department of Bioengineering, University of Maryland, College Park, MD 20742, USA

L. Jin • H.-W. Wang • Q. Tang • H. Guo • Y. Chen (✉)
Fischell Department of Bioengineering, University of Maryland, College Park, MD 20742, USA
e-mail: yuchen@umd.edu

© Springer International Publishing Switzerland 2016

Q. Luo et al. (eds.), *Oxygen Transport to Tissue XXXVIII*, Advances in Experimental Medicine and Biology 923, DOI 10.1007/978-3-319-38810-6_45

management strategy for optimal outcome. Andrews et al. investigated the effects of ischemia on kidney morphology and function using tandem scanning confocal microscopy. In their study, as the ischemic time increased from 1 to 72 h, the kidney underwent tubular swelling and necrosis. After transplantation, they showed distinct delayed graft function from a couple of days to 1 week [1]. However, confocal microscopy has a limited penetration depth of ~100 μm, which could not image through the capsule surrounding the human kidney.

Optical coherence tomography (OCT) is a novel imaging technology that produces high resolution cross-sectional images of the internal microstructure of living tissue [2]. OCT imaging depths exceeding 2 cm have been demonstrated in transparent tissues, including the eye [3]. In the skin and other highly scattering tissues, OCT can image small blood vessels and other structures as deep as 1–2 mm beneath the surface [4]. As OCT can provide deeper penetration than confocal microscopy, in our previous work [5] we performed OCT imaging of living rat kidneys before, during, and after an ischemic insult, which enabled visualization and comparison of the rat kidney morphology. Therefore, OCT represents an exciting new approach to visualize, in real-time, the pathological changes in the living kidney in a non-invasive or minimally-invasive fashion. Doppler OCT (DOCT) is a functional extension of OCT and is currently employed in several clinical areas to quantify blood flow in vivo. In our previous work [6] we investigated the feasibility of DOCT to image kidney microcirculation, specifically, glomerular blood flow. Two-photon microscopy (TPM) can provide unprecedented anatomical, cellular, molecular and functional information in vivo, which is a form of light microscopy that uses localized nonlinear optical effects induced by two-photon excitation [7]. TPM can provide kidney images with higher lateral spatial resolution than OCT [8].

In this preliminary study, we investigated the effects of different ischemia times on renal morphology and function using multi-modality optical imaging: OCT, DOCT and TPM. We used 5-month-old female Munich-Wistar rats for this study. We performed OCT/DOCT and TPM to observe the rat renal tubule lumens and glomerulus blood flow before, during, and after ischemia. We scanned multiple sites of a rat kidney using OCT/DOCT first for all animals and then using TPM for some animals. For ischemia times of 30 and 75 min, we observed recovered sites with open tubule lumens and functioning glomerulus. For ischemia times of 90 and 120 min, we observed unrecovered areas, that tubule lumens were closed and the glomerulus had no blood flow. We saw similar trends using TPM with a higher resolution than OCT to visualize tubular and glomerular blood flow at the cellular level.

2 Methods

A high-speed, high-resolution OCT system was used in this study. The details of the OCT system have been described previously [9]. Briefly, a Fourier-domain OCT system consisting of a swept-source laser with 100 nm bandwidth at 1310 nm center wavelength yielding an axial resolution of ~10 μm in tissue was used. A 10× objective was used in the sample arm. The laser source operated at a swept rate of 16 kHz

allowing a series of two-dimensional cross-sectional images to be captured in real time. Two-photon fluorescence imaging has become an important method for intravital studies [7]. Here it was performed with a microscopy system equipped with a Ti:sapphire laser (Coherent Mira 900) operating at 790 nm, 150 fs pulse width, and 76 MHz repetition rate. The excitation laser beam was focused with a 20×/1.0NA objective (Olympus XLUMPlanFL N) onto the kidney. The animal protocol was approved by the committees on animal care and use at the University of Maryland. Five-month-old female Munich-Wistar rats were used in this study. Each animal's weight, 24-h urine volume and blood creatinine were measured before the operation and all animals had a normal range of kidney functions. Rats were anesthetized with isoflurane, incised at the midline of the abdomen, the left side of the kidney and renal artery were exposed, and the renal artery clamped for various times of ischemia from 30 to 120 min. We performed OCT/DOCT and TPM to observe in vivo rat kidney before, during, and after ischemia.

3 Results and Discussion

First, we performed OCT/DOCT to observe the renal tubule lumens and glomerulus before, during, and after ischemia of 5-month-old female Munich-Wistar rats with various ischemia times at 30, 75, 90, and 120 min. Before ischemia, we observed many opened tubule lumens as shown in Fig. 45.1a and blood flow signals in the DOCT image (Fig. 45.1b) that were attributed to either the glomerulus or blood vessels. During ischemia the tubule lumens were closed, as shown in Fig. 45.1c. We did not see color signals in the DOCT image in Fig. 45.1d, indicating no significant or reduced blood flow from either the glomerulus or blood vessels. After ischemia, in the recovered location, the tubule lumens were re-opened as shown in Fig. 45.1e and there were color signals in the DOCT image, as shown in Fig. 45.1f. In the unrecovered location, the tubule lumens were still closed (Fig. 45.1g) and there was no color signal in the corresponding DOCT image (Fig. 45.1h).

To quantitate the kidney dysfunction with various ischemia times using OCT/DOCT imaging, we performed the following analysis. We quantitated one animal for each ischemia time. For each animal, we quantitated five random locations of the kidney imaged. There were 50 frames of images in each location. We calculated the percentage of the fully closed area, almost closed area, partially opened area, and fully opened area from 50 frames. In detail, we counted the number of frames containing open tubule lumens N to evaluate each location. The fully open areas have $N \geq 10$. The partially open areas have $5 \leq N < 10$. The almost closed areas have $1 \leq N < 5$, and the fully closed areas have $N = 0$. The results are shown in Table 45.1. For example, for the animal with ischemic time of 30 min at location 1, the number of frames that showed an almost closing tubule area is 3 and the percentage in the total 50 frames is 6 %. The number of frames in which the tubule lumens were partially opened is 47 and the percentage in the total 50 frames is 94 %. If we observed the Doppler signals in 50 frames for the specific location, in Table 45.1 the Doppler signals are recorded as 'yes', otherwise they are recorded as 'no'.

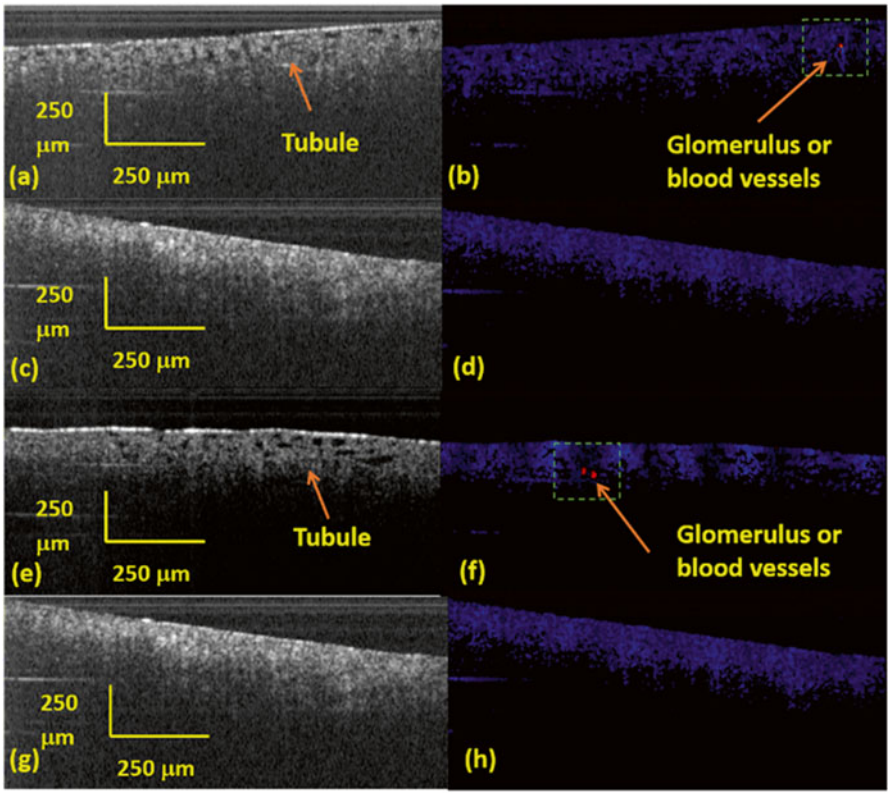

Fig. 45.1 OCT/DOCT images of in vivo rat kidney before (**a**, **b**), during (**c**, **d**), and after ischemia (**e**–**h**). The left column is OCT images and the right is DOCT images. (**e**, **f**) showed a recovered area. (**g**, **h**) showed an unrecovered area

From Table 45.1, when the ischemic times were 30 and 75 min, we did not find locations where the tubule lumens were entirely closed; all five locations had fully or partially opened tubules. These results show that most parts of the kidney were recovered in the ischemic time of 30 and 75 min. However, when the ischemic times were extended to 90 and 120 min, some locations were almost fully closed (e.g. Location 1 and 2 in 90 min, and Location 3 and 5 in 120 min). Meantime, we still find that some locations are fully open or partially open (e.g. Location 4 and 5 in 90 min and Location 1, 2 and 4 in 120 min). These results show that some parts of the kidney are not recovered after ischemic times of 90 and 120 min. In addition, there are more locations with Doppler signals after ischemic times of 30 and 75 min than those of 90 and 120 min ischemic times, indicating the glomerulus and blood vessels are also not recovered after the ischemic times of 90 and 120 min.

TPM provided higher resolution images than OCT to visualize tubular and glomerular at the cellular level. We used the TPM results to verify the OCT results. Before ischemia, we observed many clearly opened tubule lumens and glomerulus, as shown in Fig. 45.2a, b. During ischemia, cells lining the uriniferous tubules

Table 45.1 Quantitation of post-ischemia renal dysfunction with various ischemia times

		30 min ($n=1$) (%)	75 min ($n=1$) (%)	90 min ($n=1$) (%)	120 min ($n=1$) (%)
Location 1	Fully closed:	0	0	84	0
	Almost closed:	6	18	16	0
	Partially open:	94	76	0	0
	Fully open:	0	6	0	100
	Doppler:	Yes	No	No	Yes
Location 2	Fully closed:	0	0	0	0
	Almost closed	0	58	86	0
	Partially open:	48	34	12	98
	Fully open:	52	8	2	2
	Doppler:	Yes	Yes	No	No
Location 3	Fully closed:	0	0	12	96
	Almost closed:	0	0	84	4
	Partially open:	6	46	2	0
	Fully open:	94	54	2	0
	Doppler:	Yes	Yes	No	No
Location 4	Fully closed:	0	0	0	0
	Almost closed:	0	0	16	0
	Partially open:	0	4	44	0
	Fully open:	100	96	40	100
	Doppler:	No	Yes	No	No
Location 5	Fully closed:	0	0	0	0
	Almost closed:	42	0	0	100
	Partially open:	58	46	94	0
	Fully open:	0	54	6	0
	Doppler:	Yes	Yes	Yes	No

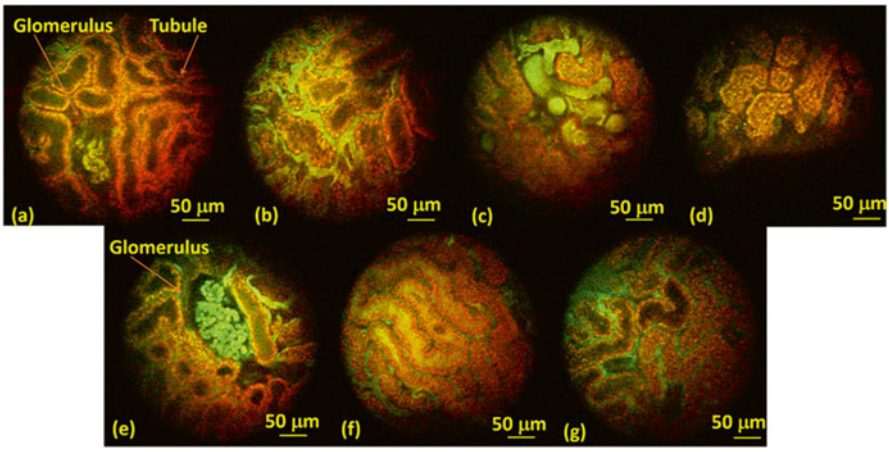

Fig. 45.2 TPM images of in vivo rat kidney before (**a**, **b**), during (**c**, **d**), and after ischemia (**e**–**h**)

swelled and the tubular lumens decreased in size, as shown in Fig. 45.2c, d. After ischemia, in the recovered location the tubule lumens re-opened and the glomerulus can be observed in Fig. 45.2e. In the unrecovered location, tubule lumens were still entirely closed as shown in Fig. 45.2f. Figure 45.2g is a location in which half is recovered and half is unrecovered.

4 Conclusions

We observed in vivo kidney dysfunction with various ischemic times of 30, 75, 90, and 120 min using OCT, DOCT and TPM. Extending the ischemic time to 90 and 120 min, we found unrecovered locations of the rat kidney after ischemia. In addition, DOCT showed a decrease of Doppler signals of glomerulus after ischemia in the longer ischemic times (90 and 120 min). We also used TPM images to verify the OCT results. In the future, we will analyze the effects of various drugs to protect against acute kidney injury due ischemia and reperfusion using OCT, DOCT and TPM.

Acknowledgments This work is partially supported by the National Institutes of Health (NIH) grants R21AG042700 and R21DK088066. We thank our collaborator Professor Peter Andrews at the Georgetown University Medical Center.

References

1. Andrews PM et al (2002) Using tandem scanning confocal microscopy to predict the status of donor kidneys. Nephron 91(1):148–155
2. Schmitt JM (1999) Optical coherence tomography (OCT): a review. IEEE J Sel Top Quant Electron 5(3):1205–1215
3. Hee MR et al (1995) Optical coherence tomography of the human retina. Arch Ophthalmol 113(3):325–332, Chicago, IL, 1960
4. Fujimoto JG et al (1995) Optical biopsy and imaging using optical coherence tomography. Nat Med 1(9):970–972
5. Andrews PM et al (2008) High-resolution optical coherence tomography imaging of the living kidney. Lab Invest 88(4):441–449
6. Wierwille J et al (2011) In vivo, label-free, three-dimensional quantitative imaging of kidney microcirculation using Doppler optical coherence tomography. Lab Invest 91(11):1596–1604
7. Chen Y et al (2013) Recent advances in two-photon imaging: technology developments and biomedical applications. Chin Opt Lett 11(1):011703
8. Ashworth S et al (2007) Two-photon microscopy: visualization of kidney dynamics. Kidney Int 72(4):416–421
9. Li Q et al (2009) Automated quantification of microstructural dimensions of the human kidney using optical coherence tomography (OCT). Opt Express 17(18):16000–16016

Chapter 46
Skeletal Muscle Oxygenation Measured by EPR Oximetry Using a Highly Sensitive Polymer-Encapsulated Paramagnetic Sensor

H. Hou, N. Khan, M. Nagane, S. Gohain, E.Y. Chen, L.A. Jarvis, P.E. Schaner, B.B. Williams, A.B. Flood, H.M. Swartz, and P. Kuppusamy

Abstract We have incorporated LiNc-BuO, an oxygen-sensing paramagnetic material, in polydimethylsiloxane (PDMS), which is an oxygen-permeable, biocompatible, and stable polymer. We fabricated implantable and retrievable oxygen-sensing chips (40 % LiNc-BuO in PDMS) using a 20-G Teflon tubing to mold the chips into variable shapes and sizes for in vivo studies in rats. In vitro EPR measurements were used to test the chip's oxygen response. Oxygen induced linear and reproducible line broadening with increasing partial pressure (pO_2). The oxygen response was similar to that of bare (unencapsulated) crystals and did not change significantly on sterilization by autoclaving. The chips were implanted in rat femoris muscle and EPR

H. Hou (✉) • N. Khan • M. Nagane • S. Gohain • A.B. Flood
Department of Radiology, Geisel School of Medicine at Dartmouth, Hanover, NH 03755, USA
e-mail: Huagang.Hou@Dartmouth.Edu

E.Y. Chen
Department of Surgery, Geisel School of Medicine at Dartmouth, Hanover, NH 03755, USA

L.A. Jarvis • P.E. Schaner
Department of Medicine, Geisel School of Medicine at Dartmouth, Hanover, NH 03755, USA

B.B. Williams • H.M. Swartz
Department of Radiology, Geisel School of Medicine at Dartmouth, Hanover, NH 03755, USA

Department of Medicine, Geisel School of Medicine at Dartmouth, Hanover, NH 03755, USA

P. Kuppusamy (✉)
Department of Radiology, Geisel School of Medicine at Dartmouth, Hanover, NH 03755, USA

Department of Medicine, Geisel School of Medicine at Dartmouth, Hanover, NH 03755, USA

Department of Radiology, EPR Center for the Study of Viable Systems, Geisel School of Medicine at Dartmouth, One Medical Center Drive, Lebanon, NH 03766, USA
e-mail: Periannan.Kuppusamy@dartmouth.edu

© Springer International Publishing Switzerland 2016

Q. Luo et al. (eds.), *Oxygen Transport to Tissue XXXVIII*, Advances in Experimental Medicine and Biology 923, DOI 10.1007/978-3-319-38810-6_46

oximetry was performed repeatedly (weekly) for 12 weeks post-implantation. The measurements showed good reliability and reproducibility over the period of testing. These results demonstrated that the new formulation of OxyChip with 40 % LiNc-BuO will enable the applicability of EPR oximetry for long-term measurement of oxygen concentration in tissues and has the potential for clinical applications.

Keywords Electron paramagnetic resonance (EPR) oximetry • Oxygen sensor • Partial pressure of oxygen (pO_2) • Skeletal muscle

1 Introduction

Measurement of partial pressure of oxygen (pO_2) in an accurate, reliable, and repeatable fashion is crucial to the understanding, diagnosis, and treatment of a number of pathophysiological conditions, including ischemic disease, reperfusion injury, oxygen toxicity, cancer, peripheral vascular disease, and wound healing [1]. Of the several methods available for measuring pO_2 in tissues [2], electron paramagnetic resonance (EPR) oximetry has some distinct advantages, including the ability to make minimally invasive, real-time (in vivo), and repeated measurements.

In addition, EPR oximetry is unique in terms of its ability to provide absolute values of pO_2 [1, 2]. Repeated measurements of pO_2, from a single location in tissue, are made possible by the use of water-insoluble crystalline probes, such as lithium phthalocyanine (LiPc) [3], lithium naphthalocyanine (LiNc) [4], or lithium octa-*n*-butoxynaphthalocyanine (LiNc-BuO) [5]. Of these crystalline probes, LiNc-BuO has some advantages over others, including high EPR sensitivity (spin density and narrow lineshape) and oxygen sensitivity, and long-term stability and responsiveness to oxygen in vivo [1].

Although, LiNc-BuO can be used in its raw (bare) crystalline form to measure oxygen, its in vivo application may be limited by particle migration within tissue leading to loss of EPR signal intensity over time, and potential biocompatibility concerns due to direct exposure of tissue to the crystals. Encapsulation of crystalline probes in a bio-inert matrix is a strategy, employed in the past, to overcome the limitations associated with the use of bare material, especially for clinical application [6, 7]. Recently, we have encapsulated LiNc-BuO in polydimethylsiloxane (PDMS), a well-characterized, biocompatible, and highly oxygen-permeable polymer, for the development of implantable, and surgically retrievable, EPR probe formulations (denoted as LiNc-BuO:PDMS and referred to hereafter as 'OxyChip') [8]. Fabrication, by cast-molding/polymerization method, and physical characterization of the OxyChips demonstrated that encapsulation in the PDMS matrix did not have any significant effect on the oxygen-sensing ability of the embedded LiNc-BuO microcrystals. The cast-molding procedure also facilitated the fabrication of OxyChips with different shapes, sizes, and spin densities [8].

In the present study, we report the biological evaluation and functional testing of OxyChips, including in vitro/in vivo biocompatibility and oxygen-sensing performance.

The results establish that the encapsulation of LiNc-BuO microcrystals in PDMS, while enhancing their biocompatibility and suitability for direct in vivo application, does not interfere with their oxygen-sensing ability.

2 Methods

2.1 Polymer-Encapsulation of LiNc-BuO Microcrystals

The synthesis and physicochemical characterization of LiNc-BuO microcrystals have been described previously [5]. Medical grade PDMS base, namely MED-4210 Platinum Silicone Elastomer, was obtained from Factor II, Inc. (Lakeside, AZ). 40 % LiNc-BuO:PDMS chips (w/w) were fabricated in the form a thin wire (diameter, 0.6 mm) using a modification of previously reported procedure [8]. Briefly, the PDMS base and catalyst/crosslinker (supplied with the PDMS elastomer) were mixed in a 10:1 ratio, as recommended by the manufacturer, after which the LiNc-BuO crystals were added. The heterogeneous dispersion/mixture was outgassed using a vacuum desiccator connected to a vacuum pump. One end of a 20-G PTFE tube was dipped into the PDMS mixture (LiNc-BuO + PDMS + Catalyst/Crosslinker) and negative pressure was applied from the other end with a 10-ml syringe to draw the PDMS mixture into the tubing to the desired length, usually about 5 cm. The PTFE tubing with PDMS mixture was cured in an oven for at least 8 h at 70 °C, followed by withdrawing (by gentle pulling) the cured PDMS chip out from the tubing. The chip (LiNc-BuO in PDMS) was further cured at 70 °C overnight. The cured chip (referred to as OxyChip) in the form of a wire (0.6-mm diameter) was cut into small segments of 5-mm lengths for use in the present study. In order to verify that mechanical stress or tearing of PDMS coating does not occur resulting in leaching of LiNc-BuO crystals, the OxyChips were suspended in water or ethanol and subjected to 72 h of continuous stirring at room temperature. After removing the OxyChips, the solution was analyzed using EPR spectroscopy, which did not show any detectable absorption due to LiNc-BuO suggesting the absence of any detectable paramagnetic debris in solution (data not shown).

2.2 In Vitro EPR Measurements

Calibration curves and the time course of response of the OxyChips were performed by measuring the EPR linewidth while the equilibrating gas content was changed from 0 to 21 % (160 mmHg) oxygen. Measurements were carried out using an L-band (1.2 GHz) EPR spectrometer (custom-built) equipped with a surface-loop resonator [9]. Gases with known concentrations of oxygen and nitrogen or air, equilibrated at 37 °C, were flushed over the samples, and the spectra were recorded every minute until equilibration, as evidenced by a steady linewidth, was achieved.

2.3 In Vivo EPR Measurements

Measurements of muscle oxygenation were performed using the same L-band (1.2 GHz) EPR spectrometer (see Sect. 2.2) using a surface-loop resonator. Animals were placed on a plastic bedplate and the previously implanted OxyChip was positioned just beneath the loop, i.e., approximately centered within the active volume of the loop resonator. Body temperature was monitored using a thermistor rectal probe, and maintained at 37 ± 1 °C using a heating pad and an infrared lamp. In order to verify that the implanted OxyChip was sensitive to changes in tissue oxygenation, the muscle tissue was subjected to temporary constriction of blood flow after baseline EPR measurement, thereby reducing the oxygen supply to the hind limb. This was achieved by gently tying the limb above the location of chip implantation using an elastic band. The constriction was maintained in place until EPR measurements were made (usually less than 5–8 min) and then removed. All animals were subjected to constriction on every other week during the course of the measurements.

2.4 Animal Preparation

All the animal procedures were approved by the Institutional Animal Care and Use Committee of Geisel School of Medicine at Dartmouth. Eight adult male Wistar rats (200–220 g, Charles River Laboratories, MA, USA) were used. One rat died on day 56 due possibly to anesthesia, but it was excluded from data analysis. For all surgical procedures, 3.0–3.5 % isoflurane in 70 % N_2:30 % (228 mmHg) O_2 was used for anesthesia induction, and 1.5–2.5 % for anesthesia maintenance. Physiologic monitoring during the procedure comprised measurement and maintenance of core (rectal) temperature at 37 ± 1 °C using a heating pad.

2.5 Evaluation of the Stability of OxyChips in the Skeletal Muscle Tissue

Prior to implantation, each piece of 0.6-mm × 5.0-mm OxyChip was suspended in 5 ml of distilled water and subjected to 72 h of continuous stirring at room temperature using a tiny magnetic stirrer pellet followed by sterilization by autoclaving at 121 °C for 30 min. Calibration curves were made before and after the washing and autoclaving procedures. For implantation of OxyChips, the animals were anesthetized by nose-cone breathing of 2–2.5 % of isoflurane in 30 % (228 mmHg) oxygen. One OxyChip was implanted in the biceps femoris of the right limb using an 18-G angiocatheter. The injected depth was 3–4 mm from the surface of the skin. Normal tissue pO_2 (baseline) was measured for 30 min when rats were anesthetized with 1.5 % isoflurane in 30 % (228 mmHg) O_2 at the following time points: day 7, day 14, day 21,

day 28, day 42, day 56, day 70 and day 84 after OxyChip implantation. Normal, ischemic and recovery tissue pO_2 (baseline pO_2 for 25 min, ischemic muscle pO_2 induced by muscle compression with a rubber band for 5–8 min and recovery from ischemia induced by release pressure for 15 min) were measured.

2.6 Statistical Analysis

Data were analyzed by Student's *t*-test. Paired *t*-test was used to compare pO_2 changes within the same group. The tests were two-sided, and a change with a *p*-value <0.05 was considered statistically significant. *N* is the number of rats and n is the number of OxyChips. All data are expressed as mean ± SEM.

3 Results and Discussion

Figure 46.1 shows the oxygen calibration of the OxyChip that was measured before and after autoclaving. The calibration remained linear, with no significant difference in oxygen sensitivity up on autoclaving. The results demonstrated the stability of the OxyChip, with no effect of autoclaving on the intended functionality of the OxyChip.

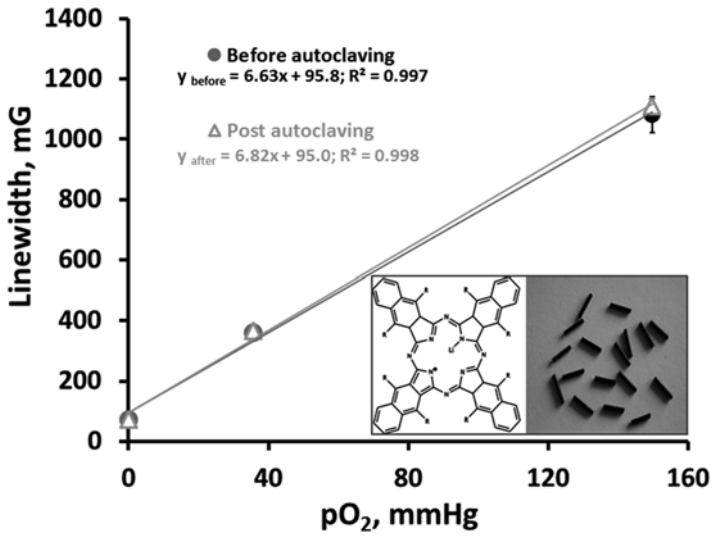

Fig. 46.1 Calibration plot of OxyChip before and after sterilization by autoclaving procedure. The response of the chip to different concentrations of perfused oxygen is shown with a linear fitting and regression coefficient (R^2). Mean ± SEM, $n = 4$ OxyChips. Inset: Molecular formula of lithium octa-*n*-butoxy-naphthalocyanine (LiNc-BuO) (*left*) and samples of 0.6-mm × 0.6-mm chips used in the oxygen measurements (*right*)

In our previous study, histological analysis of excised muscle tissue surrounding the implant after 4 weeks of implantation showed that the chip elicited a characteristic wound-healing response, with the recruitment of inflammatory cells and the formation of a thin fibrous capsule [11]. However, the fibrous coating of the chip did not have any significant effect on the in vivo oxygen-sensing ability of the implant. In the present study, the OxyChip remained intact in the muscle and enabled repeated measurements of tissue pO_2 for 11 weeks from the same rats. The pO_2 measurements established the ability of the OxyChip to provide repeated measurements of in vivo tissue oxygenation over the 11-week duration, and possibly longer. Further, in order to verify if the implanted OxyChip was responsive to changes in tissue pO_2, blood flow to the muscle was temporarily constricted using an elastic band and subsequently released. The decrease in blood flow, during the constriction, leads to a decrease in oxygen supply to the muscle.

Figure 46.2a shows that the implanted chip was capable of reporting the dynamic change in tissue oxygenation induced by the muscle constriction in an individual rat. The muscle pO_2 also returned to normal levels when the constriction was removed. Comparison of constricted-state pO_2 readouts with normal muscle pO_2 revealed a significant difference between the two, confirming that the constriction was effective and that the OxyChip was able to report the changes in muscle pO_2 (Fig. 46.2b). The results showed the mean baseline muscle pO_2 ranged from 18 to 27 mmHg over the 11-week period, which is within the range of rat gastrocnemius muscle pO_2 values reported previously [4, 10]. The differences in the baseline pO_2 values on different weeks may be due to the differences in the local physiology of the muscle.

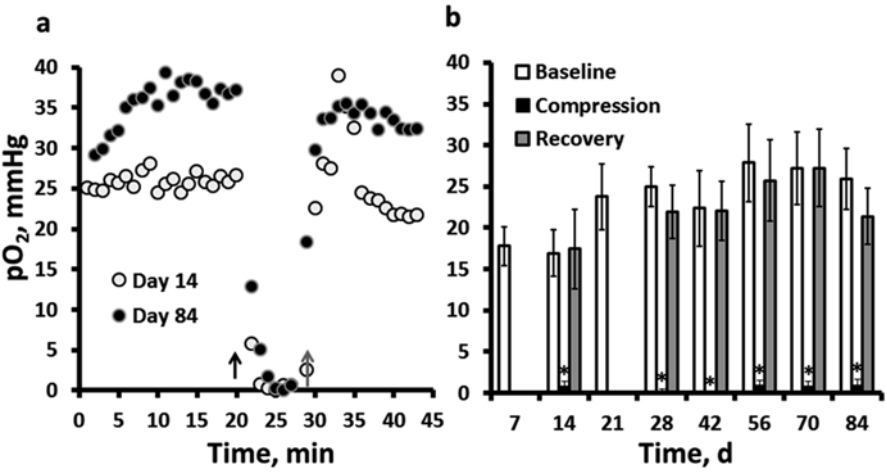

Fig. 46.2 Time course of pO_2 in biceps femoris of right limb in a single rat (**a**) and group mean (**b**) prior to, during and post leg muscle compression. Baseline is the average pO_2 from measurements of the last 15 min of 30-min baseline period. Compression is the average pO_2 in the 5–8 min period of the muscle constriction. Recovery is the average pO_2 in the last 10 min of a 20-min recovery period of measurements when the constriction was removed. The *black arrow* indicates the beginning of compression and the *gray arrow* indicates start of pressure release. Data represent Mean ± SEM; $N = 7$ rats. $^*p < 0.01$, compared to baseline on the same day (paired *t*-test)

4 Conclusion

We have successfully carried out biological evaluation and functional testing of a new EPR oximetry sensor, the OxyChip, containing 40 % LiNc-BuO in PDMS. Calibration of the OxyChips was not affected by sterilization procedures. The suitability and applicability of the chip for long-term in vivo oximetry was established by monitoring the oxygenation of rat muscle tissue for an extended period. Overall, we have established that the new OxyChip is a promising choice for clinical EPR oximetry.

Acknowledgments These developments were supported by National Institutes of Health grants R01 EB004031 and P01 CA190193.

References

1. Khan N, Williams BB, Hou H et al (2007) Repetitive tissue pO_2 measurements by electron paramagnetic resonance oximetry: current status and future potential for experimental and clinical studies. Antioxid Redox Signal 9:1169–1182
2. Swartz HM, Hou H, Khan N et al (2014) Advances in probes and methods for clinical EPR oximetry. Adv Exp Med Biol 812:73–79
3. Liu KJ, Gast P, Moussavi M et al (1993) Lithium phthalocyanine: a probe for electron paramagnetic resonance oximetry in viable biological systems. Proc Natl Acad Sci U S A 90(12):5438–5442
4. Ilangovan G, Manivannan A, Li H et al (2002) A naphthalocyanine-based EPR probe for localized measurements of tissue oxygenation. Free Radic Biol Med 32(2):139–147
5. Pandian RP, Parinandi NL, Ilangovan G, Zweier JL, Kuppusamy P (2003) Novel particulate spin probe for targeted determination of oxygen in cells and tissues. Free Radic Biol Med 35(9):1138–1148
6. Dinguizli M, Jeumont S, Beghein N et al (2006) Development and evaluation of biocompatible films of polytetrafluoroethylene polymers holding lithium phthalocyanine crystals for their use in EPR oximetry. Biosens Bioelectron 21(7):1015–1022
7. Eteshola E, Pandian RP, Lee SC, Kuppusamy P (2009) Polymer coating of paramagnetic particulates for in vivo oxygen-sensing applications. Biomed Microdevices 11(2):379–387. doi:10.1007/s10544-008-9244-x
8. Meenakshisundaram G, Eteshola E, Pandian RP et al (2009) Fabrication and physical evaluation of a polymer-encapsulated paramagnetic probe for biomedical oximetry. Biomed Microdevices 11(4):773–782
9. Swartz HM, Walczak T (1998) Developing in vivo EPR oximetry for clinical use. Adv Exp Med Biol 454:243–252
10. Hou H, Khan N, Lariviere J et al (2014) Skeletal muscle and glioma oxygenation by carbogen inhalation in rats: a longitudinal study by EPR oximetry using single-probe implantable oxygen sensors. Adv Exp Med Biol 812:97–103
11. Meenakshisundaram G, Eteshola E, Pandian RP et al (2009) Oxygen sensitivity and biocompatibility of an implantable paramagnetic probe for repeated measurements of tissue oxygenation. Biomed Microdevices 11:817–826

Chapter 47
Determination of Optical and Microvascular Parameters of Port Wine Stains Using Diffuse Reflectance Spectroscopy

Zhihai Qiu, Guangping Yao, Defu Chen, Ying Wang, Ying Gu, and Buhong Li

Abstract Characterizing port wine stains (PWS) with its optical parameters [i.e. absorption coefficient (μ_a) and reduced scattering coefficient (μ_s')] and microvascular parameters [i.e. blood volume fraction (BVF), mean vessel diameter (MVD), and oxygen saturation (StO_2)] is extremely important for elucidating the mechanisms for its light-based treatments, such as pulsed dye laser and photodynamic therapy. In this study, a customized diffuse reflectance spectroscopy (DRS) probe with an appropriate source-detector distance was used to measure the diffuse reflectance spectra of PWS lesions in clinical practice. The results demonstrate that optical parameters of different types of PWS lesions can be accurately extracted by fitting the DRS with diffusion equation. Since the sampling depth of the probe coincides with the depth distribution of abnormal vasculature in PWS, the obtained microvascular parameters of PWS lesions that changed from pink to purple are in agreement with the corresponding physiological conditions. This study suggests that DRS can be utilized to quantitatively determine the optical and microvascular parameters of PWS lesions, which have the potential for planning the protocol and predicting the efficiency for light-based PWS treatments.

Keywords Port wine stains • Diffuse reflectance spectroscopy • Optical parameters • Microvascular parameters

Z. Qiu • G. Yao • B. Li (✉)
MOE Key Laboratory of OptoElectronic Science and Technology for Medicine, Fujian Provincial Key Laboratory for Photonics Technology, Fujian Normal University, Fuzhou 350007, China
e-mail: bhli@fjnu.edu.cn

D. Chen • Y. Wang • Y. Gu
Department of Laser Medicine, Chinese PLA General Hospital, Beijing 100853, China

© Springer International Publishing Switzerland 2016

Q. Luo et al. (eds.), *Oxygen Transport to Tissue XXXVIII*, Advances in Experimental Medicine and Biology 923, DOI 10.1007/978-3-319-38810-6_47

1 Introduction

Port wine stain (PWS), a congenital and progressive vascular malformation, is histologically characterized by ecstatic capillaries and post-capillary venules in the upper dermis [1]. PWS lesions initially appear as flat pink macules and, over time, lesions tend to darken from red to purple and become gradually thickened as vascular nodules develop [2]. PWS occurs in approximately 0.3–0.5 % of infants, affecting both males and females and all racial groups equally. Although PWS can affect any part of the body, they are mainly located on the face and neck areas and may therefore have a serious emotional and physical impact [2].

To date, pulsed dye laser (PDL) and photodynamic therapy (PDT) are the two main modalities that have been proposed to treat PWS lesions. However, the treatment outcomes of PDL and PDT are strongly dependent on the characteristics of the individual PWS lesion and treatment protocols, and the mechanisms for achieving complete bleaching are still not fully understood. PDL is based on selective thermal coagulation of blood vessels without damaging the normal overlying epidermis, and the mean vessel diameter (MVD) is one of the determining factors for therapeutic efficiency [3]. Several studies have suggested that PDL is extremely effective for PWS treatment if the MVD is not less than 30 μm. On the other hand, as a key factor of PDT for PWS treatment, oxygen concentration in the blood vessels can influence treatment efficiency. Since the skin color contains information on the blood volume fraction (BVF), MVD, melanin content and the optical properties of PWS lesions, measurement of color determined from diffuse reflectance spectroscopy (DRS) has been widely applied to predict the efficacy of both PDL and PDT treatment [4].

During the past two decades DRS has been intensely applied for determining tissue optical properties, but the accuracy and the sensitivity of the derived values are largely dependent on the source-detector (S-D) distance of the DRS system, the calculation method, and the corresponding selected model [5]. Kim et al. have reported that the sensitivity range for the determined optical properties parameters, e.g. absorption coefficient (μ_a), reduced scattering coefficient (μ_s') varied with the S-D distance of the DRS probe. In particular, the measured DRS are almost insensitive to the variation of μ_s' when a DRS probe with a larger S-D distance was used [6]. Meanwhile, the sampling depth of DRS probe is also critical for achieving accurate measurement, which should coincide with the depth of the target lesion.

Based on our preliminary studies, the feasibility of a probe with an S-D distance of 520 nm for sampling the abnormal vasculature and monitoring vascular parameters during PDT of PWS was performed [7]. Herein, DRS of four types of PWS lesions were measured using our customized system. The optical parameters (i.e. μ_a and μ_s') and microvascular parameters (i.e. BVF, MVD and StO_2) of PWS lesions were then quantitatively determined by fitting the calibrated DRS using the established Farrell's equation with a compensation of a vessel packaging correction factor. In addition, validation was assessed by testing whether the obtained results coincided with the physiological characteristics of different kinds of PWS and by comparing the data with those of previous studies.

2 Patients and Methods

A total of 28 patients (13 males, 15 females) with facial PWS, undergoing PDT treatment for the first time, were recruited for the present study at the Department of Laser Medicine, Chinese PLA General Hospital, Beijing, China. PWS lesions were classified into four groups by experienced clinicians: Type I, pink, flat (mean age 4 ± 3); Type II, red, flat (mean age 5 ± 2); Type III, purple, slightly thicker (mean age 13 ± 6), and Type V, purple, significantly thicker (mean age 28 ± 9). The research protocol for this study was approved by the Ethics Committee of the Chinese PLA General Hospital, and an informed consent form was obtained from each subject.

The system and analyzing model employed in this study have been described previously by Qiu *et al* [7], and the feasibility of monitoring BVF and StO_2 during V-PDT of PWS has been validated. Before the DRS measurement, a real-time background spectrum and a reference spectrum for the diffuse reflectance standard (WS-1, Ocean optics, USA) was measured to subtract the background noise and to compensate the potential variation of lamp output, respectively. Patients were given 5 min to adjust to the ambient temperature of 25 ± 0.6 °C. Additionally, each lesion was cleaned thoroughly with alcohol pads and dried; the measurement of an uneven lesion assessed by a* value from color measurement was not included in the analysis in order to reduce the intra-patient variation. Five measurements were recorded at each relatively small homogeneous lesion area, and the DRS of the control lesion from each patient were also recorded for comparative study. During DRS measurement, the fiber probe was kept vertically and in slight contact with the lesion surface. Each average spectrum was determined from five independent measurements with a typical integration time for each measurement of about 70 ms. Diffuse reflectance spectra from 450 to 800 nm were recorded for data processing.

Based on our established protocol, the raw DRS spectra for PWS lesions were calibrated before fitting, using the well-known Farrell's equation which is a dipole approximation to diffusion theory. In addition, the determined optical and microvascular parameters for PWS lesions from DRS measurements were statistically analyzed. The paired Wilcoxon test was used to analyze differences, using $P < 0.05$ for the level of significance.

3 Results

The representative raw diffuse reflectance spectra for the four types of PWS lesions and their corresponding contralateral control sites are shown in Fig. 47.1a. A significant difference was found in the diffuse reflectance spectra between the PWS lesion and its control site. The absorbance peaks of oxyhemoglobin at 542 and 577 nm can be clearly seen; as expected, the PWS lesions have a more intense absorption than the control sites due to the abundant blood vessels. Figure 47.1b provides a comparison of the calibrated diffuse reflectance spectra for four types of

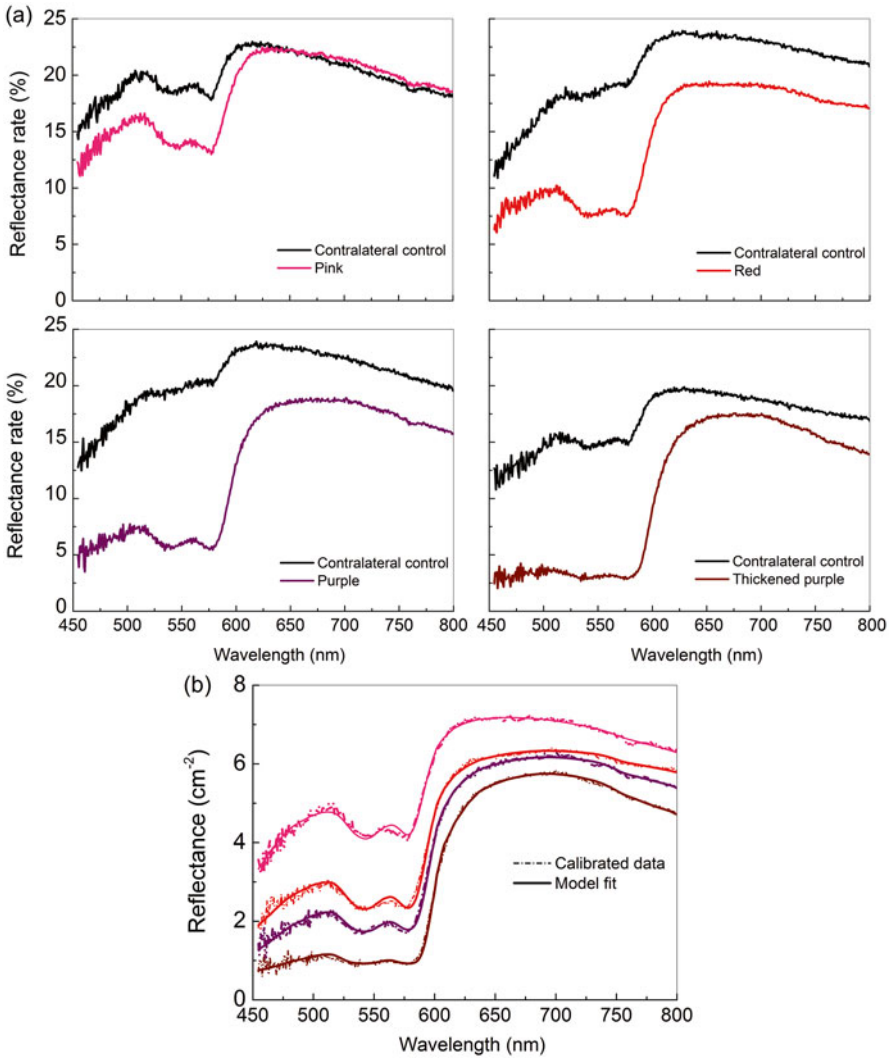

Fig. 47.1 The representative (**a**) raw diffuse reflectance spectra for the four types of PWS lesions and their corresponding contralateral control sites, and (**b**) calibrated diffuse reflectance spectra for four types of PWS lesions and their fitting curves using the well-known Farrell's equation

PWS lesions; the absorption of PWS gradually increases with the stages in lesion development from pink to red, to purple and to thickened purple, which resulted in the lower diffuse reflectance. Furthermore, the spectra can be fitted very well (r^2>0.99) using the Farrell's equation with the implementation of blood vessel package correction factor.

Table 47.1 summarises the optical parameters for four types of PWS lesions at 532 nm, including μ_a, μ_s', effective attenuation coefficient $\mu_{eff}=[3\mu_a(\mu_{a+}\mu_s')]^{1/2}$ and

Table 47.1 Optical parameters for the four types of PWS lesions ($\lambda = 532$ nm)

Lesion types	μ_a (cm^{-1})	μ_s' (cm^{-1})	μ_{eff} (cm^{-1})	δ (μm)
Pink	9.7 ± 3.4	32.4 ± 11.8	35.0 ± 8.0	285.7 ± 65.1
Red	14.8 ± 2.9	31.4 ± 10.2	45.3 ± 6.8	220.8 ± 33.3
Purple	16.8 ± 4.8	29.9 ± 13.4	48.5 ± 10.1	206.1 ± 43.0
Thickened purple	21.5 ± 6.6	31.1 ± 10.2	58.2 ± 11.2	171.7 ± 33.0

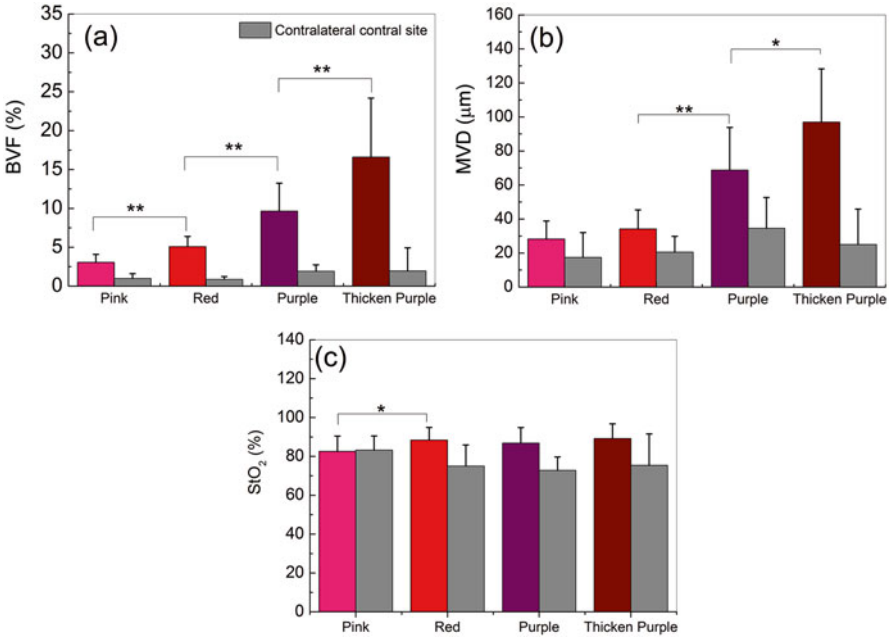

Fig. 47.2 Microvascular parameters of the four types of PWS lesions and contralateral control sites: (**a**) BVF, (**b**) MVD and (**c**) StO_2. (*$P < 0.05$, **$P < 0.01$, the error bar represents the standard deviation)

light penetration depth $\delta = \mu_{eff}^{-1}$. The $\mu_a(\lambda)$ and $\mu_s'(\lambda)$ are about 1–25 cm^{-1} and 15–45 cm^{-1} for four types of PWS lesions, respectively. There are no significant differences in μ_s' between the four types of PWS lesions, and the differences in δ is mainly attributed to the changes of μ_a.

Figure 47.2 shows the statistical data of BVF, MVD and StO_2 for the four types of PWS lesions and contralateral control sites, respectively. The BVF for pink to thickened purple PWS were (3.05 ± 1.02) %, (5.09 ± 1.29) %, (9.64 ± 3.60) %, and (16.60 ± 7.58) %, respectively. Between the different types of PWS, there were significant differences in BVF but no significant difference was observed between PWS and their contralateral control sites (Fig. 47.2a). In correspondence with the development of PWS from pink to thickened purple, an increased trend in MVD, from (28.24 ± 10.59) μm, (34.18 ± 11.21) μm, and (68.74 ± 28.10) μm to

(96.94 ± 31.36) μm, was also found. However, there was no significant difference in MVD between the pink and red PWS lesions (Fig. 47.2b). A significant difference in StO_2 was only observed between the pink (82.55 ± 7.87) % and the red PWS lesions (88.39 ± 6.52) %, while no significant difference in BVF was seen between the red (88.39 ± 6.52) %, purple (86.86 ± 7.95) %, and thickened purple (89.22 ± 7.54) % PWS lesions (Fig. 47.2c).

4 Discussion

For the optical parameters of PWS lesions at 532 nm, the obtained values range from 9.7 to 21.5 cm^{-1} and agree well with the average μ_a value of three PWS lesions with a range of 13–24 cm^{-1} measured by the spatial frequency domain image technique [8]. In addition, the μ_s' for the control sites has an average value of 31.5 ± 8.8 cm^{-1} (data not shown), which is consistent with the value of 30.16 ± 9.03 cm^{-1} for normal human skin, as summarized by Jacques [9]. Meanwhile, the average μ_s' for the four types of PWS lesions also consistent with the value of normal human skin. The μ_s' is known to be dominated by the scattering of mitochondria, cell nuclei, and other cytoplasmic organelles in skin tissue [10], which implies that there are no significant changes of nuclei and organelles in PWS lesion, as confirmed by the historical characteristics of PWS. Since it is unrealistic and unethical to compare the measured microvascular parameters with the biopsy sample in the clinic, we compared our results with values in the literature. The increasing tendency of MVD from 28.24 ± 10.59 μm for pink PWS to 68.74 ± 25.10 μm for purple PWS (Fig. 47.2b) is similar to the tendency measured by histological examination, as reported by Fiskerstrand et al. [11], in which the MVD were determined from 16.5 to 51.2 μm for pink to purple PWS. The confocal microscope showed that the MVD in normal human skin in vitro is about 15.4 (6.2–28.9) μm [12], which is also similar to the values for contralateral healthy control sites in the present study. The previous results showed that the StO_2 of normal skin is 71.5 ± 2.2 % and PWS ranges from 71.5 to 86.1 % (Fig. 47.2c) and these agree well with the values for normal skin ranges from 72.8 to 83.2 % and PWS ranges from 82.6 to 89.2 %, respectively [8]. These results suggest that microvascular parameters changing from pink to thickened purple are in agreement with physiological changes.

5 Conclusions

The probe with an S-D distance of 520 μm is suitable for measuring DRS from PWS. After implementing the vessel package effect correction factor, the DRS measured from PWS at different stages (from pink to thickened purple), could be fitted successfully with the well-known Farrell's equation. Testing under clinical conditions showed that absorption and reduced scattering coefficients of PWS can be

extracted. For coinciding with sampling depth and covering the optical properties dynamic range, the obtained microvascular parameters changing from pink to thickened purple are in agreement with physiological changes. The results indicate that our setup is reliable and that the DRS are sensitive to the variation in lesion.

Acknowledgments This study was supported by the National Natural Science Foundation of China (61275216, 61520106015, and 61036014), the Natural Science Foundation of Fujian Province (2014 J07008), and Joint Funds of Fujian Provincial Health and Education Research (WJK-FJ-30).

References

1. Chen JK, Ghasri P, Aguilar G et al (2012) An overview of clinical and experimental treatment modalities for port wine stains. J Am Acad Dermatol 67:289–304
2. Tallman B, Tan OT, Morelli JG et al (1991) Location of port-wine stains and the likelihood of ophthalmic and/or central nervous system complications. Pediatrics 87:323–327
3. Savas JA, Ledon JA, Franca K et al (2013) Pulsed dye laser-resistant port wine stains: mechanisms of resistance and implications for treatment. Br J Dermatol 168:941–953
4. Kienle A, Lilge L, Vitkin IA et al (1996) Why do veins appear blue? A new look at an old question. Appl Opt 35:1151–1160
5. Lister T, Wright PA, Chappell PH (2012) Optical properties of human skin. J Biomed Opt 17:90901
6. Kim A, Roy M, Dadani F et al (2010) A fiberoptic reflectance probe with multiple source-collector separations to increase the dynamic range of derived tissue optical absorption and scattering coefficients. Opt Express 18:5580–5594
7. Qiu Z, Chen D, Wang Y et al (2014) Monitoring blood volume fraction and oxygen saturation in port-wine stains during vascular targeted photodynamic therapy with diffuse reflectance spectroscopy: results of a preliminary case study. Photon Lasers Med 3:273–280
8. Mazhar A, Sharif SA, Cuccia JD et al (2012) Spatial frequency domain imaging of port wine stain biochemical composition in response to laser therapy: a pilot study. Lasers Surg Med 44:611–621
9. Jacques SL (2013) Optical properties of biological tissues: a review. Phys Med Biol 58:37–61
10. Mourant JR, Freyer JP, Hielscher AH et al (1998) Mechanisms of light scattering from biological cells relevant to noninvasive optical-tissue diagnostics. Appl Opt 37:3586–3593
11. Fiskerstrand EJ, Svaasand LO, Kopstad G et al (1996) Laser treatment of port wine stains: therapeutic outcome in relation to morphological parameters. Br J Dermatol 134:1039–1043
12. Selim MM, Kelly KM, Nelson JS et al (2004) Confocal microscopy study of nerves and blood vessels in untreated and treated port wine stains: preliminary observations. Dermatol Surg 30:892–897

Chapter 48
EPR Oximetry for Investigation of Hyperbaric O_2 Pre-treatment for Tumor Radiosensitization

Benjamin B. Williams, Huagang Hou, Rachel Coombs, and Harold M. Swartz

Abstract A number of studies have reported benefits associated with the application of hyperbaric oxygen treatment (HBO) delivered immediately prior to radiation therapy. While these studies provide evidence that pre-treatment with HBO may be beneficial, no measurements of intratumoral pO_2 were carried out and they do not directly link the apparent benefits to decreased hypoxic fractions at the time of radiation therapy. While there is empirical evidence and some theoretical basis for HBO to enhance radiation therapy, without direct and repeated measurements of its effects on pO_2, it is unlikely that the use of HBO can be understood and optimized for clinical applications. In vivo EPR oximetry is a technique uniquely capable of providing repeated direct measurements of pO_2 through a non-invasive procedure in both animal models and human patients. In order to evaluate the ability of pretreatment with HBO to elevate tumor pO_2, a novel small animal hyperbaric chamber system was constructed that allows simultaneous in vivo EPR oximetry. This chamber can be placed within the EPR magnet and is equipped with a variety of ports for multiplace gas delivery, thermoregulation, delivery of anesthesia, physiologic monitoring, and EPR detection. Initial measurements were performed in a subcutaneous RIF-1 tumor model in C3H/HeJ mice. The mean baseline pO_2 value was 6.0 ± 1.2 mmHg ($N = 7$) and responses to two atmospheres absolute pressure HBO varied considerably across subjects, within tumors, and over time. When an increase in pO_2 was observed, the effect was transient in all but one case, with durations lasting from 5 min to over 20 min, and returned to baseline levels during HBO administration. These results indicate that without direct measurements of pO_2 in the tissue of interest, it is likely to be difficult to know the effects of HBO on actual tissue pO_2.

Keywords HBO • EPR • Radiosensitization • Oximetry

B.B. Williams (✉) • H. Hou • R. Coombs • H.M. Swartz
Dartmouth EPR Center, Geisel School of Medicine at Dartmouth, Hanover, NH 03755, USA
e-mail: Benjamin.B.Williams@dartmouth.edu

© Springer International Publishing Switzerland 2016

Q. Luo et al. (eds.), *Oxygen Transport to Tissue XXXVIII*, Advances in Experimental Medicine and Biology 923, DOI 10.1007/978-3-319-38810-6_48

1 Introduction

It has been recognized for over 60 years that hypoxia has a profound effect on the radiosensitivity of tissue and that hypoxic cells are approximately three times less sensitive to radiation than well oxygenated cells. A practical consequence of this fact is that tumors with significant hypoxic fractions that are treated with radiation therapy (RT) have decreased probabilities for complete tumor control and reduced patient survival rates. Despite the fundamental importance of tumor oxygenation during RT, measurements of pO_2 are not routinely performed in the clinical setting due, at least in part, to the lack of an available quantitative non-invasive measurement technique. EPR oximetry is a technique that is capable of providing direct measurements of pO_2 through a repeatable and non-invasive procedure, following one-time implantation of a paramagnetic oxygen reporter, such as India ink. Oxygen-dependent broadening of the EPR signal from the implanted India ink reports the pO_2 of the surrounding has been used successfully in a wide array of animal studies [1–3] and in human subjects [4–6].

A number of studies have reported benefits associated with the application of HBO immediately preceding RT [7–10]. The hypothesis behind these studies is that increased tumor oxygenation due to HBO treatment is maintained for a significant period following decompression and a return to room pressure, and that this provides a window where the hypoxic fraction of the tumor is decreased and RT can be applied precisely using the most modern technology. While the above studies provide evidence that pre-treatment with HBO can be beneficial, no measurements of intratumoral pO_2 were carried out in these studies, and they do not directly link the apparent benefits to decreased hypoxic fractions at the time of RT nor do they provide insights as to the mechanism by which HBO affects the tissue pO_2. The effects of HBO on physiological parameters such as perfusion and cell metabolism make it difficult to conclude that an effect on outcomes has occurred simply due to increased pO_2 in the circulation. Data describing normal tissue and tumor oxygen dynamics following HBO are limited. The oxygenation of normal rat cerebral tissues following exposure to four atmospheres absolute pressure (ATA) HBO were measured by Jamieson and van den Brenk using polarographic electrodes and found to be elevated for over 30 min [11]. Kinoshita et al. [12] monitored tumor oxygenation in subcutaneous SCCVII tumors of C3H/He mice following HBO (2 ATA) using semi-quantitative T1-weighted MRI and found that the oxygen-dependent signal intensity remained elevated for more than 60 min. They also reported that the signal intensity in normal muscle tissue declined much more rapidly. Becker et al. [13] measured pO_2 in squamous cell cancers of the head and neck in seven patients using polarographic electrodes during and following HBO at 2.4 ATA and found that significantly elevated pO_2 values were maintained in all patients for 5–25 min after leaving the hyperbaric chamber. They also report that maximum pO_2 values during HBO were achieved after 10–33 min of treatment, with a mean of 17 min. Beppu et al. [14] measured pO_2 in clinical glioblastoma tumors and peritumoral tissue ($n = 18$) using Clark-type electrodes at 5-min intervals following the application of

HBO (60-min at 2.8 ATA, w/ 20-min (de)compression periods). The intratumoral pO_2 remained significantly higher than the baseline level for 30 min following decompression. These measurements indicate that pO_2 in various tissues remains elevated following HBO, but there is variability across tissues and individual tumors. Under these conditions, especially in a clinical setting, confirmation of reduced hypoxia and optimal application of RT would require direct pO_2 measurements during and following HBO.

In summary, while there is some good empirical evidence and some theoretical basis for HBO to enhance radiation therapy, without direct and repeated measurements of the effects on pO_2 it is unlikely that the use of HBO can be understood and optimized for clinical applications. To date, no studies have combined RT and HBO pre-treatment with direct measurement of the tumor pO_2. Without such measurement of pO_2, especially in the face of variability across subjects, it is not possible to determine if RT was performed at a time of increased oxygenation as expected. As investigation of this promising treatment protocol continues, such confusion could lead to inaccurate assessment of the effects of the combined therapy. Furthermore, optimization of the application of HBO and the timing of RT following HBO will benefit from knowledge of the pO_2 values in the tumor tissue and the rates at which pO_2 declines once HBO application ceases.

2 Methods

2.1 Animal and Tumor Model

Developments and studies were performed using the subcutaneous RIF-1 tumor model in C3H/HeJ mice (6–8 weeks, The Jackson Laboratory) [1, 2]. This tumor model was chosen because it has been widely studied within the radiobiology community and it has a significant hypoxic fraction of 1–11 % [15]. Established procedures for cell culture and implantation were followed [2]. Approximately 12 days after subcutaneous inoculation with tumor cells within the hind leg, when the tumors are 100–200 mm^3, aggregates of the EPR oxygen probe lithium phthalocyanine (LiPc) were introduced into the tumor. These paramagnetic crystals are biologically inert and have EPR spectra which broaden linearly with increasing pO_2. LiPc was introduced at 2 sites within each tumor to sample pO_2 within the tumor volume. Each group of LiPc crystals encompassed a volume of approximately $0.5 \times 0.5 \times 1.5$ mm^3 with a separation between sites of 4 mm.

EPR oximetry measurements were acquired at least 24 h after insertion of the LiPc aggregates to allow for resolution of the minimal acute trauma of the procedure [16]. Mice were anesthetized using an intraperitoneal bolus injection of ketamine (90 mg/kg) and xylazine (9 mg/kg). Following anesthetization, mice were intubated according to procedures described by Hallowell EMC (Pittsfield, MA, USA) and using an otoscope and supplies within the Hallowell mouse intubation

package. Mice were then positioned and secured on the animal tray and mechanical ventilation was initiated. Prior to insertion of the mouse into the HBO chamber and EPR system, a boost of anesthesia (0.5× initial dose) was applied; this combination of bolus and boost was sufficient to typically provide the 1.5 h of anesthesia necessary for the measurement protocol. A rectal thermometer was used to monitor the core temperature of the mice, which was maintained at 37 ± 1 °C throughout the experiments through use of an IR lamp prior to installation in the chamber and the radiant heat supply surrounding the mouse within the chamber.

2.2 HBO Application Protocol

Hyperbaric oxygen was applied using a customized small animal hyperbaric chamber (Model B11, Reimers Systems Inc, Springfield VA, USA) in operation at the Dartmouth EPR Center (Fig. 48.1). This chamber is capable of delivering 100 % O_2 at pressures of up to 3.72 ATA. It is equipped with a variety of ports for drug delivery, physiologic monitoring, and EPR detection. An additional set of ports allow the use of an existing external small animal ventilator (Model SAR-830, CWE Inc.), which is rated for use with pure oxygen and at hyperbaric pressures. In addition to supporting the respiratory function, the ventilator allows the chamber to be operated as a multiplace hyperbaric chamber where the chamber is filled with an inert gas (e.g. N_2) and O_2 is supplied directly to the animal. This increases safety tolerances and alleviates the need for time consuming O_2 flushing of the chamber. The chamber can be installed inside the permanent magnet of the clinical EPR spectrometer and it is constructed entirely of non-magnetic materials. A customized EPR resonator and animal warming bed have been constructed for use in the chamber. For all

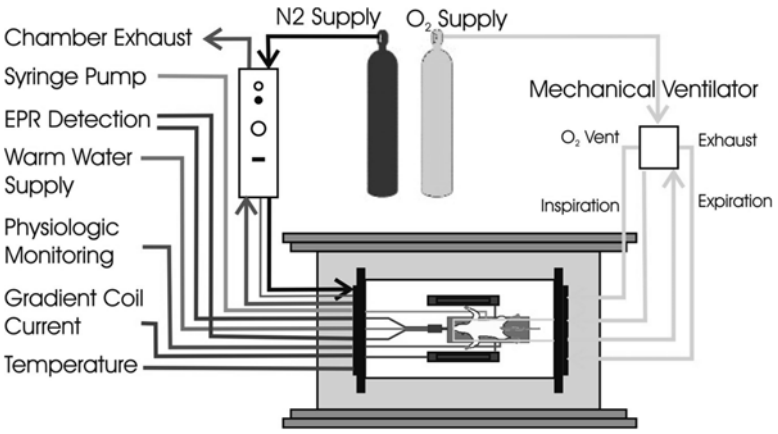

Fig. 48.1 Schematic diagram of the HBO chamber, EPR magnet, and associated equipment used for HBO measurements. Components associated with EPR detection, HBO pressurization, mechanical ventilation and O_2 supply to mouse, and physiologic monitoring and control are shown

experiments in this initial study, mice were exposed to HBO at 2 ATA, though the duration of HBO exposure varied. Compression and decompression of the chamber were performed over 2-min periods, resulting in biologically acceptable rates of ~15 (feet of seawater)/min.

2.3 In Vivo EPR Oximetry

Mice were positioned with tumors centrally located with respect to the magnet and directly under the surface loop detector [17]. Multi-site EPR spectroscopy was used to simultaneously measure the EPR signals from each site, characterize their spectral shapes, and estimate pO_2 at their locations. Quality assurance spectra were acquired during the study to verify proper calibration of the instrumental settings that could affect the observed linewidth and derived pO_2 estimates. Instrumental parameters, such as the Zeeman modulation amplitude and RF power, were set adaptively based on the measured spectra to optimize the precision and accuracy of the pO_2 measurements. Throughout periods of baseline (normobaric air breathing), HBO (2ATA with 100 % O_2), and recovery periods with normobaric air, the pO_2 was measured continuously using spectra collected with periods of 10 seconds. EPR spectra were analyzed using least-squares fitting to estimate the oxygen-dependent linewidth and linewidths were converted to pO_2 through an established oxygen calibration curve.

3 Results

Following series of normobaric trials and studies to assess the role of the ketamine/xylazine anesthesia, pO_2 measurements were accomplished in seven mice during the application of HBO. The mean baseline pO_2 value was 6.0 ± 1.2 mmHg, which is consistent with prior measurements in this mouse tumor model [16]. Responses to the application of HBO varied considerably across subjects and for individual subjects at the 2 measurement sites. In 6/7 mice a change in pO_2 of at least 2 mmHg was observed for at least one of the measurement sites. In one mouse there was no response to HBO. When an increase in pO_2 was observed, the effect was transient in all but one case, with durations lasting from 5 min to over 20 min. A typical response is shown in Fig. 48.2. HBO was initiated at the 21-min time point and ceased 30 min later. In one of the measurement sites (Site #1) a ~4 mmHg increase in pO_2 was observed within the initial 10 min of HBO, after which the pO_2 returned to the baseline values of ~6 mmHg. The second measurement site (Site #2) remained near its baseline value of 9 mmHg throughout the measurement and did not exhibit any increase in pO_2 when HBO was applied.

Within this set of measurements, and consistent with all other measurements, there was a very large degree of variability in the response to HBO. This highlights

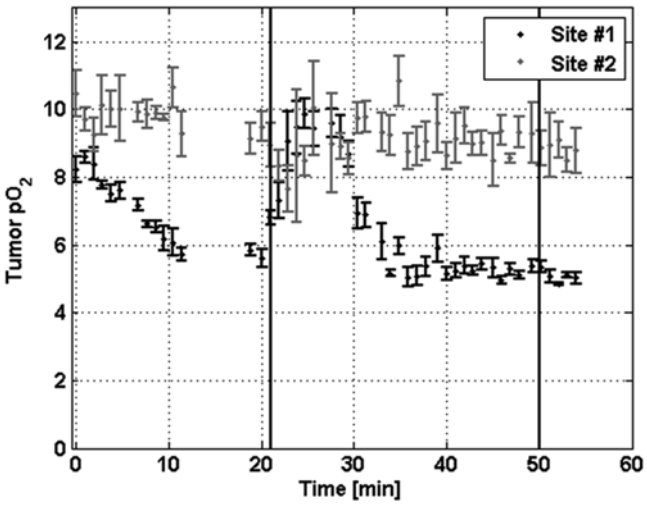

Fig. 48.2 Tumor pO_2 dynamics in response to the application of HBO. Tumor pO_2 is expressed in mmHg

the need for such measurements of tumor pO_2 if the radiosensitizing ability of HBO is to be assessed and investigated effectively.

4 Discussion and Conclusions

We have developed the instrumentation and procedures necessary to perform tumor pO_2 measurements during and following the application of HBO treatment. The developments of the instrumentation and procedures have enabled initial measurement of tumor pO_2 in the mouse tumor model prior to, during, and after HBO. We observed a large degree of inter- and intra-subject variability in the response of tumor tissue to the application of HBO. Variability in the existence, timing, and level of response were observed. The methods were designed to enable adequate physiologic controls to minimize the impact of likely confounders, including ventilation and temperature. The role of anesthesia as a potential confounder must be further considered. Additional systematic studies are warranted to provide more definitive characterization of the effects of HBOT in pertinent tumor model systems and normal tissues, and eventually within clinical trials. Currently the use of HBO for enhancing therapy has been limited by a lack of knowledge of the optimum conditions for enhancing therapy in regard to both the HBO parameters to be used to maximize radiation sensitization and the effects of radiation on the effectiveness of repeated HBO applications to change tumor pO_2. In the face of variability such as that observed in our study, especially without knowledge of the individual

pO_2 dynamics, effective use of HBO to radiosensitize tumors prior to treatment would likely not be possible. Our research is ongoing to better understand the sources and patterns of the observed variations, including both physiologic and experimental considerations, with the aim of enhancing the effectiveness of radiation therapy. Recently, clinical EPR systems have been developed [4] which will allow measurement of human tumor pO_2 following HBO treatment and, with the use of multiplace HBO chambers, could provide data during HBO as well.Acknowledgments This research was supported by a grant from the GEMI Fund, Lidingö, Sweden and American Cancer Society Research Grant #IRG-82-003-22.

References

1. Goda F, O'Hara JA, Rhodes ES, Liu KJ, Dunn JF, Bacic G, Swartz HM (1995) Changes of oxygen tension in experimental tumors after a single dose of X-ray irradiation. Cancer Res 55(11):2249–2252
2. O'Hara JA, Goda F, Demidenko E, Swartz HM (1998) Effect on regrowth delay in a murine tumor of scheduling split-dose irradiation based on direct pO_2 measurements by electron paramagnetic resonance oximetry. Radiat Res 150(5):549–556
3. O'Hara JA, Goda F, Liu KJ, Bacic G, Hoopes PJ, Swartz HM (1995) The pO_2 in a murine tumor after irradiation: an in vivo electron paramagnetic resonance oximetry study. Radiat Res 144(2):222–229
4. Swartz HM, Williams BB, Zaki BI, Hartford AC, Jarvis LA, Chen EY, Comi RJ, Ernstoff MS, Hou H, Khan N and Swarts SG (2014) Clinical EPR: unique opportunities and some challenges. Acad Radiol 21(2):197–206
5. Khan N, Williams BB, Swartz HM (2006) Clinical applications of in vivo EPR: rationale and initial results. Appl Magn Reson 30:185–199
6. Swartz HM, Khan N, Buckey J, Comi R, Gould L, Grinberg O, Hartford A, Hopf H, Hou H, Hug E, Iwasaki A, Lesniewski P, Salikhov I, Walczak T (2004) Clinical applications of EPR: overview and perspectives. NMR Biomed 17(5):335–351
7. Kunugita N, Kohshi K, Kinoshita Y, Katoh T, Abe H, Tosaki T, Kawamoto T, Norimura T (2001) Radiotherapy after hyperbaric oxygenation improves radioresponse in experimental tumor models. Cancer Lett 164(2):149–154
8. Kohshi K, Kinoshita Y, Terashima H, Konda N, Yokota A, Soejima T (1996) Radiotherapy after hyperbaric oxygenation for malignant gliomas: a pilot study. J Cancer Res Clin Oncol 122(11):676–678
9. Kohshi K, Kinoshita Y, Imada H, Kunugita N, Abe H, Terashima H, Tokui N, Uemura S (1999) Effects of radiotherapy after hyperbaric oxygenation on malignant gliomas. Br J Cancer 80(1–2):236–241
10. Kohshi K, Yamamoto H, Nakahara A, Katoh T, Takagi M (2007) Fractionated stereotactic radiotherapy using gamma unit after hyperbaric oxygenation on recurrent high-grade gliomas. J Neurooncol 82(3):297–303
11. Jamieson D, Van Den Brenk HAS (1963) Measurement of oxygen tensions in cerebral tissues of rats exposed to high pressures of oxygen. J Appl Physiol 18(5):869–876
12. Kinoshita Y, Kohshi K, Kunugita N, Tosaki T, Yokota A (2000) Preservation of tumour oxygen after hyperbaric oxygenation monitored by magnetic resonance imaging. Br J Cancer 82(1):88–92

13. Becker A, Kuhnt T, Liedtke H, Krivokuca A, Bloching M, Dunst J (2002) Oxygenation measurements in head and neck cancers during hyperbaric oxygenation. Strahlenther Onkol 178(2):105–108
14. Beppu T, Kamada K, Yoshida Y, Arai H, Ogasawara K, Ogawa A (2002) Change of oxygen pressure in glioblastoma tissue under various conditions. J Neurooncol 58(1):47–52
15. Clifton K, Briggs R, Stone HB (1966) Quantitative radiosensitivity studies of solid carcinomas in vivo: methodology and effect of anoxia. J Natl Cancer Inst 36:965–974
16. Hou H, Lariviere JP, Demidenko E, Gladstone DJ, Swartz HM, Khan N (2009) Repeated tumor pO2 measurements by multi-site EPR oximetry as a prognostic marker for enhanced therapeutic efficacy of fractionated radiotherapy. Radiother Oncol 91(1):126–131
17. Salikhov I, Walczak T, Lesniewski P, Khan N, Iwasaki A, Comi R, Buckey J, Swartz HM (2005) EPR spectrometer for clinical applications. Magn Reson Med 54(5):1317–1320

Chapter 49
Design of a Compact, Bimorph Deformable Mirror-Based Adaptive Optics Scanning Laser Ophthalmoscope

Yi He, Guohua Deng, Ling Wei, Xiqi Li, Jinsheng Yang, Guohua Shi, and Yudong Zhang

Abstract We have designed, constructed and tested an adaptive optics scanning laser ophthalmoscope (AOSLO) using a bimorph mirror. The simulated AOSLO system achieves diffraction-limited criterion through all the raster scanning fields (6.4 mm pupil, 3° × 3° on pupil). The bimorph mirror-based AOSLO corrected ocular aberrations in model eyes to less than 0.1 μm RMS wavefront error with a closed-loop bandwidth of a few Hz. Facilitated with a bimorph mirror at a stroke of ±15 μm with 35 elements and an aperture of 20 mm, the new AOSLO system has a size only half that of the first-generation AOSLO system. The significant increase in stroke allows for large ocular aberrations such as defocus in the range of ±600° and astigmatism in the range of ±200°, thereby fully exploiting the AO correcting capabilities for diseased human eyes in the future.

Keywords Optical design • Raster scanning • Adaptive optics • Confocal microscopy • Ophthalmic optics

These authors contributed to the work equllly and should be considered co-first authors.

Y. He (✉) • L. Wei • X. Li • J. Yang • G. Shi (✉) • Y. Zhang
The Key Laboratory on Adaptive Optics, Chinese Academy of Sciences, Chengdu 610209, China

The Laboratory on Adaptive Optics, Institute of Optics and Electronics, Chinese Academy of Sciences, Chengdu 610209, China
e-mail: heyi_job@126.com; ioe_eye@126.com

G. Deng
Department of Ophthalmology, The Third People's Hospital of Changzhou, Changzhou, Jiangsu, China

© Springer International Publishing Switzerland 2016

Q. Luo et al. (eds.), *Oxygen Transport to Tissue XXXVIII*, Advances in Experimental Medicine and Biology 923, DOI 10.1007/978-3-319-38810-6_49

1 Introduction

The newest generation of confocal scanning laser ophthalmoscopes (SLO) with adaptive optics (AO) correction of ocular aberrations provides retinal images of unprecedented resolution, allowing real-time imaging information on cellular and sub-cellular structures in the living eye [1, 2]. More recently, motion contrast processing techniques were applied to AOSLO to improve visualization of retinal capillary features [3]. Active image stabilization has also been integrated into AOSLO for precise imaging and targeting of retinal structures [4]. A slightly different AOSLO system has been implemented in our laboratory and has been reported in a series of publications [5, 6]. Oxygen saturation in small retinal vessels with a diameter of 27 μm is assessed by the AOSLO for the first time [7].

In fact, the deformable mirror (DM) plays a key role in the realization of the AOSLO systems. A mechanical DM was first successfully employed to correct high-order ocular aberrations in several AOSLO systems [8, 9]. Vargas-Martin et al. exploited a transmissive liquid-crystal spatial light modulator to improve the image quality [10]. Zhang et al. explored a microelectromechanical system (MEMS) DM for AO in the human eye [11]. More recently, Zhou et al. operated a bimorph DM to overcome ocular aberrations in a fundus camera [12].

In this paper, we develop an AOSLO system using a bimorph mirror with a compact optical design. The simulated AOSLO system based on off-axis spherical mirrors achieves diffraction-limited criteria through all the raster scanning fields (6.4 mm pupil, 3° × 3° on pupil), and has a size only half that of the first-generation AOSLO. Facilitated with a bimorph mirror at a stroke of ±15 μm with 35 elements, it has five times stroke compared to our first-generation AOSLO; the significant increase in stroke allows for large ocular aberrations such as defocus in the range of ±600° and astigmatism in the range of ±200°.

2 Method

As shown in Fig. 49.1, the AOSLO system use spherical mirrors in an off-axis arrangement to avoid undesired back-reflections that would be comparable to the light scattered by the retina. These mirrors are used in pairs creating an afocal telescope to preserve conjugate planes and match optics apertures. For clarity, the systems have been drawn in a plane arrangement. Note that the wavefront sensor and PMT detector are on-axis optical modular which are relatively free from aberrations, and these parts are excluded in the optical design work.

In the AOSLO, a small spot focused on the retina, and two scanning mirrors provide raster scanning of the bright spot of the retina in the field of view (FOV). Two multi-configuration surfaces representing two scanning mirrors and 17 configuration points expanding the full FOV are set in Zemax. Simulated multi-configurations are shown in Fig. 49.2; a 3° × 3° field on pupil projects an approximate

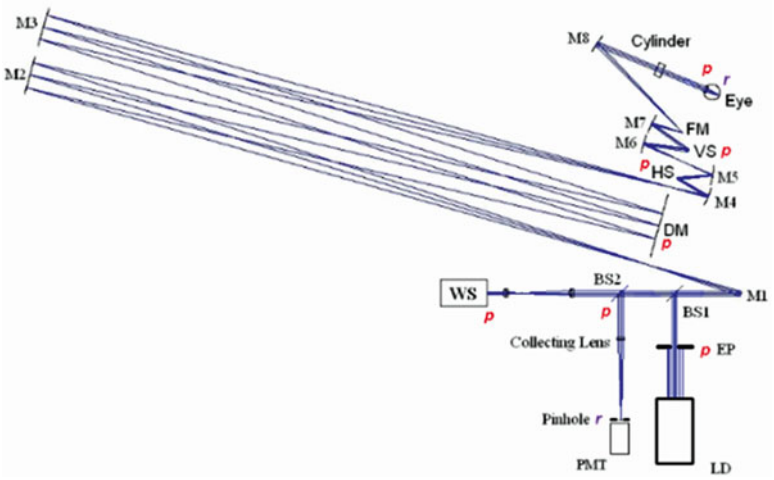

Fig. 49.1 The schematic of evaluated AOSLO optical paths

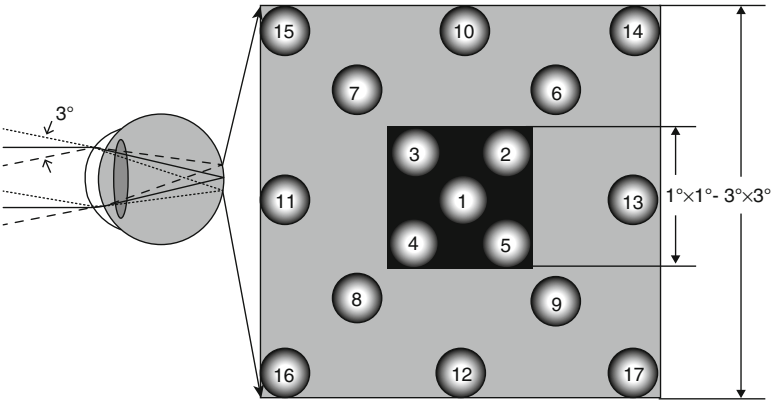

Fig. 49.2 Multi-configurations of raster scanning

900 μm × 900 μm square on the retina plane. It is desirable to achieve diffraction limited performance through the entire field, and a compact design of an AOSLO layout.

An illumination wavelength of 650 nm was assumed for all modeling work. The diameter assumed at the pupil of the eye was 6.4 mm, which determined the *f*-number of the optical system of the AOSLO, and all pupil relays have unit *f*-number, to keep the AOSLO instrument dimensions and optical aberrations to a minimum.

A pair of pupil relay mirrors between two scanners are selected off the optical plane to compensate astigmatisms, and tilting angles of other mirrors are optimized to minimize astigmatisms. Tilting angles and distances between mirrors are useful to minimize coma, because the vergence of the beam which is reflected from the

mirror determines the sign and value of coma. Each mirror in the system can be adjusted to compensate for coma generated by a previous system. In addition, high-order aberrations are minimized through optimizing the system.

The optimization methodology introduced in this research requires the root-mean-square (RMS) wavefront error for each point on the retina to be minimized as far as possible. During the optimization, operands' weights in error functions can be adjusted to balance the contribution of each configuration. For example, the central field was compromised to help the corner field performance.

3 Results and Experiment

After a complicated optimization, all evaluated configurations are diffraction-limited according to Marechal's criterion on the retinal plane. Figure 49.3a is the spot diagram of the simulated AOSLO. The squares from inside to outside represent the same field as in Fig. 49.2. The spot diagram is symmetrical horizontally but asymmetrical vertically, which is in agreement with the off-plane in x-axis in order to minimize the off-axis aberrations. Performances on a central field of $1° \times 1°$ were degraded to balance marginal FOV, while they are still in Airy disk. The maximum RMS radius on the marginal field is 1.86 μm, and the Airy disc radius is 2.84 μm, so they are in the Airy disk.

Note that the human retinal curvature has a radius of −12 mm; it is critical to minimize the field curvature aberration. Figure 49.3b shows the field curve of all the configurations. In this design, along with the increasing field configurations, the field curvature is greatly reduced to zero, but then it is inversely increased. The maximum field curvature is less than 16 μm, and is much smaller than the limit of

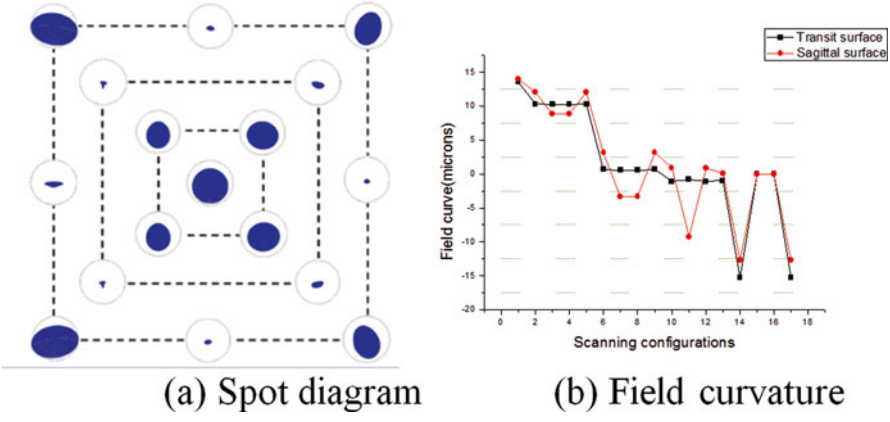

Fig. 49.3 Spot diagram (**a**) and field curvature (**b**) of the whole scanning field. Airy disk diameter is about 5.67 μm. Maximum field of curve on the transit surface of configuration 17 is −15.3 μm

theoretical axial resolution with a value of 50 μm. Therefore, such a small field curvature has no influence on the imaging quality, and is completely acceptable in view of the large retinal curvature.

The simulated AOSLO system achieves diffraction-limited criteria through all the FOV, and we present a bimorph mirror-based AOSLO system. The AOSLO system was tested in a model eye, which is composed of a perfect lens ($f = 22.8$ mm, EPD = 6.4 mm) and a curved retina with a scattered surface. To characterize the performance of the AO system for dynamically correct aberrations, we added an optometry lens to simulate defocus and astigmatism aberrations in the model eyes. We acquired and processed aberration correcting experiments in which AO correction was active during 40 iterations, and the Zernike coefficients and wavefront error maps were calculated in a typical manner [13]. Figure 49.4 shows the results.

Figure 49.4 represent the wavefront error maps averaged over frames acquired without and with AO correction, respectively. Columns of the Fig. 49.4 show the corresponding wavefront without and with AO close-loop corrections. With AO correction, defocus aberrations in the range of ±600° were corrected, and the RMS wavefront error was decreased from 0.82 μm to less than 0.1 μm within tens of close-loop times; meanwhile, astigmatism in the range of ±200° can be corrected, and the RMS error was less than 0.1 μm with AO correction and 0.24 μm without AO correction.

We also recorded images before and after AO corrections, which are plotted in the upper part of Fig. 49.5. Simulated defocus and astigmatism aberrations produced a dark and unclear image on the left. With AO correction, aberrations were perfectly compensated, the contrast and resolution of the right image were dramatically improved. One can visually distinguish more than five particles in the scale bar of 20 μm on the AO corrected image, so this proved that the resolution of the AOSLO system is less than 4 μm. The last part of Fig. 49.5 plots the AO correction as a function of close-loop times for the imaging data shown in the upper part of Fig. 49.5. The RMS error was 0.08 μm after AO correction and 0.82 μm before AO correction. Considering that the sampling rate of the AOSLO system is 20 frames per second, the 10–90 % rise-time measured was 0.8 s (16 close-loop frame times) for a measured close-loop bandwidth of 1.25 Hz. In fact, the simulated aberration was far too large and degraded the closed-loop bandwidth. In an ordinary RMS error of 0.5 μm, the AO correction was finished within ten close-loop times with a RMS error of 0.08 μm, and the closed-loop bandwidth reached 2 Hz.

4 Conclusion

Although the AOSLO has been used for an increasing range of scientific and clinical applications, there are significant impediments to its widespread application in the clinic, partly due to the restriction of deformable mirrors. We have developed a bimorph mirror for AO systems that has a stroke of ±15 μm with 35 elements and an

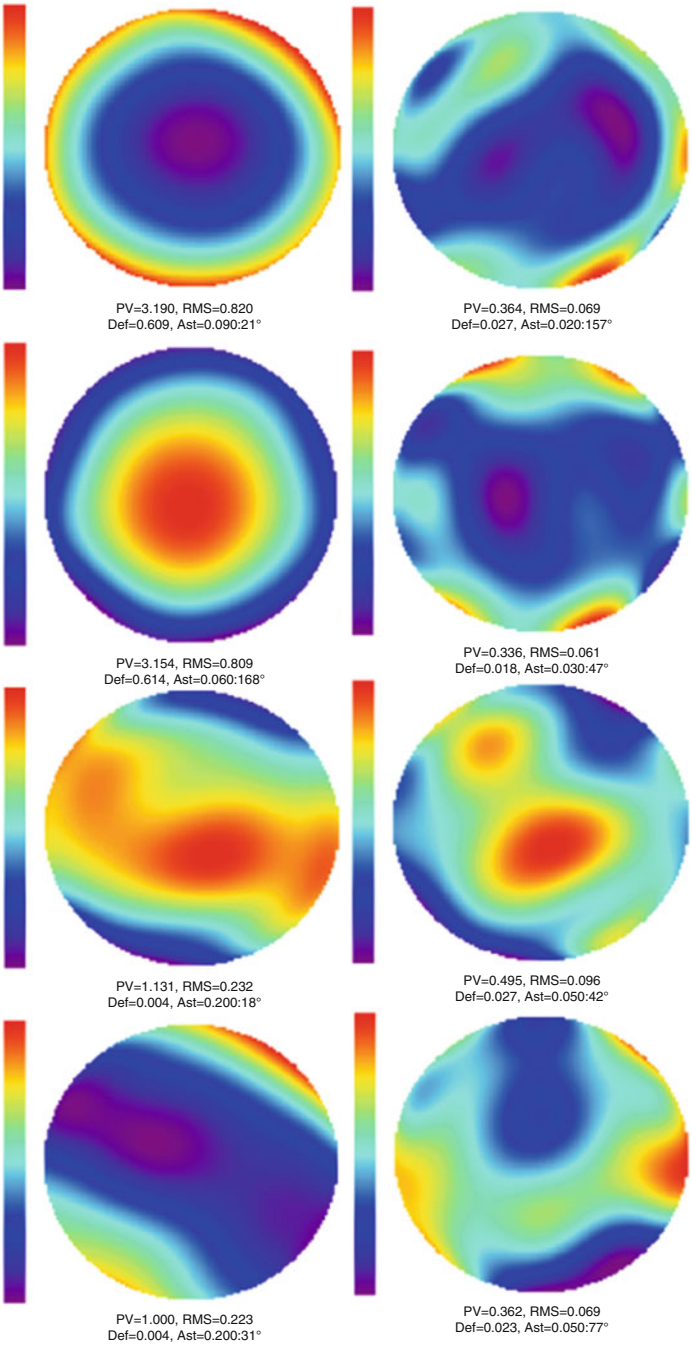

Fig. 49.4 Summary of the AO performances. Wavefront aberrations without AO correction are on the *left*, and the aberrations with AO correction are shown on the *right* side

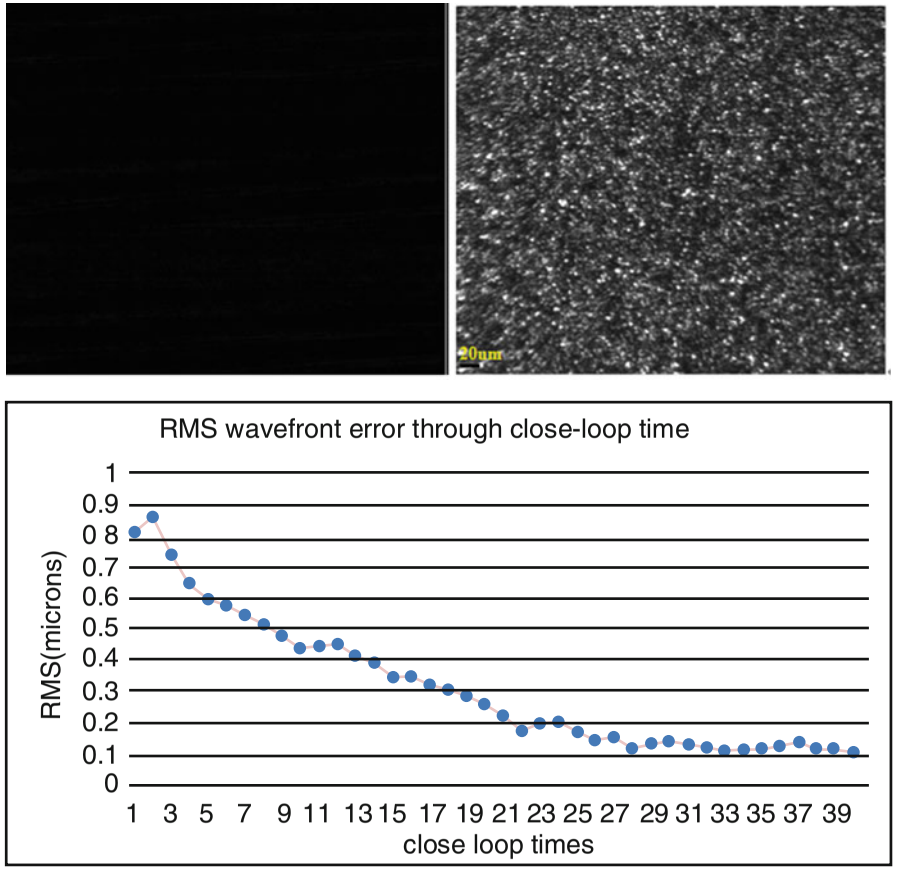

Fig. 49.5 Model eye imaging results without AO correction and with AO correction, the lower part shows the RMS wavefront error through close-loop time. Scale bar, 20 μm

aperture of 20 mm. This article describes how we designed, constructed, and tested a bimorph mirror-based AOSLO system.

Spherical mirrors are used in pairs for pupil relay arranged off the optical plane to compensate astigmatisms, and tilting angles and distances of mirrors are optimized to minimize astigmatisms and coma aberrations. The optical design of the AOSLO achieves diffraction-limited criterion through all the raster scanning fields (6.4 mm pupil, $3° \times 3°$ on pupil).

The bimorph-based AOSLO system corrected ocular aberrations in model eyes to less than 0.1 μm RMS wavefront error with a closed-loop bandwidth of a few Hz. This bandwidth, although not high, is sufficient to compensate for the majority of dynamic aberrations at rates of 2 Hz [13]. In fact, the bimorph mirror is noteworthy for the large stroke and a relative aperture, and the new AOSLO system has a size only half that of the first-generation AOSLO system. Thus, the new AOSLO system can even correct the defocus aberration in the range of ±600° and astigmatism in the range of ±200°.

These advances will aid in the development of new AOSLO systems in ophthalmology. The bimorph mirror-based AOSLO is a potential choice with a large stroke, relatively small aperture and low cost. We have begun to investigate this bimorph mirror in our new AOSLO system, and the significant increase in stroke allows for a large range of ocular aberrations such as defocus and astigmatism, thereby fully exploiting the AO correcting capabilities for diseased human eyes.

Acknowledgments This work is supported by the Outstanding Young Scientists of the Chinese Academy of Sciences, the National Instrumentation Program (NIP, Grant No. 2012YQ120080), the Zhejiang Province Technology Program (Grant No. 2013C33170), the National Science Foundation of China (Grant No. 61108082), the Sichuan Youth Science & Technology Foundation (Grant No. 2013JQ0028) and the West Light Foundation of the Chinese Academy of Sciences. The authors would like to thank Hao Li and Jing Lu for many helpful discussions regarding this project.

References

1. Roorda A, Romero-Borja F et al (2002) Adaptive optics scanning laser ophthalmoscopy. Opt Express 10:405–412
2. Chui TY, Vannasdale DA, Burns SA (2012) The use of forward scatter to improve retinal vascular imaging with an adaptive optics scanning laser ophthalmoscope. Biomed Opt Express 3(10):2537–2549
3. Hammer DX, Ferguson RD et al (2012) Multimodal adaptive optics retinal imager: design and performance. J Opt Soc Am A 29:2598–2607
4. Sheehy CK, Yang Q et al (2012) High-speed, image-based eye tracking with a scanning laser ophthalmoscope. Biomed Opt Express 3(10):2611–2622
5. Lu J, Li H et al (2011) Superresolution in adaptive optics confocal scanning laser ophthalmoscope. Acta Phys Sin 60(3):034207
6. Li H, Lu J et al (2010) Tracking features in retinal images of adaptive optics confocal scanning laser ophthalmoscope using KLT-SIFT algorithm. Biomed Opt Express 1(1):31–40

7. Li H, Lu J et al (2011) Measurement of oxygen saturation in small retinal vessels with adaptive optics confocal scanning laser ophthalmoscope. J Biomed Opt 16(11):110504
8. Hammer DX, Ferguson RD et al (2006) Adaptive optics scanning laser ophthalmoscope for stabilized retinal imaging. Opt Express 14:3354–3367
9. Zhang YH, Wang XL et al (2014) Photoreceptor perturbation around subretinal drusenoid deposits as revealed by adaptive optics scanning laser ophthalmoscopy. Am J Ophthalmol 158(3):584–596
10. Vargas-Martin F, Prieto PM, Artal P (1998) Correction of the aberrations in the human eye with a liquid-crystal spatial light modulator: limits to performance. J Opt Soc Am A 15:2552–2562
11. Zhang H, Poonja S, Roorda A (2006) MMS-based adaptive optics scanning laser ophthalmoscopy. Opt Lett 31:268–1270
12. Zhou Guan CL, Dai Y (2013) Bimorph deformable mirrors for adaptive optics of human retinal imaging system. Acta Optica Sinica 33(2):0211001
13. Thibos LN et al (2002) Standards for reporting the optical aberrations of eyes. J Refractive Surg 18:S652–S660

Chapter 50
Development of Portable, Wireless and Smartphone Controllable Near-Infrared Spectroscopy System

Takashi Watanabe, Rui Sekine, Toshihiko Mizuno, and Mitsuharu Miwa

Abstract We have developed portable near-infrared tissue oxygenation monitoring systems, called the "PocketNIRS Duo" and the "PocketNIRS HM", which features wireless data communication and a sampling rate of up to 60 data readings per second. The systems can be controlled by smartphone or personal computer. We demonstrate the efficacy of the systems for monitoring changes in brain and arm muscle hemodynamics and oxygenation in breath-holding and cuff-occlusion tests, respectively.

Our systems should prove to be useful as an oxygenation monitor not only in research but also in healthcare applications.

Keywords Near-infrared spectroscopy (NIRS) • Oxygenation • Portable • Wireless • High sampling rate

1 Introduction

Near-infrared spectroscopy (NIRS) technologies are used for the non-invasive determination of the amount of absorbing molecular species in tissue, especially oxyhemoglobin and deoxyhemoglobin [1–5]. NIR light in the wavelength range of 700–1000 nm, which is called the "optical window for tissues", is able to penetrate

T. Watanabe (✉) • R. Sekine
Optical Diagnostic Technology Group, Development Center, Hamamatsu Photonics K.K., Hamamatsu, Japan
e-mail: tk-wat@crl.hpk.co.jp

T. Mizuno
DynaSense Inc., Hamamatsu, Japan

M. Miwa
Development Center, Hamamatsu Photonics K.K., Hamamatsu, Japan

© Springer International Publishing Switzerland 2016

Q. Luo et al. (eds.), *Oxygen Transport to Tissue XXXVIII*, Advances in Experimental Medicine and Biology 923, DOI 10.1007/978-3-319-38810-6_50

several centimeters into a variety of tissues because of the low absorbance of hemoglobin and water at these wavelengths. There are three fundamental approaches to measuring oxygenation in tissue non-invasively: the continuous wave (CW), frequency resolved and time resolved techniques. NIRS using CW is the simplest and most practical of these technologies, although it is difficult to acquire the absolute hemoglobin concentration with this method.

Several CW NIRS systems are commercially available. However, these systems exhibit poor portability owing to their size and weight, fragile optical fibers that are easy to break, and slow data acquisition rates, all of which can make their use inconvenient. We have developed a portable, fiber-free, battery-operated, low noise, highly sensitive, wireless NIRS system with a fast sampling rate and two-channel probe operation. The product is called the "PocketNIRS Duo". We expect that our wireless and portable NIRS system will prove to be a useful device in a number of fields including the healthcare industry, brain research, and brain–machine interfaces.

2 Instrumentation

2.1 PocketNIRS Duo

The PocketNIRS Duo consists of three main parts, as shown in Fig. 50.1: the optical probes, the controller, and the interface device (smartphone or personal computer). The optical probe has three built-in NIR light emitting diodes (LEDs) as light sources and a single silicon PIN photodiode as an optical detector which is positioned 3 cm from the LEDs. The analog signal from the photodiode is amplified and converted to a digital signal within the optical probe and then transferred to the

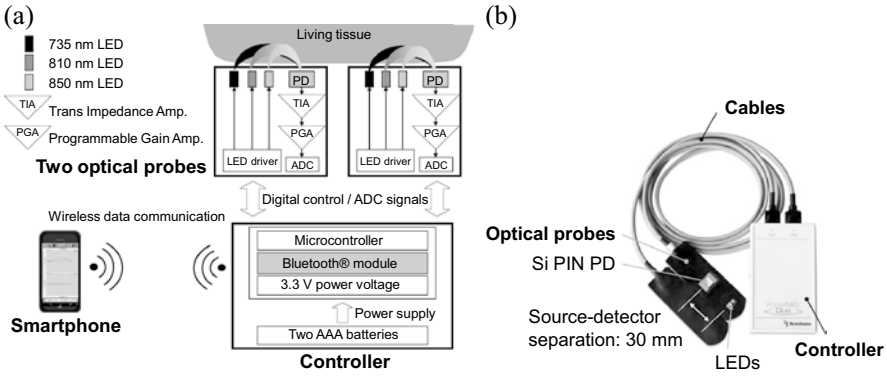

Fig. 50.1 Our wireless NIRS system "PocketNIRS Duo" (**a**) Schematic diagram (**b**) External view

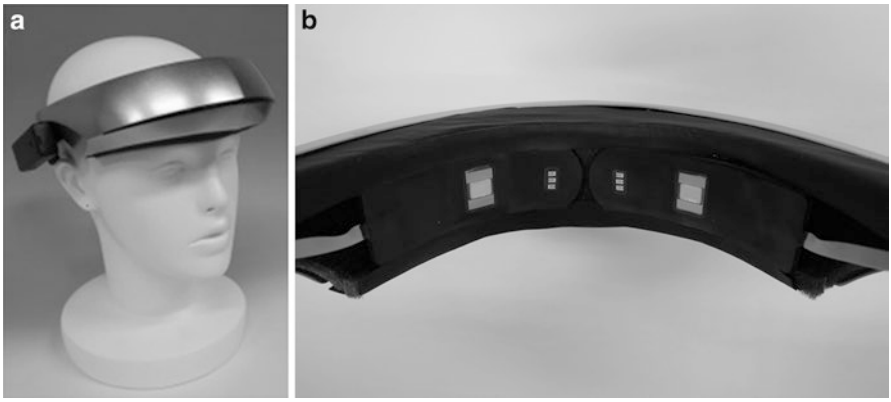

Fig. 50.2 PocketNIRS HM (**a**) External view (**b**) Internal view

controller via a 1 m long electrical cable. Digitization of the analogue signal prior to data transfer helps to preserve signal quality. The programmable gain amplifier (PGA) enables the measurement of signals over a wide dynamic range. The smartphone acquires and analyzes the data transmitted from the controller by Bluetooth® wireless technology, and then displays the results.

2.2 PocketNIRS HM

The PocketNIRS Duo has been designed for the analysis of oxygenation and hemodynamics in a number of tissues including brain and muscle.

The requirement for measuring the oxygenation state of the brain is increasing. We have therefore designed a variant of the PocketNIRS, the "PocketNIRS HM", specifically for the measurement of brain oxygenation (Fig. 50.2). All specifications are the same as those described for the PocketNIRS Duo. The control circuit, two optical probes, Bluetooth wireless data transmitter and battery are all integrated into a plastic helmet. This device does not require the use of double-sided tape on the optical probe. The PocketNIRS HM is simply mounted onto the head of the subject, the power turned on, and the start button on the smartphone pressed. The system then starts measurements immediately.

3 The Principles of the PocketNIRS Duo

The changes in tissue concentrations of oxyhemoglobin and deoxyhemoglobin can be determined using the modified Beer-Lambert law. When the NIR light sources illuminate a tissue, the photodetector receives backscattered photons from the tissue. The penetration depth of detection is approximately one half the distance

between the light sources and the photodetector. For example, if the light source and photodetector are separated by a distance of 3 cm, then the penetration depth is expected to be approximately 1.5 cm.

The attenuation of incident light intensity can be formulated as follows:

$$OD(\lambda,t) = \log_{10} \frac{I_{in}(\lambda,t)}{I_{out}(\lambda,t)} = A(\lambda,t) + S(\lambda,t), \tag{50.1}$$

where $I_{in}(\lambda, t)$ is the incident light intensity, $I_{out}(\lambda, t)$ is the detected intensity, and $OD(\lambda, t)$ is the optical density for wavelength λ at time t and is defined as the attenuation in light intensity as a function of the wavelength λ at time t. This attenuation can also be defined as the superposition of absorption $A(\lambda, t)$ and scattering $S(\lambda, t)$ of NIR light. Oxyhemoglobin and deoxyhemoglobin are the main absorbers of light in the NIR region in human tissue and their concentrations at a given point in time can be used to derive the light absorbance. Therefore, light absorbance can be formulated as follows:

$$A(\lambda,t) = \varepsilon_{HbO_2}(\lambda)[HbO_2](t)L(\lambda,t) + \varepsilon_{Hb}(\lambda)[Hb](t)L(\lambda,t), \tag{50.2}$$

where $\varepsilon_{HbO_2}(\lambda)$ and $\varepsilon_{Hb}(\lambda)$ are the respective extinction coefficients of oxyhemoglobin and deoxyhemoglobin at wavelength λ [6], $[HbO_2]$ (t) and $[Hb]$ (t) are the respective concentrations of oxyhemoglobin and deoxyhemoglobin, and $L(\lambda, t)$ is the optical path length of the wavelength λ at time t. The optical path length can be expressed in terms of the source–detector separation distance as follows:

$$L(\lambda,t) = DPF(\lambda,t) \cdot d, \tag{50.3}$$

where d is the distance between the light sources and the photodetector and $DPF(\lambda, t)$ is the differential path length factor [7–9].

When scattering $S(\lambda, t)$ is assumed to be constant with respect to both wavelength and time, the differential OD value at time t can be expressed as:

$$\Delta OD(\lambda,t) = \varepsilon_{HbO_2}(\lambda)\Delta\{[HbO_2]L(\lambda,t)\} + \varepsilon_{Hb}(\lambda)\Delta\{[Hb]L(\lambda,t)\}, \tag{50.4}$$

using Eqs. (50.1) and (50.2), and the measurement of the OD value at initial time t_0.

In addition, the measurement of the differential OD value can be obtained as follows:

$$\Delta OD(\lambda,t) = \log_{10} \frac{I_{in}(\lambda,t)}{I_{out}(\lambda,t)} - \log_{10} \frac{I_{in}(\lambda,t_0)}{I_{out}(\lambda,t_0)} = \log_{10} \frac{I_{out}(\lambda,t_0)}{I_{out}(\lambda,t)}, \tag{50.5}$$

In the above, $I_{in}(\lambda, t)$ at time t is equal to $I_{in}(\lambda, t_0)$ at initial time t_0 because $I_{in}(\lambda, t)$ is kept constant during measurement.

The relationship between changes in the product of the concentration and the optical path length and the differential OD values is derived from Eqs. (50.4) and (50.5), and least squares method as follows:

$$\left({}^{t}\mathbf{AA}\right)\mathbf{C} = {}^{t}\mathbf{AM}, \text{with}\,\mathbf{A} = \begin{bmatrix} \varepsilon_{HbO_2}(735) & \varepsilon_{Hb}(735) \\ \varepsilon_{HbO_2}(810) & \varepsilon_{Hb}(810) \\ \varepsilon_{HbO_2}(850) & \varepsilon_{Hb}(850) \end{bmatrix},$$
$$\mathbf{C} = \begin{bmatrix} \Delta\{[HbO_2](t)L(t)\} \\ \Delta\{[Hb](t)L(t)\} \end{bmatrix} \text{and}\,\mathbf{M} = \begin{bmatrix} \Delta OD(735,t) \\ \Delta OD(810,t) \\ \Delta OD(850,t) \end{bmatrix}, \tag{50.6}$$

where $L(t)$ is the optical path length assuming, for simplicity, that the path length of all wavelengths are approximately equal. Changes in the product of the concentration and the optical path length, $\Delta\{[HbO_2](t)L(t)\}$ and $\Delta\{[Hb](t)L(t)\}$, can be determined by solving Eq. (50.6).

In addition, change in the product of the total hemoglobin concentration and the optical path length, $\Delta\{[tHb](t)L(t)\}$, is obtained as follows:

$$\Delta\{[tHb](t)L(t)\} = \Delta\{[HbO_2](t)L(t)\} + \Delta\{[Hb](t)L(t)\} \tag{50.7}$$

4 Evaluation

4.1 Solid Phantom Test

To evaluate the performances of our NIRS system, an epoxy based solid phantom (absorption coefficient $[\mu_a] = 0.04\,\text{mm}^{-1}$ and reduced scattering coefficient $[\mu_s'] = 0.8\,\text{mm}^{-1}$) was used. The signal-to-noise ratio (SNR) is limited by shot noise generated by the random arrival of incidence photons at the photodetector.

The solid phantom test revealed that an SNR of at least 60 dB was obtainable with our system.

4.2 Arm Cuff Occlusion Test

The ability of the PocketNIRS Duo to measure oxygenation in human subjects was evaluated using an arm cuff occlusion test. The optical probe was placed on the left forearm of the subject. The PocketNIRS Duo clearly detected changes in forearm hemodynamics following cuff occlusion at 200 mmHg for 3 min (Fig. 50.3 shows the typical plots of one subject among five subjects).

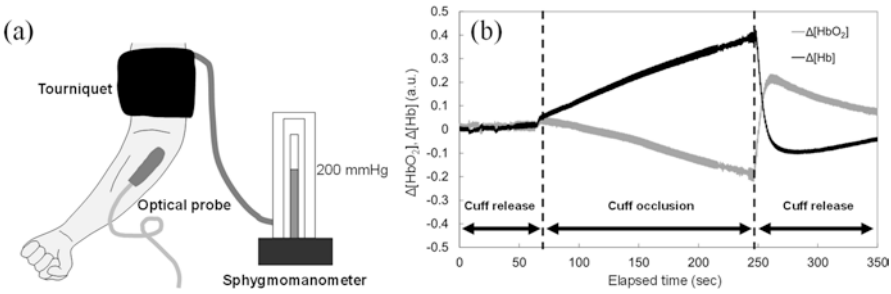

Fig. 50.3 Result of the arm cuff occlusion test (**a**) Experimental setup (**b**) Plots of changes in the product of hemoglobin concentrations and the optical path length in the left forearm of a subject

4.3 Breath-Holding Experiment

To evaluate the ability of the PocketNIRS HM to measure brain hemodynamics we performed a breath-holding experiment. The optical probe was placed on the left side of the subject's forehead and a commercial pulse-oximeter sensor (8000R, Nonin Medical Inc.), which source-detector separation was approximately 7.5 mm, was attached on the right side of the forehead. The commercial pulse-oximeter sensor (SR-5C, Konica Minolta Inc.) was attached on the right forefinger. The forehead hemodynamics and forefinger S_pO_2 (blood oxygen saturation level) data are presented in Fig. 50.4, which shows typical plots of one subject among five subjects. The subject held their breath 30 s after the commencement of measurements. In response to breath-holding, the S_pO_2 value recorded by the pulse oximeter gradually decreased. The PocketNIRS HM detected a decrease in $\Delta[HbO_2]$ and an increase in $\Delta[Hb]$ a few tens of seconds after an increase in $\Delta[HbO_2]$ and $\Delta[Hb]$. The subject restarted breathing approximately 136 s later. Following rebreathing, $\Delta[HbO_2]$ increased and $\Delta[Hb]$ decreased but the S_pO_2 of the right forehead recovered later than these signals. Especially, the recovery and the initiation of S_pO_2 in the right forefinger was delayed approximately 10 s than that in the right forehead. A small wave, the period of which is approximately 0.96 Hz (57 bpm), could be observed in $\Delta[HbO_2]$ signal, which could be attributed to the subject's heartbeat.

The PocketNIRS HM therefore demonstrates sufficient sensitivity to clearly monitor brain hemodynamics and has a data acquisition rate sufficient to detect pulsation due to heartbeat.

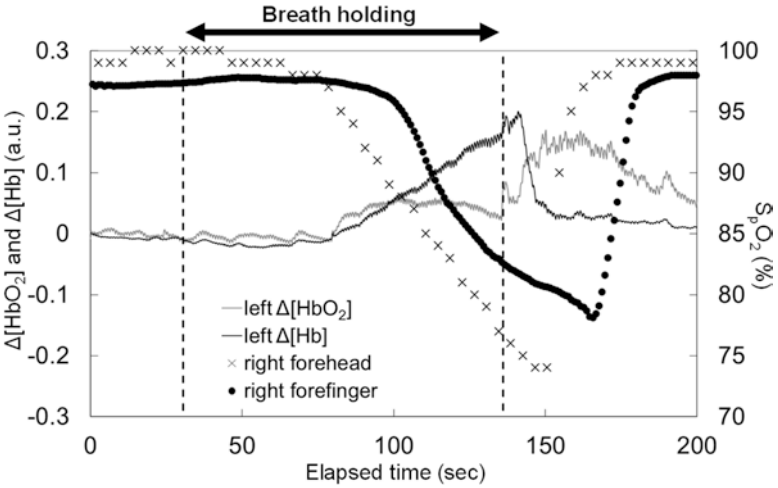

Fig. 50.4 Changes in brain oxygenation during a breath-holding experiment

5 Conclusion

We have developed a portable wireless NIRS system, the PocketNIRS Duo, and the related PocketNIRS HM system that specifically facilitates the analysis of brain hemodynamics. The primary features of these systems are their ability to measure changes in oxyhemoglobin, deoxyhemoglobin and total hemoglobin concentration. These systems demonstrate a high SNR (greater than 60 dB), fast data acquisition rate (up to 60 Hz), and simultaneous two-channel probe operation capability. Furthermore, the small size and light weight (requiring only two AAA batteries for operation), and the wireless capabilities of these systems (which are controllable by either smartphone or personal computer) make these devices ideal tools not only for clinical applications but also for healthcare monitoring at home, sports medicine, and the field of brain research.

References

1. Jöbsis FF (1977) Noninvasive, infrared monitoring of cerebral and myocardial oxygen sufficiency and circulatory parameters. Science 198:1264–1267
2. Barlow CH, Burns DH, Callis JB (1989) Breast biopsy analysis by spectroscopic imaging. In: Chance B (ed) Photon migration in tissues. Plenum Press, New York, pp 111–119
3. Wahr JA, Tremper KK, Samra S et al (1996) Near-infrared spectroscopy: theory and applications. J Cardiothoracic Vasc Anesth 10:406–418
4. Chance B, Alfano R (eds) (1997) Optical tomography and spectroscopy of tissue: theory, instrumentation, model, and human studies II. Proc SPIE 2979

5. Chance B, Alfano R, Tromberg B (eds) (1999) Optical tomography and spectroscopy of tissue: theory, instrumentation, model, and human studies III. Proc SPIE 3597
6. Cope M, Delpy DT (1988) A system for long-term measurement of cerebral blood and tissue oxygenation in newborn infants by near infrared transillumination. Med Biol Eng Comput 26:289–294
7. Delpy DT, Cope M, van der Zee P et al (1998) Estimation of optical pathlength through tissue from direct time of flight measurement. Phys Med Biol 33:1433–1442
8. Boas DA, Franceschini MA, Dunn AK et al (2002) Noninvasive imaging of cerebral activation with diffuse optical tomography. In: Frostig RD (ed) In vivo optical imaging of brain function. CRC Press, Boca Raton, pp 193–221, Chap. 8
9. Zhao H, Tanikawa Y, Gao F et al (2002) Maps of optical differential pathlength factor of human adult forehead, somatosensory motor and occipital regions at multi-wavelengths in NIR. Phys Med Biol 47:2075–2093

Chapter 51
Monitoring the Oxygen Dynamics of Brain Tissue In Vivo by Fast Acousto-Optic Scanning Microscopy: A Proposed Instrument

Zhenqiao Zhou, Dayu Chen, Zhiqiang Huang, Shaofang Wang, and Shaoqun Zeng

Abstract The function of the brain neural circuit is highly dependent on oxygen supply. Imaging the precise oxygen distribution and dynamics are critical for understanding the relationship between neuronal activity and oxygen dynamics of the nearby capillaries. Here, we develop fast acousto-optic scanning two-photon microscopy. Combined with oxygen probes, such as PtP-C343, we can monitor oxygen dynamics at the submicron level by this real-time microscopy. In this fast acousto-optic scanning microscopy, an acousto-optic deflector (AOD), an inertialess scanner, is used to scan the femtosecond laser. A cylindrical lens is used to compensate the 'cylindrical lens effect' of AOD and a prism is used to compensate the chromatic dispersion of AOD. An electro-optical modulator (EOM) and a sCMOS camera are gated to measure the phosphorescence lifetime. With a 40× water objective lens, this set-up can image a 100 μm × 100 μm field of view at a speed of 20 frames per second and a 25 μm × 8 μm field of view at a speed of 500 frames per second. This real-time two-photon microscopy is expected to be a good tool for observing and recording the precise rapid oxygen dynamics in the cerebral cortex, which will facilitate studies of oxygen metabolism in neurosciences.

Keywords Oxygen dynamics • Neuronal activity • Acousto-optic • Two-photon microscopy • Phosphorescence lifetime

---

$ Author contributed equally with all other contributors.

Z. Zhou • Z. Huang • S. Wang • S. Zeng (✉)
Wuhan National Laboratory for Optoelectronics, Britton Chance Center for Biomedical Photonics, Huazhong University of Science and Technology, 1037 Luoyu Road, Wuhan 430074, China
e-mail: sqzeng@mail.hust.edu.cn

D. Chen
Department of Neurosurgery, Wuhan General Hospital of Guangzhou Military, 627 Wuluo Road, Wuhan 430070, China

© Springer International Publishing Switzerland 2016

Q. Luo et al. (eds.), *Oxygen Transport to Tissue XXXVIII*, Advances in Experimental Medicine and Biology 923, DOI 10.1007/978-3-319-38810-6_51

1 Introduction

The function of the brain neural circuit is highly dependent on oxygen supply. Neural activity is associated with changes in oxygen metabolism, blood flow and energy metabolism. Thanks to the metabolic activity of the neural circuits, both vascular and tissue partial oxygen pressure (*pO2*) are changing all the time. Therefore, changes of oxygen transport and consumption are taken as indicators of neuronal activity [1].

Several noninvasive imaging techniques, such as functional magnetic resonance imaging (fMRI), have been used to measure blood oxygen level-dependent (BOLD) signals. Studies have shown that neuronal spiking frequency is related to the BOLD signals [2]. However, the spatial resolution of fMRI is not sufficient to distinguish precise structures, such as capillary and synapse. Therefore, the precise mechanism of neuronal activity related to oxygen dynamics of the nearby capillaries is still unclear.

Optical microscopy has the advantage of high spatial resolution at submicron level, which can be used to analyze the precise neurovascular coupling at subcellular level. Using the oxygen-dependent phosphorescence quenching method, partial oxygen pressure (*pO2*) can be measured by optical microscopy [3–7]. Phosphorescence lifetime provides absolute measurement of pO_2, which is unaffected by optical p**roperties and local probe concentration.**

Near-infrared (NIR) femtosecond laser can penetrate deep into the biological tissue, and cause multiphoton absorption and emission process. Therefore, two-photon microscopy can obtain high-quality images of oxygen distribution in the deep cerebral cortex. New types of oxygen phosphorescence probes, such as the PtP-C343, have been developed for two-photon application [8].

However, previous studies that used two-photon microscopy to measure the phosphorescence lifetime were slow, i.e. about 0.5 s per point [5]. Thus, it is not possible to monitor fast oxygen dynamics in real-time. Here, we develop fast acousto-optic scanning two-photon microscopy. Combining with oxygen phosphorescence probes, we can monitor oxygen dynamics of local capillaries in real-time by this microscopy. With a 40× water objective lens, this set-up can image a 100 μm × 100 μm field of view at a speed of 20 frames per second and a 25 μm × 8 μm field of view at a speed of 500 frames per second.

2 Fast Acousto-Optic Scanning Two-Photon Microscopy

Figure 51.1a is a schematic diagram of our fast acousto-optic scanning two-photon microscopy. An acousto-optic deflector (AOD) is used to scan the femtosecond laser. A sCOMS camera is used to detect phosphorescence intensity. An electro-optical modulator (EOM) and the camera are gated to measure the phosphorescence lifetime. Figure 51.1b shows the fast acousto-optic scanning unit. Detailed design parameters of this set-up are described below.

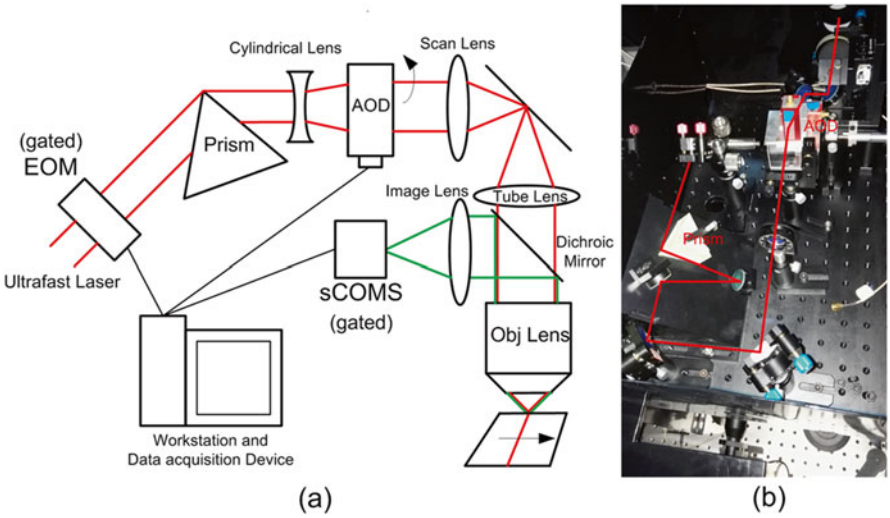

Fig. 51.1 (**a**) Schematic diagram of the fast acousto-optic scanning two-photon microscopy. An acousto-optic deflector (AOD) is used to scan the femtosecond laser. A sCOMS camera is used to detect phosphorescence intensity. An electro-optical modulator (EOM) and the camera are gated to measure the phosphorescence lifetime. (**b**) Picture of the fast acousto-optic scanning unit

The laser source is a Ti: sapphire femtosecond laser (Chameleon Ultra II, Coherent); its average power is over 1.5 W from 750 to 920 nm and the pulse width is 140 fs.

A cylindrical lens changes the collimated laser to an uncollimated laser, and then a focal line (not a focal point) is formed in the focal plane of the objective lens. An acousto-optic deflector (DTSXY400, AA Opto-electronic Inc) is used to scan the focal line, and then a planar illumination region is formed.

An AOD is an inertia-less scanner. It uses ultrasonic waves to form a diffraction grating and then scans the laser. An AOD can scan the laser faster and has better stabilization than a galvanometer. In this set-up, the AOD can scan a planar region within 25 μs.

When used in fast two-photon microscopy, the AOD met problems of chromatic dispersion and astigmatism, which have been solved by our work.

A custom prism (SF11, apex angle 65.4°) is placed in front of the AOD to simultaneously compensate the spatial and temporal dispersion of the AOD [9]. The incident angle is set to 72° to provide a dispersion of 0.135 mrad/nm at 920 nm. It can completely compensate the spatial dispersion at the center frequency of the AOD. The crystal length of the AOD is 14 mm, so the material dispersion produced by the AOD is about 8000 fs^2. Together with dispersion from the other optical components in this set-up, the total dispersion is estimated to be 18,000 fs^2. The distance between the prism and the AOD is set to be 55 cm. In this condition, the signal intensity is maximum, which proves that the temporal dispersion is compensated completely.

When the AOD is working in linear chirp mode, it behaves like a cylindrical lens, which will cause astigmatism and then blur the images. Another cylindrical lens with inverse focus length (not shown in Fig. 51.1) is used to compensate the 'cylindrical lens effect' of the AOD. To avoid much diffraction beam deformation, the focal length of the compensated cylindrical lens is set to be 2400 mm and a suitable scanning speed, 1 m/s, is selected [10].

In the phosphorescence detection part, a dichroic mirror (FF670-Di-25×36, Semrock) is used to reflect the phosphorescence to a high-sensitive high-speed sCMOS camera (ORCA Flash 4.0, Hamamatsu) and a barrier filter (FF01-680-SP, Semrock) is used to block the redundant NIR laser. The fastest readout mode of this camera can be 25 k frames per second with 2048×8 image sizes. Thus, the minimum readout period of this camera is about 40 μs.

To measure the phosphorescence lifetime, an EOM (ConOptics) is gated to control the illumination time. The pulse length of the excitation gate is 25 μs, which depends on the scan period of the AOD. The sCOMS camera is also gated to measure the phosphorescence intensity in a different time window. Each time window lasts for 1–2 μs. In each time window, an image of the phosphorescence intensity distribution is obtained by the camera. The phosphorescence lifetime is calculated every 5–10 images.

Figure 51.2 is a schematic diagram of measuring the phosphorescence lifetime by gate-control technology with two time windows per cycle. At time point t_1, the phosphorescence intensity is I_1; at time point t_2, the phosphorescence intensity is I_2. Because the phosphorescence intensity-time curves obey a simplex exponential model [3], the phosphorescence lifetime τ can be calculated by Eq. (51.1).

$$\tau = \frac{t_2 - t_1}{\mathrm{In}\left(I_1 / I_2\right)} \tag{51.1}$$

Custom-written software (in LabVIEW platform) is used to control the EOM, AOD and the sCMOS camera. The control signal of the AOD and EOM is generated by a multifunction data acquisition device (PXI6363, National Instrument). Data acquisition is accomplished by a 100 MS/s digitizer (PXI5122, National Instrument).

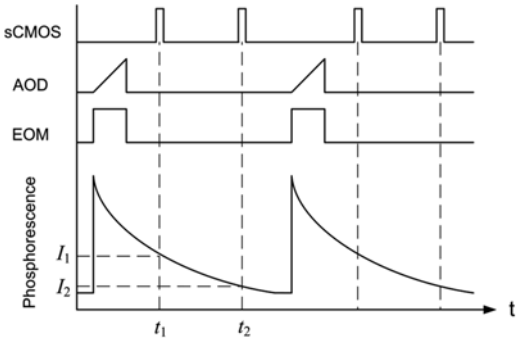

Fig. 51.2 Schematic diagram of measuring the phosphorescence lifetime by gate-control technology with two time windows per cycle

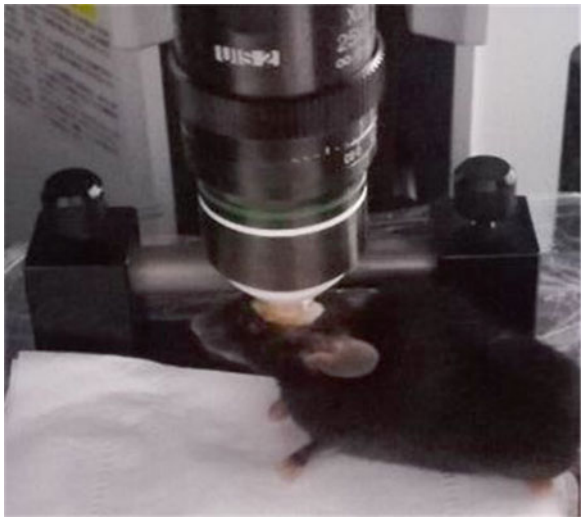

Fig. 51.3 In vivo two-photon imaging: a mouse aged 1–6 months was anaesthetized with an intraperitoneal injection. A small skull region (~300 μm in diameter), located based on stereotactic coordinates, was carefully thinned down to ~20 μm. Then the oxygen dynamics of the cerebral cortex can be imaged using fast acousto-optic scanning two-photon microscopy

The phosphorescence lifetime is calculated automatically by the software, and the reconstructed images of partial oxygen pressure are displayed to the experimenters in real-time.

With a 40× water objective lens (0.8 NA, Olympus), this set-up can image a 100 μm × 100 μm field of view at a speed of 20 frames per second and a 25 μm × 8 μm field of view at a speed of 500 frames per second. When choosing a low magnification objective lens, the field of view can further increase.

The surgical procedure for in vivo two-photon imaging refers to previous work [11]. All experiments were performed in accordance with the guidelines of the Experimental Animal Ethics Committee at Huazhong University of Science and Technology. Mice aged 1–6 months were anesthetized with an intraperitoneal injection (5.0 ml per kg body weight) of 17 mg/ml ketamine and 1.7 mg/ml xylazine in 0.9 % NaCl. The skull was exposed with a midline scalp incision. A small skull region (~300 μm in diameter), located based on stereotactic coordinates, was carefully thinned down to ~20 μm through a high-speed drill and a micro-surgical blade. Oxygen dynamics of the cerebral cortex was then imaged through the thinned skull using our fast acousto-optic scanning two-photon microscopy, as shown in Fig. 51.3.

3 Discussion

Oxygen metabolism is an important process in brain physiology and pathology. The study of oxygen metabolism in the neural circuit will facilitate our understanding of the relationship between energy metabolism and brain function both in normal and pathological individuals.

In the past, the lack of optical methods for monitoring the precise oxygen distribution and dynamics in real-time was the major limiting factor in studies of oxygen metabolism. Above, we have shown a fast acousto-optic scanning two-photon microscopy that can monitor oxygen distribution and dynamics of a small two-dimensional region with submicron spatial resolution and millisecond time resolution. To achieve the aim of millisecond time resolution, an acousto-optic deflector was used to scan a small two-dimensional region within 25 μs, and a fast sensitive sCMOS camera was used to obtain several phosphorescence images during the phosphorescence lifetime, and then the phosphorescence lifetime could be calculated. Moreover, the deep penetration depth of near-infrared laser allowed this microscopy to image the deep cerebral cortex region.

To monitor the oxygen dynamics in awake animals, our system should combine with optical fiber and GRIN lenses [12]. In this situation, the spatial resolution would be reduced a certain extent, and additional dispersion compensation to the optical fiber should be considered.

Though the principle of this system is straightforward, there are several technical challenges remaining to be addressed to get better application. The key issue is the signal-to-noise ratio or the sensitivity of the probe. The probe itself might be sensitive to detect small changes in oxygenation level, but the low two-photon excitation cross section for this probe is really a limiting factor. Currently progress in nanomaterial oxygenation sensors [13] may help to solve this problem. On the other hand, animal surgery also limits the throughput of our experiments, and need further improvements.

In summary, this real-time two-photon microscopy is expected to be a good tool for observing and recording the precise rapid oxygen dynamics in the cerebral cortex, which will facilitate studies of oxygen metabolism in neurosciences.

Acknowledgments This work was supported by the National Natural Science Foundation of China (81327802).

References

1. Tsytsarev V, Arakawa H, Borisov S et al (2013) In vivo imaging of brain metabolism activity using a phosphorescent oxygen-sensitive probe. J Neurosci Methods 216(2):146–151
2. Tiret P, Chaigneau E, Lecoq J et al (2003) Two-photon imaging of capillary blood flow in olfactory bulb glomeruli. Proc Natl Acad Sci U S A 100(22):13081–13086
3. Rumsey WI, Vanderkooi JM, Wilson DF (1998) Imaging of phosphorescence: a novel method for measuring distribution of oxygen in perfused tissue. Science 241(4873):1649–1651
4. Wilson DF, Vinogradov SA, Vaccarezza GP et al (2005) Oxygen distribution and vascular injury in the mouse eye measured by phosphorescence-lifetime imaging. Appl Opt 44(25):5239–5248
5. Sakadzic S, Roussakis E, Yaseen MA et al (2010) Two-photon high-resolution measurement of partial pressure of oxygen in cerebral vasculature and tissue. Nat Methods 7(9):755–759

6. Lloyd D, Williams CF, Vijayalakshmi K et al (2014) Intracellular oxygen: similar results from two methods of measurement using phosphorescent nanoparticles. J Innov Opt Health Sci 7(2): 1350041(14 pages)
7. Dědic R, Stíbal A, Vyklický V et al (2015) Parallel fluorescence and phosphorescence monitoring of singlet oxygen photosensitization in rats. J Innov Opt Health Sci 8(6): 1550037(14 pages)
8. Finikova OS, Lebedev AY, Aprelev A et al (2008) Oxygen microscopy by two-photon-excited phosphorescence. Chemphyschem 9(12):1673–1679
9. Zeng S, Li D, Lv X et al (2007) Pulse broadening of the femtosecond pulses in a Gaussian beam passing an angular disperser. Opt Lett 32(9):1180–1182
10. Zhou Z, Li L, Wang J et al (2015) Beam deformation within an acousto-optic lens. Opt Lett 40(10):2197–2200
11. Grutzendler J, Kasthuri N, Gan WB (2002) Long-termdendritic spine stability in the adult cortex. Nature 420:812–816
12. Yan W, Peng X, Lin D (2015) Fluorescence microendoscopy imaging based on GRIN lenses with one- and two-photon excitation modes. Front Optoelectron 8(2):177–182
13. Gainer CF, Romanowski M (2014) A review of synthetic methods for the production of upconverting lanthanide nanoparticles. J Innov Opt Health Sci 7(2): 1330007(11 pages)

Chapter 52
Magnetization Transfer MRI Contrast May Correlate with Tissue Redox State in Prostate Cancer

Rongwen Tain, He N. Xu, Xiaohong J. Zhou, Lin Z. Li, and Kejia Cai

Abstract Developing imaging biomarkers for non-invasive measurement of the tissue redox state is a key research area. Recently, we presented the first non-invasive MR imaging method that demonstrated the correlation between the endogenous chemical exchange saturation transfer (CEST) contrast and the tissue redox state. It is well known that the broadband magnetization transfer (MT) can occur via chemical exchange (CEST) and/or dipole–dipole interactions. The present study investigated if the broadband MT also correlated with the tissue redox state. The preliminary result for the prostate tumor xenografts indeed showed a significant correlation between the broadband MT contrast and the NADH redox ratio quantified with the optical redox scanning. In vivo MT contrast, once calibrated, may potentially serve as an imaging biomarker for tissue redox state.

Keywords Oxidative stress • Redox state • Magnetization transfer • CEST • Prostate cancer • MRI

R. Tain • X.J. Zhou • K. Cai (✉)
Department of Radiology, Center for MR Research, University of Illinois at Chicago, 2242 w. Harrison st., Chicago, IL 60612, USA
e-mail: kcai@uic.edu

H.N. Xu
Britton Chance Laboratory of Redox Imaging, Johnson Research Foundation; Department of Radiology, University of Pennsylvania, Philadelphia, PA 19104, USA

L.Z. Li
Molecular Imaging Laboratory, Department of Radiology, Britton Chance Laboratory of Redox Imaging, Johnson Research Foundation, Department of Biochemistry and Biophysics, Perelman School of Medicine, University of Pennsylvania, Philadelphia, PA 19104, USA

© Springer International Publishing Switzerland 2016

Q. Luo et al. (eds.), *Oxygen Transport to Tissue XXXVIII*, Advances in Experimental Medicine and Biology 923, DOI 10.1007/978-3-319-38810-6_52

1 Introduction

It has been shown that the development of cancer cells and tumor progression is associated with altered intra- and extracellular redox regulation. Redox state alterations have been associated with tumor malignancy [1, 2] and aggressiveness for breast cancer, melanoma, colon cancer, etc. [3–6].

Despite the importance of tissue redox state, so far there is no endogenous imaging contrast that can be used for the in vivo mapping of tissue redox status. Recently, we presented a non-invasive MR imaging method that demonstrated a significant correlation between the tissue redox state and the endogenous chemical exchange saturation transfer (CEST) contrast [7]. CEST MRI, on the basis of the proton exchange between metabolites and tissue bulk water, has been employed to non-invasively imaging tissue amide protons [8], liver glycogen [9], cartilage glycosaminoglycans [10], brain myo-inositol [11], and glutamate [12] with a spatial resolution down to sub-millimeters. In our recent study [7], CEST MRI has been employed to characterize intratumoral heterogeneity and to correlate with cancer redox states in xenografts of two breast cancer cell lines, MDA-MB-231 and MCF-7. We found a higher level of intratumoral CEST heterogeneity, calculated as the tumor rim-to-core ratio of CEST, in the aggressive (metastatic) MDA-MB-231 tumors than in the less aggressive (less metastatic or indolent) MCF-7 tumors. CEST contrasts from individual tumor rims and cores are linearly correlated with the NADH redox ratios quantified by the optical redox scanning where NADH is the reduced form of nicotinamide adenine dinucleotide.

It is well known that the broadband MT can occur via chemical exchange (CEST) and/or dipole–dipole interactions. The purpose of this study is to investigate whether broadband MT also correlates with the tissue redox state.

2 Methods

All in vivo animal studies were performed according to an Institutional Animal Care and Use Committee approved protocol at the University of Pennsylvania. The propagated cells of human prostate cancer of PC-3 and DU-145 were implanted subcutaneously into the upper thighs of athymic nude mice (~7 million cells/site). Tumor sizes were monitored once a week to obtain tumor volumes ($V = ab^2/2$, where a is the long axis and b is the short axis) [7]. After 5 weeks post implantation, mice bearing DU-145 and PC-3 prostate tumor xenografts ($n = 3$ for DU-145 and $n = 4$ for PC-3tumors) were scanned at a Varian horizontal 9.4 T MRI scanner. Note that one PC-3 tumor was not included in the analysis due to image artifacts induced by severe B_1 inhomogeneity.

MTR spectra were collected from tumor central cross-sections using a custom sequence with a frequency selective rectangle saturation pulse (B1 = 250 Hz, 1 s) followed by Fast Low-Angle Shot (FLASH) readout [7]. Other parameters were:

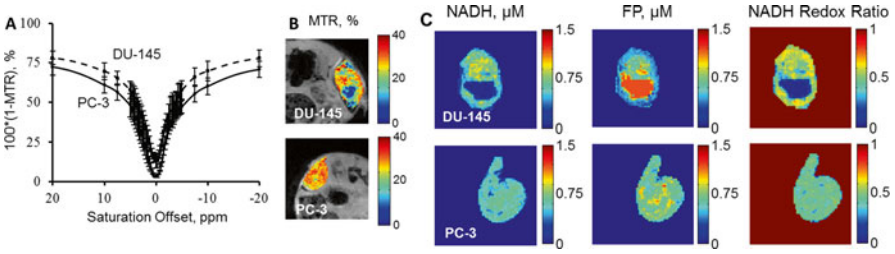

Fig. 52.1 (**a**) Z-spectra of DU-145 (*dashed line*) and PC-3 (*solid line*) prostate tumors. Data were averaged within entire tumor and across all tumors for each tumor line. (**b**) Representative MTR maps of a typical DU-145 tumor and a typical PC-3 tumor. (**c**) Optical redox scanning of representative DU-145 and PC-3 tumors, providing NADH, FP and NADH redox ratio maps

flip angle = 15°, readout TR/TE = 6.2/2.9 ms, in-plane resolution = 0.27 × 0.27 mm^2. One saturation pulse followed with 64 segment acquisition was repeated every 4 s. The MT MRI contrast or MT ratio (MTR) was quantified as $(1\text{-}MT_{\text{on}}/MT_{\text{off}}) \times 100\,\%$, where MT_{on} and MT_{off} referred to images acquired with saturation "on" at a specific frequency offset and "off" at 100 ppm, respectively. Except for Fig. 52.1a, all MTR shown and presented were for 20 ppm offset. MTR maps clearly desalinate solid tumor boundaries. After MRI, mice under anesthesia underwent snap-freezing procedures for tumor harvest. The excised frozen tumors were embedded for multi-slice fluorescence imaging of NADH, oxidized flavoprotein (Fp), and NADH redox ratio (NADH/(Fp + NADH) using the Chance redox scanner [3, 4]. The redox images of the sections closest to the MRI imaging lume slices were chosen for the quantitative analysis and correlation with the MRI contrast.

Histograms of the MTR contrast and NADH redox ratio from each tumor were fit with two Gaussian distributions to separate the generally more oxidized tumor core and less oxidized rim [7]. One-tailed paired Student's t-test was performed for comparing the redox or MRI indices between tumor rim and core. Tumor core and rim values were pooled together for the correlation analysis between redox ratio and MTR, using the Excel data analysis regression tool. Statistical significance was attained when $P < 0.05$. Results are reported as mean ± standard error (SE).

3 Results

The average size of a prostate tumor 5 weeks after implantation for all mice was 164.3 ± 20.1 mm^3 while the size of the DU-145 tumor was slightly larger than that of the PC-3 tumor (185.4 ± 31.2 vs. 143.1 ± 24.7 mm^3, $P = 0.2$).

In vivo MTR spectra from prostate tumors are shown in Fig. 52.1a. Overall, reduced MT contrast was seen from DU-145 tumors compared to PC-3 tumors. Representative MTR maps (Fig. 52.1b) show typical hypointense tumor cores associated with DU-145 tumors, leading to higher levels of intratumoral

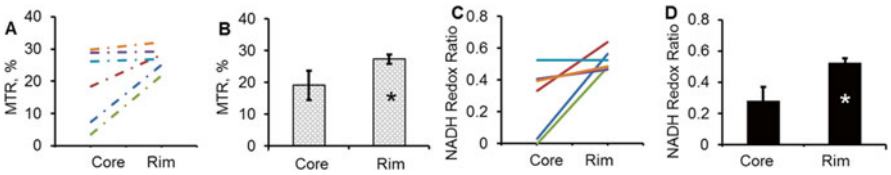

Fig. 52.2 MTR and NADH redox ratio of tumor core and rim from individual tumors (**a** and **c**, DU-145 and PC-3 tumors were grouped together) and the averaged values (**b** and **d**, $*P<0.05$)

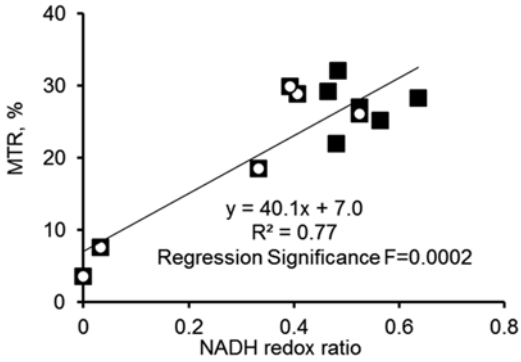

Fig. 52.3 The MTR contrasts and the redox ratios from tumor cores and rims were significantly correlated (significance $P<0.05$). The hollow black squares are derived from tumor cores and the solid ones are derived from tumor rims

inhomogeneity. As shown in Fig. 52.1c, NADH redox ratio maps of DU-145 and PC-3 tumors produced by ex vivo optical redox scanning present similar patterns as the corresponding in vivo MTR maps (Fig. 52.1b).

Figures 52.2a, c show the mean values of MTR and NADH redox ratios for each tumor. Overall, MTR and NADH redox ratio are higher in tumor rims than that in tumor cores (Fig. 52.2b, d, $P<0.05$). Furthermore through a linear regression analysis pooling all data of tumor cores and rims, we found that the MTR contrasts were significantly correlated with the NADH redox ratios (Fig. 52.3, $R^2=0.77$, $P=0.0002$). The 95% confidence interval for the fitted linear coefficient was between 24.8 and 55.5 and that for the intercept between 0.1 and 13.8.

4 Discussion

This study validates and strengthens the hypothesis that the redox imbalance may affect magnetization transfer contrast and, furthermore, supports and shows consistency with our previous study [7]. The significant correlation between MT and NADH redox ratio found in this study indicates that in vivo MT contrast may potentially serve as an imaging biomarker for tissue redox status.

We hypothesize that the correlation between MT contrast and tissue redox status may be through proton/electron transfer in redox reactions, which are in a general form of $\mathbf{RH_2 + NAD^+ \leftrightarrow R + NADH + H^+}$, where R is a substrate or tissue metabolite.

Our previous study demonstrated that CEST MRI may probe proton transfer in redox reactions and that the reduced metabolites generally expressed higher CEST contrast than their oxidized counterparts, which is likely due to the reception of mobile protons. As a result, higher CEST contrast corresponds to a more reduced redox state. Similarly, the MT effect from tissue metabolites may also be affected by their redox states. It is well known that MT can occur via chemical/proton exchange and/or dipole–dipole interactions. Metabolite oxidation leads to the loss of exchangeable protons or the mobile protons that generate MT contrast. In other words, MT MRI quantifies the steady-state redox states of all in vivo redox-sensitive metabolites, including small molecules, peptides, proteins and DNAs, whose redox states may be affected due to oxidative stress.

We could not rule out that there might be necrosis in some tumor core regions. In the clinic, tumor tissues are commonly classified into viable and necrotic regions, and there is not much interest in the necrotic regions from the pathologists in general. However, this binary tissue classification could be an over-simplified picture of tumor progression because cancer cells may still survive in necrotic regions, as shown previously in mouse xenografts of human breast cancer and melanomas [4, 13, 14]. These numerous viable cells in the tumor cores and their typically highly oxidized redox states could provide information on tumor metastatic potential [4, 13, 14]. Nevertheless, we still need to investigate whether this is the case for the prostate cancer models. Since MT contrast may include contributions from macromolecules in extracellular space, we also need to investigate whether the correlation between MT and redox state of tumor cores and rims still hold in the presence of known necrosis.

Compared to the CEST technique, broadband MT may have less sensitivity in the correlation with tissue redox state, particularly during the early phase of tumor growth. CEST contrast, but not MT, can differentiate the intratumoral core/rim heterogeneity of an aggressive breast cancer at small size [7].

A limitation of this study is that it is based on relatively small sample sizes. Although a significant correlation was found between NADH redox ratio and MTR contrast, larger sample size and longitudinal studies may improve the accuracy of the correlation between MT and tissue redox state. It is also worth noting that the MT contrast in vivo can be affected by many other factors, including tissue T_1 and T_2 relaxation times. We are currently investigating their possible contributions to the observed intratumoral MTR heterogeneity and their contributions to the correlation between MTR and redox ratios. Nevertheless, MT MRI for the characterization of tissue redox state requires calibration.

In conclusion, MT MRI contrast was found to significantly correlate to the prostate tumor NADH redox ratio measured by optical redox scanning. This correlation indicates that MT MRI may be sensitive to tissue redox state. Non-invasive MT MRI, once further confirmed, may have a great potential for clinical applications.

Acknowledgments The work was supported in part by grants from the National Institute of Health (1S10RR028898, UL1RR029879 and R01CA155348). The authors acknowledge the

Department of Radiology and the 3T Program of the Center of Magnetic Resonance Research at the University of Illinois at Chicago College of Medicine for the research support. The authors are also grateful to E. James Delikatny for providing the prostate cancer cell lines and Ravinder Reddy at the University of Pennsylvania for valuable discussions.

References

1. Xu HN, Tchou J, Feng M et al (2015) Differentiating cancerous from normal breast tissue by redox imaging. Proc. SPIE 9303, Photonic Therapeutics and Diagnostics 6: 93032R
2. Walsh AJ, Cook RS, Manning HC et al (2013) Optical metabolic imaging identifies glycolytic levels, subtypes, and early-treatment response in breast cancer. Cancer Res 73:6164–6174
3. Li LZ, Zhou R, Xu HN et al (2009) Quantitative magnetic resonance and optical imaging biomarkers of melanoma metastatic potential. Proc Natl Acad Sci USA 106:6608–6613
4. Xu HN, Nioka S, Glickson JD (2010) Quantitative mitochondrial redox imaging of breast cancer metastatic potential. J Biomed Opt 15:36010
5. Xu HN, Feng M, Moon L et al (2013) Redox imaging of the p53-dependent mitochondrial redox state in colon cancer ex vivo. J Innov Opt Heal Sci 6:1350016
6. Xu HN, Li LZ (2004) Quantitative redox imaging biomarkers for studying tissue metabolic state and its heterogeneity. J Innov Opt Health Sci 7:1430002-1-20
7. Cai K, Xu HN, Singh A et al (2014) Breast cancer redox heterogeneity detectable with chemical exchange saturation transfer (CEST) MRI. Mol Imaging Biol 16:670–679
8. Zhou JY, Tryggestad E, Wen ZB et al (2011) Differentiation between glioma and radiation necrosis using molecular magnetic resonance imaging of endogenous proteins and peptides. Nat Med 17:130–U308
9. Van Zijl PC, Jones CK, Ren J et al (2007) MRI detection of glycogen in vivo by using chemical exchange saturation transfer imaging (glycoCEST). Proc Natl Acad Sci USA 104: 4359–4364
10. Ling W, Regatte RR, Navon G et al (2008) Assessment of glycosaminoglycan concentration in vivo by chemical exchange-dependent saturation transfer (gagCEST). Proc Natl Acad Sci USA 105:2266–2270
11. Haris M, Cai K, Singh A et al (2011) In vivo mapping of brain myo-inositol. Neuroimage 54:2079–2085
12. Cai K, Haris M, Singh A et al (2012) Magnetic resonance imaging of glutamate. Nat Med 18:302–306
13. Xu HN, Zhou R, Nioka S et al (2009) Histological basis of MR/optical imaging of human melanoma mouse xenografts spanning a range of metastatic potentials. Adv Exp Med Biol 645:247–253
14. Xu HN, Zheng G, Tchou J et al (2013) Characterizing the metabolic heterogeneity in human breast cancer xenografts by 3D high resolution fluorescence imaging. Springerplus 2:73

Chapter 53
Comparison of Two Algorithms for Analysis of Perfusion Computed Tomography Data for Evaluation of Cerebral Microcirculation in Chronic Subdural Hematoma

Alexey O. Trofimov, George Kalentiev, Oleg Voennov, Michail Yuriev, Darya Agarkova, Svetlana Trofimova, and Denis E. Bragin

Abstract The aim of this work was comparison of two algorithms of perfusion computed tomography (PCT) data analysis for evaluation of cerebral microcirculation in the perifocal zone of chronic subdural hematoma (CSDH). Twenty patients with CSDH after polytrauma were included in the study. The same PCT data were assessed quantitatively in cortical brain region beneath the CSDH (zone 1), and in the corresponding contralateral brain hemisphere (zone 2) without and with the use of perfusion calculation mode excluding vascular pixel 'Remote Vessels' (RV); 1st and 2nd analysis method, respectively. Comparison with normal values for perfusion indices in the zone 1 in the 1st analysis method showed a significant ($p<0.01$) increase in CBV and CBF, and no significant increase in MTT and TTP. Use of the RV mode (2nd analysis method) showed no statistically reliable change of perfusion parameters in the microcirculatory blood flow of the 2nd zone. Maintenance of microcirculatory blood flow perfusion reflects the preservation of cerebral blood flow autoregulation in patients with CSDH.

A.O. Trofimov (✉)
Department of Neurosurgery, Nizhniy Novgorod State Medical Academy, 10/1, Minin Str., Nizhniy Novgorod 603950, Russia

Department of Neurosurgery, University of New Mexico School of Medicine, University of New Mexico, 1, MSC 10 5615, Albuquerque, NM 87131, USA

Department of Polytrauma and Critical Care, Regional Hospital named after N.A. Semashko, 190, Rodionov str., Nizhny Novgorod 603126, Russian Federation
e-mail: xtro7@mail.ru

G. Kalentiev • O. Voennov • M. Yuriev • D. Agarkova • S. Trofimova • D.E. Bragin
Department of Neurosurgery, Nizhniy Novgorod State Medical Academy, 10/1, Minin Str., Nizhniy Novgorod 603950, Russia

Department of Neurosurgery, University of New Mexico School of Medicine, University of New Mexico, 1, MSC 10 5615, Albuquerque, NM 87131, USA

© Springer International Publishing Switzerland 2016

Q. Luo et al. (eds.), *Oxygen Transport to Tissue XXXVIII*, Advances in Experimental Medicine and Biology 923, DOI 10.1007/978-3-319-38810-6_53

Keywords Chronic subdural hematoma • Perifocal zone • Perfusion computerized tomography • Cerebral microvasculature

1 Introduction

A chronic subdural hematoma (CSDH) is a multi-etiological disease, characterized by the formation of a capsule around a subdural hemorrhage causing local and general compression of the brain [1, 2]. The most frequently occurring CSDH are formed after a craniocerebral trauma [3]. One of the key aspects determining the clinical course and outcome in patients with CSDH, is the reaction of the microvasculature in the adjacent cerebral cortex area, called a perifocal zone [4]. However, information on the status of the cerebral microcirculation and autoregulation in this zone remains contradictory. One explanation for this may be the imperfection of software algorithms for the calculation of cerebral perfusion in computer tomography [5, 6]. Nevertheless, after the development of computer-tomographic algorithms for the calculation of perfusion parameters, excluding data on blood flow in large cortical vessels, it became possible to evaluate the character of pial blood flow in the 'region of interest' [7, 8]. Thus, it seems possible to expand perceptions on the state of cerebral blood flow and to clarify the mechanisms that maintain microcirculation in the perifocal zone of CSDH, based on the state of cerebral autoregulation in patients with CSDH.

The aim of this work was to compare two perfusion computed tomography (PCT) data analysis algorithms for evaluation of cerebral microcirculation in the perifocal zone of CSDH.

2 Materials and Methods

The protocol for this single-center prospective study was approved by the local research ethics committee. Twenty patients with CSDH after polytrauma were included to the study for the period from January 2013 to March 2014. Inclusion criteria were CSDH on CT or magnetic resonance scans, indication for surgery, and signed informed consent to participate in the study. Exclusion criteria were age younger than 16 years, bilateral CSDH, serum blood creatinine level >120 mg/l, and acute deterioration necessitating decompressive craniotomy.

After PCT all patients were subjected to a single burr hole craniotomy under general anesthesia. The cavity of the hematoma was washed out with warm Ringer's solution. After sufficient drainage of the hematoma, the drainage catheter Pleurofix® (B.Braun Melsungen AG, Germany) was placed in the cavity for 2 days.

2.1 Perfusion Computed Tomography

All patients underwent PCT within the first day before surgery using a 64-slice Philips Ingenuity CT® (Philips Medical systems, Cleveland, USA). The perfusion examination report included an initial native CT of the brain followed by 4 extended scanning of the 'region of interest', 32 mm in thickness, within 55 s, with a contrast agent administered (the Brain Perfusion mode). The scanning parameters were: 120 kVp, 70 mA, 70 mAs and 1000 ms. The contrast agent (Ultravist 370, Shering AG, Germany) was administered with an automatic syringe-injector (Stellant, One Medrad, Indianola, PA, USA) into a peripheral vein through a standard catheter (20 G) at a rate of 4–5 ml/s in a dose of 30–50 ml per examination.

Acquired data were transferred to a Philips Ingenuity Core workstation (Philips Healthcare Nederland B.V., the Netherlands, 2013, v.3.5.5.25007). Artery and vein marks were automatically recorded followed by manual control of indices in a time-concentration diagram.

Color-coded perfusion maps were produced to describe cerebral perfusion: cerebral blood volume (CBV), cerebral blood flow (CBF), mean transit time (MTT), and time to peak concentration of the contrast (TTP). The same PCT data were assessed quantitatively in cortical brain region beneath the CSDH (zone 1), and in the corresponding contralateral brain hemisphere (zone 2) without and with use of the perfusion calculation mode excluding vascular pixel 'Remote Vessels' (RV), 1st and 2nd analysis method, respectively.

Pixels that characterized vascular structures were excluded from the calculations at a moment when the peak concentration of the contrast in the vessel exceeded the concentration of contrast in the superior sagittal sinus [9].

2.2 Statistical Analysis

Data are shown as a mean ± standard deviation. A statistical analysis of all the results was performed using the paired Student's *t*-test. $p < 0.01$ was considered statistically significant.

3 Results

Sex distribution had a male predominance (8 women, 12 men). Mean age was 54.7 ± 15.6 (range 17–87) years. CSDH was located in the left hemisphere in 11 patients and on the right side in nine patients. The average volume of the CSDH was 84.2 ± 12.4 (range 56–17) cm^3. The mean shift in the septum pellucidum was 7.1 ± 1.4 (range 5–12) mm. The wakefulness level according to the Glasgow Coma Score was 13.1 ± 0.5 (range 11–15). The severity level according to the Markwalder Grading Score was 1.8 ± 0.5 (range 0–3).

Table 53.1 Data on comparison of the analyzed parameters

		CBV (ml/100 g)	CBF (ml/100 g × min)	MTT (s)	TTP (s)
1	1st analysis method (zone 1 without RV)	11.07 ± 2.82	149.15 ± 33.18	4.48 ± 0.66	27.57 ± 0.83
2	1st analysis method (zone 2 without RV)	9.31 ± 2.33	122.84 ± 29.52	4.63 ± 0.76	27.78 ± 1.13
3	2nd analysis method (zone 1 with RV)	5.66 ± 0.96	88.36 ± 16.2	3.84 ± 0.61	27.47 ± 0.84
4	2nd analysis method (zone 2 with RV)	5.16 ± 0.8	75 ± 20.97	4.08 ± 0.86	27.94 ± 1.3
5	Normal value [10]	4.5 ± 0.6	64.02 ± 0.6	4.3 ± 0.8	–
	P (1–2)	0.04	0.011	0.53	0.52
	P (1–3)	<0.001*	<0.001*	0.004*	0.70
	P (2–4)	<0.001*	0.002*	0.05	0.70
	P (3–4)	0.09	0.04	0.32	0.19

*Significant difference ($p < 0.01$)

The acquired and analyzed data are summarized in Table 53.1.

Comparison with normal values for perfusion indices [10] in the zone 1 in the calculation algorithm with flow in cortical vessels (1st analysis method) showed a significant ($p < 0.01$) increase in CBV and CBF, and no significant increase in MTT and TTP ($p > 0.01$). However, when using the RV mode (2nd analysis method), comparison of perfusion parameters in the zone 1 with normal values showed the changes to be nonsignificant ($p > 0.01$).

In the zone 2 (side contralateral to the hematoma), comparison with normal values for perfusion indices revealed in the 1st analysis method a statistically reliable increase in CBV and CBF ($p < 0.01$), but no significant change in MTT and TTP. At the same time, use 2nd analysis method showed no statistically reliable change of perfusion parameters ($p > 0.01$) in the microcirculatory blood flow on the zone 2.

4 Discussion

One of the fundamental properties of the cerebral circulation is the ability to maintain constant microvascular perfusion under fluctuating arterial blood and intracranial pressure [11]; this property is called cerebral autoregulation [11]. It was noted that indicators of cerebral perfusion and the state of autoregulation are in close interdependence and microvasculature perfusion disorders result from damage of the autoregulation mechanism [12, 13]. It has been proposed that CSDH disrupts the mechanisms of cerebral blood flow autoregulation, as evident through cerebral microcirculation disorders with the development of congestion and hyperperfusion syndromes. Thus, there was a fair increase in CBV as

compared to the symmetrical zones of the opposite hemisphere, while time characteristics have not significantly changed corresponding to congestion and hyperperfusion patterns, indicating cerebral autoregulation disorder [4, 14]. Nevertheless, these findings, as well as the fact that the studies were carried out without using algorithms, appeared to be the basis for critical comments on the work. In our study we used a CT analysis algorithm which excludes pixels from large vessels thus enabling to adequately assess perfusion in the pial bed of the perifocal zone of the CSDH.

We think that we can use the 2nd algorithm in the «intact» hemisphere because microcirculation in this area is also abnormal in the patients with CSDH. Microcirculatory disturbances in the «intact» hemisphere are due to the venous drainage failure and the intracranial hypertension. This belief is based on the data of other investigators [1, 4].

Our data prove the stability of microvasculature perfusion in the CSDH perifocal zone and, consequently, preserved cerebral blood flow autoregulation in patients with such pathology. Hyperemia and hyperperfusion in the perifocal zone of CSDH described in previous studies [4] do not affect the microcirculation, as no pial perfusion disorders were revealed. A possible reason for the development of such syndromes in the perifocal zone could be the formation of de novo blood vessels in the capsule, with the development of over-capillary shunting phenomena causing an increasing volume blood flow rate. In practice, our results show that the onset of foci of local cerebral hyperperfusion non-affecting the pial bed direction is probably an early marker of de novo angiogenesis in the capsule formation with the development of brain compression [15]. Clarification of this statement might be the basis for early diagnosis of compression formation based on the detection of the characteristic features of cerebral perfusion.

It should be noted that our study has some methodological limitations, the main one being the impossibility of dynamic non-invasive assessment of the state of perfusion in the perihematomal area without PCT rescanning. Moreover, taking into account the characteristics of our study design, we were unable to assess the perfusion characteristics of the perifocal zone in patients with a bilateral CSDH or in patients with a CSDH at a decompensated state. Both these issues require further study.

5 Conclusion

The detection of hyperemia and hyperperfusion in the perifocal zone of the CSDH in the 1st analysis method is apparently associated with the change in blood flow and blood supply at the level of resistive and capacitive vessels and does not affect the capillary bed.

The perfusion indices of blood flow in the perifocal zone of the CSDH show no significant differences from the symmetrical zone of the contralateral hemisphere.

The maintenance of microcirculatory blood flow perfusion reflects the preservation of cerebral blood flow autoregulation in patients with chronic subdural hematomas. Exclusion of large vessels from the analysis of microcirculation (2nd method) is more suitable for evaluation of cerebral blood flow status in patients with CSDH.

References

1. Aries MJ, Budohoski K (2013) Cerebral perfusion in chronic subdural hematoma. J Neurotrauma 19:1680
2. Tang J, Ai J (2011) Developing a model of chronic subdural hematoma. Acta Neurochir Suppl 111:25–29
3. Germano A (2014) Pre- and postoperative cerebral perfusion assessment in chronic subdural hematoma. J Neurotrauma 31:A1–A73
4. Slotty PJ, Kamp MA, Steige HJ (2012) Cerebral perfusion in chronic subdural hematoma. J Neurotrauma 30:347–351
5. Kudo K, Terae S, Katoh C (2003) Quantitative cerebral blood flow measurement with dynamic perfusion CT using the vascular-pixel elimination method: comparison with H2(15)O positron emission tomography. AJNR Am J Neuroradiol 24:419–426
6. Abels B, Villablanca J (2012) Acute stroke: a comparison of different CT perfusion algorithms and validation of ischaemic lesions by follow-up imaging. Eur Radiol 22:2559–2567
7. Campbell B, Christensen S, Levi C (2011) Cerebral blood flow is the optimal CT perfusion parameter for assessing infarct core. Stroke 42(12):3435–3440
8. Kamalian S, Maas M (2012) CT perfusion mean transit time maps optimally distinguish benign oligemia from true "at-risk" ischemic penumbra, but thresholds vary by postprocessing technique. Am J Neuroradiol 33(3):545–549
9. Miles K, Eastwood J (2007) Multidetector computed tomography in cerebrovascular disease. CT perfusion imaging. Informa Healthcare, London
10. Zakharova N, Kornienko V, Potapov A (2014) Neuroimaging of traumatic brain injury. Springer, Heidelberg, New York, London
11. Varsos G, Richards H, Kasprowicz M (2013) Critical closing pressure during intracranial pressure plateau waves. Neurocrit Care 18:341–348
12. Bivard A, Levi C, Krishnamurthy V (2014) Defining acute ischemic stroke tissue pathophysiology with whole brain CT perfusion. J Neuroradiol 41:307–315. doi:10.1016/j.neurad.2013.11.006
13. Turowski B, Haenggi D, Wittsack J (2007) Cerebral perfusion computerized tomography in vasospasm after subarachnoid hemorrhage: diagnostic value of MTT. Rofo 179:847–854
14. Cao W, Campbell B (2014) Relative filling time delay based on CT perfusion source imaging: a simple method to predict outcome in acute ischemic stroke. Am J Neuroradiol 35: 1683–1687
15. Hong HJ, Kim YJ, Yi HJ (2009) Role of angiogenic growth factors and inflammatory cytokine on recurrence of chronic subdural hematoma. Surg Neurol 71:161–166

Chapter 54
MMP-14 Triggered Fluorescence Contrast Agent

Mai-Dung Nguyen and Kyung A. Kang

Abstract Matrix metalloproteinase-14 (MMP-14) is involved in cancer invasion, metastasis, and angiogenesis. Therefore, it is considered to be a biomarker for aggressive cancer types, including some of the triple-negative breast cancer. Accurate (i.e., specific) and sensitive detection of MMP-14 can, thus, be important for the early diagnosis of and accurate prognosis for aggressive cancer, including the breast cancer caused by cell line MDA-MB 231. Fluorophore-mediated molecular sensing has been used for detecting biomarkers, for a long time. One way to increase the specificity of the sensing is designing the fluorophore to emit its fluorescence only when it encounters the biomarker of interest. When a fluorophore is placed on the surface of, or very close to a gold nanoparticle (GNP), its fluorescence is quenched. Applying this relationship between the GNP and fluorophore, we have developed a GNP-based, near-infrared fluorescent contrast agent that is highly specific for MMP-14. This agent normally emits only 14–17 % fluorescence of the free fluorophore. When the agent encounters MMP-14, its fluorescence gets fully restored, allowing MMP-14 specific optical signal emission.

Keywords MMP-14 • Gold nanoparticle • MDA-MB 231 • Breast cancer detection • Cypate

1 Introduction

Matrix metalloproteinases (MMPs) are zinc dependent endopeptidases involved in tissue remodeling. Some MMPs (e.g., MMP-14) are, however, involved in tumor invasion, metastasis and angiogenesis [1]. MMP-14 is a cell-membrane bound enzyme and expressed during the early stage of several aggressive cancer types, including the breast cancer caused by cell line MDA-MB 231 [2, 3]. MMP-14 strongly promotes tumor angiogenesis. It also activates MMP-2, −9 and −13, which

M.-D. Nguyen • K.A. Kang (✉)
Department of Chemical Engineering, University of Louisville, Louisville, KY 40292, USA
e-mail: kyung.kang@louisville.edu

© Springer International Publishing Switzerland 2016

Q. Luo et al. (eds.), *Oxygen Transport to Tissue XXXVIII*, Advances in Experimental Medicine and Biology 923, DOI 10.1007/978-3-319-38810-6_54

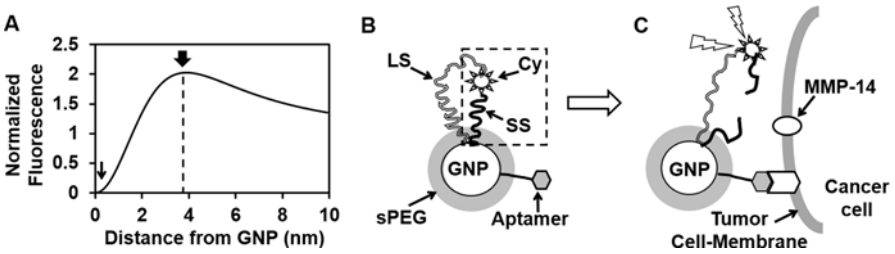

Fig. 54.1 (**a**) Computer simulated Cypate fluorescence levels with the distance from a 10 nm GNP surface. The fluorescence is quenched when Cypate is placed close to the GNP and enhanced at ~4 nm. (**b**) Schematic diagram of our agent: sPEG coated GNP; Cypate; a SS and a LS that connect a GNP and Cypate; and an aptamer that targets tumor cells. The agent emits little fluorescence because SS holds Cypate close to the GNP (the *dotted rectagle* is the focus on the study reported). (**c**) When the aptamer binds to the tumor cell, MMP-14 in the cell membrane cleaves SS and Cypate fluoresces at an enhanced level

destroy extracellular matrices to allow cancer cells to migrate [4–6]. High expression of MMP-14 is, thus, frequently associated with cancer malignancy and poor prognosis. Breast cancer cell line MDA-MB 231 lacks receptors for estrogen, progesterone, and epidermal growth factor HER-2 (i.e., triple negative) and does not respond well to current therapies. Therefore, detecting MMP-14 accurately and sensitively can be important for early diagnosis of aggressive cancer types, so as to initiate a proper treatment immediately.

Fluorophore-mediated molecular sensing/imaging has been extensively used for biomedical purposes. Since fluorescence is generated when electrons of the fluorophore change their energy states, the fluorescence level can be artificially altered by placing the fluorophore in a localized electro-magnetic (EM) field. Gold nanoparticles (GNPs) are good for this purpose because they can provide a strong local EM (plasmon) field. The plasmon field of a GNP is strongest immediately outside its surface and decreases with the distance from it. If a fluorophore is placed on the surface or very close to the GNP, its fluorescence is significantly quenched (thin arrow in Fig. 54.1a). On the other hand, its fluorescence can be significantly enhanced (thick arrow in Fig. 54.1a) at a particular distance from the GNP surface, depending upon the GNP size and fluorophore properties, [7, 8].

Utilizing the relationship between the GNP and fluorophore, we are developing a GNP-based fluorescent contrast agent for detecting MMP-14 in a highly specific and sensitive manner. The agent includes a GNP; short spacers (SSs) containing MMP-14 substrate motives, which can hold our fluorophore Cypate (Cy) close to the GNP; long spacers (LSs) that place Cypate to the GNP at a distance that can enhance the fluorescence maximally; cancer-cell targeting aptamer; and bio-polymer (sPEG) that coat the GNP surface, where the spacers have not occupied (Fig. 54.1b). Cypate is a derivative of FDA-approved, near-infrared (NIR) fluorophore Indocyanine Green (ICG), with the excitation (Ex) and emission (Em) wavelengths of 780 and 830 nm, respectively [7, 9, 10]. We selected an NIR fluorophore for in vivo use in the future because NIR penetrates well into the tissue with a minimal background

noise caused by tissue auto-fluorescence. Normally, this agent emits very little fluorescence (thin arrow in Fig. 54.1a, b). When the agent binds to the cancer cell *via* the aptamer and if the cell produces MMP-14, the SS gets cleaved. Cypate is then released from the SS and placed at a distance of the LS length from the GNP, generating its maximum fluorescence (thick arrow in Fig. 54.1a, c).

In this article, we report the first part of this multi-functional agent development, which is the contrast agents specific to MMP-14 (dotted rectangle in Fig. 54.1b), i.e., the agent with SS alone, without LS or the aptamer.

The plasmon field strength is determined by the GNP size and Cypate. For our purpose, the field strength should fit for both the fluorescence quenching by SS and enhancement by LS. According to our previous studies [7, 8, 11, 12], the GNP size meeting this dual condition was found to be approximately 10 nm. Therefore, we selected 10 nm GNPs for this study (Fig. 54.1a).

In designing the SS, we first selected a substrate-peptide sequence exhibiting a good specificity to MMP-14, i.e., amino acid sequence of ATRLFGIRGS, from the list reported by Kridel et al. [13]. For an additional SS candidate, we shortened the length by removing two amino acids from each end of it. A Cysteine (C) was then added to the C-terminus of each sequence to provide a thiol group to bind on to the GNP surface. The resulting SS sequences are, therefore, CRLFGIR-Aca (SS_1), where Aca denotes **a**mino**c**aproic **a**cid and CATRLFGIRGS (SS_2). Before binding them onto the GNP, they were conjugated to Cypate to form SS-Cy.

The GNP coating polymer sPEG is thiol group added, (11-Mercaptoundecyl) tri (ethylene glycol). sPEG is hydrophobic at one end and hydrophilic at the other end, to form a thin self-assembled-monolayer on the GNP surface that are unoccupied by the SS, and provides hydrophilicity to the outside by ethylene glycol. By varying its molar ratio to that of SS, the number of SS (i.e., Cypate) conjugated onto the GNP can be controlled [7–9, 11].

The fluorescence level of the resulting GNP-SS-Cy, with and without MMP-14, was then tested to verify its efficacy as an MMP-14 specific contrast agent.

2 Materials, Methods, and Instruments

A total of 10 ml of GNPs at 9.47 nM (Ted Pella; Redding, CA) was centrifuged at 15,700 × *g*, for 1 h, and the resulting pellet was re-dispersed in its supernatant to form a 3.0 ml GNP solution (~31.5 nM). 1.2 μmol sPEG (Asemblon; Redmond, WA) and 0.06 μmol SS-Cy (commissioned to Peptides International; Louisville, KY) were dissolved in 100 % ethanol to make the final volume of 3 ml (molar ratio of sPEG to SS-Cy, 15:1. The amount of the sPEG and SS-Cy, reacted with GNPs was nine times of the estimated number of SH binding sites on the 10 nm GNPs [7] to assure the GNP surface fully covered by them. The GNP solution was then added to the (sPEG + SS-Cy) solution in a 15 ml centrifuge tube, and the mixture was reacted gently on a rotator at room temperature for 4 h. The resulting solution was placed in a dialysis cassette (20,000 MWCO; Thermo Scientific; Rockford, IL) to

be dialyzed in 3.0 L of 1.0 mM PBS solution, overnight. The dialyzed product was then centrifuged at 15,700 × *g* for 1 h. The resulting pellet was re-dispersed in 1.0 mM PBS to make a final volume of 5 ml.

To characterize the product, its absorption spectrum (500–900 nm) was obtained, along with those of GNP and SS-Cy alone, using a Beckman DU520 Spectrophotometer (Beckman Instruments; Fullerton, CA). Fluorescence was measured at 830 nm (Ex, at 780 nm) using a Spectra Gemini XPS Fluorometer (Molecular Devices; Sunnyvale, CA), with SS-Cy as a control.

For studying the conditional fluorescence emission of the product, MMP-14 (EMD Millipore; Billerica, MA) was added to GNP-SS-Cy solution (2.0 μM Cypate) at a concentration of 3.0 mg/ml in a 1.0 mM PBS solution containing cofactors 5.0 mM $CaCl_2$ and 50.0 μM $ZnCl_2$. The reaction was carried out at 37 °C, and the fluorescence was recorded over 1.5 h, with free SS-Cy and GNP-SS-Cy without MMP-14, as controls.

3 Results and Discussion

3.1 Conjugation of sPEG and SS-Cy to GNP

The conjugation state of sPEG and SS-Cy onto the GNPs was examined by analyzing the absorption spectra of the reactants and products. Figure 54.2a shows the normalized absorption spectra of GNP-SS_1-Cy, GNP-SS_2-Cy, GNP, and SS-Cy. The absorption peak of 10 nm GNPs is at 520 nm (Fig. 54.2a, dotted arrow). As seen in the figure, the peak of GNP-SS_1-Cy and GNP-SS_2-Cy spectrum was at 525 nm (Fig. 54.2a, solid arrow), 5 nm red-shifted from the GNP peak. This peak shifting indicates that the particle size increased, implying that sPEG, SS-Cy, or both were successfully conjugated onto the GNP. The amount of the GNP and Cypate in the products were quantified via the absorption at 525 nm (product absorption peak)

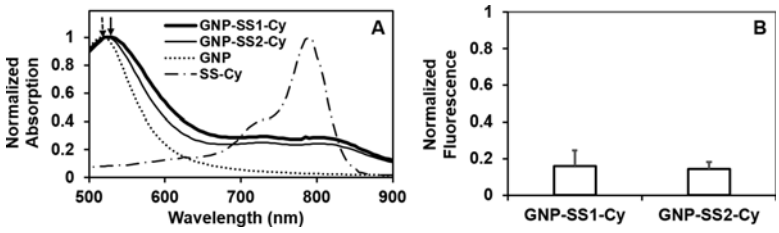

Fig. 54.2 (**a**) Normalized absorption spectra of GNP-SS_1-Cy, GNP-SS_2-Cy, GNP and SS-Cy. The peaks of GNP-SS-Cys red-shifted by 5 nm and the absorbance at 780 nm increased, implying that sPEG and SS-Cys were successfully conjugated onto the GNP. (**b**) Fluorescence of GNP-SS_1-Cy and GNP-SS_2-Cy, normalized to that of free SS-Cy. Cypate conjugated to GNP via SS emits only 14–17 % fluorescence of free Cypate

and 780 nm (Cypate absorption peak), respectively. The molar ratios of Cypate to GNP in the products were found to be 315 ± 19 and 287 ± 42 for SS_1-Cy and SS_2-Cy, respectively, indicating that the SS-Cys were successfully conjugated.

The fluorescent emissions by the products were measured for the level of Cypate fluorescence quenched by the GNP. Figure 54.2b shows the fluorescence level of the two GNP-SS-Cys, normalized by the free SS-Cy fluorescence at the same concentration. As in the figure, conjugating SS_1-Cy and SS_2-Cy to the GNP reduced their fluorescence by 83 ± 8 and 86 ± 3 %, respectively, indicating that our SSs placed Cypate molecules sufficiently close to the GNP for the desired fluorescence quenching.

3.2 Fluorescence Restoration of GNP-SS-Cy by MMP-14

The fluorescence restoration of the products by MMP-14 was tested by adding MMP-14 to the product solution. Figure 54.3 shows the time course of the normalized fluorescence level of the products, with and without MMP 14, starting at the time of MMP-14 addition. In the figure, only one control GNP-SS_2-Cy was included to avoid crowdedness. The fluorescence slowly increased in time, and by 90 min the fluorescence reached the level of its free SS-Cy, or even higher. This fluorescence increase indicates that MMP-14 cleaved the SS and that the released Cypate molecules moved away from the GNP. For the SS_1, the fluorescence increased faster than for SS_2, and after 60 min its fluorescence level became even greater than that of the free SS-Cy. This unexpected fluorescence increase might be because the freed Cypate molecules moved and reached where the plasmon field strength would enhance the fluorescence (Fig. 54.1a). This phenomenon is expected to disappear when the Cypate molecules move even farther from the GNP. It should be noted that the GNP-SS-Cy complex was stable for several weeks after the production (data not shown).

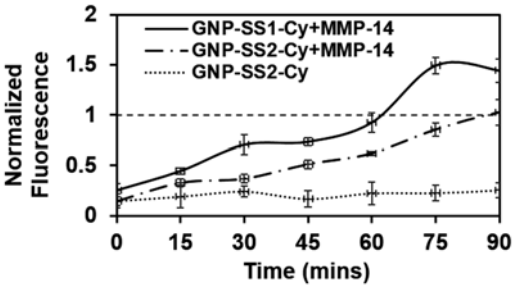

Fig. 54.3 Time course of normalized fluorescence of GNP-SS_1-Cy and GNP-SS_2-Cy with MMP-14. The fluorescence of GNP-SS_1-Cy and GNP-SS_2-Cy were fully restored after 90 min, while the fluorescence of GNP-SS_2-Cy without MMP-14 (control) remained constant during the time of measurements

The experimental results on the low fluorescence level of GNP-SS-Cys and their conditional fluorescence restoration by MMP-14 demonstrate that our contrast agents can detect MMP-14 in a highly specific manner.

4 Conclusions

MMP-14 is associated with aggressive cancer types, including the triple-negative breast cancer cell line MDA-MB 231. Thus, detecting MMP-14 in the breast tissue in a specific and sensitive manner can be important for early diagnosis of aggressive breast cancer and for accurate prognosis of the disease. By taking advantage of the unique nature of GNPs, we have developed GNP-based, NIR fluorescent contrast agents, which emit fluorescence only in the presence of MMP-14. Two MMP-14 substrate-motif containing short spacers (SS_1 and SS_2) were designed to place NIR fluorophore Cypate close to the GNP, and the resulting products exhibited the fluorescence level at 14–17 % of its free Cypate. When the product GNP-SS-Cy was exposed to MMP-14, the fluorescence was fully restored, demonstrating that our contrast agents provide signals specific for MMP-14. The next step of our design will be to develop the contrast agent having both high specificity and sensitivity for MMP-14 detection, and also the targeting aptamer, as described in the introduction section.

Acknowledgments The authors acknowledge the financial supported from the NIH Grant 1R15CA173693.

References

1. Yao G, He P, Chen L, Hu X et al (2013) MT1-MMP in breast cancer: induction of VEGF-C correlates with metastasis and poor prognosis. Cancer Cell Int. doi:10.1186/1475-2867-13-98
2. Lu SY, Wang Y, Huang H et al (2013) Quantitative FRET imaging to visualize the invasiveness of live breast cancer cells. Plos One. doi:10.1371/journal.pone.0058569
3. Haage A, Nam DH, Ge X et al (2014) Matrix metalloproteinase-14 is a mechanically regulated activator of secreted MMPs and invasion. Biochem Biophys Res Commun 450:213–218
4. Curran S, Murray GI (1999) Matrix metalloproteinases in tumour invasion and metastasis. J Pathol 189:300–308
5. Malemud CJ (2006) Matrix metalloproteinases (MMPs) in health and disease: an overview. Front Biosci 11:1696–1701
6. Stamenkovic I (2000) Matrix metalloproteinases in tumor invasion and metastasis. Semin Cancer Biol 10:415–433
7. Kang KA, Wang JT (2014) Conditionally activating optical contrast agent with enhanced sensitivity via gold nanoparticle plasmon energy transfer: feasibility study. J Nanobiotechnol. doi:10.1186/s12951-014-0056-2
8. Kang KA, Wang JT, Jasinski JB et al (2011) Fluorescence manipulation by gold nanoparticles: from complete quenching to extensive enhancement. J Nanobiotechnol 9:16–29

9. Wang JT, Achilefu S et al (2011) Gold nanoparticle-fluorophore complex for conditionally fluorescing signal mediator. Anal Chim Acta 695:96–104
10. Ye YP, Bloch S, Kao J et al (2005) Multivalent carbocyanine molecular probes: synthesis and applications. Bioconjug Chem 16:51–61
11. Wang JT, Moore J, Laulhe S et al (2012) Fluorophore-gold nanoparticle complex for sensitive optical biosensing and imaging. Nanotechnology. doi:10.1088/0957-4484/23/9/095501
12. Kang KA, Wang JT (2014) Smart dual-mode fluorescent gold nanoparticle agents. Wiley Interdisciplinary Rev Nanomed Nanobiotechnol 6:398–409
13. Kridel SJ, Sawai H, Ratnikov BI et al (2002) A unique substrate binding mode discriminates membrane type-1 matrix metalloproteinase from other matrix metalloproteinases. J Biol Chem 277:23788–23793

Chapter 55
Boundary Element Method for Reconstructing Absorption and Diffusion Coefficients of Biological Tissues in DOT/MicroCT Imaging

Wenhao Xie, Yong Deng, Lichao Lian, Dongmei Yan, Xiaoquan Yang, and Qingming Luo

Abstract The functional information, the absorption and diffusion coefficients, as well as the structural information of biological tissues can be provided by the DOT(Diffuse Optical Tomograph)/MicroCT. In this paper, we use boundary element method to calculate the forward problem of DOT based on the structure prior given by the MicroCT, and then we reconstruct the absorption and diffusion coefficients of different biological tissues by the Levenberg-Marquardt algorithm. The method only needs surface meshing, reducing the complexity of calculation; in addition, it reconstructs a single value within an organ, which reduces the ill-posedness of the inverse problem to make reconstruction results have good noise stability. This indicates that the boundary element method-based reconstruction can serve as an new scheme for getting absorption and diffusion coefficients in DOT/MicroCT multimodality imaging.

Keywords Multimodality imaging • Boundary element method • Image reconstruction • Absorbing coefficients • Diffusion coefficients

W. Xie • Y. Deng (✉) • L. Lian • D. Yan • X. Yang
Wuhan National Laboratory for Optoelectronics, Britton Chance Center for Biomedical Photonics, Huazhong University of Science and Technology, Wuhan 430074, China

Key Laboratory of Biomedical Photonics of Ministry of Education, Department of Biomedical Engineering, Huazhong University of Science and Technology, Wuhan 430074, China
e-mail: ydeng@mail.hust.edu.cn

Q. Luo
Britton Chance Center for Biomedical Photonics, Wuhan National Laboratory for Optoelectronics, Huazhong University of Science and Technology, Wuhan 430074, China

© Springer International Publishing Switzerland 2016

Q. Luo et al. (eds.), *Oxygen Transport to Tissue XXXVIII*, Advances in Experimental Medicine and Biology 923, DOI 10.1007/978-3-319-38810-6_55

1 Introduction

Diffuse optical tomography (DOT) is a non-invasive and highly sensitive optical imaging technique. It can reconstruct the absorption and diffusion coefficients of different biological tissues either in 2D or 3D [1, 2]. In recent years, the multimodality imaging technique has become a worldwide research focus, where structural information provided by XCT or MRI can be used in DOT reconstruction as prior information, hence the contrast and resolution of the reconstructed image can be improved [3].

The most commonly used technique in solving the forward problem of DOT/MicroCT multimodal imaging is the finite element method (FEM) [4]. The inverse problem can be solved by conjugate gradient method and Newton method [5]. The boundary element method (BEM), compared with FEM, can get more accurate numerical solutions and thus leads to a more accurate reconstruction. The BEM approach requires only surface discretization, alleviating the meshing complexity compared to volume meshing in FEM. Furthermore, the optical parameters to be reconstructed reduce to several piecewise constant values in each region, reducing the ill-posedness of the inverse problem [6–8]. In this paper, we use BEM to solve the forward problem of DOT/Micro-CT, and then present a BEM-based reconstruction scheme.

2 Methods

2.1 Forward Model

Although the biological organizations are very complex, they can be seen as a collection of organs with similar components. The optical coefficients in each organ are assumed to be piecewise constant. Diffusion approximation has been commonly used to model light transport in these organizations where scattering dominates over absorption and the Robin-type boundary condition is used [1]. We assume that the body is divided into n subregions with L smooth boundaries. Each region is characterized by constant optical coefficients. The diffusion equations in this case are several coupled Helmholtz equations [7]:

$$\nabla^2\Phi_l(r) - \omega_l^2\Phi_l(r) = -q_l \qquad l = 1,2\ldots L \tag{55.1}$$

where $\Phi(r)$ is the photon fluence at position r, $q(r)$ is the isotropic source and

$$\begin{cases} \omega_l^2 = \dfrac{\mu_{\alpha,l}}{\kappa_l} \\ q_l = \dfrac{q_1(r)}{\kappa_1}\cdot\delta_{i,1} \end{cases} \tag{55.2}$$

where $\mu_a(r)$ is the absorption coefficient and κ_1 is the diffusion coefficient. The source term is non-zero only on the outmost boundary. The three-dimensional fundamental solution is presented here:

$$\mathrm{G}\left(r,r'\right)=\frac{1}{4\pi\left|r-r'\right|}e^{-\kappa\left|r-r'\right|} \tag{55.3}$$

where r denotes the field position, r' the source position and $\hat{v}$ the outer normal direction on the boundaries.

We can get the following boundary integral equation by applying the second Green's theorem:

$$c_l\Phi_l+\int_{\Gamma_l}\left(\partial_l\mathrm{G}_l\cdot\mathrm{U}_l-\frac{\mathrm{G}_l}{\kappa_l}\cdot\mathrm{V}_l\right)=\int_{\Omega_l}\mathrm{G}_l q_l \tag{55.4}$$

where the term c_l is a constant due to the singularities on the boundary. In the case of a smooth surface, $c_l=\frac{1}{2}$.

We use constant element to discretize the boundary Γ_l in to N_l elements, we define two factors:

$$\begin{cases}\mathrm{a}^l_{mm'}=\int_{\Gamma_l}\partial_l\mathrm{G}_l dS\\ \mathrm{b}^l_{mm'}=\int_{\Gamma_l}\frac{\partial_l\mathrm{G}_l}{\kappa_l}dS\end{cases}\qquad m,m'=1,2.....N_l \tag{55.5}$$

Assembling all $\mathrm{a}^l_{mm'}$, $\mathrm{b}^l_{mm'}$,we get two matrixes $\boldsymbol{A}^l_{nn'}$, $\boldsymbol{B}^l_{nn'}$.

All the discretized boundary integral equations combined together produce a system of linear equations, and the photon fluence and photon flux on the boundary can be obtained by solving these equations.

2.2 Inverse Problem

The inverse problem in DOT/MicroCT multimodal imaging, namely the image reconstruction, is to reconstruct the optical coefficients of the tissue from boundary measurements. This is usually modeled as a nonlinear least square optimization problem [9]:

$$\min_{\mathbf{x}}\Omega=\mathbf{y}-\mathbf{F}\left(\mathbf{x}\right)^2 \tag{55.6}$$

where **y** is the boundary measures, **F**(**x**) is the calculations of the forward model with the predicted optical properties.

The BEM-based reconstruction is based on the assumption that the optical properties are piecewise constant. In comparison to the FEM-based reconstruction, the reduction in the number of optical properties to be reconstructed leads to a less ill-posed problem.

Equation (55.6) was solved by Levenberg-Marquardt algorithm [5], and we also used the logarithmic data to improve the original poor-scaled problem.

3 Results

In the inverse problem of DOT/Micro-CT, we did a simulation study to demonstrate the BEM-based DOT image reconstruction, showing the accuracy and noise stability of the BEM-based reconstruction method. First, we used the Micro-CT built in our laboratory to image a mouse [10]. Then the mice model for simulation was obtained by extracting the boundaries of different organs of the mouse including heart, liver, lung and the outmost boundary. We aimed to reconstruct the absorption and diffusion coefficient of different tissues. Table 55.1 gives the absorbing coefficients and diffusion coefficients of these tissues [11]. These coefficients were then used to generate the simulated measurements for the subsequent reconstruction.

We reconstructed μ_a and κ of different organs with three different levels of Gaussian noise (which are 1, 3 and 5 %) added to the simulated data; the reconstruction results are show in Table 55.2. The initial values of the absorbing coefficients and diffusion coefficients were set to be 0.01 and 0.3 mm^{-1} before the iteration in the inverse problem. The iteration stopped after 20 iterations.

Table 55.1 Absorbing coefficient μ_a and diffusion coefficient κ

Optical properties/mm^{-1}	Heart	Liver	Lung	Other tissue
μ_a	0.035	0.06	0.025	0.03
κ	0.19	0.25	0.11	0.22

Table 55.2 Reconstruction results (reconstructed (μ_a,κ)/relative error) of absorbing coefficient μ_a and diffusion coefficient κ under three different noise levels

Tissue type	1 % Gaussian noise	3 % Gaussian noise	5 % Gaussian noise
Heart	(0.0354, 0.1952)/ (1.03 %, 2.72 %)	(0.3318, 0.2052)/ (5.52 %, 8.01 %)	(0.0372, 0.2040)/(6.29 %, 7.37 %)
Liver	(0.0595, 0.2462)/ (0.75 %, 1.53 %)	(0.0612, 0.2546)/ (2.05 %, 1.85 %)	(0.0584,0.2550)/(2.67 %, 2 %)
Lung	(0.0260, 0.1063)/(4 %, 3.33 %)	(0.0219, 0.1049)/ (12.30 %, 4.63 %)	(0.0310, 0.1051)/(24 %, 4.45 %)
Other tissue	(0.0310, 0.2247)/ (0.35 %, 2.14 %)	(0.0310, 0.1974)/ (3.17 %, 10.26 %)	(0.0283, 0.1863)/(5.67 %, 15.32 %)

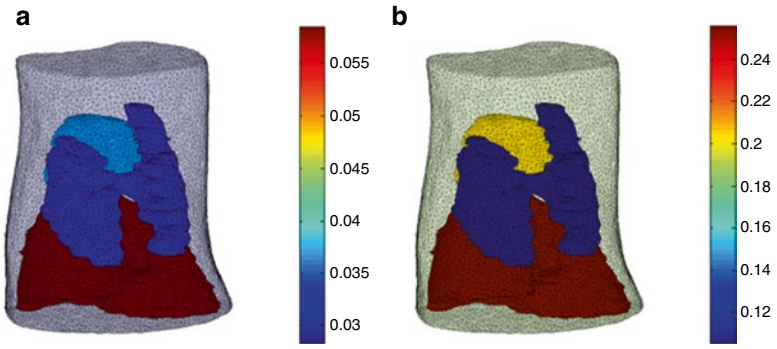

Fig. 55.1 (**a**) Reconstructed μ_a. (**b**) Reconstructed κ

The reconstruction errors are relatively small. Figure 55.1a, b show the reconstructed distribution of μ_a and κ, respectively, with 5 % Gaussian noise added to the simulated data.

4 Conclusions

In this paper, we used BEM to solve the forward problem. As a numerical method, BEM can also be as important as FEM in the field of biomedical imaging. Since BEM only needs surface meshing of different organs which is much easier and more efficient than the volume meshing required in FEM, it is more suitable for a large-scale problem. We used the Levenberg-Marquardt algorithm to reconstruct the optical properties of different organizations of mice based on a 3D mice model provided by MicroCT. The reconstruction showed that the BEM-based reconstruction had good accuracy and noise stability. Compared with FEM based reconstruction scheme, BEM based reconstruction also has some limitations. Its calculation complexity increases with the increase of the boundaries of different organs, and its reconstruction quality depends highly on the accuracy of the extraction of these boundaries.Acknowledgments This research was supported by National Key Scientific Instrument & Equipment Development Program of China (No. 2012YQ030260); National Major Scientific Research Program of China (No. 2011CB910401); National Natural Science Fund (No. 61078072); Science Fund for Creative Research Group (No. 61421064).

References

1. Arridge SR (1999) Optical tomography in medical imaging. Inverse Probl 15:R41–R93
2. Kim HK, Hielscher AH (2010) A diffusion–transport hybrid method for accelerating optical tomography. J Innov Opt Heal Sci 03:293–305

3. Tian J, Bai J, Yan XP et al (2008) Multimodality molecular imaging. IEEE Eng Med Biol 27:48–57
4. Arridge SR, Schweiger M, Hiraoka M et al (1993) A finite element approach for modeling photon transport in tissue. Med Phys 20:299–309
5. Schweiger M, Arridge SR, Nissila I et al (2005) Gauss–Newton method for image reconstruction in diffuse optical tomography. Phys Med Biol 50:2365–2386
6. Elisee J, Gibson A, Arridge S (2011) Diffuse optical cortical mapping using the boundary element method. Biomed Opt Express 2:568–578
7. Srinivasan S, Pogue BW, Carpenter C et al (2007) A boundary element approach for image-guided near-infrared absorption and scatter estimation. Med Phys 34:4545–4557
8. Elisee J, Bonnet M, Arridge S (2011) Accelerated boundary element method for diffuse optical imaging. Opt Lett 36:4101–4103
9. Yalavarthy PK, Pogue BW, Dehghani H et al (2007) Weight-matrix structured regularization provides optimal generalized least-squares estimate in diffuse optical tomography. Med Phys 34:2085–2098
10. Yang X, Meng Y, Gong H et al (2012) Abnormal pixel detection using sum-of-projections symmetry in cone beam computed tomography. Opt Express 20:11014–11030
11. Zhang B, Gao F, Wang M et al (2014) In vivo tomographic imaging of lung colonization of tumour in mouse with simultaneous fluorescence and X-ray CT. J Biophotonics 7:110–116

Chapter 56
Mathematical Model of an Innate Immune Response to Cutaneous Wound in the Presence of Local Hypoxia

Guennadi Saiko, Karen Cross, and Alexandre Douplik

Abstract We developed a 2D multi-agent stochastic model of interaction between cellular debris, bacteria and neutrophils in the surface cutaneous wound with local hypoxia. Bacteria, which grow logistically with a maximum carrying capacity, and debris are phagocytosed by neutrophils with probability determined by the partial pressure of oxygen in the tissue, $pO_2 = 4$–400 mmHg, according to the Michaelis-Menten equation with $K_m = 40$ mmHg. The influx of new neutrophils depends linearly ($k = 0.05$–0.2) on the amount of (a) platelets and (b) neutrophils, which are in contact with bacteria or debris. Each activated neutrophil can accomplish a certain amount of phagocytosis, $n_{max} = 5$–20, during its lifespan, $T = 1$–5 days. The universe of outcomes consists of (a) bacteria clearance (high k and n_{max}), (b) infection is not cleared by neutrophils (low k and n_{max}), and (c) intermittent (quasiperiodic) bursts of inflammation. In the absence of infection, phagocytosis stops within 48 h. We found that pO_2 alone did not change the type of outcome, but affects the number of recruited neutrophils and inflammation duration (in the absence of infection by up to 10 and 5 %, respectively).

Keywords Wound healing • Inflammation • Neutrophils • Phagocytosis • Hypoxia

1 Introduction

When the wound is not healed within 6 weeks, it is considered chronic. Chronic wounds are a major source of patients' discomfort and a serious health issue leading to complications, significant morbidity and mortality. Only diabetic foot ulcers and ischemic limbs cost health care in the USA $80 billion per year [1].

G. Saiko (✉) • A. Douplik
Department of Physics, Ryerson University, Toronto, ON, Canada M5B 2K3
e-mail: gsaiko@ryerson.ca

K. Cross
Division of Plastic Surg., St. Michael's Hospital, Toronto, ON, Canada M5B 1W8

© Springer International Publishing Switzerland 2016

Q. Luo et al. (eds.), *Oxygen Transport to Tissue XXXVIII*, Advances in Experimental Medicine and Biology 923, DOI 10.1007/978-3-319-38810-6_56

Typically, a chronic wound develops in case of disruption of the inflammatory phase or the proliferative phase and is related to tissue hypoxia. Oxygen is an important factor during all stages of wound healing. The K_m for enzymes involved in bacterial killing, collagen synthesis, angiogenesis and re-epithelialization requires pO_2 levels in wound tissue ranging from 25 to 100 mmHg [2]. Inflammatory phase in acute wounds is the first oxygen-dependent step in wound healing and, consequently, the effect of local hypoxia on the kinetics of the inflammatory phase is of importance for wound management and prevention of chronic wounds. The aim of this work is to investigate the effect of local hypoxia on the kinetics of the early inflammatory phase in acute wounds.

The influx of neutrophils is the first line of an innate immune defense in an acute wound. Neutrophils are normally found in the bloodstream, where they are inactive and swept along at high speed or marginally and reversibly attached to the endothelial cells of the blood vessel wall.

Once they have received the proper signals (proteins from bacteria, clotting system peptides, cytokines), it takes them about 30 min to leave the blood and reach the site of an infection: they adhere to endothelium, exit the blood through generated gaps between the endothelial cells (diapedesis), and migrate towards the site of infection (chemotaxis), where they engulf (phagocytosis) and kill the bacteria. Circulating neutrophils have a half-life of 6–10 h and undergo apoptosis, after which they are cleared in the spleen. In a wound, they do not return to the blood and their apoptosis is delayed by the activated endothelium [3] up to 5 days.

Phagocytosis of bacteria by human neutrophils takes on average 9 min [4] and is accompanied by a large burst (by a factor of 50–100 [5]) in oxygen consumption. The respiratory burst is brief in nature, reaching a maximum rate at 3 min after stimulation and being undetectable after 30–60 min post stimulation. With this large oxygen consumption, neutrophils become susceptible to tissue perfusion. In particular, it is known that neutrophils lose their killing ability if the partial pressure of oxygen, pO_2, is below 40 mmHg.

Previously published mathematical models [6] of bacterial kinetics and inflammatory processes present a conceptual framework for our study. Most of the studies use systems of ordinary differential equations to describe bacterial pathogenesis. Xue et al. [7] developed a model based on partial differential equations in 1D (cylindrical) geometry to investigate the process of ischemic wound healing. However, use of scalar (number of bacteria) or 1D (bacteria distribution) values to characterize outcomes may be insufficient for such a heterogeneous environment as wounds. We propose a 2D multi-agent probabilistic model, which can be adjusted to realistic geometries of the wound.

2 Mathematical Model

We developed a 2D multi-agent stochastic model, which depicts the interaction between cellular debris, bacteria population and the neutrophils in the surface cutaneous wound with local hypoxia. Numerical simulation of the model was done

using a multi-agent environment NetLogo 5.1.0 [8], where users can give instructions (rules) to multiple agents, which behave independently. NetLogo is well suited for modelling complex system developing over time. Parameter values used to simulate models are given in the text.

2.1 The Lattice Model

The wound is represented by *LxL* square lattice. The system evolves in time with fixed time steps Δt. On each step, a bacterium can replicate, a neutrophil can enter the wound, phagocyte, move to a nearby location, or die. The rules that govern these process are specified below.

We selected our time step $\Delta t = 30$ min, which is a reasonable estimate for the doubling time of bacteria (e.g. *E. coli*) and signaling-recruitment-migration events.

2.2 Geometry

The size of the lattice cell can be determined using (a) the distance travelled by each neutrophil on one time step, or (b) the size of the area served by each capillary loop. The velocity of migrating neutrophil is close to 10 μm min^{-1} [9] and their directionality (ratio of the shortest linear distance between the start point and end point of the migration path compared with the total distance traveled by the cell) is around 0.7 [9]. Thus, the overall displacement over time step Δt will be around 200 μm, which is in good agreement with the size of the area served by each capillary loop. Therefore, we can set the lattice cell size to 200 μm.

Lattice size *L* was set to 51 for most of the calculations (a 10×10 mm wound). We emulated a larger wound with cyclical boundary conditions.

2.3 Bacteria Growth

A number of bacteria (in CFU) at any particular lattice cell is *b*. Bacteria grow logistically with growth rate *r* and a maximum tissue carrying capacity, K_p. When a bacterium divides, the new bacterium goes to a nearby cell. For simplicity, we will consider the case where $r\Delta t = 1$. If we consider the surface wound, then the active volume of the wound, which corresponds to each lattice cell will be $0.2 \times 0.2 \times 2$ mm $= 0.08$ mm^3. Thus, to convert the number of bacteria (or carrying capacity) to CFU/ml units we need to multiply it by the 1.25×10^4 factor.

2.4 Neutrophil Recruitment

Neutrophils' recruitment, activation, and migration are regulated by various growth factors and other cytokines, produced by cells and bacteria. We incorporated signaling through two major mechanisms: initial release of cytokines by platelets and secondary cytokine signaling by leukocytes.

Most types of injury damage blood vessels and coagulation is an immediate response to initiate protection from excessive blood loss. With the adhesion, aggregation and degranulation of circulating platelets within the forming fibrin clot, a number of mediators and cytokines are released, including PF4 and TGF-β1, which elicits the rapid chemotaxis of neutrophils and monocytes to the wound site in a dose-dependent manner.

Autocrine expression of TGF- β1 by leukocytes and fibroblasts, in turn, induces these cells to generate additional cytokines including tumor necrosis factor alpha (TNF-α), interleukin 1 β (IL-1 β) and PDGF, as well as chemokines, as components of a cytokine cascade, which recruit and activate neutrophils.

Even though these cytokines have slightly different kinetics, we will model them as one type: cytokines are produced at a rate α pg ml^{-1} cell^{-1} h^{-1} from platelets (2.1 10^{-2} pg ml^{-1} cell^{-1} h^{-1} [6]) and are degraded at a rate d_c per hour (0.83 h^{-1} [10]). Then, their steady-state concentration is $c^* = \alpha/d_c$ or 0.025 pg ml^{-1} cell^{-1}. The cytokine signalling recruits neutrophils at a rate η (1.33 cells (pg/ml)$^{-1}$h^{-1} [6]). Thus, we can estimate the influx of new neutrophils as $k = \eta c^*$ or $k = 0.033$ cell^{-1} h^{-1}. In our model the influx of new neutrophils depends linearly ($k = 0.05$–0.2) with time delay (Δt) on the amount of (a) platelets and (b) neutrophils, which are in contact with bacteria or cellular debris.

2.5 Phagocytosis

Neutralization of bacteria can be considered as a two-stage process

$$extracellular\ bacteria \xrightarrow{k_1} intracellular\ bacteria \xrightarrow{k_2} killed\ bacteria$$

Hampton et al. [4] found that each stage could be described by a first order kinetics equation. They also found coefficients k_1 and k_2 for two clinically relevant bacteria: *E.coli* (0.073 and 0.36 min^{-1}, respectively) and *S.aureus* (0.077 and 0.11 min^{-1}, respectively).

According to the first order kinetics equation for engulfing, if initially we had B_0 bacteria, then after some period T we will have $B_0\ exp(-k_1T)$ free bacteria. This means that we can consider $exp(-k_1T)$ as a probability for a bacterium to escape and $p(T) = 1 - exp(-k_1T)$ as a probability to get engulfed during the period T.

One can expect that the k_1 (and k_2) will be proportional to V, the pO_2-modulated velocity of engulfing (or killing), which depends on pO_2 according to the

Michaelis-Menten equation with half maximal velocity, K_m. Moreover, V is the first nonzero term in this expansion (obviously $k_1 = 0$ if $pO_2 = 0$).

We will use the expression for $p(T)$ and $k_1 \sim V$ relationship to calculate the probability of phagocytosis during one time step Δt. We consider pO_2 in the range from 4 mmHg (hypoxia) to 400 mmHg (HBOT or TOT), K_m was set at 40 mmHg.

A neutrophil phagocytes a bacterium or debris located in the same cell with probability $p(\Delta t)$. If it is not engaged in phagocytosis, the neutrophil moves one step within the wound. Each activated neutrophil has a certain lifespan in the wound, $T = 1$–5 days, and can accomplish a certain amount of phagocytosis during its lifespan, $n_{max} = 5$–20. Apoptotic material and remaining debris will be cleared by macrophages at later stages.

We also modeled extreme hypoxia by introducing the notion that neutrophil during phagocytosis can deplete oxygen from some spatial area (one lattice cell), and tissue requires some time (certain number of time steps Δt) to replenish it. During this period, any new phagocytosis in this area is prohibited.

3 Results, Discussion, and Conclusions

The universe of outcomes of the model consists of (a) bacteria clearance (high k and n_{max}), (b) infection is not cleared by neutrophils (low k and n_{max}), and (c) intermittent (quasiperiodic) bursts of inflammation: see Fig. 56.1 for typical cases.

We ran multiple simulations with various parameters and tracked the duration of neutrophil presence in the wound and their maximal accumulation. We found that pO_2 alone does not change the type of outcome, but affects the number of recruited neutrophils and inflammation duration (in the absence of infection by up to 10 and 5 %, respectively). In the case of extreme hypoxia, we found that inflammation duration is increased significantly, and lengthy inflammation with a high number of neutrophils is the most probable outcome.

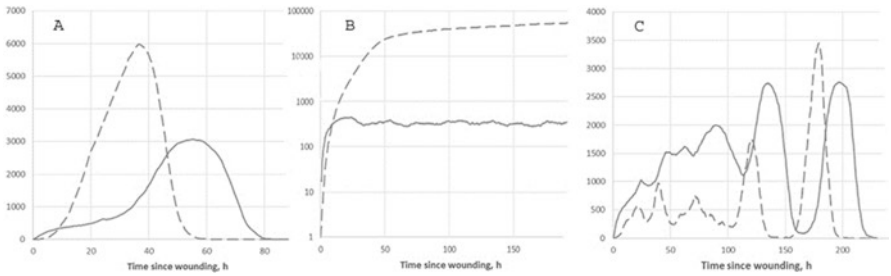

Fig. 56.1 Typical kinetics of bacteria (*dashed line*) and neutrophils (*solid line*) for $T = 1$d and $K_p = 6$: (**a**) bacteria clearance ($k = 0.1$, $n_{max} = 20$), (**b**) neutrophil system is overwhelmed ($k = 0.1$, $n_{max} = 10$), (**c**) intermittent inflammation ($k = 0.2$, $n_{max} = 10$)

To refine the impact of hypoxia we studied the wound without bacterial contamination. In Table 56.1 we present the aggregated results with various parameters (in columns and rows) for the duration of neutrophil presence in the wound (measured in Δt units) for $T = 1$d. In each cell three values correspond to different pO_2: 400 mmHg (upper), 4 mmHg (middle), and 4 mmHg with depletion for one time interval Δt (lower), respectively. Each value is accompanied by its standard deviation (in brackets). We also run a t-test for each group of simulations to find out where hypoxia induces significant changes. Statistically significant values ($p = 0.05$, two-sided test) are underscored.

We did not find a significant influence of pO_2 on the kinetics of initial accumulation of neutrophils in the absence of infection. This is an expected result because this process is driven primarily by platelets signalling, which in our model is pO_2-independent. The initial accumulation depends mostly on k, which incorporates signalling/neutrophil recruiting, and platelets density, which is linked to the surface density of damaged blood vessels.

Maximum accumulation of neutrophils depends on pO_2. We found that hypoxia increases the peak value up to 10 % for the wide range of conditions.

In the absence of infection, phagocytosis stops within 48 h. The duration of neutrophil presence in the wound is determined mostly by their lifespan T. However, in many cases (e.g. for low platelets density) they may stay in the wound much longer than usual ('tails'). We found that hypoxia increases inflammation duration for a wide range of parameters (see Table 56.1).

Our model (with scaling factor 10^4) reasonably well explains the results from a mouse model [11] in term of kinetics and neutrophil density. In particular, it was found [11] that the neutrophil accumulation in the wound reached $\sim 6 \times 10^6$ by day 2 and decreased progressively from day 5 to wound closure (day 9).

Table 56.1 The duration of neutrophil presence in the wound (measured in Δt units) for pO_2: 400 mmHg (upper), 4 mmHg (middle), and 4 mmHg with depletion (lower)

Time of neutrophil presence in the wound (in 30 min)				Cellular debris density			
				0.1		1	
				New neutrophils, k		New neutrophils, k	
				0.1	0.2	0.1	0.2
Platelets density	1	Max kills, n_{max}	20	67.8(3.9) 66.9(2.0) 69.0(1.5)	60.9(1.7) 62.5(2.2) **64.3(1.6)**	66.0(2.6) 67.0(3.3) **73.2(4.7)**	60.7(1.0) 60.3(1.3) **66.6(1.9)**
			5	69.6(3.5) 68.2(1.9) 70.0(4.3)	61.8(1.9) 61.4(1.2) **64.0(1.8)**	71.3(4.8) 69.2(2.5) **76.4(3.6)**	62.0(2.4) 61.7(1.3) **67.2(2.0)**
	0.1	Max kills, n_{max}	20	341.6(581) 109.7(396) 99.7(22)	82.2(6.1) 81.4(5.8) 82.6(5.4)	99.0(8.6) 94.4(7.2) 102.4(7.7)	81.1(4.3) 81.3(5.2) 84.6(3.0)
			5	202.8(189.3) 93.2(6.8) 113.6(55.0)	80.9(5.1) 80.6(3.8) 82.4 (4.1)	321.7(589.9) 198.1(132.3) 333.9(378.1)	94.1(9.1) 88.1(4.3) 93.5(7.3)

The proposed model is quite flexible and allows multiple expansions: (a) to increase the number of agents (e.g. macrophages, re-epithelization), and (b) to investigate various geometries of the wound, e.g. full depth wounds or cuts with various width, which can be modelled with 3D models, etc.

In summary, we developed a 2D multi-agent stochastic model, which depicts the interaction between cellular debris, bacteria and neutrophils in the surface cutaneous wound with local hypoxia. The proposed model can be used to better understand oxygen balance during wound healing and to optimize infection prevention, wound dressings, and adjuvant wound healing therapies, e.g. TOT.

References

1. Centre for Disease Control. June 2014. http://www.cdc.gov/diabetes/pubs/statsreport14.htm
2. Allen DB, Maguire JJ, Mahdavian M et al (1997) Wound hypoxia and acidosis limit neutrophil bacterial killing mechanisms. Arch Surg 132:991–996
3. Coxon A, Tang T, Mayadas TN (1999) Cytokine-activated endothelial cells delay neutrophil apoptosis in vitro and in vivo. A role for granulocyte/macrophage colony-stimulating factor. J Exp Med 190:923–934
4. Hampton MB, Vissers MC, Winterbourn CC (1994) A single assay for measuring the rates of phagocytosis and bacterial killing by neutrophils. J Leukoc Biol 55(2):147–152
5. Morel F, Doussiere J, Vignais PV (1991) The superoxide-generating oxidase of phagocytic cells—physiological, molecular and pathological aspects. Eur J Biochem 201:523–546
6. Smith A, McCullers J, Adler F (2011) Mathematical model of a three-stage innate immune response to a pneumococcal lung infection. J Theor Biol 276:106–116
7. Xue C, Friedman A, Sen CK (2009) A mathematical model of ischemic cutaneous wounds. Proc Natl Acad Sci U S A 106(39):16782–16787
8. Wilensky U (1999) NetLogo. http://ccl.northwestern.edu/netlogo/. Center for Connected Learning and Computer-Based Modeling, Northwestern University, Evanston, IL
9. Mathias JR, Perrin BJ, T-Xi L et al (2006) Resolution of inflammation by retrograde chemotaxis of neutrophils in transgenic zebrafish. J Leukoc Biol 80:1281–1288
10. Cloff C, Willis R (1992) Pharmacokinetics and metabolism of therapeutic cytokines. In: Ferraiolo B, Mohler M, Gloff C (eds) Protein pharmacokinetics and metabolism. Springer, New York, pp 127–150
11. Kim M-H, Liu W, Borjesson DL et al (2008) Dynamics of neutrophil infiltration during cutaneous wound healing and infection using fluorescence imaging. J Invest Dermatol 128(7):1812–1820

Chapter 57
Analytical Expression for the NO Concentration Profile Following NONOate Decomposition in the Presence of Oxygen

Zimei Rong and Zhihui Ye

Abstract We have derived an analytical expression for the time dependent NO concentration from NONOate donors in the presence of oxygen for the process of NO release from NO donors following autoxidation. This analytical solution incorporates the kinetics of the releases with the autoxidation and is used to fit the simulated NO concentration profile to the experimental data. This allows one to determine the NO release rate constant, k_1, the NO release stoichiometric coefficient, v_{NO}, and the NO autoxidation reaction rate constant, k_2. This analytical solution also allows us to predict the real NO concentration released from NO donors under aerobic conditions, while v_{NO} is reportedly two under aerobic conditions, it falls to lower values in the presence of oxygen.

Keywords NONOate • Decomposition • Nitric oxide • Autoxidation • Mathematical mode

1 Introduction

The brain responds to hypoxia with an increase in cerebral blood flow (CBF). Many vasodilatory mechanisms have been proposed for this hypoxic vasodilation but none has gained universal acceptance. Nitric oxide (NO) was suggested to play a significant role in this response [1]. Both the formation and removal of this gas are pO_2 dependent and, therefore, CBF is a complex function of oxygen concentration. To test this hypothesis quantitatively, we incorporated the NO vasodilatory mechanism

Z. Rong (✉)
Centre for English Language Education, University of Nottingham Ningbo China, Ningbo 315100, China
e-mail: zimeirong@hotmail.com

Z. Ye
Department of Built Environment, London South Bank University, London SE1 0AA, UK

© Springer International Publishing Switzerland 2016

Q. Luo et al. (eds.), *Oxygen Transport to Tissue XXXVIII*, Advances in Experimental Medicine and Biology 923, DOI 10.1007/978-3-319-38810-6_57

into the BRAINSIGNALS model [2], which was designed to assist in the interpretation of multimodal noninvasive clinical measurements. Previously, we incorporated NO generation by deoxyhemoglobin [3] and NO metabolism by oxidised cytochrome *c* oxidase (CCO) [4] and oxyhemoglobin [5] into the BRAINSIGNALS model to reproduce the experimental human CBF versus pO_2 curves digitised from literature [6]. However, we were still unable to reproduce the exact CBF versus pO_2 curve and, in particular, the threshold phenomenon: CBF remaining unchanged until pO_2 decreased to a threshold value triggering a rise in CBF.

We considered looking for either an increase in NO production with decreasing pO_2 or a decrease in NO metabolism with decreasing pO_2 from a steeper NO versus O_2 curve, to reproduce the threshold in a CBF versus pO_2 curve. NO autoxidation is a third order reaction, i.e., first order with respect to oxygen and second order with respect to NO. For our simulation, we need the reaction rate constant, which varies a lot according to different researchers [7]. We reviewed the literature on NO autoxidation, which was studied with two systems, either a mixture of NO and oxygen, or NO released from donors followed by an aerobic removal. For the former, injecting the concentrated NO solution as a bolus may lead to heterogeneous NO oxidation at the tip of the syringe [8]. In the latter case, NO donors were used to provide continuous NO sources for characterization of NO autoxidation [9, 10] and NO formation and autoxidation has been modelled by numerical methods [9, 10].

In this work, we obtain an analytical expression that describes NO release from NO donors and NO oxidation, and use this to simulate NO concentration profiles and hence simultaneously determine three parameters: the NO release rate constant (k_1), the NO release stoichiometric coefficient (v_{NO}), and the NO autoxidation rate constant (k_2).

2 Mathematical Model

In a biochemical system, an NO donor such as ProliNO (disodium 1-(hydroxy-NNO-azoxy)-L-proline) releases NO which is then oxidised by O_2. We will first consider the release of NO by ProliNO.

$$\text{ProliNO} \rightarrow v_{NO}\text{NO} \tag{57.1}$$

where v_{NO} is the stoichiometric coefficient of NO release, i.e., v_{NO} moles of NO molecules are released from one mole of ProliNO. ProliNO decomposition follows first order kinetics with a decay rate constant k_1 in s^{-1} as:

$$\frac{d\left[\text{ProliNO}\right]}{dt} = -k_1\left[\text{ProliNO}\right] \tag{57.2}$$

The solution to Eq. (57.2) can be expressed as:

$$[\text{ProliNO}] = [\text{ProliNO}]_0 \exp(-k_1 t) \tag{57.3}$$

The rate of NO formation can be obtained as:

$$\frac{d[\text{NO}]}{dt} = v_{\text{NO}} k_1 [\text{ProliNO}] = v_{\text{NO}} k_1 [\text{ProliNO}]_0 \exp(-k_1 t) \tag{57.4}$$

We use x to represent NO concentration in M, and P ($v_{\text{NO}}[\text{ProliNO}]_0$) to represent the maximum NO concentration in the absence of decay, i.e., the initial ProliNO concentration ($t=0$) multiplied by v_{NO}. Equation (57.4) can be simplified as

$$\frac{dx}{dt} = k_1 P \exp(-k_1 t) \tag{57.5}$$

Now we consider NO autoxidation as:

$$4\text{NO} + \text{O}_2 + 2\text{H}_2\text{O} \rightarrow 4\text{NO}_2^- + 4\text{H}^+ \tag{57.6}$$

The rate equation of NO autoxidation can be expressed as:

$$\frac{dx}{dt} = -k_3 [\text{O}_2] x^2 = -4k_4 [\text{O}_2] x^2 = -k_2 x^2 \tag{57.7}$$

where k_3 (NO consumption) and k_4 (oxygen consumption) are the NO autoxidation rate constants with units $\text{M}^{-2}\ \text{s}^{-1}$ and k_2 is the NO autoxidation rate constant, k_3 that incorporates the oxygen concentration in unit $\text{M}^{-1}\ \text{s}^{-1}$. Historically, k_2, k_3 and k_4 have been used by different researchers to characterize NO autoxidation.

The overall reaction is a cascade chemical reaction. We need to solve a combined equation with an initial condition $x(t=0)=0$ as:

$$\frac{dx}{dt} = Pk_1 \exp(-k_1 t) - k_2 x^2 \tag{57.8}$$

For simplicity we introduce an intermediate, dimensionless, parameter b as:

$$b = 2\sqrt{Pk_2 / k_1} \tag{57.9}$$

and an intermediate, dimensionless, variable y as:

$$y = b \exp\left(-\frac{k_1 t}{2}\right) \tag{57.10}$$

The solution is given as:

$$x = \frac{2P}{b}\exp\left(-\frac{k_1 t}{2}\right)\frac{I_1(b)K_1(y) - I_1(y)K_1(b)}{I_1(b)K_0(y) + I_0(y)K_1(b)} \tag{57.11}$$

where $I_0(I_1)$ is a modified Bessel function of the first kind with the order of zero (one). $K_0(K_1)$ is a modified Bessel function of the second kind with the order of zero (one) [15]. $b(y)$ is the value at which to calculate the function. These two special engineering functions are built in Microsoft Excel with syntaxes of BESSELI(z, n) and BESSELK(z, n), where z is the variable and n is the order of the Bessel functions.

We can determine the rate constant k_1, b and P by fitting the simulated NO concentration x to experimental data i.e., minimising the standard deviation.

$$\sigma = \sum_{i=1}^{n}\left(x_{\text{sim}i} - x_{\text{exp}i}\right)^2 \tag{57.12}$$

where $x_{\text{exp}} = x_{\text{obs}} - x_{\text{base}}$, since a base line correction is usually needed.

For a best fit, the initial parameters for k_1, b and P are needed. P is the initial ProliNO concentration. There are several ways to obtain the initial parameters k_1 and $b(k_2)$. Firstly, for an existing question, the published data can be used as the initial parameters. Secondly, we can estimate the initial parameters by assuming only NO release (k_1), at the beginning part of the curve, and only NO oxidation (k_2), at the later part of the curve. Finally, we can differentiate Eq. (57.11) to obtain the maximum point (t_m, x_m).

$$x_\text{m} = \frac{2P}{b}\exp\left(-\frac{k_1 t_\text{m}}{2}\right) \tag{57.13}$$

$$I_1(b)\left(K_1(y_\text{m}) - K_0(y_\text{m})\right) = K_1(b)\left(I_1(y_\text{m}) + I_0(y_\text{m})\right) \tag{57.14}$$

Substituting Eq. (57.13) into Eq. (57.14), we obtain Eq. (57.15)

$$I_1(b)\left(K_1\left(b^2 x_\text{m}/2P\right) - K_0\left(b^2 x_\text{m}/2P\right)\right) = K_1(b)\left(I_1\left(b^2 x_\text{m}/2P\right) + I_0\left(b^2 x_\text{m}/2P\right)\right) \tag{57.15}$$

From Eq. (57.15) we can calculate the initial value b, which is substituted into Eq. (57.13) to calculate the initial value k_1.

3 Results and Discussion

The autoxidation of NO was considered too slow to be biologically relevant because the reaction rate depends on the NO concentration squared and the physiologically low NO concentration [8]. The rate of NO autoxidation could be increased by a

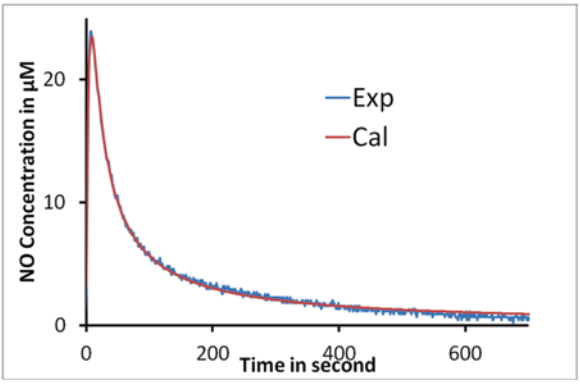

Fig. 57.1 The simulated and observed NO concentration profile after 40 µM proliNO adding to a 100 mM potassium phosphate buffer with pH 7.4 at 30 °C with oxygen concentration of 0.212 mM

higher reaction rate constant in membrane than in water or by higher local NO and O_2 concentrations in hydrophobic media.

Equation (57.11) can be used to simulate the NO concentration profile for a process combining NO generation and autoxidation. From a best fit of the simulated NO concentration profile to experimental data as shown in Fig. 57.1 [11] with Excel determined at oxygen concentration of 212 µM, the following values were obtained: $k_1 = 0.265\ s^{-1}$, $b = 0.857$, and $P = 31.345$ µM. From the obtained P value, we can calculate $v_{NO} = P/[\text{ProliNO}]_0 = 0.78$. From the value of b, we get $k_2 = 1.55 \times 10^3\ M^{-1}\ s^{-1}$, and $k_3 = 7.31 \times 10^6\ M^{-2}\ s^{-1}$.

Pogrebnaya was the first researcher to propose stoichiometrical NO autoxidation in aqueous solution and reported the kinetic reaction parameter $k_3 = 9 \times 10^6\ M^{-2}\ s^{-1}$ [12]. A wide range of kinetic reaction constants $k_3 = 6 \times 10^6\ M^{-2}\ s^{-1}$ [13], $k_3 = 8 \times 10^6\ M^{-2}\ s^{-1}$ [10], $k_3 = 9.2 \times 10^6\ M^{-2}\ s^{-1}$ [9], $k_3 = 12 \times 10^6\ M^{-2}\ s^{-1}$ [14], and $k_3 = 17 \times 10^6\ M^{-2}\ s^{-1}$ [8] were reported to be independent of pH [14]. Our NO autoxidation reaction rate constant is consistent with the reported values [8–14].

The rate of NO release from NO donors depends more upon experimental conditions such as pH. Therefore the characterization of NO release becomes more significant compared with the autoxidation which is independent of pH. DEANO releases NO at rate constants of $k_1 = 1.4 \times 10^{-3}\ s^{-1}$ [9] and $k_1 = 1.3 \times 10^{-3}\ s^{-1}$ [10], and were much slower than ProliNO with a rate constant of $k_1 = 0.265\ s^{-1}$. ProliNO release NO and NO autoxidation were studied [8, 11] but NO release rate constants were not reported.

In principle, 2 mol of NO can be released from 1 mol of the donor molecule. In reality, the stoichiometric coefficient is usually less than 2 and depends on the experimental conditions. v_{NO} of DEANO was determined to be 1.0 [9] but varies from 1.5 [10] to 2.0 [9]. Under anaerobic conditions, v_{NO} of ProliNO was measured to be 1.94 [11], which is very different from v_{NO} of 0.78 under aerobic conditions. From the analytical solution, it can be found that the NO concentration depends on v_{NO} in a complex way. Therefore v_{NO} can be determined from a fit of the simulated curve to the experimental data.

NO donors decompose at physiological pH and continuously release NO to allow studying of the effect of NO on biological systems even in long-term experiments. Therefore, the prediction of NO concentration evolution in such systems becomes very important. Schmidt et al. [9] developed a numerical model for NO decomposition and autoxidation in aqueous solution and also presented a graphical plot of NO concentration evolution, which was used to estimate the actual NO concentration. The analytical solution provides an improved way to forecast NO concentration produced from NO donors under aerobic conditions. Thus, it may contribute to elucidation of hypoxic vasodilation: the CBF increases to maintain the constant cerebral metabolic rate of O_2 when $[O_2]$ decreases [15].

4 Conclusions

We have derived an analytical solution for NO donor decomposition in aerobic solutions. This solution was used to characterize the decomposition rate constant of NO donors and the stoichiometric coefficient of NO release, and the reaction rate constant of NO autoxidation. NO donors can be used as continuous NO sources in biochemical systems and the analytical solution can be used to predict the actual NO concentration in such systems. In general, characterization of the kinetics of NO autoxidation enhances one's fundamental understanding of how nitric oxide can serve in many physiological processes. Furthermore, this mathematical model provides a simple way to study the variation of v_{NO}, clearly reported in the literature, with such parameters as $[O_2]$. This variation is important to characterize if one is to use NONOates to generate NO in biological system with different $[O_2]$.

Acknowledgments I thank Professor Michael Wilson (University of Essex) for helpful discussion and help with manuscript preparation and Professor Peter Nicholls (University of Essex) for the experimental data.

References

1. Gladwin MT, Kim-Shapiro DB (2008) The functional nitrite reductase activity of the hemeglobins. Blood 112:2636–2647
2. Banaji M, Mallet A, Elwell CE et al (2008) A model of brain circulation and metabolism: NIRS signal changes during physiological challenges. PLoS Comput Biol 4(11):e1000212. doi:10.1371/journal.pcbi.1000212, BRAINSIGNALS: an open source modelling environment http://www.medphys.ucl.ac.uk/braincirc/download/repos/NIRSmodel.html
3. Rong Z, Cooper C (2013) Modelling hemoglobin nitrite reductase activity as a mechanism of hypoxic vasodilation? Adv Exp Med Bio 789:361–368
4. Rong Z, Banaji M, Moroz T, Cooper CE (2013) Can mitochondrial cytochrome oxidase mediate hypoxic vasodilation via nitric oxide metabolism? Adv Exp Med Bio 765:231–238
5. Rong Z, Cooper C (2016) Hemoglobin effects on nitric oxide mediated hypoxic vasodilation. Adv Exp Med Bio 876:121–127

6. Brown M, Wade J, Marshall J (1985) Fundamental importance of arterial oxygen content in the regulation of cerebral blood flow in man. Brain 108:81–93
7. Ford PC, Wink DA, Stanbury DM (1993) Autoxidation kinetics of aqueous nitric oxide. FEBS Lett 326:1–3
8. Möller MN, Li Q, Vitturi DA et al (2007) Membrane "Lens" effect: focusing the formation of reactive nitrogen oxide from the NO/O_2 reaction. Chem Res Toxicol 20:709–714
9. Schmidt K, Desch W, Klatt P et al (1997) Release of nitric oxide from donors with known half life: a mathematical model for calculating nitric oxide concentrations in aerobic solutions. Naunyn-Schmiedeberg's Arch Pharmacol 355:457–462
10. Griveau S, Dumézy C, Goldner P et al (2007) Electrochemical analysis of the kinetics of nitric oxide release from two diazeniumdiolates in buffered aqueous solution. Electrochem Comm 9:2551–2556
11. Silkstone RS, Mason MG, Nicholls P, Cooper CE (2012) Nitrogen dioxide oxidizes mitochondrial cytochrome *c*. Free Rad Bio Med 52:80–87
12. Pogrebnaya VL, Usov AP, Baranov AV et al (1995) Oxidation of nitric oxide by oxygen in the liquid phase. J Appl Chem USSR 48:1004–1007
13. Wink DA, Darbyshire JF, Nims RW et al (1993) Reactions of the bioregulatory agent nitric oxide in oxygenated aqueous media: determination of the kinetics for oxidation and nitrosation by intermediates generated in the NO/O_2 reaction. Chem Res Toxicol 6(1):23–27
14. Goldstein S, Czapski G (1995) Kinetics of nitric oxide autoxidation in aqueous solution in the absence and presence of various reductants. The nature of the intermediates. J Am Chem Soc 117:12078–12084
15. Wehrli FW, Rodgers ZB, Jain V et al (2014) Acad Radiol 21:207–214

Erratum to: The Effects of Passive Cycling Exercise for 20 min on Cardiorespiratory Dynamics in Healthy Men

Sayuri Fuse, Ryotaro Kime, Takuya Osada, Norio Murase, and Toshihito Katsumura

Erratum to:
Chapter 35 in: Q. Luo et al. (eds.), *Oxygen Transport to Tissue XXXVIII*, Advances in Experimental Medicine and Biology 923, DOI 10.1007/978-3-319-38810-6_35

In the original version of this chapter, the title was incorrect. The title should read "The Effects of Passive Cycling Exercise for 20 min on Cardiorespiratory Dynamics in Healthy Men". The title is corrected through this erratum.

The updated original online version for this chapter can be found at http://dx.doi.org/10.1007/978-3-319-38810-6_35

© Springer International Publishing Switzerland 2016

Q. Luo et al. (eds.), *Oxygen Transport to Tissue XXXVIII*, Advances in Experimental Medicine and Biology 923, DOI 10.1007/978-3-319-38810-6_58

Errata to: Oxygen Transport to Tissue XXXVIII

Qingming Luo, Lin Z. Li, David K. Harrison, Hua Shi, and Duane F. Bruley

Errata to:
Q. Luo et al. (eds.), *Oxygen Transport to Tissue XXXVIII*, Advances in Experimental Medicine and Biology 923, DOI 10.1007/978-3-319-38810-6

Chapters 24, 26 and 33 were originally published © Springer International Publishing Switzerland, but have now been made available © The Author(s) under a CC BY 4.0 license.

The updated online versions of these chapters can be found at
http://dx.doi.org/10.1007/978-3-319-38810-6_24
http://dx.doi.org/10.1007/978-3-319-38810-6_26
http://dx.doi.org/10.1007/978-3-319-38810-6_33
http://dx.doi.org/10.1007/978-3-319-38810-6

© Springer International Publishing Switzerland 2017

Q. Luo et al. (eds.), *Oxygen Transport to Tissue XXXVIII*, Advances in Experimental Medicine and Biology 923, DOI 10.1007/978-3-319-38810-6_59

Index

© Springer International Publishing Switzerland 2016

Q. Luo et al. (eds.), *Oxygen Transport to Tissue XXXVIII*, Advances in Experimental Medicine and Biology 923, DOI 10.1007/978-3-319-38810-6